Manual of Head and Neck Imaging

Prashant Raghavan
Sugoto Mukherjee
Mark Jameson
Max Wintermark

Springer

Manual of Head and Neck Imaging

Prashant Raghavan • Sugoto Mukherjee
Mark J. Jameson • Max Wintermark

Manual of Head and Neck Imaging

Springer

Prashant Raghavan, MD
Division of Neuroradiology
Department of Diagnostic Radiology
and Nuclear Medicine
University of Maryland School
of Medicine
Baltimore, MD
USA

Sugoto Mukherjee, MD
Division of Neuroradiology
Department of Radiology
and Medical Imaging
University of Virginia Health System
Charlottesville, VA
USA

Mark J. Jameson, MD, PhD, FACS
Division of Head and Neck Surgical
Oncology
Department of Otolaryngology – Head
and Neck Surgery
University of Virginia Health System
Charlottesville, VA
USA

Max Wintermark, MD
Department of Radiology
and Medical Imaging
University of Virginia Health System
Charlottesville, VA
USA

ISBN 978-3-642-40376-7 ISBN 978-3-642-40377-4 (eBook)
DOI 10.1007/978-3-642-40377-4
Springer Heidelberg New York Dordrecht London

Library of Congress Control Number: 2013955233

Foreword

Despite the technical challenges and expertise necessary to be a skillful head and neck radiologist, most in the discipline of neuroradiology have historically focused upon the central nervous system and not the head and neck, an anatomic region whose composition is both fascinating and complicated. Additionally, as the specialty of otolaryngology–head and neck surgery continues to mature, the requirement for both radiologist and surgeon to be adept at recognizing the best scan to order as well as interpreting them becomes increasingly important. The authors of this book represent expertise not only in this radiologic subspecialty but also in all aspects of otolaryngology–head and neck surgery, sharing with the reader their knowledge in conjunction with high quality, up-to-date radiologic examples of the pathology to create a guide for both the inexperienced as well as the skillful practitioner in both fields as well as their trainees.

Paul A. Levine, MD, FACS
Department of Otolaryngology – Head and Neck Surgery
University of Virginia Health System
Charlottesville, VA, USA

Preface

There are several outstanding reference books on the incredibly complex topic that is head and neck imaging. Of these, the most authoritative and popular are perhaps *Head and Neck Imaging* by Drs. Som and Curtin and *Diagnostic Imaging: Head and Neck* by Drs. Harnsberger, Hudgins, Wiggins and Davidson. These are considered essential reading for any serious student of the subject, and we recommend them too.

Ours is a concise book, written with the intention of serving as an introductory text. It is written with the hope that residents and fellows, both in radiology and otolaryngology, can easily consume it, perhaps during the course of a rotation. The material contained in it is the basics of what one must know about cross-sectional head and neck imaging. Practical anatomical concepts and the imaging findings in the more common disease entities are emphasized. Also included, in each chapter, is a brief section written by a surgeon to provide a clinical perspective. Each chapter also has suggestions for further reading. As with any book of this size, we run the risk of excluding certain entities.

We would like to thank our teachers – those who we have had the fortune to know personally and also those that have influenced us through their books and lectures. Of the former, we are most grateful to Dr. C. Douglas Phillips, MD, FACR, Professor of Radiology and Director of Head and Neck Imaging at the Weill Cornell Medical Center, New York-Presbyterian Hospital, and Dr. Paul Levine MD FACS, Robert W. Cantrell Professor and Chairman, Department of Otolaryngology – Head and Neck Surgery, University of Virginia Health System. Behind every image in this book is a patient – to every one of them, we are grateful. We are also thankful to Philip J. Cohen for his assistance with the artwork. To our families, who have stood by us throughout this sometimes taxing, but always rewarding, endeavor, we owe everything.

Baltimore, MD — Prashant Raghavan, MD
Charlottesville, VA — Sugoto Mukherjee, MD
Charlottesville, VA — Mark J. Jameson, MD, PhD, FACS
Charlottesville, VA — Max Wintermark, MD

Contents

Contributors

J. Jared Christophel, MD, MPH Division of Facial Plastic and Reconstructive Surgery, Department of Otolaryngology – Head and Neck Surgery, University of Virginia Health System, Charlottesville, VA, USA

David Clopton, MD Department of Radiology and Medical Imaging, University of Virginia Health System, Charlottesville, VA, USA

Matthew A. Hubbard, MD Department of Otolaryngology – Head and Neck Surgery, University of Virginia Health System, Charlottesville, VA, USA

Mark J. Jameson, MD, PhD, FACS Division of Head and Neck Surgical Oncology, Department of Otolaryngology – Head and Neck Surgery, University of Virginia Health System, Charlottesville, VA, USA

Bradley W. Kesser, MD Division of Otology and Neurotology, Department of Otolaryngology – Head and Neck Surgery, University of Virginia Health System, Charlottesville, VA, USA

Rachita Khot, MD Division of Body Imaging, Department of Radiology and Medical Imaging, University of Virginia Health System, Charlottesville, VA, USA

Sugoto Mukherjee, MD Division of Neuroradiology, Department of Radiology and Medical Imaging, University of Virginia Health System, Charlottesville, VA, USA

Thomas J.E. Muttikal, MD Department of Radiology and Medical Imaging, University of Virginia Health System, Charlottesville, VA, USA

Steven A. Newman, MD Department of Ophthalmology, University of Virginia Health System, Charlottesville, VA, USA

Prashant Raghavan, MD Division of Neuroradiology, Department of Diagnostic Radiology and Nuclear Medicine, University of Maryland School of Medicine, Baltimore, MD, USA

David C. Shonka Jr., MD Division of Head and Neck Surgical Oncology, Department of Otolaryngology – Head and Neck Surgery, University of Virginia Health System, Charlottesville, VA, USA

Max Wintermark, MD Department of Radiology and Medical Imaging, University of Virginia Health System, Charlottesville, VA, USA

Brian M. Trotta, MD Coastal Radiology Associates, PLLC, New Bern, NC, USA

Christopher R. Durst, MD Clinical Instructor, Department of Radiology and Medical Imaging, Division of Neuroradiology, Charlottesville, VA, USA

Spaces of the Neck

1

Christopher R. Durst, Mark J. Jameson, Max Wintermark, Prashant Raghavan, and Sugoto Mukherjee

1.1 Introduction

This chapter describes an anatomic approach to pathology of the neck. A solid understanding of the anatomic boundaries of the spaces of the neck allows one to elucidate a focused differential diagnosis and evaluate for specific invasion or extension; these insights help the surgeon determine optimal operative management. This chapter will focus on the parapharyngeal, masticator, carotid, and posterior spaces. The parotid, submandibular/sublingual, and pharyngeal mucosal spaces are discussed in detail in other chapters.

Accurate interpretation of head and neck imaging requires an understanding of fascial layers, which cannot be precisely delineated with imaging; in practice, key anatomic landmarks define these fascial layers. The superficial cervical fascia (SCF) envelops fat, loose connective tissue, the platysma, and the external jugular veins. The deep cervical fascia (DCF) is further divided into superficial (SLDCF), middle (MLDCF), and deep (DLDCF) layers that form the boundaries of the spaces of the suprahyoid neck described in detail below.

1.2 Imaging Evaluation

Conventional radiography has largely been replaced by cross-sectional imaging in the evaluation of the soft tissues of the neck.

In the appropriate setting, ultrasound is a valuable tool in evaluation of the neck. Superficial lesions can typically be adequately imaged and described in the hands of an experienced sonographer. Ultrasound provides the added benefit of providing real-time image guidance for biopsy or drainage. However, ultrasound is inadequate in the evaluation of the deeper spaces of the neck.

CT is the mainstay of evaluation of neck lesions. Intravenous contrast is recommended, as lesions often cannot be delineated from adjacent normal tissues without

P. Raghavan et al., *Manual of Head and Neck Imaging*,
DOI 10.1007/978-3-642-40377-4_1, © Springer-Verlag Berlin Heidelberg 2014

it. Dental amalgam can sometimes present a challenge in evaluation of masses in the pharyngeal mucosal, sublingual, submandibular, and masticator spaces; this can often be overcome by angling the gantry at 15–25° (so-called butterfly cuts) and reimaging through the oral cavity.

MRI is a very useful tool for evaluating head and neck masses. When used with a dedicated neck coil, the deep and superficial structures of the neck can be clearly identified. Intravenous contrast is recommended to help characterize masses and enable accurate detection of tumor spread. When evaluating for spread of malignancy, it is vital to obtain precontrast T1-weighted images without fat suppression. The bright signal intensity of fat on this sequence provides a useful background against which the soft tissue intensity of tumor can be detected. The addition of fat suppression to post-contrast sequences facilitates better delineation of the enhancing tumor margins. The main disadvantages of neck MRI are the artifacts produced by dental hardware or amalgam and the length of time the patient may have to remain in the scanner (often 30–60 min), which frequently results in motion artifact.

1.2.1 Parapharyngeal Space

1.2.1.1 Anatomy

In clinical otolaryngology, the term "parapharyngeal space" has been used inclusively to refer to what is described above as the PPS and the carotid space. In this nomenclature scheme, the two distinct compartments were identified as the prestyloid and poststyloid compartments, respectively. For the purposes of consistency in this discussion, the terms PPS (prestyloid compartment) and carotid space (poststyloid compartment) will be used.

The parapharyngeal space (PPS) can be thought of as an inverted pyramid extending from the inferior surface of the petrous bone to the lesser horn of the hyoid bone. Its central location in the deep spaces of the suprahyoid neck results in a complex fascial anatomy (Fig. 1.1). The PPS extends medially to the aerodigestive tract; the visceral fascia is its medial border. The visceral fascia (deepest layer of MLDCF) adheres to the visceral structures of the neck, including the pharynx, larynx, esophagus, trachea, thyroid gland, and parathyroid glands. Anteriorly and laterally, the PPS abuts the masticator and parotid spaces, respectively. The SLDCF splits to envelop these spaces. As such, the anterior and lateral walls of the parapharyngeal space are leaflets of the SLDCF. The DLDCF of the carotid space and that of the lateral margin of the retropharyngeal space demarcate the posterior margin of the PPS. Some texts indicate that there is no fascial separation between the PPS and the submandibular space, allowing direct spread of infection or tumor between the two spaces.

The PPS is predominantly comprised of fat, making it readily identifiable on CT and MRI (Fig. 1.1). Also present are small branches of the mandibular division of

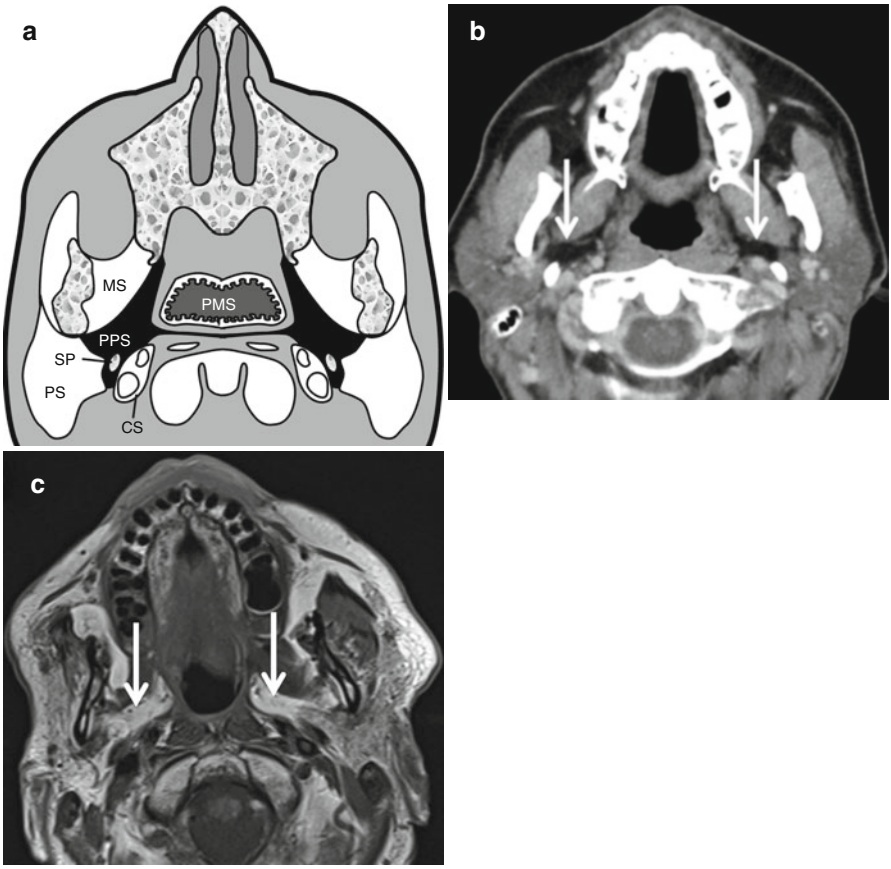

Fig. 1.1 Neck spaces. Axial graphic (**a**), CT (**b**), and T1-weighted MR (**c**) images show the normal anatomy of the parapharyngeal space (*PPS*). This space predominantly contains fat and can be easily identified (*arrows* in **b** and **c**) on both CT (hypodense on CT) and MR (bright on T1-weighted sequences) images. The central location of this space is the reason for its displacement in lesions arising from the adjacent masticator space (*MS*), parotid space (*PS*), carotid space (*CS*), and the pharyngeal mucosal space (*PMS*). The styloid process (*SP*) is along the posterior aspect of the parapharyngeal space. Note that, infrequently, lesions can arise primarily from within the parapharyngeal space and can be completely surrounded by adjacent fat

the trigeminal nerve (V3), the ascending pharyngeal artery, the internal maxillary artery, lymph nodes, and minor salivary rests (Box 1.1).

When a mass arises in an adjacent space, the fat in the parapharyngeal space can become deformed and displaced. Observation of the direction in which the mass displaces the parapharyngeal fat can help determine the origin of the mass (Fig. 1.2). Box 1.2 summarizes the expected effect of adjacent masses on the parapharyngeal space.

1.2.1.2 Pathology

Primary masses of the PPS are rare. More commonly, tumors arise from the deep lobe of the parotid gland or from an adjacent space and extend into the PPS. The most common masses involving the parapharyngeal and the adjacent spaces are listed in Box 1.1.

Of the primary PPS neoplasms, benign tumors account for 80 %. The most common is a pleomorphic adenoma (benign mixed tumor) arising from a minor salivary

Box 1.1. Spaces of the Neck: Contents and Lesions

Space	Contents	Lesions
Parapharyngeal space	Fat	Benign mixed tumors – either from ectopic rests in parapharyngeal space or from deep lobe of the parotid
	Ectopic rests of salivary glands	Lipoma
	Branches of mandibular division of trigeminal nerve	Schwannomas
	Internal maxillary artery	Cellulitis/abscess
	Ascending pharyngeal artery	
	Pharyngeal venous plexus	
[a]Masticator space	Internal maxillary artery and its branches	Odontogenic abscess
	Mandibular nerve and its branches	Sarcomas
	Ramus/body of mandible	Neurogenic tumors
	Muscles of mastication	Vascular malformations
		Perineural spread of carcinomas
		Secondary involvement from jaw, skull base, and pharyngeal mucosal space lesions
Carotid space	Internal carotid artery	Internal carotid artery aneurysm/ dissection
	Internal jugular vein	Internal jugular vein thrombosis
	Cranial nerves IX–XII	Schwannomas/neurofibromas of the cranial nerves IX–XII and sympathetic chain
	Cervical sympathetic chain	Paragangliomas – carotid body tumors, glomus vagale
	Glomus bodies	Inferior extension of lesions from jugular foramen (schwannomas/neurofibromas/ meningiomas/glomus jugulare)
	Jugular chain nodes	Metastatic adenopathy
[a]Parotid space	Parotid gland	Salivary gland tumors
	Intraparotid lymph nodes	Metastatic tumors
	Facial nerve and branches	Lymphomas
	Internal carotid artery	Perineural extension through facial nerve
	Retromandibular vein	Cystic lesions

Space	Contents	Lesions
[a]Pharyngeal mucosal space	Squamous epithelial mucosa	Squamous cell cancers incl. nasopharyngeal carcinomas
	Lymphoid and tonsillar tissue	Lymphomas
	Minor salivary glands	Minor salivary gland tumors
[a]Visceral space	Larynx and hypopharynx	Squamous cell cancers
	Thyroid and parathyroid	Thyroid and parathyroid tumors
	Esophagus	Vascular malformations
		Thyroglossal and branchial cysts
		Benign mesenchymal and neurogenic tumors
		Dermoids/epidermoids
Retropharyngeal space	Fat	Metastatic adenopathy
	Medial and lateral retropharyngeal nodes	Lymphoma
Perivertebral space	Prevertebral/paravertebral muscles	Abscess/osteomyelitis
	Cervical vertebra	Osseous metastasis
	Phrenic and cervical nerves	Schwannomas/neurofibromas

[a]These spaces have been discussed in details in chapters elsewhere in the book

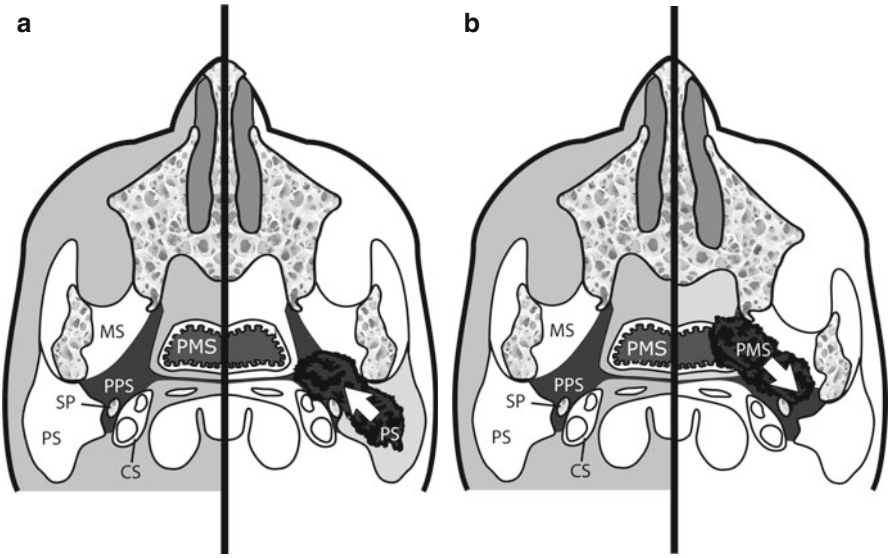

Fig. 1.2 Displacement of fat in the parapharyngeal space (PPS) by lesions in adjacent spaces which are masticator space (MS), parotid space (PS), carotid space (CS), and the pharyngeal mucosal space (PMS). The styloid process (SP) is along the posterior aspect of the parapharyngeal space. These include anteromedial displacement (**a**) by a lesion arising from the deep lobe of the parotid gland from PS (such as a pleomorphic adenoma), posterolateral displacement (**b**) of the fat by a pharyngeal mucosal space (PMS) lesion (such as a nasopharyngeal carcinoma), posteromedial displacement (**c**) from a masticator space (MS) lesion, or anterior displacement (**d**) from a lesion arising from the carotid space (CS) lesion (nerve sheath tumors or paragangliomas)

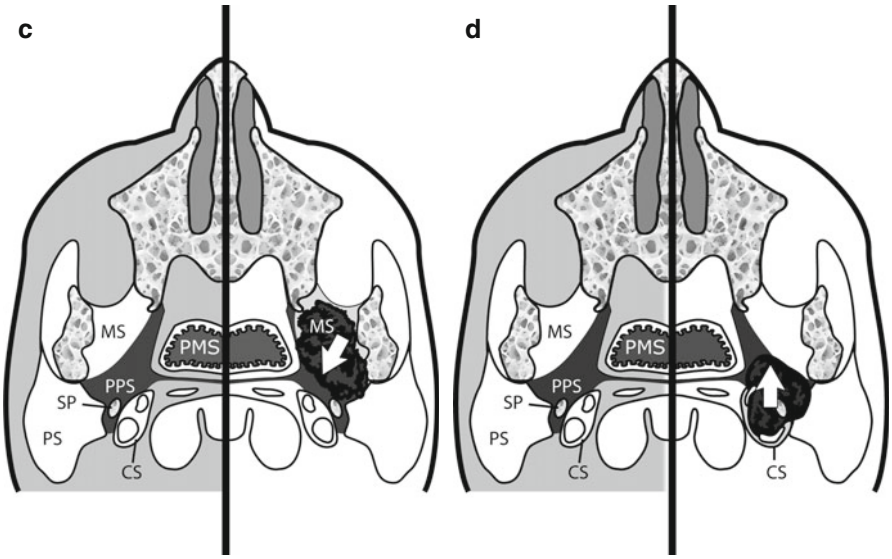

Fig. 1.2 (continued)

Box 1.2. Lesion Localization in Suprahyoid Neck

Lesion location	Displacement
Pharyngeal mucosal space	Posterolateral displacement of parapharyngeal fat Posterior displacement of styloid process
Masticator space	Posteromedial displacement of parapharyngeal fat Posterior displacement of styloid process
Carotid space	Anterior displacement of parapharyngeal fat and styloid process
Parotid space	Anteromedial displacement of parapharyngeal fat
Retropharyngeal	Anterolateral displacement of parapharyngeal fat Anterior displacement of styloid process

gland rest. As shown in Fig. 1.3, pleomorphic adenomas are typically well marginated and bright on T2 with heterogeneous enhancement. It is important to distinguish a pleomorphic adenoma arising from a minor salivary gland rest in the PPS from those arising from the deep lobe of parotid gland as this has significant surgical implications: masses centered in the PPS should be fully encompassed by PPS fat. The presence of small branches from V3 gives rise to neurogenic tumors (schwannomas and neurofibromas), which tend to be well defined, but are typically less bright on T2 than pleomorphic adenomas; they may, however, be indistinguishable. This distinction is not vital, as long as the radiologist is confidently able to place the mass in the PPS. Lipomas are rare encapsulated fatty tumors that follow

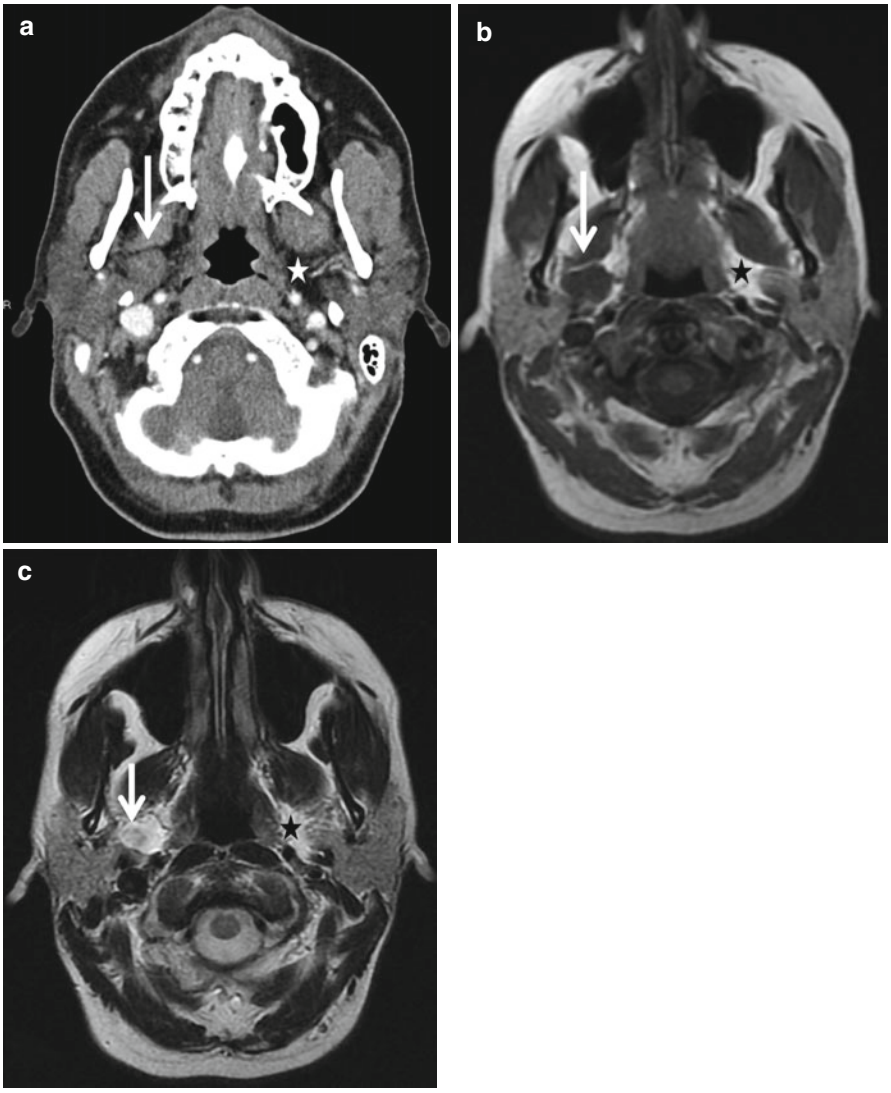

Fig. 1.3 Pleomorphic adenoma. Axial CT (**a**) and T1- and T2-weighted MR images (**b** and **c**) display a well-circumscribed lesion centered within the right parapharyngeal space (*white arrow*). Note the thin rim of fat surrounding the lesion. The contralateral normal left parapharyngeal space demonstrates normal fat (*star*). Fat appears hypodense on CT (with negative Hounsfield Units) and is hyperintense on both T1 and T2 sequences. Pleomorphic adenomas usually appear hyperintense on T2-weighted sequences, as seen on image (**c**)

fat signal and density on all MR sequences and CT, respectively. Malignant neoplasms, such as adenoid cystic carcinoma and mucoepidermoid carcinoma are uncommon. As in other spaces, malignant neoplasms are infiltrative and demonstrate avid, though not always uniform, enhancement.

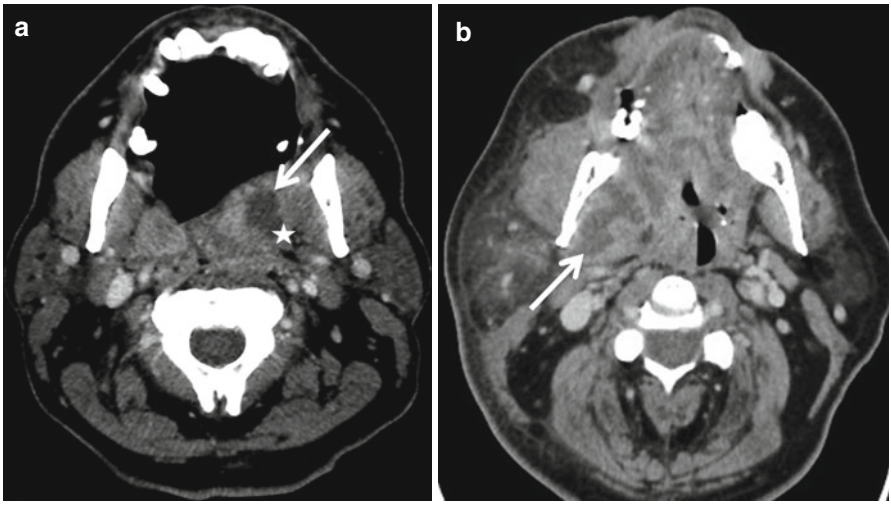

Fig. 1.4 Peritonsillar abscess. Axial contrast-enhanced CT shows low-density irregular left peritonsillar abscess (*white arrow* in **a**) with extension in the left parapharyngeal space (*star*). The right tonsil demonstrates mildly striated enhancement, which is suggestive for inflammation. Another case (**b**) shows extension from the right masticator space (*arrows*) due to right mandibular periodontal disease

Infection of the PPS is most commonly the result of direct spread from the pharyngeal mucosal space (tonsillitis) or the masticator space (sinus or odontogenic infection) (Fig. 1.4). Additionally, infections can spread to the PPS via direct communication with the submandibular space. Early infection may show only mild fat stranding or inflammation. A thicker rim of enhancement and a central necrotic core consisting of fluid and debris can distinguish late infection with abscess formation. These patients are usually acutely ill, so clinical setting can help establish the diagnosis.

The most common congenital lesions of the PPS include the second branchial cleft cyst (BCC) and venolymphatic malformations. The second branchial sinus extends from the skin of the lateral neck to the palatine tonsil. A second BCC may occur anywhere along this tract, typically at the anterior margin of the sternomastoid near the angle of the mandible. Rarely, a second BCC may arise within the PPS. As in its more typical location at the angle of the mandible, a second BCC in the PPS should be cystic with a thin, nonenhancing rim (Fig. 1.5). Venolymphatic malformations are typically lobular, transspatial masses with cystic components. The presence of phleboliths, best depicted on CT, is specific for this entity.

1.2.2 Masticator Space

1.2.2.1 Anatomy

At the angle of the mandible, the SLDCF splits into superficial and deep leaflets to enclose the masticator space. The superficial leaflet extends superiorly to enclose the zygomatic arch and temporal fossa. The deep leaflet extends cranially to the

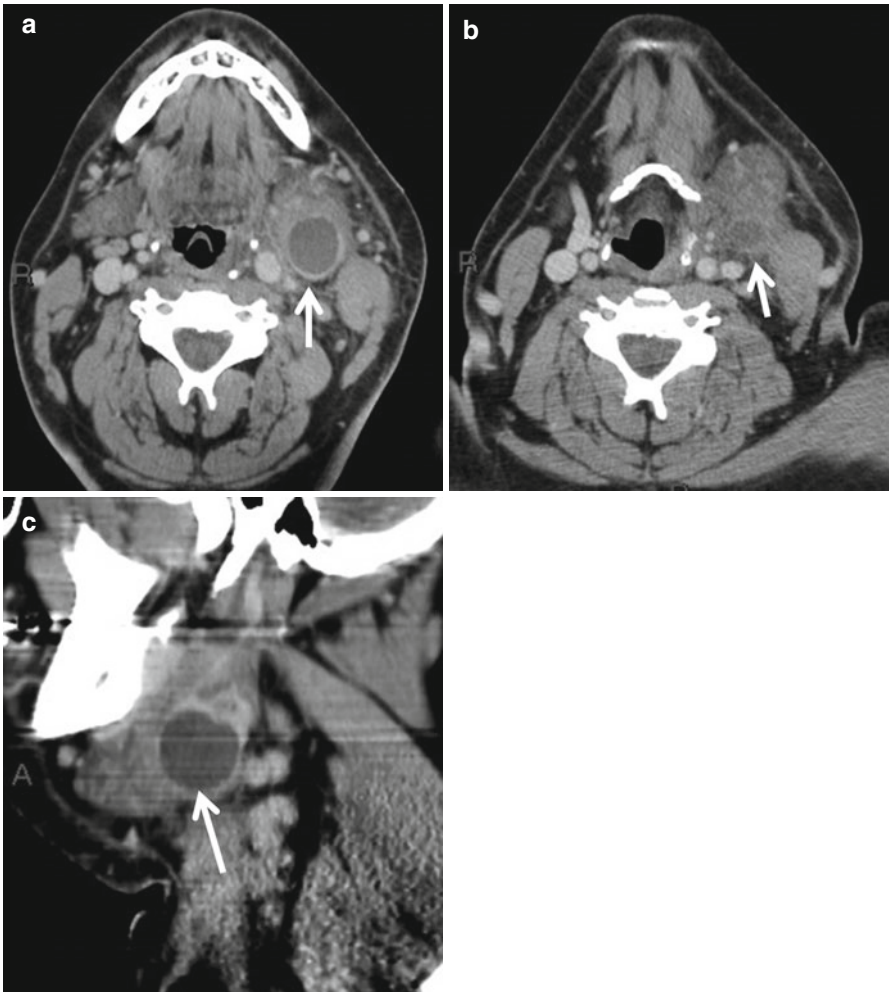

Fig. 1.5 Infected second branchial cleft cyst. Axial and sagittal contrast-enhanced CT images (**a**, **b**) show an infected second branchial cleft cyst (*arrow*) involving the left inferior parapharyngeal space. The lesion is in between the submandibular gland anteriorly, carotid sheath posteriorly, and the sternocleidomastoid laterally. The sagittal images (**c**) demonstrate the lesion at the angle of the mandible, a common location (*arrow*)

skull base from the medial pterygoid plate to the sphenoid spine, enclosing the foramen ovale within the masticator space.

The masticator space (consisting of the supra- and infrazygomatic segments) extends from the temporalis muscle insertion high on the parietal calvarium to the angle of the mandible; this is important to remember, as there is a tendency to only consider the infrazygomatic portion of the space when evaluating imaging. The mandibular ramus and posterior body, muscles of mastication, branches of V3, and inferior alveolar artery and vein are included within this space (Box 1.1).

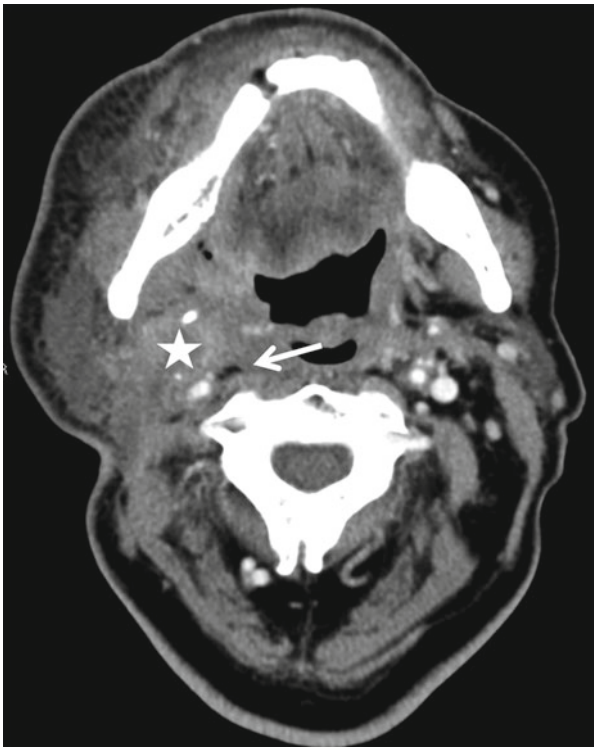

Fig. 1.6 Tumor masticator space. Recurrent tumor in the right masticator space (*star*) with involvement of the right parapharyngeal and carotid spaces. Note the minimal amount of preserved fat along the posterior aspect of the right parapharyngeal space (*arrow*)

Masses of the masticator space should be centered within the muscles of mastication or arising from the posterior body or ramus of the mandible. The mass should displace the PPS posteriorly and medially (Fig. 1.6). When there is concern for a malignant process in the masticator space, it is important to evaluate the entire course of V3 from the Meckel's cave through foramen ovale for signs of perineural spread.

1.2.2.2 Pathology

When a patient presents with trismus, the masticator space must be carefully evaluated. Trismus is especially worrisome in a patient with an oral cavity or oropharyngeal cancer and may imply invasion of the pterygoid musculature. Inflammation in the masticator space, most commonly odontogenic in origin, can also irritate the muscles of mastication and cause trismus. However, there are other considerations within the masticator space, as indicated in Box 1.1.

Odontogenic abscesses, particularly from the third molar, are the most common masses of the masticator space. As with other abscesses, CT or MR should demonstrate a thick rim of enhancement with central necrosis (Fig. 1.7). To establish the abscess as odontogenic, CT is recommended to evaluate the dentition for periapical disease and cortical disruption. Alternatively, clinical history of a recently extracted tooth can suggest the diagnosis. Documentation of the tooth or teeth of origin will

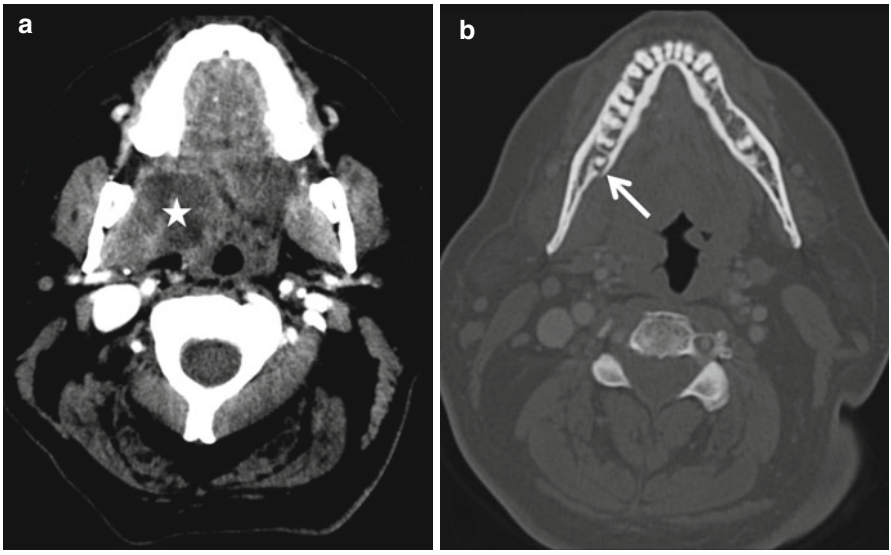

Fig. 1.7 Abscess masticator space. Rim-enhancing abscess (*star* in **a**) within the right masticator space secondary to spread from periodontal disease involving the mesial root of right mandibular molar with loss of lingual cortex (*arrow* in **b**)

help guide treatment. It is then important to evaluate the mandible for signs of osteomyelitis, including mottled bone destruction and periostitis as this may necessitate prolonged antibiotic therapy.

Benign soft tissue tumors in the masticator space include neurogenic tumors and leiomyomas. Schwannomas and neurofibromas may arise anywhere along V3; these are ovoid, enhancing masses along its course. Occasionally, they can encroach upon and expand foramen ovale or the inferior alveolar canal. They may also occur elsewhere in the space if they originate from smaller branches of the nerve. If neurogenic tumors grow adjacent to bone, smooth remodeling is noted. Leiomyomas are rare and are indistinguishable from neurogenic tumors.

Benign and malignant mandibular tumors may present as masticator space masses and will be discussed in greater detail in the chapter on Jaw imaging (Chap. 11).

Primary malignant tumors of the masticator space are rare, but rhabdomyosarcoma, leiomyosarcoma, osteosarcoma, and liposarcoma can occur. A necrotic heterogeneous masticator space mass in a young patient is likely to be a rhabdomyosarcoma. Liposarcomas, when relatively well differentiated, may contain macroscopic fat; when poorly differentiated, they resemble other sarcomas. Osteosarcoma can have a varied radiographic appearance ranging from osteolytic to mixed to osteogenic pattern of bone. New bone formation when identified, is helpful in narrowing the diagnosis (Fig. 1.8). The presence of an aggressive tumor in the masticator space warrants careful evaluation for perineural spread and for direct invasion of contiguous spaces. Tumors in the masticator space may gain access to the middle cranial fossa through the foramen ovale.

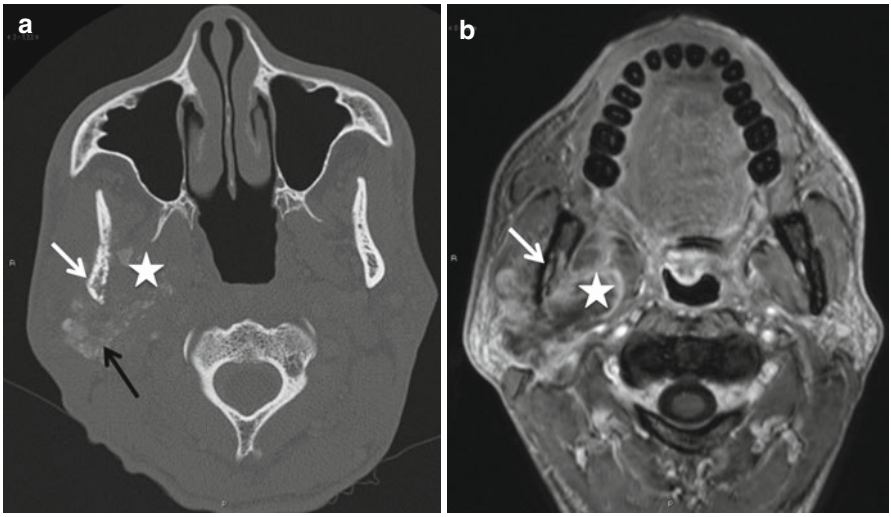

Fig. 1.8 Mandibular osteosarcoma. Axial CT (**a**) and post-contrast MR (**b**) show a heterogeneous aggressive tumor within the right masticator space arising from the right mandible (*white arrow*). Note the large soft tissue component of the tumor completely effacing the right parapharyngeal space along with new bone formation on the CT (*black arrow* in **a**) (*white star* in **a** and **b**)

Other lesions of the masticator space include venolymphatic malformations, which tend to be lobular and transspatial with scattered cystic spaces. Specific to the masticator space is benign hypertrophy of the muscles of mastication caused by bruxism. Typically, this is bilateral but can be unilateral; there should be no unusual enhancement or asymmetric edema.

1.2.3 Carotid Space

1.2.3.1 Anatomy

The fascial anatomy of the carotid space is complex, including layers from the SLDCF, MLDCF, and DLDCF. Grossly, the SLDCF forms the lateral wall, the DLDCF forms the posterior wall, the MLDCF forms the anterior wall, and the medial wall is comprised of either or both of the MLDCF and DLDCF. Below the level of the carotid bulb, the fascia completely encloses the carotid space. Above the bifurcation, however, there are areas of dehiscence of the fascia, providing a means for direct extension of an infiltrating mass into or out of the carotid space.

The carotid space begins at the skull base and extends throughout the entire length of the neck to the aortic arch. At the skull base, the fascial envelope encloses the carotid canal, jugular foramen, and hypoglossal canal. Within this space are the common and internal carotid arteries, internal jugular vein (IJV), cranial nerves IX through XII, the sympathetic plexus, and numerous lymph nodes (Box 1.1). Below

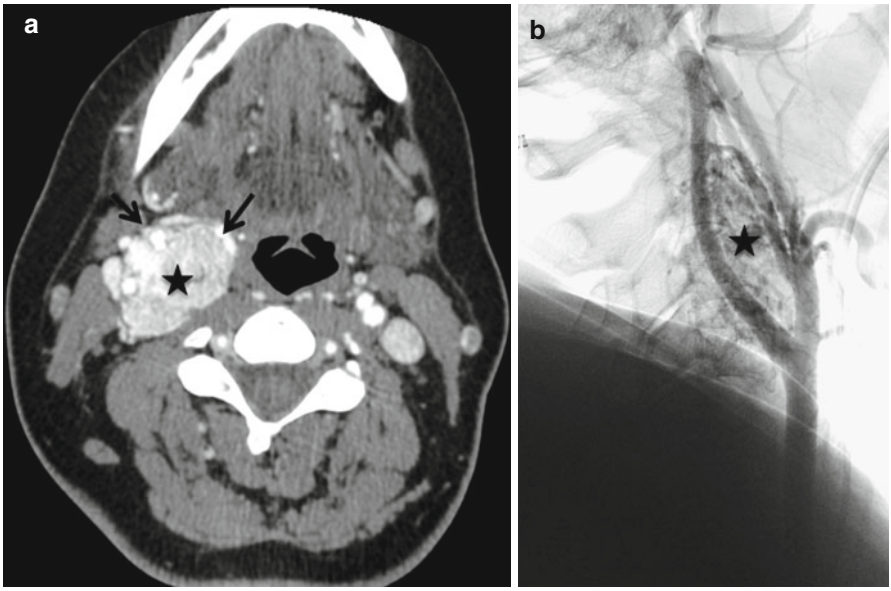

Fig. 1.9 Carotid body tumor. Axial CT (**a**) and catheter angiogram (**b**) demonstrate the intense enhancement along with the hypervascular blush of this lesion within the right carotid space (*black star*). The lesion splays the carotid vessels (*small arrows*) and completely effaces the right parapharyngeal fat which is displaced anteriorly

the level of the hyoid, only the vagus nerve remains with the carotid arteries and IJV within the carotid space.

Masses arising within the carotid space may displace the PPS or styloid process anteriorly and the posterior belly of the digastric muscle or parotid gland laterally (Fig. 1.9). A carotid space mass may engulf, displace, or splay the carotid arteries and IJV. Observation of the effect on the vessels can suggest a foremost diagnosis.

1.2.3.2 Pathology

The presence of the carotid artery, cranial nerves, paraganglia, and sympathetic plexus give rise to several masses unique to this space (Box 1.1). Schwannomas and paragangliomas are the most common benign tumors of the carotid space. Schwannomas may arise from any of the cranial nerves or the sympathetic plexus within the carotid space. Classically, schwannomas appear well circumscribed and enhance uniformly. However, cystic degeneration may result in a heterogeneous appearance with variable enhancement. The vagus nerve (X) traverses the carotid sheath between the common carotid artery and the IJV. Thus, a vagal schwannoma will often splay the common carotid artery and the IJV (Fig. 1.10a). The sympathetic chain courses along the posteromedial margin of the carotid vessels so sympathetic chain schwannomas displace both vessels but do not increase the distance between them (Fig. 1.10b). Paragangliomas include glomus

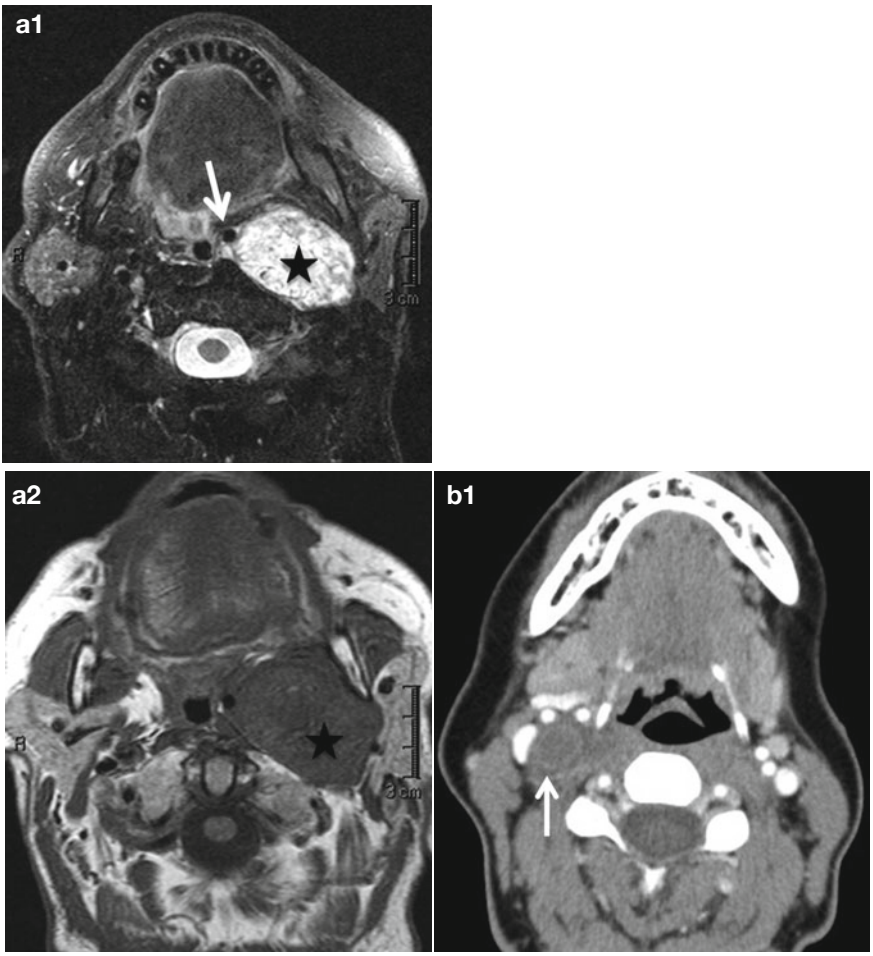

Fig. 1.10 (**a**) Vagal schwannoma. Axial T2 and T1 (**a1** and **a2**) MR images of a left carotid space vagal schwannoma, which is T2 hyperintense, with heterogeneous peripheral enhancement and central necrosis. (not shown here). The mass displaces the internal carotid artery anteromedially (*arrow* in **a**) and completely effaces the internal jugular vein. (**b**) Sympathetic trunk schwannoma. CT (**b1**) and MR images (**b2** and **b3**) of a hypodense right carotid space well-defined lesion, which is T2 hyperintense and has a tubular configuration, best appreciated on the coronal post-contrast sequences (*arrow* in **b3**). The internal and external carotid branches are displaced anteriorly, while the internal jugular vein is displaced laterally. On resection, this was a schwannoma arising from the sympathetic trunk. (**c**). Glomus vagale. Sagittal and axial post-contrast MR images (**c1** and **c2**) of a left-sided glomus vagale paraganglioma, as a heterogeneously enhancing mass in the left carotid space. This lesion extends superiorly towards the jugular foramen (*arrow* in **c2**) and shows a focal blush (*arrow* in **c4**) on the left common carotid angiogram. These lesions usually arise within 1–2 cm below the skull base. (**d**) Carotid body tumor. Intensely enhancing left carotid space mass lesion (**d1**, **d3**, **d4**, **d5**), with small flow voids (**d2**) along with the characteristic location at the carotid bifurcation, splaying the internal and external carotid branches on the MR angiogram (**d4**) and the catheter angiography (**d5**), consistent with a carotid body paraganglioma

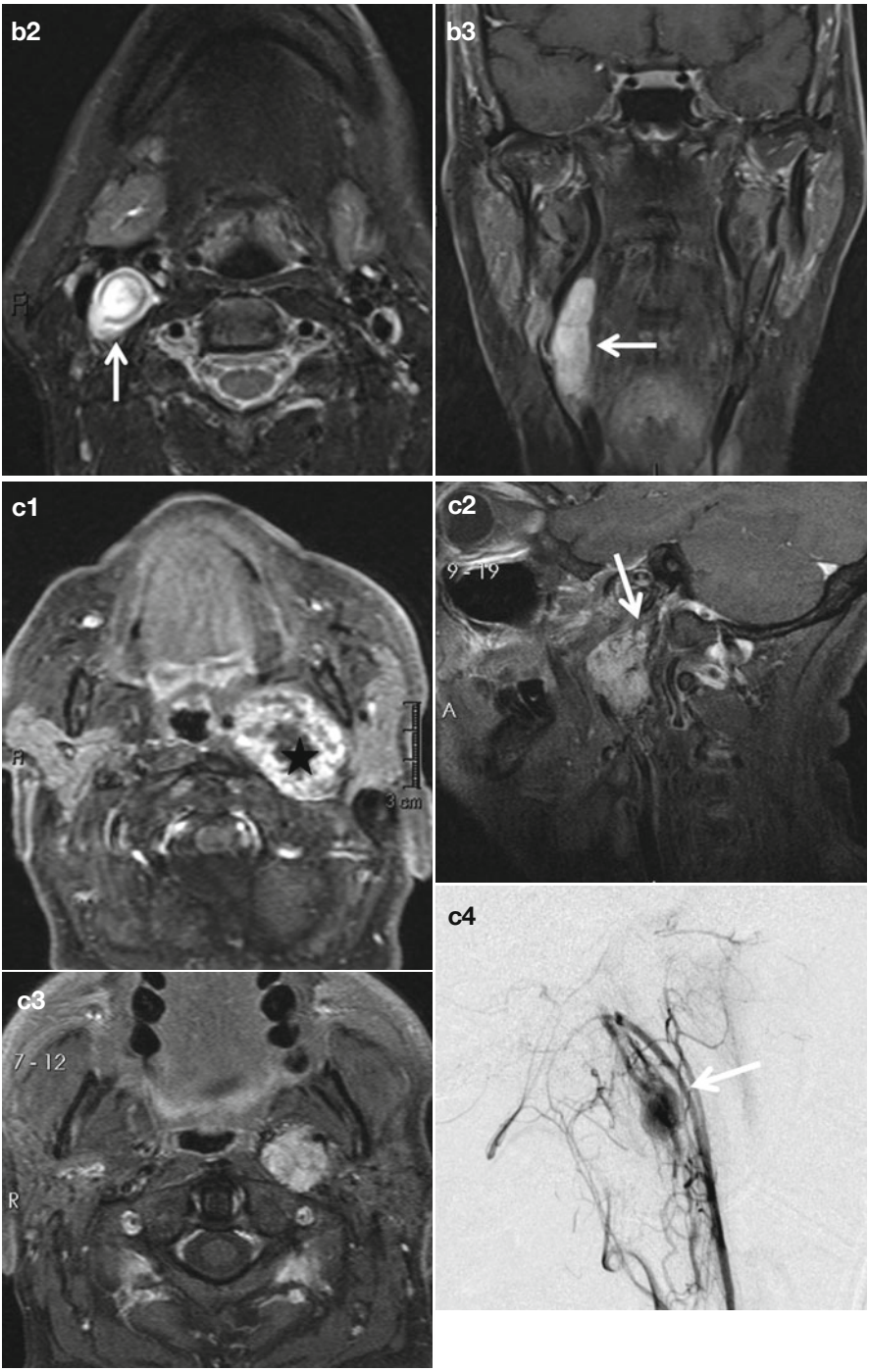

Fig. 1.10 (continued)

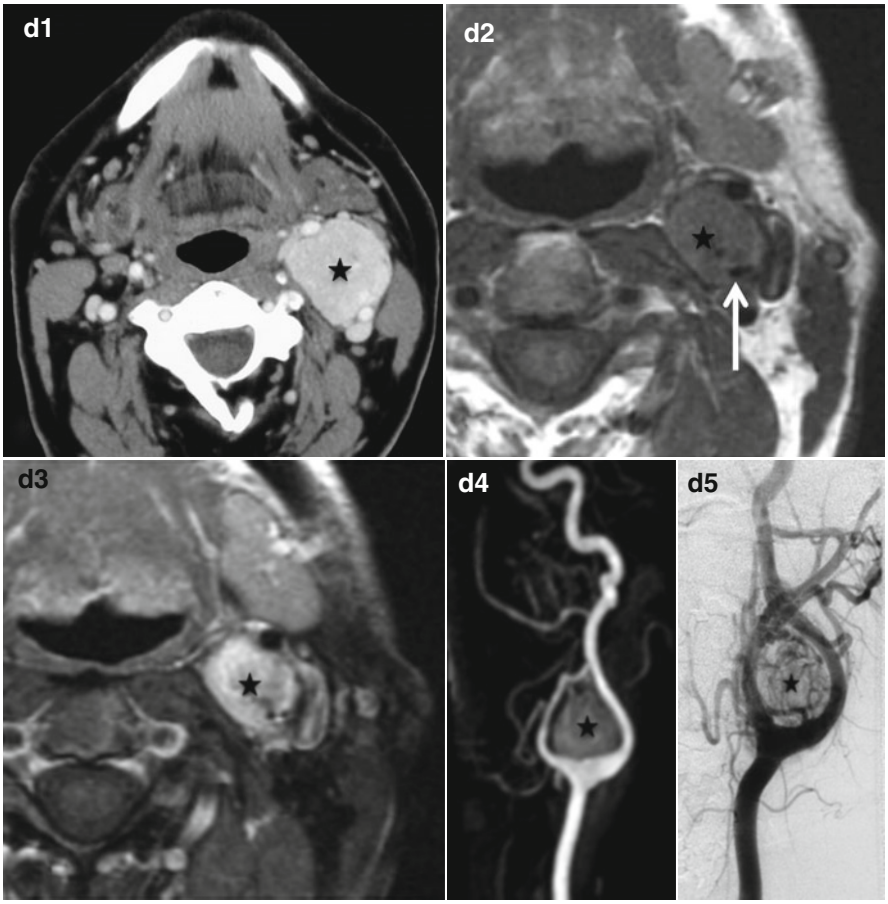

Fig. 1.10 (continued)

jugulare, glomus vagale, and carotid body tumors. On unenhanced MRI, flow voids can often be identified, giving them a salt-and-pepper appearance. However, these are not always evident, especially in smaller tumors. Upon administration of gadolinium, paragangliomas demonstrate rapid wash-in and wash-out as opposed to the more slow and steady enhancement of a schwannoma. Glomus jugulare tumors may extend through the jugular foramen, invading the jugular vein and often leading to mottled bony destruction of the foramen itself. Glomus vagale tumors typically occur several centimeters below the skull base (Fig. 1.10c). Carotid body tumors occur at the carotid bifurcation and tend to splay the internal and external carotid arteries (Fig. 1.10d). Due to their origin at the crux of the carotid bifurcation, it is important to comment on arterial involvement: tumors that are adherent to the artery, partially surround the vessel, or

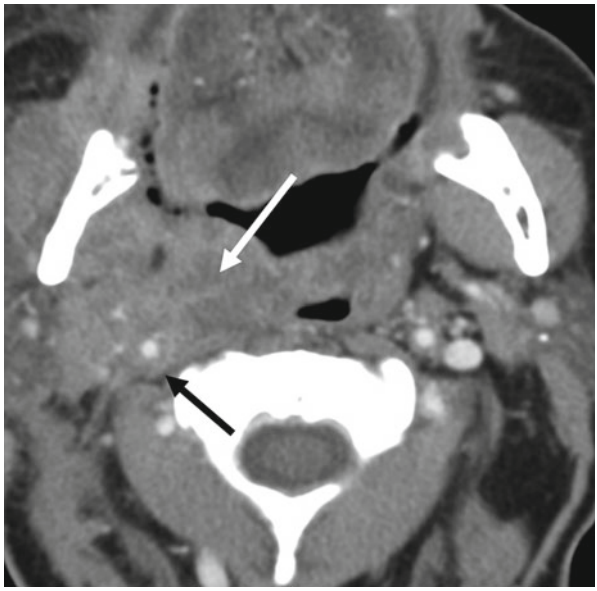

Fig. 1.11 Carotid encasement. Contrast-enhanced axial CT image in a patient with a large right tonsillar SCC (*white arrow*) that extends to the skull base and encases the right internal carotid artery (*black arrow*)

completely encase the artery put the patient at higher risk for injury to the artery and cranial nerves during resection.

Primary malignant neoplasms are particularly rare within the carotid space. However, involvement of the space from metastatic lymphadenopathy from squamous cell carcinoma or by lymphoma can occur. When evaluating lymphadenopathy, particularly with extracapsular spread, it is important to comment on the extent of involvement of the carotid artery. If less than 270° of the circumference of the artery is involved, the surgeon can generally resect the mass without sacrificing the artery (Fig. 1.11).

Commonly, "masses" of the carotid space will be vascular in etiology. Fibrofatty atherosclerotic disease of the carotid artery can be mistaken for a mass. Ectasia or fusiform or saccular aneurysmal dilation of the carotid artery may also be mistaken for a true mass. In each of these cases, the mass will typically be pulsatile and vascular imaging will demonstrate the "mass" as intraluminal, clinching the diagnosis (Fig. 1.12). IJV thrombosis may also simulate a mass (Fig. 1.13). In a patient with a recent indwelling venous line, thrombosis should be considered and US is very good for screening. However, if the thrombus propagates beyond the thoracic inlet and if knowledge of the extent will help direct treatment, CT or MRI will be necessary. Infrequently, a patient may present with tenderness over the carotid bifurcation and be diagnosed with carotidynia. Commonly, there is no associated radiographic or pathologic finding associated with the neck pain. However, CT or MR may occasionally demonstrate abnormal enhancing tissue surrounding the symptomatic carotid artery corresponding to the focus of tenderness (Fig. 1.14).

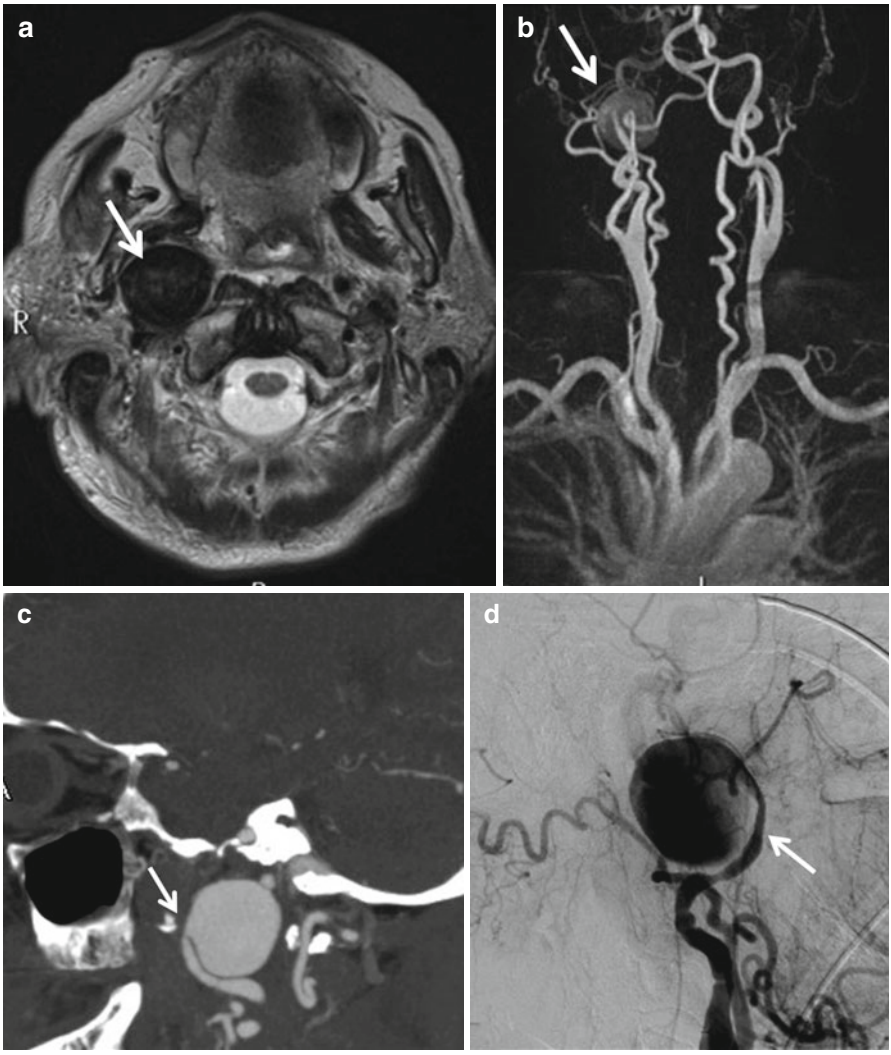

Fig. 1.12 Internal carotid artery aneurysm. Axial T2-weighted MR (**a**) shows a T2 hypointense lesion within the right carotid space, which clearly appears to arise from the right internal carotid artery (*white arrow*) on the MR angiogram of the neck (**b**), CT angiogram (**c**), and the catheter angiogram (**d**)

1.2.4 Posterior Spaces

1.2.4.1 Anatomy

The posterior spaces of the neck include the retropharyngeal space, danger space, and the perivertebral or prevertebral space. As these three spaces are in continuity and share similar fascia, anatomic boundaries, and pathologies, they will be discussed together.

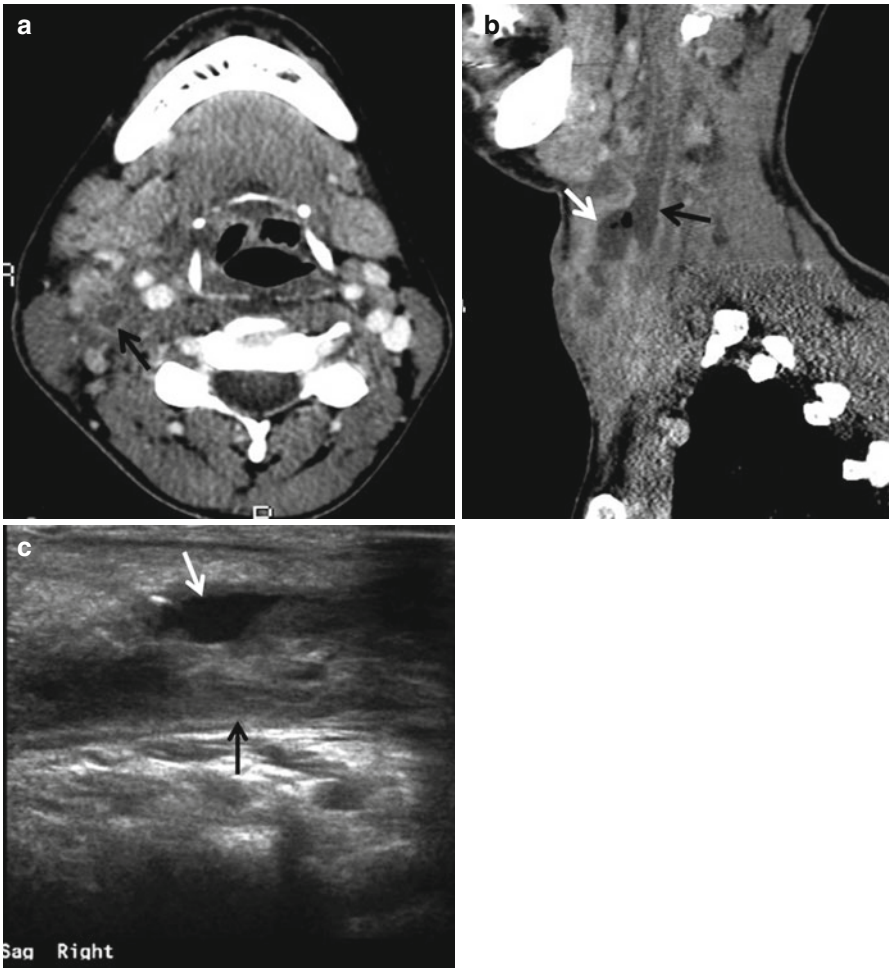

Fig. 1.13 Internal jugular vein thrombosis with abscess. Axial and sagittal CT (**a**, **b**) and sagittal USG (**c**) demonstrate thrombosed right internal jugular vein (*black arrow*) in this young patient with history of intravenous drug abuse. The patient injected the drug directly into her right internal jugular vein. Note the abscess anterior to the thrombosed vein (*white arrow* in **b** and **c**)

The most anterior of the three spaces is the retropharyngeal space, which courses along the posterior margin of the pharyngeal mucosal space and extends from the skull base to T3. The retropharyngeal space is bordered anteriorly by the visceral fascia, which is a component of the MLDCF, and posteriorly by the alar fascia, a component of the DLDCF. The danger space is a potential space that lies immediately posterior to the retropharyngeal space and is sometimes referred to as the posterior compartment of the retropharyngeal space. The danger space extends from the skull base to the diaphragm and is bordered anteriorly

Fig. 1.14 Carotidynia. Axial CT with contrast clearly demonstrates a small cuff of soft tissue (*white arrow*) surrounding the left carotid artery in this patient with pain overlying the left neck in the same location. This is a self-limited condition and resolves in a few weeks with supportive treatment

by the alar fascia and posteriorly by the prevertebral fascia, both components of the DLDCF. The perivertebral space extends from the skull base to the upper mediastinum and is completely enclosed by the prevertebral fascia, a component of the DLDCF.

The retropharyngeal space can be divided into a suprahyoid component and an infrahyoid component. The infrahyoid retropharyngeal space is made up only of fat, while the suprahyoid portion contains fat and lymph nodes (Box 1.1). The lymph nodes can be divided into medial and lateral groups. The medial nodes are located along the midline, but are not always present. The lateral nodes can be found overlying the vertebral transverse processes.

The danger space is a potential space and has no contents; it only becomes evident when invaded or edematous.

The perivertebral space was classically referred to as the prevertebral space, but more recently has been described as the perivertebral space to account for the inclusion of the paraspinal musculature and the posterior elements of the vertebral bodies. However, discussions of the perivertebral space typically refer to the prevertebral component, which is comprised of the prevertebral and scalene muscles, the vertebral artery, the brachial plexus, phrenic nerve, the vertebral body, and the intervertebral disc (Box 1.1).

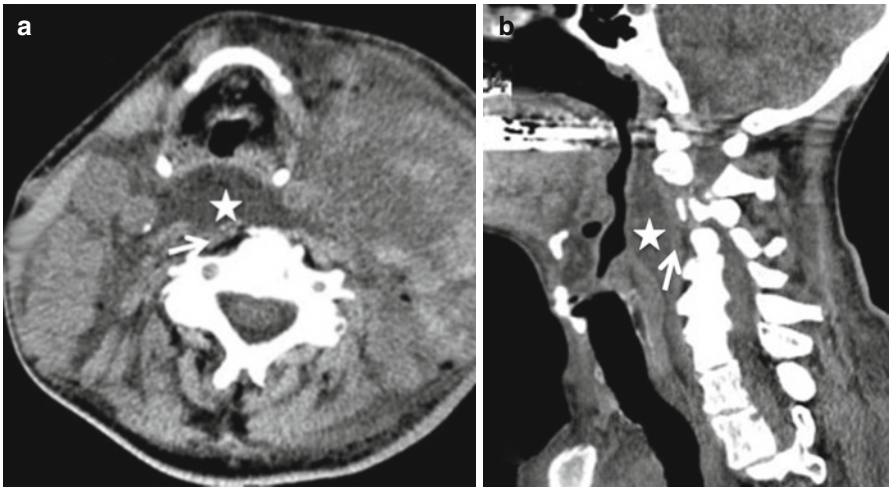

Fig. 1.15 Retropharyngeal edema. Axial and sagittal CT images (**a**, **b**) show large retropharyngeal effusion (*white star*) in this patient with bilateral pathological adenopathy status postradiation therapy. This is not an uncommon situation and retropharyngeal effusions have been described in various other infectious and inflammatory conditions. Note its location anterior to the prevertebral muscles (*small white arrows*)

Differentiating masses of the retropharyngeal space from those of the perivertebral spaces can best be accomplished by observing the effect on the prevertebral musculature. Retropharyngeal lesions arise in the potential space between the aerodigestive tract and the prevertebral muscles, so lesions in this space should displace the musculature posteriorly. The perivertebral space is a potential space between the prevertebral musculature and the anterior column of the vertebrae. Lesions in this space should displace the prevertebral musculature anteriorly. If a mass directly involves the vertebral body, it can be conclusively described as a perivertebral space lesion.

1.2.4.2 Pathology

The differential diagnosis for a mass centered in the retropharyngeal space is limited. Most commonly, visualization of the retropharyngeal space is due to the presence of edema from radiation treatment, trauma, or infection (Fig. 1.15). Discrete lesions of the retropharyngeal space are most commonly reactive or suppurative nodes resulting from pharyngitis or tonsillitis. If reactive, the nodes should appear well defined, round, and homogeneous. Suppurative nodes can appear similar but may progress to a more heterogeneous density, eventually becoming cystic. If left untreated, suppurative nodes may rupture, forming a retropharyngeal abscess (Fig. 1.16). Differentiation of an abscess from edema can often be made based on past medical history and clinical symptoms. CT will show a peripherally enhancing fluid collection, often in conjunction with tonsillitis or pharyngitis if an abscess is present.

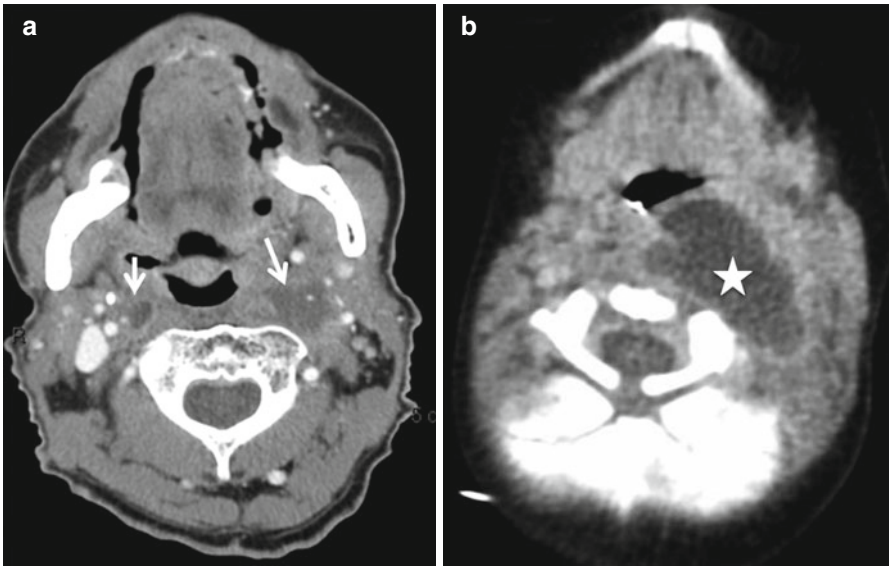

Fig. 1.16 Suppurative retropharyngeal abscess. Axial contrast-enhanced CT (**a**) in this patient shows bilateral suppurative retropharyngeal adenopathy (*white arrow* in **a**). CECT in a different patient (**b**) with shows a large retropharyngeal abscess, presumably originating from a suppurative left retropharyngeal node. The large abscess involves the left parapharyngeal space with mass effect on the airway (*white star* in **b**)

Retropharyngeal lymphadenopathy may be a sign of lymphoma or metastatic disease (Fig. 1.17). While retropharyngeal nodes are not a primary drainage pathway for head and neck cancers, they frequently become involved with recurrences after neck dissection. Initially, the lymph nodes increase in size and appear well rounded. With continued growth, they may become necrotic. Eventually, the capsule of the lymph node is disrupted, and the mass can appear very irregular.

The danger space is a potential space, only becoming evident when edema or abscess dissects between the alar fascia and the prevertebral fascia. An infection in the danger space could directly communicate with the thoracic cavity leading to mediastinitis and pericarditis, hence the name "danger space."

Masses centered in the perivertebral space most frequently arise from the vertebral bodies. Spondylosis is common. Associated anterior disc protrusions or bulges and osteophytes may cause local mass effect. Metastases to the vertebral bodies will replace the normal fatty bone marrow signal, appearing hypointense on T1 with varying levels of enhancement. As with the other posterior spaces, infection should always be considered. However, as opposed to the retropharyngeal and danger spaces where the source of infection is typically oropharyngeal, an infection in the perivertebral space is typically discogenic or vertebral in origin, though involvement of the cervical spine is much less frequent than the lumbar spine. Discitis results in loss of disc height, end plate irregularity, increased T2 signal in the disc space, and

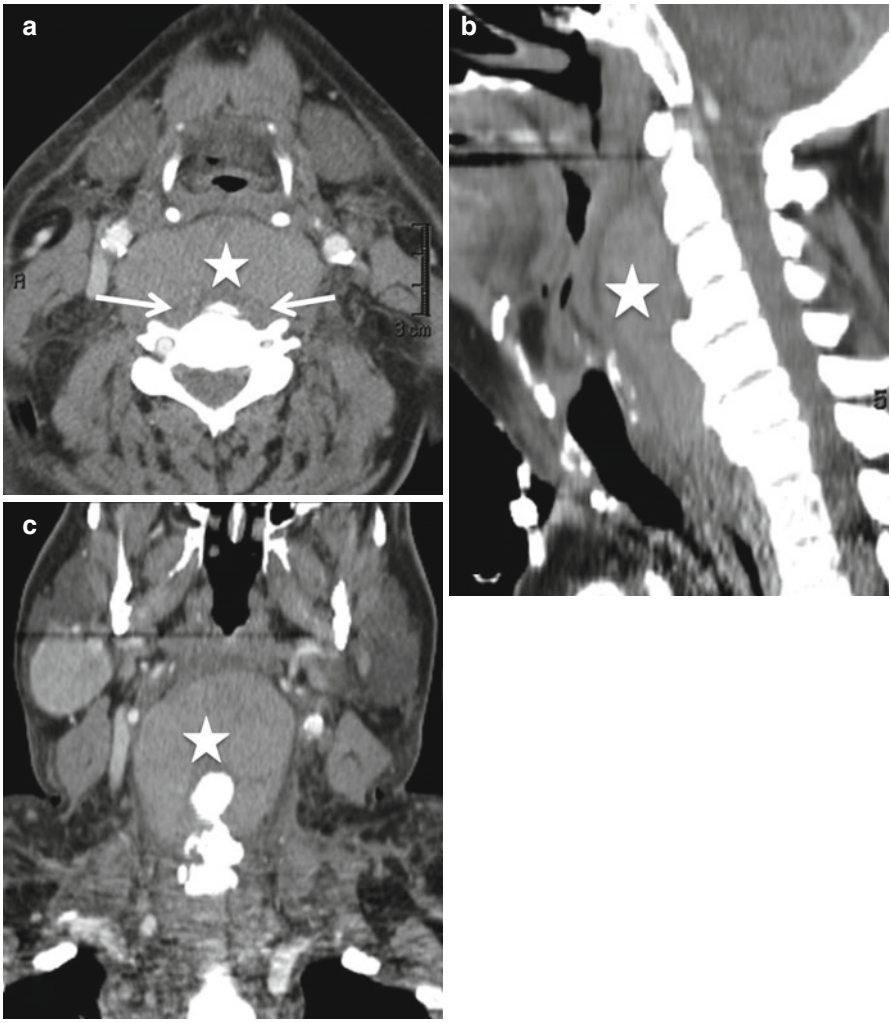

Fig. 1.17 Retropharyngeal lymphadenopathy. Bulky non-necrotic retropharyngeal lymphadenopathy (*white star*) is seen in this patient with non-Hodgkin's lymphoma on the axial, sagittal, and coronal (a, b and c) contrast-enhanced CT images. Note the location of the prevertebral muscles, immediately posterior to the nodal mass (*white arrows* in **a**)

irregular T2 signal and enhancement in the adjacent soft tissues. As the infection spreads to the adjacent vertebral bodies, the end plates demonstrate low T1 signal, high T2 signal, enhancement, and increased end plate irregularity with eventual collapse. Another musculoskeletal cause which is unique to the perivertebral space and can be a cause of diagnostic dilemma on imaging is calcific tendonitis. The reactive retropharyngeal effusion can be mistaken for an infection, and unless the signal dropout from the calcium is recognized, the patient may be subjected to unnecessary

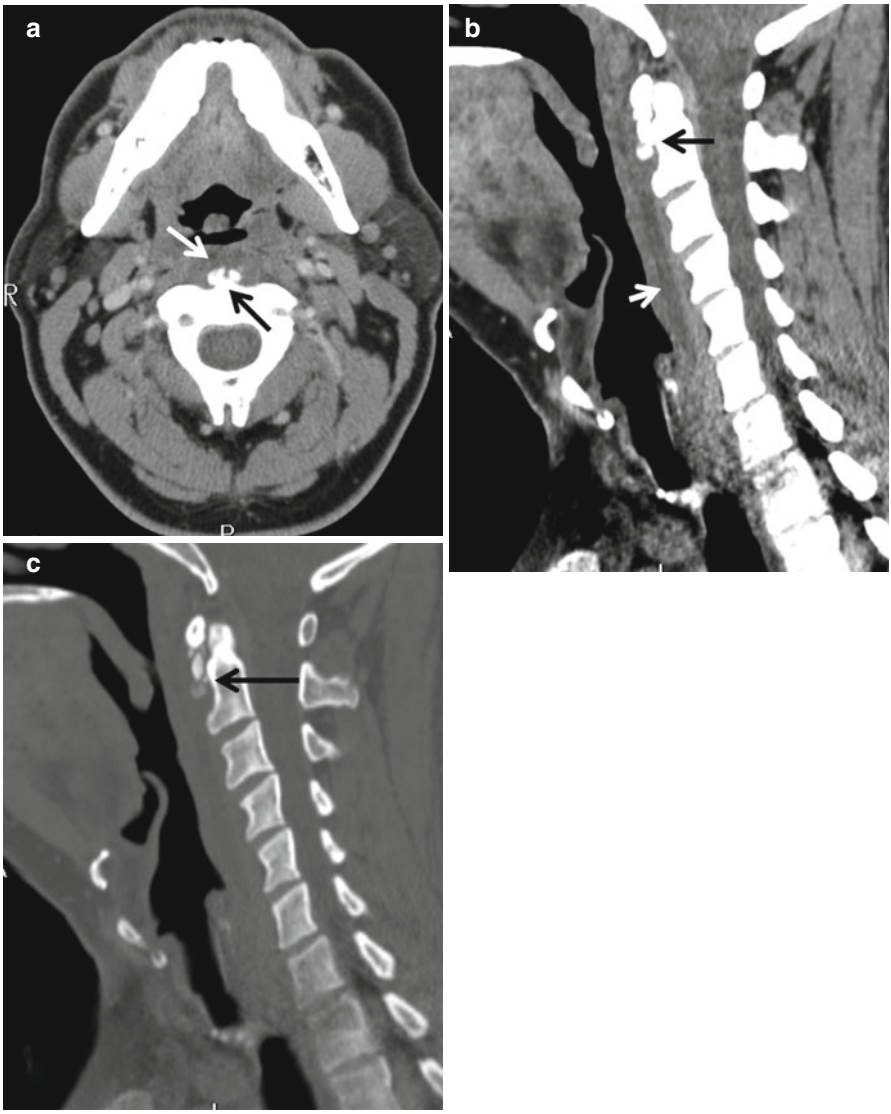

Fig. 1.18 Acute calcific prevertebral tendinitis. Axial (**a**), soft tissue (**b**), and bony window (**c**) sagittal images shows the characteristic calcification (*black arrow*) due to calcium hydroxyapatite in the longus colli muscles at the C2 level with associated retropharyngeal effusion (*white arrow*). This patient presented with headache, slight fever, and other signs concerning for meningitis. This is a self-limiting condition which responds to NSAIDS and rest

treatment (Fig. 1.18). As midline structures, the vertebral bodies may also give rise to chordomas, which are classically T2 hyperintense and enhance avidly.

The cervical spinal nerves, brachial plexus, and the phrenic nerve in the perivertebral space may give rise to neurogenic tumors, including schwannomas and

neurofibromas. Patients with neurofibromatosis (NF) types 1 and 2 may develop multiple nerve sheath tumors (Fig. 1.19). The multiplicity of the tumors helps in diagnosis. Neurogenic tumors tend to be T2 hyperintense and enhance avidly. The classical "Target sign" in plexiform neurofibromas on MRI is due to a T2 hypointense core (central fibrocollagenous tissue) with a rim of T2 hyperintense signal (peripheral myxomatous tissue). Other mesenchymal lesions such as sarcomas can also arise in this location from the adjacent muscles and nerves (Fig. 1.20).

1.3 The Surgeon's Perspective

While masses in the PPS are often discovered incidentally on imaging obtained for other reasons, a common presentation is a submucosal oropharyngeal mass. These masses can typically be accessed for core biopsy under imaging guidance, but this may be unnecessary when the diagnosis is reasonably well established by standard imaging and the treatment approach is resection regardless of the pathology. Biopsy is most helpful when there is concern for malignancy, as this will impact the approach and extent of surgery, but as described above, malignancy is uncommon in this space.

The PPS contains the retromandibular portion of the deep lobe of the parotid gland, and when evaluating masses in the PPS, it is important to determine if they originate within the PPS or in the deep lobe of the parotid gland. Tumors of parotid origin require total parotidectomy for removal in order to carefully preserve facial nerve function. Inherent tumors of the PPS do not require parotidectomy (although such an approach may be employed in some cases) and can usually be resected by a transcervical approach. For tumors high in the PPS, transection of the stylomandibular ligament allows anteromedial displacement of the mandible and broader access via the transcervical route. With adequate exposure, removal of well-encapsulated benign tumors is usually straightforward. While mandibulotomy has been described to improve access, removal of the external aspect of the mandibular angle can dramatically improve exposure without disrupting mandibular continuity.

Malignancy involving the PPS is managed with much more aggressive surgical approaches that often require combined parotidectomy, mandibulectomy, and oral/oropharyngeal resection; these require significant reconstructive surgery to restore form and function. Before undertaking such surgery, the pterygoid musculature, skull base, and regional nerves must be examined for tumor spread. Involvement of these structures may not per se make the tumor unresectable, but will dramatically worsen the patient's prognosis, potentially making a palliative approach more appropriate.

Trismus is an important clinical finding that should be explained radiographically. Trismus can be mechanical or secondary to pain/inflammation. When trismus is due to mechanical limitation, it will not be improved by analgesia, sedation, or paralysis; thus, access (e.g., to an intraoral or pharyngeal tumor, to the airway) will not improve in the operating room as it will when mandibular excursion is limited

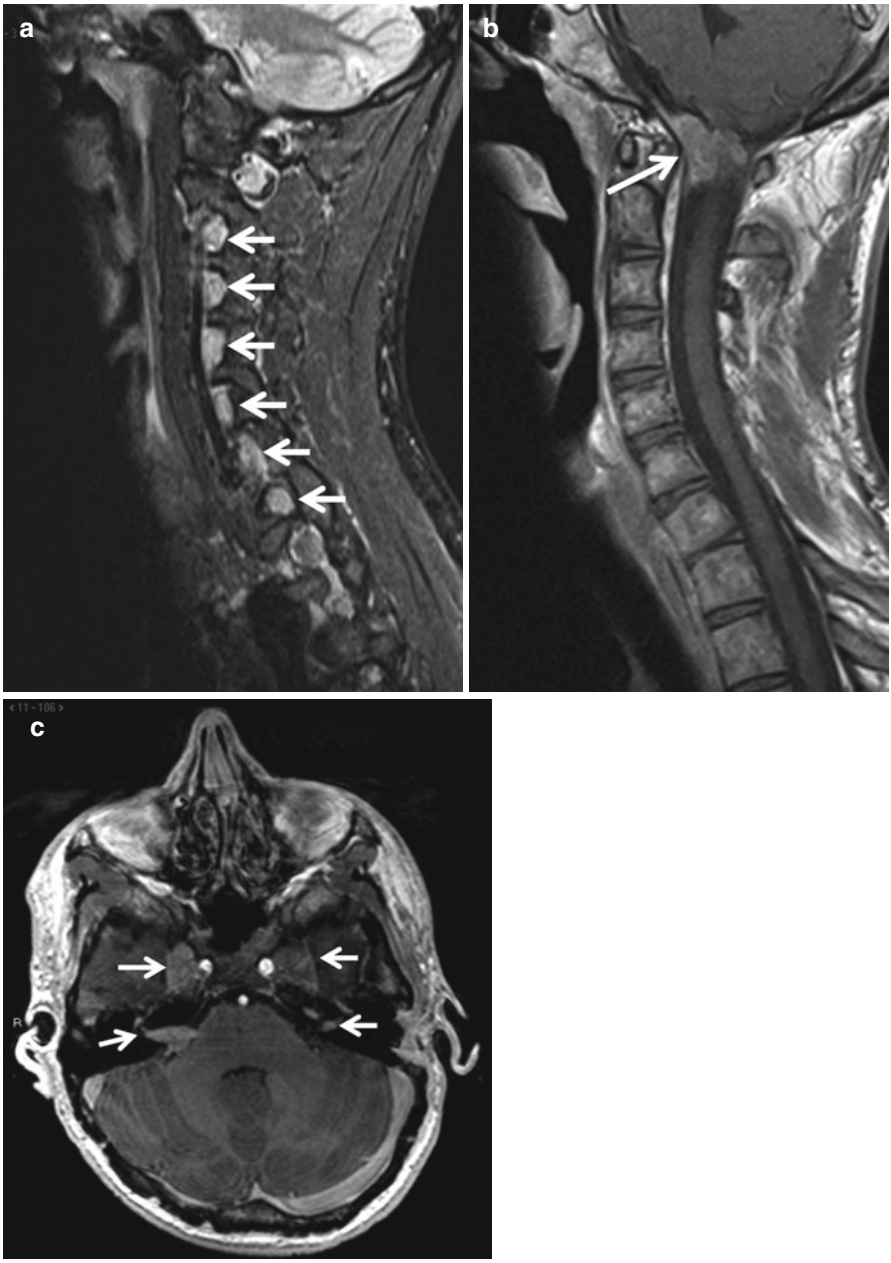

Fig. 1.19 Neurofibromatosis 2. Parasagittal T2, sagittal post-contrast T1, and axial post-contrast T1 sequences demonstrate multiple nerve sheath tumor involving the cervical nerves (*small arrows* in **a**), a skull base meningioma (*arrow* in **b**), and multiple cranial nerve sheath tumors involving bilateral Meckel's cave and internal auditory canals (*small arrows* in **c**)

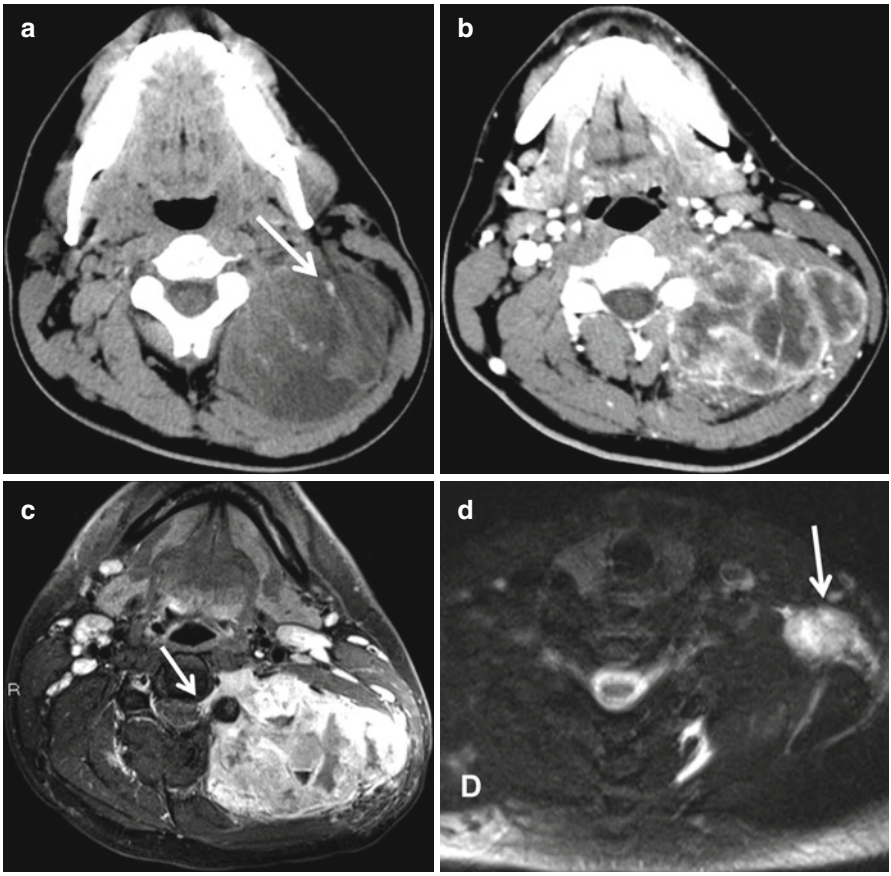

Fig. 1.20 Synovial cell sarcoma. Axial pre- (**a**) and post-contrast (**b**) images in this teenager shows a large lobulated heterogeneously enhancing soft tissue mass in the left posterolateral intramuscular soft tissues, containing scattered calcifications (*arrow* in **a**) and enhancing septations (**b**). Axial post-contrast MR (**c**) shows the intraspinal extension of the lesion, (*arrow* in **c**) while a pathological level V node is seen on the axial T2 fast saturated sequences (*arrows* in **d**)

by pain or inflammation. Mechanical limitation of jaw excursion may warrant an endoscopic approach to airway management or even an awake tracheotomy in some cases, and it is crucial to be aware of this before attempting a standard approach to airway management.

Management of benign tumors in the carotid space is based on diagnosis and symptoms. While paragangliomas are often treated without significant morbidity, resection of neurogenic tumors will almost always result in neurologic functional deficits. Thus, treatment of neurogenic tumors is often delayed until symptoms are noted. Since many of these tumors are discovered incidentally and grow slowly

(or not at all), they are often observed for a period of time (6–12 months) to determine their growth rate before making treatment decisions. In such cases, it is important for the radiologist to compare the present images to previous studies to determine the rate of change over time. Tumors in the carotid space are often quite vascular, and particularly if they are larger or close to the skull base resulting in somewhat more difficult access, it can be valuable to consider preoperative embolization to reduce intraoperative bleeding.

Evaluation and management of retropharyngeal infections should be prompt and definitive to avoid extension into the danger space and risk of thoracic extension. In children that do not appear toxic, retropharyngeal abscesses may be managed with IV antibiotics and close observation for 24–48 h; with improvement, surgery can usually be avoided. However, most adults are with significant retropharyngeal abscesses are treated surgically. In some cases, retropharyngeal infections are associated with cervical spine hardware placed by the neurosurgeons or orthopedic surgeons. In these cases, it is important to determine if there is a pharyngeal or esophageal leak that has resulted in contamination of the hardware; any approach to treatment will require a plan to repair the leak. Preoperative evaluation usually includes a contrasted swallow study. Regardless of the presence of a leak, the contaminated cervical hardware must be removed to adequately treat the infection.

Further Reading

Batsakis JG, Sneige N (1989) Pathology consultation: parapharyngeal and retropharyngeal space diseases. Ann Otol Rhinol Laryngol 98:320–321

Chong VFH, Fan YF (1996) Pictorial review: radiology of the carotid space. Clin Radiol 51:762–768

Harnsberger HR, Osborn AG (1991) Differential diagnosis of head and neck lesions based on their space of origin. 1. The suprahyoid part of the neck. AJR Am J Roentgenol 751:147–154

Hughes KV, Olsen KD, McCaffrey TV (1995) Parapharyngeal space neoplasms. Head Neck 17: 124–130

Mukherji SK, Castillo M (1998) A simplified approach to the spaces of the suprahyoid neck. Radiol Clin North Am 36(5):761–780, v

Som PM, Sacher M, Stollman AL, Biller HF, Lawson W (1988) Common tumors of the parapharyngeal space: refined imaging diagnosis. Radiology 169:81–85

Yousem DM (2000) Suprahyoid spaces of the head and neck. Semin Roentgenol XXXV(1): 63–71

Lymph Nodes

2

Sugoto Mukherjee, Mark J. Jameson, Max Wintermark, and Prashant Raghavan

2.1 Introduction

While there are a variety of causes of cervical lymphadenopathy (see Box 2.1), the primary role for imaging in cervical lymphadenopathy is to diagnose metastatic disease in head and neck squamous cell carcinoma (HNSCC), which significantly impacts treatment. Other nonneoplastic causes of cervical lymphadenopathy, including various infectious and inflammatory diseases, usually do not require routine imaging. This chapter reviews the anatomy and classification of cervical lymph nodes, diagnostic criteria, and imaging findings of lymph node metastasis and the imaging appearance of other benign cervical lymphadenopathies.

Box 2.1. Causes of Cervical Lymphadenopathy

Neoplastic	Squamous cell carcinoma
	Lymphoma
	Thyroid carcinoma (papillary most common)
	Kaposi sarcoma
	Metastases (lung, breast, melanoma, renal cell, carcinoid)
Infection	Bacterial
	Mycobacterium tuberculosis
	Infectious mononucleosis
	Cytomegalovirus
	Rubella
	Cat-scratch disease
	Brucellosis
	Lyme disease
Granulomatous disease	Sarcoidosis
	Langerhans cell histiocytosis
Miscellaneous	Castleman's disease (angiofollicular lymphoid hyperplasia)
	Posttransplantation lymphoproliferative disease
	Sinus histiocytosis with massive lymphadenopathy
	Kimura disease

P. Raghavan et al., *Manual of Head and Neck Imaging*,
DOI 10.1007/978-3-642-40377-4_2, © Springer-Verlag Berlin Heidelberg 2014

2.2 Anatomy and Pathophysiology

Given that regional nodal metastasis is the single most important prognostic factor for HNSCC, evaluation of cervical nodes is an essential component of staging and treatment planning. Cross-sectional imaging significantly improves accuracy of detection of metastatic nodal disease, particularly when non-palpable.

Knowledge of cervical anatomy and nodal classification is essential to accurately describe cervical nodal metastases in HNSCC. The American Joint Committee on Cancer (AJCC) has classified neck lymph nodes from levels I through VII. Level I refers to nodes in the submandibular and submental regions. Levels II, III, and IV refer to lymph nodes along the anterior cervical chain. Level V and VI nodes are in the posterior and visceral compartments of the neck, respectively, and level VII nodes are in the superior mediastinum (Fig. 2.1).

The essential anatomic landmarks used for imaging classification are depicted in Fig. 2.1 and are described in Box 2.2. Certain nodes are still classified according to their anatomic names, including supraclavicular, retropharyngeal, parotid, facial, occipital, and postauricular.

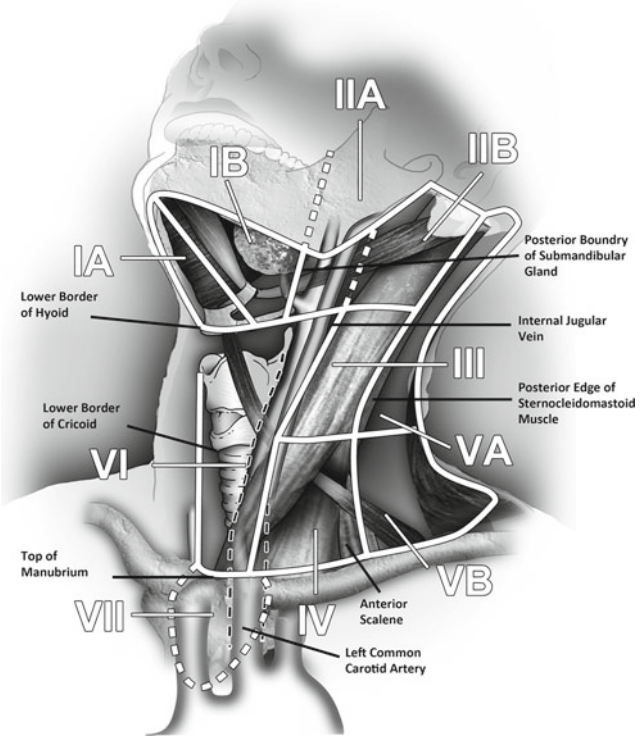

Fig. 2.1 Oblique sagittal graphic showing the relevant anatomic landmarks for imaging-based nodal classification. The important landmarks visible on this graphic include lower border of hyoid (levels *I* and *II*), lower border of cricoid (levels *III* and *IV*), (levels *VA* and *VB*) top of manubrium (levels *VI* and *VII*), anterior belly of digastric (levels *IA* and *IB*), posterior border of submandibular gland (levels *IB* and *IIA*), and posterior border of internal jugular vein (levels *IIA* and *IIB*). The anterior scalene (levels *IV* and *VB*) and carotid arteries (levels *II* and *IV* from *VI*) are not well visualized on this image

Box 2.2. Imaging-Based Nodal Classification

Levels	Boundaries			
	Superior	Inferior	Anterior (medial)	Posterior (lateral)
IA Submental group	Symphysis of mandible	Body of hyoid	Anterior belly of contralateral digastric muscle	Anterior belly of ipsilateral digastric muscle
IB Submandibular group	Body of mandible	Posterior belly of digastric muscle	Anterior belly of digastric muscle	Stylohyoid muscle
IIA Upper jugular group nodes	Skull base	Horizontal plane defined by the inferior border of hyoid bone	Stylohyoid muscle	Vertical plane defined by the spinal accessory nerve
IIB Upper jugular group nodes	Skull base	Horizontal plane defined by the inferior border of hyoid bone	Vertical plane defined by the spinal accessory nerve	Lateral border of the sternocleidomastoid muscle
III Mid-jugular group	Horizontal plane defined by the inferior border of hyoid bone	Horizontal plane defined by the inferior border of cricoid cartilage	Lateral border of the sternohyoid muscle	Lateral border of the sternocleidomastoid muscle or sensory branches of the cervical plexus
IV Lower jugular group	Horizontal plane defined by the inferior border of cricoid cartilage	Clavicle	Lateral border of the sternohyoid muscle	Lateral border of the sternocleidomastoid muscle or sensory branches of the cervical plexus
VA Posterior triangle group	Apex of the convergence of sternocleido-mastoid and trapezius muscles	Horizontal plane defined by the inferior border of the cricoid cartilage	Lateral border of the sternocleido-mastoid muscle or sensory branches of the cervical plexus	Anterior border of the trapezius muscle
VB Posterior triangle group	Horizontal plane defined by the inferior border of cricoid cartilage	Clavicle	Lateral border of the sternocleido-mastoid muscle or sensory branches of the cervical plexus	Anterior border of the trapezius muscle

Levels	Boundaries			
	Superior	Inferior	Anterior (medial)	Posterior (lateral)
VI Central or anterior group	Hyoid bone	Top of manubrium	Common carotid artery	Common carotid artery
VII Superior mediastinal group	Top of manubrium	Innominate vein	Common carotid artery	Common carotid artery

Note: Other superficial nodal groups continue to be referred to by their anatomic names including parotid, facial, and postauricular lymph nodes

The clinically important internal jugular nodes are classified as level II, III, or IV nodes (previously referred to as upper, mid-, and lower jugular nodes). On axial imaging, levels II and III are separated by the bottom of the body of the hyoid bone, and levels III and IV are separated by the bottom of the arch (anterior rim) of the cricoid cartilage (Figs. 2.2 and 2.3). All three levels are bounded posteriorly by the posterior edge of sternocleidomastoid muscle (SCM). Level II is also bounded posteriorly by the posterior edge of the submandibular gland. Level IIA nodes lie adjacent to the internal jugular vein (IJV); any level II nodes that are posterior to the IJV and are separated from the vein by a fat plane are level IIB nodes. Level I nodes are above the hyoid bone, below the mylohyoid muscle, and anterior to posterior margin of submandibular gland. They are subdivided into levels IA (submental) and IB (submandibular) based on whether they are medial or posterolateral to the anterior belly of digastric muscle, respectively. Level III nodes lie anterior to the posterior margin of the SCM and in between the lower margin of the body of the hyoid bone and the lower margin of the cricoid cartilage arch. Level III nodes also lie lateral to the medial margin of either the common carotid artery or the internal carotid artery. On each side of the neck, the medial margin of these arteries separates level III (lateral) from level VI (medial) nodes. Level IV nodes lie between the level of the lower margin of the cricoid cartilage arch and the level of the clavicle as seen on each axial scan. These nodes are anteromedial to a line drawn through the posterior edge of the SCM and the posterolateral edge of the anterior scalene muscle on each axial image. Also, the medial aspect of the common carotid artery separates level IV (lateral to the artery) from level VI nodes (medial to the artery) (Figs. 2.1 and 2.4).

Level V nodes extend from the skull base, at the posterior border of the attachment of the SCM, to the level of the clavicle as seen on each axial scan. Level VA (upper level V) nodes lie between the skull base and the lower margin of the cricoid cartilage arch, behind the posterior edge of the SCM, while level VB (lower level V) nodes lie between the level of the lower margin of the cricoid cartilage arch and the level of the clavicle as seen on each axial scan. Their anterior boundary if formed by the posterior edge of the SCM (Figs. 2.1, 2.2, and 2.3).

Identification of the clavicle allows one to separate the supraclavicular from axillary nodes on axial CT slices. When any portion of the clavicle is seen on the scan, the visible nodes are classified as supraclavicular nodes, while any nodes below the level of the clavicle and lateral to the ribs are classified as axillary nodes.

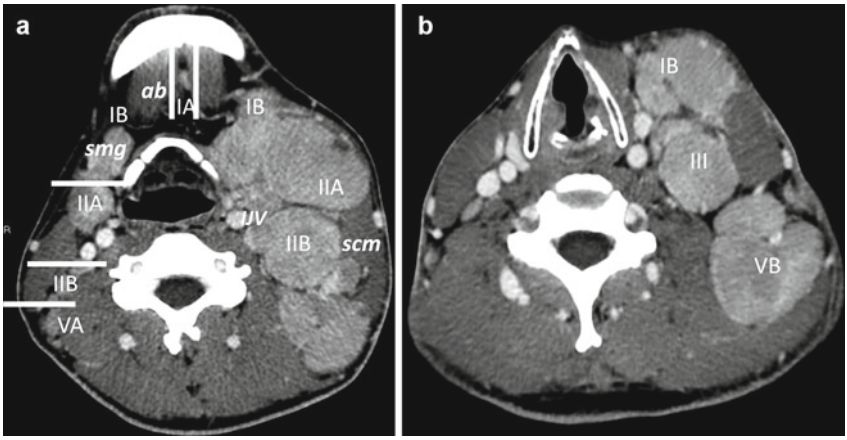

Fig. 2.2 (**a** and **b**) A 23 year-old with Hodgkin's lymphoma above and below the hyoid cartilage. *ab* anterior belly of digastric, *smg* submandibular gland, *scm* sternocleidomastoid, *IJV* internal jugular vein. *White lines* divide the different nodal compartments. Level *IA* is in between the anterior belly of digastric, while level *IB* is in between the anterior belly of digastric and posterior margin of submandibular gland. Levels *II/III/IV* are separated from level *V* by posterior border of sternocleidomastoid. Levels *IIA* and *IIB* are divided by internal jugular vein (*IJV*). Nodes that lie anterior or contact IJV are *IIA* nodes. Levels *II* and *III* and *III* and *IV* are defined by the inferior borders of hyoid and cricoid cartilages, respectively

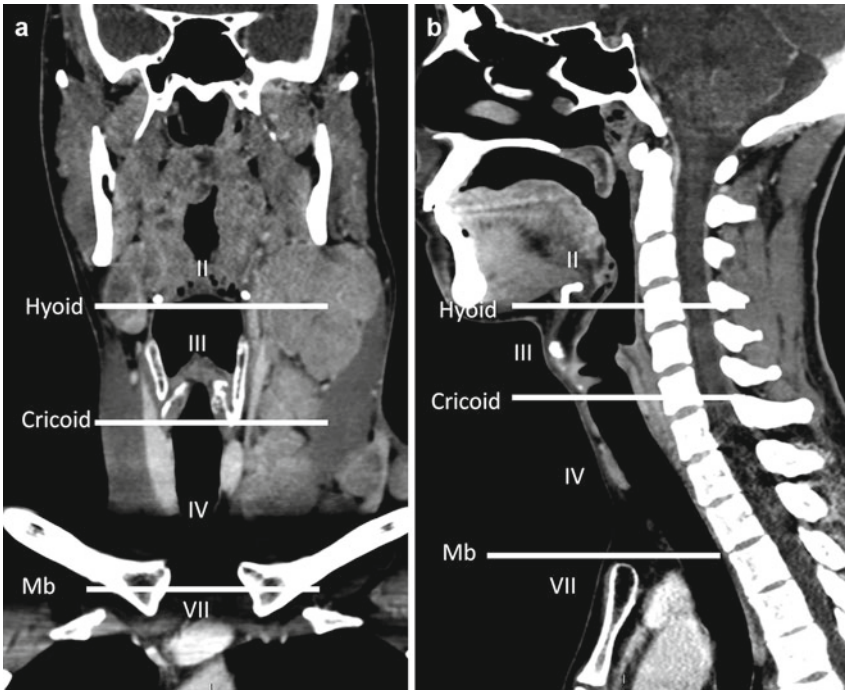

Fig. 2.3 (**a** and **b**) Coronal and sagittal CT images show levels *II*, *III*, and *IV* sites divided by inferior border of hyoid and inferior border of cricoid. Levels *VI* and *VII* are separated by the superior border of manubrium

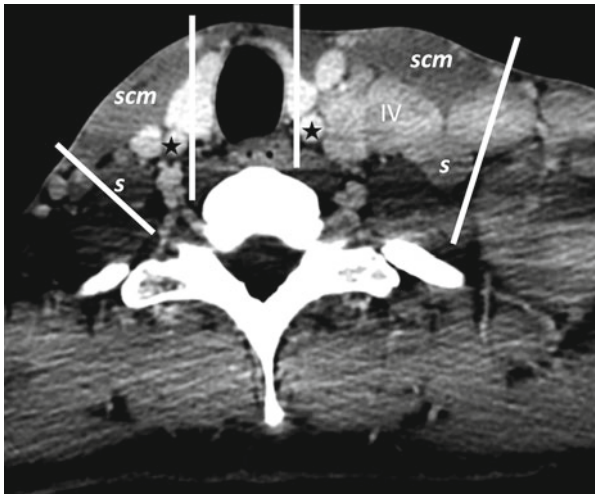

Fig. 2.4 Axial contrast-enhanced CT scans through the infrahyoid lower neck show levels IV, V, and VI sites, defined by medial margin of common carotid artery (*star*) and oblique line from lateral anterior scalene muscle (*s*) to posterior border of sternocleidomastoid muscle (*scm*)

Level VI nodes or the visceral nodes lie inferior to the lower body of the hyoid bone, superior to the top of the manubrium, and between the medial margins of the left and right common carotid arteries or the internal carotid arteries. Level VII nodes lie inferior to the top of the manubrium in the superior mediastinum, between the medial margins of the common carotid arteries. These superior mediastinal nodes extend caudally to the level of the innominate vein (Figs. 2.3 and 2.4).

2.3 Imaging Evaluation

2.3.1 CT and MRI

On imaging, the radiologist needs to identify the pathological nodes based on size, shape, and abnormal nodal architecture. Laterality (ipsilateral, contralateral, or bilateral) must also be noted. Other important features that affect management such as the presence of extracapsular spread of tumor, carotid encasement, and fixation of the tumor to the skull base or prevertebral space also needs to be identified and mentioned. According to the 50 % rule for pathological nodes, presence of nodal metastases decreases the patient's morbidity and mortality by 50 %; presence of bilateral nodes, extracapsular spread, and nodal fixation each lowers the prognosis by an additional 50 %.

The established size criteria for pathological lymph nodes are somewhat arbitrary and controversial and vary among different institutions and practitioners. A commonly used set of size criteria places cutoffs of ≥1.5 cm for levels I and II, ≥1 cm for levels III–V, and ≥8 mm for retropharyngeal nodes (Fig. 2.5). However, many malignant nodes are normal in size, whereas enlarged nodes may be benign. Malignant lymph nodes appear more rounded as compared to benign nodes, which are bean-shaped. Thus, another criterion is based on the ratio of long-axis to

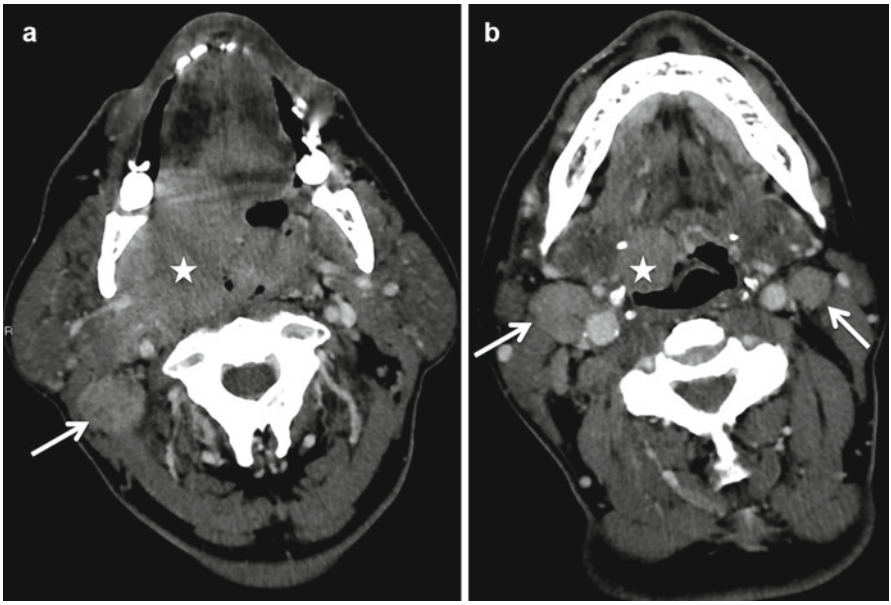

Fig. 2.5 Large T4b invasive tonsillar tumor (*star*) with bilateral pathological adenopathy. Note the rounded shape with loss of internal hilar fat of these enlarged right level IIB (*arrow* in **a**) and bilateral IIA nodes (*arrows* in **b**)

short-axis measurements, with a ratio >2 favoring a benign node and a ratio <2 being concerning for malignancy. Size criteria alone are not reliable, with a false-positive and false-negative rates of ranging from 15 to 20 %. Retropharyngeal lymph nodes are always abnormal when necrotic in the setting of cancer, irrespective of their size (Fig. 2.6). Intraparotid lymph nodes should be suspected to be abnormal in the setting of scalp skin malignancies (Fig. 2.7).

For neck nodes, the presence of hilar fat (easily identified on CT or MR) indicates benignity; this should be distinguished from necrosis, which is usually centrally located in a rounded node (Fig. 2.8). In patients with HNSCC, nodal necrosis implies regional metastasis until proven otherwise. Necrotic nodes can appear cystic when the intranodal contents demonstrate fluid-like imaging appearance with a thin enhancing wall; this is particularly common with human papillomavirus (HPV)-related HNSCC, and the inner cystic component can have complex signal characteristics (Fig. 2.9). The likelihood of necrosis in a metastatic lymph node increases with lymph node size, with more than 50 % of nodes ≥1.5 cm demonstrating necrosis. In addition to HNSCC, necrotic or cystic nodes are not uncommonly seen in metastatic papillary thyroid cancer (PTC).

Cervical lymph node calcification (Fig. 2.10) is rare (~1 %). Presence of nodal calcification is not a reliable predictor of either benign or malignant disease; however, it does provide a limited differential diagnosis. Calcification in cervical lymph nodes is most common in PTC and is occasionally seen in metastatic mucinous adenocarcinoma, treated lymphoma, and granulomatous diseases.

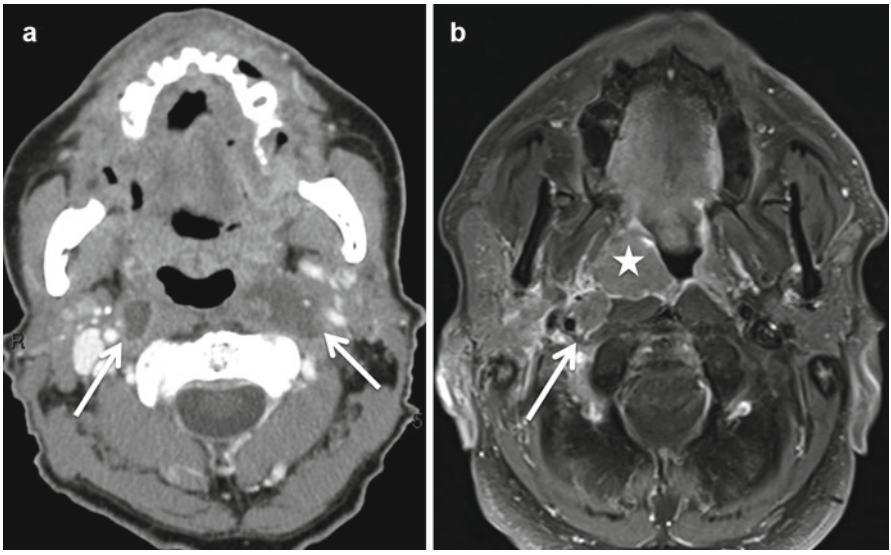

Fig. 2.6 Contrast-enhanced CT (**a**) in a patient with sinonasal tumor demonstrates bilateral necrotic retropharyngeal nodes (*arrows*). Another 55-year-old patient (**b**) with tonsillar cancer (*star*) has a pathological 1 cm right retropharyngeal node (*arrow*)

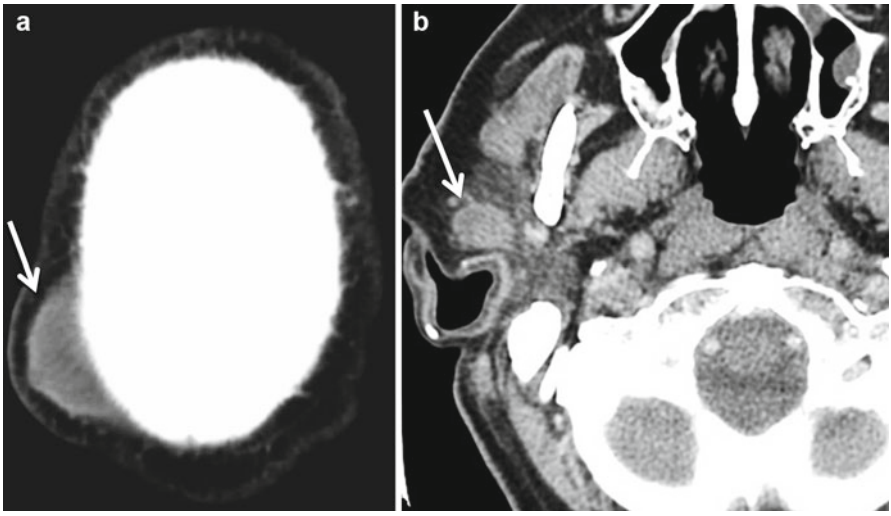

Fig. 2.7 A 65 years old with right vertex squamous cell carcinoma (*arrow* in **a**) with pathological intraparotid adenopathy (*arrow* in **b**). These nodes represent the first echelon of drainage for cutaneous malignancies of the scalp

The presence of extracapsular spread (ECS) of metastatic nodal disease is associated with increased local recurrence rates and decreased survival in patients with HNSCC. Extracapsular extension is identified by poorly defined nodal margins and/

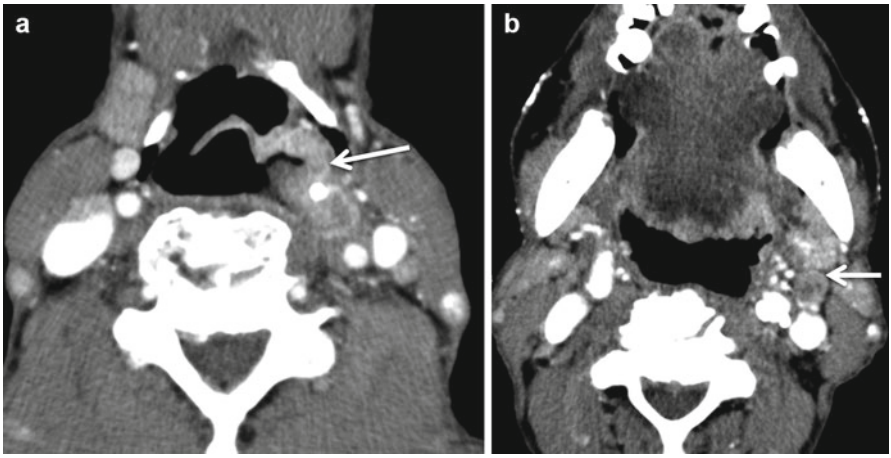

Fig. 2.8 A 55-year-old with left pyriform sinus cancer (*arrow* in **a**) and a pathological left level IIA node (*arrow* in **b**) with loss of hilar fat and central necrosis. Although the level IIA nodes are not pathological by size criteria, the presence of central necrosis along with the known primary suggests that this node is pathological

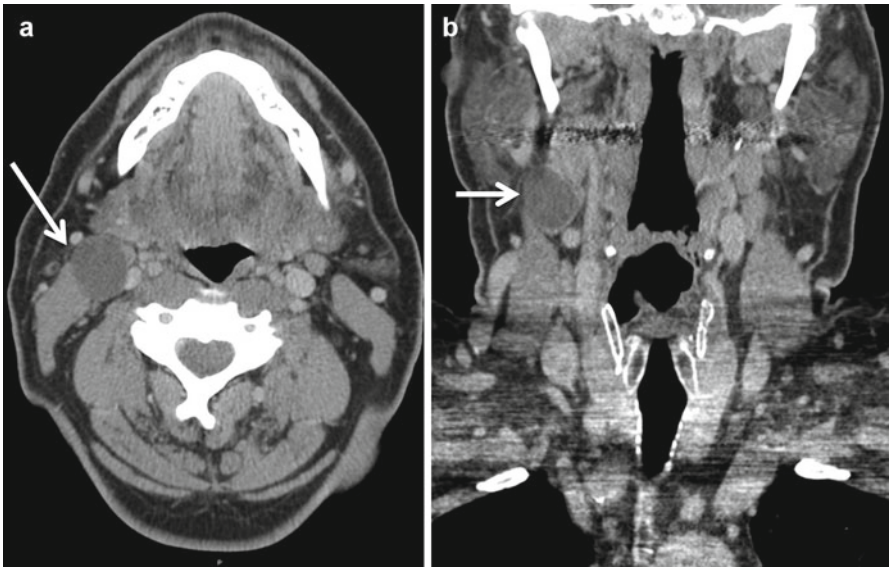

Fig. 2.9 Axial (**a**) and coronal (**b**) contrast-enhanced CT scans in this 52-year-old male with right level II cystic mass (*white arrows*). No primary was identified on endoscopic-guided biopsies. CT-guided FNA showed a metastatic node from a squamous cell carcinoma. This is a common presentation of HPV (human papillomavirus)-associated oral and oropharyngeal cancers which are known for cystic nodal level II metastasis

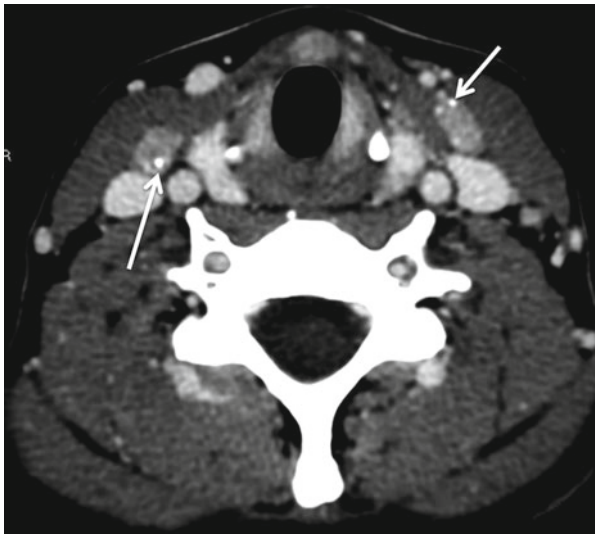

Fig. 2.10 Bilateral pathological level IV enhancing nodes in this patient with papillary carcinoma of the thyroid with small specks of calcification (*arrows*)

or soft tissue infiltration or stranding of the muscles or fat in the neck with loss of normal tissue planes (Fig. 2.11). Also, increasing lymph node size is an indicator of ECS with larger nodes more frequently demonstrating ECS.

Some of the other advanced imaging techniques, which are infrequently used, include diffusion-weighted MRI (DWI), perfusion imaging with dynamic contrast-enhanced MRI (DCE-MRI), and CT perfusion. These techniques, particularly CT and MR perfusion imaging, may allow us to predict biological behavior of these cancers and identify early responders and nonresponders and allow alternative treatment as well as earlier treatment modification.

2.3.2 Ultrasonography

Sonography is used both for detecting nodes and for guiding fine needle aspiration (FNA). A high-frequency linear transducer with Doppler capability is the preferred tool. Normal nodes appear oval/oblong with an echogenic hilum, hypoechoic cortex, and minimal or no intranodal blood flow on color Doppler. Increased short-axis diameter (rounding) and absence of central hilar echogenicity are the criteria most predictive of lymph node metastasis (Fig. 2.12). Doppler imaging can detect peripheral vascularity with or without central vascularity, which significantly improves the overall accuracy of sonography in identifying metastatic nodes. Lymphoma is an exception, as involved nodes may only have hilar flow. Other signs of malignancy include focal or eccentric hypertrophy of the peripheral cortex, absence of an echogenic hilus, indistinct margin (suggests ECS), and necrotic/cystic changes within the substance of the node. Most metastatic nodes appear hypoechoic to adjacent muscle, except for metastatic PTC. US-guided FNA is an extremely reliable and efficient technique to obtain cells for cytologic evaluation and confirmation of suspected metastatic disease and to obtain samples for microbiologic evaluation (Fig. 2.12).

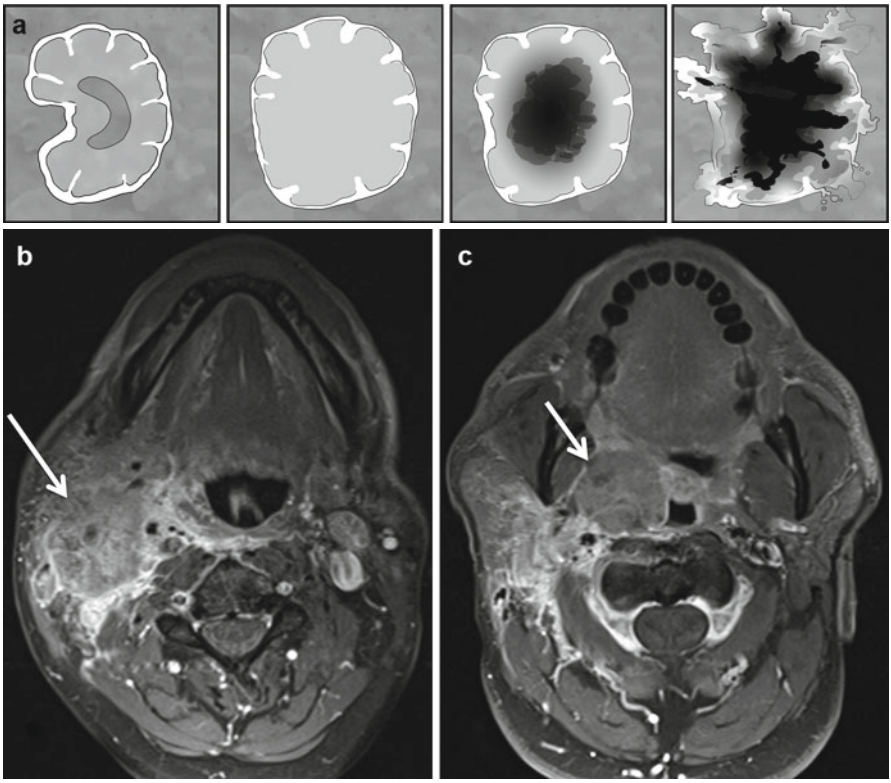

Fig. 2.11 (**a**) Graphic shows the progressive changes in a node when it is involved in metastatic disease. The first image shows the reniform shape of the node, with hilar fat and distinct margins. The involved node loses its normal shape, becomes more rounded followed by central necrosis in the third image. Later stages result in disease spilling out of the node with extracapsular extension. This is seen on imaging as irregular shape, with loss of clear nodal margins and abnormal appearance of the adjacent fat on CT and MR. (**b** and **c**) Axial post-contrast fat-saturated images show extracapsular spread of the right level II nodal mass (*arrow* in **b**) with loss of surrounding tissue planes. The nodal mass has completely infiltrated the right posterior masticator space, the parapharyngeal fat, and possibly the right carotid space. Note the right tonsillar primary (*arrow* in **c**)

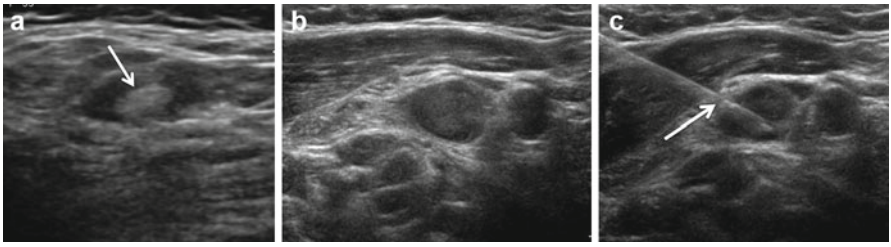

Fig. 2.12 Gray-scale transverse view US image showing a normal lymph node (**a**), with oval shape and echogenic central hilum (*arrow*). Pathological lymph node (**b**) shows a rounded shape with loss of central echogenic fatty hilum, in a patient with thyroid cancer. US (**c**) also helps in providing guidance (*arrow*) for fine needle aspiration cytology and biopsy

2.3.3 PET

Out of various available advanced imaging techniques, 18FDG-PET is most commonly used in clinical practice. FDG-PET has been used in the pretreatment setting for indeterminate nodes on CT/MR, distant metastasis (Fig. 2.13); higher tumor burden with less nodal disease than expected and for baseline scans. FDG-PET is also used for evaluation of residual nodal disease in postradiation setting. Other adjunct uses include directing biopsy/FNA and in patients with unknown primary. Limitations of FDG-PET include false-positive results due to physiological uptake and false negative in necrotic lymph nodes, which may simply not contain sufficient metabolically active tissue to take up FDG.

2.3.4 Posttreatment Evaluation of Residual/Recurrent Nodal Disease

After radiation therapy, routine CT and MR imaging with contrast is insensitive in identifying residual/recurrent nodal disease secondary to scar, fibrosis, and granulation tissue. On a conventional neck CT scan, residual and or recurrent nodal disease may manifest as increasing size or new nodal lesions, as well as persistent intranodal hypodensity (concerning for nodal necrosis). FDG-PET scanning has a role in this setting and can help in identifying residual/recurrent disease in some of these patients (Fig. 2.14).

2.4 Other Pathology

Various other malignancies, infections, and granulomatous/inflammatory diseases can involve neck nodes (Box 2.1), the most common of which are discussed below.

2.4.1 Lymphoma

Lymphoma is the second most common malignancy in the head and neck after squamous cell carcinoma. Hodgkin's disease accounts for 25 % of all lymphomas and extranodal involvement is rare. Non-Hodgkin's lymphoma, however, may present as both nodal and extranodal disease. Lymphoma typically involves deep lymphatic chains, such as the internal jugular, spinal accessory, and transverse cervical chains. Typical imaging reveals one or more well-demarcated homogeneous nodes (Fig. 2.15). Extranodal tumor extension, nodal necrosis, calcification, and hemorrhage are rare but may be seen posttreatment. On MR imaging when compared to muscle, involved nodes are iso- to hypointense on T1-weighted images and hyperintense on T2-weighted images; they exhibit homogenous enhancement. An important caveat here is the protean manifestations of extranodal lymphoma,

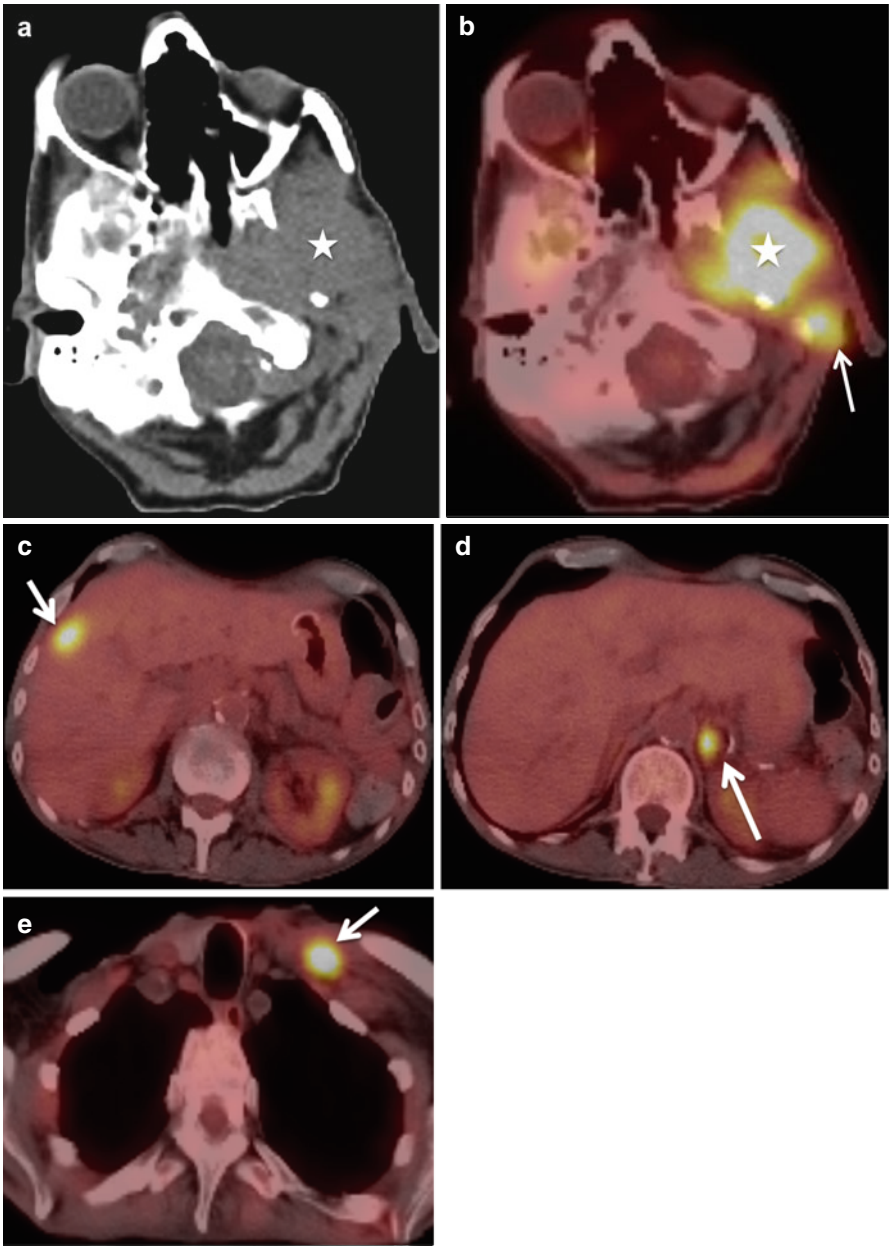

Fig. 2.13 (**a** and **b**) 18FDG-PET scan demonstrates T4b oropharyngeal carcinoma with involvement of the left nasopharynx, left masticator, nasopharyngeal spaces, and the deep lobe of the parotid (*star* in **a** and **b**). A level VA metastatic lymph node is also evident (*arrow* in **b**). (**c**–**e**) Whole body PET scan demonstrated distant metastasis in the left supraclavicular node, right lobe of liver and left adrenal gland (*arrows* in **c**, **d** and **e**)

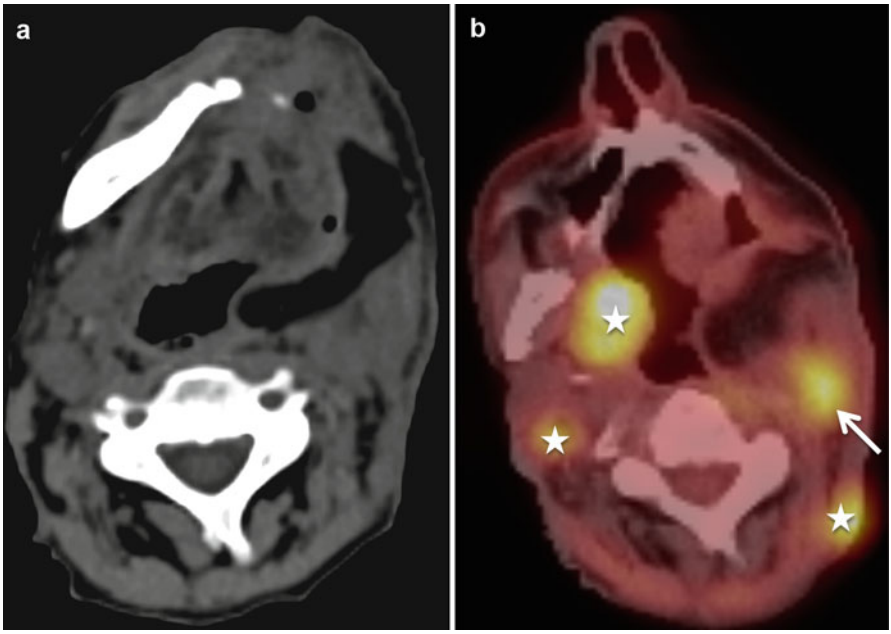

Fig. 2.14 (**a** and **b**) Posttreatment 18FDG-PET scan in this patient status post left hemimandibulectomy, left-sided selective neck dissection, and pectoralis flap reconstruction demonstrates multiple sites of recurrent tumor, both within the postsurgical site (*arrow* in **b**) as well as ipsilateral and contralateral metastatic nodal disease (*star* in **b**)

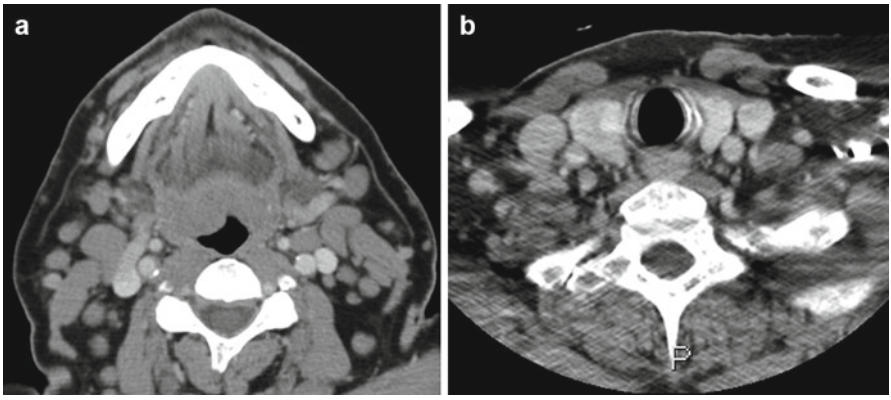

Fig. 2.15 (**a** and **b**) A 55-year-old male with Hodgkin's lymphoma shows multilevel bilateral discrete nodes, both within the suprahyoid and infrahyoid neck. The nodes are rounded with loss of inner hilar fat

which can include infiltrative lesions involving the orbits, nasal cavity, bones, thyroid gland, and/or salivary glands (Fig. 2.16). Extranodal B cell lymphomas can spread along vessels and nerves and can mimic other lesions.

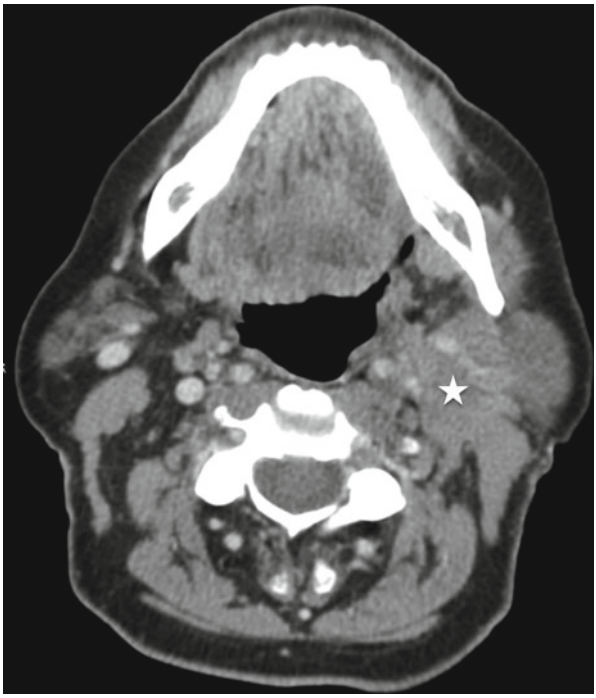

Fig. 2.16 A 55-year-old with diffuse large B cell lymphoma demonstrates an infiltrative mass (*star*) involving the left parapharyngeal space, the left carotid space, and the deep lobe of the left parotid

2.4.2 Papillary Thyroid Carcinoma

Papillary thyroid carcinoma (PTC) frequently metastasizes to cervical lymph nodes. A unique imaging feature of PTC metastases is areas of T1 hyperintensity, which is thought to represent a high concentration of thyroglobulin or intranodal hemorrhage (Fig. 2.17). Other considerations for hemorrhagic nodal disease include metastasis from renal cell carcinoma or melanomas. Nodal calcifications, seen on both CT and ultrasound imaging using high-frequency transducers, can also be seen in metastatic PTC (Fig. 2.18). PTC can also present with purely cystic nodal metastasis.

2.4.3 Bacterial Infection

Many of the infectious causes of cervical lymphadenopathy have a nonspecific imaging appearance. An important imaging feature, which suggests infection rather than neoplasm, is the presence of adjacent fascial thickening and fat infiltration. Suppurative infectious adenopathy can be indistinguishable from malignant necrotic nodal disease, and the clinical context is paramount.

A common clinical scenario is acute nodal enlargement in children, which is frequently due to *S. aureus* infection. An infected node may undergo suppurative necrosis, which manifests as a low-density center surrounded by shaggy enhancement and stranding of the adjacent fat on CT.

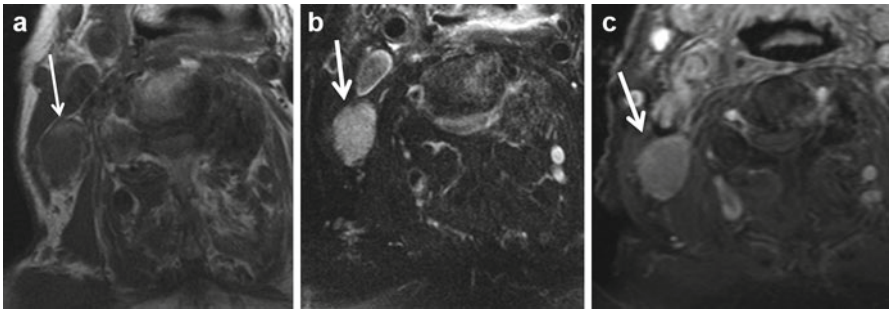

Fig. 2.17 Metastatic right level III lymph node from a papillary thyroid primary. This node is slightly hyperintense, most prominent along the anterior aspect, on the T1-weighted images (*arrow* in **a**) and is hyperintense on the fat-saturated T2-weighted image (*arrow* in **b**). It demonstrates homogeneous enhancement on the post-contrast fat-suppressed T1-weighted image (*arrow* in **c**)

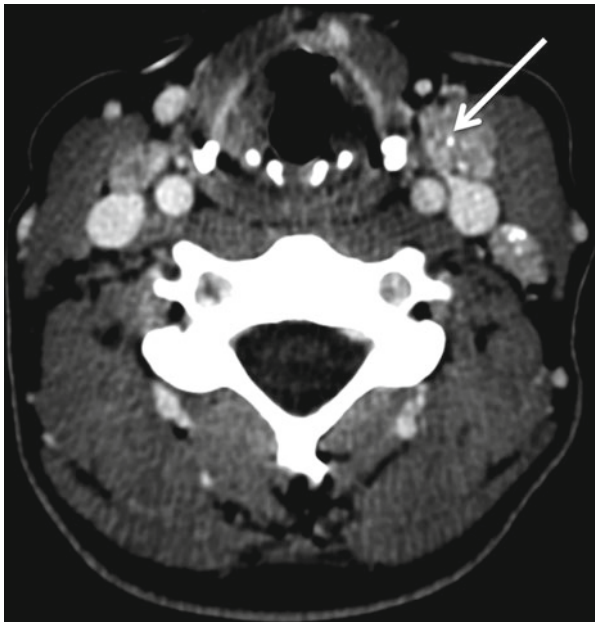

Fig. 2.18 Papillary carcinoma with nodes. Multiple small specks of calcification are seen in the abnormally enhancing left level IV nodes (*arrow*)

2.4.4 Tuberculous and Mycobacterial Lymphadenitis

Mycobacterial infections are divided into tuberculous and nontuberculous infections. Both most commonly involve infrahyoid nodes, with the internal jugular and posterior triangle nodes most frequently affected. Unlike patients with nonmycobacterial lymphadenitis, patients with tubercular adenitis have few generalized symptoms and may present with a painless neck mass. The imaging appearance depends on the stage on the infection: nodes are homogenously enhancing in the initial phase and then become centrally necrotic in the subacute phase with progression to fibrocalcific changes in the posttreatment or chronic state. On CT, the nodes may demonstrate variable enhancement with areas of nodal necrosis and

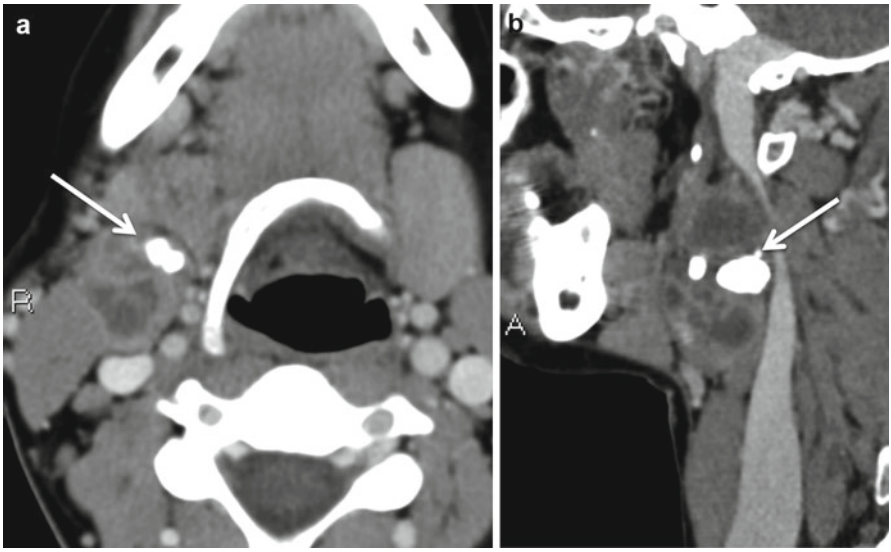

Fig. 2.19 (**a** and **b**) Known HIV positive patient with tuberculosis shows right level II necrotic node with thick calcification (*arrows*)

variable calcification (Fig. 2.19). Similarly, on MR, the nodes might appear complex depending on the stage of disease. Eggshell calcification, which is sometimes seen in tuberculous nodes, can be seen in silicosis and sarcoidosis.

Nontuberculous mycobacterial infections are the commonest granulomatous infection in children and are caused by *M. avium intracellulare*, *M. bovis*, and other nontuberculous mycobacterial species. The imaging findings are similar to tuberculous adenitis, commonly affecting children between 2 and 4 years of age.

2.4.5 Viral Infection

Viral infections including mononucleosis, HIV infection, and mumps generally present as bilateral diffuse lymphadenopathy without necrosis, similar in radiographic appearance to noninfectious causes such as lymphoma and sarcoidosis. Viral adenitis is also common in the pediatric age group, resulting in reactive lymphadenopathy. Tonsillar enlargement and large nodal lesions can be seen in patients with infectious mononucleosis (Fig. 2.20). HIV infection can have unique imaging signs, including enlarged adenoids and multiple bilateral benign intraparotid lymphoepithelial cysts (Fig. 2.21).

2.4.6 Other Inflammatory Conditions

Some of the other rare causes of lymphadenopathy include sarcoidosis, Langerhans cell histiocytosis, Castleman's disease (angiofollicular lymphoid hyperplasia), Kimura disease, Kikuchi disease, sinus histiocytosis with massive lymphadenopathy

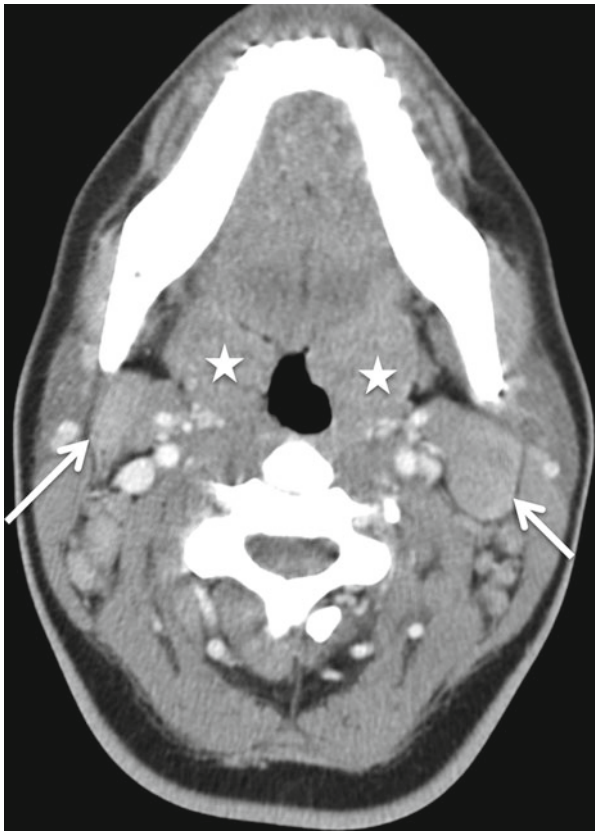

Fig. 2.20 Bilateral multiple enhancing nodes (*arrows*) with enlarged bilateral tonsillar tissue (*star*) are seen in this 19 years old with infectious mononucleosis

Fig. 2.21 A 25-year-old HIV patient with the classical imaging appearance of multiple bilateral benign intraparotid lymphoepithelial cysts (*arrows*)

(Rosai-Dorfman disease), and posttransplantation lymphoproliferative disease (PTLD) (see Box 2.1).

Common head and neck manifestations of sarcoidosis include cervical lymphadenopathy with parotid gland, facial nerve, ocular, and lacrimal involvement. The nodal disease in sarcoidosis is usually bilateral, non-tender, and non-necrotic with diffuse homogenous enhancement and well-defined margins. Eggshell calcification may be seen. The combination of bilateral enlarged parotids with bilateral nodal disease and pulmonary involvement suggests sarcoidosis.

Castleman's disease (angiofollicular hyperplasia) involves head and neck nodes in 10–15 % of cases and is usually of the hyaline-vascular subtype, which is characterized by vascular proliferation. Thus, involved nodes usually demonstrate intense contrast enhancement with a prominent adjacent vessel (Fig. 2.22).

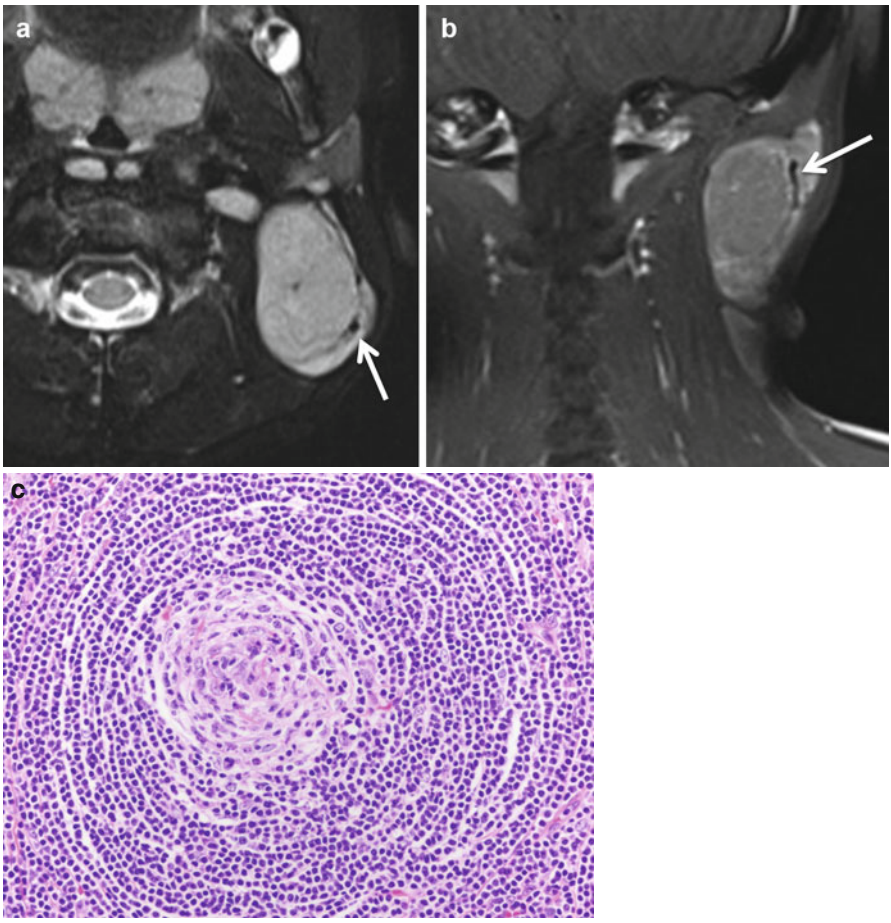

Fig. 2.22 Castleman's disease. Biopsy-proven hyaline-vascular variant of Castleman's disease in this young adult with persistent lymphadenopathy. Note the large dominant posterior neck node with the adjacent flow void. (*arrow* in **a** and **b**). The pathology slide (**c**) demonstrates the classical findings of lymphoid follicle with central hyalinized blood vessels and "onion skin" arrangement of lymhocytes in the hyaline vascular variant of Castleman's disease

Rosai-Dorfman disease (sinus histiocytosis with massive lymphadenopathy) is a rare benign histiocytic proliferation that occurs in young patients. It is characterized by massive painless cervical lymphadenopathy with homogenous enhancement. Associated orbital and salivary gland lesions are seen in 20–30 % of patients.

PTLD (posttransplant lymphoproliferative disease) can demonstrate cervical lymphadenopathy; it can present as a dominant large nodal mass with low central attenuation or as diffuse bilateral nodal disease (Fig. 2.23).

Kimura disease is an inflammatory disease seen in younger Asian men, consisting of cervical adenopathy, peripheral eosinophilia, and elevated serum IgE. Imaging findings of Kimura disease are nonspecific, but markedly enhancing nodes are common.

2.5 The Surgeon's Perspective

When evaluating a patient with cervical lymphadenopathy, imaging is a powerful tool, but clinical examination and patient context are paramount. While experienced examiners can identify cervical masses as enlarged lymph nodes, it is important to be aware that other neck structures, normal and abnormal, can masquerade as lymph nodes. For example, ptotic submandibular glands are common in elderly patients, and this diagnosis can be made clinically without costly imaging. Similarly, many thin

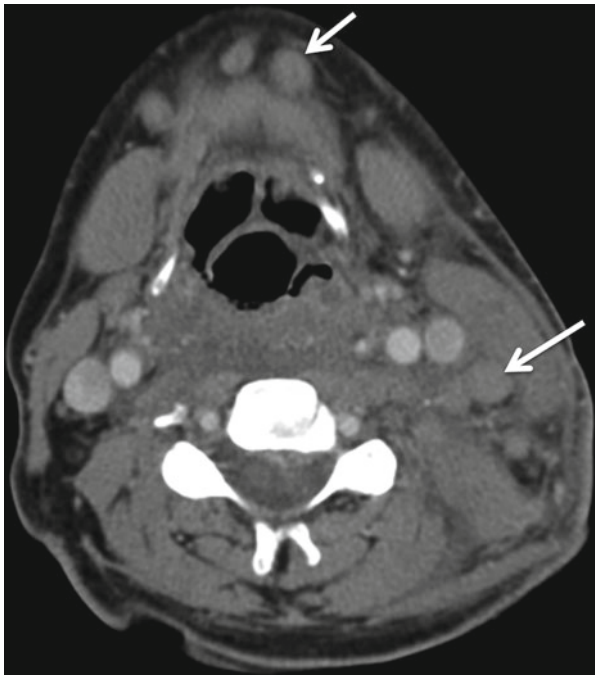

Fig. 2.23 Multiple hypo-enhancing nodes (*arrows*) are seen in this patient with PTLD (posttransplant lymphoproliferative disease). These lesions can present as both multiple small nodes and a large dominant nodal mass

patients have prominent carotid bulbs, and these should not be imaged (or biopsied!). In both scenarios, the patient context complements the clinical examination, and this information is valuable to not only the otolaryngologist but also the radiologist.

A middle-aged adult smoker with cervical lymphadenopathy has cancer until proven otherwise, and imaging and FNA biopsy are in order rather than one or more courses of antibiotics. Children and young adults (especially nonsmokers) with lymphadenopathy are more likely to have a benign infectious illness and, when the clinical context is clear, may be treated with appropriate medical care without imaging. When the imaging does not fit this picture and is more suggestive of malignancy, the radiologist must be aware that the most likely source is the upper aerodigestive tract, rather than metastasis from more distant sites, so that patients are sent on for evaluation by an otolaryngologist – head and neck surgeon in a timely fashion.

One must be aware of the increasing incidence of HPV-related oropharyngeal SCC, which often occurs in young adults with no smoking history. This disease is unique to HPV-negative SCC and often presents with a large cystic node and a very small primary tumor (Fig. 2.24). A common pitfall is to misdiagnose such a node as a branchial cleft cyst. First presentation of a branchial cleft cyst in an adult is extremely rare. Thus, detection of a cystic neck mass in an adult should prompt the radiologist to look for HNSCC, especially in the tonsils and tongue base. Even if the primary is not detectable on imaging, the radiologist should suggest thorough

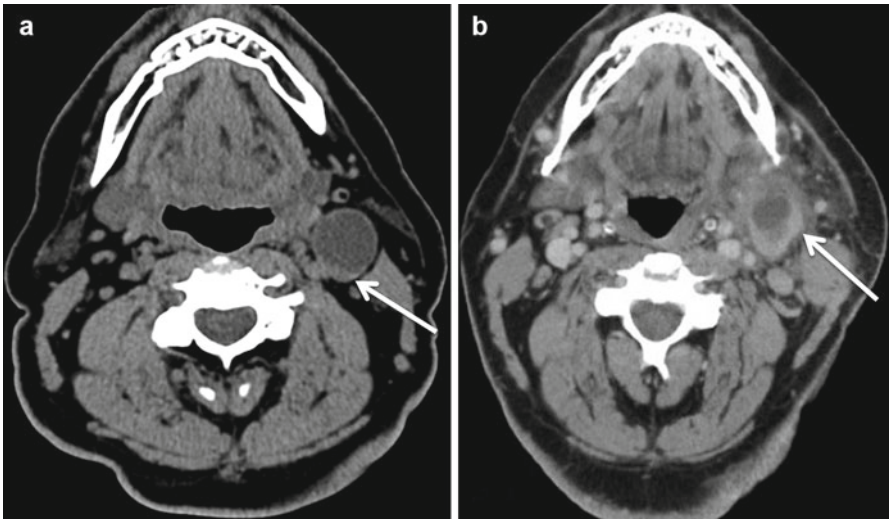

Fig. 2.24 A 45-year-old female who presented with a cystic left neck mass, (*arrow*) on contrast-enhanced CT scan (**a**), mimicking a branchial cleft cyst. Note the minimal soft tissue along the posterior margin. No identifiable primary was obvious on the scan. Speculative biopsies under endoscope revealed a left tonsillar primary. Radiologists should be aware of this pitfall in adult patients presenting with cystic level II lesion, which represents cystic nodal metastasis and is common in HPV-associated oral/oropharyngeal cancers. Infected branchial cleft cysts in adult patients can mimic the appearance of cystic necrotic nodes (*arrow* in **b**), although they are quite rare

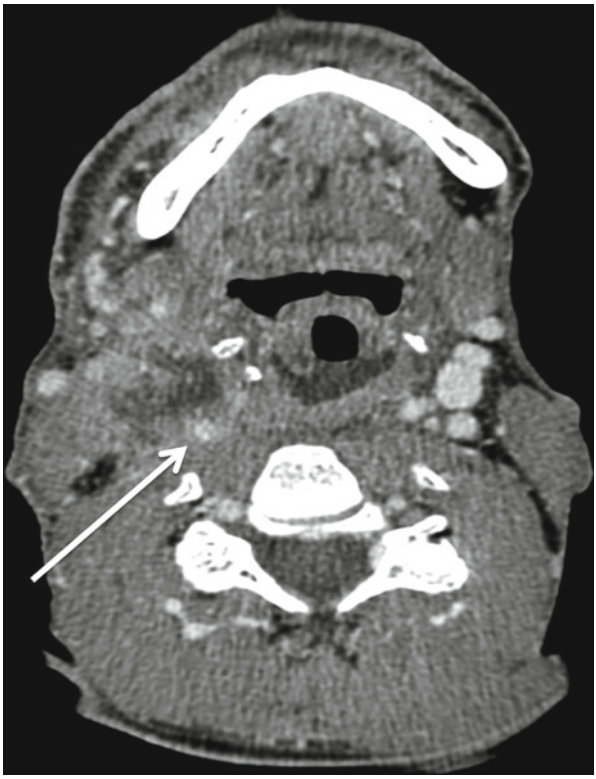

Fig. 2.25 Right carotid sheath invasion is seen in this patient with recurrent right-sided neck disease. Note the lack of tissue planes and loss of fat adjacent to the carotid sheath, with occluded jugular vein (not visible) and a visibly narrowed right carotid artery (*arrow*)

endoscopic evaluation of the oropharynx and FNA biopsy of the node. This approach will often be futile without ultrasound guidance, which allows for specific sampling of the solid cancerous rim of the node. Incorrect diagnosis of these nodes as branchial cleft cysts obviously leads to unnecessary delay in treatment of the patient's HNSCC.

With few exceptions (e.g., T1 glottic SCC), CT or MR imaging are a necessary component of staging for head and neck cancers. While it is important to carefully evaluate all neck levels for nodal abnormalities, it is useful to be well versed in the predicted nodal drainage patterns so that, given a specific primary, the status of the most likely nodal targets can be clearly delineated (Box 2.3). When nodes at the expected regional metastasis locations exhibit borderline or equivocal characteristics, this should be reported as it may impact clinical management. Several features of nodal metastases should be communicated because they impact prognosis and management. The number of positive nodes should be clearly delineated, as the presence of multiple nodes often indicates the need for dual modality therapy for that side of the neck. The presence of ECS is a high-risk feature that warrants additional therapy. The presence of carotid encasement or invasion, or extension to or involvement of the skull base, or prevertebral space may render the patient inoperable and dramatically change treatment planning (Fig. 2.25).

Box 2.3. Most Frequently Affected Nodal Levels by Head and Neck Cancers

Location of primary cancers	Most frequently involved nodal stations
Floor of mouth and oral tongue	Ipsilateral levels I and II
Base of tongue and tonsils	Ipsilateral levels II and III and contralateral level II
Soft palate	Ipsilateral and contralateral level II, ipsilateral level III
Nasopharynx	Ipsilateral and contralateral levels I and V
Supraglottic larynx	Ipsilateral levels II and III and contralateral level II
Glottis	Ipsilateral levels II and III

HNSCC can present with metastatic lymph node(s) only and no identifiable primary on physical exam (unknown primary, T0). Again, a thorough knowledge of the lymphatic drainage pathways is extremely helpful, in this setting to identify the primary (Box 2.3). Primaries that are not detectable on physical exam are often identifiable on high-resolution CT or MR imaging; PET/CT can be additionally helpful in identifying very small primaries, often within lymphoid tissue. Findings on these studies can guide biopsies and result in a higher rate of primary identification, which allows for more focused therapy, rather that the broad radiation to Waldeyer's ring that is required for primaries that cannot be formally diagnosed. HPV and EBV testing of the nodal biopsy can also be helpful in directing the search for the primary. It is important to remember that, in rare cases, the primary is outside the head and neck region, requiring a whole-body work-up.

Management of the cervical nodes is warranted in patients staged N1 or greater or in patients stage N0 who carry a greater than 20 % risk of occult nodal metastasis (Box 2.4). Neck nodes can be treated with radiation or surgically by neck dissection (ND), which involves removal of the fibrofatty tissue of the neck in which the nodes reside. NDs can be therapeutic (for N+ disease) or prophylactic (for N0 disease) and are classified as radical, modified radical (comprehensive), selective, or extended. Box 2.5 summarizes the neck dissection terminology and definitions. Imaging in these cases would reveal deformity, loss of normal contour, and tissue planes in the neck along with absence of the removed nonlymphatic structures. Given the extent of surgery in extended ND, this is reserved for special cases with bulky nodal disease and/or extranodal spread and often requires some form of reconstruction.

Box 2.4. American Joint Committee on Cancer Nodal Staging and Features in Head and Neck Cancers

Stage N0	No nodes
Stage N1	Single, ipsilateral node $\leq$3 cm
Stage N2a	Single, ipsilateral node >3 cm and $\leq$6 cm
Stage N2b	Multiple, ipsilateral nodes $\leq$6 cm
Stage N2c	Bilateral, or contralateral nodes $\leq$6 cm
Stage N3	Nodal metastases >6 cm

Adjusted from American Joint Committee on Cancer Staging (2010) American Joint Committee on Cancer Staging manual. 7th edn. Springer

Box 2.5. Summary of Neck Dissection Terminology and Definitions

Type of neck dissection	Lymph node Levels removed	Nonlymphatic structures removed
Radical neck dissection (RND)	I, II, III, IV, V	Sternocleidomastoid muscle, internal jugular vein, spinal accessory nerve
Modified radical neck dissection (MRND) (includes functional neck dissection)	I, II, III, IV, V	Sparing at least 1 of the following: Sternocleidomastoid muscle, internal jugular vein, spinal accessory nerve
Extended neck dissection (END)	I, II, III, IV, V, and additional nodal stations	Structures removed in RND and additional structures such as carotid artery, overlying skin, strap and paraspinal muscles, platysma, and hypoglossal and vagus nerves

Many HNSCCs are treated with definitive radio- or chemoradiotherapy (C/RT). There is a substantial body of literature that supports observation if nodal metastatic disease is completely resolved on post-C/RT imaging. If post-C/RT imaging demonstrates persistent soft tissue concerning for residual malignancy, options include (1) empiric ND, which often yields no viable tumor; (2) directed needle biopsy, which has a high false-negative rate in the setting of microscopic residual disease; or (3) functional imaging with PET/CT, which has a very low false-negative rate but a high false-positive rate before 12 weeks posttreatment and thus can result in delayed ND in the setting of persistent disease. The approach in these cases varies by institution and surgeon (Box 2.6).

Box 2.6. Pearls and Pitfalls

- Know the landmarks for nodal stations and where different cancer subsites drain
- Comment on extracapsular extension, unilaterality/bilateral and contralateral, presence of nodes while describing nodal involvement in head and neck cancers, etc.
- Always remember to look for commonly missed nodal disease, e.g., retropharyngeal nodes
- Parotid lymph nodes represent the primary site for drainage of skin cancers from the scalp and skin cancers of the adjacent region. Skin cancers can also metastasize to level V and other superficial nodes, such as postauricular, facial, and occipital nodes
- Know about imaging appearance of HPV-related oral/oropharyngeal cancer-related cystic nodes (potential mimic for type 2 branchial cysts in young adults).

Further Reading

Som PM, Curtin HD, Mancuso AA (2000) Imaging-based nodal classification for evaluation of neck metastatic adenopathy. AJR Am J Roentgenol 174:837–844

Nasopharynx

3

Sugoto Mukherjee, David C. Shonka Jr., Max Wintermark, and Prashant Raghavan

3.1 Introduction

The nasopharynx is located at the crossroads between the skull base superiorly, the nasal cavity anteriorly, and the oropharynx inferiorly. Disease processes can spread to and from the nasopharynx through well-defined anatomic pathways. The focus of this chapter will be on nasopharyngeal carcinoma, with a brief overview of a few other lesions.

3.2 Anatomy and Physiology

The nasopharynx is located posterosuperior to the hard palate and contains adenoidal lymphoid tissue and an abundance of minor salivary glands. It is bound by the floor of the sphenoid sinus and clivus superiorly, by the nasal choanae anteriorly, by the posterosuperior surface of the soft palate anteroinferiorly, by the prevertebral musculature and clivus posteriorly, and by the parapharyngeal spaces laterally. It is continuous with the oropharynx inferiorly. The lateral wall of the nasopharynx includes the fossa of Rosenmüller, located lateral and posterior to the torus tubarius (the cartilaginous opening of Eustachian tube); the fossa is the most common site of primary nasopharyngeal carcinoma (NPC) (Figs. 3.1 and 3.2). Also along the lateral wall are the tensor and levator veli palatini muscles, separated by a small fat pad, the effacement of which is an early radiographic sign of NPC (Figs. 3.2 and 3.3).

NPCs have a high propensity to invade local structures; the extent of local invasion significantly impacts staging and prognosis. An important avenue for expansion is via the sinus of Morgagni, a potential gap in the pharyngobasilar fascia between the superior edge of the superior constrictor muscle and the skull base. This sinus allows NPC to enter the parapharyngeal and other adjacent deep extra mucosal spaces.

The lateral retropharyngeal nodes of Rouvier represent the first echelon nodes in nasopharyngeal lymphatic drainage. They are typically ventral to the prevertebral musculature and medial to the carotid sheath (Fig. 3.3).

P. Raghavan et al., *Manual of Head and Neck Imaging*,
DOI 10.1007/978-3-642-40377-4_3, © Springer-Verlag Berlin Heidelberg 2014

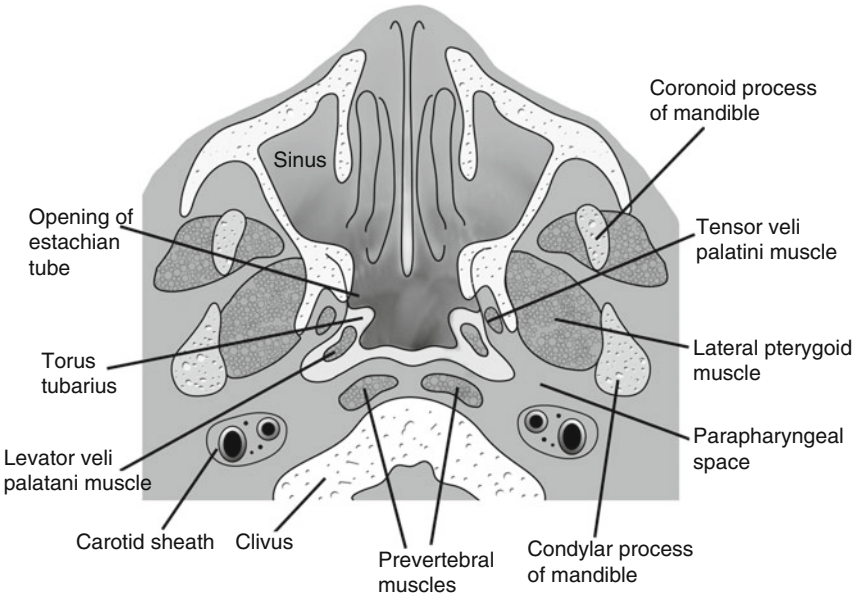

Fig. 3.1 Axial graphic of the nasopharynx showing the important landmarks. Just behind the elevated torus tubarius lies a fat-filled mucosal recess known as fossa of Rosenmüller. Evaluation of this recess is critical for identifying early nasopharyngeal carcinomas

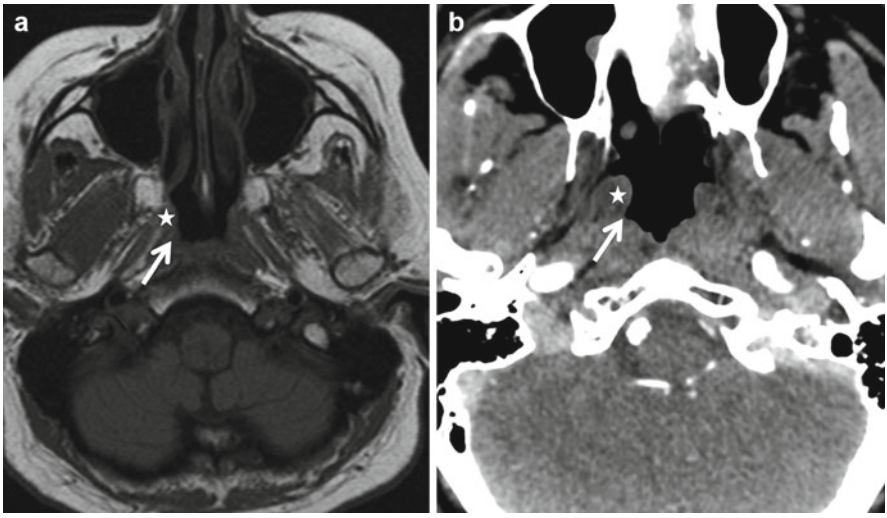

Fig. 3.2 Normal axial CT and MR of the nasopharynx. (**a**) (CT) and (**b**) (T1 MR) showing the relevant anatomy, consisting of torus tubarius (*white star*) and the fossa of Rosenmüller (*white arrow*) behind it. Effacement of the fat in this region with asymmetrical fullness is seen in early nasopharyngeal carcinomas

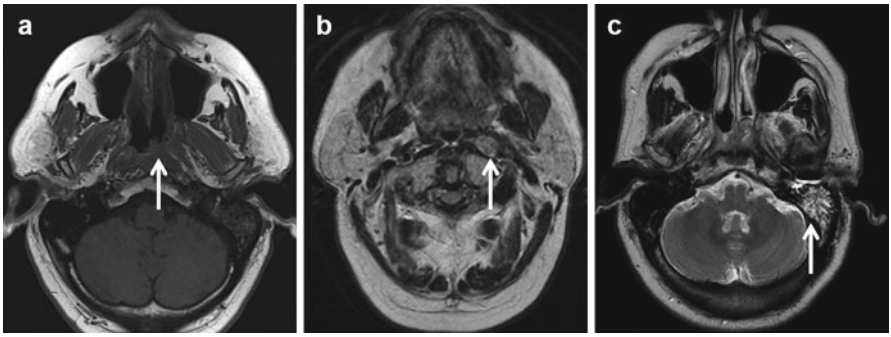

Fig. 3.3 Early nasopharyngeal carcinoma. Subtle effacement with fullness along the left lateral nasopharyngeal wall (*arrow* in **a**), along with pathological left retropharyngeal node (*arrow* in **b**), and left mastoid effusion (*arrow* in **c**), due to Eustachian tube dysfunction in this patient with biopsy-proven nasopharyngeal carcinoma

3.3 Pathology

The nasopharynx can be involved by congenital lesions such as notochord remnant (e.g., Thornwaldt's cyst) basal encephaloceles and epidermoids, dermoids, hamartomas, and neurenteric cysts. Lesions arising from the sella and the clivus can also extend inferiorly to involve the nasopharynx. Benign acquired lesions of the nasopharynx include squamous papillomas, antrochoanal polyps, and hemangiomas. Infectious and inflammatory changes of the nasopharynx occur secondary to involvement of the adenoids. Extension of infection can also occur from the sinuses or from osteomyelitis of the central skull base. Many of these aggressive infections are either fungal or granulomatous (e.g., tuberculosis) and are usually associated with immunocompromise; thus, they should be considered in patients with HIV, undergoing active immune suppression, (e.g., posttransplant, autoimmune disorders), being treated with chemotherapy, or with poorly controlled diabetes mellitus.

NPC represents the predominant malignancy in the nasopharynx, comprising almost 80 % of the known malignant lesions with lymphomas being the next most common. Rarer malignancies include nasopharyngeal melanomas, rhabdomyosarcomas, and minor salivary gland malignancies. The predominant benign tumor of the nasopharynx is the juvenile nasopharyngeal angiofibroma (JNA). These arise from the sphenopalatine foramen and frequently involve the nasopharynx (Fig. 3.4); they are discussed in the sinonasal chapter.

3.4 Imaging Evaluation

Nasopharyngeal lesions are usually evaluated using a combination of contrast-enhanced CT and MRI scans. Axial and coronal views are the mainstays. On CT scans, thin (0.5–1 mm) sections are usually obtained and reformatted in multiple planes to provide the requisite soft tissue and bony detail. MRI scans are usually

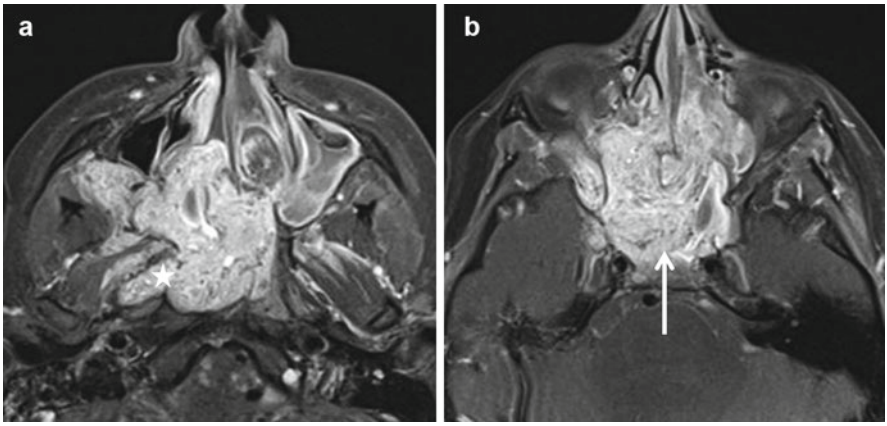

Fig. 3.4 Axial post-contrast MR images (**a**, **b**) demonstrate a large heterogeneously enhancing mass involving the right pterygopalatine fossa, sinonasal cavity, nasopharynx, and central skull base (*arrow* in **b**). Note the extension of the tumor laterally from the nasopharynx into the right fossa of Rosenmüller, torus tubarius, and Eustachian tube orifice (*white star* in **a**). This was a biopsy-proven juvenile angiofibroma

obtained with 3–4 mm sections and a field of view of approximately 10–15 cm. A combination of fat-suppressed pre- and post-contrast T1- and T2-weighted images, in axial, coronal, and sagittal planes is obtained for adequate evaluation. MRI is superior for evaluating locoregional extent of tumors, including skull base and intracranial extent. CT provides better definition of local bony destruction. FDG-PET can be helpful for detecting distant metastases and in the evaluation of therapeutic response posttreatment. Catheter angiography is sometime used in the evaluation of nasopharyngeal lesions such as JNAs.

3.5 Nasopharyngeal Carcinoma

NPC is unique when compared to squamous cell carcinomas elsewhere in the head and neck. It is more common in people from Southeast Asia, especially those from southern China. In the USA, NPC is more commonly seen in Americans of Chinese ancestry. The World Health Organization (WHO) has classified NPC into three broad histological patterns: Type 1, keratinizing squamous carcinoma; Type 2, non-keratinizing squamous carcinoma (with or without lymphoid stroma); and Type 3, undifferentiated carcinoma (with or without lymphoid stroma). Types 2 and 3 comprise the bulk of NPC. Nasopharyngeal carcinoma has a bimodal presentation: a subset of younger (15–30 years old) patients with Type 3 cancers (in patients from

Box 3.1. TNM Staging of Nasopharynx Cancer

Category	Description
T	Primary tumor
T1	Tumor confined to the nasopharynx, oropharynx and/or nasal cavity
T2	Tumor with parapharyngeal extension
T3	Tumor involves bony structures of skull base and/or paranasal sinuses
T4	Tumor with intracranial extension and/or involvement of cranial nerves, hypopharynx, or orbit, or with extension to the infratemporal fossa/masticator space
N	Regional lymph nodes
N1	Unilateral metastasis in cervical lymph nodes ≤6 cm in greatest dimension, above the supraclavicular fossa, and/or unilateral or bilateral retropharyngeal lymph nodes ≤6 cm in greatest dimension (midline nodes are considered ipsilateral nodes)
N2	Bilateral metastasis in cervical lymph nodes ≤6 cm in greatest dimension, above the supraclavicular fossa (midline nodes are considered ipsilateral nodes)
N3	Metastasis in a lymph node >6 cm and/or to the supraclavicular fossa (midline nodes are considered ipsilateral nodes)
N3a	>6 cm in dimension
N3b	Extension to the supraclavicular fossa
M	Distant metastasis
M0	No distant metastasis
M1	M1 Distant metastasis

Modified from Edge SB, Byrd DR, Compton CC et al (eds) (2010) AJCC cancer staging manual, 7th edn. Springer, New York

China and of Chinese descent) and a second subset of older patients (>40 years old) who typically have Type 1 and Type 2 cancers. A small group of aggressive, poorly differentiated NPC (pediatric NPC) occurs in adolescents, with a propensity for advanced locoregional and distant spread.

The TNM classification for nasopharyngeal carcinoma is summarized in Box 3.1. Involvement of parapharyngeal space (PPS) (T2 lesion) results in a worse prognosis as compared to involvement of the nasal cavity or oropharynx (Fig. 3.5). Other landmarks to be noted include osseous structures of the skull base and paranasal sinuses for T3 lesions (Fig. 3.6); intracranial extension and/or involvement of cranial nerves and orbits or with extension to the infratemporal fossa/masticator space, which are T4 lesions (Figs. 3.6 and 3.7).

The most common imaging appearance of NPC is a mass centered at the lateral nasopharyngeal recess (fossa of Rosenmüller) with deeper extension and associated cervical nodal disease (Fig. 3.8). Frequently, the tumor is identified extending

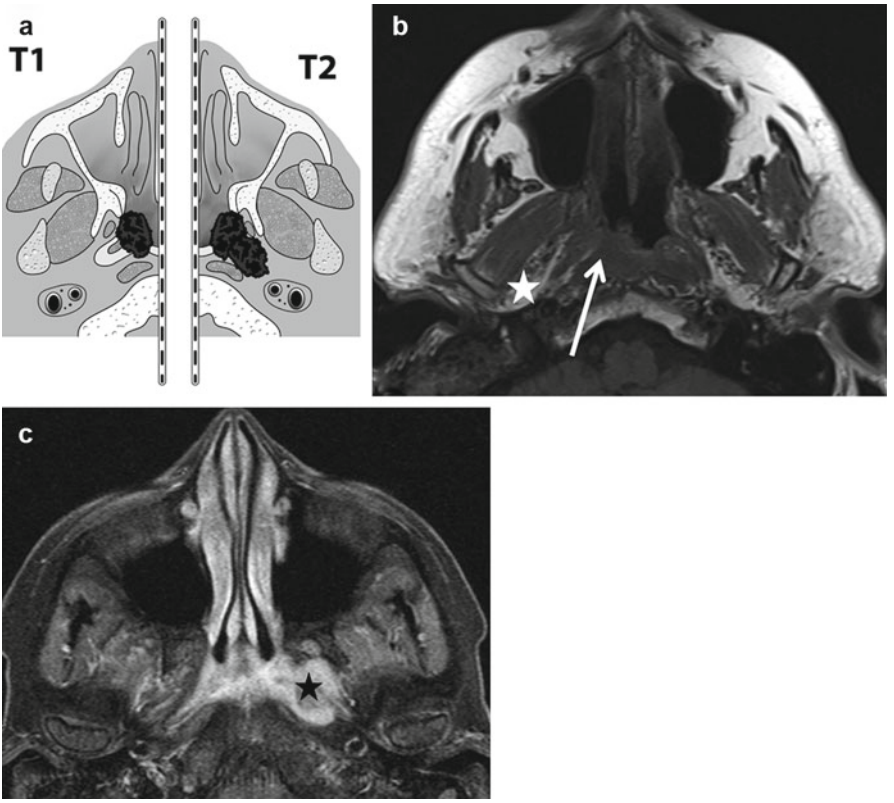

Fig. 3.5 Axial graphic (**a**) shows T1 and T2 lesions. T2 lesions extend into the adjacent parapharyngeal space. Axial T1 non-contrast MR elegantly demonstrates the subtle loss of T1 fat signal in the right lateral nasopharyngeal recess (*white arrow*), with preserved normal right parapharyngeal fat of a T1 tumor (*white star* in **b**). Axial T2 fat saturated sequences show a T2 tumor on the left (*black star* in **c**) with involvement of the left parapharyngeal recess

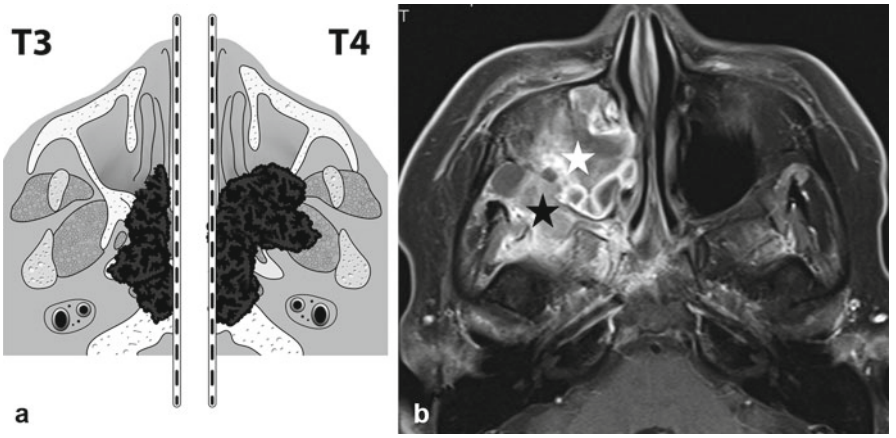

Fig. 3.6 Axial graphic (**a**) showing T3 (extension into the bony structures and paranasal sinuses) and T4 tumors (extension into masticator space). Axial T1 post-contrast sequences (**b**) demonstrates a T4 lesion on the right which involves both the right maxillary sinus (*white star*) and the right infratemporal masticator space and central skull base (*black star*)

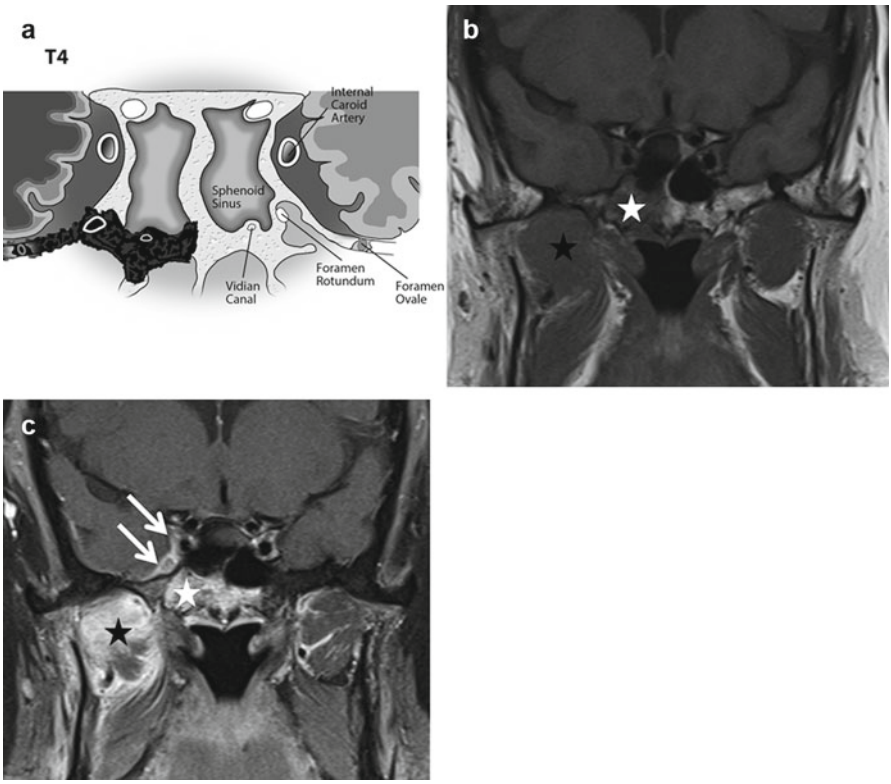

Fig. 3.7 Coronal graphic (**a**) demonstrating T4 lesion extending to the right central skull base and the foramen rotundum and foramen ovale with intracranial extension. Axial T1 pre- (**b**) and post-contrast sequences (**c**) show a T4 lesion in the right masticator space (*black star*) involving the central skull base/clivus (*white star*) with intracranial extension into the right cavernous sinus through the right foramen rotundum along the V2 division of the right trigeminal nerve (*white arrows*)

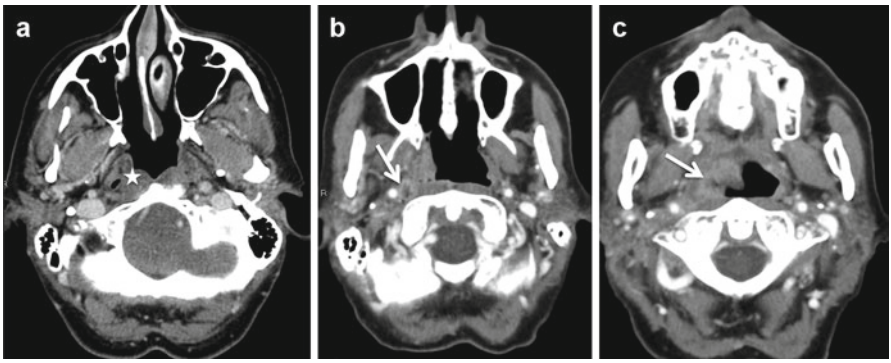

Fig. 3.8 Axial contrast-enhanced CT images (**a**, **b** and **c**) demonstrate the common imaging appearance of NPC as a mass centered at the lateral nasopharyngeal recess (fossa of Rosenmüller) (*star* in **a**) with pathological retropharyngeal adenopathy (*arrow* in **b**). Note the inferior extension along the right nasopharyngeal wall (*arrow* in **c**)

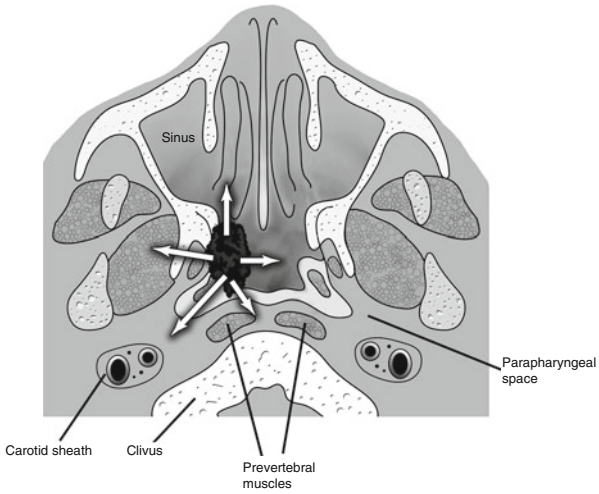

Fig. 3.9 An axial graphic showing the various pathways of spread of a NPC. These include anterior extension into the nasal cavity; lateral extension into the parapharyngeal, masticator, and carotid spaces; and posterior extension into the prevertebral space. NPC is also notorious for superior extension into the clivus and skull base with intracranial extension

Box 3.2. Nasopharynx carcinoma evaluation: Pearls and Pitfalls

- Always remember to look at the lateral nasopharyngeal recess (fossa of Rosenmüller) when confronted with a pathological retropharyngeal node in an adult to identify early NPCs
- Subtle effacement of fat within the fossa of Rosenmüller is one of the earliest signs and should be actively looked for in suspected nasopharyngeal carcinomas
- Know the various patterns of spread of NPCs to better stage the tumors
- Look for the replacement of normal fat within the marrows of the clivus and central skull base to avoid missing osseous invasion

beyond the nasopharynx into adjacent spaces. NPCs spread along these well-defined routes (Fig. 3.9), and care should be taken to evaluate these areas on imaging (Box 3.2):

1. Lateral spread is the most common via the sinus of Morgagni into the parapharyngeal space. This appears as effacement of the parapharyngeal fat triangle. From there, the tumor might extend into the masticator space and involve the pterygoid muscles which are associated with trismus, or into the carotid sheath (Fig. 3.10), impacting the great vessels and IX–XII cranial nerve functions. Invasion of the masticator space allows a potential pathway for intracranial perineural spread along the mandibular nerve (V3) through foramen ovale (Fig. 3.11). Retrograde perineural extension can occur all the way back to the pons (Fig. 3.11) with denervation atrophy changes in the muscles of mastication (Fig. 3.12).

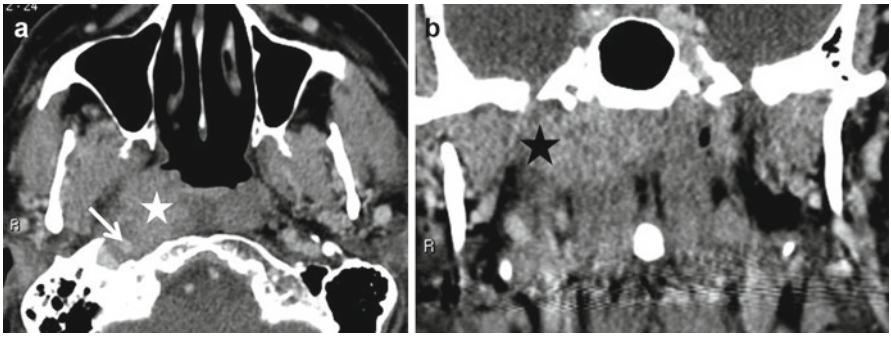

Fig. 3.10 Axial and coronal post-contrast CT images demonstrate a right nasopharyngeal mass (*white star*) encasing the right carotid artery (*white arrow* in **a**), with loss of fat all around the artery. Note the involvement of right parapharyngeal fat, well appreciated (*black star*) on the coronal (**b**) images

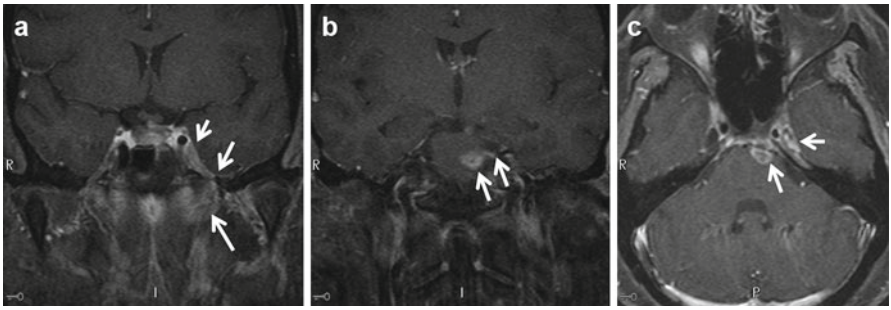

Fig. 3.11 Coronal (**a**, **b**) and axial (**c**) post-contrast T1 MR images show retrograde extension of nasopharyngeal cancer along the mandibular division of trigeminal nerve (V3) through the left foramen ovale and left cavernous sinus and all the way back to the pons (*white arrows*)

2. Anteriorly, the tumor can spread to the nasal cavity, pterygopalatine fossa, and the orbital apex (Fig. 3.13). Obliteration of the normal fat within the pterygopalatine fossa (Fig. 3.14) is an indication of infiltration, which allows for perineural spread into the cranial vault via the foramen rotundum along the maxillary nerve (V2), or into the orbit through the inferior orbital fissure and then into the cavernous sinus via the superior orbital fissure.
3. Superiorly, tumor can extend intracranially by multiple pathways: (a) by direct involvement of the skull base, (b) along the attachment of levator or tensor veli palatini, or (c) by direct invasion of the sphenoid sinus (Figs. 3.14 and 3.15). The more common route for intracranial extension is through the foramen ovale via perineural infiltration of the mandibular nerve (Fig. 3.14). This allows the tumor to access the intracranial segment of the mandibular nerve including the trigeminal (Gasserian) ganglion in Meckel's cave and the preganglionic segment of

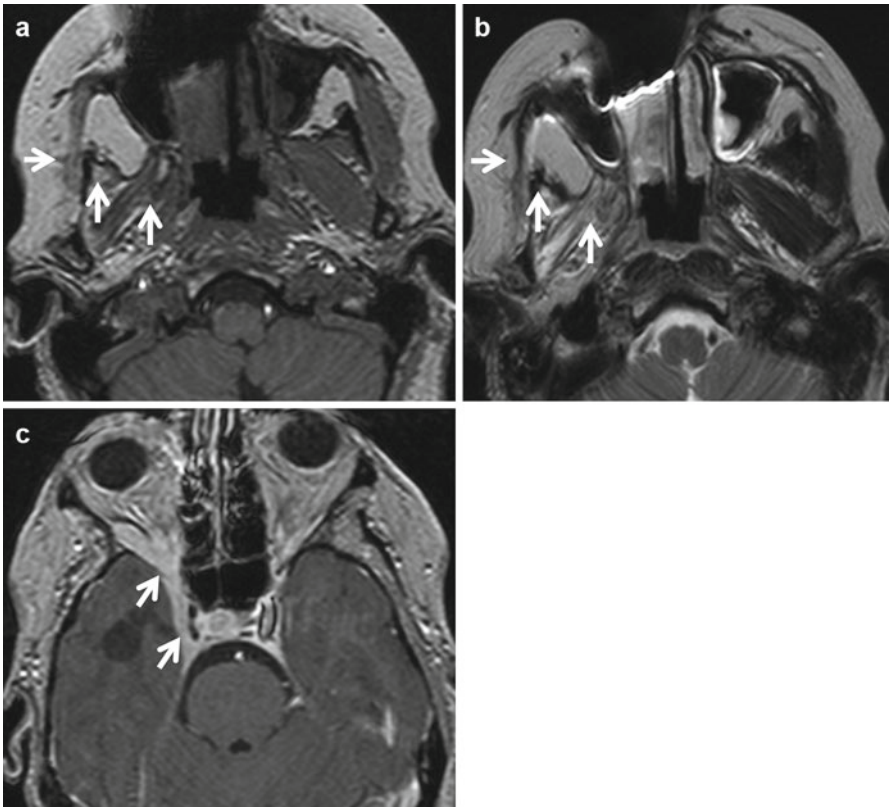

Fig. 3.12 Axial T1 (**a**), T2 (**b**), and post-contrast T1 images show changes of denervation fatty atrophy involving the right medial and lateral pterygoid muscles, masseter muscle, and temporalis muscles (*arrows* in **a** and **b**) secondary to persistent tumor in the right cavernous sinus and right orbital apex (*arrows* in **c**). Compare with the normal musculature on the left side

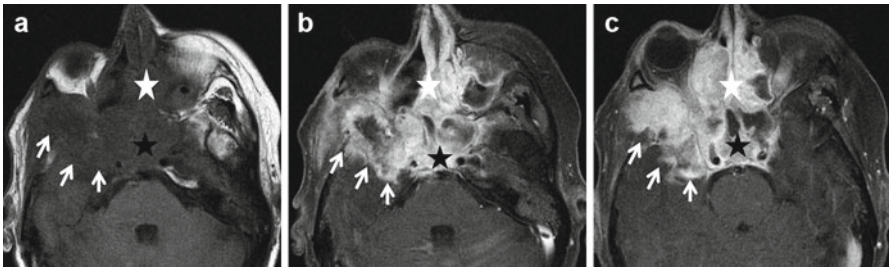

Fig. 3.13 Anterior and superior spread of large nasopharyngeal carcinoma is seen on these axial pre- (**a**) and post-contrast (**b**, **c**) sequences, involving the nasal cavity (*white star*), orbital apex, and inferior orbital fissure (*black star*). Note the extensive intracranial extension through the central skull base and right middle cranial fossa with brain invasion (*white arrows*). Note the shaggy irregular enhancement with T1 hypointensity of the right temporal lobe in image (**c**), consistent with brain parenchymal invasion

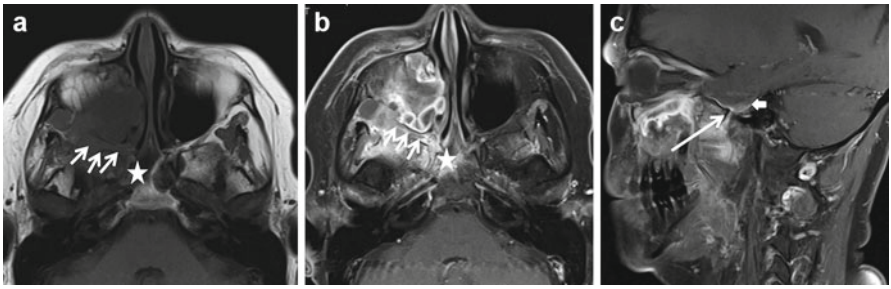

Fig. 3.14 Axial pre- (**a**) and post-contrast (**b**) and sagittal post-contrast (**c**) show superior tumor extension through direct sphenoid sinus and clival invasion (*white star*). The tumor involves the right infratemporal masticator space, right pterygopalatine fossa (*small white arrows*), and right foramen ovale (*long white arrow*) with abnormal dural enhancement in the right middle cranial fossa (*solid white arrow* in **c**). This likely represents intracranial extension of tumor through both direct extension and perineural extension

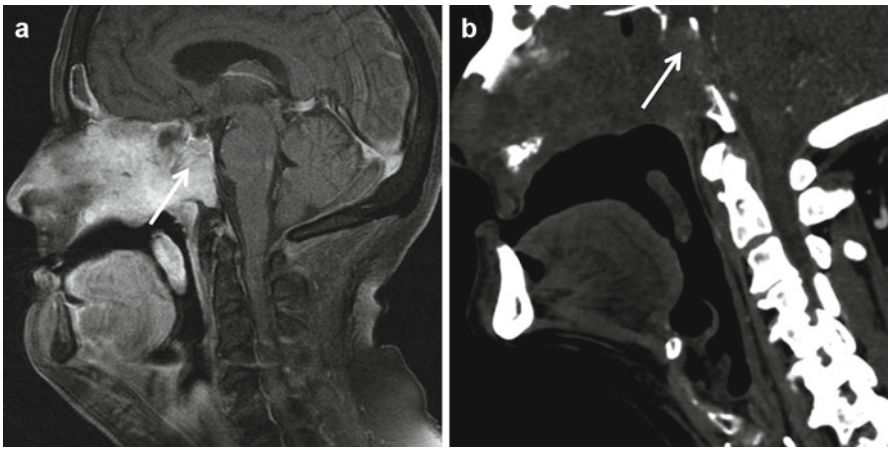

Fig. 3.15 Sagittal post-contrast MR (**a**) and CT images (**b**) demonstrate direct superior extension with abnormal enhancement on MR with complete bony destruction on CT (*white arrow*)

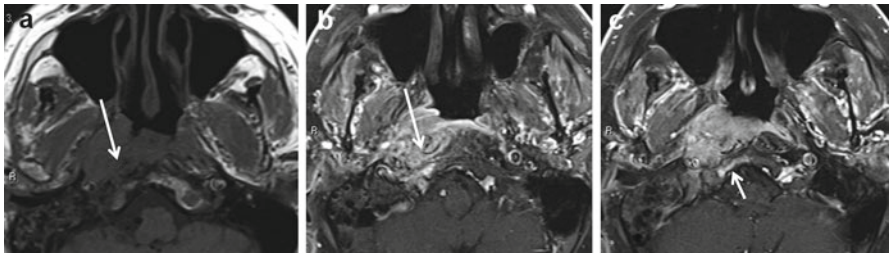

Fig. 3.16 Axial T1 pre- (**a**) and post-contrast MRs (**b**, **c**) demonstrate posterior extension of a right sides NPC into the right longus colli/prevertebral space (*arrows* in **a** and **b**) with abnormal enhancement in the right half of the clivus small white arrow in (**c**). Note the loss of normal marrow signal on the axial T1 (**a**)

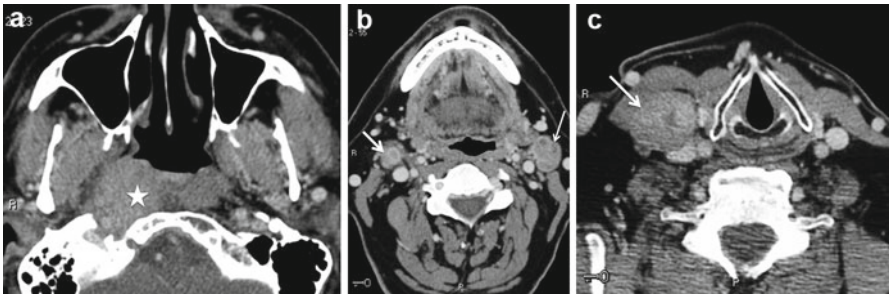

Fig. 3.17 Axial contrast-enhanced CT images in this patient with right-sided NPC (*star* in **a**) demonstrates bilateral level II (*arrows* in **b**) and large right level IV (*arrow* in **c**) nodal metastasis. Nodal metastasis is quite often the presenting symptom in NPC and usually involves the retropharyngeal lymph nodes and the deep jugular nodes (levels II, III, and IV)

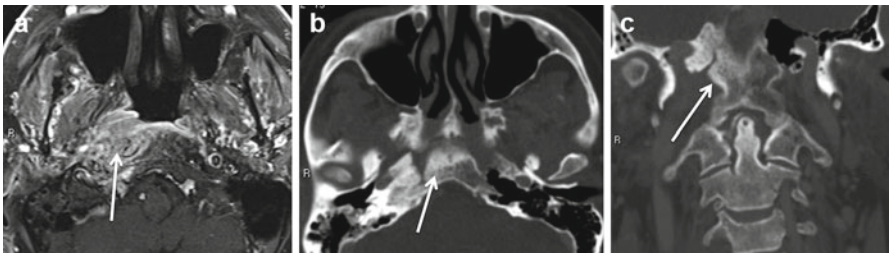

Fig. 3.18 Axial T1 post-contrast MR (**a**) and axial (**b**) and coronal (**c**) CT scans demonstrate clival invasion on the right (*arrows*), which is manifested as sclerosis on the CT. NPC involvement in the clivus and skull base can present with both lytic and sclerotic changes

trigeminal nerve (V). Another route involves infiltration of the foramen lacerum and petrous apex, which allows the tumor to crawl along the carotid canal into the cavernous sinus with potential involvement of cranial nerves III–VI. Inferiorly, the tumor can spread submucosally to involve the oropharynx.

4. Posteriorly, the tumor can involve the retropharyngeal and prevertebral spaces with obliteration of the fat stripe between the two (Fig. 3.16). Larger tumors can involve the vertebral column with extension into spinal canal. Invasion of the jugular and hypoglossal canals is infrequent.

Nodal metastasis is frequent in NPC and typically involves the retropharyngeal lymph nodes as well as the deep jugular nodes (levels II, III, and IV) (Fig. 3.17). Supraclavicular nodal metastasis increases the incidence of distant metastasis, which is most commonly in the bones (20 %), lungs (13 %), and liver (9 %).

The destructive bony changes are associated with both lytic and sclerotic changes on CT involving the posterior skull base, the clivus as well as the pterygoid plates (Fig. 3.18). Although MRI has several advantages over CT, CT is effective at evaluating the extent of bony erosion. It is often used for radiotherapy planning and is often performed as a combined study with FDG-PET imaging. The soft tissue extension is more clearly evident on MR imaging: within the lesion the appearance is hypo- to isointense to the adjacent muscle, and it can be seen replacing the normal fat within the clivus, sphenoid bone, and vertebral bodies. Involvement of the skull base with

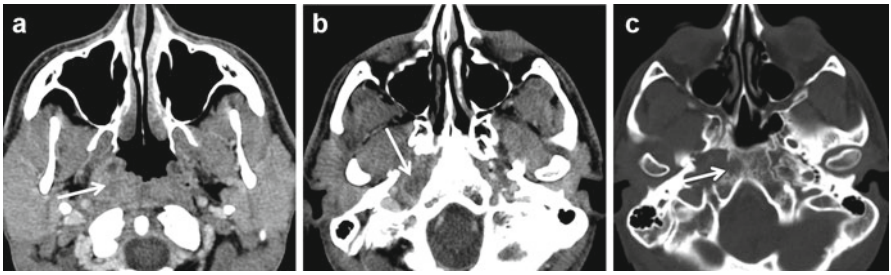

Fig. 3.19 A 45-year-old with right nasopharyngeal lesion (*arrows*) with erosive changes in the right half of clivus on axial CT images (**a**, **b** and **c**). Biopsy revealed a skull base osteomyelitis with positive Pseudomonas cultures. On CT, the initial diagnosis was a NPC

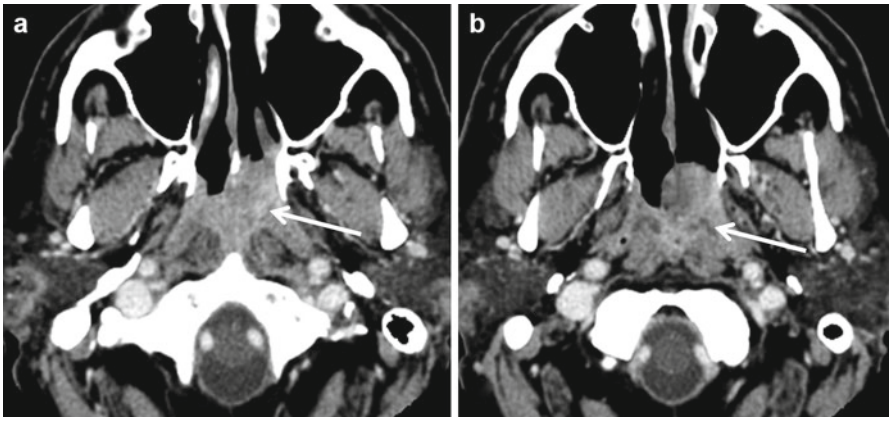

Fig. 3.20 Left-sided nasopharyngeal melanoma (*arrow* in **a** and **b**), mimicking a NPC. No unique imaging features are present to distinguish between the two on a CT scan

obliteration of the normal fat adjacent to the skull base represents direct spread. Perineural spread is seen as obliteration of neural fat pad adjacent to the neurovascular foramina, or neuroforaminal expansion with enlargement and/or abnormal enhancement of the nerve. The tumor itself is usually hyperintense and demonstrates heterogeneous/moderate enhancement. A combination of CT and MR can elegantly evaluate the extent of bony and soft tissue and skull base extent of the lesion. PET/CT is helpful in the detection of distant metastasis and can be used for posttreatment evaluation.

Other processes that can mimic NPC include lymphomas, aggressive infectious processes (e.g., skull base osteomyelitis (Fig. 3.19), nasopharyngeal melanomas (Fig. 3.20), minor salivary gland malignancies (e.g., adenoid cystic carcinoma), and pseudotumor of the nasopharyngeal mucosal space (Fig. 3.21)). Differentiating imaging features of lymphomas (as compared to NPC) include a more midline location, less osseous destruction, lower apparent diffusion coefficient values on diffusion-weighted imaging, and involvement of regional and distant nodes (Fig. 3.22).

NPCs are exquisitely radiosensitive tumors, and radiotherapy is the primary mode of treatment. A posttreatment scan is usually obtained for comparison with future scans. It is important for the radiologist to be able to distinguish granulation tissue

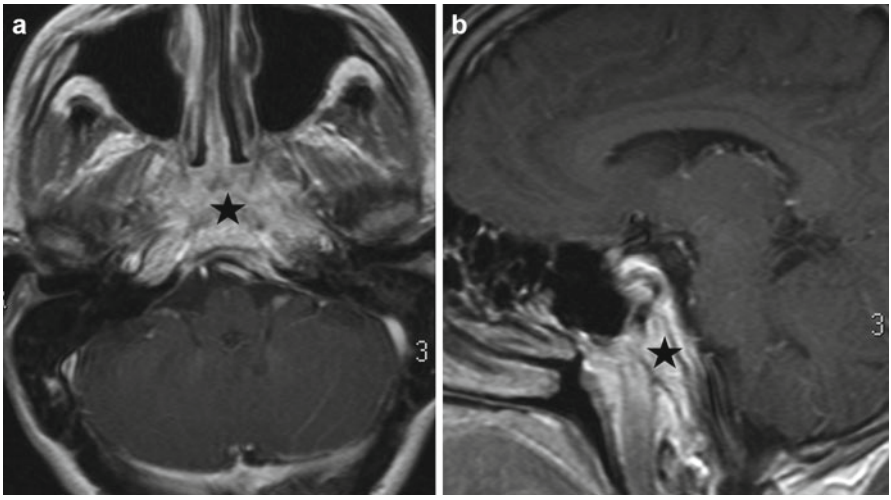

Fig. 3.21 Axial (**a**) and sagittal (**b**) post-contrast T1 images in a patient with biopsy-proven pseudotumor of the central skull base, involving the nasopharyngeal mucosal space, the clivus, and adjacent neck soft tissues (*black star*). These are difficult to distinguish from NPCs

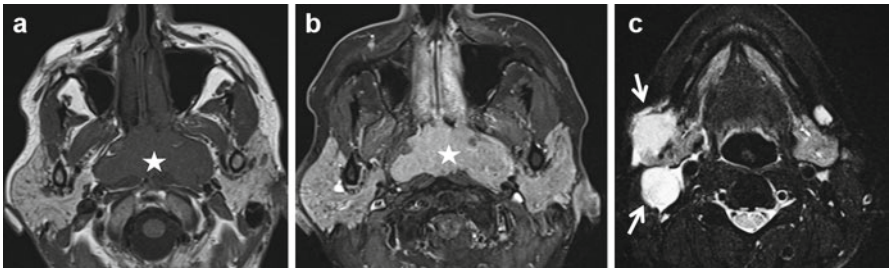

Fig. 3.22 Axial T1 (**a**), post-contrast (**b**), and T2 (**c**) images show a large, non-necrotic, midline mass (*star* in **a** and **b**) with homogenous enhancement. Note right level II non-necrotic pathological adenopathy (*arrows* in **c**), in this patient with non-Hodgkin's lymphoma

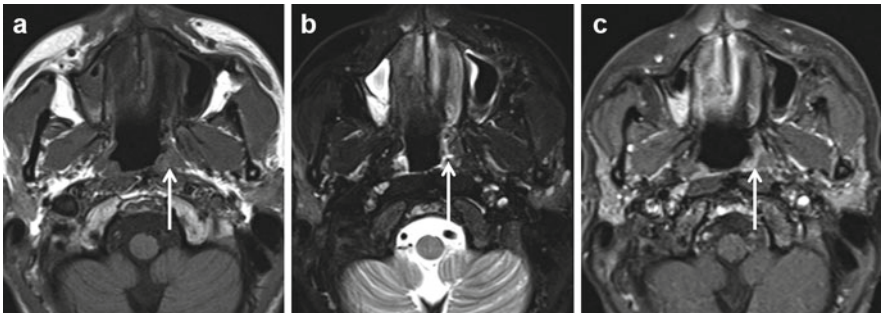

Fig. 3.23 Post treatment granulation tissue. Axial T1, (**a**) T2, (**b**) and T1 post-contrast (**c**) images in a treated left-sided NPC with heterogenous low T2 signal (*arrow* in **b**) and irregular minimal enhancement (*arrow* in **c**), consistent with granulation tissue

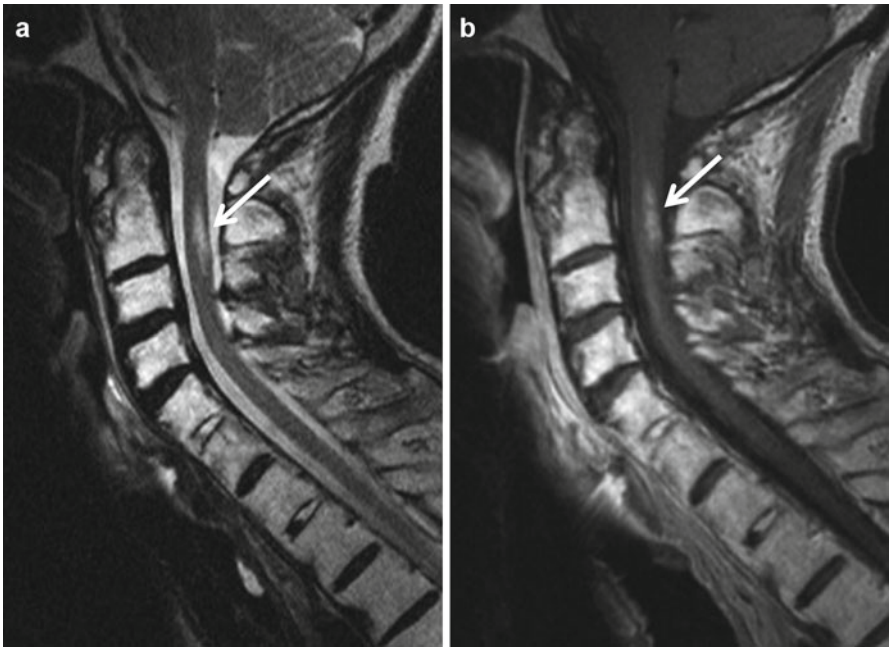

Fig. 3.24 Postradiation injury within the upper cervical cord (*arrows* in **a** and **b**) with increased T2 signal and abnormal enhancement on sagittal T2 (**a**) and post-contrast T1 images (**b**)

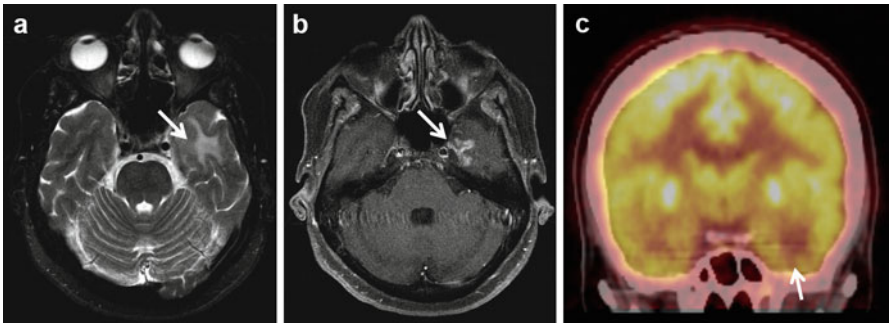

Fig. 3.25 Axial T2 (**a**), post-contrast (**b**), and coronal PET images show left temporal lobe cortical and white matter injury postradiation with edema (*arrow* in **a**), enhancement (*arrows* in **b**), and decreased uptake along the inferior left temporal lobe on PET (*arrow* in **c**)

from residual tumor, because early detection of locoregional failure is crucial for patient outcomes. Both MRI with contrast and FDG-PET/CT are viable options. Unlike recurrent cancer on MRI, mature granulation tissue does not demonstrate significant enhancement and also appears hypointense on T2-weighted sequences (Fig. 3.23). However, immature granulation tissue can demonstrate contrast enhancement and intermediate to high T2 signal, making it extremely challenging to

differentiate from residual/recurrent tumor; FDG-PET/CT imaging may be a better option in this scenario. Other signs of recurrence include a new pathological lymph node and new lesions elsewhere, such as meningeal or dural enhancement. FDG-PET/CT scans are extremely helpful in the diagnosis of persistent/recurrent locoregional disease, with limitations in the evaluation of skull base and intracranial tumor spread.

The radiologist should pay close attention to radiation-induced complications including osteoradionecrosis (ORN), temporal lobe injury, and radiation-induced tumors. ORN frequently occurs months after radiation and appears as a mixed pattern of sclerosis and lysis within the radiation portal. Sometimes, the associated inflammatory soft tissue simulates a recurrent cancer, especially in the skull base. The skull base, upper cervical spine, and mandible are most commonly involved with ORN (Fig. 3.24). Temporal lobe injury can be either unilateral or bilateral depending on the irradiated area and usually occurs years after the initial treatment. Changes can involve both the cortex (more common) and white matter and can demonstrate enhancement and necrosis as they progress (Fig. 3.25). MR spectroscopy or PET can be used in correctly diagnosing the challenging cases. Radiation-induced sarcomas and carcinomas can occur anywhere in the radiation field, generally 5–10 years after completion of radiation. On imaging, these appear as rapidly progressing heterogeneous destructive masses. Radiation-induced sarcomas often contain ossification or calcification.

3.5.1 Nasopharyngeal Lymphoma

Lymphomas of the nasopharynx are of the non-Hodgkin's type and affect older patients. They arise from the extranodal lymphoid tissue of the pharyngeal mucosal space. Nasopharyngeal lymphomas are generally bulky, diffuse, superficial but submucosal, non-necrotic masses that do not infiltrate the surrounding soft tissues (vs. NPC). On CT and MR, lymphomas demonstrate moderate, homogenous contrast enhancement. Additional suggestive imaging features that include enlarged non-necrotic lymph nodes in atypical drainage locations and the presence of extranodal lesions elsewhere. Frequently, the imaging appearance of lymphoma is very similar to that of NPC, and tissue sampling is required for diagnosis (Fig. 3.22).

3.5.2 Other Nasopharyngeal Lesions

3.5.2.1 Pseudolesions

Nasopharyngeal pseudomass results from asymmetry of the fossa of Rosenmüller due to incomplete aeration, inflammatory debris, or asymmetrical lymphoid tissue. In doubtful cases, the radiologist should evaluate for preservation of the adjacent soft tissue planes and sometimes recommend clinical examination by an otolaryngologist to confirm that the nasopharyngeal mucosa is indeed intact.

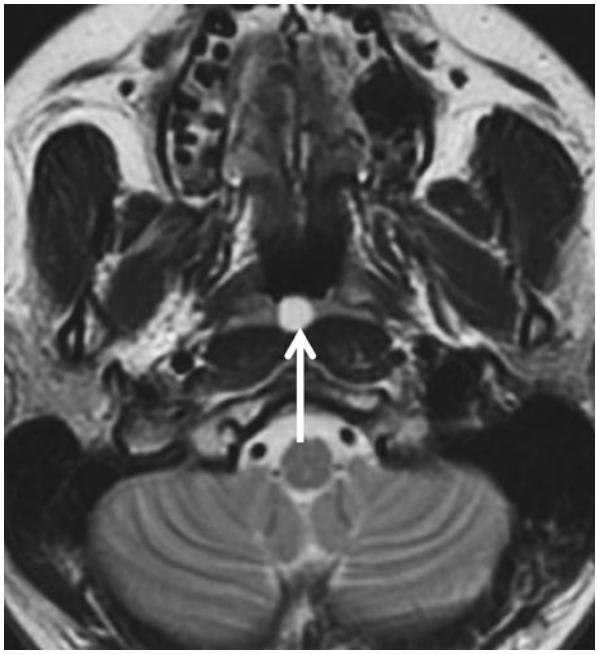

Fig. 3.26 Thornwaldt's cyst. Axial T2 image showing a Thornwaldt's cyst as midline T2 hyperintense lesion (*arrow*)

3.5.2.2 Congenital Lesions

Congenital abnormalities are associated with defects in skull base development. Basal encephaloceles result from a persistent craniopharyngeal canal which allows the pituitary gland to herniate inferiorly into the nasopharynx producing a midline nasopharyngeal polypoid mass. It is very important to evaluate the skull base on CT and MR studies in younger patients with polypoid nasopharyngeal lesions to avoid inappropriate biopsy or resection, which could result in hypopituitarism and/or CSF leak.

Thornwaldt's cysts result from adhesion of the pharyngeal mucosa to the notochord remnant and usually present as asymptomatic, incidentally discovered well-circumscribed, thin-walled midline cystic protrusions from the posterior nasopharyngeal wall. On CT, they may be hypo- or hyperdense depending on the cyst contents. Similarly on MR, although many of these demonstrate increased T1 signal, they can appear variable in signal intensity, depending on the protein content. Peripheral enhancement may be present (Fig. 3.26).

3.5.2.3 Infectious and Inflammatory Lesions

Hypertrophied adenoids appear as homogenous fullness that encroaches on the nasopharyngeal airway; the imaging signal is similar to the adjacent muscles on both CT and MRI. Enlarged adenoids can cause significant airway obstruction and lead to obstructive sleep apnea (OSA). A soft tissue lateral neck radiograph is adequate to document the enlarged adenoid in most cases (Fig. 3.27). Beyond the adenoids, the inflammatory and infectious processes of the nasopharyngeal mucosa can

Fig. 3.27 Enlarged adenoids. Large adenoids (*white star*) narrowing the airway (*black star*) in this young patient with OSA

be primary or secondary to adenoid or tonsil pathology. Other infectious sources include skull base osteomyelitis involving the clivus, sphenoid, bone, or the petrous apex, aggressive sinonasal infections can also spread to the skull base and involve the nasopharynx and adjacent structures (Fig. 3.19). The Eustachian tube and petrous apex represent a pathway for spread of infection from the middle ear and mastoid. Many of these changes are better seen with MR, especially given its ability to depict inflammation in the marrow of the skull base.

3.6 The Surgeon's Perspective

NPC is the most common malignant tumor of the nasopharynx. Nasopharyngeal carcinoma commonly present with an otherwise asymptomatic neck mass. Even small cancers can result in significant adenopathy. The bilateral lymphatic drainage pattern allows for cervical metastatic disease ipsilateral and contralateral to the primary tumor. The nasopharynx is also in close proximity to a number of cranial nerves (particularly CN III–VI), and patients who present with an unexplained neuropathy of one or more of these should have a careful endoscopic evaluation of the nasopharynx and imaging as clinically appropriate. A common complaint of patients with NPC at the time of initial presentation is unilateral hearing loss, which is

usually an ipsilateral conductive loss due to Eustachian tube obstruction and an associated middle ear effusion. Thus, in the absence of an established otologic diagnosis, any adult with a unilateral middle ear or mastoid effusion should undergo careful endoscopic examination of the nasopharynx for a mass lesion obstructing the Eustachian tube. Similarly, advanced NPC can be associated with neuropathies of CN IX–XII or trismus, and if these symptoms are otherwise unexplained, the nasopharynx should be evaluated carefully.

The first step in the evaluation of patients with signs or symptoms concerning for NPC is flexible or rigid endoscopic examination of the nasopharynx. The fossa of Rosenmüller is visualized posterior to the Eustachian tube orifice and torus tubarius; lesions identified in this location can often be biopsied in the office with rigid endoscopy and biopsy forceps after adequate topical anesthesia and decongestion. CT and MRI can be complementary for accurate staging of NPC; however, MRI is of particular importance for the ability to assess skull base invasion and cranial nerve involvement. Because this area is extremely difficult to access surgically and because negative margins are difficult to achieve, the primary treatment for NPC is radiation therapy; chemotherapy is added for more advanced disease. These tumors are often quite radiosensitive, and nonsurgical treatment has a high success rate. Other less common neoplastic processes of the nasopharynx include lymphoma and minor salivary gland tumors.

Benign processes involving the nasopharynx include adenoid hypertrophy, Thornwaldt's cyst, and mucus retention cysts. Cysts of the nasopharynx are common and are generally asymptomatic. Thornwaldt's cysts occur in the midline and are well circumscribed with a thin mucosal covering. Surgical treatment of Thornwaldt's cysts or mucus retention cysts of the nasopharynx is rarely necessary, but they can be associated with recurrent/chronic infections that are poorly treated with antibiotics, in which case resection or broad marsupialization is warranted.

Adenoid hypertrophy is a common problem in the pediatric population. Along with tonsillar hypertrophy, adenoid hypertrophy contributes to obstructive sleep apnea in children. It can also contribute to chronic Eustachian tube dysfunction and resulting chronic otitis media, hearing loss, and delayed speech development. In the pediatric population, adenoid hypertrophy is usually diagnosed clinically given its association with tonsillar hypertrophy and Eustachian tube dysfunction. Since endoscopic visualization of the nasopharynx is often difficult in a child in the clinic setting, adenoid hypertrophy is often diagnosed and surgically addressed while the child is anesthetized in the operating room in conjunction with a planned tonsillectomy for sleep apnea or pressure equalization tube insertion for chronic otitis media. Some practitioners use lateral neck plain films to evaluate adenoid hypertrophy in children, but variability is quite high. When adenoid hypertrophy is incidentally identified on imaging in an adult, HIV infection should be considered.

Further Reading

Chong VFH et al (1998) Carcinoma of the nasopharynx. Semin Ultrasound CT MR 19:449–462
Kim YI et al (2003) Nasopharyngeal carcinoma: post treatment changes of imaging findings. Am J Otolaryngol 24(4):224–230

Oral Cavity and Oropharynx

4

Sugoto Mukherjee, Brian M. Trotta, Mark J. Jameson, Max Wintermark, and Prashant Raghavan

4.1 Introduction

Squamous cell carcinomas (SCCs) represent the vast majority of lesions in the oral cavity and oropharynx (OC/OP). The imaging appearance of these cancers and their common pathways of spread are the focus of this chapter, and a few of the other lesions of the OC/OP are reviewed.

4.2 Anatomy

The oral cavity is separated from the sinonasal region by the hard and soft palate and from the oropharynx by the circumvallate papilla of the tongue, soft palate, and anterior tonsillar pillars (Fig. 4.1). The maxillary tuberosity serves as the radiographic border between the oral cavity and oropharynx.

From an imaging standpoint, the oral cavity can be subdivided into four distinct regions: (1) the oral mucosal surface, including the floor of mouth; (2) the root of the tongue; (3) the sublingual space; and (4) the submandibular space (Fig. 4.2). All the surfaces of the oral cavity structures are covered with keratinizing stratified squamous epithelium along with minor salivary gland rests.

The tongue is divided into an oral part (anterior two-thirds within the oral cavity), the base (posterior one-third within the oropharynx), and the root. The circumvallate papilla of the tongue separates the oral tongue from the base of tongue, which also includes the lingual tonsils. The tongue consists of extrinsic muscles (genioglossus, hyoglossus, styloglossus, and palatoglossus), which predominantly move the tongue body, and the intrinsic muscles (superior and inferior longitudinal, transverse, and vertical muscles), which alter tongue shape during swallowing and speech. The root of the tongue consists of the genioglossus-geniohyoid complex and the lingual septum; it extends from the extrinsic tongue muscles superiorly to the mylohyoid sling inferiorly (Fig. 4.3). The vasculature of the tongue consists of the lingual artery (second branch of external carotid) and corresponding lingual vein within the sublingual space. The hypoglossal nerve provides the motor supply and enters the

P. Raghavan et al., *Manual of Head and Neck Imaging*,
DOI 10.1007/978-3-642-40377-4_4, © Springer-Verlag Berlin Heidelberg 2014

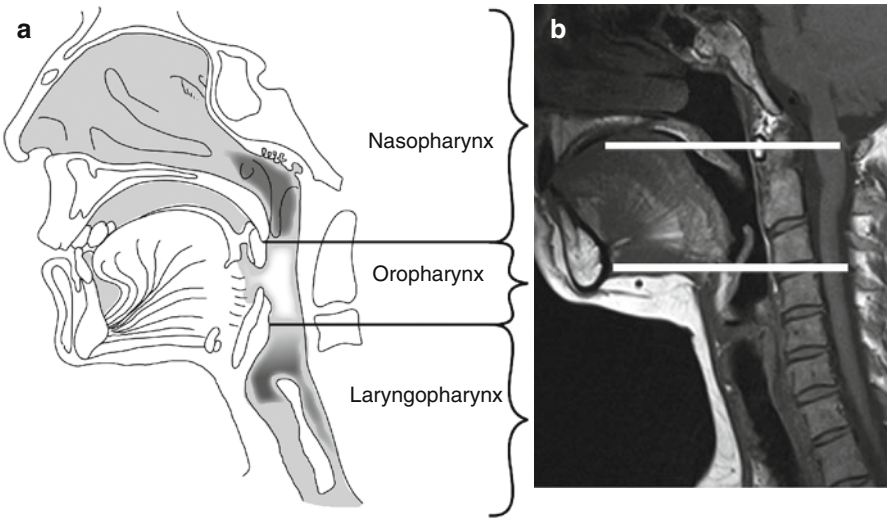

Fig. 4.1 Sagittal graphic (**a**) showing the anatomical landmarks of the oropharynx in between the nasopharynx and laryngopharynx. The oropharynx lies. It is the area in between the hard/soft palate and the pharyngo-epiglottic folds at the level of the inferior epiglottis, marked by the two *horizontal white lines* on the sagittal MR image (**b**)

sublingual space just lateral to the posterior hyoglossus. Sensory supply for the anterior two-thirds is by the lingual nerve, while the posterior one-thirds is supplied by branches from glossopharyngeal nerve (CN IX). The chorda tympani nerve, a branch from the facial nerve (CN VII), carries the taste fibers from the anterior two-thirds within the lingual nerve. All these run in the sublingual space (Fig. 4.2).

The floor of the mouth includes the mylohyoid muscle, the hyoglossus muscle, and the sublingual space, which is located between these two muscles (Fig. 4.2). The sublingual space is a horizontal horseshoe-shaped space deep to the oral tongue that communicates posteriorly within the submandibular space and the inferior parapharyngeal space. It lies in between the mylohyoid muscle inferolaterally and the genioglossus muscle medially. The contents of the sublingual space include the lingual artery and vein, distal segments of CNs IX and X, the lingual nerve containing sensory fibers from CN V3 (mandibular branch of trigeminal) as well as taste fibers through the chorda tympani from CN VII (facial), the sublingual gland and ducts, the deep portion of the submandibular gland, and the submandibular duct.

The submandibular space is a vertical horseshoe-shaped space, inferolateral to the mylohyoid muscle and superior to the hyoid bone. It communicates both with the inferior parapharyngeal space and the posterior aspect of the sublingual space. The submandibular space contains the larger superficial portion of the submandibular gland, anterior belly of the digastric, the facial vein and artery, the inferior loop of the hypoglossal nerve (CN XII), and the submental and submandibular lymph node groups (Fig. 4.2).

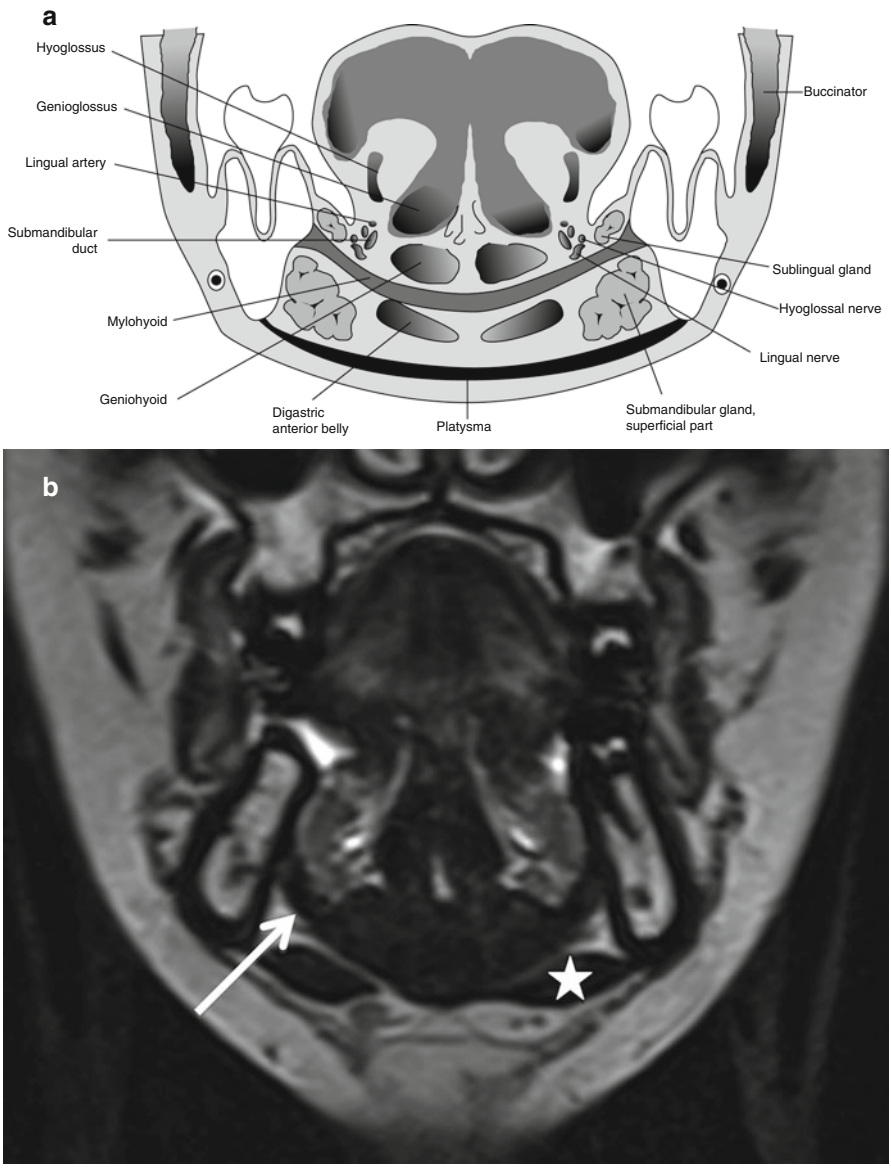

Fig. 4.2 Coronal graphic (**a**) shows the relationship of the sublingual and the submandibular spaces with the mylohyoid muscle. Also note the neurovascular pedicle (consisting of lingual artery and vein, lingual nerve) within the sublingual space. The hypoglossal nerve courses both in the posterior submandibular and sublingual spaces and runs along the surface of hyoglossus muscle before terminating within the tongue. Coronal MR (**b**) shows the mylohyoid muscle as a dark curvilinear sling (*arrow*)-like structure separating the upper sublingual and the inferior submandibular spaces. Also note the paired anterior belly of digastric below the mylohyoid (*star*)

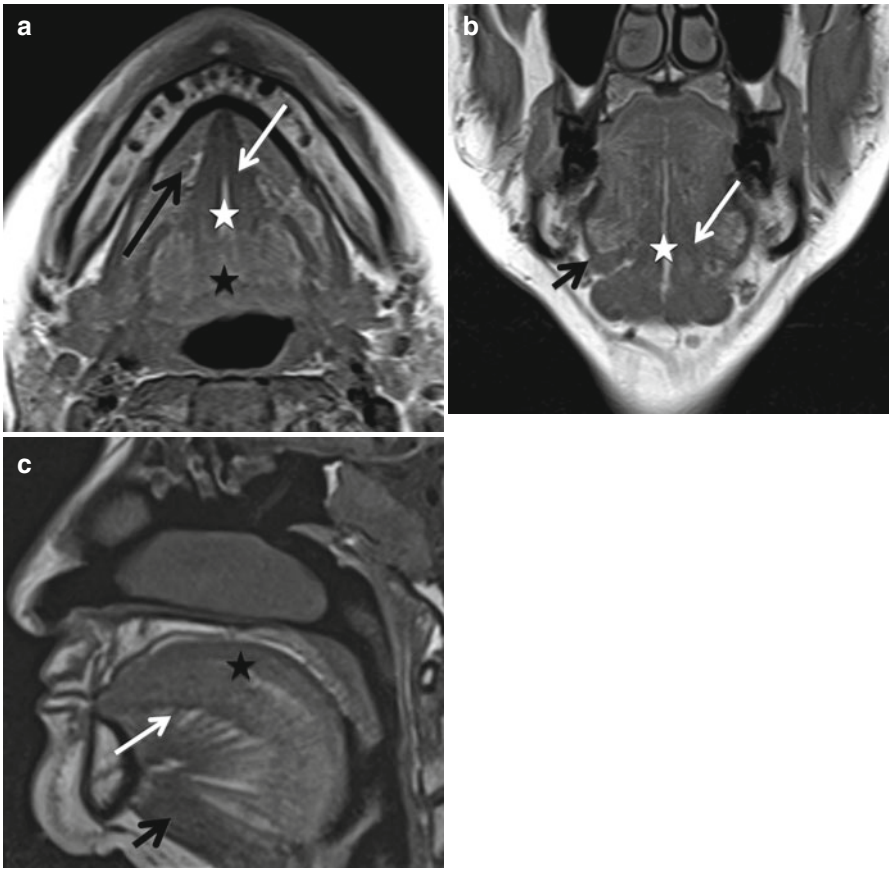

Fig. 4.3 Tongue anatomy is elegantly identified on MR images. On axial T1 (**a**), the lingual septum (with linear T1 hyperintense fat within it) (*white star*), the adjacent genioglossus muscles (*white arrow*), and the intrinsic muscles (*black star*) which are posterior to it. Also note the sublingual spaces lateral to the genioglossus (*long black arrow*). Coronal T1 (**b**) images also show the lingual septum (*white star*), genioglossus as well as the mylohyoid (*short black arrow*). Finally, sagittal T1 (**c**) images show the characteristic fan-like shape of the genioglossus (*white arrow*) along with the geniohyoid and mylohyoid muscles inferiorly (*short black arrow*). The intrinsic tongue muscles are superior to the genioglossus on this sagittal image

The oropharynx includes the posterior third of tongue (base of tongue), the vallecula, the palatine tonsils and tonsillar fossa, the soft palate, the uvula, and the posterior and lateral pharyngeal walls from the soft palate superiorly to the pharyngo-epiglottic folds inferiorly (Fig. 4.1).

Regional nodal metastasis from oral cavity and base of tongue cancers commonly occurs to the submental, submandibular, and upper and mid-cervical lymph chains (levels I–III); for tonsil and pharyngeal wall cancers, regional metastases rarely involve level I.

4.3 Squamous Cell Carcinoma

The most commonly recognized risk factors for SCCs in the head and neck include long-term overuse of alcohol and tobacco. Recently, human papillomavirus (HPV) has been shown to be responsible for the majority of new oropharyngeal SCCs, with HPV-16 accounting for 90–95 % of such cases. Radiologists should be aware of a unique presentation of HPV-associated oropharyngeal cancers, which have an increased tendency to present with large cystic/necrotic level IIa nodal metastases. Given that they have a tendency to occur in younger nonsmokers, these can easily be misinterpreted as second branchial cleft cysts, resulting in missed diagnosis and/or delayed treatment (Fig. 4.4). While second branchial cleft cysts also present as level IIa cystic lesions, they typically present in the first two decades and, unless infected, appear smooth, well circumscribed, and unilocular without any stranding of surrounding structures and without thick or nodular walls. Thus, the presence of an underlying head and neck primary cancer should always be excluded in a young adult with a newly diagnosed level II neck mass.

4.3.1 Radiographic Staging

As with other head and neck SCCs, OC/OP SCCs are staged using the TNM classification system (Boxes 4.1a and 4.1b). Although much of the staging is accomplished

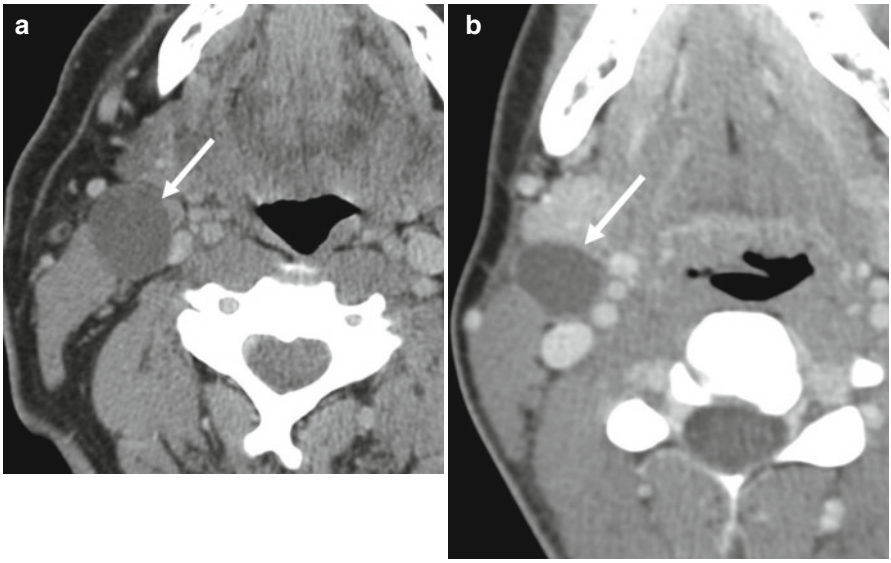

Fig. 4.4 Axial contrast-enhanced CT images from two different patients demonstrate an enlarged fluid density cystic lymph node in a patient with known tonsillar SCC and (*arrow* in **a**) a thin-walled fluid density lesion in the same location in a different patient (*arrow* in **b**) which was found to represent a type II branchial cleft cyst

Box 4.1a. TNM Classification of Squamous Cell Carcinomas of the Oral Cavity and Oropharynx[a]

Disease category	Defining characteristics
	Primary tumor of oral cavity
Tx	Primary tumor cannot be assessed
T0	No evidence of primary tumor is seen
Tis	Primary tumor is carcinoma in situ
T1	Primary carcinoma has a maximal diameter of 2 cm or less
T2	Primary carcinoma has a maximal diameter of 2–4 cm
T3	Primary carcinoma has a maximal diameter of more than 4 cm
T4a	
Lip	Primary tumor invades through cortical bone or involves inferior alveolar nerve, floor of mouth, skin of chin or nose
Oral cavity	Primary tumor invades through cortical bone or involves extrinsic tongue muscles, maxillary sinus, skin of face
T4b	Primary tumor involves masticator space, pterygoid plates, skull base, internal carotid artery
	Primary tumor of oropharynx
Tx	Primary tumor cannot be assessed
T0	No evidence of primary tumor is seen
T1	Primary carcinoma has a maximal diameter of 2 cm or less
T2	Primary carcinoma has a maximal diameter of 2–4 cm
T3	Primary carcinoma has a maximal diameter of more than 4 cm
T4a	Primary tumor involves the larynx, extrinsic muscles of the tongue, medial pterygoid, hard palate, or mandible
T4b	Primary tumor involves the lateral pterygoid muscle, pterygoid plates, lateral nasopharynx, skull base, carotid artery

Modified from Edge SB, Byrd DR, Compton CC et al (eds) (2010) AJCC cancer staging manual, 7th edn. Springer, New York

[a]N and M staging have been covered in Chap. 2

by clinical exam and endoscopy, final staging is heavily dependent upon cross-sectional imaging. Issues of key importance to staging that are clarified or determined by imaging include extent of the primary lesion, invasion of nearby bone, neural and/or vascular involvement, and cervical nodal status, including subclinical cervical nodal metastases and extracapsular spread (ECS) beyond involved nodes. In this process, it is crucial to note involvement of structures that raise concern for resectability (e.g., carotid encasement, pterygoid involvement, skull-base involvement).

4.3.2 Routes of Spread

The general routes of spread of OC/OP SCC are the same for all subsites: (a) direct extension over mucosal surfaces, muscle, and bone; (b) lymphatic drainage

Box 4.1b. Oral Cavity and Oropharyngeal Squamous Cell Carcinoma Stage Grouping Based on TNM Classification

Cancer stage	T category	N category	M category
0	Tis	N0	M0
I	T1	N0	M0
II	T2	N0	M0
III	T3	N0	M0
III	T1 to T3	N1	M0
IVA	T4a	N0 or N1	M0
	T1 to T4a	N2	M0
IVB	T4b	Any N	M0
	Any T	N3	M0
IVC	Any T	Any N	M1

Modified from Edge SB, Byrd DR, Compton CC et al (eds) (2010) AJCC cancer staging manual, 7th ed. Springer, New York

pathways; and (c) extension along neurovascular bundles. However, the particular subsite of involvement of the oral cavity or oropharynx may dictate routine assessment of certain anatomic structures. The relevant imaging anatomy and the patterns of spread for each primary site are summarized in the Boxes 4.2a and 4.2b.

Box 4.2a. Oral Cavity Subsites

Oral cavity subsite	Imaging anatomy	Imaging patterns of tumor spread
Lip	Most often arises along vermilion border	Laterally: Involvement of skin
	Only infiltrative lesions require imaging	Deep: Involvement of orbicularis oris muscle or osseous involvement of buccal surface of maxillary or mandibular ridge
		Lymphatics: Primarily level I and II lymph nodes
Buccal mucosa and gingiva	Buccal mucosa covers lips and cheeks and is continuous with the buccal aspect of the gingiva of the maxillary and mandibular alveolar ridge	Superficial spread most common along buccinator muscle
	Most commonly occurs on lateral walls	Deep: Osseous involvement of maxilla or mandible
	Continuous with retromolar trigone	Posteriorly: To retromolar trigone and pterygomandibular raphe (see below)
		Superiorly: Paranasal sinuses
		Lymphatics: Primarily level I and II lymph nodes

Oral cavity subsite	Imaging anatomy	Imaging patterns of tumor spread
Retromolar trigone	Triangular-shaped mucosa behind last mandibular molar	Anteriorly: Along alveolar ridge
	Either primary site of SCCA or secondarily involved	Posteriorly: Along masticator space, mandibular ramus, and perineural spread along V3
	Pterygomandibular raphe – fascial band extending from posterior mylohyoid ridge to medial pterygoid hamulus	Superiorly: Along pterygomandibular raphe to medial pterygoid plate
	Provides pathway for tumor spread between buccal, masticator space, and floor of mouth.	Inferiorly: Along pterygomandibular raphe and mylohyoid ridge and muscle.
	Medial pterygoid involvement is heralded clinically by trismus	Also osseous involvement of mandible and perineural spread along inferior alveolar nerve
Floor of the mouth	Crescent-shaped mucosa supported by the mylohyoid, which separates it from the submandibular space	Inferior: Along mylohyoid muscle or along neurovascular bundles
	Divided in half by the lingual frenulum	Anterior and lateral: To gingiva and mandible. Assess for crossing of midline
	Posterior border is tongue and anterior tonsillar pillars	Posteriorly: Along hyoglossus muscle
		Lymphatics: Primarily levels I and II lymph nodes can be bilateral for lesions approaching midline
Oral tongue	Consists of anterior and middle thirds of tongue	Laterally: Along gingiva and mandible. Assess for crossing of midline
	Mostly occur along lateral and ventral surfaces	Inferiorly: Along floor of mouth, intrinsic and extrinsic muscles of the tongue and along neurovascular bundles
		Posteriorly: Along base of tongue and intrinsic/extrinsic muscles of the tongue
		Lymphatics: Primarily levels I and II but regional spread to levels III and IV can occur without involvement of higher levels
Hard palate	Primary SCC of the hard palate is rare	Lateral: Maxillary alveolar ridge
	Most commonly represents direct extension	Superiorly: Into nasal cavity and maxillary sinuses. Perineural spread along greater and lesser palatine nerves which provide pathway to pterygopalatine fossa

Box 4.2b. Oropharyngeal Subsites

Oropharynx subsite	Imaging anatomy	Imaging patterns of tumor spread
Base of the tongue	Extends from circumvallate papillae anteriorly to the vallecula inferiorly	Laterally: Along tonsillar pillars. Assess for crossing of midline Anteriorly: To the sublingual space and oral tongue Posteriorly/Inferiorly: Along intrinsic muscles of the tongue. Under valleculae and into preepiglottic space Lymphatics: Primarily to level II, III, and IV, tongue base has bilateral nodal drainage
Tonsils	Anterior and posterior tonsillar pillars or palatine tonsils Most arise in anterior tonsillar pillar	Superiorly: Along palatoglossus muscle to hard and soft palates. Along tensor and levator palatini muscles and pterygoid muscles. Invasion of nasopharynx and skull base Anteriorly: Along superior constrictor muscles to pterygomandibular raphe (may then involve skull base) Posteriorly: Retropharyngeal or carotid space Inferiorly: Base of tongue Osseous involvement: Primarily pterygoid plates and maxilla Lymphatics: Primarily levels II and III, contralateral involvement higher when HPV related

Evaluation of direct extension is most effectively accomplished by direct visualization, particularly in the case of superficial lesions, but the overall extent of the a tumor is often underestimated by physical examination due to submucosal extension or direct invasion of adjacent structures. The radiologist report should describe in detail the entire extent of the tumor and address all the issues relevant to treatment planning.

4.3.3 Radiographic Evaluation

The key concepts in evaluating oral cavity and oropharyngeal SCCs (Box 4.3) are:

1. *Primary subsite evaluation*: One of the most important concepts in OC/OP carcinoma imaging is to correctly localize the tumor subsite (Fig. 4.5). This helps in accurate description of local tumor extension as well as spread beyond the subsite, e.g., into the adjacent masticator and/or buccal spaces and deep neck structures. Specific features to look for at different subsites include:
   (a) *Lip carcinoma*: Evaluate the depth of soft tissue invasion and look for underlying bony erosion usually along the buccal aspect of maxillary or mandibular ridge (Fig. 4.6). Cases involving the mandible may warrant MRI to assess the inferior alveolar nerve if clinically important.

Box 4.3 Key Imaging Concepts in Oral Cavity/Oropharynx Cancer Imaging

T4 lesions	Know the discriminators for T4 lesions: invasion through cortical bone or involvement of extrinsic tongue muscles, maxillary sinus, facial skin, pterygoid muscles, nasopharynx, skull base, carotid artery, soft tissues of the neck, prevertebral muscles, or larynx
Preepiglottic space	Primary vallecular and BOT tumors can invade the preepiglottic space altering management
Nodal disease	Unilateral or bilateral, size and extracapsular spread
Midline extension	Describe extension of tumor across midline for tongue/BOT/FOM lesions
Spread	Know pathways of tumor spread (see Boxes 4.2a and 4.2b)
Mandible	Mandibular periosteal versus frank cortical involvement
Airway issues	Note should be made of possible airway compromise in larger lesions which would require direct communication and immediate intervention

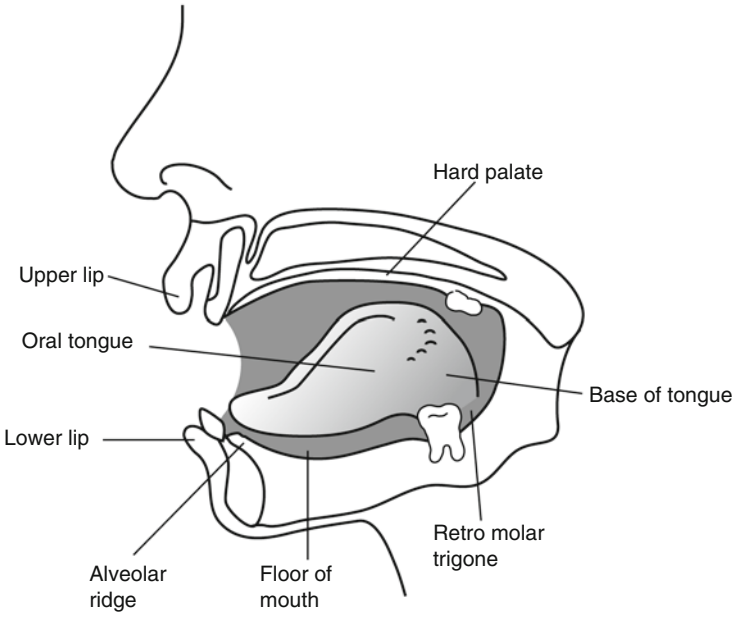

Fig. 4.5 Graphic showing the various subsites of the oral cavity and the oropharynx (base of tongue). Squamous cell carcinomas can arise from any of these subsites. The subsite origin predicts the pattern of cancer spread and consequently affects management and prognosis of these cancers

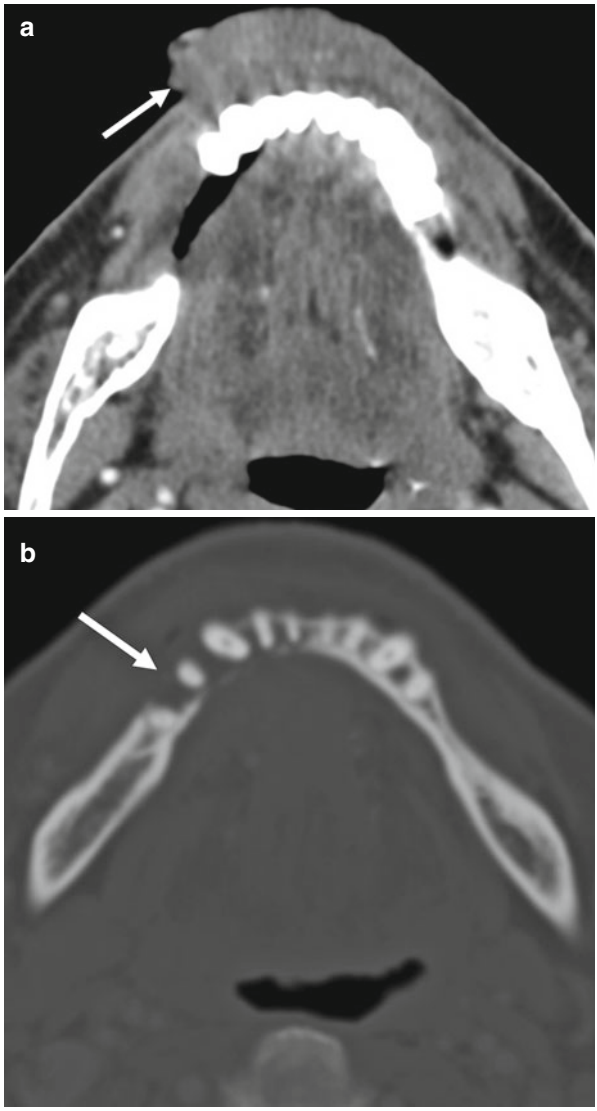

Fig. 4.6 Axial contrast-enhanced CT images in soft tissue and bone windows demonstrate (**a**) a lobulated soft tissue mass arising from the lip which was found to represent SCC and (**b**) cortical destruction of the mandible with loss of normal marrow trabeculae

(b) *Buccal carcinoma*: The primary considerations here are submucosal extension and osseous involvement (Fig. 4.7). On CT, a puffed cheek maneuver may help in identifying smaller lesions (Fig. 4.8).

(c) *Retromolar trigone* (*RMT*) *carcinoma*: Key features to describe are submucosal spread, osseous involvement, and perineural invasion. Often the extent of RMT SCC cannot be determined clinically (Fig. 4.9), regardless of whether the SCC arose primarily from the RMT or represents regional extension of a nearby lesion (Fig. 4.10). Extension along the pterygomandibular raphe allows access to the floor of the mouth.

Fig. 4.7 Axial contrast-enhanced CT image demonstrates a soft tissue mass arising from the left buccal mucosa and extending into the adjacent subcutaneous fat, consistent with SCC

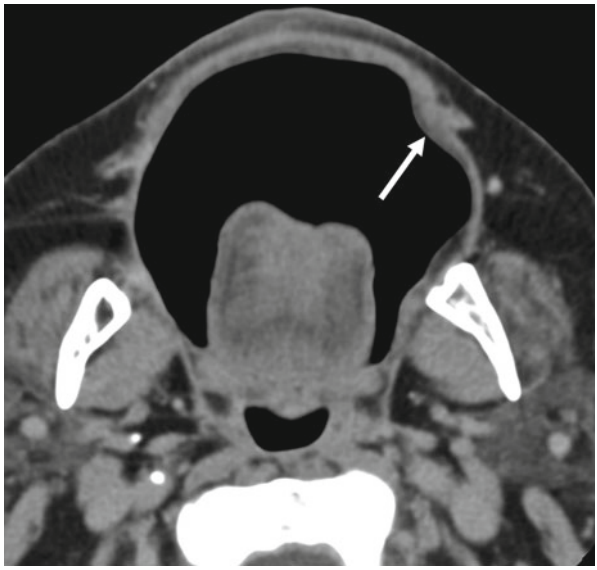

Fig. 4.8 Axial CT image using the "puffed cheek" technique to identify a small SCC arising from the left buccal mucosa (*arrow*). The scan is performed with the patient holding their breath and puffing their cheeks out to increase conspicuity of small lesions

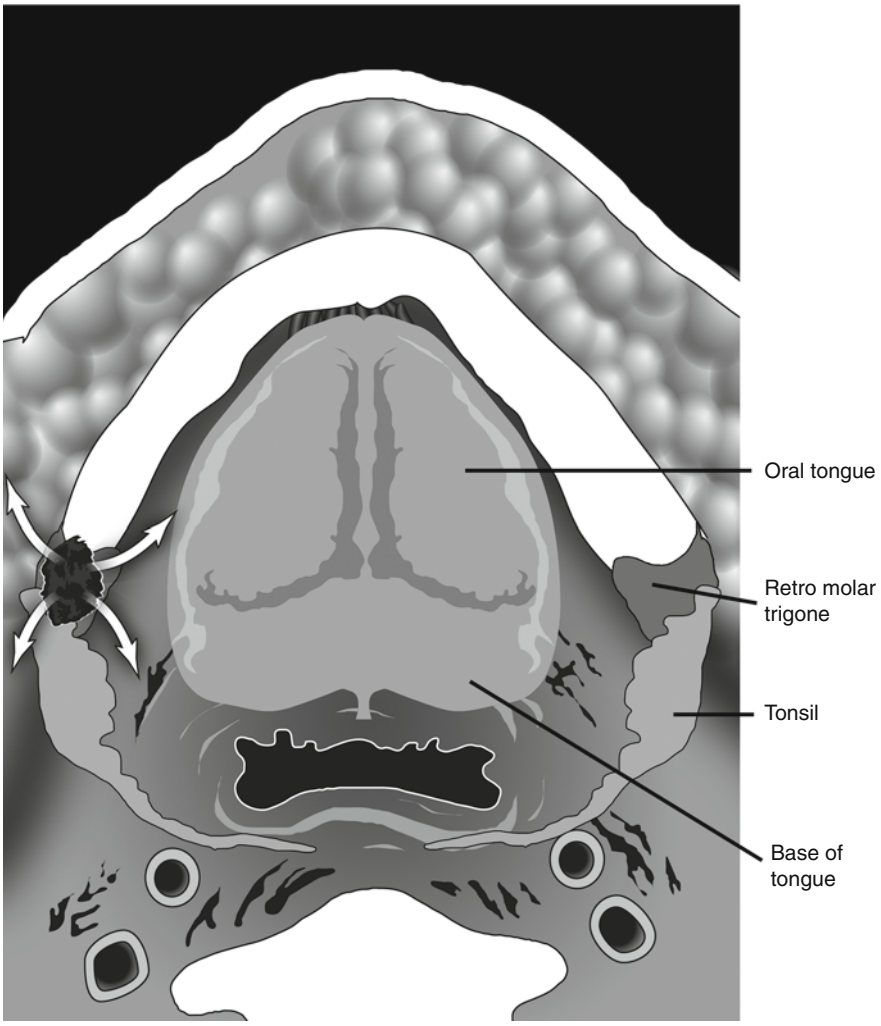

Fig. 4.9 Axial graphic showing normal retromolar trigone (see normal left RMT) situated at the crossroads between oral cavity, oropharynx, masticator space, and buccal space. Consequently, tumor arising in this region, (see right RMT), can spread to all these regions (*white arrows*)

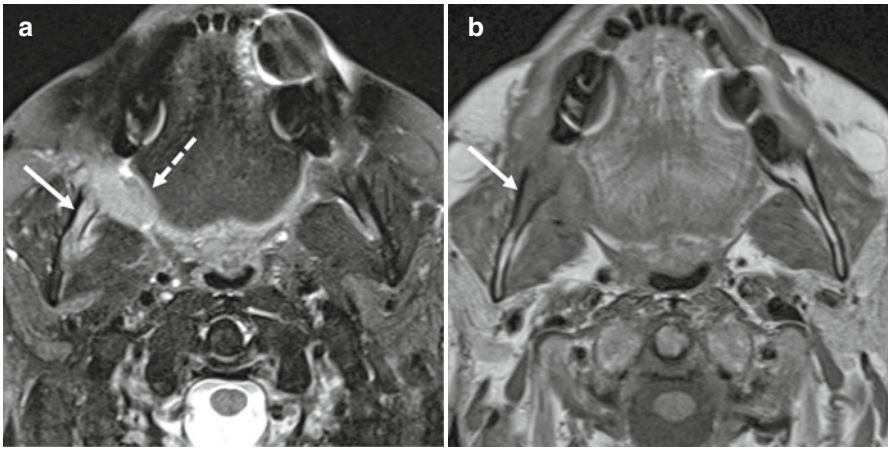

Fig. 4.10 Axial T2-weighted MR image (**a**) with fat saturation demonstrates a T2-hyperintense SCC (*dotted arrow*) arising from the right retromolar trigone with invasion of the mandible (*solid arrow*) as evidenced by abnormal increased T2 signal within the involved bone marrow. Axial T1-weighted image (**b**) of the same patient demonstrates abnormal low T1 signal within the marrow of the right mandible, consistent with osseous invasion

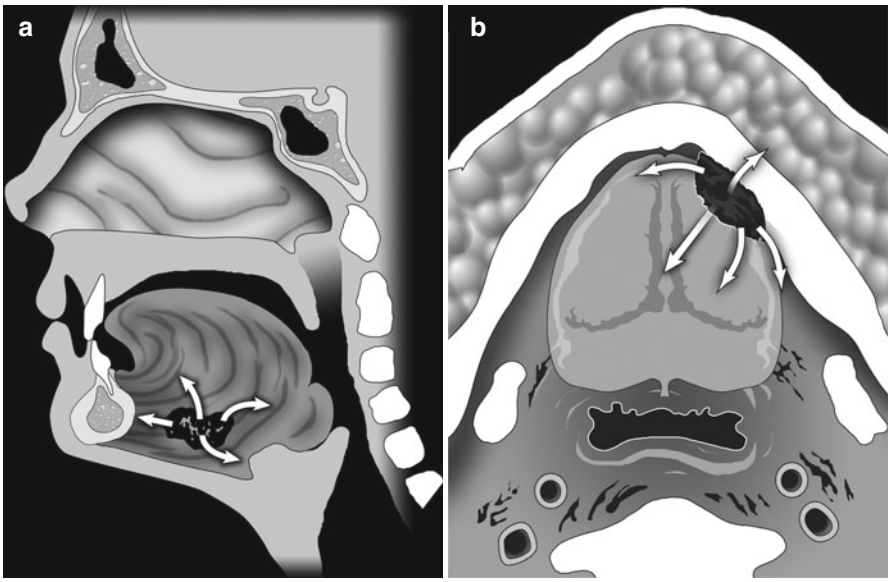

Fig. 4.11 Floor of mouth cancer spread. Sagittal and axial graphic (**a**, **b**) shows the common pathways of spread of a floor of mouth carcinoma into oral tongue, mandible, buccal space, and posteriorly into the base of tongue (*arrows*)

(d) *Floor of mouth* (*FOM*) *carcinoma*: Deep extension along the mylohyoid and hyoglossus muscles should be noted. The relationship to both the ipsilateral and contralateral (if the lesion crosses the midline) neurovascular bundles should be mentioned. Tongue base and osseous invasion must be reported (Figs. 4.11 and 4.12).

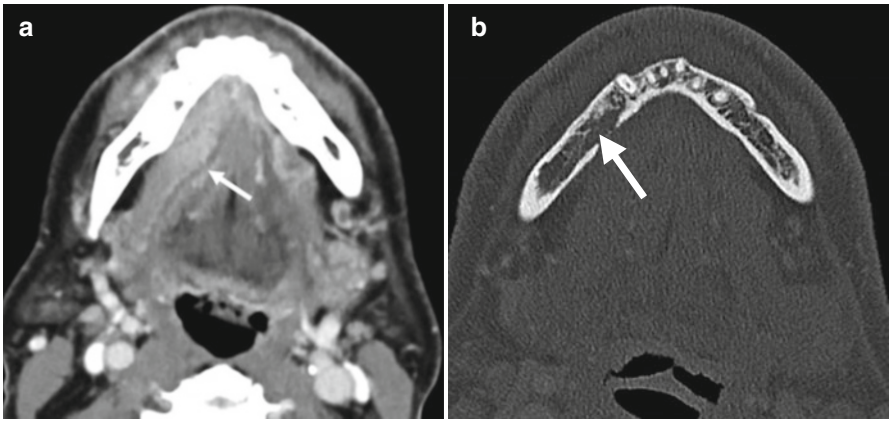

Fig. 4.12 Axial contrast-enhanced CT images in (**a**) soft tissue and (**b**) bone windows demonstrate SCC involving the right floor of the mouth with dilated submandibular duct (*arrow* in **a**) and erosion of the mandibular cortex (*arrow* in **b**)

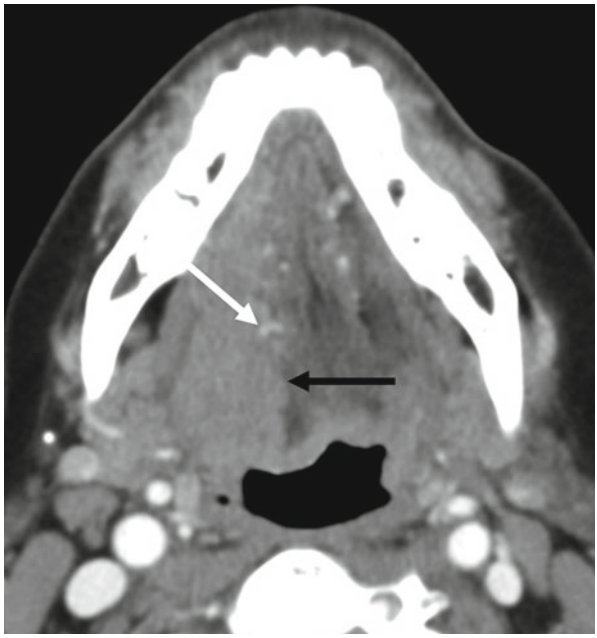

Fig. 4.13 Axial contrast-enhanced CT image in a patient with SCC (*black arrow*) involving the right base of the tongue and oral tongue with involvement of the right lingual neurovascular bundle (*white arrow*). Not that the SCC does not cross the midline of the tongue, an important feature for surgical planning

(e) *Oral tongue*: Note extension across midline, invasion of ipsilateral or contralateral neurovascular bundle, and inferior extension to the floor of mouth (Figs. 4.13, 4.14, and 4.15). Involvement of extrinsic muscles should be mentioned, as these are T4a lesions. Look for osseous involvement of the mandible or perineural extension along the neurovascular bundle.

(f) *Gingiva and hard palate carcinoma*: These rare cancers are best evaluated on coronal and sagittal images due to the axial plane of the hard palate. Bony

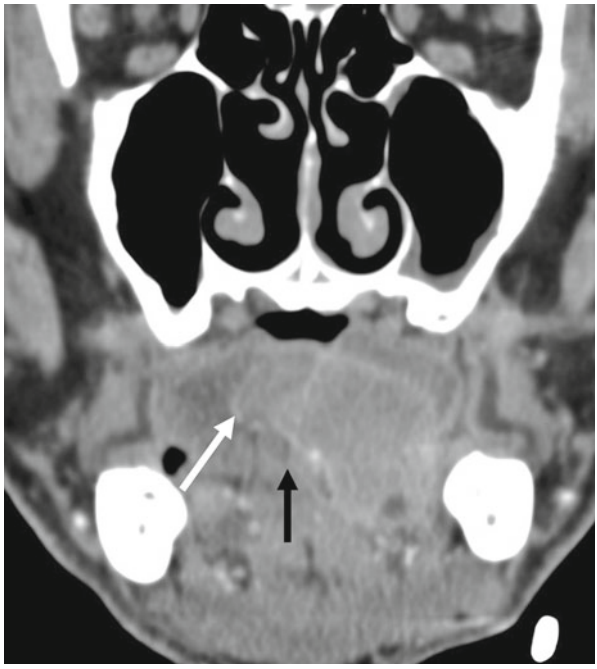

Fig. 4.14 Coronal contrast-enhanced CT image with SCC involving the oral tongue and sublingual space. The left-sided mass crosses to the right of midline (*white arrow*). The *black arrow* indicates the hypodense lingual septum, a useful structure for identifying the midline

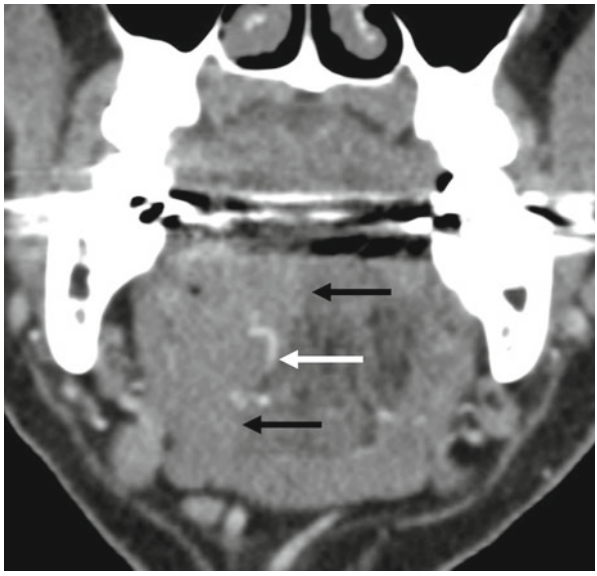

Fig. 4.15 Coronal contrast-enhanced CT image in a patient with SCC (*black arrows*) of the oral tongue and sublingual space with involvement of the lingual neurovascular bundle (*white arrow*)

erosion and perineural invasion of the greater and lesser palatine foramen and the incisive canal are key issues in these cancers (Fig. 4.16).

(g) *Base of tongue* (*BOT*) *carcinoma*: As with FOM SCC, evaluation of the full extent of the tongue involvement is necessary, including extent across midline (Fig. 4.17; *precludes hemiglossectomy*) and involvement of the extrinsic

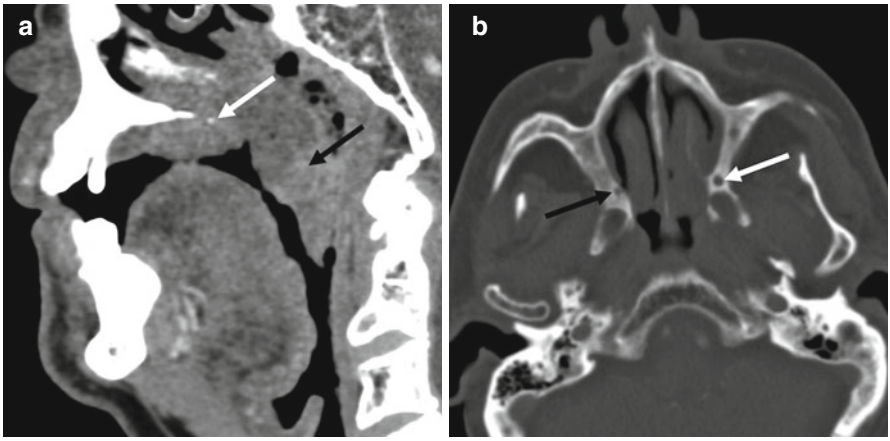

Fig. 4.16 (**a**) Contrast-enhanced sagittal CT image in a patient with SCC involving the soft palate (*black arrow*) with erosion of the hard palate (*white arrow*). (**b**) Axial CT image in the same patient with enlargement and sclerosis of the left greater palatine foramen (*white arrow*) as compared to the normal right greater palatine foramen (*black arrow*) likely indicating perineural spread along the left greater palatine nerve

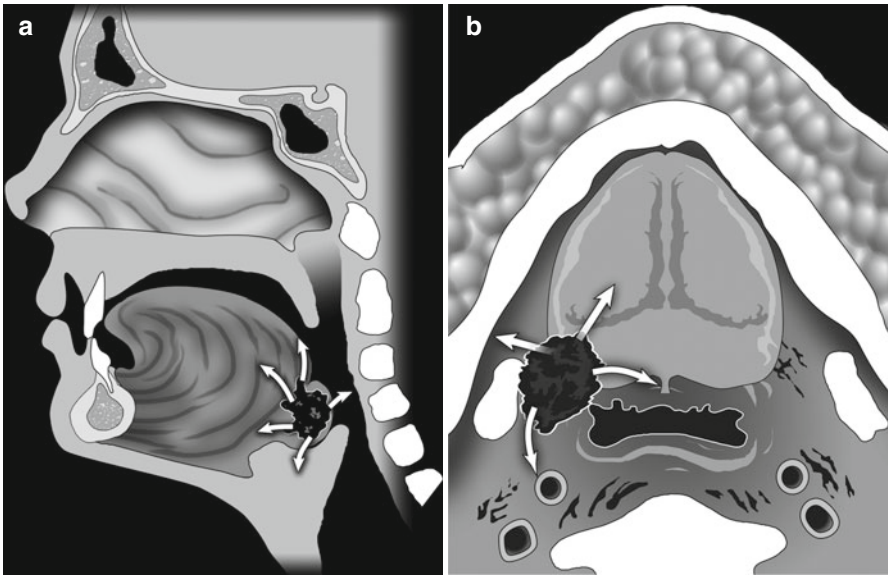

Fig. 4.17 Sagittal (**a**) and axial (**b**) graphic of base of tongue cancer spread. A base of tongue cancer can spread (*arrows*) into oral tongue, floor of mouth, and into the parapharyngeal and carotid paces. Posteriorly, it can extend into the retropharyngeal and prevertebral spaces

musculature (*T4a lesion*; Fig. 4.17). Other features to note include spread to the FOM (including involvement of neurovascular bundle and perineural spread), the anterior tonsillar pillar, and/or the larynx via involvement of the preepiglottic fat (*precludes partial glossectomy*; Figs. 4.17 and 4.18). Axial

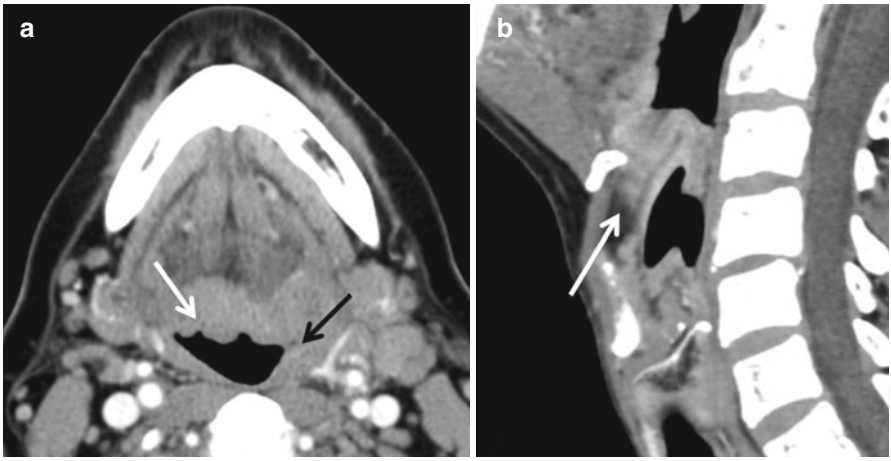

Fig. 4.18 Axial contrast-enhanced CT image (**a**) in a patient with SCC involving the left base of the tongue as well as the entire left side of the oropharynx (*black arrow*). The lesion also crosses the midline of the base of the tongue (*white arrow*). Sagittal CT image (**b**) in the same patient demonstrates tumor anterior to the epiglottis with hazy soft tissue density within the preepiglottic fat, consistent with invasion of the larynx

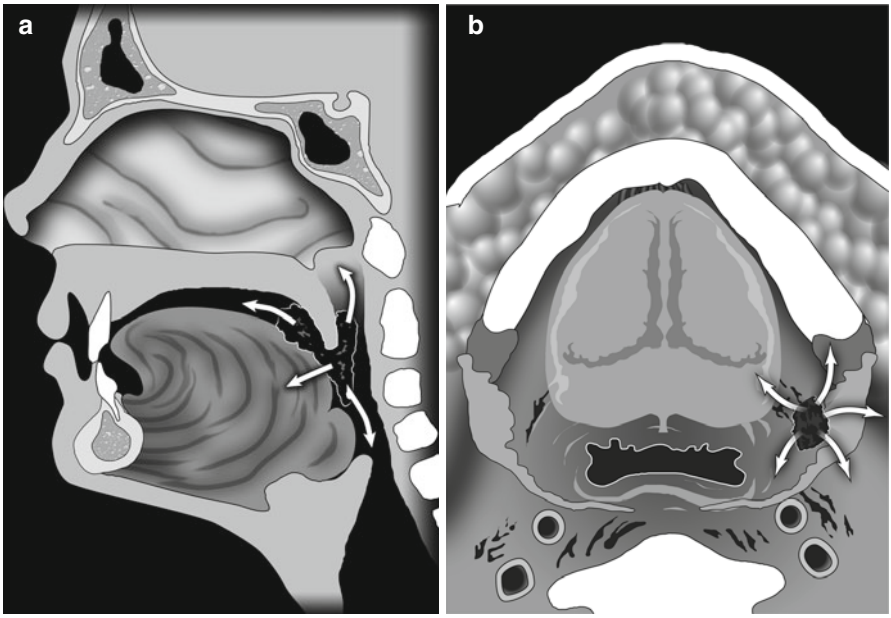

Fig. 4.19 Tonsillar carcinoma spread. Sagittal (**a**) and axial (**b**) graphic shows the common pathways for tonsillar cancer spread into the tongue base, deeper into the parapharyngeal and carotid space, and superiorly and inferiorly along the oropharyngeal walls (*arrows*)

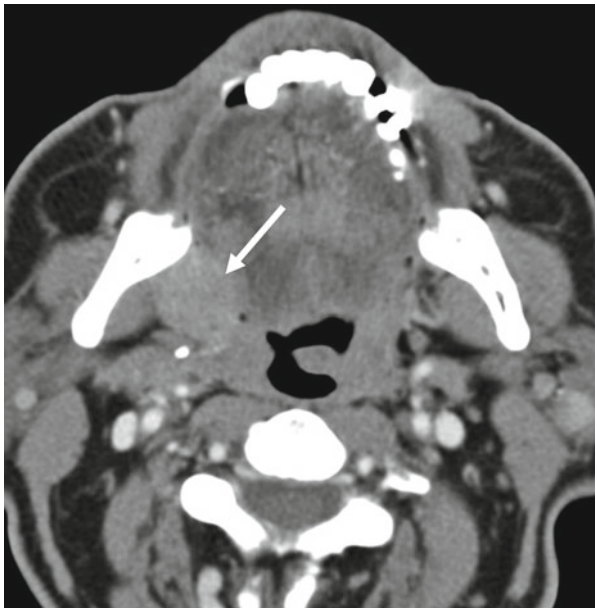

Fig. 4.20 Contrast-enhanced CT image demonstrating SCC arising from the right tonsillar fossa (*arrow*) and involving the right anterior tonsillar pillar

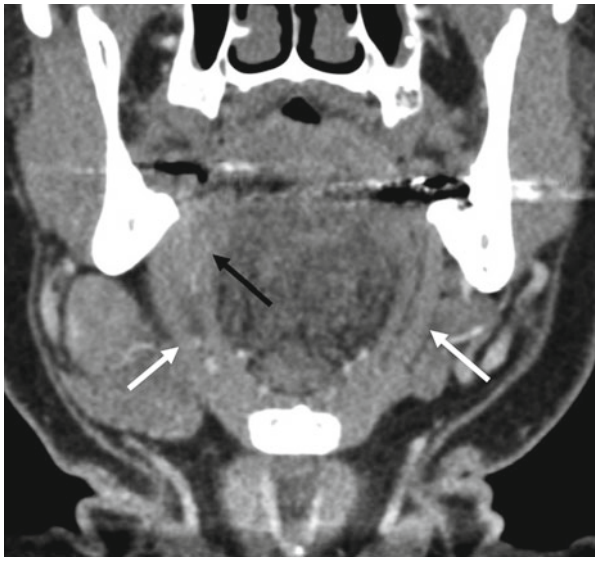

Fig. 4.21 Coronal contrast-enhanced CT image in a patient with right tonsillar SCC (*black arrow*) with loss of the fat plane between the lesion and the mylohyoid muscle, indicating invasion of the mylohyoid muscle and possible extension into the submandibular space

and sagittal T1-weighted MR images are particularly useful in the evaluation of the preepiglottic fat.

(h) *Tonsillar carcinoma*: Describe tongue base invasion and deeper extension into the parapharyngeal space (Figs. 4.19, 4.20, and 4.21). Describe carotid sheath invasion (Fig. 4.22), as well as skull-base, osseous, and prevertebral space involvement (Fig. 4.22). Given that new transoral surgical techniques are

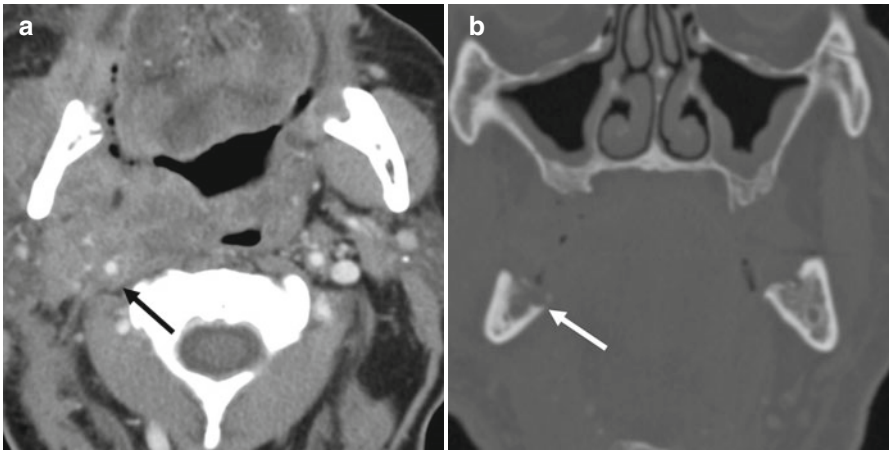

Fig. 4.22 (**a**) Contrast-enhanced axial CT image in a patient with a large right tonsillar SCC which extends to the skull base and encases the right internal carotid artery. (**b**) Coronal CT image in the same patient demonstrates erosion of the adjacent mandibular cortex

contraindicated in the presence of a retropharyngeal carotid artery, the positions of the carotids should be noted whether or not they are involved by cancer.

2. *Osseous involvement*: This includes presence or absence usually of mandibular and, less often, maxillary or palatine involvement. When tumor completely penetrates the bony cortex, all oral cavity and oropharynx lesions are staged as T4. CT can best assess cortical involvement of bone where findings such as cortical erosion, aggressive periosteal reaction, abnormal attenuation, and pathologic fractures indicate involvement (Figs. 4.6 and 4.12). MRI may also be used to assess osseous involvement although studies have shown a lower specificity for tumor involvement. MR imaging findings suggestive of osseous involvement include loss of normal low signal intensity cortex, replacement of high signal intensity marrow on T1-weighted images by intermediate signal tumor, and contrast enhancement of nerves, particularly the inferior alveolar nerve in the mandible (Fig. 4.10). However, it is important to be mindful of potential false positives such as artifacts (Fig. 4.23), recent dental extraction, radiation-induced fibrosis, and osteoradionecrosis. The presence of osseous involvement necessitates at least partial resection of the bone if the tumor is to be treated surgically.
3. *Neurovascular involvement*: A critical part of imaging evaluation in these cancers is to detect perineural spread along CN's XII and V3, the greater and lesser palatine nerves, and the posterior superior alveolar nerves. Imaging features suggestive of perineural spread include enlargement of the nerve on contrast-enhanced MR images and foraminal enlargement with replacement of normal fat within the neural foramen (Fig. 4.24). Although CT may demonstrate foraminal enlargement, MRI best detects perineural spread. The most commonly involved neurovascular bundles include the inferior alveolar nerve in cases of mandibular invasion (Fig. 4.25), the lingual neurovascular bundle in cases with involvement of the oral tongue and FOM (Figs. 4.13 and 4.15), and the greater and lesser palatine nerves

Fig. 4.23 Axial CT image in the same patient in Fig. 4.22 demonstrates invasion of the right medial pterygoid muscle (*arrow*)

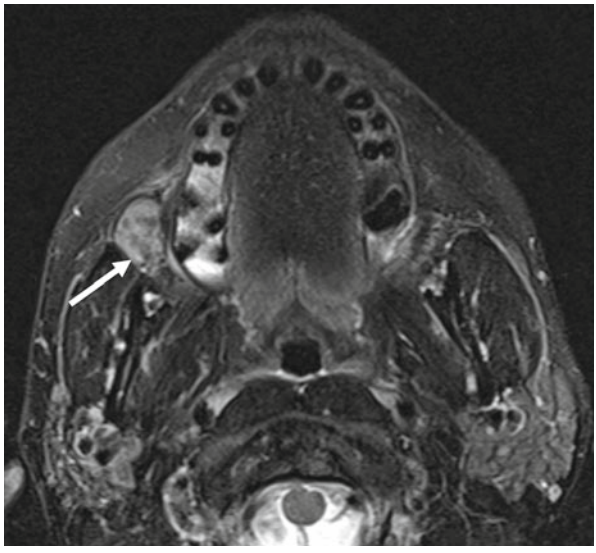

Fig. 4.24 Axial T2-weighted MR image with fat saturation demonstrates a T2- hyperintense mass (*arrow*) arising from the right buccal mucosa. Increased T2 signal within the right maxilla is secondary to artifact from dental hardware

when there is involvement of the hard palate (Fig. 4.16). Therefore, SCC involvement of these subsites requires evaluation for possible neurovascular spread.

4. *Evaluation of regional lymph nodes*: As with all head and neck SCC's, a thorough evaluation should be done for bilateral nodal disease, including presence of extracapsular spread and possible involvement of critical anatomic structures (Fig. 4.26). Cervical nodal imaging is covered in detail in Chap. 2.

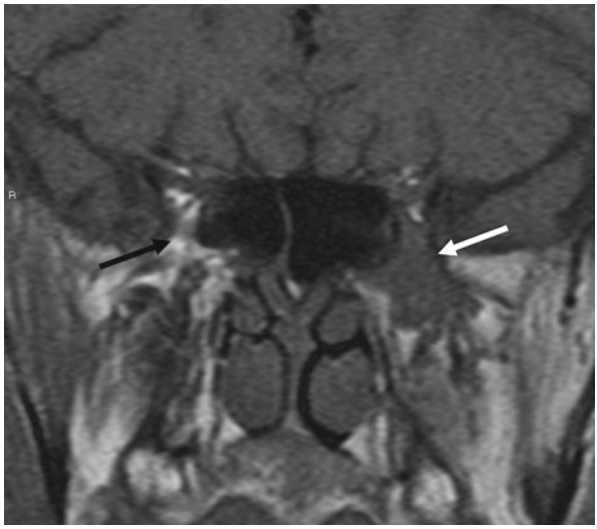

Fig. 4.25 Coronal T1-weighted MR image demonstrating perineural spread of tumor. There is replacement of the normal fat within the left pterygopalatine fossa (*white arrow*) with soft tissue. Compare with the normal appearance of the right pterygopalatine fossa (*black arrow*)

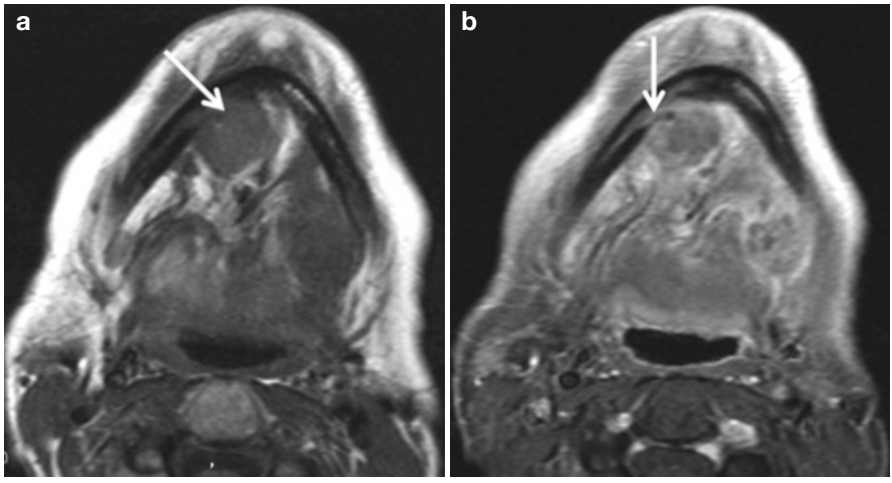

Fig. 4.26 Axial pre-contrast T1 (**a**) and post-contrast fat-saturated images (**b**) demonstrate a large recurrence within the flap with mandibular invasion and perineural extension along the right inferior alveolar nerve. Note loss of the predominant fat signal within the flap with mass-like enhancing soft tissue recurrent tumor within it (*white arrow*)

4.3.4 Posttreatment Imaging in Oral and Oropharyngeal Cancers

Treatment in OC/OP cancers involves surgery, radiation, and/or chemotherapy. An understanding and familiarity with the surgical techniques and with the expected post-radiation changes is essential in interpreting posttreatment scans. Imaging is targeted at identifying response to therapy and/or residual/recurrent tumor.

Although FDG PET-CT has a high sensitivity (80–100 %) for detection of residual and recurrent cancers and nodal disease after radiotherapy, its specificity is quite

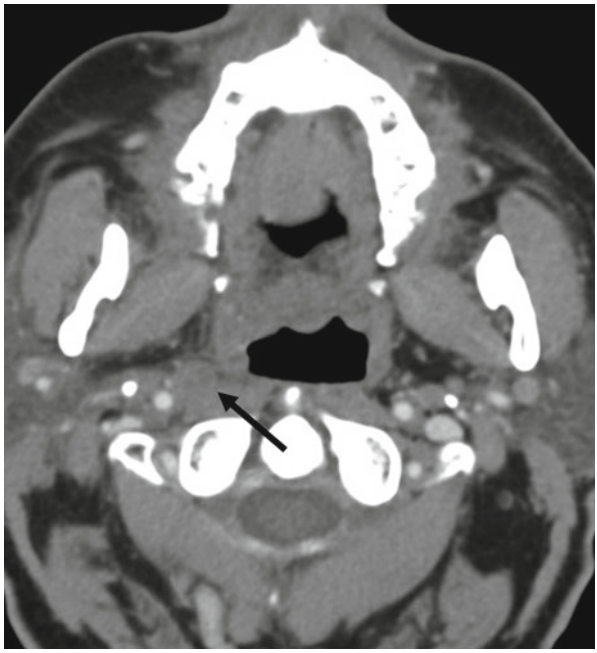

Fig. 4.27 Axial contrast-enhanced CT image with a right retropharyngeal lymph node (*black arrow*) in a patient with tonsillar SCC

low and variable (60–90 %). It is far better for detection of regional and distant recurrences than for local recurrence (Fig. 4.27). In the initial posttreatment setting, false positives are due to posttreatment inflammation or infection. Causes for false negatives are more nebulous; they may represent decreased perfusion because of radiation-induced vascular damage or a state of temporarily decreased glucose uptake, possibly due to depression of glucose transporters. The accuracy of FDG PET-CT improves markedly at 12 weeks or more after treatment, but the 12-week interval is considered too long for patients with disease persistence in whom surgical intervention is warranted. In such patients, a window of 4–8 weeks minimizes fibrosis and optimizes healing. Consequently, National Comprehensive Cancer Network (NCCN) guidelines currently recommend contrast-enhanced CT or MRI within 4–8 weeks of (chemo) radiotherapy in higher-risk patients or those with suspected disease persistence/progression.

Newer techniques such as perfusion CT and diffusion-weighted MR imaging are being used as adjuncts, though further studies are needed to validate results. Baseline posttreatment imaging is very helpful in many of these situations.

Curative surgical resection for locally advanced OC/OP cancers is frequently repaired using complex flap reconstructions for both cosmesis and function. Flaps can be pedicled (retaining native blood supply) or free (primary vascular pedicle detached and reanastomosed to local vasculature). The most common free flap used in OC/OP reconstruction is the radial forearm free flap, but a variety of others are used as well. The most common pedicled flap remains the pectoralis major; it is used in patients that are poor candidates for free tissue transfer or in cases where soft tissue bulk and/or improved vascularization are required within its anatomic range. When imaged over time, myocutaneous flaps demonstrate fatty atrophy and

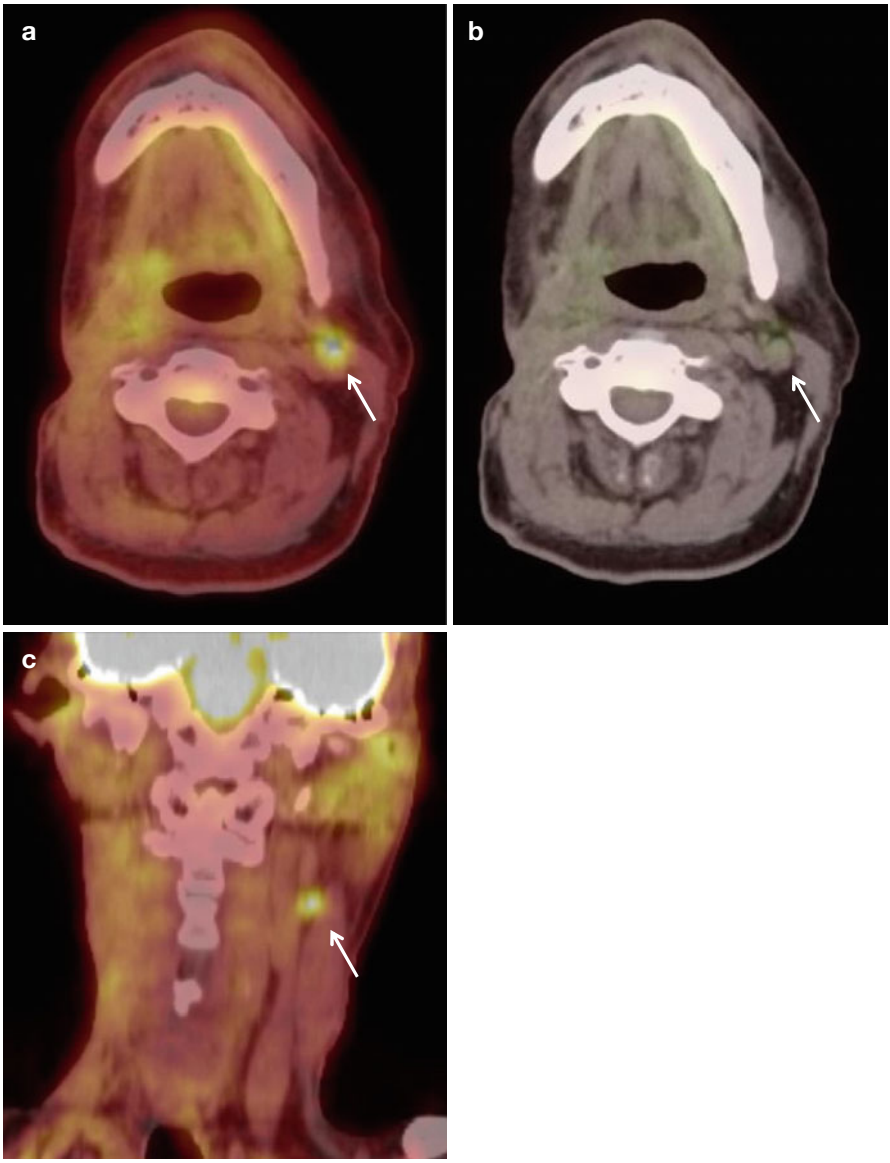

Fig. 4.28 PET-CT can play a very helpful role in posttreatment evaluation as in this case. Patient has had multiple surgeries and radiotherapy for a T2N3M0 lesion, with extensive postsurgical and RT changes; PET was specifically requested as CT imaging interpretation was difficult due to altered anatomy. Axial (**a**) and coronal (**b**, **c**) PET shows abnormal uptake in a left level II node, (*arrow* in **a**, **b** and **c**) consistent with residual nodal disease. Diffuse uptake in the right neck is secondary to posttreatment changes

decreased bulk due to denervation atrophy (Fig. 4.28). Consequently, any increase in bulk or any focally enhancing mass, particularly at the margin of the flap, is concerning of recurrent tumor (Fig. 4.29).

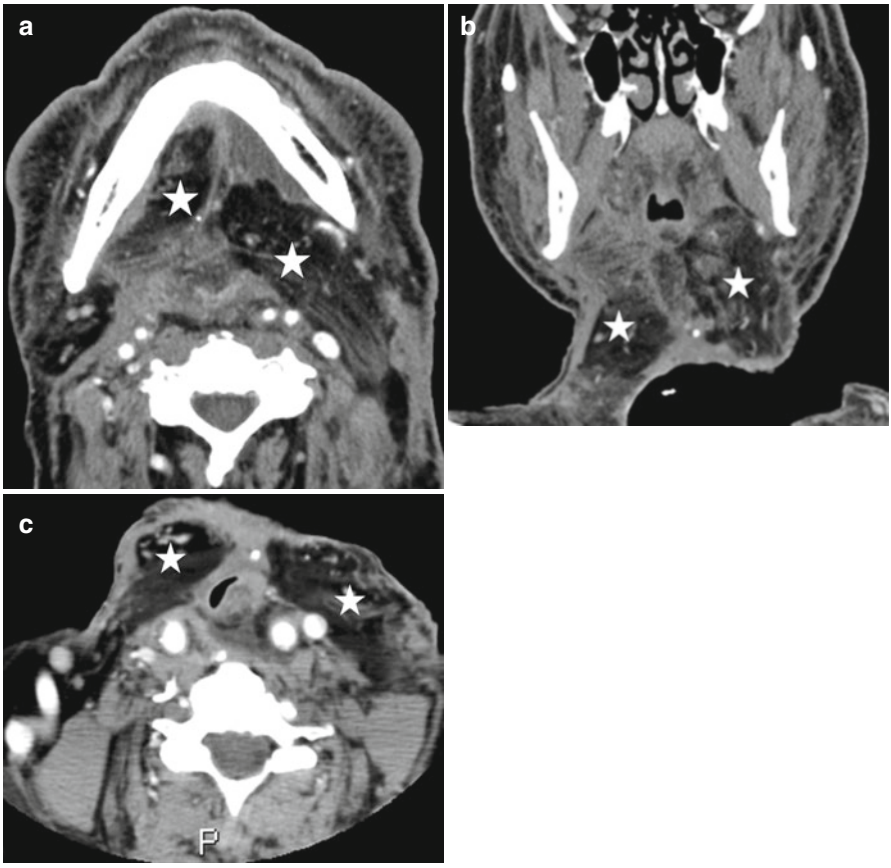

Fig. 4.29 A 51-year-old with floor of mouth cancer and extensive bilateral nodal disease status tumor resection and bilateral flap reconstruction. Six-month follow-up scans axial (**a**, **c**) and coronal (**b**) demonstrates bilateral pectoralis major myocutaneous flaps (*stars* in **a**, **b** and **c**) with changes of denervation atrophy (volume loss and fatty replacement)

Other postoperative changes include secondary infections, fistulas (Fig. 4.30), and abscesses as well as hematomas and seromas. Postsurgical changes of the various kinds of neck dissections are discussed in Chap. 2.

Radiation induces necrosis, mucosal changes, soft tissue fibrosis, and mandibular osteoradionecrosis in the local field (Fig. 4.31). Additionally, radiotherapy impacts other tissues such as brain, upper cervical spinal cord, and upper lungs. Head and neck radiologists should be accustomed to post-radiation changes. The early changes are very common and reversible and include findings of mucositis and skin desquamation. Late changes are more worrisome and include soft tissue necrosis, vascular complications, osteoradionecrosis, and secondary malignancies. Post-radiation changes can be easily identified on CT and MR imaging and include any combination of reticulation of the subcutaneous fat, edema in the retropharyngeal spaces, thickened skin and platysma, and increased enhancement within the

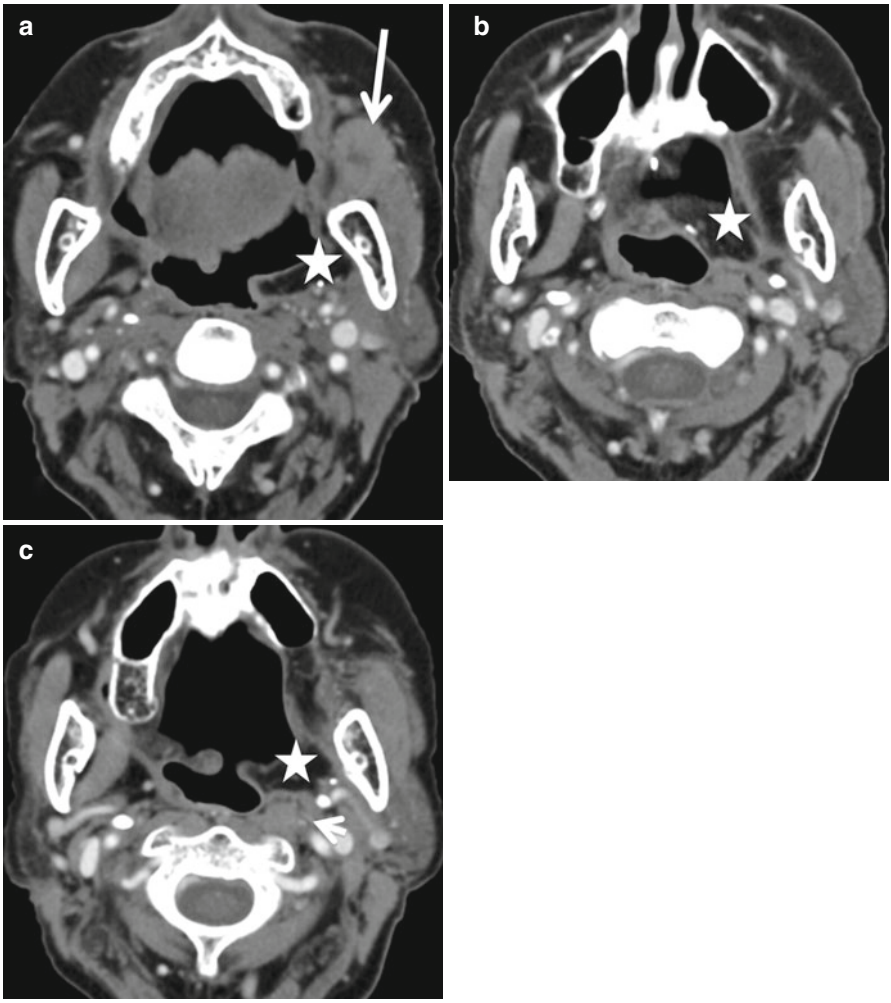

Fig. 4.30 A left buccal space recurrence in a 55-year-old with left oropharyngeal cancer status post-tumor resection and flap reconstruction. Axial CT images (**a**, **b** and **c**) show a heterogeneously enhancing mass (*arrow* in **a**) adjacent to the flap (*star* in **a**, **b** and **c**). Also note the pathological new left-sided retropharyngeal node (*smaller arrow* in **c**)

pharyngeal mucosa and the salivary glands (Fig. 4.32). Later changes include more fibrosis within the skin, platysma, and deeper soft tissue structures as well as atrophy of the salivary glands.

4.4 Other Oral and Oropharyngeal Neoplasms

The presence of lymphoid tissue in the tonsils and BOT as well as the presence of minor salivary gland tissue throughout the OC/OP accounts for the spectrum of neoplasms seen in addition to carcinomas, which principally includes salivary

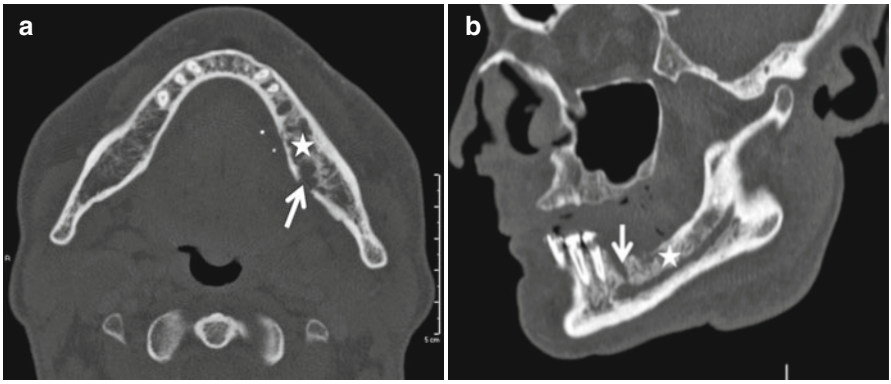

Fig. 4.31 Axial (**a**) and sagittal (**b**) CT images in a patient treated 2 years prior with radiation, for left-sided tongue cancer. Findings of mandibular osteoradionecrosis are seen with loss of lingual cortex (*arrow*) and resorption of the trabeculae (*star*)

tumors and lymphomas; these are reviewed in Chaps. 1 and 9. Although a variety of mesenchymal and other neoplastic lesions can involve the OC/OP, they are quite rare and most have no distinct imaging features. Boxes 4.4 and 4.5 summarize both the neoplastic and nonneoplastic lesions within the sublingual and submandibular spaces.

4.5 Nonneoplastic Lesions

Nonneoplastic lesions within the OC/OP run the whole gamut. Developmental and congenital lesions including benign cysts (e.g., ranula (Fig. 4.33), thyroglossal ducts remnants, dermoids, and epidermoids) and vascular malformations. Most of these have been discussed in Chaps. 9, 10, and 11. Infectious and inflammatory lesions, predominantly odontogenic in origin, represent the vast majority of nonneoplastic processes and are discussed below. Jaw lesions are covered in detail in Chap. 13.

4.5.1 Inflammatory Lesions of the Oral Cavity and Oropharynx

The OC/OP is frequently involved with infectious/inflammatory processes, secondary to odontogenic or tonsillar infections or to salivary gland obstruction. Odontogenic disease is the most frequent source of oral cavity infection in adults, whereas the palatine tonsils are the most frequent source in children and young adults.

4.5.2 Odontogenic Infections

Odontogenic infections can be dental or periodontal in origin with resultant periapical abscess. These can then spread to maxillary sinus, masticator space, buccal

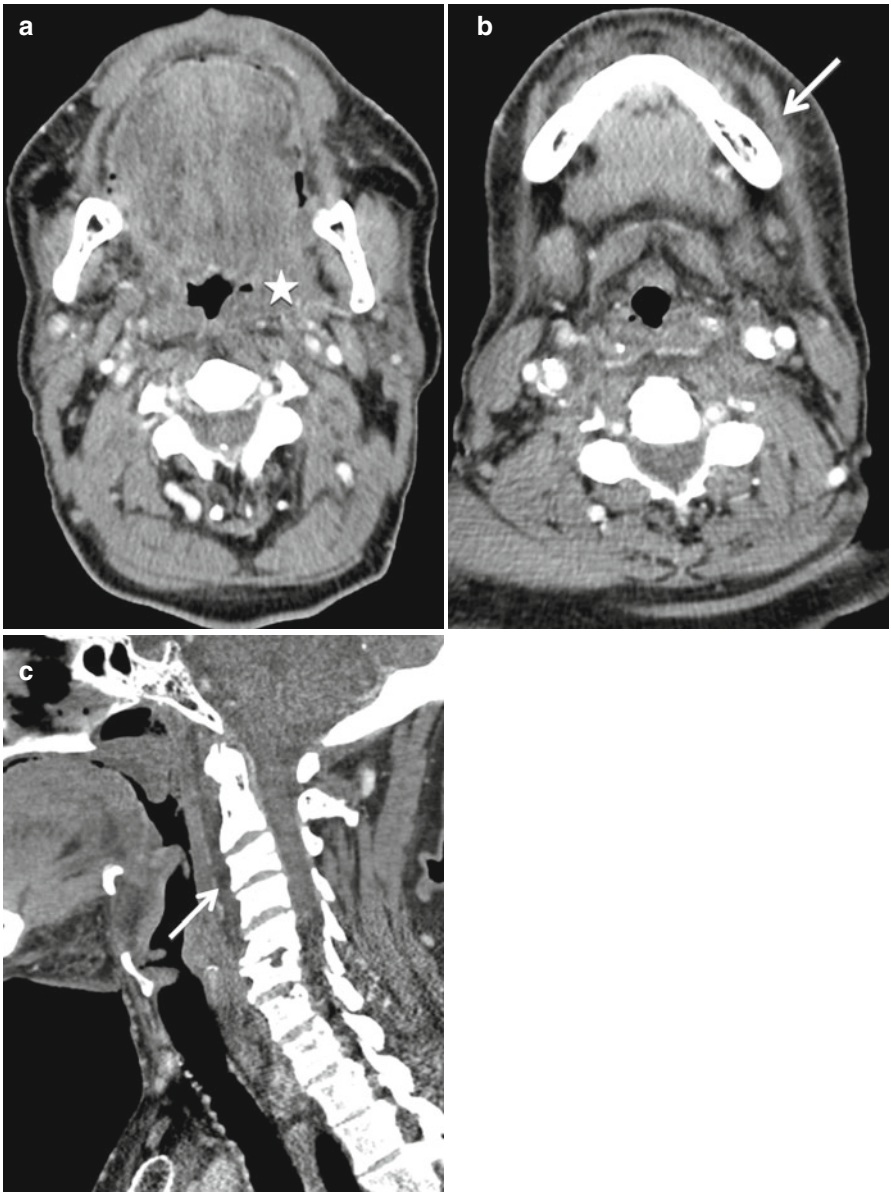

Fig. 4.32 Post-radiation changes in a patient with left-sided tonsillar tumor (*star* in **a**) show expected changes of soft tissue thickening and stranding, including platysma thickening and retropharyngeal edema. Figure (**a**) is the axial pretreatment scan, while figures (**b**, **c**) are axial posttreatment scans

Box 4.4. Sublingual Space/Floor of Mouth Lesions

Cystic lesions	Ranula (simple or plunging), dermoid and epidermoid cysts
Infectious/inflammatory processes	Phlegmon-cellulitis, abscess, submandibular duct stenosis, and calculi
Developmental	Lingual thyroid
Vascular malformations	Arteriovenous malformations (high and low flow), hemangiomas, lymphatic malformations, venous and mixed venolymphatic malformations
Neoplastic lesions	Benign lesions (lipomas, nerve sheath tumors, benign mixed tumor) and malignant tumors (squamous cell carcinomas and salivary gland tumors)
Pseudolesion	Tongue atrophy from hypoglossal palsy

Box 4.5. Submandibular Space Lesions

Cystic lesions	Thyroglossal duct cyst, dermoid and epidermoid cyst, second branchial cleft cyst
Inflammatory processes	Phlegmon-cellulitis, abscess, reactive adenopathy
Submandibular diseases	Stenosis and calculi, mucocele
Vascular malformations	Arteriovenous malformations (high and low flow), hemangiomas, lymphatic malformations, venous and mixed venolymphatic malformations
Neoplastic lesions	Benign lesions (lipomas, nerve sheath tumors, benign mixed tumor) and malignant tumors (squamous cell carcinomas and salivary gland tumors)
Pseudolesions	Secondary to mandibular nerve atrophy, small mylohyoid, anterior belly of digastric

space, and sublingual/submandibular spaces (Fig. 4.34). The attachment of the mylohyoid muscle to the mylohyoid ridge dictates the spread to sublingual and submandibular spaces. Infections arising in the anterior mandibular teeth (incisors, canines, premolars, and first molars) spread to the sublingual space due to their position above the mylohyoid line (Fig. 4.35), whereas those arising in the second and third molars spread to the submandibular space as their apices lie below the mylohyoid line. Imaging findings include edematous changes in the muscles, salivary glands, and soft tissues with obscurations of fat planes with stranding. On

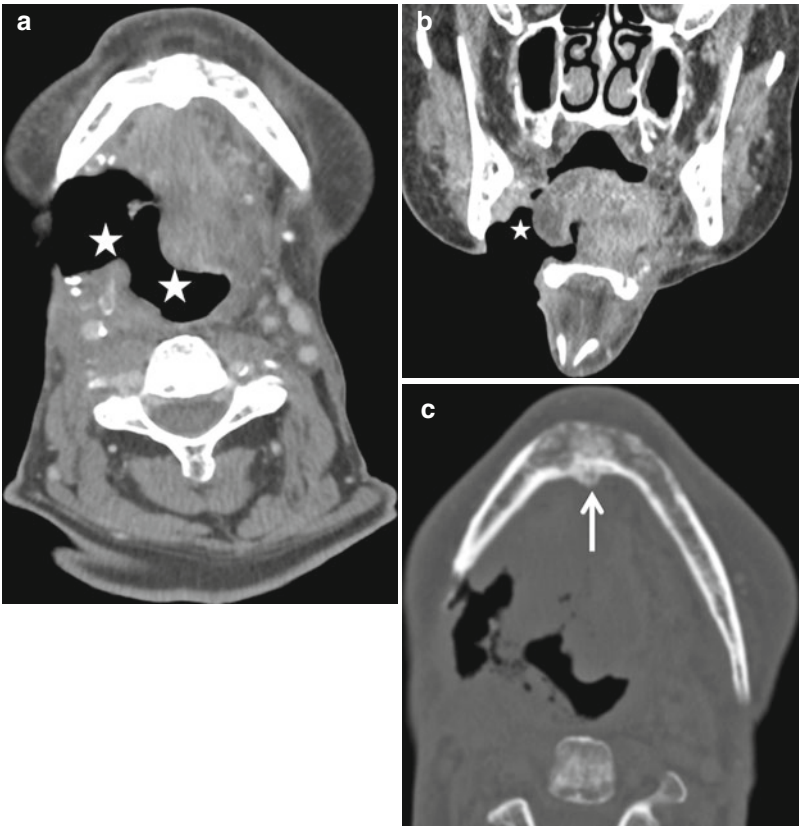

Fig. 4.33 Axial (**a**) and coronal (**b**, **c**) CT images of a patient with extensive right-sided neck surgery and radiation for recurrent oropharyngeal cancer with a large right side pharyngocutaneous fistula (*star* in **a**, **b**). Also note the changes of osteoradionecrosis within the mandible (*arrow* in **c**)

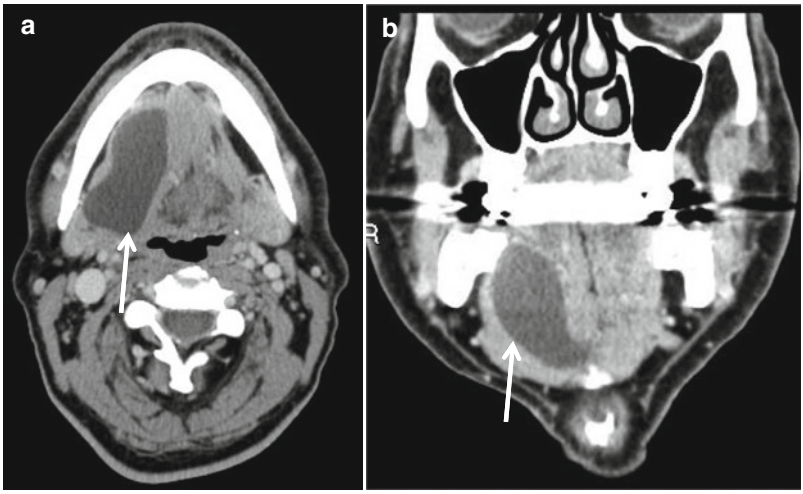

Fig. 4.34 A well-defined hypodense lesion (*arrow*) is seen in these axial (**a**) and coronal (**b**) CT scans, centered within the right sublingual space, consistent with a ranula

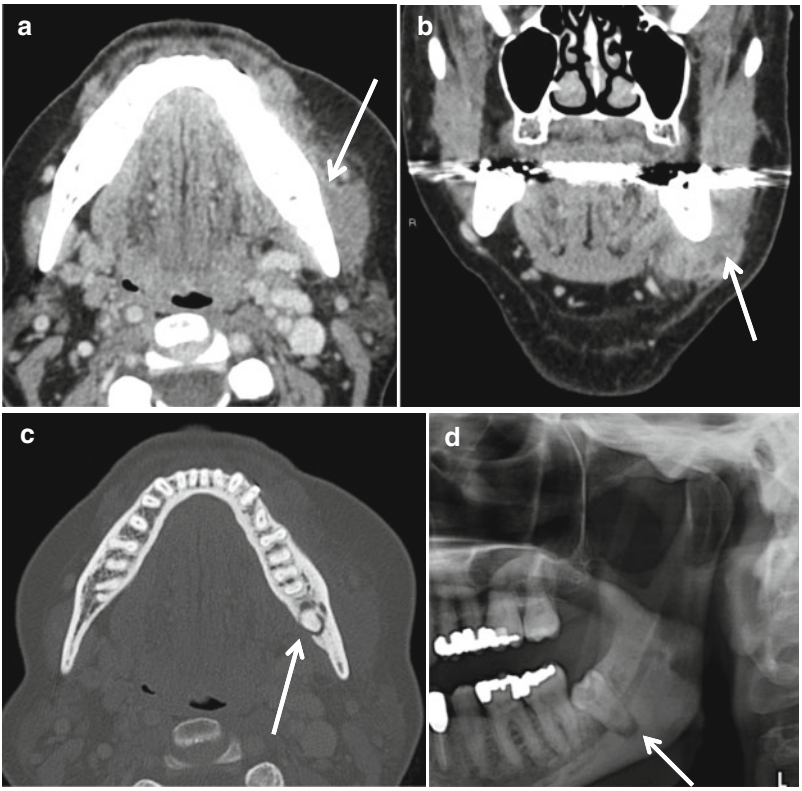

Fig. 4.35 Axial (**a**)- and coronal (**b**)-contrasted CT images in a patient with left submandibular abscess (*arrow* in **a** and **b**). The bony windows (**c**) demonstrate left mandibular molar periodontal lucency (*arrow*) with loss of lingual cortex. The periodontal lucency (*arrow*) can also be well identified on the panorex view (**d**)

contrast-enhanced CT, one can identify changes consistent with phlegmon, with more organized rim-enhancing abscesses becoming more obvious later in the course of the illness.

4.5.3 Infections of Salivary Gland Origin

Sialadenitis and related sialolithiasis are discussed in detail in Chap. 9.

4.5.4 Tonsillar/Peritonsillar Infections, Peritonsillar Abscess

Routine imaging is not performed in acute tonsillitis, which is very common in children. Uncomplicated tonsillitis appears as edematous, enlarged palatine tonsils. Imaging in tonsillitis may be warranted patients with potential complicating features such as progressive difficulty in swallowing, trismus, ear pain, torticollis, and

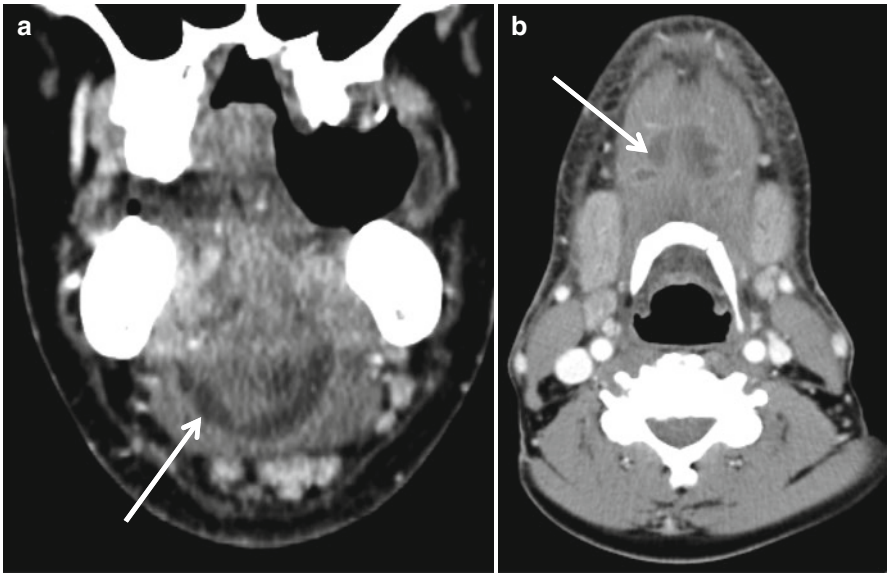

Fig. 4.36 Coronal (**a**) and axial (**b**) post-contrast CT scan images demonstrate a well-defined rim-enhancing abscess (*arrows*) in the sublingual space. Note the abscess location in between the tongue superiorly and the mylohyoid muscle inferiorly. Multiple enhancing reactive nodes are present

bulging of the pharyngeal wall, concerning for a retropharyngeal abscess. Routine peritonsillar abscesses are diagnosed clinically and do not require imaging; they occur when infection extends outside the tonsillar capsule and into the lateral pharyngeal space between the tonsillar capsule and superior constrictor muscle. Peritonsillar abscesses appear as rim-enhancing collection, limited laterally by the superior constrictor muscle. However, they may extend into the parapharyngeal or retropharyngeal spaces, which must be mentioned in the radiology report, as this can affect the surgical approach (Figs. 4.36 and 4.37).

4.5.5 Suppurative Lymphadenitis

Level Ia and Ib lymph nodes can be affected by infectious processes but rarely undergo necrosis to form an intranodal abscess. This is most commonly seen in children due to *Staphylococcus aureus* infection and is known as suppurative adenitis.

4.5.6 Necrotizing Fasciitis

Necrotizing fasciitis, which can affect any part of the body, can also involve the superficial and deep tissues of the neck. It is a rare, severe, rapidly progressive bacterial infection, which can destroy tissues across fascial planes, including skin,

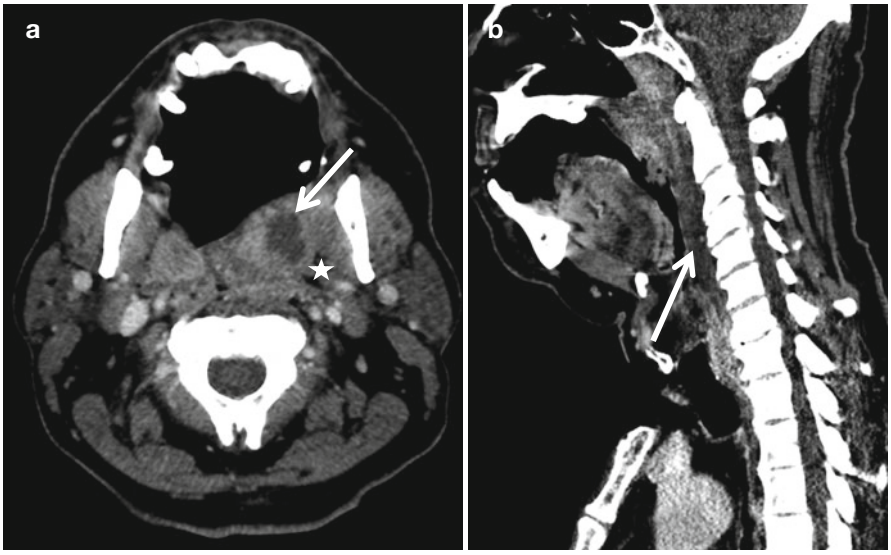

Fig. 4.37 Axial (**a**) and sagittal (**b**) contrast-enhanced CT shows low-density irregular left intra/peritonsillar abscess (*white arrows* in **a**) with minimal stranding in the left parapharyngeal space (*star* in **a**). The right tonsils demonstrate mildly striated enhancement, which is suggestive for inflammation. Note the large sympathetic effusion in retropharyngeal space (*white arrow* in **b**)

muscles, and other soft tissues. A variety of aerobic and anaerobic bacteria can be involved. On imaging, a combination of diffuse cellulitis, fasciitis, and myositis of the superficial and deep soft tissues is seen, sometimes with small pockets of air.

4.5.7 Ludwig's Angina

Ludwig's angina is a rare condition and represents a head and neck therapeutic emergency. It involves a diffuse life-threatening infection of the sublingual space with associated severe sublingual and lingual edema resulting in expansion and retropulsion of the tongue with airway obstruction. Infection often extends to the submandibular spaces with clinical findings of dysphagia, trismus, and induration of the upper neck soft tissues. Most of these are odontogenic in origin, usually due to an infection of the third molar or the gums surrounding a partially erupted third molar, and caused by *Streptococcus* species. On cross-sectional imaging, there is diffuse infiltration and edema centered in the sublingual region that is phlegmonous in appearance without a discrete abscess. The submandibular spaces, submandibular glands, and other immediate fascial spaces are frequently involved. Given the potential for airway compromise, and other serious complications (jugular thrombophlebitis, empyema, mediastinitis, etc.), this process requires urgent intervention. On imaging, attention should be paid to airway patency and the identification of any drainable abscess.

4.5.8 Other Lesions

Various other lesions, including congenital lesions and vascular malformations, are discussed elsewhere in this book (Chap. 11).

4.6 The Surgeon's Perspective

4.6.1 Oral Cavity Lesions

As in other areas of the head and neck, imaging of the OC/OP is crucial for accurate diagnosis, staging, and therapeutic planning. When considering OC lesions, superficial noninvasive lesions can be managed without imaging, but all invasive lesions should undergo head and neck CT or MRI. OC SCC, particularly oral tongue, FOM, and buccal cancers, have a high rate of occult cervical nodal metastases and continue to have relatively poor survival despite aggressive therapy. Since all patients with N+ disease are at least stage III, imaging evaluation often differentiates between early stage (I/II) and late stage (III/IV) cancers. This is crucial because, while single modality therapy (e.g., surgery alone) may be an option for early stage OC cancers, advanced disease is always treated with a multimodal approach (e.g., surgery and postoperative radiotherapy ± chemotherapy).

It is important to have completed a thorough clinical examination when reviewing OC imaging, since some imaging findings can be misleading. For instance, a lesion that is clearly isolated to the lateral tongue on physical exam with the tongue protruded may appear on imaging to involve the FOM or lingual gingiva of the mandible since the tumor abuts these areas with the tongue at rest in the mouth. Similarly, a recently extracted tooth may leave behind ragged, eroded bone on imaging but may be clearly free of tumor on physical exam; while it is important to note bony erosion on imaging, it is equally important that this be clearly associated with the cancer and not present for another reason.

OC imaging is particularly important for determining depth of invasion and bony involvement. On physical exam, deep infiltrative invasion of the tongue may not be palpable but may be readily recognized on CT or MRI. While tumors that are fixed to the periosteum on physical exam have a high risk of bone invasion, this cannot be clearly delineated without imaging. As a general rule, tumors that abut the periosteum can be managed surgically with periosteal resection without bone removal. In this case, a section of periosteum should undergo intraoperative pathological evaluation, and if positive, a rim mandibulectomy should be performed. In cases where the periosteum is clearly invaded but the bone is pristine on imaging, a rim mandibulectomy should be performed. If the bony cortex is breached by tumor, the patient should undergo a segmental mandibulectomy. Many surgeons submit bone marrow at the cut edges of bone for frozen section analysis at the time of resection. While not infallible, this is the best approach to confirming negative bony margins intraoperatively since the bone itself cannot be assessed. Given that these approaches dramatically change the extent and duration of surgery and the reconstructive

approach, it is crucial to have as much information as possible before proceeding with surgery.

While surgical reconstructive approaches are well beyond the scope of this text, it behooves the head and neck radiologist to be comfortable with these in terms of the postoperative imaging appearance. Since they are often unique, good communication between the surgeon and the radiologist as to the details of the surgical intervention is necessary so that the imaging report does not reflect a normal reconstructive element as concerning for recurrence. Preoperative imaging is often essential for reconstructive planning, particularly when bony reconstruction will be required, particularly as new imaging-based computer-assisted reconstructive planning tools become more commonplace.

4.6.2 Oropharynx Lesions

For OP SCC, imaging is perhaps even more important. BOT and tonsil cancers are difficult to evaluate by physical exam in the clinic and even under general anesthesia. When tonsil cancers are mobile on exam, they are almost always T1/2 and surgically resectable via transoral approaches, which are becoming more popular as they have the potential to allow for reduced use of the chemotherapy and/or radiotherapy. This is important in terms of improving long-term morbidity, particularly in an era where most new OP cancers are HPV related, with, in general, younger, nonsmoking patients. To consider a transoral surgical approach, the surgeon must understand the extent of the tumor and its relationship to the carotid vessels, as well as the relative position of these vessels to the pharyngeal walls. Superior extent of tonsil tumors should be assessed carefully since soft palate resection will have significant functional consequences for the patient and reconstruction may be required. For BOT tumors, careful consideration is given to the lingual vascular pedicles; tumors that cross the midline are generally considered poor candidates for transoral surgery since both vascular pedicles are likely to be ligated during the procedure, resulting in necrosis of the distal tongue. Additionally, BOT tumors that extend into the preepiglottic and/or paraglottic spaces require at least supraglottic laryngectomy for complete surgical removal; these findings may push treatment planning toward primary chemoradiotherapy.

Accurate staging is also important for nonsurgical treatment planning for OP cancers. Again, early stage lesions can undergo unimodality therapy (e.g., radiotherapy alone), but advanced cancers generally require multimodality therapy (e.g., chemoradiotherapy). Mid-stage cancers (e.g., T1N1 tonsil) may be considered for unimodality therapy unless extracapsular spread (ECS) is present around the metastatic cervical node, and thus the imaging report should always comment on the present or absence of ECS. BOT tumors routinely require treatment of both the left and right cervical nodal basins. Imaging is also commonly obtained for infectious processes in the OP. However, this is rarely necessary. Tonsillar cellulitis and peritonsillar abscess are diagnosed clinically and can almost always be managed without imaging. In settings where these commonly present (emergency departments,

student health organizations), primary providers should be encouraged to obtain clinical consultation with an otolaryngologist or other experienced provider rather than relying on imaging, which, in this case, involves unnecessary expense and radiation exposure for the patient.

In similar clinical settings, Ludwig's angina is a common question but is rarely seen. In most cases, these are perimandibular infections that result in extensive submandibular swelling with edema and possibly abscess inferior to the mylohyoid muscle. In true cases of Ludwig's angina, significant swelling is present in the floor of mouth due to cellulitis in the sublingual space superior to the mylohyoid muscle. This results in superior and posterior displacement of the tongue with OP compression and airway obstruction. When this situation presents, securing the airway is paramount and takes priority over CT imaging. In the unexpected situation where these findings are present but not advanced enough to cause airway obstruction, the radiologist should communicate rapidly to the requesting physician with a recommendation for acute airway evaluation.

Further Reading

Mukherji SK, Weissmann JL, Holliday RA (2003) Pharynx. In: Som PM, Curtin HD (eds) Head and neck imaging, 4th edn. Mosby, St Louis

Smoker WRK (2003) The oral cavity. In: Som PM, Curtin HD (eds) Head and neck imaging, 4th edn. St Louis Smoker WRK, Mosby

Larynx and Hypopharynx

5

Prashant Raghavan, David C. Shonka Jr., Max Wintermark, and Sugoto Mukherjee

5.1 Introduction

This chapter will focus on the imaging evaluation of squamous cell carcinoma of the larynx and hypopharynx. Although several other malignant neoplasms can occur in the larynx, these are uncommon and will not be addressed in detail. Imaging of traumatic and inflammatory processes and vocal cord paralysis is also briefly discussed.

5.2 Anatomy (Box 5.1)

Box 5.1. Key Anatomical Terms

Divisions

Supraglottis

Subsites

Epiglottis – suprahyoid (tip, lingual, and laryngeal surfaces)

Epiglottis – infrahyoid

Aryepiglottic folds – laryngeal surface

False vocal cords

Arytenoid cartilages

Glottis

True vocal cords

Anterior commissure

Posterior commissure (inter-arytenoid area)

Subglottis

Cartilages

Unpaired

Epiglottis

(continued)

P. Raghavan et al., *Manual of Head and Neck Imaging*,
DOI 10.1007/978-3-642-40377-4_5, © Springer-Verlag Berlin Heidelberg 2014

Box 5.1 (continued)
Thyroid
Cricoid
Paired
Arytenoid
Corniculate
Cuneiform
Triticeous
Ligaments
Hyoepiglottic
Thyroepiglottic
Ventricular ligament – false vocal cord
Vocal ligament – true vocal cord
Spaces
Preepiglottic space
Paraglottic space
Membranes and fascia
Quadrangular membrane
Conus elasticus
Thyrohyoid membrane
Cricothyroid membrane
Joints
Cricoarytenoid joints
Cricothyroid joints
Muscles
Thyroarytenoideus – forms bulk of true cords
Posterior and lateral cricoarytenoid – antagonistic muscles that abduct and adduct the TVCs

The laryngeal skeleton is comprised of the hyoid bone, three unpaired (epiglottis, thyroid, cricoid), and four paired (arytenoid, corniculate, cuneiform, triticeous) cartilages (Fig. 5.1). The corniculate and cuneiform cartilages (located along the aryepiglottic folds) and the triticeous (located in the thyrohyoid membrane) are of no clinical significance. The epiglottis is attached to the laryngeal skeleton by the hyoepiglottic and thyroepiglottic ligaments. The mucosa of the lingual surface is contiguous with that of the vallecula and tongue base (Fig. 5.1). The epiglottis has little resistance to tumor invasion.

The thyroid cartilage is comprised of two laminae attached at the midline. Superior and inferior cornua project from the posterior edge of each lamina. The thyroid cartilage is connected to the hyoid bone by the thyrohyoid membrane, which is pierced by the superior laryngeal neurovascular bundle; this provides a pathway for extralaryngeal tumor spread. The thyroid cartilage is connected to the cricoid cartilage by the cricothyroid membrane. The inferior cornua articulate with a small

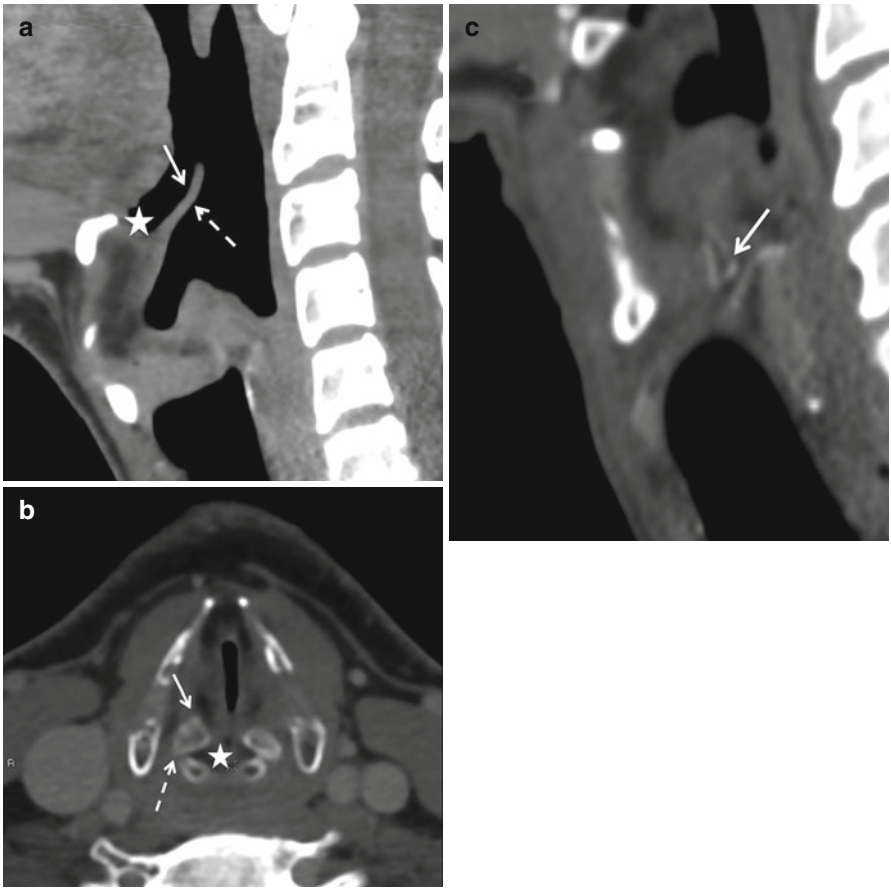

Fig. 5.1 The laryngeal cartilages. (**a**) The epiglottis has a lingual (*solid arrow*) and laryngeal (*dashed arrow*) surface. The valleculae (*asterisk*) lie between the lingual surface and the base of the tongue. (**b**) The thyroid cartilage can be variably calcified/ossified. The arytenoid cartilages are comprised of a vocal (*solid arrow*) and a muscular process (*dashed arrow*). The vocal processes provide attachment to the true cords. The mucosa between the arytenoid cartilages is the interarytenoid area (*asterisk*). The cricoarytenoid joint space is best seen on the sagittal plane (**c**). Note that the height of the cricoid ring is greater posteriorly than anteriorly

facet on each side of the cricoid cartilage. In young people, the thyroid cartilage, like other laryngeal cartilages, is of soft tissue density on CT scan. It mineralizes with age in a central to peripheral direction. Ossified foci of cartilage often contain fatty marrow (Fig. 5.1).

The cricoid cartilage is shaped like a signet ring and has an anterior arch and a flat posterior quadrate lamina (Fig. 5.1). Along the superior edge of the lamina on either side of the midline are two facets for articulation with the pyramidal arytenoid cartridges. The cricoid cartilage is the foundation upon which the framework the larynx rests. Tumor involvement of this structure precludes any type of voice preservation surgery.

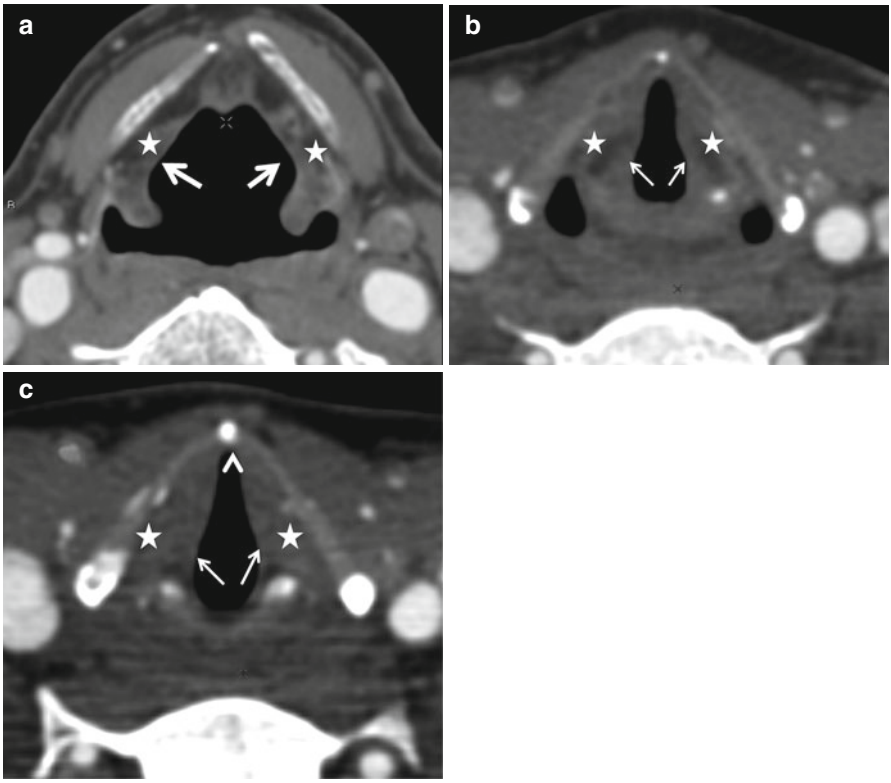

Fig. 5.2 (**a**) The aryepiglottic folds (*arrows*, **a**) descend on either side from the lateral margins of the epiglottis. The AE folds are supported by the conus elasticus. Their free edges form the false cords (**b**). The false cords contain fat as opposed to the true cords which are nearly entirely comprised of the thyroarytenoideus muscle (*arrows*, **c**). The *arrowhead* in (c) points to the anterior commissure. The *asterisks* indicate the paraglottic spaces

The arytenoid cartilages articulate with the cricoid cartilage by true synovial joints, which are susceptible to all the disease processes that may afflict synovial joints elsewhere in the body. An anterior vocal process provides attachment to the vocal ligament. The lateral muscular process provides attachment to the lateral and posterior cricoarytenoid muscles (Fig. 5.1). With age, the arytenoid cartilage can undergo mineralization which may be markedly asymmetric.

The aryepiglottic folds arise from each lateral edge of the epiglottis and extend to the arytenoids. They are supported by a fibrous fascial sheet called the quadrangular membrane. The lower free edge of the aryepiglottic fold forms the false vocal cord, and the associated edge of the quadrangular membrane forms the ventricular ligament. The aryepiglottic folds also form the medial margin of the paraglottic spaces (Fig. 5.2).

Each true vocal cord is comprised of mucosa covering the fibrous vocal ligament medially and the thyroarytenoid (vocalis) muscle laterally. The anterior commissure is an important anatomic landmark where the fibers of the vocal ligament directly pierce the thyroid cartilage. The absence of a protective perichondrium in this location permits tumors to access the thyroid cartilage (Fig. 5.2). The space between the

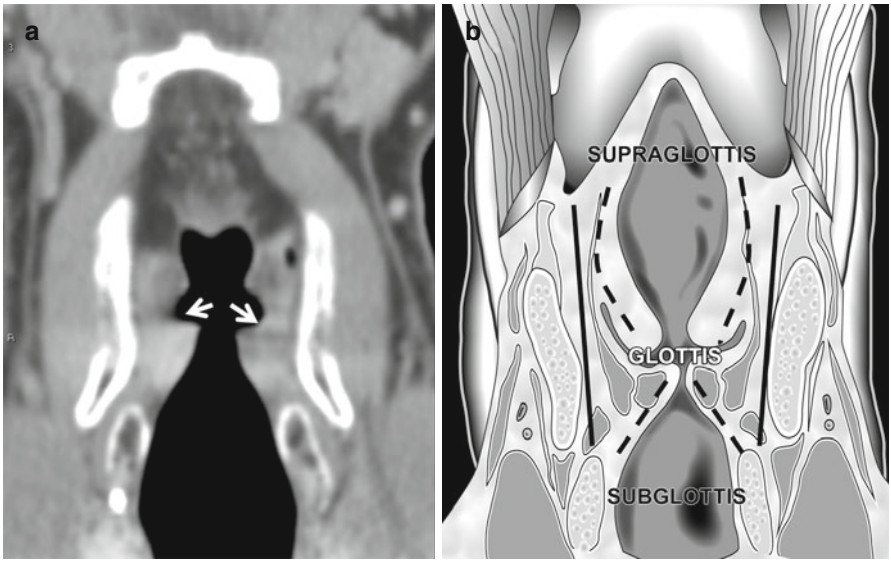

Fig. 5.3 The laryngeal ventricle and the divisions of the larynx. The laryngeal ventricle (*arrows*, **a**) is the space between the false and the true cords and is best seen on a coronal view. The glottis includes the ventricle and about 1 cm of the airway inferiorly. The subglottis extends from this point to the lower margin of the cricoid cartilage. The *paired dashed upper lines* in (**b**) correspond to the conus elasticus and the inferior *pair of dashed lines*, to the cricovocal membrane. Note that the paraglottic spaces run nearly the entire length of the larynx (*black lines* in **b**) and are limited inferiorly by the cricovocal membrane

true and false vocal cords is the laryngeal ventricle. The saccule/appendix of the laryngeal ventricle is lined by mucus glands and may extend into the paraglottic space. The posterior commissure is the region between the two arytenoid cartilages (inter-arytenoid area) (Fig. 5.3).

The conus elasticus is a thick membrane that extends from the vocal ligament to the upper margins of the cricoid cartilage. This membrane is an effective barrier to inferior submucosal spread of glottic malignancy (Fig. 5.3).

It is crucially important to understand the radiology of two spaces in the larynx (Fig. 5.4). The preepiglottic space is a fat-containing midline space located anterior to the epiglottis, posterior to the hyoid bone and thyrohyoid membrane, and contained between the hyoepiglottic ligament superiorly and the thyroepiglottic ligament inferiorly (Fig. 5.4). The preepiglottic space continues on each side as the paraglottic spaces which are bounded laterally by the thyroid cartilage and thyrohyoid membrane and medially by the quadrangular membrane (aryepiglottic folds). The space spans the entirety of the supraglottis and glottis and is limited interiorly by the conus elasticus. Paraglottic space involvement allows submucosal extension of laryngeal malignancy, which may not be visible on endoscopy; it upstages laryngeal cancer and is associated with increased risk of regional metastatic lymphadenopathy. Tumors that arise outside of the larynx may also involve these spaces: the preepiglottic space may be involved by base of tongue malignancy, and the paraglottic space may be involved by invasive pyriform sinus cancers.

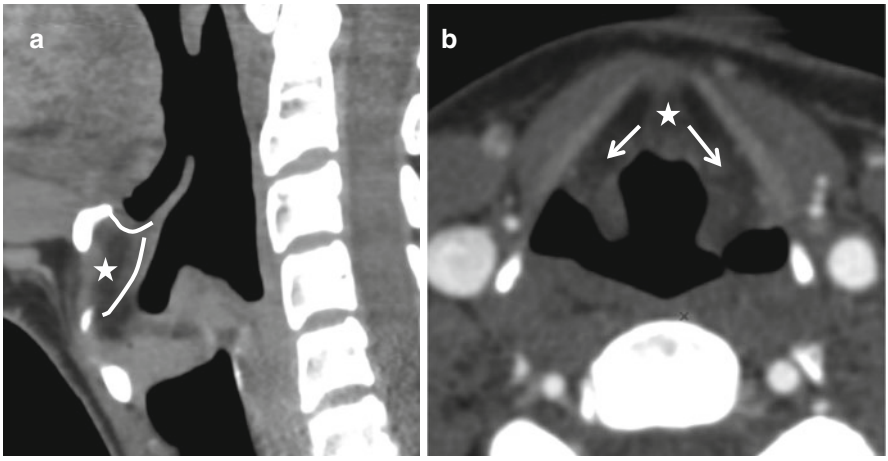

Fig. 5.4 The laryngeal spaces. The preepiglottic space (*asterisk* in **a** and **b**) is enclosed between the hyoepiglottic and thyroepiglottic ligaments and contains a pad of fat. It is best seen on a sagittal view. The preepiglottic space is contiguous with the paraglottic spaces on either side (*arrows*, **b**)

The larynx is divided into the supraglottis, glottis, and subglottis. The supraglottis is cephalad to a plane across the apex of the ventricles. The glottis lies between this plane and a plane drawn 1 cm more caudal; it encompasses the floor of the ventricle, the anterior and posterior commissures, and the true vocal cords. The subglottis extends from the second plane to the inferior margin of the cricoid cartilage (Fig. 5.3).

The supraglottic larynx is drained bilaterally by a rich lymphatic network, and supraglottic squamous cell carcinomas (SCCs) tend to spread to level II and III lymph nodes bilaterally. The glottis, especially the true vocal cord, is poorly served by lymphatics. Small true vocal cord tumors almost are never associated with cervical lymphadenopathy. The subglottis drains to central compartment (level VI) lymph nodes.

The recurrent laryngeal nerve (RLN), a branch of the vagus, innervates all the laryngeal muscles except for the cricothyroid, which is supplied by the superior laryngeal nerves. The right RLN loops under the right subclavian artery before ascending along the tracheoesophageal groove to enter the larynx. The left RLN loops under the arch of the aorta.

The hypopharynx is divided into three subsites: the postcricoid area, the posterior pharyngeal wall, and the pyriform sinuses (Fig. 5.5). The pyriform sinuses may be imagined as inverted cone-shaped outpouchings of the hypopharynx lateral to the larynx. The medial walls of the pyriform sinuses are formed by the aryepiglottic folds. The lateral walls are formed by the thyroid cartilage. It is important to note that the paraglottic space lies directly anterior to the pyriform sinuses. The apices of the pyriform sinuses lie roughly at the level of the superior margin of the cricoid cartilage; cancer in this location is almost invariably treated by a total laryngectomy due to the need for cricoid resection to obtain adequate margins. As the cricoid cartilage is the structural foundation of the larynx, its removal necessitates total laryngectomy.

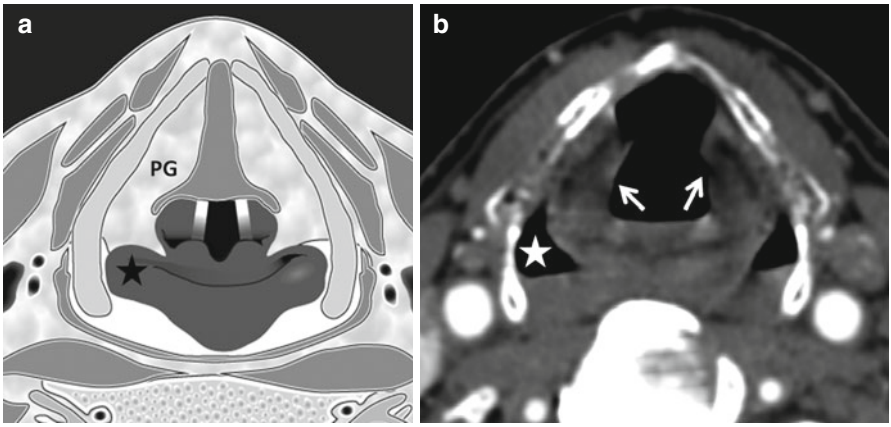

Fig. 5.5 The pyriform sinuses. The pyriform sinuses (*asterisks* in **a** and **b**) are paired outpouchings of the hypopharynx, sandwiched between the aryepiglottic folds (*arrows*, **b**) and the thyroid cartilages. It is important to note that the paraglottic spaces (*PG*) are immediately anterior to the pyriform sinuses and tumor spread between the larynx and hypopharynx can easily occur here

5.3 Imaging Evaluation

Plain radiography plays little to no role in the evaluation of laryngeal pathology, except perhaps in the localization of foreign bodies. Computed tomography is mainstay of laryngeal imaging and is best performed on helical scanners where the entire larynx may be covered in one breath hold. It is important to obtain axial planes along the axis of laryngeal ventricles in order to be able to assess anatomy accurately. This is easily achieved by educating the technologist to reconstruct a set of axial images parallel to the C2–C3 intervertebral disc space. This space is roughly parallel to the plane of the ventricles. Coverage must extend from the skull base to the aortopulmonary window, especially when vocal cord paralysis is being evaluated. Intravenous contrast improves tumor delineation and characterization of lymph nodes.

MRI is rarely used for laryngeal imaging, but may be valuable when assessment of laryngeal cartilage invasion is of critical importance. A typical MR study should consist of precontrast axial and sagittal T1-weighted sequences to depict low-signal-intensity tumor against a background of high-intensity fat contained in ossified cartilage marrow and in the preepiglottic and paraglottic spaces. Fat-suppressed T2-weighted sequences enable detection of high-signal-intensity tumors amid dark suppressed fat. Post-contrast fat-suppressed T1-weighted obtained in axial, coronal, and sagittal planes highlight enhancing tumor and enable differentiation from non-enhancing edema. MR images are often degraded by respiratory and pulsation artifact. In routine clinical practice, most questions can be answered by CT alone.

PET/CT does not aid significantly in establishing the extent of primary laryngeal tumors. It is also not definitively useful in pretreatment evaluation for regional metastasis, which can be adequately accomplished by standard CT and clinical exam. PET/CT may have value in staging advanced tumors that are at risk for distant metastasis and in the evaluation of recurrent disease in the posttreatment neck.

5.4 Squamous Cell Carcinoma

5.4.1 Radiographic Staging

Accurate interpretation of imaging for laryngeal SCC rests upon a thorough understanding of the TNM staging criteria (Box 5.2). The task of the radiologist is not primarily to diagnose SCC but to assist in staging it. Clinical T stage is assigned based on data obtained from endoscopic evaluation and cross-sectional imaging.

Box 5.2. Simplified T Staging System for Laryngeal Squamous Cell Carcinoma

Primary tumor (*T*)

TX: Primary tumor cannot be assessed

T0: No evidence of primary tumor

Tis: Carcinoma in situ

Supraglottis

T1: Tumor limited to one subsite with normal vocal cord mobility

T2: Tumor involves more than one adjacent subsite or involves glottis, vallecula, tongue base, or medial wall of pyriform sinus with normal vocal cord mobility

T3: Tumor limited to larynx with vocal cord fixation and/or invades postcricoid area, preepiglottic space, paraglottic space, and/or minor thyroid cartilage erosion

T4a: Tumor invades through thyroid cartilage, and/or extralaryngeal spread (trachea, soft tissues of the neck including deep extrinsic muscle of the tongue, strap muscles, thyroid gland, or esophagus)

T4b: Tumor invades prevertebral space, encases carotid artery, or invades mediastinum

Glottis

T1:

T1a: Tumor limited to one vocal cord

T1b: Tumor involves both vocal cords

Anterior or posterior commissure may be involved, normal cord mobility

T2: Tumor extends to supraglottis and/or subglottis and/or with limited vocal cord mobility

T3: Tumor limited to the larynx with vocal cord fixation and/or invades paraglottic space and/or minor thyroid cartilage erosion (e.g., inner cortex)

T4a and T4b are staged as for supraglottic cancers

Subglottis

T1: Tumor limited to the subglottis

T2: Tumor extends to vocal cord(s) with normal or impaired mobility

T3: Tumor confined to larynx but with vocal cord fixation

T4a and T4b are staged as for supraglottic cancers

Adapted from AJCC Cancer Staging Manual. 7th edn. Springer, New York

Although tumors of the supraglottis, glottis, and subglottis are staged slightly differently, the principles behind such staging, such as extent of tumor, impairment of cord mobility, cartilage invasion, and involvement of extralaryngeal structures remain the same. Key concepts in the imaging evaluation are:

1. *Subsite involvement*: The supraglottic subsites include the suprahyoid epiglottis, the infrahyoid epiglottis, the aryepiglottic folds, the false vocal cords, and the arytenoids. Involvement of more than one subsite indicates at least a T2 lesion (Fig. 5.6). Although endoscopy in most cases can assess the number of subsites involved accurately, the radiologist must attempt to accurately describe all locations involved, especially when bulky tumors prevent adequate visualization.
2. *Cord mobility*: Fixation of the vocal cords indicates at least a T3 tumor. Determination of vocal cord mobility is best made on endoscopy. Fixation of the true cords may occur from tumor infiltration of the thyroarytenoid muscle or of the cricoarytenoid complex. Involvement of the latter precludes partial laryngectomy.
3. *Preepiglottic space involvement*: The preepiglottic space is comprised almost entirely of fat, which is hypodense on CT and hyperintense on T1-weighted MRI; replacement of this fat by soft tissue indicates invasion, which indicates at least stage T3 for supraglottic tumors and increases the risk of cervical lymphadenopathy (Fig. 5.7).
4. *Paraglottic space involvement*: This space is in direct communication with the preepiglottic space and is also comprised almost entirely of fat. A large amount of submucosal tumor can exist in this space and remain undetected by the endoscopist. Tumor in the paraglottic space can cross the laryngeal ventricle, a finding that is best appreciated on coronal images. A tumor in the paraglottic space that spans the ventricle is considered to be "transglottic." Involvement of this space indicates at least stage T3 for supraglottic and glottis tumors and increases the risk of both lymphadenopathy and extralaryngeal spread (Fig. 5.8).

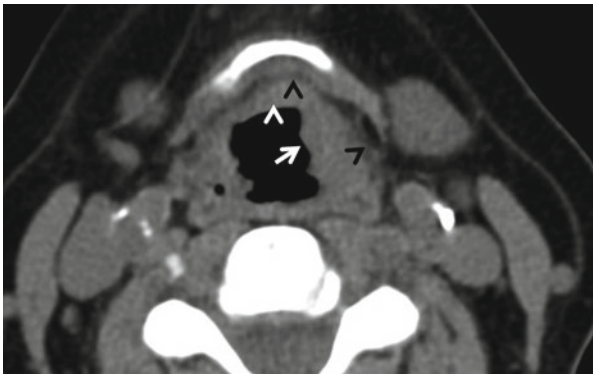

Fig. 5.6 T2 supraglottic squamous cell carcinoma. Note the nodular soft tissue thickening of the mucosa of the left aryepiglottic fold (*arrow*) and root of the epiglottis (*white arrowhead*). A thin rim of intact preepiglottic and paraglottic fat is visible (*black arrowheads*). The patient's left vocal cord demonstrated normal motility on examination. A combination of clinical and imaging findings stages this tumor as T2 lesion

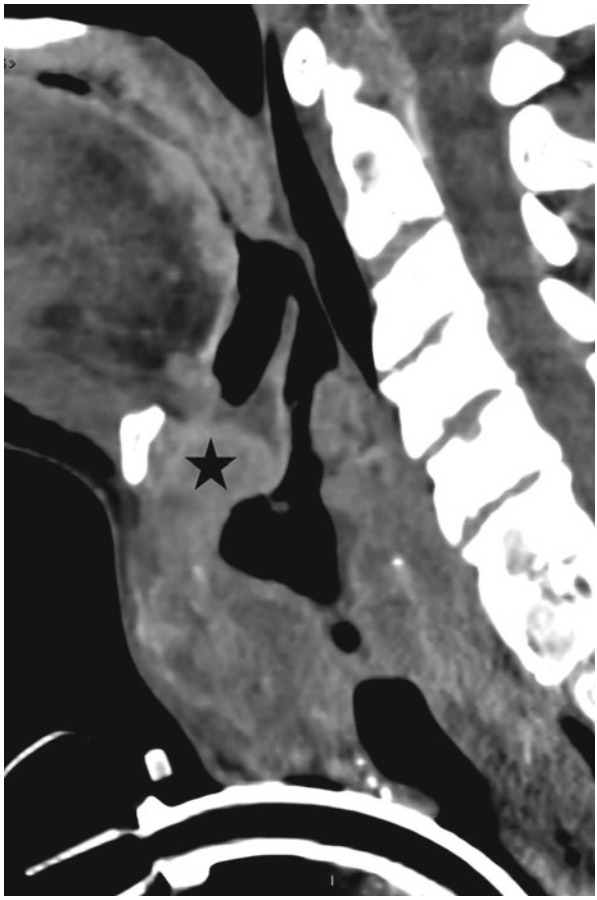

Fig. 5.7 Invasion of the preepiglottic space by a large transglottic malignancy. The fat that is normally encountered in this space is replaced entirely by tumor (*asterisk*)

5. *Cartilage invasion*: Primary laryngeal tumors exhibiting superficial cartilage invasion and complete cartilage penetration are staged as at least T3 and T4a, respectively. Both CT and MR have limitations in the assessment of cartilage invasion because of the highly variable degree of mineralization that is a normal part of aging. Calcified/ossified cartilage is hyperdense on CT and may contain fatty marrow demonstrable as foci of hypodensity on CT and T1 hyperintensity on MRI. Unossified cartilage is of intermediate density on CT and of intermediate signal intensity on MRI. The only reliable sign of involvement by tumor on both CT and MRI is the presence of tumor on both sides of the cartilage (Fig. 5.9). On CT, the presence of focal erosions or sclerosis contiguous with tumor may indicate invasion, but these findings are neither sensitive nor specific; it is not uncommon for normal cartilage, especially the thyroid cartilage, to appear irregular and sclerotic. Asymmetry also occurs commonly: one arytenoid cartilage may be densely sclerotic while the other may be of soft tissue density on CT scan, even when uninvolved by tumor.

Fig. 5.8 Paraglottic space invasion. The graphic (**a**) clearly illustrates how only a fraction of a tumor may be apparent on examination, while the bulk of it remains hidden submucosally in the paraglottic space. In the subglottis, this tumor is limited by the tough cricovocal membrane (*black line* in **b**). In (**c**), the tumor has also invaded the left arytenoid cartilage (*arrow*)

When evaluating MRI studies for cartilage invasion, it is best to begin with the unenhanced T1-weighted images. If the cartilage contains fatty marrow, intermediate signal intensity tumor may be demonstrable against a background of bright fat. On T2-weighted images, with fat suppression, both tumor and tumor-induced edema may appear as areas of hyperintensity against dark suppressed fat. Distinction between the two may be possible on post-contrast fat-suppressed sequences, in which tumor enhances while edema

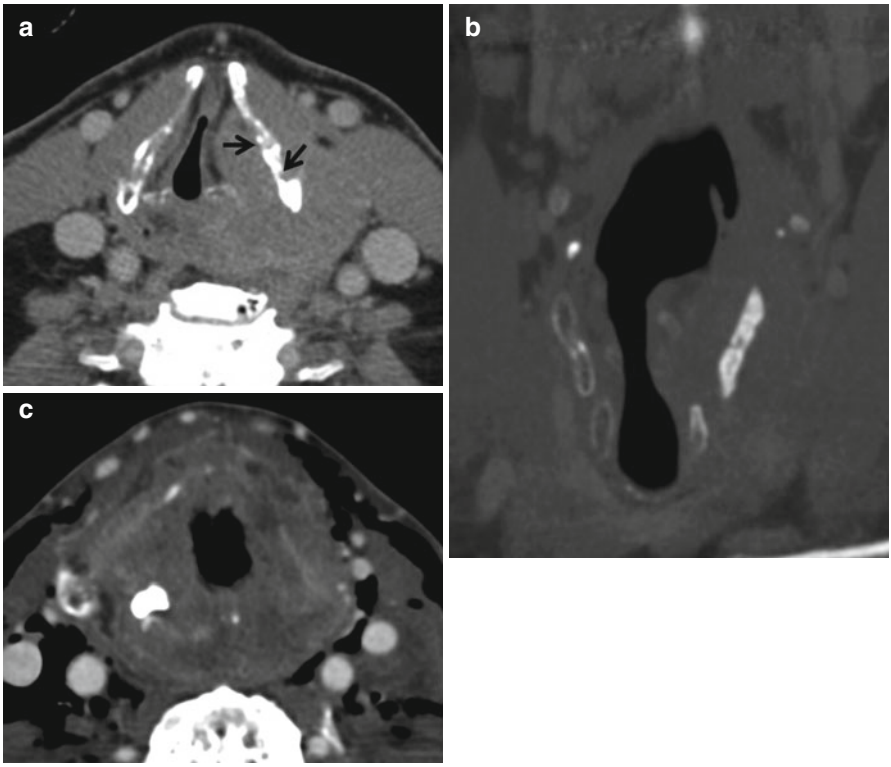

Fig. 5.9 Cartilage invasion. In (**a**), the left lamina of the thyroid cartilage is eroded (*arrows*) and also sclerotic. In (**b**), the left lamina of the thyroid cartilage is diffusely sclerotic. Erosion and sclerosis are not specific signs of cartilage invasion – irregularly ossification may simulate erosion and asymmetric sclerosis can be seen as a normal phenomenon. The only definitive sign of cartilage invasion remains demonstration of tumor on both sides of cartilage, as in (**c**), where tumor is present in the strap muscles after invading the entirety of the thyroid cartilage. The left arytenoid and cricoid lamina have been completely destroyed. The sclerotic right arytenoid cartilage was also found to contain tumor on pathology

does not (Fig. 5.10). Conspicuity between tumor and the adjacent cartilage may not be as evident when there is no fatty marrow. For all practical purposes, the radiologist must call invasion by tumor if tumor is present on both sides of cartilage and must suspect it if erosions or sclerosis are present contiguous to tumor.

6. *Prevertebral space and carotid sheath involvement*: Tumors involving the prevertebral space or carotid sheath are considered unresectable and staged as T4b. The prevertebral space is separated from the aerodigestive tract by a slender fat plane. Loss of this fat plane on CT or MRI may be the earliest sign of invasion, but this plane is not reliably seen in all patients and may be lost due simply to effacement by tumor. MR is perhaps a little more sensitive than CT in detecting

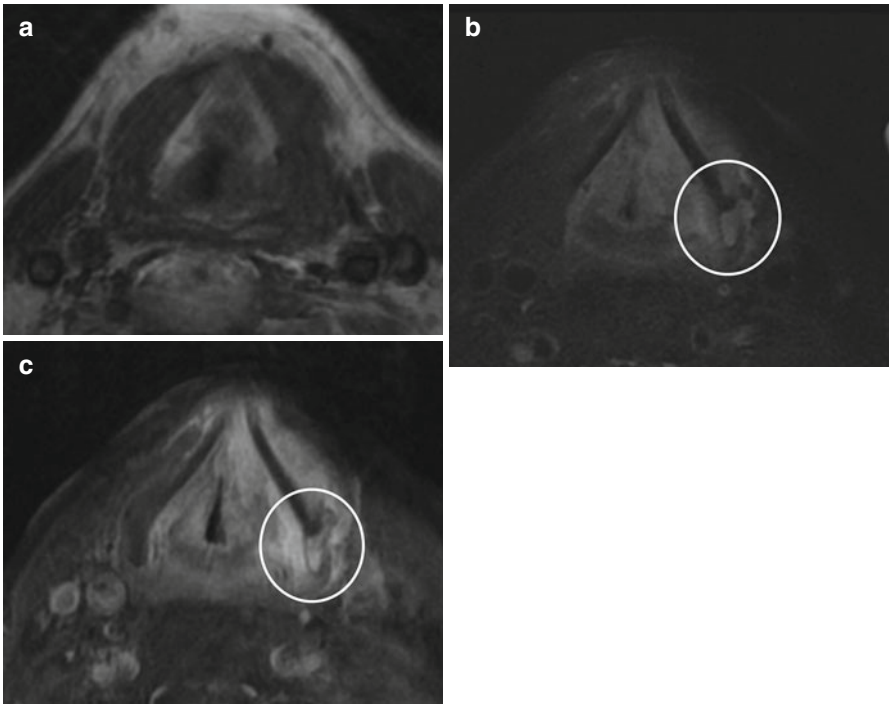

Fig. 5.10 MRI of cartilage invasion. Axial precontrast T1 (**a**), fat-suppressed T2 (**b**), post-contrast fat-suppressed T1 (**c**)-weighted images of a transglottic squamous cell carcinoma. In (**a**), involvement of the left thyroid lamina is difficult to discern from the signal intensity of uninvolved sclerotic cartilage. In (**b**), abnormal T2 hyperintensity in the posterior part of the left thyroid lamina is evident. This area also shows abnormal enhancement in (**c**). This finding is however nonspecific. The only specific sign of invasion is presence of tumor on both sides of cartilage (Courtesy of Dr William P. Dillon, University of California, San Francisco)

prevertebral space invasion. Abnormal signal intensity and enhancement of the longus colli may indicate invasion on MRI (Fig. 5.11). CT and MRI are also not sensitive enough to detect invasion of the adventitia of the carotid arteries. If the extent of arterial encasement is more than three-fourths of the arterial circumference (>270°) on axial images, one can reasonably predict that the adventitia is invaded. If not, only the extent of contact between the tumor and the arterial wall is reported (Fig. 5.12).

7. *Esophageal involvement*: Subglottic and hypopharyngeal malignancies can involve the esophagus (Fig. 5.13). On axial CT sections, the cross section of the hypopharynx appears circular due to the cricopharyngeus. The esophagus on the other hand is oval in cross section. This transition occurs roughly at the lower border of the cricoid cartilage. If one can see a normal circular configuration of the cricopharyngeus below the level of visible tumor, it may be surmised that esophageal invasion has not occurred.

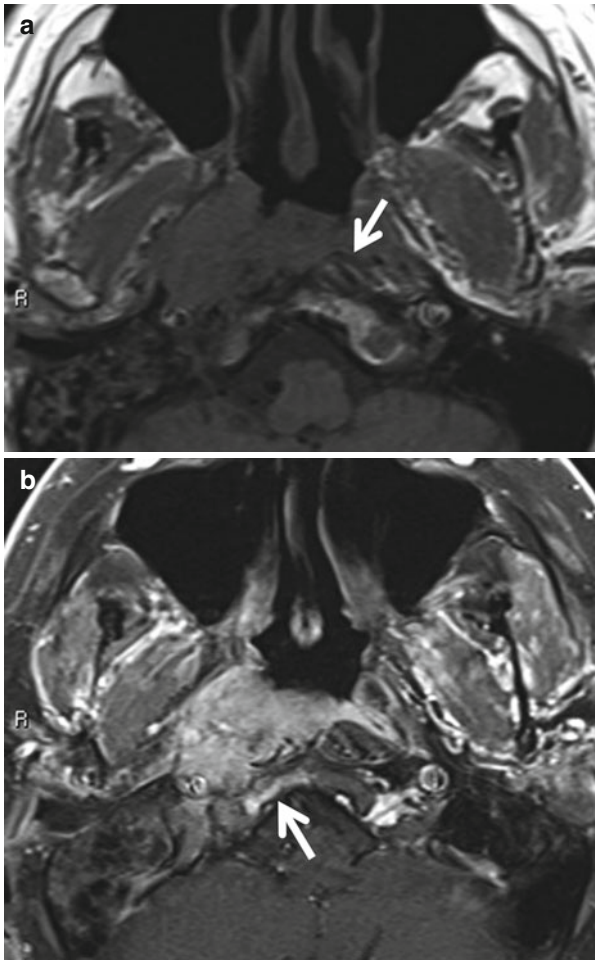

Fig. 5.11 Prevertebral space and skull base invasion by a posterior pharyngeal wall squamous cell carcinoma. In (**a**), an unenhanced T1W image, note the contrast between the uninvolved left longus colli (*arrow*) in which hyperintense striations from fat are visible and the right longus colli, which is engulfed by tumor. In (**b**), in addition to involvement of the prevertebral space, enhancement of the clival marrow, indicating skull base invasion, is also present

5.4.2 Posttreatment Imaging

Treatment-related inflammatory changes and anatomic distortion can make detection of tumor recurrence challenging on posttreatment imaging. It is always useful to read the treatment notes (e.g., radiation summary, operative reports) before attempting to interpret these scans. On CT, the radiated larynx is characterized by thickening of the supraglottic soft tissues, which may persist for several (or many) months after treatment is complete. Collapse and resorption of the laryngeal cartilages in the absence of an associated mass is indicative of radiation chondronecrosis. Recurrent tumor can be completely indistinguishable from postoperative granulation and fibrosis. However, the presence of an enhancing soft tissue abnormality is always worrisome, especially if it is necrotic (Fig. 5.14). PET/CT can be

invaluable in detecting persistent or recurrent disease, but has a high false-positive rate due to the residual inflammation; these should not be obtained less than 8 weeks after treatment is complete, and more ideally at least 12 weeks. A negative PET/CT at this stage virtually excludes a recurrence.

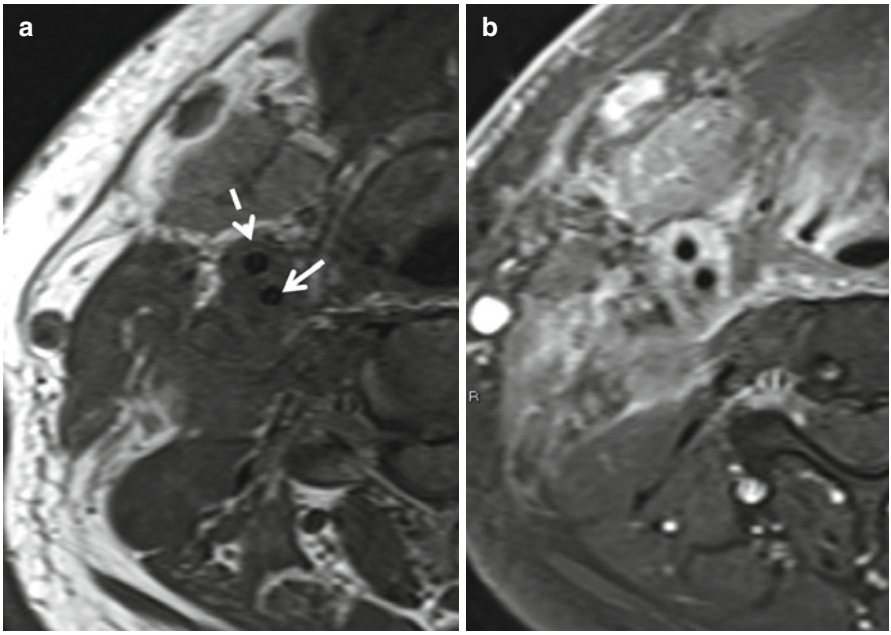

Fig. 5.12 Vascular Involvement by metastatic laryngeal squamous cell carcinoma. The pre- and post-contrast axial T1W images (**a**, **b**) reveal circumferential encasement of the internal (*solid arrow*) and external (*dashed arrow*) carotid arteries by tumor. Encasement of greater than 270° of arterial circumference is the only reliable sign of vascular involvement

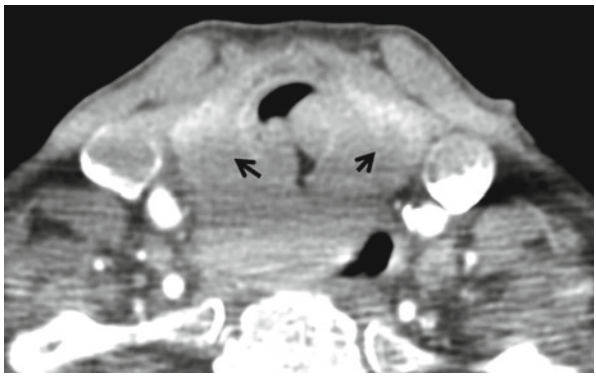

Fig. 5.13 Esophageal invasion by subglottic squamous cell carcinoma. No fat plane is discernible between this extensive tumor and the anterior esophageal wall. Note that the tumor has also transgressed the cricoid ring and invaded the thyroid gland (*arrows*)

Fig. 5.13 (continued)

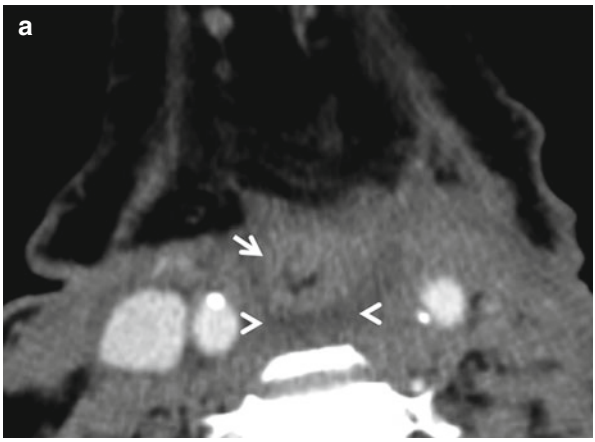

Fig. 5.14 Peristomal recurrence after total laryngectomy. The neopharynx (*arrow*) is rounded in cross section in (**a**). A small amount of fluid and/or edema (*arrowheads*) in the retropharyngeal space can persist for up to a few months after surgery. (**b**) Is an image from the same patient 6 months after surgery. Note the nodular foci of tumor recurrence on either side of the stoma (*star*). On the left, tumor has enveloped nearly the entirety of the circumference of the left common carotid artery (*arrow*)

Fig. 5.14 (continued)

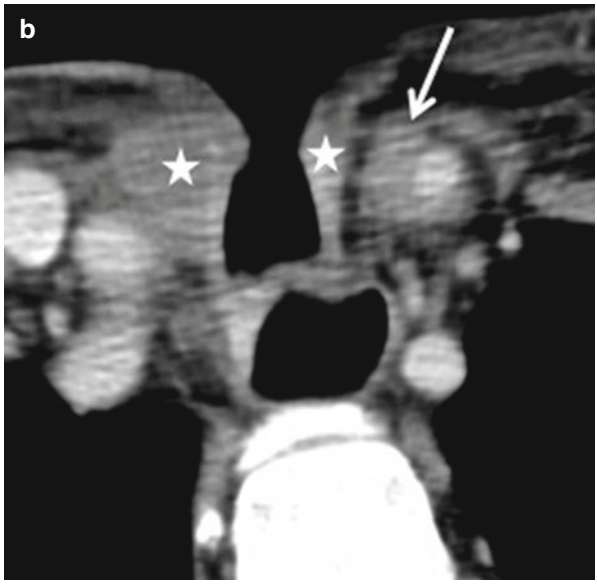

5.5 Other Laryngeal Neoplasms

A number of malignant laryngeal epithelial, glandular, mesenchymal, and hematological tumors including spindle cell carcinoma, adenocarcinoma, neuroendocrine carcinoma, adenoid cystic carcinoma, mucoepidermoid carcinoma, chondrosarcoma, lymphoma, and plasmacytoma can occur. In general, these are indistinguishable from each other on imaging. Chondrosarcomas may be the exception. They usually arise from the cricoid cartilage. The presence of curvilinear foci of intralesional calcification on CT and marked hyperintensity on T2-weighted images is suggestive of a chondrosarcoma (Fig. 5.15).

A number of benign epithelial and mesenchymal neoplasms occur in the larynx as well. Of these, lipomas are easily recognized due to the characteristic CT density and MR T1 hyperintensity. Benign chondroid lesions may be indistinguishable from chondrosarcomas. Hemangiomas and low-flow vascular malformation can also occur in the larynx. Typically, laryngeal hemangioma occurs in children in the subglottis; they are compressible red/blue masses on endoscopy. Imaging may be obtained in order to determine the extent of these lesions which may cause significant airway compromise, especially in the setting of an upper respiratory tract infection. Subglottic hemangiomas are usually diagnosed on endoscopy as compressible bluish-red masses in neonates with respiratory distress, and imaging is not absolutely essential. Laryngeal papillomas are probably the most common benign epithelial neoplasm of the larynx. Imaging for these is rarely obtained. Occasionally, a paraganglioma may manifest as an intensely enhancing supraglottic mass.

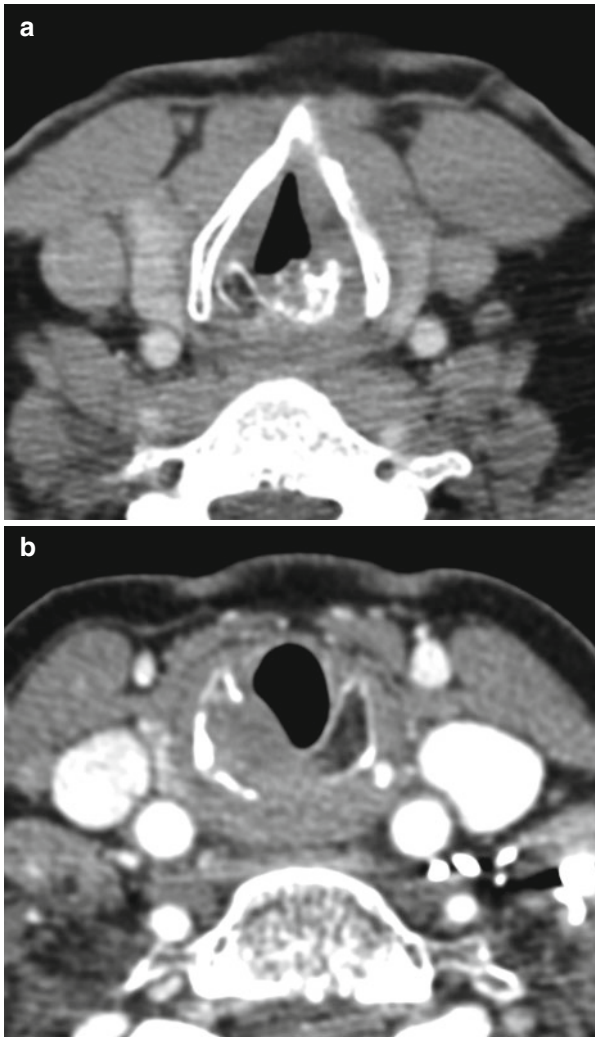

Fig. 5.15 Two examples of laryngeal chondrosarcoma. In (**a**), a calcified mass arising from the left arytenoid cartilage is present. In (**b**), an expansile mass arising from the cricoid cartilage is seen, devoid of calcifications. Calcifications are a useful but not invariable sign of chondrosarcoma

5.6 Infectious and Inflammatory Disorders

Croup and epiglottitis are perhaps the two most important acute inflammatory laryngeal conditions. Both are more common in children. Epiglottitis caused by *Haemophilus influenza*, now rare in children because of effective vaccination, can occur in adults where there is usually inflammation of the remainder of the supraglottis as well. These conditions are rarely imaged. On the frontal radiograph, the loss of the subglottic arch results in the appearance of a "steeple sign" in patients with croup. In epiglottitis, the thickened epiglottis on a lateral plain film produces the "thumb sign" (Fig. 5.16). Because the inflamed epiglottis can rapidly compromise the airway, epiglottitis can be life-threatening, and attempts at visualization and imaging are contraindicated. Radiography must only be attempted when absolutely necessary and only under conditions where an airway can be quickly obtained if needed (intubation or tracheotomy).

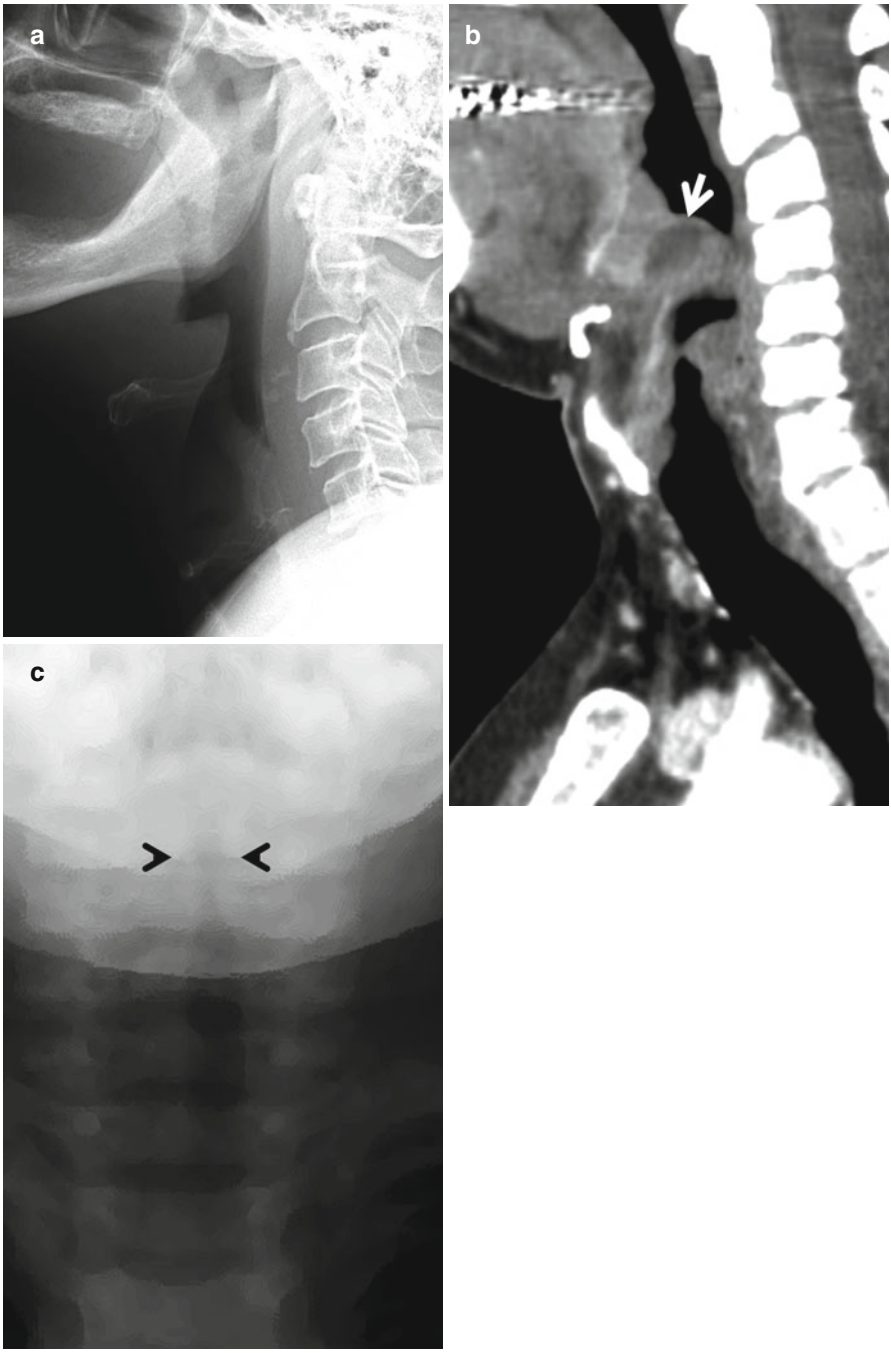

Fig. 5.16 (**a**,**b**) Acute epiglottitis. Note the swollen epiglottis with a thumb-like appearance. Radiography is unnecessary in acute epiglottitis and must not be undertaken lightly but occasionally may be performed to exclude a foreign body. It is best performed with the patient in a sitting position to keep the airway open. Epiglottitis can be life-threatening and resources to secure the airway must be available at all times. The CT image shows an edematous epiglottis containing an abscess (*arrow*). CT is unnecessary for acute epiglottitis. (**c**) Croup – "steeple" like narrowing of the subglottic airway (*arrowheads*)

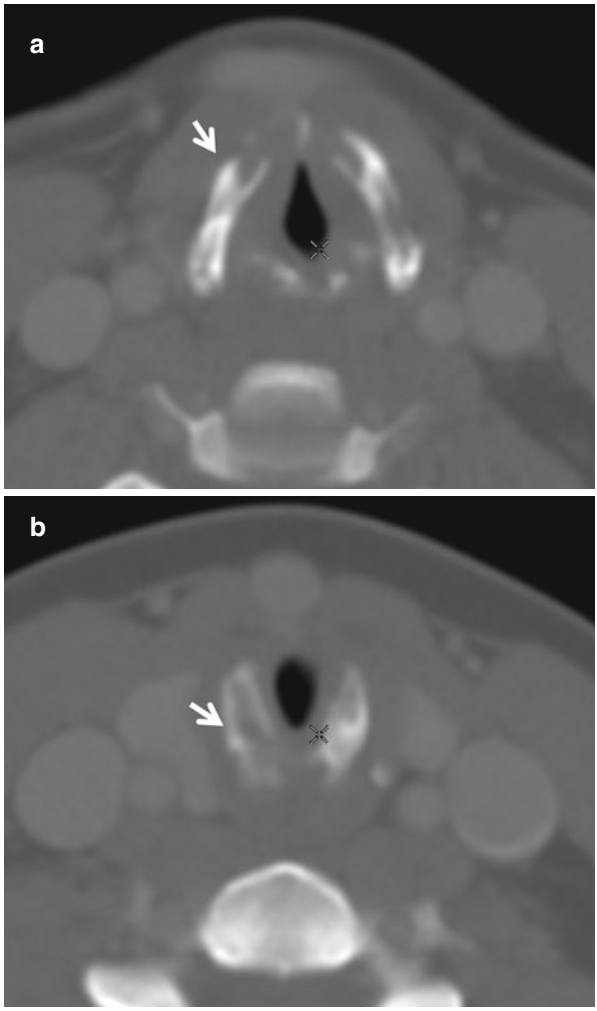

Fig. 5.17 Relapsing polychondritis. Cartilage calcification in relapsing polychondritis is usually smooth and linear and tends to affect the subglottic airway, the nosa, pinna, and external auditory canal. The "tram-track" calcification of the thyroid lamina and the cricoid arch (*arrows*, **a** and **b**) as in this case are a less common pattern

Chronic tuberculous, mycotic, and syphilitic infections can produce a chronic laryngitis. None of these are likely to be encountered in routine practice. Chronic laryngeal inflammation especially involving the cartilages and their articulations can occur with connective tissue disease. Relapsing polychondritis is characterized by recurrent inflammation of the laryngeal cartilages which ultimately leads to sclerosis, thickening, and collapse of the laryngeal cartilages and of the tracheal rings (Fig. 5.17). A similar picture can be seen in patients with radiation-related chondritis after treatment for laryngeal cancer.

5.7 Trauma

Laryngeal trauma may be the result of penetrating or blunt forces and is best evaluated by CT. Blunt force may cause fracture and/or joint dislocation. Fractures are most common in the thyroid cartilage and may be transverse or vertical in orientation. Cricoid cartilage fractures tend to be multifocal as the cricoid is a ring. The task of the radiologist is to identify fracture fragments that compromise the airway and to determine if a hematoma, which may be focal or concentric, is present (Fig. 5.18).

5.8 Laryngocele

A laryngocele is a dilatation of the laryngeal saccule filled with fluid or air that appears as a smooth submucosal mass on laryngoscopy. Small incidental laryngoceles are not uncommon on CT scans obtained for other indications. An internal laryngocele is confined to the larynx; an external laryngocele insinuates into the extralaryngeal soft tissues through the thyrohyoid membrane. When fluid filled, it is important to scrutinize the laryngeal ventricle for a subtle obstructive tumor. On CT scans, laryngoceles are typically well-defined, rounded, fluid- or air-filled structures in the paraglottic space. An infected laryngocele (laryngopyocele) demonstrates peripheral enhancement (Fig. 5.19).

5.9 Vocal Cord Paralysis

The CT appearance of the paralyzed vocal cord is characteristic (Fig. 5.20): the affected cord is small due to atrophy of the thyroarytenoid muscle, the ipsilateral ventricle is expanded, and the pyriform sinus and vallecula are also sometimes expanded. Close inspection may also reveal fatty atrophy of the posterior cricoarytenoid muscle, seen on the dorsal aspect of the cricoid cartilage. A CT study for vocal cord palsy, especially on the left, must include images down to the level of the aortopulmonary window. The entire course of the vagus from the medulla through the jugular foramen, along the carotid sheath (where the nerve lies posterior to the artery and vein), must be evaluated. Increased relative uptake may be seen in the normal unaffected cord on PET/CT imaging, and this must not be construed as an abnormality. When a paralyzed vocal cord has been medialized surgically, images showing injected or implanted material must not be mistaken for pathology (Fig. 5.21).

5.10 Laryngeal Stenosis

True congenital laryngeal stenosis is rare; most cases of airway stenosis are acquired and are subglottic and/or upper tracheal in location and occur after prolonged endotracheal intubation or other iatrogenic injury. Stenosis can occur after trauma or corrosive

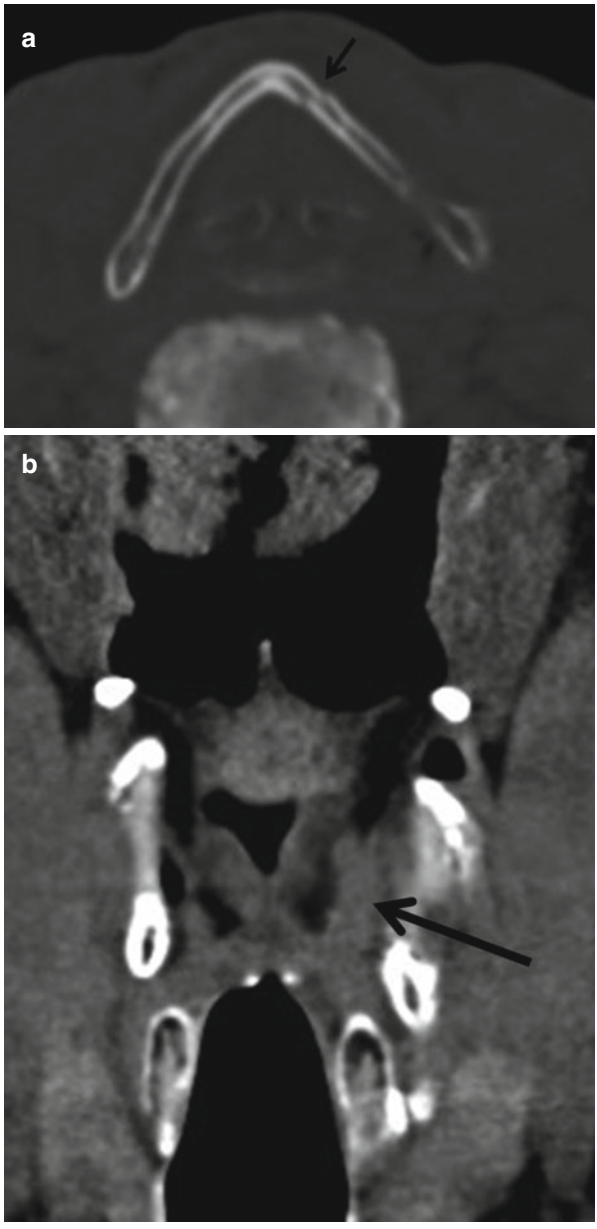

Fig. 5.18 Vertical fracture of the left lamina of the thyroid cartilage (*arrow* in **a**) associated with a hematoma in the paraglottic space (*arrow*, **b**). The conspicuity of laryngeal fractures is a function of the extent of mineralization. Airway compromise may occur from a combination of fracture fragment encroachment and hematoma

ingestion/aspiration. Treatment ranges from observation to intraluminal scar lysis and dilation to resection and reconstruction, depending on the extent and severity of the problem. Laryngeal stenosis is best evaluated with CT. "Virtual" endoscopic images can be reconstructed from the source CT data set and may be useful for surgical planning. The radiologist must indicate the length and diameter of the stenotic segment, describe if it is due to soft tissue or cartilage, and indicate the upper and lower limit of the stenosis in relation to an anatomic landmark (e.g., ventricle, cricoid, carina) (Fig. 5.22).

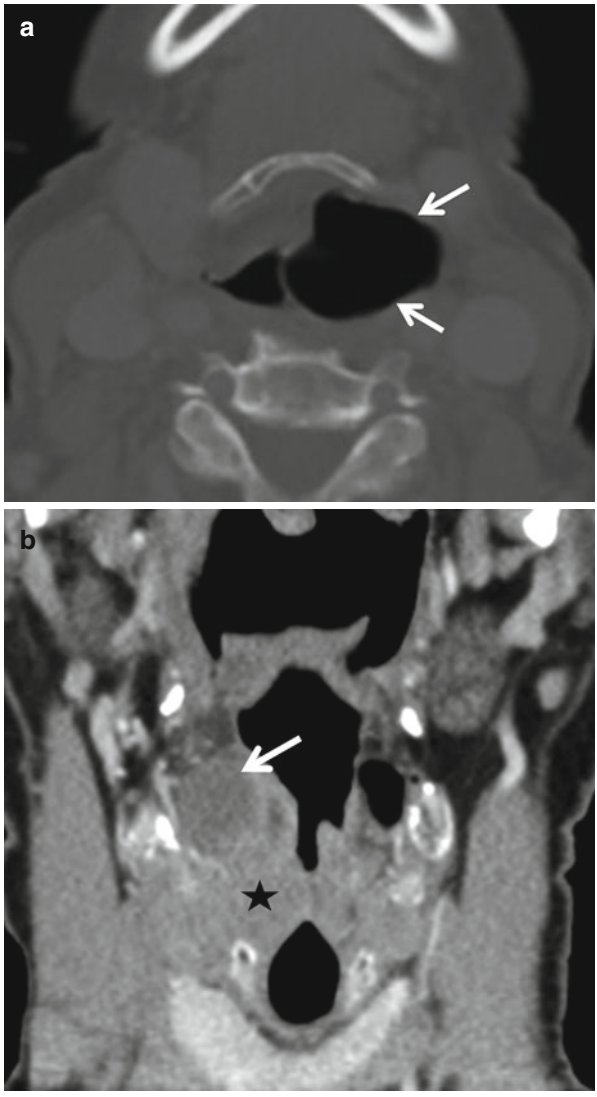

Fig. 5.19 (**a**) Air-containing laryngocele. In (**b**), the laryngocele contains fluid. This should always prompt close evaluation of the glottis to exclude an obstructing malignancy (*asterisk*)

5.11 The Surgeon's Perspective

5.11.1 Laryngeal and Hypopharyngeal Malignancy

Patients with laryngeal or hypopharyngeal neoplasms can present with a range of complaints including dysphonia, throat pain, neck mass, dysphagia, odynophagia, hemoptysis, otalgia, shortness of breath, fatigue, or weight loss. These patients usually have a history of excessive tobacco and/or alcohol use. A thorough head and neck examination is required when a patient with risk factors presents with these complaints, and this should include indirect mirror examination of the larynx or flexible fiberoptic

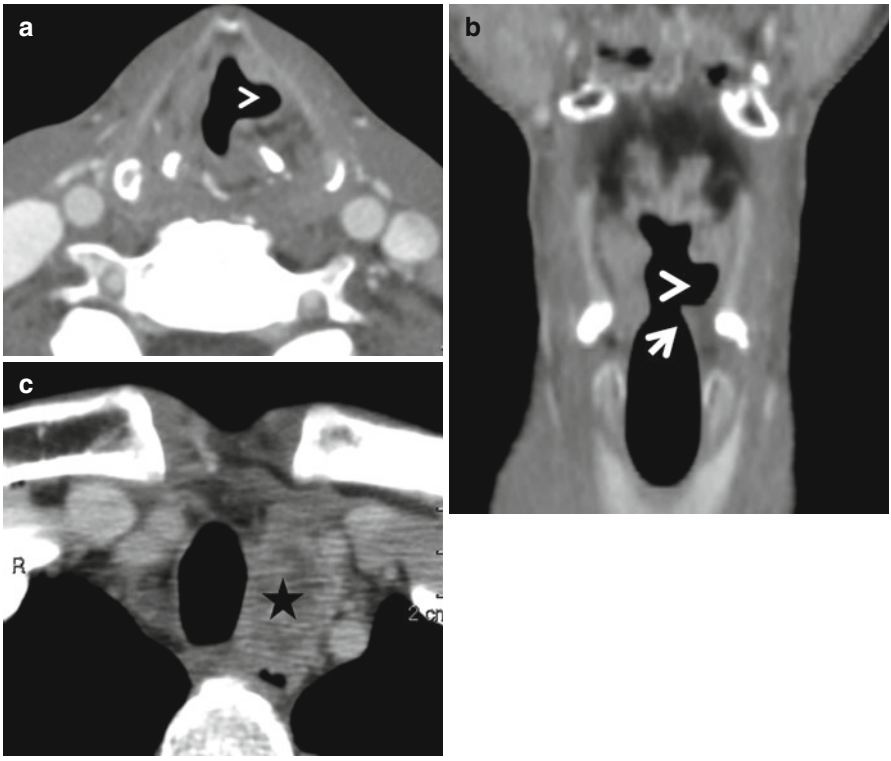

Fig. 5.20 Vocal cord paralysis. Figures (**a**, **b**) show the typical appearance of a paralyzed cord – the cord is in a paramedian position (*arrow*, **b**), and the laryngeal ventricle is dilated (*arrowheads*). The necrotic metastatic lymph node in the left tracheoesophageal groove responsible for recurrent laryngeal nerve invasion is seen in (**c**) (*asterisk*)

Fig. 5.21 Typical appearance of medialization laryngoplasty for vocal cord paralysis with Teflon (*arrow*). This must not be mistaken for pathology

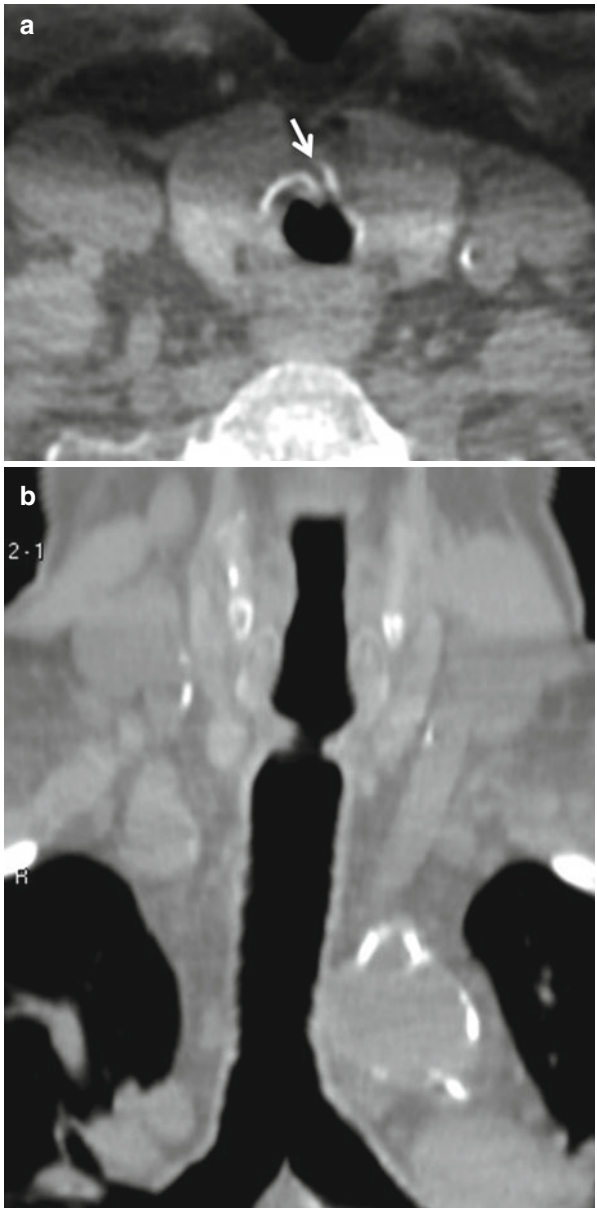

Fig. 5.22 Subglottic stenosis after tracheostomy. This is a "hard" stenosis produced by fragmentation of the anterior tracheal wall and inward displacement of the cartilage fragments (*arrow*, **a**). The coronal reformation (**b**) demonstrates the longitudinal extent of stenosis. Stenosis may also occur due to formation of scar tissue

laryngoscopy. This allows the physician to ascertain the presence of a neoplasm, determine its location, assess for patency of the airway, and evaluate vocal cord function. Direct laryngoscopy under general anesthesia is utilized to determine the mucosal extent of the tumor and to obtain tissue for diagnosis. Evaluation of vocal cord function is limited in this setting and is better performed while the patient is awake in the office.

The clinical stage is determined by a combination of laryngoscopy and imaging findings and is the beginning of treatment planning. As described in detail above, a contrasted neck CT is the preferred study for the initial evaluation of a laryngeal neoplasm. This step may be unnecessary in patients with T1 glottic cancers because of the low likelihood of cervical nodal metastasis and because the entirety of the primary tumor can be visualized. For other patients, imaging is utilized to evaluate the submucosal extent of the primary tumor, which cannot be determined on physical examination or laryngoscopy, and to clarify cervical nodal disease.

Given that hypopharyngeal cancers are generally considered to be more aggressive, are often discovered at a more advanced stage, and often abut or involve the cricoid cartilage, they are generally treated with total laryngectomy and partial pharyngectomy followed by radiation or chemoradiation as appropriate based on pathologic findings.

Treatment options for patients with laryngeal malignancies utilize either surgery or radiation as the primary modality. In general, early stage malignancies (stage I and II) can be treated with a single modality, whereas advanced stage tumors (stage III and IV) require at least dual modality therapy (i.e., surgery and radiation, radiation and chemotherapy). Treatment approaches using definitive radiation ± chemotherapy are referred to as "organ preservation" approaches. There are several imaging findings that have a significant impact on selection of the best treatment approach. T4 primary tumors, particularly those with extension into the thyroid cartilage, are best treated with total laryngectomy and postoperative radiation, rather than attempted organ preservation with definitive chemoradiation therapy. Other key radiographic findings include invasion of prevertebral or paraspinous musculature and circumferential carotid involvement which indicate unresectable disease.

There is a range of surgical options for treatment of laryngeal cancer. When considering surgery as the primary treatment modality, imaging findings can be important in determining if a voice preserving laryngeal procedure is feasible. Treatment of early stage tumors is usually feasible using a transoral laser approach; most commonly this would involve cordectomy for early glottic cancers or supraglottic laryngectomy for early supraglottic cancers. Supraglottic laryngectomy (unilateral or bilateral) (Fig. 5.23) can also be performed using a transoral robotic approach and can be performed as a transcervical procedure as well. The inferior limit of resection for a supraglottic laryngectomy passes through the laryngeal ventricle. The true vocal cords are spared, as are the arytenoid and cricoid cartilages. A supraglottic laryngectomy is contraindicated if there is vocal cord fixation or if tumor involves (1) the true vocal cord or ventricle; (2) the thyroid, cricoid, or arytenoid cartilage; or (3) the tongue base to less than 1 cm from the circumvallate papillae. Thus, it is valuable to determine the vertical extent of the tumor on CT, and for this, coronal images can be particularly useful.

Vertical hemilaryngectomy (Fig. 5.23) is another transcervical partial laryngectomy procedure that is voice preserving and appropriate in some patients with limited well-lateralized glottic disease. The limit of resection is in the sagittal plane; the

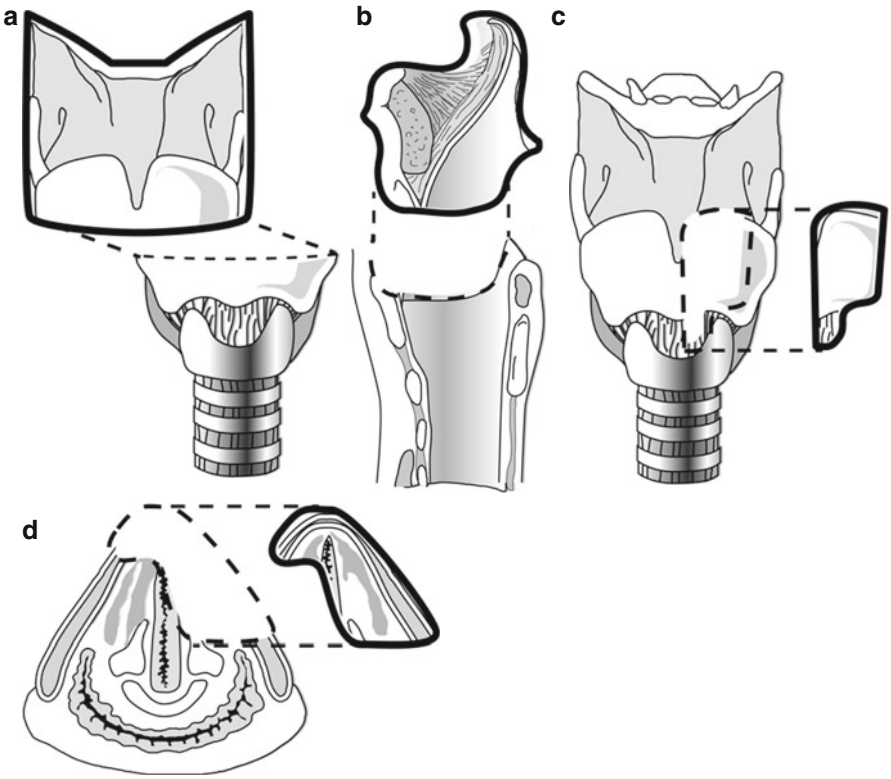

Fig. 5.23 Structures removed in supraglottic laryngectomy (**a**, **b**) and vertical hemilaryngectomy (**c**, **d**) (Modified from Becker M (2000) Neoplastic invasion of laryngeal cartilage: radiologic diagnosis and therapeutic implications. Eur J Radiol 33(3):216–229)

procedure is contraindicated if the tumor crosses the anterior commissure, especially if it involves more than the anterior third of the contralateral true cord. Defining the lower limit of tumor involvement is important. Because the cricoid cartilage is higher posteriorly that it is anteriorly, 5 mm of downward growth from the true cords posteriorly, as opposed to 10 mm anteriorly is permissible. If tumor extent inferiorly is any greater than this, the cricoid cartilage will have to be removed and a total laryngectomy is the only option.

When necessary and appropriate, total laryngectomy is still a very effective operation, and speech and swallowing rehabilitation after this procedure allow for a reasonable quality of life in most patients. After a total laryngectomy, a "neopharynx" is constructed by reapproximating the hypopharyngeal mucosa. If an associated partial pharyngectomy is required or if the total laryngectomy is a salvage procedure in a radiated field, many surgeons employ regional pedicled flaps or free flaps to more effectively and durably reconstruct the pharynx. On CT, the neopharynx appears as a tubular structure with a rounded cross section (Fig. 5.14).

Box 5.3. Imaging Checklist of Laryngeal/Hypopharyngeal Malignancy

1. Is it supraglottic, glottis, glottis, subglottic, or transglottis?
2. What are the subsites involved?
3. Is the base of the tongue involved?
4. Is the preepiglottic space involved?
5. Is the paraglottic space involved?
6. Does the tumor cross the laryngeal ventricle?
7. Does the tumor cross the anterior commissure? If so, how much of the contralateral true cord is involved?
8. Is their cartilage involvement? If so, is it superficial erosion or is it penetration with extralaryngeal spread?
9. Is the cervical esophagus involved?
10. Is the prevertebral space violated?
11. Is the carotid space invaded?
12. What is the extent of metastatic cervical lymphadenopathy, if any? Is there evidence of nodal necrosis or extracapsular spread?

5.11.2 Other Laryngeal Pathology

Imaging plays a major role in the evaluation of other laryngeal pathology in addition to laryngeal and hypopharyngeal neoplasms. When unilateral vocal cord paralysis is identified in a patient with voice complaints without a corresponding surgical history (lung, cervical spine, thyroid, etc.), it is important to evaluate the entire course of the recurrent laryngeal nerve. This can be the presenting finding in patients with tumors of the thyroid gland, thymus, mediastinum, or apex of the lung. Patients with blunt trauma to the neck may be best managed operatively if displaced fractures of the laryngeal skeleton are identified on CT. Finally, CT can determine the extent of tracheal stenosis when the stenosis is too extensive to permit direct visualization endoscopically.

Laryngeal anatomy is a key predictor of tumor behavior. The radiologist's role is to understand this concept and assist the otolaryngologist in answering two fundamental questions about tumor spread: "How low does it go?" and "How deep does it go?" (Box 5.3). Accurate interpretation of posttreatment scans rests upon a sound understanding of the treatment option(s) employed.

Further Reading

Becker M, Zbären P, Delavelle J, Kurt AM, Egger C, Rüfenacht DA, Terrier F (1997) Neoplastic invasion of the laryngeal cartilage: reassessment of criteria for diagnosis at CT. Radiology 203(2):521–532

Becker M, Burkhardt K, Dulguerov P, Allal A (2008) Imaging of the larynx and hypopharynx. Eur J Radiol 66(3):460–479

Blitz AM, Aygun N (2008) Radiologic evaluation of larynx cancer. Otolaryngol Clin North Am 41(4):697–713

Curtin HD (1989) Imaging of the larynx: current concepts. Radiology 173(1):1–11

Mukherji SK, Weadock WJ (2002) Imaging of the post-treatment larynx. Eur J Radiol 44(2):108–119

Salivary Glands

6

Prashant Raghavan, Mark J. Jameson, Max Wintermark, and Sugoto Mukherjee

6.1 Introduction

The salivary glands may be afflicted by a wide variety of inflammatory, infectious, and neoplastic processes. This often creates difficulty in arriving at a specific imaging diagnosis. Knowledge of glandular anatomy and pertinent clinical data is vital to the radiologist to arrive at a reasonably short list of differential diagnoses and provide information that is of importance to the otolaryngologist for surgical planning. This chapter discusses basic salivary gland anatomy and imaging appearances of the more common glandular disorders and also provides a table of differential diagnosis based on pattern recognition. A brief section that discusses the otolaryngologist's approach to the evaluation of salivary gland disease is also included.

6.2 Anatomy

- Box 6.1 summarizes a summary of glandular anatomy, ductal and lymphatic drainage.
- The parotid, submandibular, and sublingual glands are the major paired glandular structures. Up to 750 minor salivary gland clusters exist in the upper aerodigestive tract, paranasal sinuses, and parapharyngeal spaces.
- The parotid gland is divided into superficial and deep lobes. This division is artificial, usually based upon the plane of the facial nerve. The part of the gland that lies external to the nerve is the superficial lobe; that which lies internal to the plane of the nerve is the deep lobe. Alternatively, this division can also be based upon the plane of the ramus of the mandible. The deep lobe passes through the stylomandibular tunnel and lies laterally to the fat of the prestyloid parapharyngeal space. The stylomandibular tunnel is bounded anteriorly by the ramus of the

P. Raghavan et al., *Manual of Head and Neck Imaging*,
DOI 10.1007/978-3-642-40377-4_6, © Springer-Verlag Berlin Heidelberg 2014

Box 6.1 Salivary Gland Anatomy

	Location	Ductal drainage	Lymphatic drainage	Secretomotor innervation
Parotid	Parotid space	Stensen's duct – pierces buccinator to open opposite upper second molar	Intraparotid notes, IIA, IIB	Inferior salivary nucleus → glossopharyngeal N → Jacobson's N →tympanic plexus → lesser petrosal N → otic ganglion → auriculotemporal N
Submandibular	Submandibular space	Wharton's duct – opens adjacent to frenulum linguae in the floor of the mouth	I	Superior salivatory nucleus →f acial N → chorda tympani→lingual N → submandibular ganglion
Sublingual	Sublingual space	Multiple ducts (Rivinus) open into floor of mouth beside frenulum linguae, some of the smaller ducts may unite to form a larger Bartholin's duct that joins Wharton's duct	I	Same as for the submandibular gland

mandible and posteriorly by the stylomandibular ligament, sternomastoid, and digastric (posterior belly) muscles (Fig. 6.1a).

- The facial nerve courses lateral to the retromandibular vein. The vein is seen as a constant structure on cross-sectional imaging and is a useful marker for the location of the nerve (Fig. 6.1b).
- Accessory parotid tissue may be located along the course of the Stensen's duct. This should not be mistaken for a mass lesion.
- The parotid gland develops before the submandibular and sublingual glands but is the last to encapsulate. This explains the inclusion of small lymph nodes in the parotid space.
- The submandibular gland wraps around the free edge of the mylohyoid muscle. The angular facial vein lies dorsal to the gland. A primary submandibular mass displaces the vein posteriorly. When the vein lies anterior to a mass in the submandibular triangle, the mass is not submandibular gland in origin. The key anatomic features of the submandibular and sublingual glands are depicted in (Fig. 6.2).

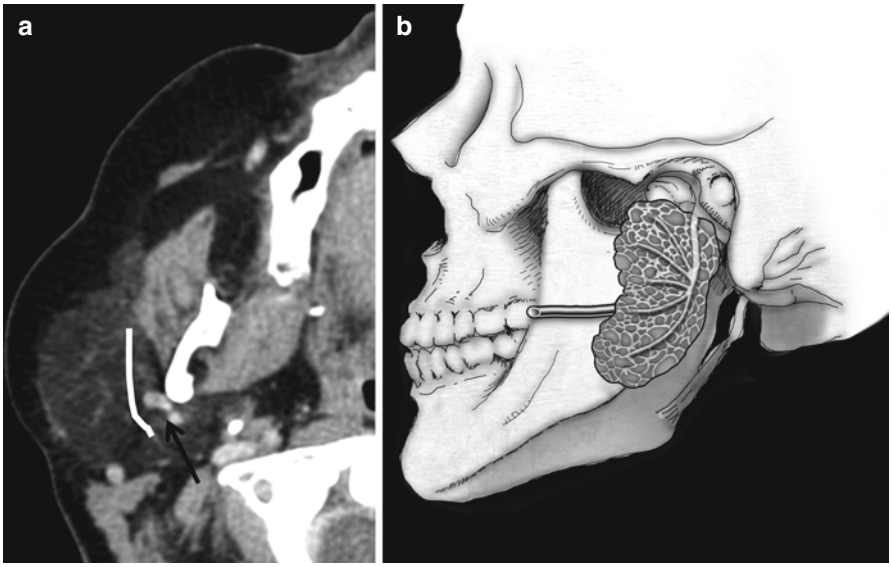

Fig. 6.1 The retromandibular vein (RMV, *arrow* in **a**) is consistently seen on cross-sectional imaging. The facial nerve although not directly visible passes lateral to the RMV in an anteroposterior direction. The parotid gland straddles the stylomandibular tunnel (**b**)

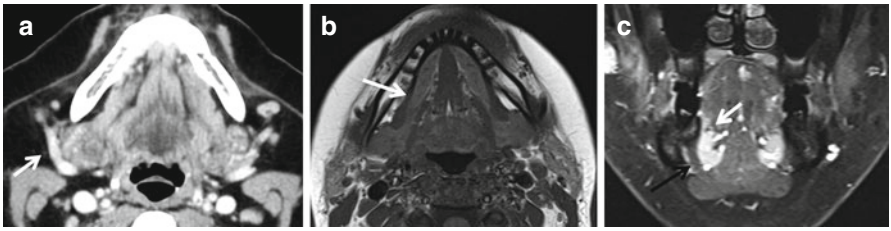

Fig. 6.2 The facial vein lies dorsal to the SMG (*arrow* in **a**). The SMG wraps around the posterior edge of the mylohyoid (*arrow* in **b**). The mylohyoid sling (*black arrow* in **c**) separates the submandibular and sublingual spaces. The sublingual glands are seen as enhancing structures on this coronal MR image (*white arrow*, **c**)

6.3 Imaging Evaluation

6.3.1 Sialography

This technique is not routinely performed in imaging practice. Cannulation of the submandibular and parotid ducts is achieved with commercially available cannulas (Rabinov). Indications for ductal cannulation include:

1. Evaluation for lucent calculi
2. Establishment of diagnoses of inflammatory salivary gland disease, most often Sjögren's syndrome
3. Delineation of the fistulae and sinuses related to the parotid glands
   A CT may be performed in conjunction with a conventional sialogram.

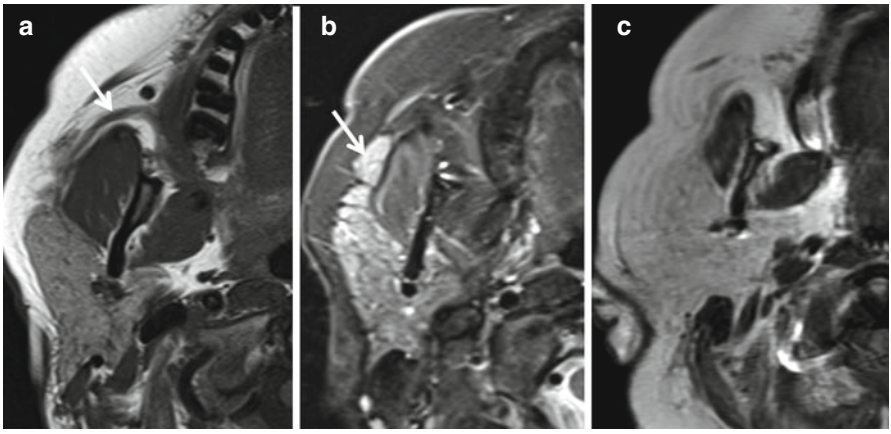

Fig. 6.3 Normal parotid gland. On the T1-weighted image (**a**), the gland is of intermediate to high signal. Stensen's duct (*arrow*) is also clearly visible. In (**b**), a T2-weighted image, the gland is hyperintense. A small lobule of accessory parotid tissue (*arrow*) is seen along Stensen's duct. In (**c**), a T1-weighted image, the gland is diffusely hyperintense due to replacement by fat

6.3.2 Cross-Sectional Imaging

CT is often the first line of investigation and is best performed after administration of IV contrast. CT is best used in inflammatory states where identification of calculi and glandular calcification may be of importance and also in the initial evaluation of palpable masses, although MR is superior in the latter. MRI with gadolinium is best used for evaluation of the local extent of salivary gland malignancy. The usage of gadolinium is a must for evaluation of involvement of the facial nerve in cases of suspected parotid malignancy. MR sialography with heavy T2-weighted sequences may be used when the ductal pathology is suspected. MRI with diffusion may aid in the differentiation of benign from malignant masses. Pleomorphic and myoepithelial adenomas especially may demonstrate increased ADC values compared to other lesions.

The appearance of the parotid gland on cross-sectional imaging is largely dependent upon the extent to which its parenchyma is replaced by fat. The gland may be completely fatty in appearance (hypodense on CT, hyperintense on T1-weighted MRI) in patients with hyperlipidemia and sialosis (Fig. 6.3). T1-weighted MRI without contrast is perhaps the most useful sequence for delineation of the margins of a parotid lesion. The salivary glands are easily insonated by ultrasound due to their superficial location. Ultrasound is best used to guide fine-needle aspiration. The role of PET CT is primarily to stage malignant neoplasms.

6.4 Pathology

6.4.1 Congenital Anomalies

Congenital anomalies are in general uncommon. Agenesis of one or more glands and their ducts has been reported. These are more likely to occur in patients with more widespread craniofacial anomalies that may be consequent to abnormal branchial arch development such as in the Treacher Collins and Goldenhar syndromes. Congenital salivary gland cysts are the most common of such anomaly encountered in practice. These may represent any of the following:
First branchial cleft cysts
Lymphoepithelial cysts
Epidermoid cysts
Congenital sialocele

A young patient with a unilocular cystic mass in the parotid gland may be assumed to have a first branchial cleft cyst (Fig. 6.4). The location of these cysts parallels the route of migration of the pinna. The pinna arises from six ectodermal hillocks, three on each side of the first branchial cleft. It migrates from a ventrocaudal location at the angle of the mandible to a dorsocranial location. A first BCC may lie at any location along this course. A type 1 first BCC lies in the preauricular region and may be associated with a tract that runs laterally to the facial nerve and terminates in the wall of the external auditory canal, usually at the junction of its bony and cartilaginous segments. A type 2 first BCC lies near the angle of the mandible and may also be associated with a tract that terminates at the EAC. The relationship of its tract with the facial nerve is however more variable. Demonstration of the tract may not always be possible with imaging. A fistulogram or a heavily T2-weighted fat-suppressed MRI sequence may help.

Congenital cysts are often indistinguishable on imaging. Most of these present as unilocular low-density masses on CT. Occasionally the fluid density of these lesions may be difficult to appreciate on CT due them being isodense to the adjacent glandular parenchyma. Fluid signal intensity is however clearly evident on MRI. Dermoid/epidermoid cysts may contain low-density foci on CT due to the presence of fat and correspondingly demonstrate high T1 signal on MRI.

6.4.2 Infectious and Inflammatory Disorders

A wide variety of bacterial and viral infectious agents may affect the salivary glands. In most cases, there is no specific imaging pattern that enables identification of the offending organism. Bilateral acute parotid enlargement in a young patient may suggest mumps as the etiology. The presence of abscesses, multiple sinuses, and associated parotid and submandibular lymphadenopathy in conjunction with an ill-defined parotid lesion on CT may indicate actinomycosis as the etiology.

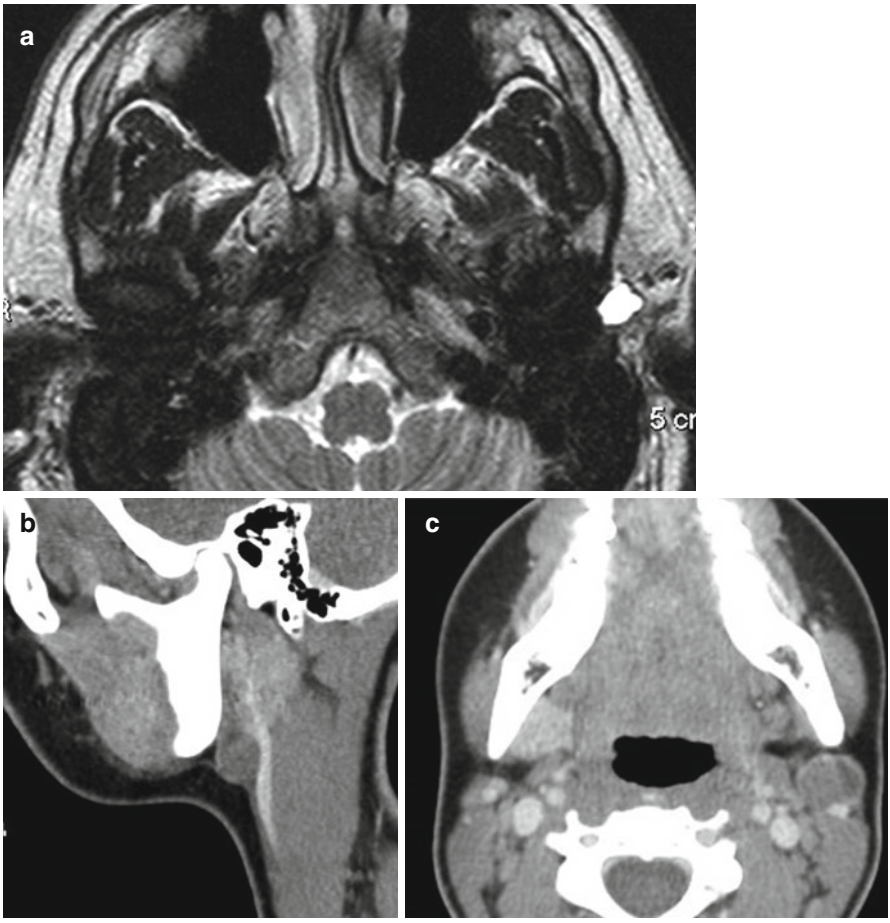

Fig. 6.4 First branchial cleft cysts. A typical type 1 first BCC is shown in (**a**). The cyst contains clear fluid and is located anterior to the external auditory canal. In the presence of degenerative joint disease, a synovial or ganglion cyst of the TM joint may also present in this location. (**b**, **c**) Type 2 first BCC. In a teenager there is faint enhancement of the cyst wall due to recent infection. In an adult, one must always exclude a cystic metastatic lymph node in this location. Mural nodularity or septations are red flags

Identification of bilateral lacrimal gland enlargement in association with multiple parotid masses is suggestive of sarcoidosis. Nonspecific chronic sialadenitis (chronic recurrent sialadenitis) is associated with heterogeneous glandular density and multiple foci of dystrophic calcification.

In the acute setting, the role of the radiologist is to determine if an obstructive calculus is present and identify the presence of potentially drainable abscesses (Fig. 6.5). In the case of chronic inflammatory disease, the radiologist may be the first to identify an imaging pattern compatible with a specific disorder such as Sjögren's syndrome or HIV-associated disease.

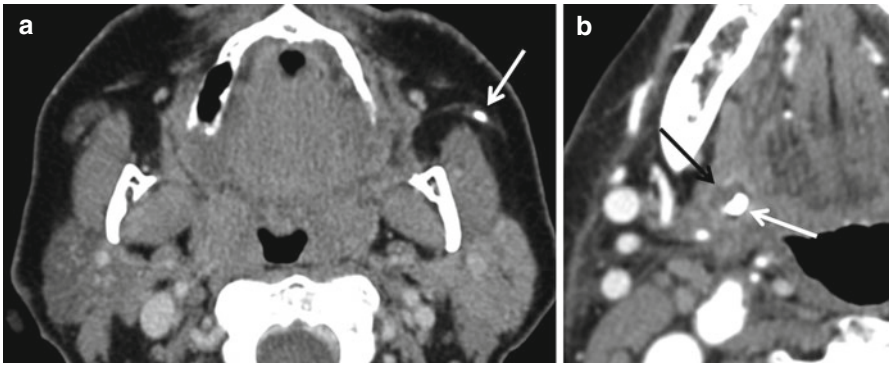

Fig. 6.5 Calculi and sialadenitis. Left Stensen's duct calculus (**a**) with early parotiditis. The left parotid gland enhances to a greater degree than the right. In (**b**), a small abscess (*black arrow*) is seen in the submandibular gland associated with an intraglandular calculus (*white arrow*)

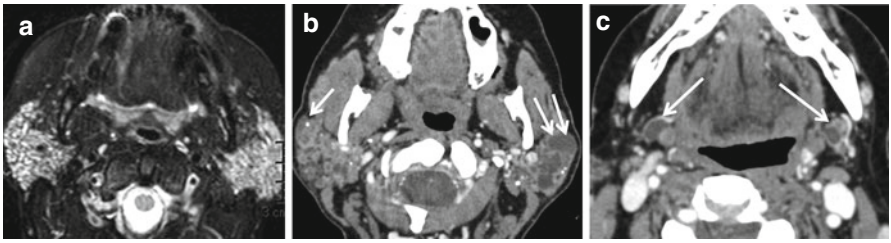

Fig. 6.6 Sjögren's syndrome. Multiple punctate hyperintensities are seen in figure (**a**) representing the "miliary" pattern of intermediate stage Sjögren's syndrome. Images of a patient with late-stage disease (**b**, **c**) where calcifications (*arrow*, **b**) and cyst formation (*double arrows* **b**, *arrows* **c**) are typical. Note the involvement of the submandibular glands in (**c**), a finding that is not seen with HIV infection

6.4.2.1 Sjögren's Syndrome

Sjögren's syndrome may be primary or secondary. Primary Sjögren's syndrome is more common in females (9:1 ratio). Secondary Sjögren's syndrome coexists with other connective tissue disorders. Sjögren's syndrome is characterized by increased B-cell retention in the major and minor salivary glands in response to autoantigenic stimulation. The inflammatory lymphoid infiltrate can conglomerate into discrete masses (benign lymphoepithelial lesions or Godwin's tumors). On conventional sialography, the characteristic finding is multiple small uniformly sized collections of injected contrast representing foci of destroyed peripheral intraglandular ducts and acini. These collections can persist for years and may be visible as punctate hyperdensities on CT. In the later stages, these coalesce to form large cysts. Similar findings are seen on MR sialography. On CT, early stages are nonspecific and may only manifest as increased glandular density. The glands progressively develop a honeycomb appearance. This however may be seen with any cause of chronic sialadenitis and is not specific for Sjögren's syndrome (Fig. 6.6). BLELs usually appear as solid

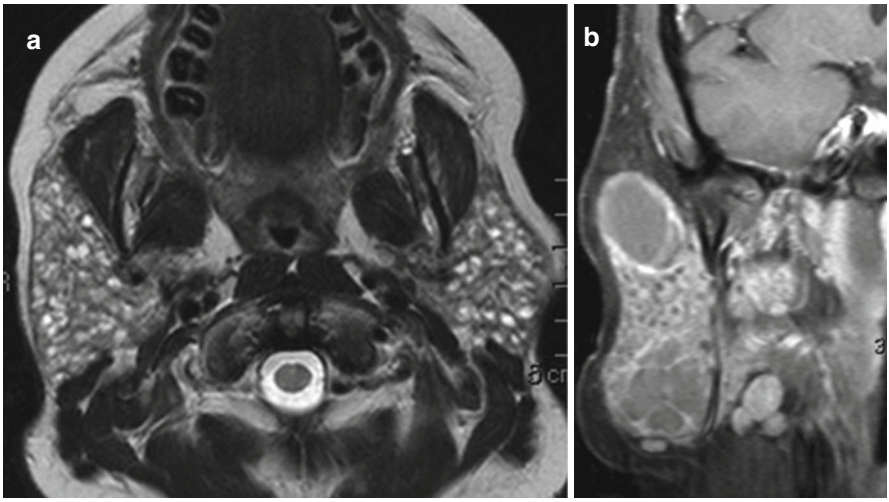

Fig. 6.7 Parotid cysts in HIV infection. Innumerable small cysts representing benign lymphoepithelial lesions are seen in both parotid glands on the T2-weighted image (**a**). In (**b**), a coronal contrast-enhanced T1-weighted image from a different patient, the cysts are much larger. These findings are identical to Sjögren's syndrome. Occasionally, the disease may be unilateral or present as a solitary cyst. The presence of adenoid or facial tonsillar hypertrophy and the lack of submandibular gland involvement are useful clues to the diagnosis

foci. They can sometimes however cavitate and appear cystic, much like those with HIV-associated disease. The latter is commonly associated with cervical lymphadenopathy, while uncomplicated Sjögren's syndrome is not. The role of the radiologist is not really to diagnose Sjögren's syndrome but, more importantly, to detect the occurrence of lymphoma. This is of the B-cell mucosa associated lymphoid tissue (MALT) variety and may be low or high grade. Any solid mass, especially one that enlarges rapidly and/or is associated with cervical lymphadenopathy, must be viewed with suspicion.

6.4.2.2 HIV Infection and AIDS-Related Parotid Cysts

This is an uncommon manifestation of HIV infection. A mixture of multiple solid and cystic foci is seen on imaging. Pathologically, cysts occur due to a combination of cyst formation in intraparotid lymph nodes and due to obstruction of small ducts by a lymphoid infiltrate. The process is very often bilateral and is frequently associated with cervical lymphadenopathy and prominent lingual and adenoid tonsillar tissue. The submandibular glands are typically spared (Fig. 6.7).

Neoplasms

Contrast-enhanced CT is the first line of investigation when one encounters a salivary gland mass in routine clinical practice. MRI with contrast is the next step, if required, to localize and assess regional extent. A specific histological diagnosis is often impossible on cross-sectional imaging, given the bewildering variety of tumors that exist, and, in most instances, with a few exceptions, is pointless to

attempt. Three quarters of parotid, one half of submandibular, and one-third of sublingual and minor salivary gland tumors are benign. In children however a salivary tumor is more likely to be malignant. The most common adult tumor is pleomorphic adenoma. Hemangiomas are the most common of such tumors in children. The classification of the more common tumors, modified from the WHO system, is provided in Box 6.2.

Box 6.2 Classification of Salivary Gland Tumors

- Adenomas
  - Pleomorphic
  - Basal cell
  - Oncocytoma
  - Warthin's tumor
  - Cystadenoma
- Carcinoma
  - Acinic cell
  - Adenoid cystic
  - Mucoepidermoid
  - Polymorphous low-grade adenocarcinoma
  - Squamous cell carcinoma
  - Carcinoma ex pleomorphic adenoma
- Nonepithelial tumors
  - Hemangioma
  - Nerve sheath tumors
- Lymphoma
- Metastases

6.4.3 Common Benign Tumors

6.4.3.1 Pleomorphic Adenoma

An unfortunate tendency to refer to these lesions as benign mixed tumors exists. These tumors although histologically benign, in about 25 % of cases, eventually degenerate to malignancy. Carcinomas ex pleomorphic adenoma and carcinosarcomas have been described to arise from these lesions. Despite being benign, rarely, these tumors may also metastasize. Histologically, they are comprised of epithelial and mesenchymal elements, which may differentiate into a wide variety of tissues, including bone and cartilage, thus explaining the pleomorphism seen under the microscope. A well-defined circumscribed lobulated salivary gland lesion, sometimes containing foci of coarse calcification and liquefaction, is usually a pleomorphic adenoma. Younger patients often tend to have low-density tumors that blend with the surrounding parenchyma. Heterogeneous adenomas may be impossible to distinguish from malignant tumors. On MRI, the key finding is high T2 signal intensity (Fig. 6.8). Often they are the brightest structure on a T2-weighted image. If a salivary gland lesion is not hyperintense on T2-weighted imaging, one should consider alternative diagnoses of other benign or malignant tumors. However, it is not

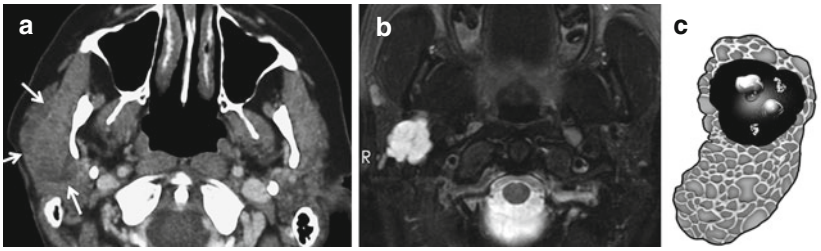

Fig. 6.8 Typical pleomorphic adenomas. In (**a**), the tumor is nearly isodense with the parotid gland and its margins are ill-defined. This is often the case in younger patients. With time, liquefaction and calcification appear causing the tumor to be more heterogeneous. In (**b**), the T2 hyperintensity is a typical finding. Although pleomorphic adenomas may be of intermediate or low signal on T2-weighted images, the lack of hyperintensity should make one consider other diagnoses. (**c**) Illustrates the typical features of a pleomorphic adenoma – lobulated, well defined, and heterogeneous due to the presence of liquefaction and calcification

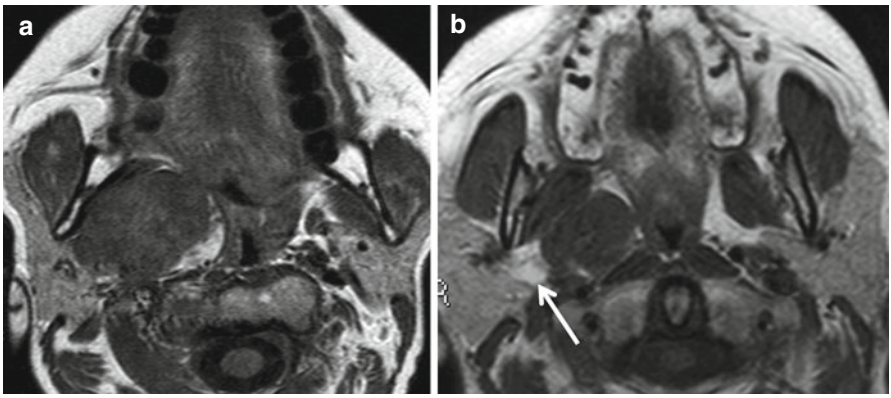

Fig. 6.9 Deep lobe parotid versus primary parapharyngeal space pleomorphic adenoma. In (**a**), there is no fat plane visible between the tumor and the parotid gland indicating that this is a deep lobe mass. In (**b**), a distinct zone of fat is evident (*arrow*) between the mass and the parotid gland, indicating that this is a primary PPS tumor

uncommon to encounter a pleomorphic adenoma that is intermediate or low signal intensity on T2-weighted images. The presence of infiltrative margins, shaggy irregular peripheral enhancement, and coexistent lymphadenopathy suggests malignancy. This is especially true with a history of pain or facial palsy. From a surgeon's perspective, it is important to differentiate between a pleomorphic adenoma of deep lobe parotid origin from that arising from minor salivary gland clusters in the parapharyngeal space (Fig. 6.9). With parapharyngeal space pleomorphic adenomas, a complete fat plane is visible on cross-sectional imaging between the tumor and the adjacent deep lobe. If a fat plane is not visible, one of three possibilities must be considered: (1) The tumor is of deep lobe origin. (2) The tumor is of parapharyngeal origin but is so large that the fat plane has simply been effaced completely. (3) The tumor is of parapharyngeal origin but has invaded the deep lobe. The last two scenarios are unlikely enough that the lack of a fat plane may be assumed to indicate a

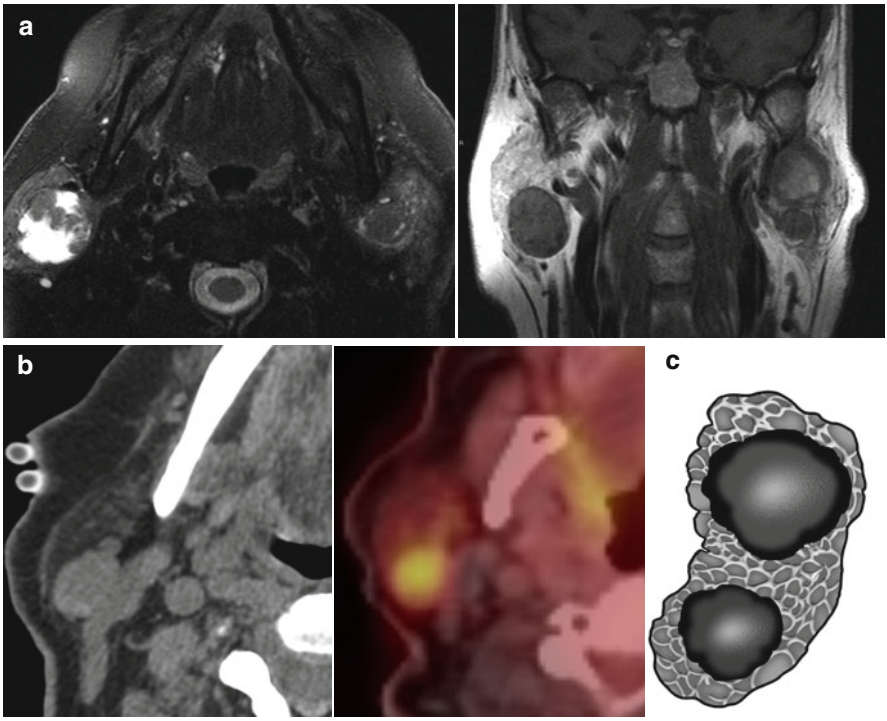

Fig. 6.10 (**a**) Multiple Warthin's tumors in an elderly male smoker. The multiplicity, smooth non-lobulated margins, and the areas of cystic change as in the right parotid lesion are highly suggestive of Warthin's tumors. A right parotid lesion shows increased T1 signal. This may be due to the high protein content of cyst fluid or, as in this case, hemorrhage. Warthin's tumors can be hot on PET, as shown in (**b**), in a patient with metastatic melanoma. It is important to be aware of this phenomenon and not assume that they are nodal metastases. The key concept to remember is that an elderly patient with a well-defined sometimes fluid containing lesion, especially if more than one is present, usually has a Warthin's tumor (**c**)

deep lobe origin. This distinction is important because a deep lobe tumor would be removed through a transparotid approach, which may entail facial nerve manipulation and a small but increased risk of nerve injury. A parapharyngeal tumor can be removed by a transcervical or trans-oral approach. The best modality to monitor recurrence is MRI, where T2 hyperintensity and a clustered appearance are characteristic.

6.4.3.2 Warthin's Tumors and Oncocytomas

A well-defined cystic-appearing parotid tumor in an elderly male, who is a smoker, is almost always a Warthin's tumor. This is especially true, if multiple such lesions are seen. These are the second most common salivary gland tumor. Histologically, they are comprised of both epithelial and lymphoid cells. Low density on CT, high T2 signal on MRI, and mural nodularity on both are frequently seen. These tumors are hot on PET and Technetium-99m scans due to the presence of mitochondria rich oncocytes (Fig. 6.10).

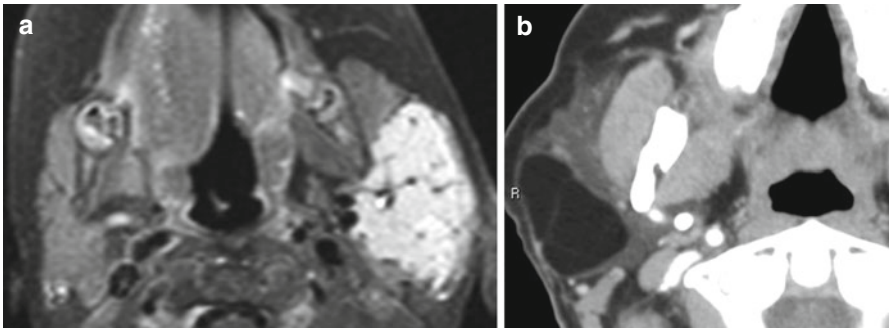

Fig. 6.11 (**a**) The most common parotid space mass in a child is a hemangioma. Hemangiomas enhance intensely with contrast and contain flow voids representing feeding vessels. As opposed to vascular malformations, which are hamartomas that tend to grow with the patient, hemangiomas are true benign neoplasms and may involute spontaneously. In (**b**), the fat density of a lipoma is obvious

Oncocytomas are uncommon tumors, also encountered in the elderly population, like Warthin's tumors. They however are more common in women. The presence of a lobulated contour, especially in association with a central nonenhancing cleft, is highly suggestive of oncocytoma. Unlike Warthin's tumors and pleomorphic adenomas, they may be hypointense on T2-weighted imaging. They too are hot on Technetium-99m scans. In about ten percent of cases, more than one tumor may be present.

6.4.4 Mesenchymal Tumors

Hemangiomas, lipomas, and nerve sheath tumors can occur in the parotid space. A lobulated enhancing mass in a child is usually a hemangioma (Fig. 6.11a). Venolymphatic malformations may also occur in and around salivary glands. These are hamartomas rather than true neoplasms. These are low flow lesions, may not enhance significantly, may be comprised of cystic elements, and can demonstrate fluid levels. The presence of phleboliths is a useful clue to their diagnosis (Fig. 6.11a). Lipomas are easily recognized by their fat density/signal intensity. Nerve sheath tumors arising from peripheral facial nerve branches do occur. They can be indistinguishable from pleomorphic adenomas. Occasionally the presence of a target sign or extension into the facial nerve canal suggests the diagnosis.

6.4.5 Malignant Neoplasms

6.4.5.1 Primary Malignancy

There is unfortunately no certain way to differentiate a benign from malignant salivary gland tumor on imaging. If a mass demonstrates the features described above, one may be able to diagnose a pleomorphic adenoma, Warthin's tumor, or oncocytoma with a reasonable degree of confidence. Fairly often, tumors do not and

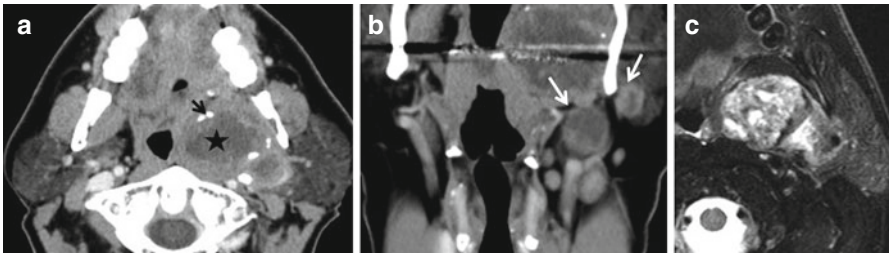

Fig. 6.12 Carcinoma ex pleomorphic adenoma of the deep lobe of the parotid gland. The foci of liquefaction (*asterisk*) and calcification (*arrows*) in this tumor (**a**) are not necessarily indicative of a malignant lesion. Large pleomorphic adenomas often degenerate this way with time. What is worrisome though is the presence of necrotic cervical lymphadenopathy (*arrows* in **b**) and the history of facial paresis. The cuff of tumor around the retromandibular vein in image (**c**) indicates that the facial nerve is likely involved by tumor

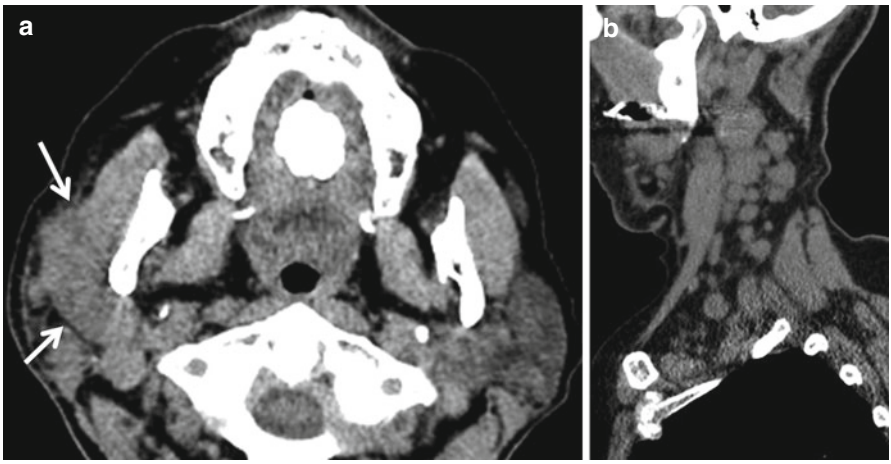

Fig. 6.13 Non-Hodgkin's lymphoma of the parotid gland. Lymphoma of the parotid gland can mimic chronic sialadenitis (**a**), as it did in this case. Here, an infiltrative process is seen replacing the right parotid parenchyma. The presence of multiple enlarged cervical lymph nodes in (**b**) is a clue that one is not dealing with simple chronic sialadenitis

a specific diagnosis is impossible. Salivary gland malignancies come in a variety of flavors, and any of them can look completely benign. Clinical history is important and a history of pain, facial paresis, and past radiation are clues that one may not be dealing with a benign lesion (Fig. 6.12). There are some reasonably special characteristic of some types of malignancies that may be useful to remember – mucoepidermoid carcinomas are the most common malignancy, acinic cell tumors can be bilateral, and adenoid cystic carcinomas have a tendency to spread perineurally. Primary lymphoma of the parotid gland is extremely uncommon. It is usually a non-Hodgkin's lymphoma of the B-cell variety. Lymphoma may also mimic chronic sialadenitis on imaging by presenting as a nodular infiltrative process and must be suspected when such an appearance is seen on CT/MR in an older patient, especially in conjunction with cervical lymphadenopathy (Fig. 6.13).

Box 6.3 TNM Staging for Salivary Gland Malignancies

Primary tumor	
TX	Primary tumor cannot be assessed
T0	No evidence of primary tumor
T1	Tumor <2 cm, no macroscopic extraparenchymal extension
T2	Tumor >2 but <4 cm, no macroscopic extraparenchymal extension
T3	Tumor >4 cm and/or macroscopic extraparenchymal extension
T4a	Tumor invades skin, mandible EAC, facial nerve (moderately advanced disease)
T4b	Tumor invades skull base, pterygoid plates, carotid artery (very advanced disease)
Regional lymph node staging	
NX	Lymph nodes cannot be assessed
N0	No evidence of lymph node metastases
N1	Metastases to single ipsilateral lymph node, <3 cm in greatest dimension
N2a	Metastases to single ipsilateral node >3 cm but <6 cm
N2b	Metastases to multiple ipsilateral nodes, none more than 6 cm
N2b	Metastases to multiple contralateral/bilateral nodes, none >6 cm
N3	Metastases to any node >6 cm
Distant metastases	
MX	Distant metastases cannot be assessed
M0	No distant metastases
M1	Distant metastases present

Adapted from *AJCC Cancer Staging Manual*. 7th edn. Springer, New York

The TNM staging for salivary gland malignancy is provided in Box 6.3. Awareness of the staging system and knowledge of anatomy of the pathways for perineural spread are vital. PNTS carries an unfortunate prognosis. Two potential pathways for PNTS from the parotid gland exist. A tumor may directly involve the facial nerve (Fig. 6.14) or use the auriculotemporal nerve to access the mandibular division of the trigeminal nerve. Depending on the pathway involved, perineural extension into the skull base can occur through the stylomastoid foramen (facial nerve) or the foramen ovale (auriculotemporal nerve). It is important to note that skip lesions may occur and that the imaging field of view must include the entirety of the courses of these nerves. The findings of PNTS may be subtle and one must actively look for them. PNTS may occasionally be evident on CT where widening of a skull base foramen, replacement of fat within it, or destruction of its walls is present. It is however more obvious on MRI, where PNTS is indicated directly by replacement of fat, nerve thickening, and enhancement and indirectly by denervation atrophy of the muscles of facial expression or mastication, depending on the nerves involved (Fig. 6.12). These findings are summarized in Box 6.4. A checklist of structures to be evaluated while assessing these lesions is provided in Box 6.5.

6.4.5.2 Secondary Malignancy

Intraparotid nodes drain the skin of the scalp, pinna, and periauricular region. Cutaneous malignancies from any of these sites may metastasize to these nodes.

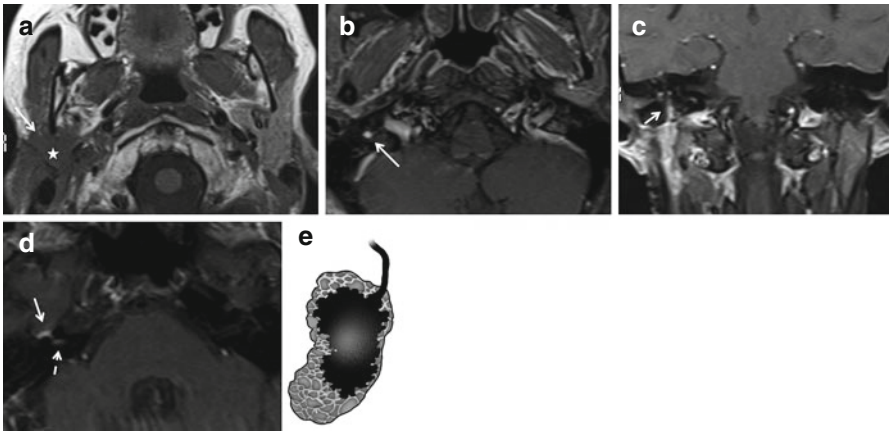

Fig. 6.14 Perineural tumor spread from adenoid cystic carcinoma of the parotid gland. The unenhanced T1-weighted image (**a**), shows an irregularly marginated right parotid tumor that has infiltrated the parenchyma around the retromandibular vein (*asterisk*), a finding that must raise the possibility of facial nerve invasion. This is confirmed on (**b**), where thickening and enhancement of the mastoid segment of the right facial nerve is evident (*arrow*). This is also clearly demonstrated on the coronal image (*arrow*, **c**). In (**d**), there is enlargement and enhancement of the right geniculate ganglion (*solid arrow*) and of the facial nerve in the fundus of the internal auditory canal (*dashed arrow*). (**e**) Illustrates the key concept of PNTS in parotid malignancy. Although adenoid cystic carcinoma is the most likely to do so, other cancers like squamous cell carcinoma, lymphoma, and melanoma can also spread perineurally. The course of the facial nerve in its entirety must always be evaluated in patients with parotid malignancy

Box 6.4 Imaging Signs of Perineural Spread

- Foraminal widening
- Loss of foraminal fat
- Destruction of bony walls of foramina
- Nerve thickening and enhancement
- Denervation atrophy

Box 6.5 Imaging Checklist for Salivary Gland Tumors

- Superficial versus deep lobe versus parapharyngeal space
- Evaluate other parotid gland for multiple masses
- Facial nerve, mandibular division of trigeminal nerve
- Mandible and temporomandibular joint
- External auditory canal
- Skin
- Carotid sheath
- Pterygopalatine fossa, pterygoid plates, and skull base foramina (foramen ovale, stylomastoid foramen)
- Lymph nodes – intraparotid, levels 1 and 2

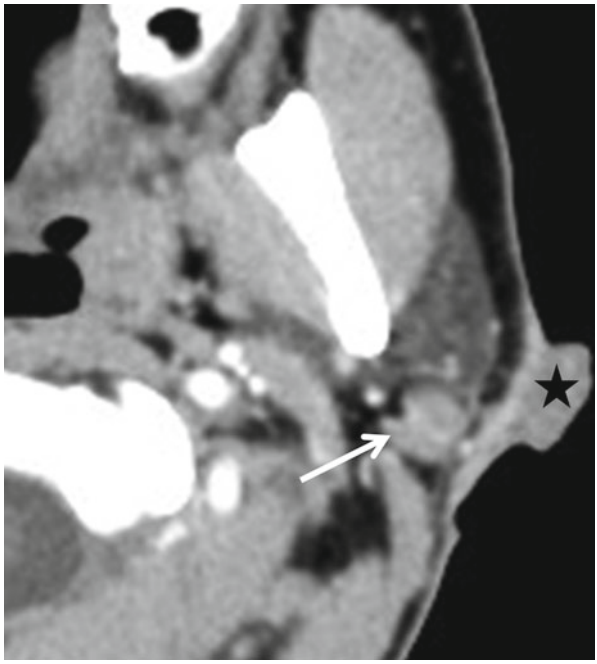

Fig. 6.15 Intraparotid nodal metastasis (*arrow*) from a preauricular cutaneous squamous cell carcinoma (*asterisk*)

An intraparotid nodal mass may be indistinguishable from a primary parotid neoplasm (Fig. 6.15). Metastatic disease to the glandular parenchyma is rare and may arise from lung, renal, or breast primaries.

6.4.6 Miscellaneous Disorders

6.4.6.1 Ranula

A ranula is a mucocele of a sublingual salivary gland and is so named for its resemblance of its surface to the underbelly of a frog (Rana). Most ranulas are confined to the sublingual space. Occasionally, they extend into the submandibular space, when they are called plunging ranulas. This may be accomplished by one or both of two ways. When large enough, they may extend in the submandibular space behind the posterior free edge of the mylohyoid. They may also do so through congenital defects in the mylohyoid sling. When they do so, differentiation from lymphangiomas, which also occur not infrequently in the submandibular space, is of importance. Lymphangiomas may be treated by sclerotherapy, while ranulas require surgical excision. A sublingual tail of extension on CT/MR is highly suggestive of a ranula. Lymphangiomas are more likely to be septated, enhance peripherally, and contain fluid levels (Fig. 6.16).

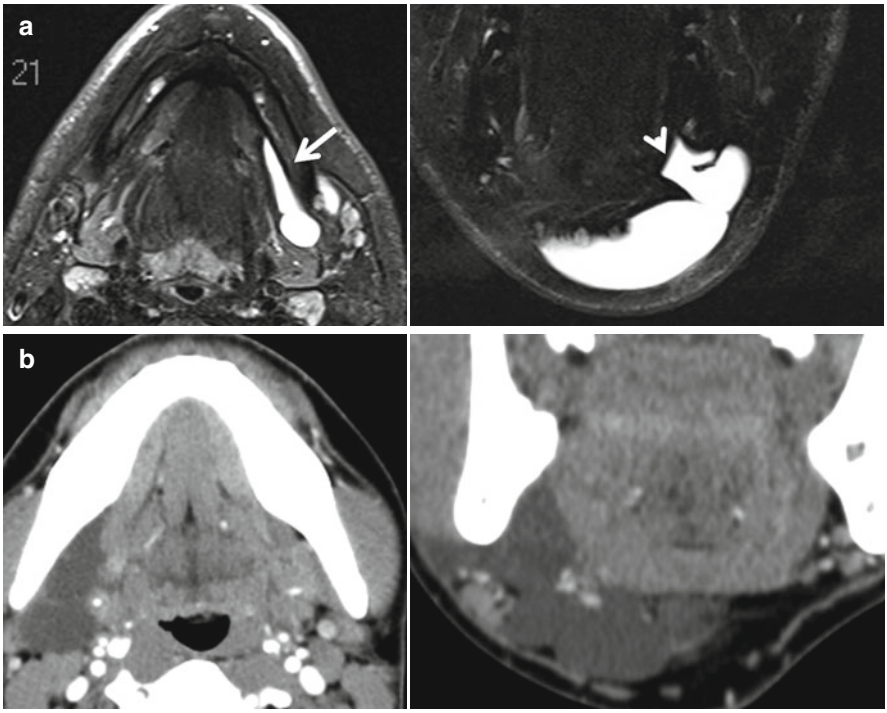

Fig. 6.16 (**a**) Simple and plunging ranula. The sublingual tail (*arrow*) is a specific sign of a ranula, when present. The plunging ranula on the left extends into the submandibular space from the sublingual space through a congenital defect in the mylohyoid (*arrowheads*). (**b**) Shows a submandibular space lymphangioma. The lobulations, septa, and lack of a sublingual component (tail) help differentiate from a plunging ranula

6.4.6.2 Sialolithiasis

Calculi are more common in the Wharton's duct than in the Stensen's duct. In about 25 % of cases, multiple calculi are seen. 90 % of submandibular and 60 % of parotid calculi can be seen on a plain film. CT is obviously more sensitive (Fig. 6.5).

6.5 The Surgeon's Perspective

The mainstays of clinical diagnosis for salivary gland complaints are physical exam and fine-needle aspiration (FNA) biopsy. Imaging must be used prudently if it has to impact patient management. The most common salivary gland diagnosis, sialadenitis, is made based on history and physical exam, and imaging need not routinely be obtained. Other common salivary gland findings such as ductal stones and bilateral parotid enlargement should be managed clinically with imaging used sparingly.

For salivary gland masses, FNA biopsy provides the most rapid and cost-effective approach to diagnosis. Since the vast majority of parotid masses are benign, proceeding to surgery without a diagnosis is not inappropriate, but most surgeons favor establishing a diagnosis so that the extent of surgery and risk to the facial nerve can be better predicted. Isolated level I cervical masses thought to involve or originate from the submandibular or sublingual glands have a much higher likelihood of malignancy and should always be assessed by FNA biopsy. If FNA is performed and fails to yield an adequate specimen or results in equivocal diagnosis, imaging and/or image-guided biopsy can be useful. A diagnosis of malignancy on FNA biopsy also warrants imaging to determine the extent of tumor, unless this is obvious on physical exam.

For benign parotid tumors involving only the superficial lobe, a superficial parotidectomy (or less) will be performed. If the tumor extends into the deep lobe, part of all of it will be removed with preservation of the facial nerve. In this case, the likelihood of transient facial paresis/paralysis is increased and thus determining the extent of the tumor with preoperative imaging can help to anticipate this and appropriately prepare the patient. For malignant parotid tumors, total parotidectomy is commonly warranted, and while preservation of the functioning facial nerve is the norm, the risk of transient paresis/paralysis is higher, as is the potential need to transect the nerve for oncologic control. Depending on the histology, selective neck dissection may also be appropriate for known or suspected regional metastasis. Thus, for malignant parotid tumors, preoperative imaging is a must. When the facial paralysis is present preoperatively, facial nerve invasion is implied and a radical parotidectomy with facial nerve sacrifice will be required. This is generally performed for aggressive malignancies and, again, preoperative imaging is crucial in determining the complete extent of the tumor and what adjunctive procedures may be required (e.g., mastoidectomy and partial mandibulectomy) to obtain oncologic control. When the malignant mass is actually a metastasis to an intraparotid lymph node, imaging can augment a complete physical exam in identifying and/or determining the extent of the primary malignancy.

What then is the best way to approach a salivary gland lesion? It is critical to be in possession of the patient's history before one begins evaluating imaging findings. In the setting of an acutely tender, swollen gland(s), the role of the radiologist is to determine if an obstructive calculus or abscess is present. When confronted with a mass, it is important to be aware if the lesion has been present for a long time or has grown rapidly and if it is associated with worrisome symptoms such as pain or those of facial paresis. The first question to be answered on imaging is this: Are there any features that indicate malignancy? The most important of these are lack of T2 hyperintensity on MR, irregular margins, and the presence of cervical lymphadenopathy. If the answer is yes, the issues outlined in the imaging checklist provided above must be addressed. If none of the above is the case, the mass may be benign or malignant. The next question to be asked then is if the lesion demonstrates features compatible with a pleomorphic adenoma, Warthin's tumor, oncocytoma, or benign cyst. Often, a definitive diagnosis is not possible and FNA or resection is warranted to clarify the issue. Box 6.6 summarizes a pattern-based approach to differential diagnosis.

Box 6.6 Pattern-Based Differential Diagnosis for Salivary Glands

Cystic salivary gland lesions
- First branchial cyst
- Sialocele
- Lymphoepithelial cyst
- Ductal cyst
- Lymphangioma
- Epidermoid cyst
- Warthin's tumor
- Low-grade mucoepidermoid carcinoma
- Oncocytic papillary cystadenoma

Multiple salivary gland masses
- Warthin's tumors
- Oncocytomas
- Lymphoepithelial cysts
- Acinic cell carcinoma
- Enlarged intraparotid lymph nodes

Calcifications
- Chronic inflammatory disease – multiple small
- Venolymphatic malformations – phleboliths
- Pleomorphic adenoma
- Calcified lymph nodes

Further Reading

Habermann CR, Arndt C, Graessner J, Diestel L, Petersen KU, Reitmeier F, Jaehne M (2009) Diffusion-weighted echo-planar MR imaging of primary parotid gland tumors: is a prediction of different histologic subtypes possible? AJNR Am J Neuroradiol 30(3):591–596

Rice DH (1999) Malignant salivary gland neoplasms. Otolaryngol Clin North Am 32(5):875

Schmalfuss IM, Tart RP, Mukherji S, Mancuso AA (2002) Perineural tumor spread along the auriculotemporal nerve. AJNR Am J Neuroradiol 23(2):303–311

Yousem DM, Kraut MA, Chalian AA (2000) Major salivary gland imaging. Radiology 216(1): 19–29

Orbits

7

Thomas J.E. Muttikal, Prashant Raghavan,
Max Wintermark, Steven A. Newman,
and Sugoto Mukherjee

7.1 Introduction

This chapter describes the imaging characteristics of the more common orbital lesions. Although a specific imaging diagnosis of orbital pathology may not always be possible, a combination of clinical information and imaging features can enable a relatively short list of differential diagnoses to be formulated in most instances.

7.2 Anatomy

The orbit is a pyramidal-shaped cavity formed by seven bones. The roof is formed by the orbital process of frontal bone and the lesser wing of sphenoid. The floor is formed by the orbital plates of the maxilla, zygoma, and the palatine bone. The medial wall is formed by the frontal process of the maxilla, the lacrimal bone, and the gracile lamina papyracea of the ethmoid bone. The greater wing of sphenoid, the zygoma, and the zygomatic process of frontal bone form the lateral wall (Figs. 7.1, 7.2, and 7.3).

The contents of the orbit include the globe, the external ocular muscles (EOM), the optic nerve, cranial nerves III and IV, the first (ophthalmic, V1) division of V and VI, the ophthalmic artery, the superior and inferior ophthalmic veins, fat, the lacrimal apparatus, and the orbital septum (Figs. 7.1, 7.2, and 7.3).

The contents of the various channels of the orbit are summarized in Box 7.1.

7.3 Imaging Modalities

7.3.1 Ultrasound

Ultrasound of the orbit is best performed with a high-frequency linear transducer, ideally 10 MHz or higher. US is used to evaluate the eye and superficial structures and provides limited evaluation of deeper intraorbital structures. It is particularly useful when ophthalmoscopic examination is limited due to the presence of

P. Raghavan et al., *Manual of Head and Neck Imaging*,
DOI 10.1007/978-3-642-40377-4_7, © Springer-Verlag Berlin Heidelberg 2014

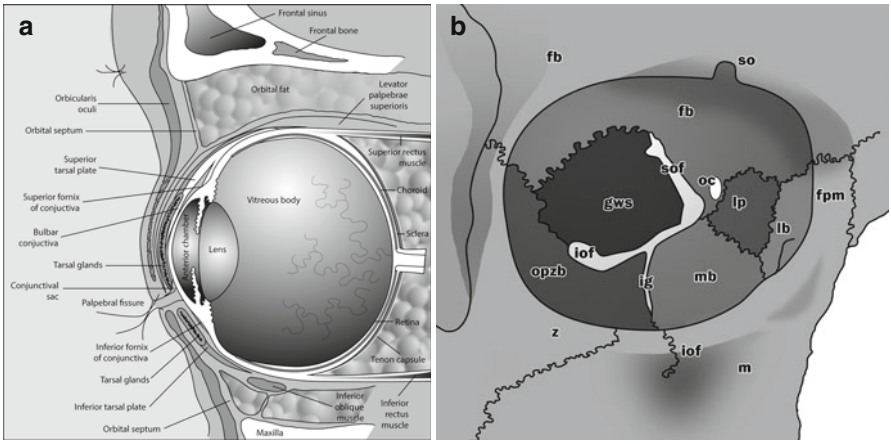

Fig. 7.1 Sagittal graphic (**a**) showing the gross anatomy of the globe and the orbit. Note the three layers of the globe consisting of retina, choroid, and sclera. The bony orbit (**b**) shows the relationships of the various foramina and fissures including the superior orbital fissure (*sof*), inferior orbital fissure (*iof*), and the optic canal (*oc*), as well as the superior (*sf*) and the inferior orbital foramina (*iof*). The bones forming the bony orbit include frontal bone (*fb*), greater wing of sphenoid (*gws*), orbital plate of the zygomatic bone (*opzb*), lacrimal bone (*lb*), frontal process of maxilla (*fpm*), supraorbital notch (*so*), infraorbital groove (*ig*), maxillary bone (*mb*), and lamina papyracea (*lp*). Other abbreviations in the figure include *m* maxilla, *z* zygomatic bone

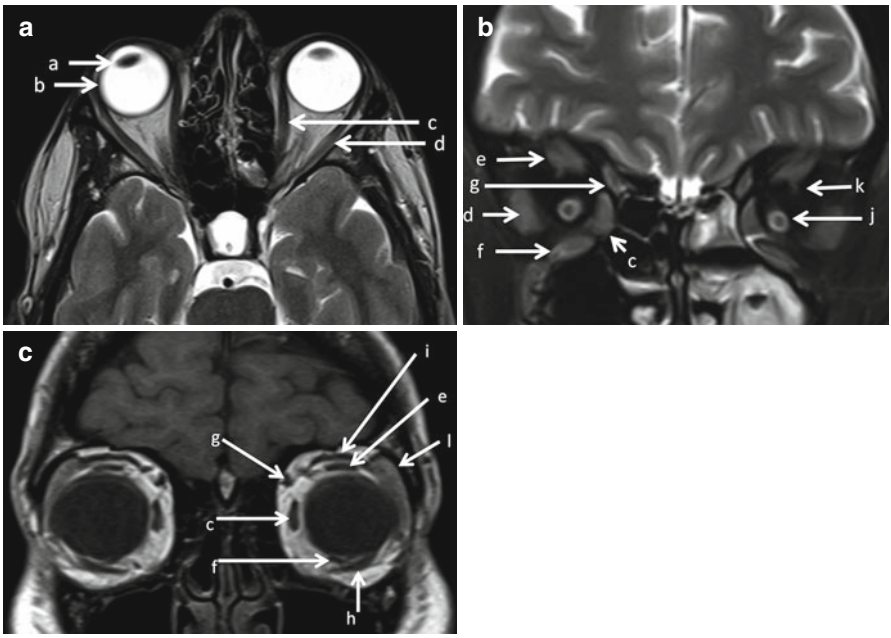

Fig. 7.2 Axial T2WI (**a**) and coronal T2WI with fat saturation (**b**) and coronal T1WI (**c**) show the easily identifiable intraorbital structures and extraocular muscles on MR. These include (*a*) lens, (*b*) globe, (*c*) medial rectus, (*d*) lateral rectus, (*e*) superior rectus, (*f*) inferior rectus, (*g*) superior oblique, (*h*) inferior oblique, (*i*) levator palpebrae superioris, (*j*) optic nerve sheath complex showing optic nerve surrounded by fluid in the optic nerve sheath, (*k*) superior ophthalmic vein, and (*l*) lacrimal gland

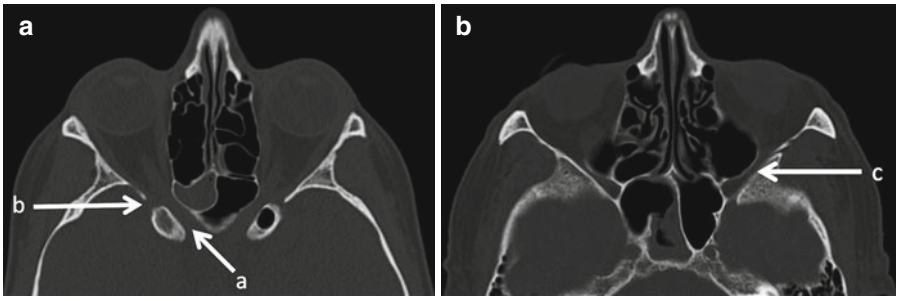

Fig. 7.3 Axial CT images (**a**, **b**) show the interrelationships of (*a*) optic canal, (*b*) superior orbital fissure, and (*c*) inferior orbital fissure

Box 7.1. Bony Channels of the Orbit

Optic canal	At apex of orbit, within the lesser wing of sphenoid bone	Optic nerve, ophthalmic artery with accompanying sympathetic fibers
Superior orbital fissure	Between the lesser and greater wings of the sphenoid	Branches of cranial nerves III, IV, and VI and cranial nerve VI, orbital branch of the middle meningeal artery, recurrent branch of the lacrimal artery and superior ophthalmic vein
Inferior orbital fissure	Between the greater wing of sphenoid, maxilla, and palatine bones	Maxillary nerve, zygomatic nerve, parasympathetics to lacrimal gland, infraorbital artery, infraorbital vein, and branch of inferior ophthalmic vein to pterygoid plexus

The infraorbital canal transmits the infraorbital nerve and vessels from the orbit to the face

opaque ocular media such as by cataract or vitreous hemorrhage. US is commonly performed by the ophthalmologist as an office procedure for evaluating a mass seen during ophthalmoscopy, to look for a mass underlying a retinal detachment, to evaluate ocular trauma, and for biometry. Color Doppler can be used to evaluate lesional vascularity.

7.3.2 Cross-Sectional Imaging

CT is the modality of choice in suspected orbital trauma, in orbital infection in the setting of sinusitis, and in the initial evaluation of an orbital mass. In patients with trauma, an unenhanced scan is sufficient. CT demonstrates bony changes and calcifications better than MRI. However, it must be employed judiciously in children and young patients where radiation exposure to the lens is a legitimate concern. CT scan and MRI can both provide complimentary information in the evaluation of orbital masses. A standard orbit MR study comprises of axial and coronal thin section unenhanced non-fat-suppressed T1-weighted images (the hyperintense fat provides excellent background contrast), a coronal fat-suppressed T2W sequence (for evaluating

Box 7.2. Multispatial Lesions

Lesion	T2	Pain	Additional helpful features
Plexiform neurofibroma	Hyperintense, central low intensity—target sign	Generally painless	Associated findings of NF1
Venous-lymphatic malformation	Heterogeneous, fluid-fluid levels	May be painful during thrombosis or sudden hemorrhage	
Orbital cellulitis	Hyperintense	Painful	Clinical features of infection
Orbital Pseudotumor	Hypointense	Painful	
Sarcoid	Hypointense	Generally painless	CNS or systemic sarcoidosis
Wegener	Hypointense	Generally painless	Other manifestation of Wegener, especially in nasal cavity and paranasal sinuses
Lymphoma	Hypointense	Painless	Restricted diffusion
Infantile hemangioma	Slightly hyperintense	Painless	

the optic nerve), and post-contrast fat-suppressed axial and coronal T1W images. CTA and MRA are useful when a vascular process such as a carotid-cavernous fistula or AV malformation is suspected.

The primary role of the radiologist is to precisely localize the lesion, estimate its site of origin and describe its extent. An attempt should be made to describe the lesion as focal or multispatial (Box 7.2), whether it involves intra or extraconal compartments, and its origin from the globe, optic nerve, lacrimal gland, vascular structures, extraocular muscles or the bony orbit.

7.4 Congenital/Developmental Anomalies

7.4.1 Coloboma

A coloboma is a focal discontinuity in the structure of the globe resulting from the failure of closure of the embryonic choroid fissure between the 5th and 7th weeks of life. Posterior colobomas, which include choroidoretinal, and optic disc colobomas are the more common type. They can occur as isolated lesions or as a part of a more widespread syndromic process. Isolated colobomas are usually unilateral, while

Fig. 7.4 Coloboma and lacrimal abscess. Axial contrast-enhanced CT scan showing incidental finding of coloboma of the right eye (*long arrow*). The patient was imaged for the left lacrimal gland abscess (*short arrow*)

syndromic forms tend to be bilateral. They appear as focal protrusions isodense to the vitreous on non-enhanced CT (NECT) scan and isointense to the vitreous of MRI, unless complicated by retinal detachment and hemorrhage (Fig. 7.4). A large coloboma may also present as an intraorbital cyst associated with a small globe (microphthalmia).

7.4.2 Persistent Hyperplastic Primary Vitreous

Persistent hyperplastic primary vitreous results from failure of regression of embryonic ocular blood supply. There are three types—posterior, anterior, and mixed. In posterior PHPV, there is an enhancing retrolental soft tissue with a stalk, representing the remnant of the primitive hyaloid artery, extending from the posterior surface of the lens to the head of the optic nerve (Fig. 7.5). Retinal detachment is frequently present and the globe is small. In anterior PHPV, the anterior chamber is shallow, the lens is thin and dysplastic, and an abnormal enhancing tissue is present in the region of the ciliary body and lens. The mixed type demonstrates features of posterior and anterior PHPV.

7.4.3 Coats' Disease

Coats' disease, seen in children, usually boys, under the age of ten, is caused by retinal telangiectasias and a leaky blood retinal barrier, which results in subretinal exudate accumulation. Coats' disease is usually unilateral and results in retinal detachment. The exudate appears hyperdense compared to vitreous on CT. The exudate, comprised mainly of cholesterol, is hyperintense on T1W MR images. Patients usually present with leukocoria and vision loss. The most important differential is retinoblastoma. On CT, the lack of calcification of the exudate of Coats enables differentiation from retinoblastoma. Also, post-contrast studies show no enhancement of the subretinal collection. Linear enhancement of the retinal detachment may however be present.

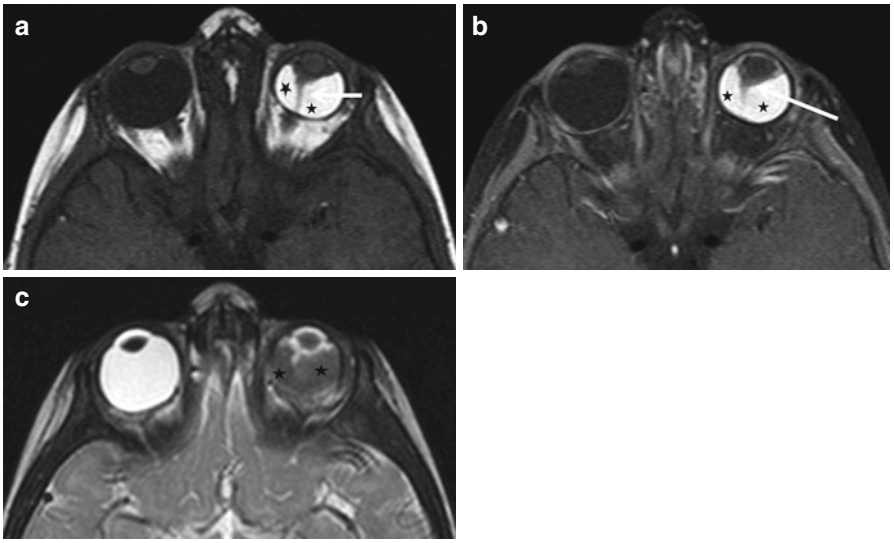

Fig. 7.5 Persistent hyperplastic primary vitreous (PHPV) in a 1-year-old patient. Axial T1 (**a**), axial fat-sat T1 post-contrast (**b**), and axial T2 (**c**) showing small left globe, stalklike hyaloid remnant extending from the posterior surface of the lens to the head of the optic nerve (*short arrow*), enhancing retrolental soft tissue (*long arrow*), and associated retinal detachment with hemorrhage (*black star*)

Box 7.3. Cystic Lesions

Dermoid
Epidermoid
Abscess
Venous-lymphatic malformation
Hemorrhage

7.4.4 Dermoids/Epidermoids

A dermoid is a congenital inclusion cyst occurring near suture lines, adjacent to the periosteum. The most common site is the superolateral portion of the orbit. Dermoid cysts commonly result in bony remodeling. They may be exophytic or endophytic. Exophytic cysts grow externally and are discovered early in childhood, while endophytic cysts grow internally and are encountered later in youth or early adulthood. Exophytic dermoids are usually small as they are identified earlier. Endophytic cysts are larger and may be associated with extensive bony changes. Other cystic lesions are summarized in Box 7.3.

They appear on unenhanced CT as well-defined fat density lesions (Fig. 7.6). The fat density is by no means universal, and it is not uncommon for them to present as fluid-containing lesions with no fat density. On MRI, the high T1 signal on fat,

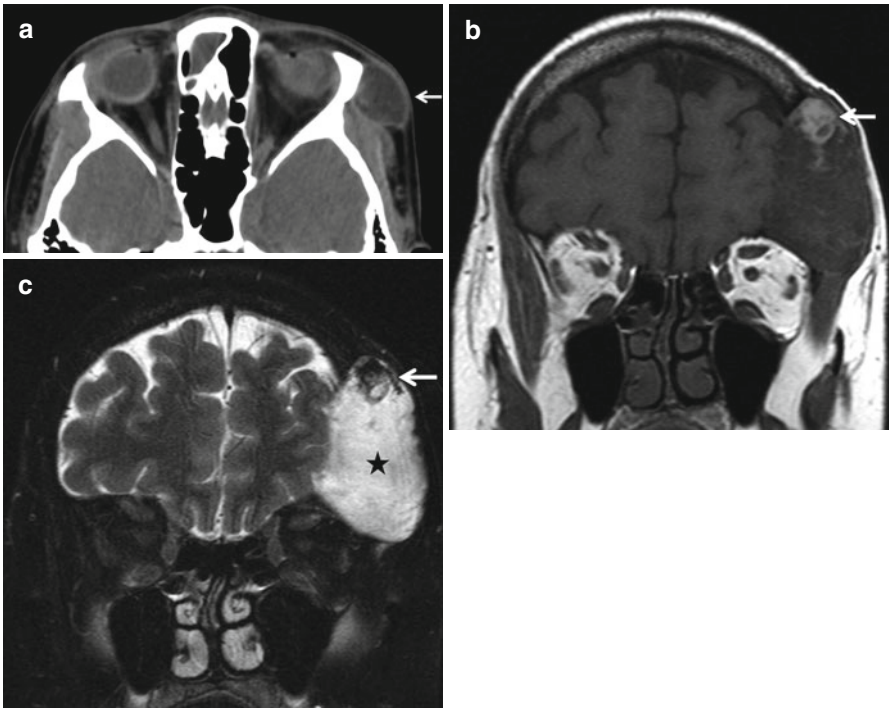

Fig. 7.6 Orbital dermoid. A 12-year-old patient presenting with gradually progressive, painless left periorbital swelling. Axial CT (**a**) showing cystic lesion without fat density along the superolateral margin of left orbit (*white arrow*). A 54-year-old patient, with long-standing history of left frontal swelling. Coronal T1WI (**b**) showing mixed signal intensity lesion with prominent fat nodule in its superior aspect (*white arrow*) with left frontal calvarial involvement. Coronal T2 fat-sat image (**c**) showing fat suppression in the superior nodular lesion (*white arrow*) and the hyperintense cystic component (*black star*). Compared to (a), this lesion is much bigger, with extensive lytic area in the frontal bone, related to the chronicity. The presence of fat within the lesion helps in diagnosis

when present, is characteristic. Occasionally a heterogeneous appearance due to intracystic debris may be encountered (Fig. 7.6). Sometimes, thin marginal enhancement on CT and MRI may be present. Irregular margins and perilesional inflammatory changes indicate rupture.

Epidermoid cysts demonstrate fluid signal/density on MRI and CT. A characteristic finding on MRI is restricted diffusion.

7.4.5 Neurofibromatosis Type 1

The ocular and orbital manifestations of NF1 include sphenoid wing dysplasia, plexiform neurofibroma, optic nerve glioma, buphthalmos, and optic nerve sheath ectasia. Sphenoid dysplasia, thinning, remodeling, or deficiency of the greater

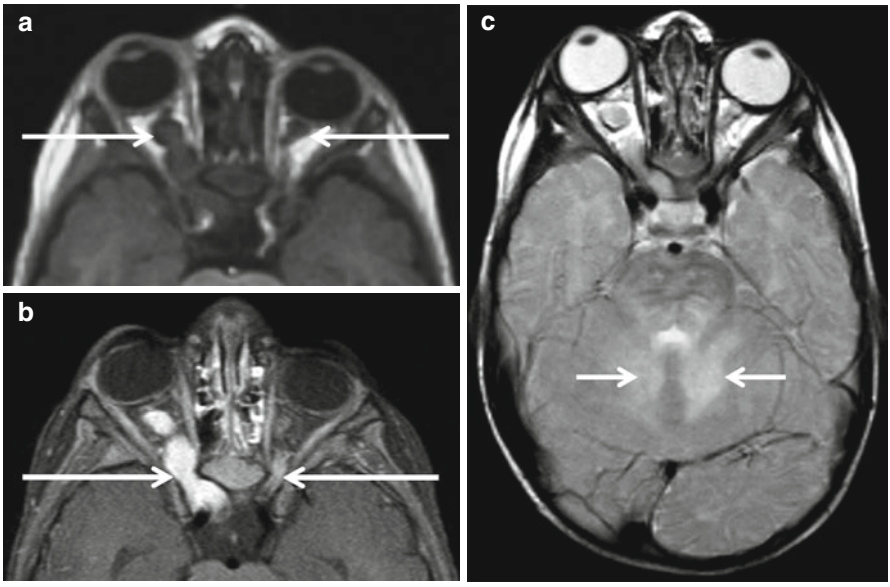

Fig. 7.7 Optic nerve gliomas in NF1. Axial T1-weighted images (**a**) showing bilateral optic gliomas (*long arrows*), right worse than left in a patient with NF1. Post-contrast axial T1 fat-sat image (**b**) shows enhancement of these lesions (*long arrows*). Axial T2-weighted sequences (**c**) show characteristic lesions of FASI (foci of abnormal signal intensity). These appear as non-enhancing foci of T2 prolongation and are thought to represent areas of myelin vacuolization (*short arrows* in **c**)

sphenoid wing, can result in the "bare orbit sign" on a frontal radiograph of the skull. Plexiform neurofibromas appear as variably enhancing infiltrative soft tissue masses on cross-sectional imaging. The target sign produced by foci of central T2 hypointensity is a typical finding. Perioptic dural sheath ectasia is an uncommon benign finding in patients with NF1. The distended CSF-filled sheaths are easily recognized on T2W MRI. Optic nerve gliomas are characterized by expansion of the nerve itself. They may be limited to the nerve or extend substantially along the visual pathway to involve the chiasm and hypothalamus (Fig. 7.7). They are low-grade neoplasms (pilocytic or fibrillary astrocytomas) and are frequently bilateral. No calcification is present on CT. They are of intermediate signal intensity and enhance variably on MRI.

7.5 Vascular Anomalies

7.5.1 Orbital Venous-Lymphatic Malformation (Lymphangioma)

Venous-lymphatic malformations are poorly marginated frequently trans-spatial multicystic lesions comprised of variable amounts of dysplastic lymphatic and venous elements. These lesions are best characterized on MRI. Cystic areas may show

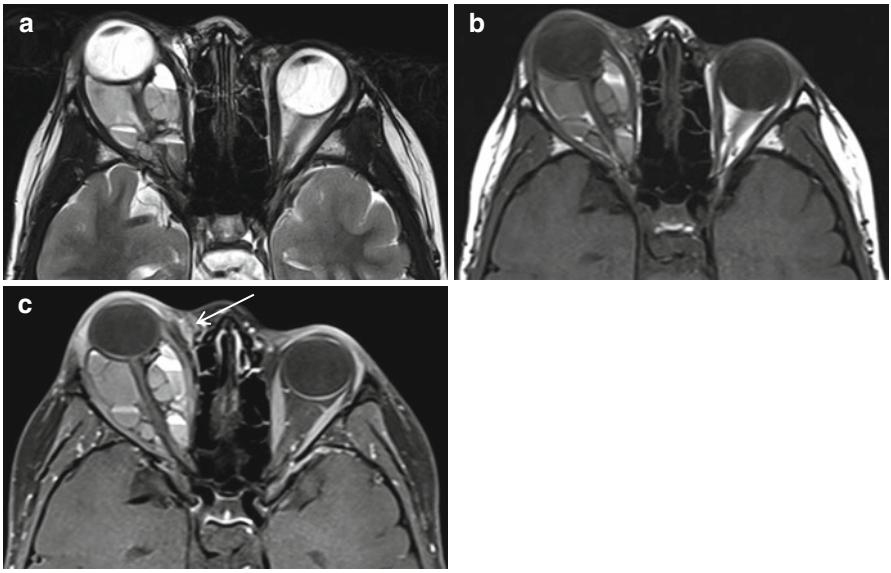

Fig. 7.8 Orbital venolymphatic malformation. Axial T2WI (**a**) showing complex multispatial lesion with multiple blood fluid levels in the right orbit in a 6-year-old patient. Axial precontrast TIWI (**b**) and post-contrast T1 fat-sat image (**c**) show a small enhancing portion (*arrow* in **c**) along the medial canthus of right eye

fluid-fluid levels and can contain blood products (Fig. 7.8). Enhancement is variable and is a function of the proportion of the venous component. Phleboliths, which appear on CT, as well-defined rounded calcific foci are a useful clue when present.

7.5.2 Venous Varix

An orbital venous varix is a distensible low-flow venous malformation connected with the systemic circulation. When large enough, it can result in intermittent reversible proptosis. Varices increase in size when systemic venous pressure increases, such as with coughing, straining, or compression of the jugular vein. Occasionally thrombosis, calcification, or hemorrhage can occur. Uncomplicated lesions appear as tubular soft tissue densities that enhance intensely with contrast. Patent varices can be made more conspicuous with the Valsalva maneuver. On MRI complex signal intensities due to slow flow and thrombosis may be present (Fig. 7.9).

7.5.3 Cavernous Hemangioma

Cavernous hemangiomas, the most commonly encountered orbital masses in adults, are vascular malformations comprised of endothelial-lined cavernous spaces with a

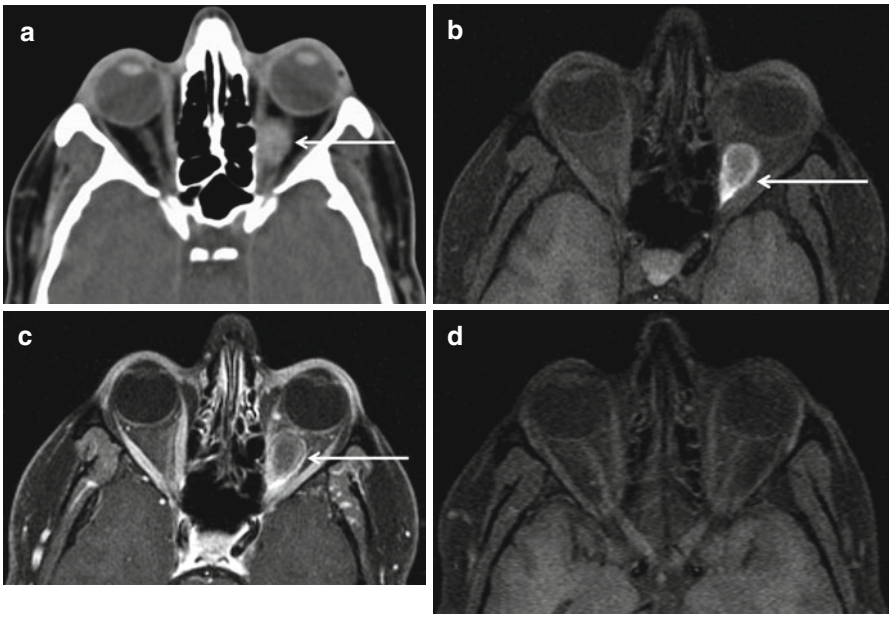

Fig. 7.9 Thrombosed venous varix. Axial CT scan (**a**) in this 42-year-old patient presenting with sudden onset left eye pain shows a well-defined hyperdense intraconal lesion (*arrow*). Axial T1 fat-sat image (**b**) also shows the T hyperintense intraconal lesion (*arrow* in **b**), without enhancement in post-contrast axial T1 fat-sat image (*arrow* in **c**). Follow-up axial T1 fat-sat image (**d**) after 3 months showing complete resolution of the lesion. The important pediatric lesions are summarized in Box 7.4

pseudocapsule of compressed normal orbital tissue. They are often incidentally detected on imaging but can present with slowly progressive painless proptosis. They are typically located in the intraconal compartment. They appear as well-defined homogeneous, noncalcified round or oval masses that exhibit progressive enhancement on delayed scans (Fig. 7.10).

7.6 Infectious and Inflammatory Disorders

The orbital complications of sinusitis are discussed in detail in Chap. 9.

These along with trauma and hemorrhage are the most common cause of acute proptosis (Box 7.5).

7.6.1 Idiopathic Orbital Inflammatory Disease

Idiopathic orbital inflammatory disease (orbital pseudotumor) is a poorly understood non-granulomatous steroid responsive disorder that can afflict any structure in the

Box 7.4. Pediatric Orbital Lesions

	Location	Important clinical feature	CT	MRI	Additional feature	DD
Dermoid	Occurs near the suture lines. Most common site is superolateral portion of orbit	Firm mass at the anterolateral portion of orbit	Bony remodeling is common. Fat density is seen in about ½ of the cases	Fat signal intensity seen in about ½ of the cases. Fluid-fluid level may be seen	If ruptured, appears irregular with adjacent inflammatory changes	Epidermoid has fluid density in CT and shows fluid signal intensity in MRI. Restricted diffusion in DWI differentiates it from dermoid
Venous-lymphatic malformation	Trans-spatial lesion	Gradually progressive proptosis, with intermittent worsening	Poorly marginated multicystic trans-spatial lesion. Calcification is rare	Fluid-fluid levels, varying blood signal intensity. Venous components and the periphery of cyst enhances		Orbital venous varix—dynamic change with Valsalva maneuver Orbital infantile hemangioma—intensely enhancing poorly marginated lesion with flow voids in MRI. Plexiform neurofibroma—infiltrative, variably enhancing lesion which appear hyperintense with central low intensity in T2-weighted imaging-target sign. Other features of NF1
Infantile hemangioma	Commonly preseptal, less commonly post-septal	Bluish skin discoloration with soft tissue mass	Lobular or infiltrative lesion	Flow voids	Imaging appearance changes with phase of involution, shows more fat content and septations	Orbital venous varix—dynamic change with Valsalva maneuver Plexiform neurofibroma Venolymphatic malformation Rhabdomyosarcoma—tendency to invade bone. Lack of flow void

(continued)

Box 7.4. (continued)

	Location	Important clinical feature	CT	MRI	Additional feature	DD
Optic glioma	Optic nerve	Decreased vision	Fusiform thickening, occasional hypodense cystic spaces	Fusiform thickening, occasional T2 hyperintense cystic spaces	May be associated with NF1 or sporadic	Optic nerve sheath ectasia can mimic optic glioma in NECT. Post-contrast imaging differentiates the two
Retinoblastoma	Arises from retina, extent depends on the tumor spread	White reflex	Calcifications in about 90 %	Hypointense in T2WI compared to vitreous. Noncalcified portion shows contrast enhancement	May have retinal detachment	Coats' disease—subretinal fluid collection, retinal detachment. No solid enhancing components Retinal astrocytic hamartoma resembles retinoblastoma radiologically. Association with tuberous sclerosis and neurofibromatosis helps to differentiate Ocular toxocariasis may show higher T2 signal intensity, which helps to differentiate. Calcification in CT is uncommon
Orbital rhabdomyosarcoma	Commonly extraconal, often contiguous with adjacent extraocular muscles	Painless proptosis	Bony erosion	T2 hyperintense		Orbital lymphoma—uncommon in children. Hypointense to isointense compared to EOM Orbital metastases can appear similar Plexiform neurofibroma—infiltrative, variably enhancing lesion which appear hyperintense with central low intensity in T2-weighted imaging-target sign. Other features of NF1

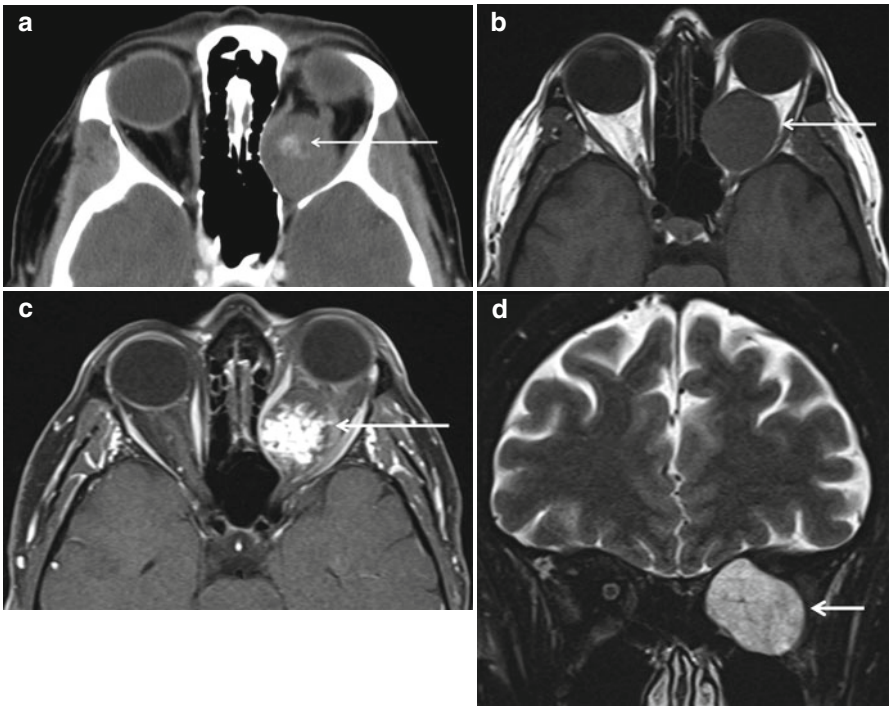

Fig. 7.10 Cavernous hemangioma. Axial CECT (**a**) showing central patchy enhancement in a well-defined intraconal lesion. In (**b** and **c**), the lesion is of intermediate signal intensity and enhances in a centripetal fashion. Coronal T2 fat-sat image (**d**) shows the characteristic T2 hyperintense nature of the lesion (*arrow*)

Box 7.5. Proptosis: Acute

Hemorrhage—hemorrhage in an underlying vascular lesion like venous-lymphatic malformation, trauma
Infection
CCF
Cavernous sinus thrombosis

orbit. IOID occurs in five forms—anterior (globe and retrobulbar soft tissues), lacrimal, myositic, apical (involvement of the orbital apex and cavernous sinus, Tolosa-Hunt syndrome), and diffuse and sclerosing (bilateral affliction of the orbits and paranasal sinuses) (Figs. 7.11 and 7.12). Painful unilateral ophthalmoplegia is the most common presenting feature. The myositic form, which on imaging is characterized by uniform enlargement of one or more extraocular muscles and their tendon sheaths, is the most frequently encountered variety of IOID. Involvement of the tendon sheaths is a typical finding in IOP and enables differentiation from thyroid ophthalmopathy, where despite smooth enlargement of the muscle belly, the tendon is unaffected. IOID may also occur as a diffusely infiltrative relatively T2

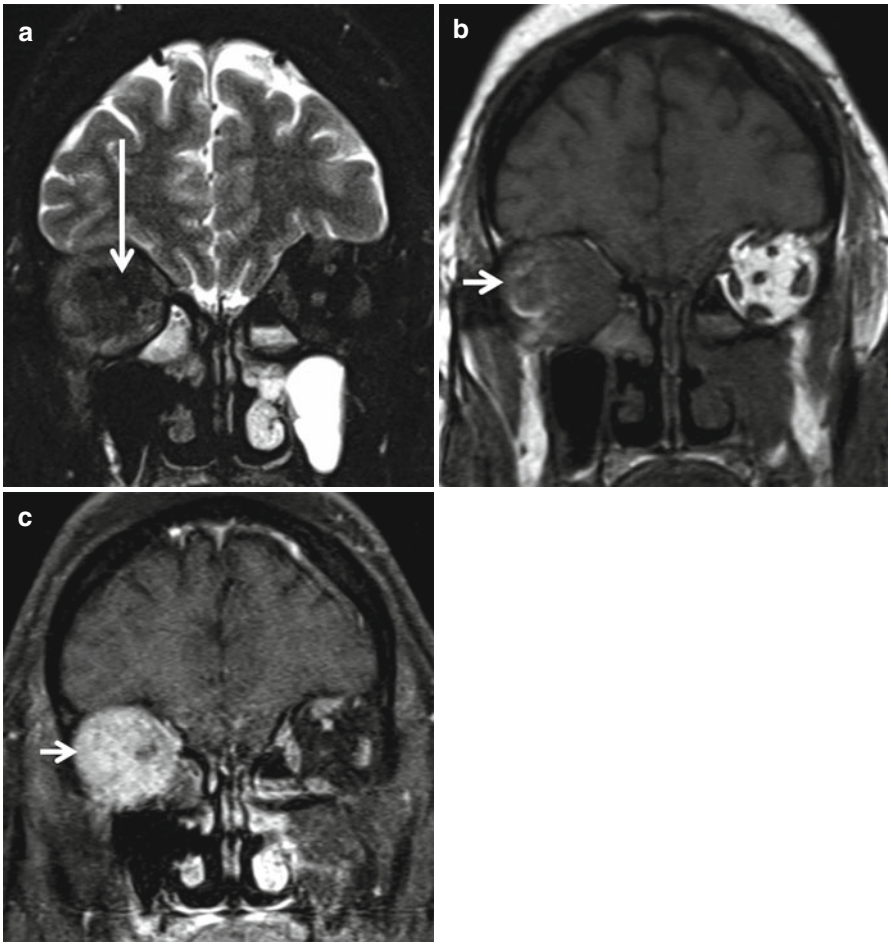

Fig. 7.11 Idiopathic orbital pseudotumor. Coronal T2 (**a**), precontrast T1 (**b**), and post-contrast T1 fat-sat (**c**) images, in a 42-year-old with painful slowly progressive proptosis, demonstrate an ill-defined T2 hypointense (compared to the extraocular muscles) (*long arrow* in **a**), enhancing lesion (*short arrow* in **b** and **c**) involving both the extra- and intraconal compartments. Typical features of this entity are T2 hypointensity on MRI, ocular pain and steroid responsiveness. These need not necessarily be present in every patient

hypointense enhancing process. When fibrosis is marked, the lesion may be profoundly T2 hypointense. Orbital lymphoma, sarcoidosis, and Wegener's granulomatosis can have very similar imaging appearances (Box 7.6), and one may have to rely on clinical data to arrive at the correct diagnosis. IgG4-related sclerosing disease is a type of orbital pseudotumor characterized by lymphoplasmacytic tissue infiltration with a predominance of IgG4-positive plasma cells, usually accompanied by fibrosis, and elevated serum levels of IgG4. IgG4-related sclerosing disease radiologically is indistinguishable from IOID.

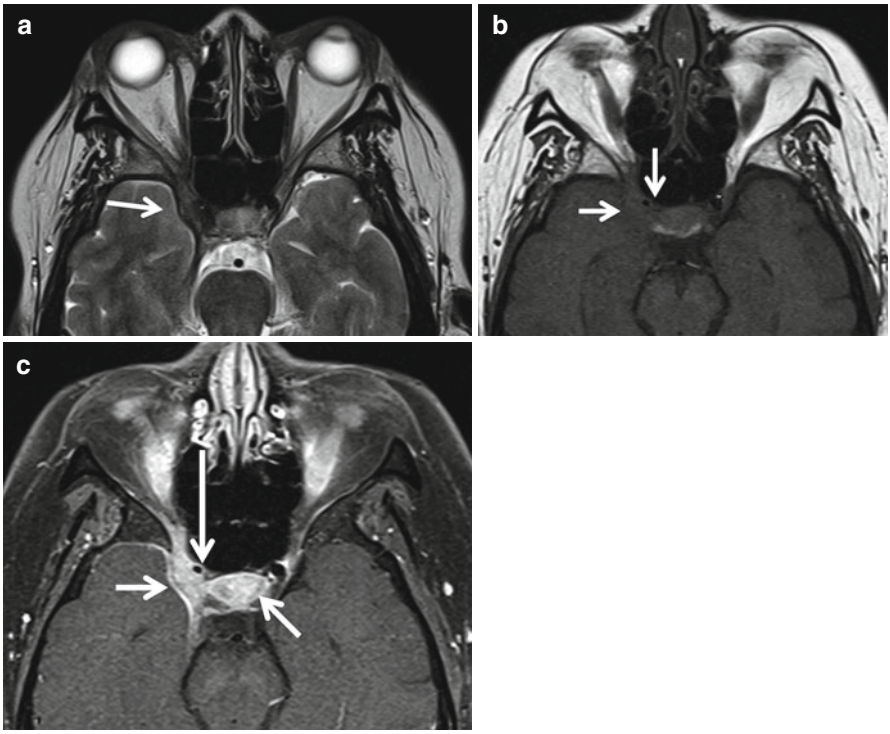

Fig. 7.12 Tolosa-Hunt syndrome in orbital pseudotumor. Axial T2 (**a**), precontrast T1 (**b**), and post-contrast fat-sat T1 images (**c**) demonstrate a T2 hypointense enhancing lesion (*short white arrows* in **a**–**c**) involving the right superior orbital fissure and the adjacent right cavernous sinus and sella. The right internal carotid artery is encased and narrowed by this lesion (*longer arrow* in **c**). This patient with an underlying diagnosis of orbital pseudotumor presented acutely with severe eye pain, headache, and external ophthalmoplegia

Box 7.6. Low T2 Signal Intensity Lesions

Orbital pseudotumor
Sarcoid
Wegener's granulomatosis
Lymphoma
Acute hematoma

7.6.2 Sarcoidosis

Although ophthalmological disease in sarcoidosis is frequent, imaging findings are uncommon. Anterior and posterior uveites are well-known phenomena associated with ocular sarcoid and are not evaluated with imaging. Soft tissue masses in the

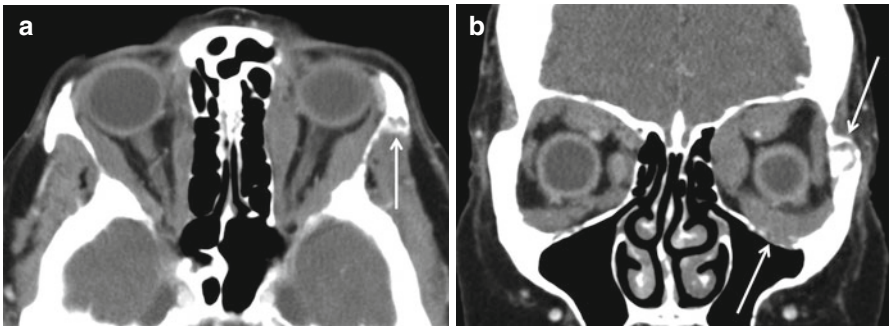

Fig. 7.13 Orbital sarcoidosis. Axial (**a**) and coronal (**b**) CECT in a 70-year-old woman presenting with gradual onset bilateral proptosis, showing bilateral enlarged external ocular muscles and bony lesions (*arrows*)

eyelids, lacrimal gland infiltration, optic nerve and sheath involvement, unilateral and bilateral retrobulbar soft tissue masses, extraocular muscle involvement, and, rarely, destructive osseous lesions have all been reported to occur (Fig. 7.13). There are no specific imaging features of orbital sarcoid, and often it is the presence of systemic disease elsewhere that points to the diagnosis.

7.6.3 Wegener's Granulomatosis

Imaging findings in Wegener's granulomatosis resemble that of sarcoidosis and IOID. Coexistent destructive sinonasal lesions are suggestive of WG, although such lesions may also be seen with sarcoidosis and IgG4-related inflammatory disease.

7.6.4 Thyroid Ophthalmopathy

Thyroid ophthalmopathy results from autoimmune orbital inflammation associated with Grave's disease. Thyroid ophthalmopathy, evident clinically as exophthalmos, may present before, during or after treatment of Grave's disease. Spindle-shaped smooth enlargement of the extraocular muscles, with sparing of the tendinous insertions, is typical of the disease. The inferior, medial, superior, and lateral rectus and oblique muscles are affected in decreasing order of frequency. These findings are usually bilateral and symmetric; however, they also may be unilateral. Additional findings include increased orbital fat, lacrimal gland enlargement, eyelid edema, stretching of the optic nerve, and tenting of the posterior globe. On CT the extraocular muscles are heterogeneous in appearance and contain foci of low density due to mucopolysaccharide deposition (Fig. 7.14). The enlarged muscles are isointense on T1WI and demonstrate increased signal intensity on fat-suppressed T2WI in the acute phase of the disease due to edema. In chronic thyroid ophthalmopathy, low signal intensity due to fibrosis may be present. Visual dysfunction may also occur due to compression of the optic nerve at the orbital apex by the enlarged

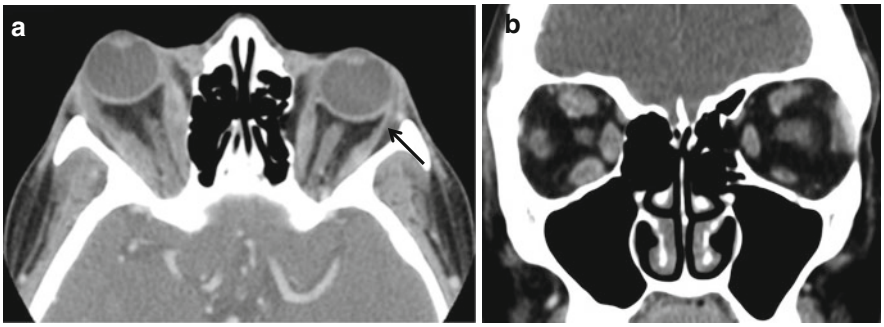

Fig. 7.14 Thyroid orbitopathy. Axial (**a**) and coronal (**b**) CT scan of a 43-year-old patient with thyroid orbitopathy showing bilateral enlarged external ocular muscles and characteristic sparing of the tendinous insertions (*arrow* in **a**). Note the tiny hypodensities within external ocular muscles in the coronal CT (**b**) due to deposition of mucopolysaccharides

Box 7.7. Extraocular Muscle Enlargement

Thyroid ophthalmopathy
Idiopathic pseudotumor
Malignancy—lymphoma, leukemia, metastases
Infectious myositis
Lymphoma, metastases
Vascular congestion—CCF, dural AV fistula, superior ophthalmic vein thrombosis

muscles. Lack of a cuff of fat around the nerve at the apex can indicate significant compression. The differential diagnosis of an enlarged extraocular muscle includes myositis pseudotumor, thyroid ophthalmopathy, and lymphoma (Box 7.7). Of these the only entity that spares the tendinous insertion is thyroid ophthalmopathy. Occasionally an EOM may be enlarged due to the presence of a metastatic deposit (usually from a lung, breast, or carcinoid primary); such enlargement is however nodular.

7.6.5 Optic Neuritis

Optic neuritis, best imaged with MRI, can occur due to a wide variety of infectious and inflammatory causes, including posttreatment (radiation-induced optic neuritis) (Figs. 7.15 and 7.16). The most common clinical scenario in which one encounters optic neuritis is in patients with multiple sclerosis (or with neuromyelitis optica), which is why it is prudent to scrutinize the entirety of the brain for demyelinating plaques. The inflamed nerve is hyperintense on fat-suppressed T2W images and enhances with gadolinium (Fig. 7.6). Occasionally, inflammation may be confined to the optic nerve head, when the term papillitis is used. There are no specific imaging patterns of optic neuritis.

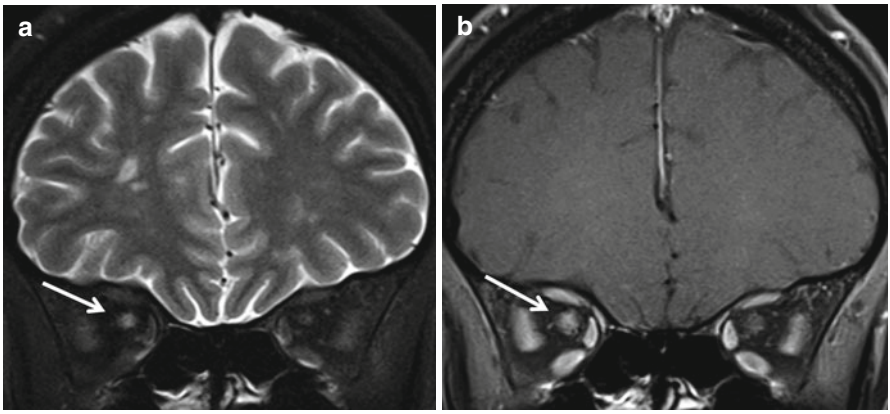

Fig. 7.15 Optic neuritis. Coronal T2 fat-sat image (**a**) showing enlarged hyperintense right optic nerve (*arrow*) in a 28-year-old patient with multiple sclerosis who presented with acute onset right-sided eye pain and vision loss. Post-contrast coronal T1 fat-sat image (**b**) showing abnormally enhancing enlarged right optic nerve (*arrow*)

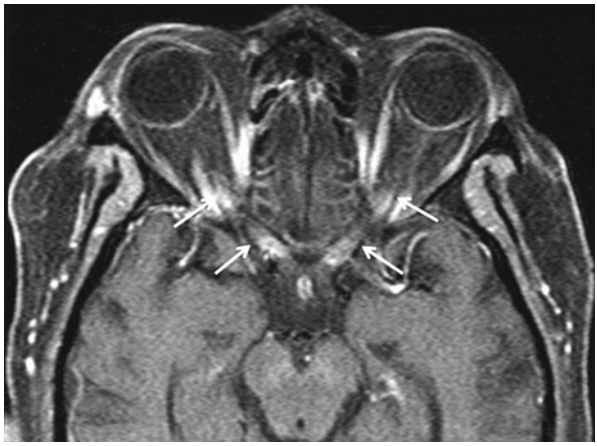

Fig. 7.16 Radiation-induced optic neuritis. Post-contrast axial T1 fat-sat image showing abnormally enhancing bilateral optic nerves (*arrows*) in this 54-year-old patient, following treatment for brain metastases

7.7 Benign Tumors

7.7.1 Infantile Hemangioma

Orbital infantile hemangioma is a benign vascular tumor, which usually appears within the first few weeks of life. Clinically, it presents as a mass with purplish discoloration of the eyelid/conjunctiva. Larger lesions may result in proptosis, diplopia, optic atrophy, and visual deterioration. Typical infantile hemangiomas grow during the first 1–2 years, stabilize, and regress spontaneously by late childhood. Most occur in the preseptal compartment. Infantile hemangiomas can appear lobular or infiltrative. Intense enhancement with intravenous contrast and prominent flow voids are a common feature (Fig. 7.17). Involuting hemangiomas can contain foci of fat and may not enhance intensely.

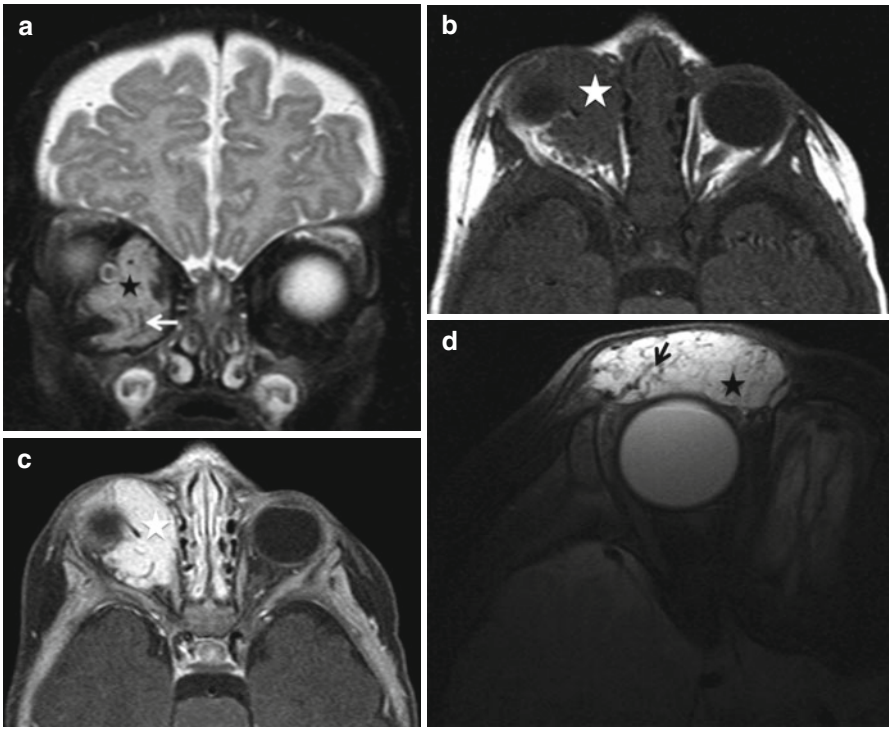

Fig. 7.17 Infantile hemangioma in a 3-month-old patient. Coronal T2 fat-sat image (**a**) showing hyperintense intraconal and extraconal irregular lesion (*star*) with flow voids (*white arrow*). Precontrast axial T1WI (**b**) shows the intermediate signal intensity of the lesion affecting preseptal and post-septal (intraconal and extraconal) compartments (*star*) with intense enhancement on the post-contrast axial T1 fat-sat image (**c**). Infantile hemangioma in another 3-month-old patient, with hyperintense lesion (*black star* in **d**) with prominent flow voids (*black arrow* in **d**) limited to the preseptal compartment

7.7.2 Optic Nerve Meningioma

Optic nerve meningiomas usually present with gradual painless, progressive vision loss. The occurrence of bilateral optic sheath meningioma is very rare and may be seen in patients with neurofibromatosis 2. They usually surround the optic nerve and grow in a tubular pattern. Occasionally a pedunculated or fusiform appearance may be present (Fig. 7.18). A linear "tram track" pattern of calcification is a typical finding (Fig. 7.18). Other lesions which can sometimes have a tram track pattern of enhancement are summarized in Box 7.8 below. They are best seen on post-contrast fat-suppressed MR images. Perioptic cysts representing trapped CSF in the optic nerve sheath, between the distal portion of the tumor and the globe may be present. Intracanalicular meningiomas represent a diagnostic challenge. They are difficult to identify and must always be actively sought for, when a patient, especially a female one, presents with painless gradual visual decline (Fig. 7.18).

Fig. 7.18 Optic nerve meningioma. A 58-year-old patient with gradual onset loss of vision of the right eye. Axial T1WI (**a**) showing intermediate signal intensity lesion near the orbital apex and in the optic canal (*arrow*). Post-contrast axial T1 fat-sat images (**b**) showing enhancing lesion which is predominantly involving the intracanalicular portion of optic nerve (*arrow*). These lesions can be missed unless specifically looked for in the dedicated contrast-enhanced fat-sat images. Coronal T2 fat-sat image (**c**) showing atrophy of the right optic nerve (*arrow*). (**d**, **e**) Optic nerve sheath meningioma. Another patient (**d**) with asymmetric enhancement along the intraorbital portion of right optic nerve (*arrow*), with atrophy of the optic nerve. Bilateral optic nerve sheath meningiomas with tram track calcification (*long arrow* **e**) in a different 53-year-old patient, who also had multiple intracranial calcified meningiomas (*short arrows*)

Box 7.8. Tram Track Enhancement

Meningioma
Perioptic neuritis
Optic neuritis
Lymphoma, leukemia, metastases
Sarcoid
Perioptic hemorrhage
Normal variant

7.7.3 Lacrimal Gland Benign Mixed Tumor

The typical appearance of a lacrimal gland pleomorphic adenoma is that of a well-defined lobulated variably enhancing mass with typical high signal on T2W images. Smooth bone remodeling may sometimes be present. Aggressive lacrimal masses such as lacrimal gland carcinomas show more irregular margins with local osseous invasion (Fig. 7.19).

7.8 Malignant Tumors

7.8.1 Retinoblastoma

Retinoblastoma is the most common intraocular childhood malignancy. Approximately 40 % of cases of retinoblastoma are due to heritable mutations, the rest being sporadic. Hereditary forms have an earlier age of onset, usually by 2 years of age and has propensity for bilateral and multifocal tumors. The nonheritable form is seen in older children and is typically solitary. Retinoblastomas result from inactivation of the retinoblastoma tumor suppressor gene on chromosome 13, at q14 locus. Although retinoblastomas can be visualized by direct ophthalmological examination, imaging plays an essential role in defining the extent of the disease (Box 7.9). Although USG, CT, and MRI are all used in the work-up in retinoblastomas, CT is ideally avoided due to concerns of increased long-term risk of malignancy. High-resolution MR imaging is the preferred modality to evaluate retinoblastomas.

On CT, the imaging findings are nonspecific, except for the appearance of calcification within the mass. Other calcified masses on CT include Coats' disease, retinal astrocytoma, phthisis bulbi, and ocular toxocariasis, all of which can be differentiated from retinoblastomas by a combination of clinical and imaging appearance.

On MR, retinoblastomas appear as heterogeneously enhancing lesions, with variable T1 (usually hyperintense to ocular fluid), with hypointense T2 signal (relative to vitreous) (Fig. 7.20a). Calcifications can be identified on either gradient echo MRI (GRE) or susceptibility-weighted imaging MRI (SWI) sequences (Fig. 7.20b). These lesions also restrict diffusion, although evaluation on this sequence can be limited due to susceptibility-related artifacts from calcifications. More importantly, MRI is done to precisely map the extent of the disease for accurate staging and management. Important intraocular findings to look for include presence of vitreous

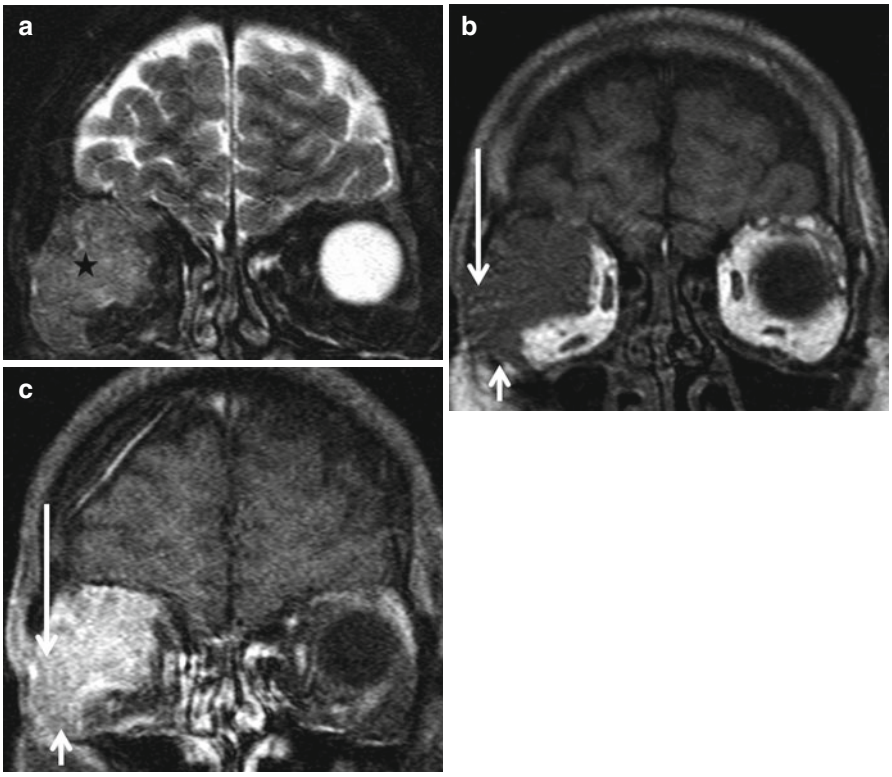

Fig. 7.19 Lacrimal gland carcinoma. Heterogeneous T2 hyperintense lesion (*star* in **a**), which demonstrates moderate enhancement on the precontrast T1 (**b**) and post-contrast T1 fat-sat images (**c**), with invasion of the lateral (*long arrow*) and inferior (*short arrow*) orbital bony walls. The bony destruction indicates that the lesion is aggressive, the location of the lesion being the only indication that the lesion may be arising from the lacrimal gland in the superolateral quadrant. The imaging appearance is nonspecific

Box 7.9. International Intraocular Retinoblastoma Classification

Group A	Tumors ≤3 mm in size, confined to retina, away from optic disc or foveola
Group B	Tumors ≥3 mm in size, confined to retina and close to optic disc or foveola
Group C	Localized (vitreous/subretinal) fine and limited seeding
Group D	Massive and/or diffuse intraocular seeding, retinal detachment
Group E	Larger tumors, with neovascular glaucoma, massive intraocular hemorrhage, anterior segment or ciliary body invasion or phthisis bulbi

Murphree AL (2005) Intraocular retinoblastoma: the case for a new group classification. Ophthalmol Clin North Am 18:41–53

seeding, retinal detachment, subretinal seeding, vitreous hemorrhage, anterior segment involvement, and choroidal/scleral invasion. Presence of vitreous hemorrhage (high T1 and low T2) may obscure tumor in MR imaging. In such cases, the tumor is usually best delineated by comparing precontrast and post-contrast T1 images.

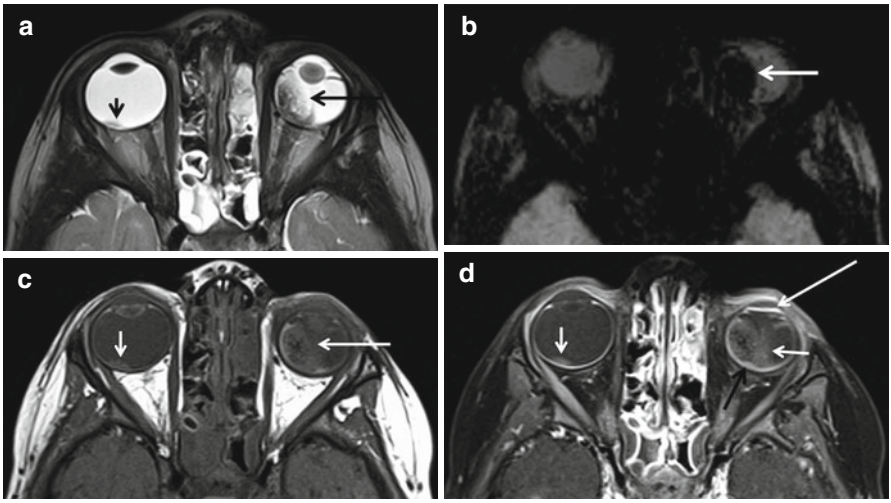

Fig. 7.20 Bilateral retinoblastoma. Axial T2 (**a**) and SWI (**b**) sequences demonstrate bilateral retinoblastomas. These appear as low signal intensity lesion in the left eye (*long black arrow*) and a small lesion in the right eye (*short black arrow*). The axial SWI (**b**) sequence nicely shows loss of signal with blooming, due to calcification within the lesion (*white arrow*) in the left eye. Axial TI sequences (**c**) shows heterogeneous hyperintensity of the lesions compared to the vitreous in the left eye (*long white arrow*) and a small lesion in the right eye (*short white arrow*). Contrast-enhanced T1 fat-sat image (**d**) showing enhancement of the lesions (*short white arrow*, *double white arrows*). Choroidal invasion is seen as focal thickening (*black arrow* in **d**). Plaque-like enhancement (*long white arrow* in **d**) of the iris is a reactive phenomenon (rubeosis iridis) and does not represent tumor spread

A potential pitfall is rubeosis iridis (the neovascularization of the iris), which appears as contrast enhancement within the anterior segment (Fig. 7.20d). This is not due to tumor spread, but is a reactive phenomenon mediated by vascular endothelial growth factors released by tissue hypoxia. Extraocular spread should be documented including extrascleral extension (abnormal enhancement of the retroorbital fat) and optic nerve involvement (whether pre- or postlaminar). However, MR has low sensitivity for predicting prelaminar optic nerve invasion. MR imaging findings of postlaminar optic nerve infiltration include focal optic nerve enhancement, with or without focal thickening of the optic nerve. Postlaminar optic nerve involvement indicates poor prognosis. MR can also document intracranial extension along optic nerve, leptomeningeal metastasis, and other primary intracranial tumors associated with bilateral retinoblastomas such as trilateral and quadrilateral retinoblastomas (pineal and suprasellar tumors).

7.8.2 Choroidal Melanoma

This is the most common primary intraocular tumor in adults. They are frequently asymptomatic or may sometimes present with painless visual disturbance. Rarely, they can result in retinal detachment. Choroidal melanomas appear as noncalcified

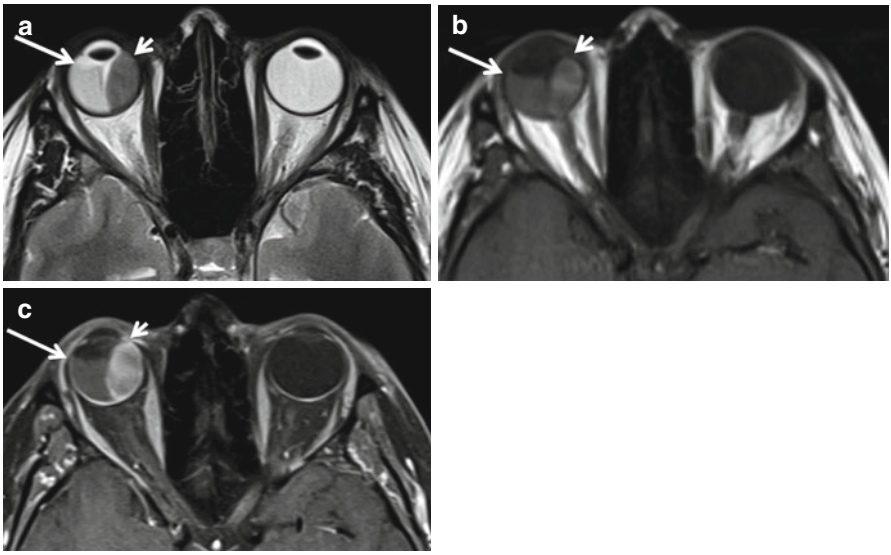

Fig. 7.21 Choroidal melanoma. Axial T2 (**a**) and T1 (**b**) sequences showing T2 hypointense (**a**), T1 hyperintense (**b**) lesion in the right eye (*short arrow*) with retinal detachment (*long arrow*). Post-contrast axial T1 fat-sat image (**c**) showing enhancing melanoma (*short arrow*) with non-enhancing retinal detachment (*long arrow*)

soft tissue masses on CT, with moderate enhancement. Depending on the melanin content, they can appear T1 hyperintense and T2 hypointense to the vitreous on MR, with moderate contrast enhancement (Fig. 7.21). Other choroidal masses such as metastasis can mimic the appearance of choroidal melanomas.

7.8.3 Orbital Rhabdomyosarcoma

Orbital rhabdomyosarcoma can be primary, arising from the primitive mesenchymal cells, or may represent secondary extension from extraocular muscles or from adjacent paranasal sinuses. These are typically found in pediatric patients and present with painless rapidly progressive proptosis and diplopia. The tumor can involve both the extra and intraconal compartments and frequently invades the bony orbit. On CT, the mass is usually mildly hyperdense with irregular enhancement. MR is helpful to delineate the entire extent of the lesion, which has treatment implications (Fig. 7.22).

7.8.4 Orbital Lymphoma

As with rhabdomyosarcomas, orbital lymphomas too can be primary or associated with systemic lymphomas. However, this is typically a disease of older patients,

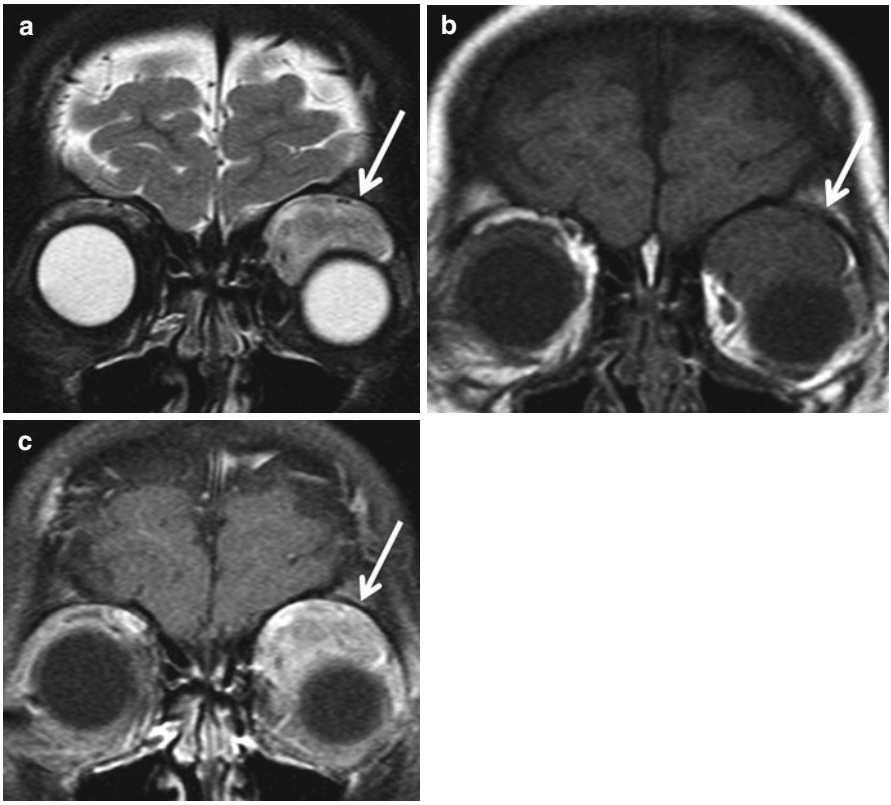

Fig. 7.22 Orbital rhabdomyosarcoma. Coronal T2 fat-sat images (**a**) in this 4-year-old patient showing heterogeneous hyperintense lesion in the superior aspect of the orbit (*arrow*), involving both the extraconal and intraconal compartments. The lesion shows intermediate signal intensity (*arrow*) in precontrast coronal T1 (**b**) with heterogeneous enhancement (**c**). Although the imaging appearance is nonspecific, the age of the patient helps in narrowing the differential diagnosis

who present with painless proptosis and diplopia. It can manifest as a unifocal lesion affecting any of the intraorbital structures or a diffusely infiltrative mass, like orbital pseudotumor. Unlike other aggressive intraorbital tumors, these lesions insinuate around the orbital structures without significant mass effect or osseous invasion (similar to orbital pseudotumors). Lymphoma may mimic thyroid ophthalmopathy by isolated involvement of the external ocular muscles. Orbital lymphomas appear isodense to hyperdense in NECT due to the hypercellularity of the tumor and show moderate contrast enhancement. On MR, these enhancing lesions are difficult to distinguish from orbital pseudotumor, because of similar imaging characteristics (Fig. 7.23). Diffusion-weighted imaging may help in differentiating these lesions, as lymphomas show restricted diffusion, due to their high cellularity (Fig. 7.23d, e).

7.8.5 Orbital Metastases

Metastatic disease to the globe is extremely uncommon. Usually, orbital metastases are either osseous or extraconal with secondary intraconal involvement. The

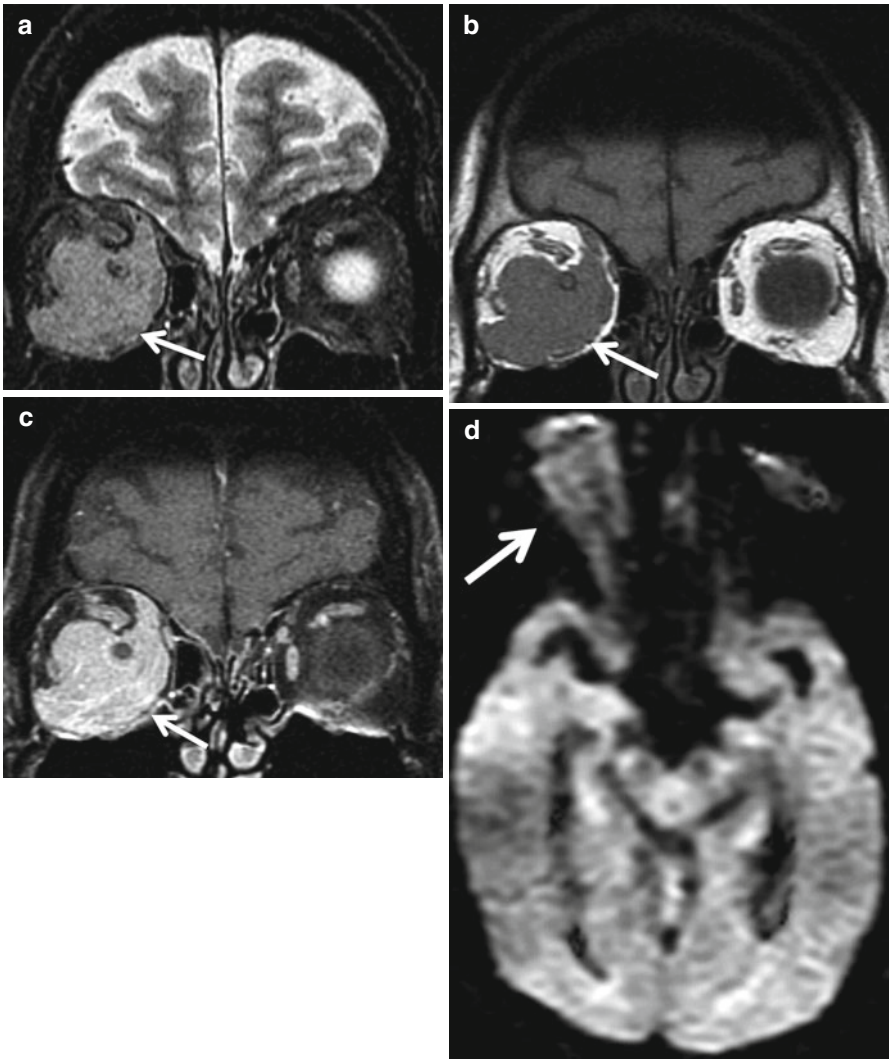

Fig. 7.23 Orbital lymphoma. Coronal T2 fat-sat image (**a**) showing slightly hyperintense infiltrative lesion (*arrow*) involving both the intraconal and extraconal compartments in this 62-year-old patient who presented with painless gradual onset proptosis. The lesion shows intermediate signal intensity in coronal T1 sequences (*arrow* in **b**) with intense contrast enhancement (*arrow* in **c**). The lesion also demonstrates restricted diffusion, (*arrows* in **d** and **e**). The absence of pain and restricted diffusion differentiates lymphoma from orbital pseudotumor

Fig. 7.23 (continued)

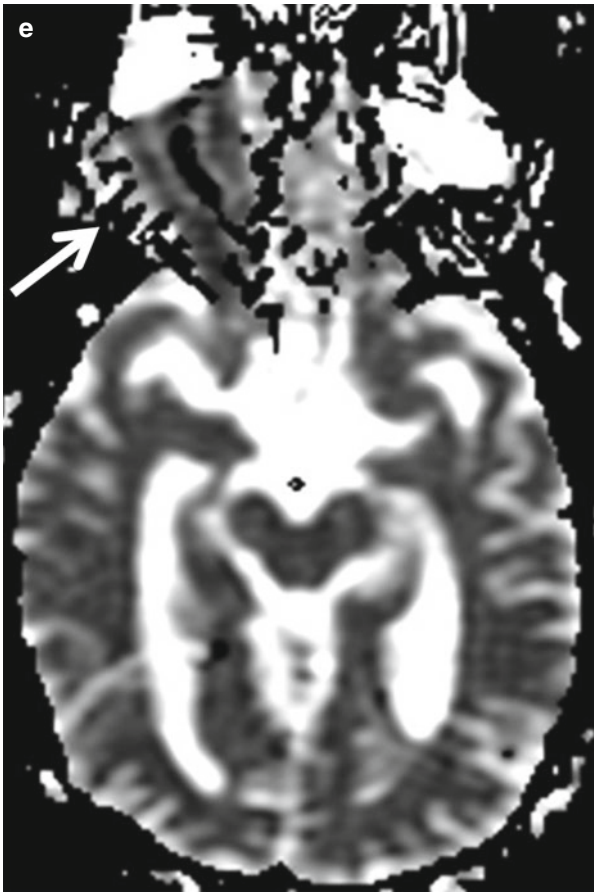

extraocular muscles are involved infrequently. More than half of the orbital metastasis is from breast and lung cancers. Although imaging findings are nonspecific, many of the metastatic lesions appear more nodular as compared to other mass lesions (Fig. 7.24).

7.9 Miscellaneous

7.9.1 Retinal Detachment

Retinal detachment refers to separation of the inner layers of the retina from the underlying retinal pigment epithelium. This results in crescent-shaped or V-shaped fluid collection on axial sections, with the apex converging at the optic disc. Retinal detachment can be spontaneous or due to underlying lesions, including tumors like retinoblastoma, choroidal melanoma, or metastases as well as other lesions such as

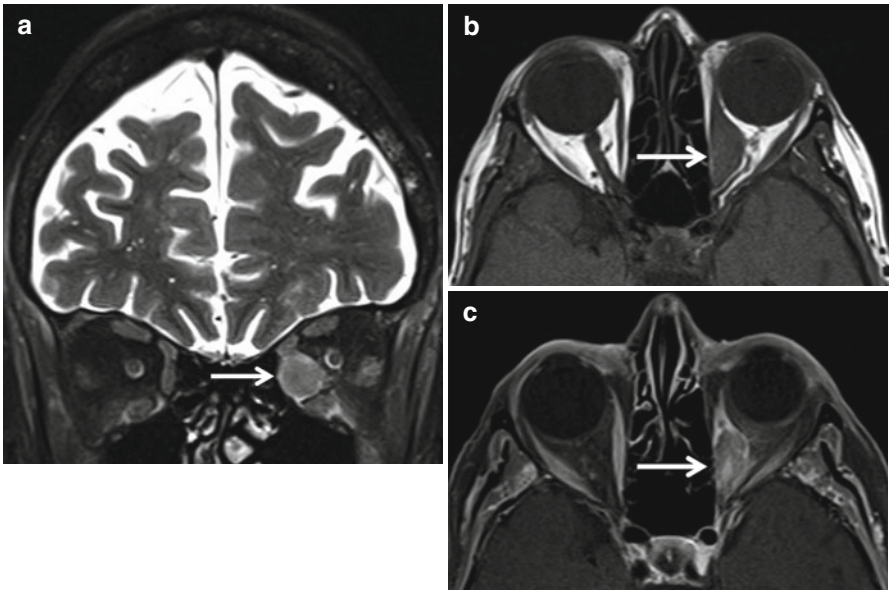

Fig. 7.24 Orbital metastases from breast cancer. Coronal T2 fat-sat image (**a**) showing slightly hyperintense lesion in left medial rectus (*arrow* in **a**). The lesion shows intermediate signal intensity in axial T1WI (*arrow* in **b**) with heterogeneous contrast enhancement (*arrow* in **c**)

trauma (due to subretinal hemorrhage), PHPV, and senile macular degeneration (Fig. 7.5).

7.9.2 Choroidal Detachment

Choroidal detachment is the separation of choroid from sclera with either serous or hemorrhagic collection, in the suprachoroidal space. These can be linear or crescentic and extend anteriorly to the ciliary bodies. Posterior extension is limited by the anchoring effect of short posterior ciliary arteries and nerves, thus sparing the posterior portion of the globe and the optic disc (unlike retinal detachments) (Fig. 7.25). Choroidal detachment can be seen with trauma, surgery, ocular hypotonia, and lesions such as choroidal melanomas.

7.10 The Surgeon's Perspective

The physical examination is a critical part of work-up for suspected orbital disease. This includes assessing the afferent visual pathways, including visual acuity, visual fields, and the presence of asymmetric optic nerve function as indicated by an afferent pupillary defect. Motility abnormalities suggesting involvement of the extraocular muscles or the cranial nerves innervating them are raised by the symptoms of

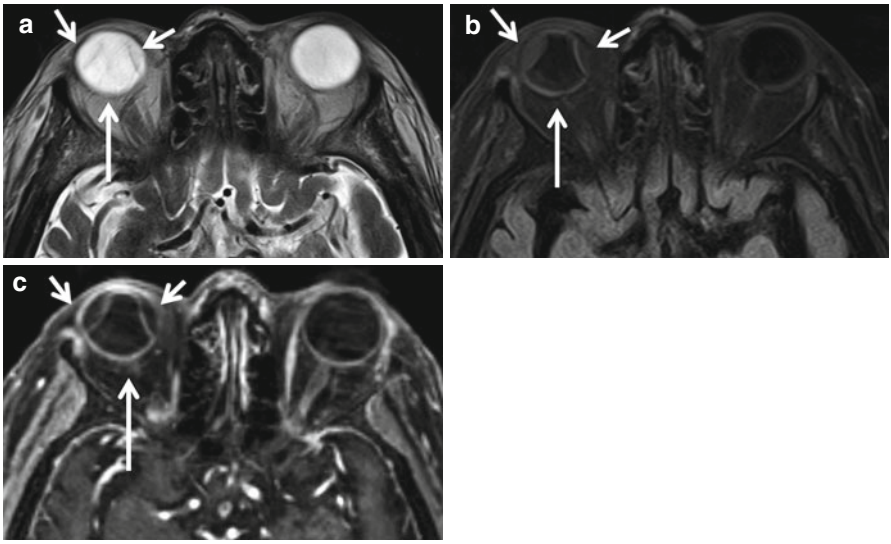

Fig. 7.25 Spontaneous choroidal detachment. Axial T2 (**a**), FLAIR (**b**), and post-contrast images (**c**) show the characteristic sparing of the posterior portion of the globe differentiating it from retinal detachment (*long arrow*). The subchoroidal fluid (*smaller white arrows*) appears hyperintense compared to vitreous in axial FLAIR (**b**)

diplopia and the findings of limited motility producing ocular malalignment. Most important to the suspicion of orbital pathology however remains, as recognized more than a thousand years ago, the presence of proptosis supplemented by abnormal lid position, resistance to retropulsion, sensory changes, and dystopia with the globe displaced in the direction opposite to the location of the lesion. More subtle findings on examination may include the presence of prominent episcleral vessels and increased intraocular pulse pressure suggestive of the presence of orbital venous hypertension, often related to carotid-cavernous fistula. Intermittent proptosis exacerbated by Valsalva maneuver may indicate the presence of an orbital venous varix.

Pathology affecting the orbit, like other locations in the body, may be congenital, developmental, inflammatory (including infectious), neoplastic, and vascular. Trauma can also affect the orbit, as can pathology arising from surrounding structures such as the paranasal sinuses and intracranially from the anterior and middle cranial fossae. Intracranial tumors that affect the orbit include most commonly meningiomas, particularly those arising from the sphenoid wing but occasionally from the floor of the anterior cranial fossa. Nasal or sinus tumors include adenocarcinoma, squamous cell carcinoma, undifferentiated carcinoma, esthesioneuroblastoma, and more rarely metastatic disease, melanomas, and adenoid cystic carcinoma. These secondary tumors are usually outlined and diagnosed by imaging and confirmed by endoscopic biopsy. Even with the most detailed history and physical examination, the specifics of localization and definitive diagnosis were usually impossible prior to the advent of imaging.

From the ophthalmologist's perspective, the most important aspect of localization on imaging is the lesions' relationship to the optic nerve. Not only does the location

suggest the optimal approach, rendering moot the conflict between whether transcranial or lateral orbitotomy is the ideal approach, in some cases, the specific characteristics of the pathology on imaging permit a diagnosis and thus suggest optimal treatment. Although other techniques, including the use of ultrasound, angiography, and venography, have been developed to play a supplementary role in the diagnosis of orbital pathology, CT and MR imaging remains the primary means of diagnosis and planning therapy in orbital disease. Imaging may also play a role in diagnosing intraocular pathology, but it usually is secondary to ophthalmoscopic evaluation and ultrasound.

Unlike intracranial pathology where MR proves superior in the majority of cases, in the orbit, CT and MR both remain extremely useful and often complimentary. Because of the contrast provided by the high fat signal intensity on CT scanning, it can often outline lesions within the orbit. As with other intracranial pathology, however, CT suffers at the bone-soft tissue interface, particularly at the orbital apex. There, especially when evaluating apical optic nerve pathology, MR offers a major advantage. CT is particularly sensitive to calcium and includes not only the bones around the orbit but also certain lesions that affect the globe including choroidal osteomas, scleral choristomas, and phthisis. While retinoblastoma often calcifies, these patients should probably not be studied with CT due to the risk of radiation-induced secondary tumors (often sarcomas) in patients with mutations in the RB1 (a tumor suppressor) gene. Retinoblastoma patients should avoid radiographic studies if possible (a combination of ultrasound and MRI are often adequate).

Soft tissue characteristics are better seen on MRI, and CT is superior for suspected foreign bodies with the possible exception of wood. Currently localization information provided by imaging includes involvement of the globe, the optic nerve, or the extraocular muscles. The pattern, whether it is infiltrative or well separated from the surrounding normal tissue, involvement of the surrounding bone provides additional information, while additional techniques may continue to provide supplementary information. One unusual characteristic of MR findings that could be helpful with orbital pathology is that of the paramagnetic features of melanin, meaning that instead of being bright on T2, melanomas are often dark on T2 and bright on T1. In orbital pathology more than any other location, imaging study remains the foundation upon which we make a diagnosis and decide on treatment.

While imaging studies are the backbone of orbital evaluation, it is far better to tailor our approach to lesions affecting the orbit based on pathology. Not all lesions need to be operated on. Malignant lesions are rarely curable with surgery and biopsy may direct treatment to radiation therapy or chemotherapy (particularly with lymphoproliferative lesions). Inflammatory or infectious pathology conversely needs to be treated with appropriate antibiotics or anti-inflammatories and other than drainage with as little surgery as possible. While specific diagnosis can sometimes be made on imaging, often tissue biopsy or cytology provided by fine needle aspiration may be necessary. Knowledge of the natural history, as provided by follow-up quantitative imaging studies supplemented by additional information including genetic testing and histopathology, provided either by biopsy or even by cytology from fine needle aspiration (especially when combined with flow cytometry,

immunohistochemical marking, and gene rearrangement studies), permits increasingly sophisticated decision making regarding orbital pathology. Although largely supplemental, ultrasound does have certain situations where it is particularly diagnostic, such as the "T sign" in patients with posterior scleritis.

It is impossible to maintain a practice in orbital pathology without a firm understanding of the role of the myriad imaging techniques now available. Ophthalmologists are encouraged to personally involve their radiologists to optimize the information obtained permitting better planning and results in taking care of patients with orbital lesions.

Further Reading

Chung EM, Smirniotopoulos JG, Specht CS et al (2007) Pediatric orbit tumors and tumorlike lesions: nonosseous lesions of the extraocular orbit. Radiographics 27:1777–1799

Gentry LR (1998) Anatomy of the orbit. Neuroimaging Clin N Am 8(1):171–194

Levin AV (2003) Congenital eye anomalies. Pediatr Clin North Am 50:55–76

Rauscheker AM, Patel CV et al (2012) High-resolution MR imaging of the orbit in patients with retinoblastoma. Radiographics 32(5):1307–1326

Smoker WR, Gentry LR, Yee NK et al (2008) Vascular lesion of the orbit: more than meets the eye. Radiographics 28:185–204

Temporal Bone and Skull Base

8

Prashant Raghavan, Bradley W. Kesser, Max Wintermark, and Sugoto Mukherjee

8.1 Anatomy

8.1.1 External Ear

The external auditory canal is comprised of an outer cartilaginous and an inner bony part and is covered entirely by skin. The tympanic membrane is located in an osseous groove (tympanic annulus) and forms a complex angle, roughly about 55° with the sagittal plane. The normal tympanic membrane may not be visible on CT scans. The anterosuperior portion of the tympanic membrane is comprised of the pars flaccida, and the remainder is the pars tensa. The pars flaccida is the most common site of cholesteatoma formation. The handle of the malleus is attached to the pars tensa (Fig. 8.1).

8.1.2 Middle Ear

The middle ear cavity is divided into the epitympanum (attic), mesotympanum, and the hypotympanum. The mesotympanum is typically what can be seen through the tympanic membrane and is separated from the epitympanum superiorly by the facial nerve and separated from the hypotympanum inferiorly by the inferior bony annulus.

The roof of the middle ear cavity is the tegmen tympani. The floor is related to the jugular bulb. The lateral wall is formed by the tympanic membrane.

The medial wall is comprised of two eminences. The superior of these is produced by the lateral semicircular canal. The inferior eminence is due to the basal turn of the cochlea and is called the promontory. The tympanic plexus of nerves is located on the promontory. The presence of paraganglia in the plexus accounts for the occurrence of glomus tympanicum tumors in this location. Between these two eminences is the oval window niche. The tympanic segment of the facial nerve lies under the lateral semicircular canal but may pass directly over the oval window if

P. Raghavan et al., *Manual of Head and Neck Imaging*,
DOI 10.1007/978-3-642-40377-4_8, © Springer-Verlag Berlin Heidelberg 2014

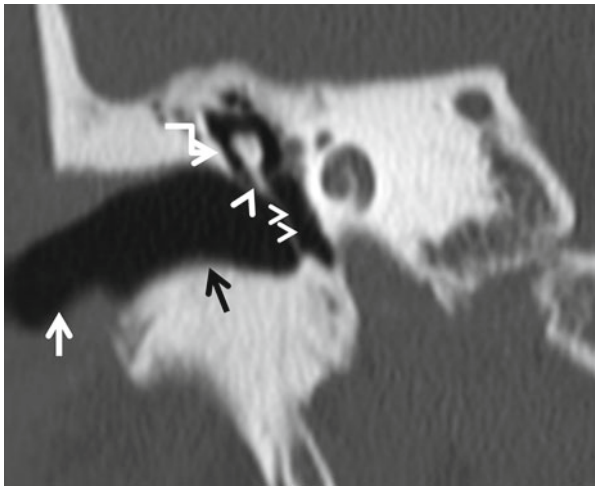

Fig. 8.1 The external auditory canal and tympanic membrane. The *white arrow* points to the cartilaginous EAC, the *black arrow* to the bony EAC. The tympanic membrane is oriented at an angle to the EAC. The *large arrow* indicates the pars flaccida, while the smaller *arrowheads* point to the pars tensa. The *hooked arrow* points to the scutum

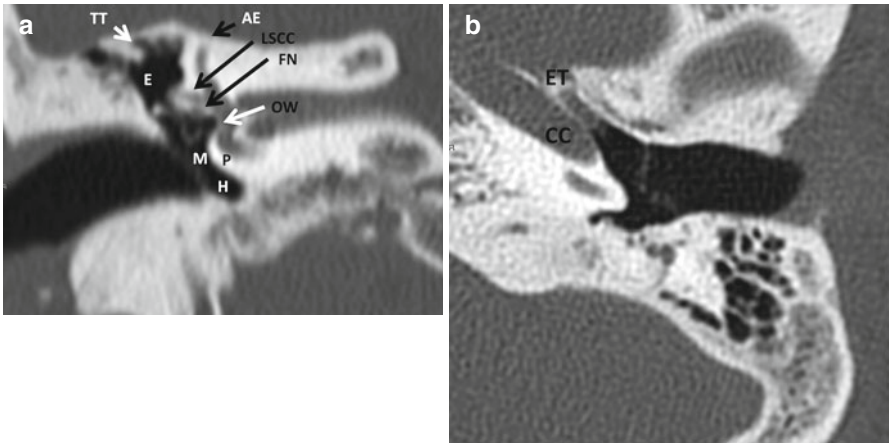

Fig. 8.2 The middle ear cavity. (**a**) Structures of the roof and medial wall, (**b**) anterior wall. *Abbreviations*: *TT* tegmen tympani, *AE* arcuate eminence, *LSCC* lateral semicircular canal, *FN* facial nerve (tympanic segment), *OW* oval window, *P* promontory, *E* epitympanum, *M* mesotympanum, *H* hypotympanum, *CC* carotid canal (horizontal segment), *ET* eustachian tube

its bony canal is dehiscent. The round window niche is located posteroinferior to the promontory at a right angle to the face of the oval window (Fig. 8.2).

The anterior wall in its upper portion contains two openings: one for the eustachian tube and the other for the entry of the tensor tympani. In its lower part, the anterior wall is related to the carotid canal (Fig. 8.2).

The posterior wall superiorly contains the aditus ad antrum, a passageway which leads to the mastoid antrum. Inferiorly are two recesses in which cholesteatoma may reside, the tympanic sinus medially and the facial recess laterally. These are

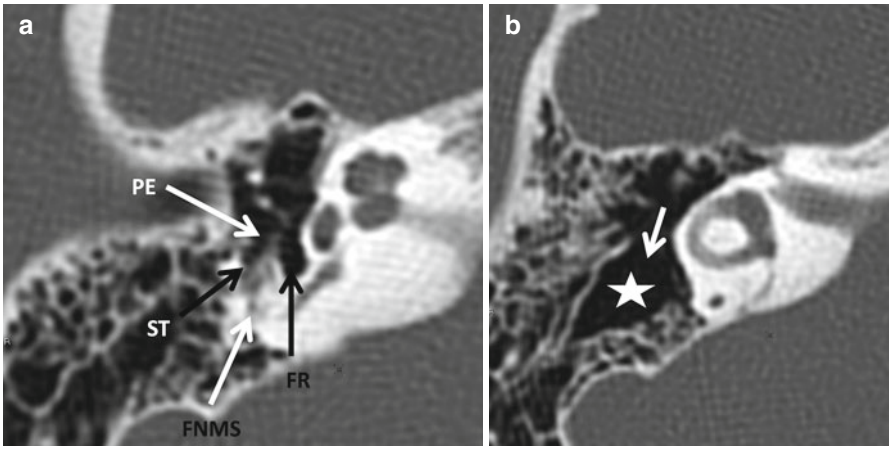

Fig. 8.3 The posterior wall of the middle ear cavity. (**a**) Inferior section through the mesotympanum at the level of the pyramidal eminence (*PE*). (**b**) Superior section through the epitympanum showing the aditus (*arrow*) and antrum (*asterisk*). *ST* sinus tympani, *FR* facial recess, *FNMS* facial nerve mastoid segment

separated by the pyramidal eminence, which contains the stapedius muscle (Fig. 8.3).

The mastoid process can be variably pneumatized. The largest air cell is referred to as the mastoid antrum. The roof of the mastoid air cells is the tegmen mastoideum. The sigmoid sinus plate separates the mastoid air cells from the sigmoid sinus. Evaluation of the integrity of the sigmoid sinus plate is of vital importance in patients with otomastoiditis. The floor of the middle ear cavity is variably related to the jugular bulb and carotid canal (Fig. 8.4).

Prussak's space is located in the epitympanum and is bounded laterally by the pars flaccida and a bony spur called the scutum. The medial wall is formed by the neck and head of the malleus. Its inferior wall is the lateral process of the malleus. The anterior and superior walls of Prussak's space are formed by the lateral mallear ligament. Acquired cholesteatoma is most often found in this space (Fig. 8.5).

The middle ear cavity contains three ossicles (Fig. 8.6). The malleus is comprised of a handle (manubrium), neck, head, and a lateral process. The incus consists of a body, a posteriorly directed short process, and a long process that descends into the mesotympanum to end in the bulbous lenticular process. The lenticular process articulates with the stapes. The malleoincudal joint appears as an "ice-cream cone" on axial CT images. The head of the malleus forms the ice cream, and the body and short process of the incus form the cone. The handle of the malleus and the long process of the incus are visible as 2 almost-parallel linear structures on axial images. An oblique reconstructed image, parallel to the long axis of the incus, provides an excellent depiction of the incudostapedial joint. The stapes consists of a head, neck, 2 crura, and a footplate. The footplate articulates through a syndesmosis with the oval window.

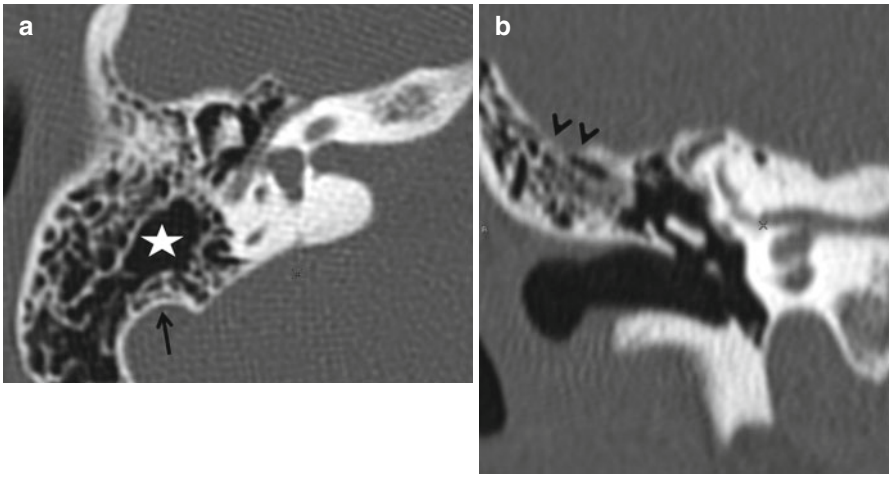

Fig. 8.4 The mastoid antrum is the largest of the mastoid air cells (*asterisk*). The sigmoid sinus plate is best seen on the axial view (*arrow*, **a**). The roof of the mastoid air cells is the tegmen mastoideum (*arrowheads* in **b**). The floor of the middle ear cavity is related to the jugular bulb. The bony plate separating the bulb from the middle ear cavity may be thin or absent

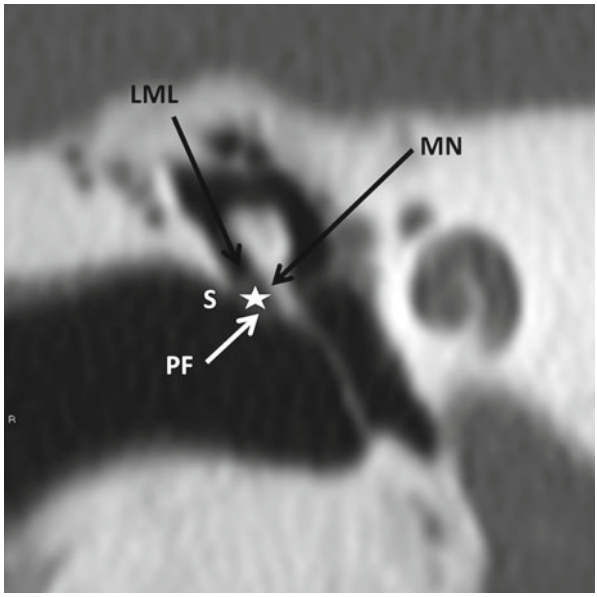

Fig. 8.5 Prussak's space (*asterisk*). *S* scutum, *PF* pars flaccida, *MN* malleus neck, *LML* lateral ligament of the malleus

8.1.3 Inner Ear

The internal auditory canal (Fig. 8.7) transmits the facial, superior vestibular, inferior vestibular, and cochlear nerves. The fundus of the IAC is divided into four quadrants, horizontally by the falciform crest and vertically in its upper half by Bill's bar. The facial nerve occupies the anterosuperior quadrant, the cochlear nerve

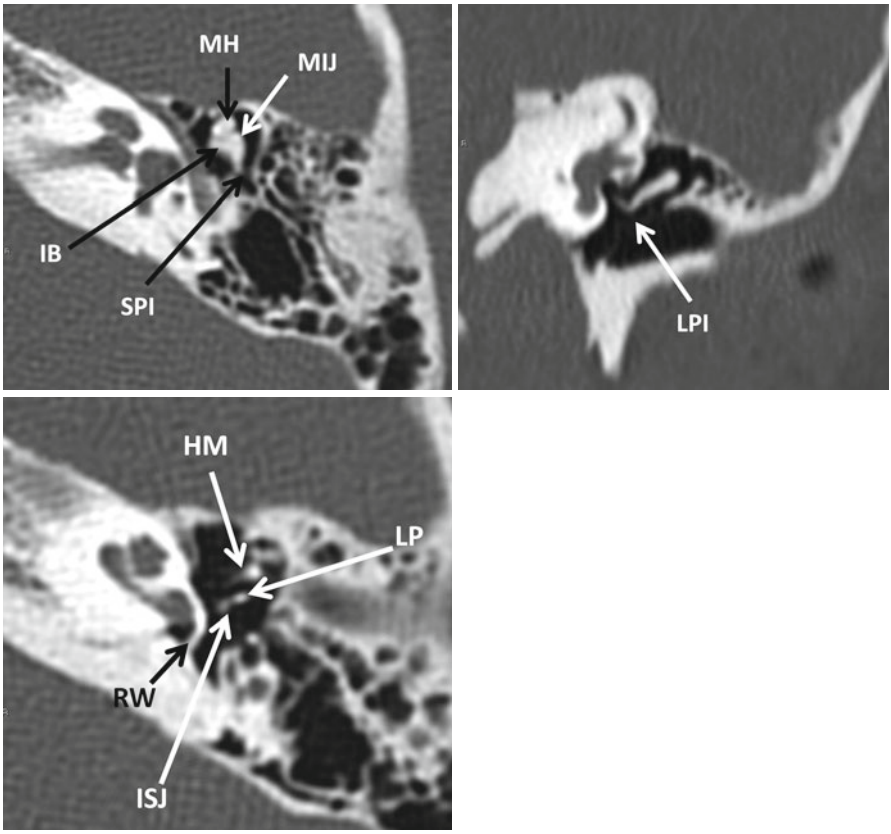

Fig. 8.6 The ossicles. *MH* malleus head, *IB* incus body, *SPI* short process of incus, *MIJ* malleo-incudal joint. *LPI* long process of incus, *LP* lenticular process, *ISJ* incudostapedial joint, *HM* handle of malleus. The round window is also seen adjacent to the basal cochlear turn

the anteroinferior quadrant, the superior vestibular nerve the posterosuperior quadrant, and the inferior vestibular nerve the posterior inferior quadrant. The singular canal leaves the posterior wall of the IAC and carries the branch of the inferior vestibular nerve to the posterior semicircular canal.

The dense bone of the osseous labyrinth encloses the delicate membranous labyrinth. The bony cochlea consists of two- and three-quarter turns and is wound around the modiolus. The interscalar septum supports the cochlear turns. At the base of the cochlea is an aperture that transmits the cochlear nerve (Fig. 8.8).

The vestibule contains the utricle and saccule. The three semicircular canals arise from it. The superior semicircular canal of one side is oriented parallel to the posterior semicircular canal of the other side. The vestibular aqueduct leaves the vestibule in a posterolateral direction. The normal vestibular aqueduct is always smaller than the adjacent posterior semicircular canal. It opens via a flared operculum into the endolymphatic sac. On high-resolution MR images, the endolymphatic sac is evident as a fluid-filled elongated structure along the posterior wall of the petrous temporal bone (Fig. 8.8).

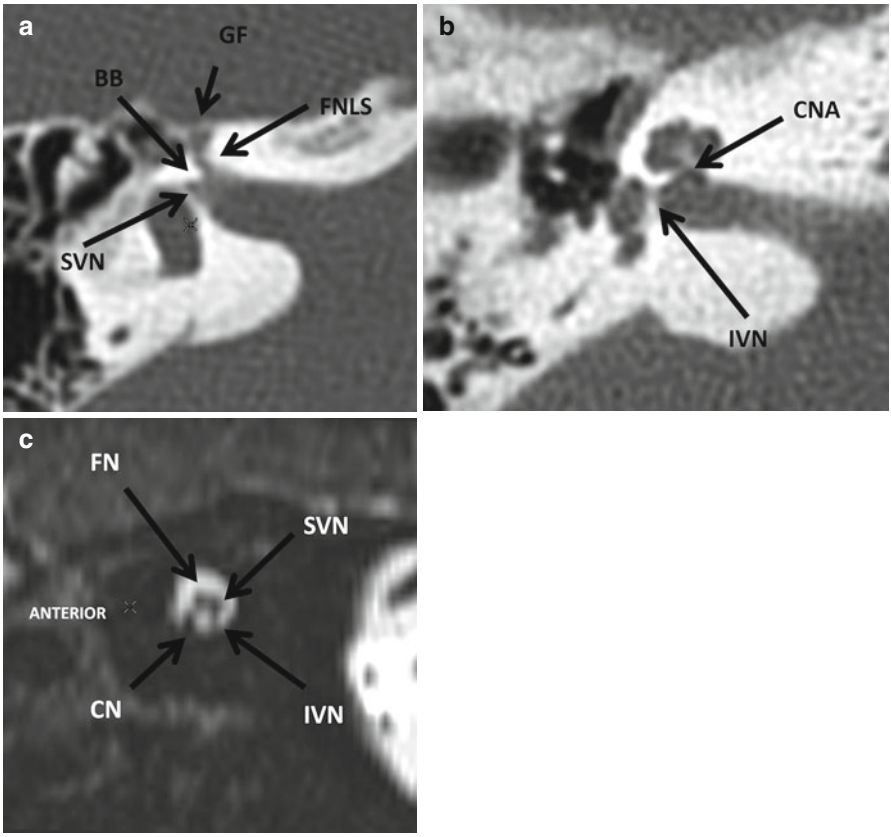

Fig. 8.7 The internal auditory canal (IAC). (**a**) axial section through the superior part of the IAC, (**b**) axial section through the superior part of the IAC, and (**c**) sagittal reformatted high-resolution 3D T2W image through the porus acusticus. *FNLS* facial nerve canal, labyrinthine segment, *GF* geniculate fossa, *BB* Bill's bar, *SVN* superior vestibular nerve canal, *CNA* cochlear nerve aperture, *IVN* inferior vestibular nerve canal; *FN* facial nerve, *CN* cochlear nerve, *SVN* superior vestibular nerve, *IVN* inferior vestibular nerve

8.1.4 Facial Nerve

The course of the facial nerve is divided into five segments: cisternal, canalicular, labyrinthine, tympanic, and mastoid. In the internal auditory canal, it occupies the anterosuperior quadrant. The labyrinthine, tympanic, and mastoid segments are enclosed in the bony Fallopian canal. The labyrinthine segment is anterolaterally directed and is relatively short. It ends in the first genu where the geniculate ganglion is located. From the anterior aspect of the geniculate ganglion, the greater superficial petrosal nerve arises. A small bony defect is usually evident at its origin. The tympanic segment is directed posteriorly from the geniculate ganglion. The segment lies under the lateral semicircular canal. If the bony canal is dehiscent, the nerve may prolapse inferiorly and lie over the oval window and stapes. This finding must always be recognized to prevent inadvertent nerve damage during surgery on the

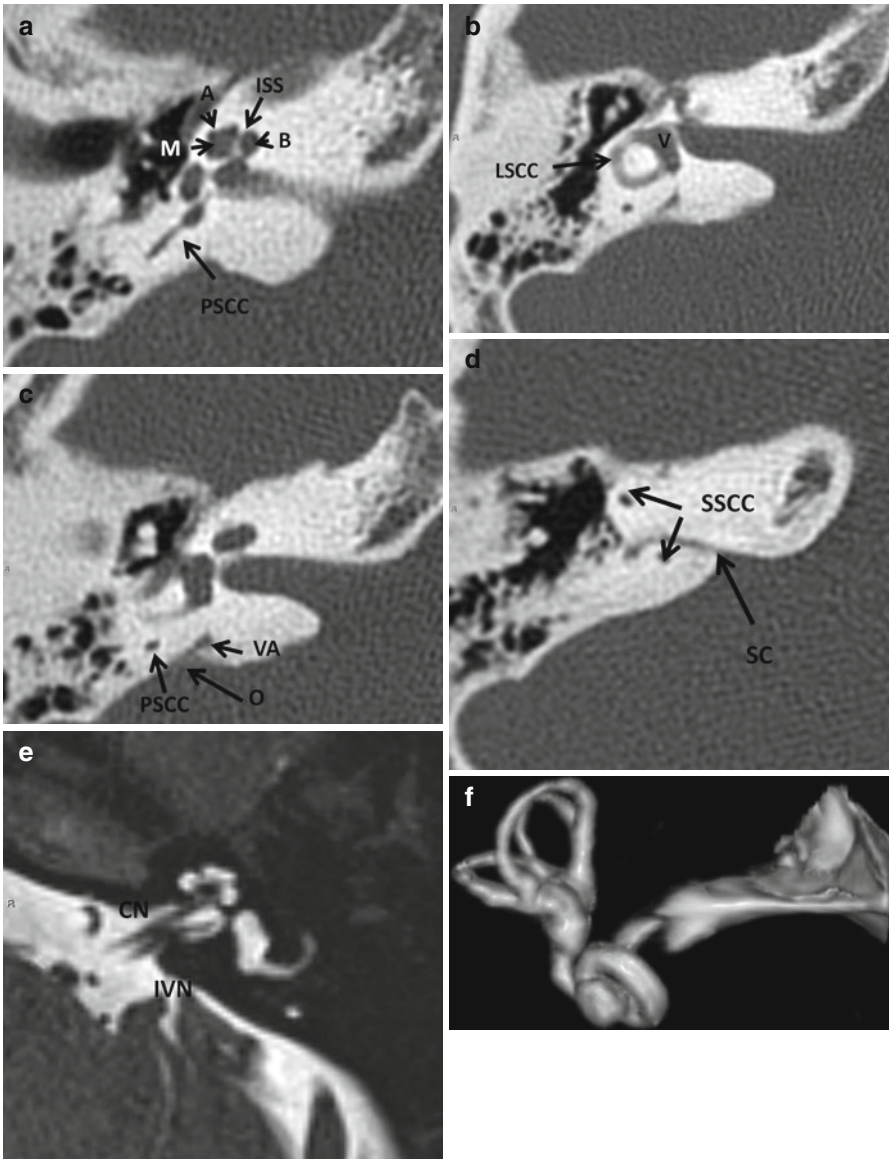

Fig. 8.8 Structures of the inner ear. In (**a**), the apical (*A*), mid (*M*), and basal (*B*) turns of the cochlea are visible. The interscalar septum (*ISS*) emanating from the modiolus is also seen. In (**b**), the vestibule (*V*) and lateral semicircular canal are demonstrated. In (**c**), the vestibular aqueduct (*VA*) with its flared operculum (*O*) is seen. The normal VA is never larger than the adjacent posterior semicircular canal (*PSCC*). In (**d**), the subarcuate canal (*SC* containing the subarcuate artery) is seen passing between the limbs of the superior semicircular canal. In (**e**), an axial high-resolution heavily T2-weighted MR image, the hypointense modiolus is seen against the background of bright endolymph within the cochlea. The interscalar septum, the cochlear nerve (*CN*), and inferior vestibular nerve (*IVN*) are also demonstrated. Volumetric images of the labyrinth (**f**) can be generated from both high-resolution CT and MR images

stapes. The tympanic segment ends in the second genu from which the mastoid segment continues. The segment is directed inferiorly. The nerve to the stapedius and chorda tympani arise from this segment. The facial nerve leaves the temporal bone through the stylomastoid foramen. It then passes anteriorly into the substance of the parotid gland where it is located lateral to the retromandibular vein. It then ramifies into five branches. The normal facial nerve in its cisternal and canalicular segments does not enhance on MRI. The remainder of the facial nerve may demonstrate enhancement. This is due to the presence of a perineural venous plexus (Fig. 8.9).

8.1.5 Jugular Foramen

The jugular foramen is a cleft between the petrous pyramid and the basiocciput. It is divided into an anteromedial pars nervosa and a posterolateral pars vascularis. The pars nervosa contains the inferior petrosal sinus and the glossopharyngeal nerve. The pars vascularis contains the jugular bulb and cranial nerves 10 and 11 (Fig. 8.10).

8.2 Imaging Evaluation

Conductive hearing loss is best imaged by high-resolution CT with images reconstructed in a bone algorithm. Sensorineural hearing loss and vertigo are best evaluated with MRI. The MRI study should consist of pre- and postcontrast T1-weighted images (maximum slice thickness of 3 mm) obtained in axial and coronal planes, supplemented with a volumetric heavily T2-weighted sequence. The precontrast images help exclude rare cases of labyrinthine hemorrhage (which appears hyperintense on T1-weighted images) and serve as a baseline to compare the postcontrast images with. The T2-weighted sequence enables detection of small tumors in the IAC and labyrinth and depiction of vascular loops in the cerebellopontine angle cistern and IAC and is extremely useful in cases of facial or vestibulocochlear nerve hypoplasia.

Tumors of the temporal bone and skull base usually require a combination of CT and MR images. The role of catheter angiography is limited to the evaluation of pulsatile tinnitus when cross-sectional imaging has failed to reveal a cause and in the preoperative evaluation and embolization of vascular skull base tumors.

8.3 Common Congenital Anomalies of the Temporal Bone

8.3.1 External Auditory Canal (EAC) Atresia and Stenosis

Atresia or stenosis of the EAC is frequently associated with abnormalities of the malleus and incus, given that these are derivatives of the first branchial arch. Inner ear anomalies are uncommon with EAC atresia, but a large vestibular

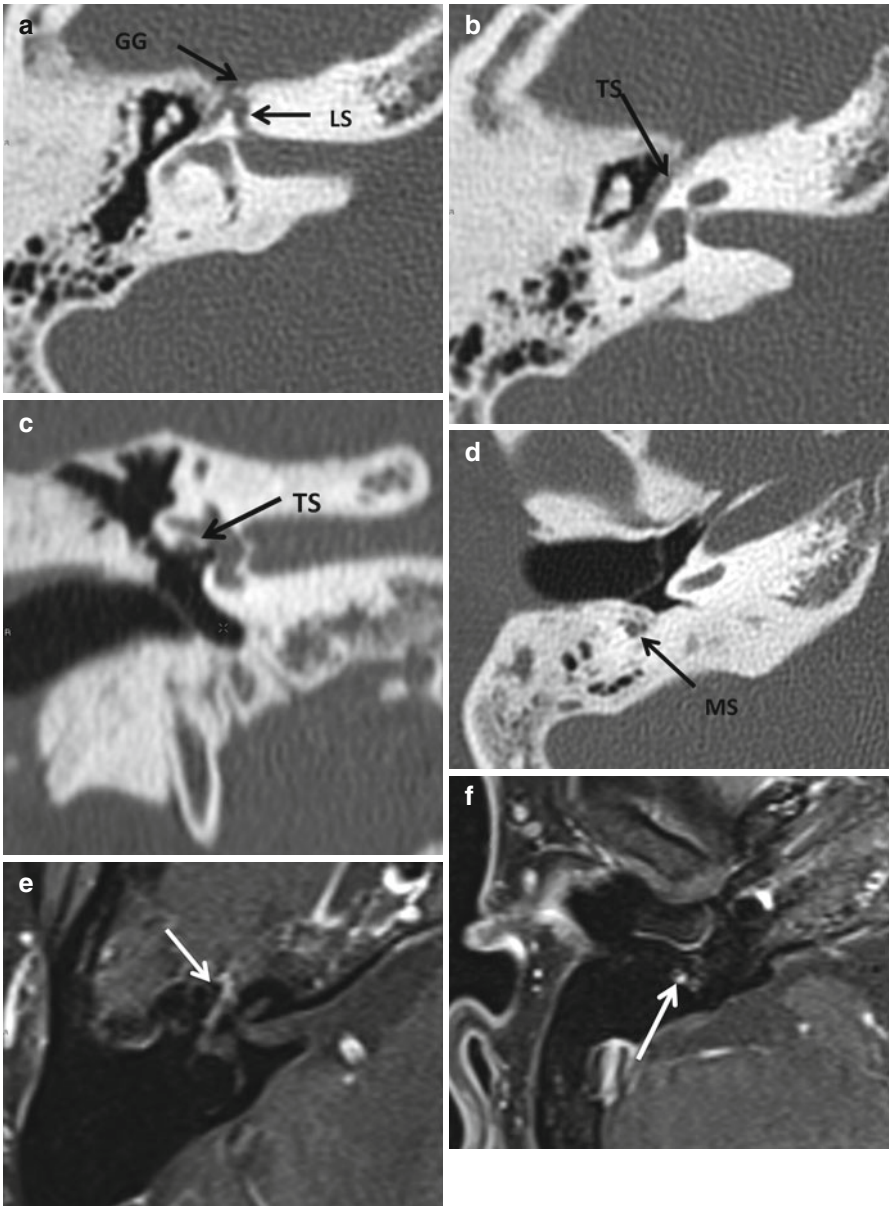

Fig. 8.9 Anatomy of the facial nerve. *LS* labyrinthine segment, *GG* geniculate ganglion, *TS* tympanic segment (note that the TS lies immediately under the LSCC (**c**) above the oval window niche. Dehiscence of this segment of the canal may cause the nerve to prolapse inferiorly and directly overlie the oval window – a finding of great surgical importance); *MS* mastoid segment. In (**e**, **f**), note that the geniculate ganglion, tympanic, and mastoid segments enhance – a normal finding, thought to occur due to the presence of a circumneural venous plexus. Enhancement of the labyrinthine, canalicular, and cisternal segments of the nerve is always abnormal

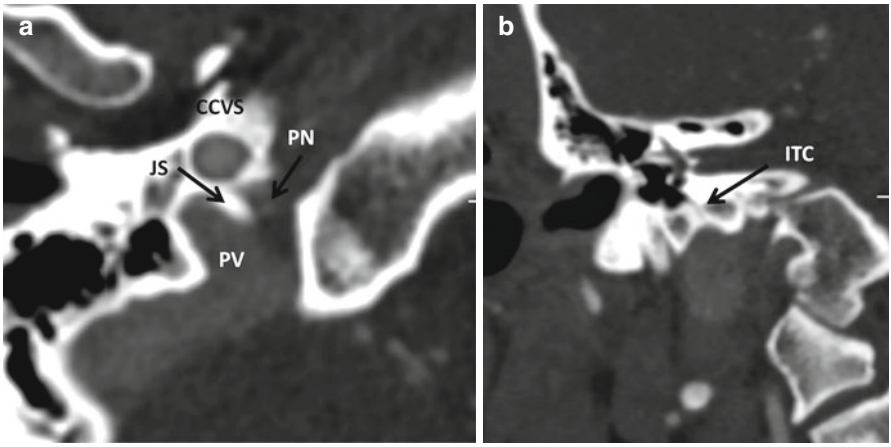

Fig. 8.10 Jugular foramen. (**a**) The jugular spine (*JS*) divides the jugular foramen into a smaller anteromedial pars nervosa (*PN*) which contains glossopharyngeal nerve and the inferior petrosal sinus and the larger posterolateral pars vascularis (*PV*) which contains the vagus nerve and its auricular branch (Arnold's nerve), the spinal accessory nerve, the posterior meningeal branch of the ascending pharyngeal artery, and the jugular bulb. *CCVS* carotid canal, vertical segment. In (**b**), the inferior tympanic canaliculus (*ITC*) which contains Jacobsen's nerve, a branch of the glossopharyngeal nerve and a small artery, is seen ascending from the bulb to the promontory, where it contributes to the tympanic plexus. Jugular paragangliomas may invade the middle ear using the ITC

aqueduct, a dysplastic lateral semicircular canal, and varying degrees of cochlear hypoplasia may occasionally be encountered. Syndromes that may be associated with EAC atresia include the Goldenhar and Treacher Collins syndromes, Pierre Robin sequence, Klippel–Feil anomaly, and hemifacial microsomia among others.

The stenotic/atretic external ear is best evaluated on high-resolution CT. Awareness of the 10-point Jahrsdoerfer and Yeakley scale for the preoperative evaluation of aural atresia is essential for optimal interpretation of these scans (Box 8.1). Prior to consideration for surgery, the patient must demonstrate evidence of normal cochlear function on audiometric testing and a normal appearance of the inner ear on imaging. The most important determinants for a successful surgical outcome are the presence of a stapes and adequate middle ear pneumatization. As indicated in Box 8.1, the presence of a stapes is assigned 2 points. An open oval window is defined as one that is greater than 2 mm in vertical dimension on the coronal view. If it is less than 1 mm, it is considered stenotic and no point is assigned. An atretic oval window is completely separated by a complete bony plate from the middle ear. A facial nerve that demonstrates an unfavorable course, for instance, when a dehiscent tympanic segment lies over the oval window, directly in the line of surgical approach, receives no points (Fig. 8.11). The course of the facial nerve in most cases of aural atresia is predictable. The tympanic segment is foreshortened, the second genu is more anteriorly located, and the mastoid segment is often directed towards the temporomandibular joint. The presence of a relatively normal malleus–incus complex is

Box 8.1. The Jahrsdoerfer Aural Atresia Scale

External ear	1
Middle ear space	1
Mastoid pneumatization	1
Malleus–incus complex	1
Incudostapedial connection	1
Stapes	2
Facial nerve	1
Oval window open	1
Round window open	1
Total score	10
A score of 7 or more indicates good prognosis for postoperative hearing improvement	

assigned 1 point. Often the malleus and incus are fused with each other and are adherent to the atresia plate (Fig. 8.11). If there is no connection between them and the remainder of the ossicular chain, no point is assigned. The incudostapedial joint is best depicted on the coronal oblique reformations where a characteristic hockey-stick appearance is noted. A sclerotic mastoid system results in no points being assigned. The round window is in most cases normal. However, when it is less than 1 mm in width, no point is assigned. The appearance of the external ear is best judged clinically.

8.3.2 Middle Ear Anomalies

Congenital cholesteatomas are a cause of conductive hearing loss in the pediatric population. They occur usually in the anterior superior epitympanum and may be seen as whitish soft tissue behind the tympanic membrane on otoscopy. They can also occur in the external ear, mastoid air cell system, facial canal, or petrous apex. There is nothing specific about their imaging appearance, but it is important to note that they can progressively enlarge and erode adjacent osseous structures much like acquired cholesteatomas do. A well-defined middle ear mass with displacement of the ossicular chain in a child is usually a cholesteatoma (Fig. 8.12). *Meningoencephaloceles* may also be seen in the middle ear associated with defects of the tegmen tympani. When a nondependent soft tissue process adjacent to a bone defect and contiguous with the cranial cavity is seen on CT, a meningoencephalocele must always be suspected and evaluated with MRI.

Isolated anomalies of the ossicular chain are uncommon but maybe occasionally encountered. Ossicles may be malformed, absent in their entirety or partially, or malpositioned (Fig. 8.13).

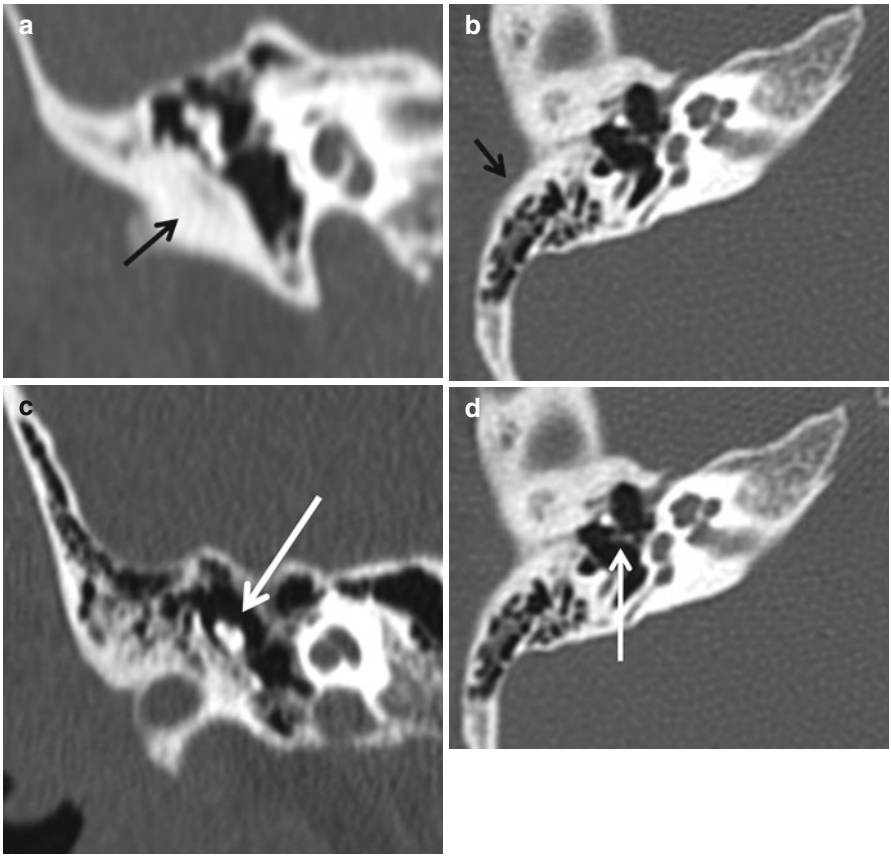

Fig. 8.11 Congenital aural atresia. In (**a**), a bony atresia plate is evident (*arrow*), whereas in (**b**), the atresia plate is pneumatized. In (**c**), a malformed malleus–incus complex fused to the atresia plate is evident – a fairly common finding in aural atresia. In (**d**), a normal stapes indicating good surgical prognosis is noted. In (**e**), note that the middle ear cleft is well aerated, a favorable surgical finding while in (**f**) the middle ear cleft is not pneumatized at all. This finding essentially precludes reconstructive surgery. In (**g**) and (**h**), the typical variant course of the facial nerve canal is demonstrated – a more obtuse than normal angle at the geniculate ganglion, a foreshortened tympanic segment (note that the facial nerve is not visible underneath the LSCC) and a mastoid segment displaced anteriorly to lie in proximity to the glenoid fossa. In (**i**), in a patient with mild atresia, the facial nerve canal is dehiscent and the nerve lies directly on the promontory. Also note that the stapes is absent. Dehiscence of the facial nerve canal is important to recognize preoperatively to prevent inadvertent nerve injury at surgery

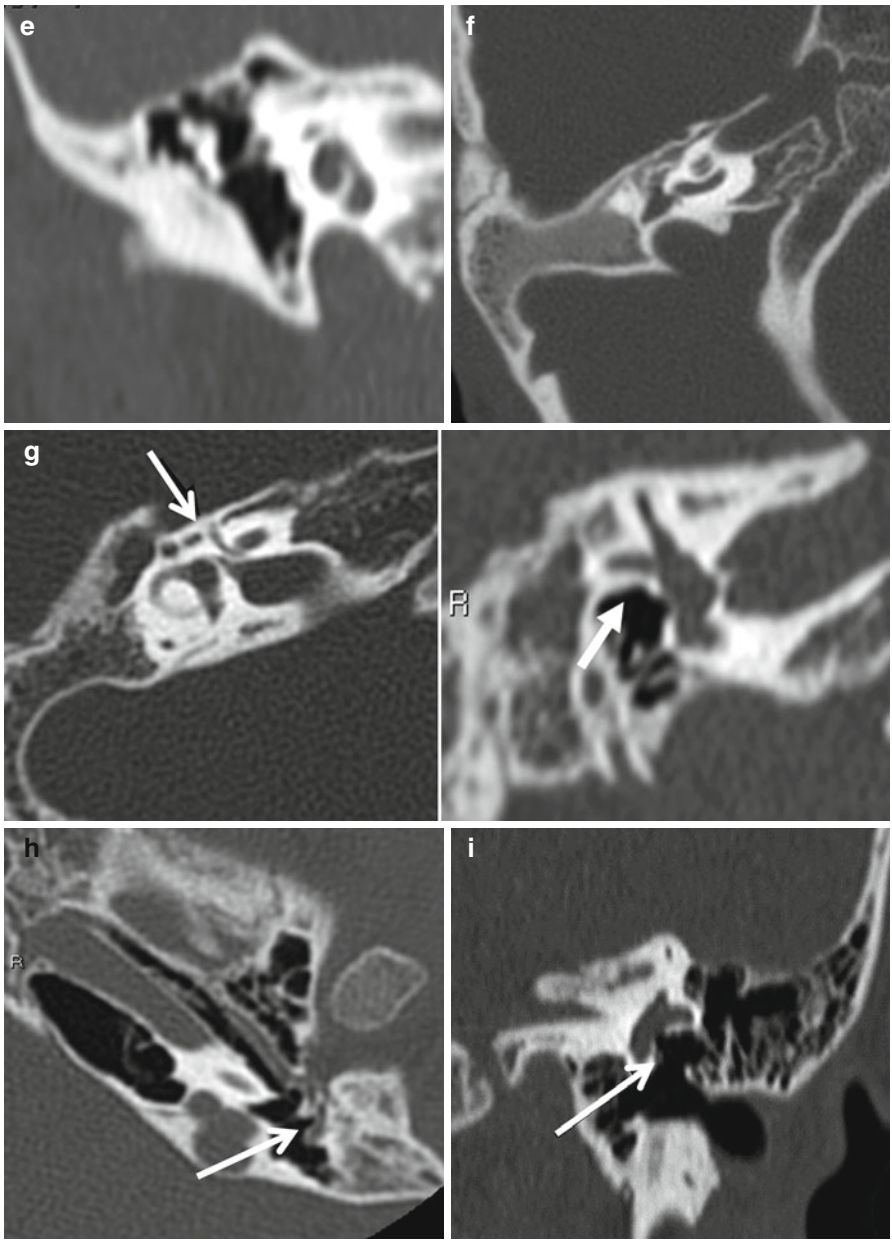

Fig. 8.11 (continued)

Fig. 8.12 Congenital cholesteatomas present as nonspecific middle ear masses that displace the ossicular chain (**a**). Stenotic EAC may also harbor a congenital cholesteatoma (*asterisk*, **b**). In (**c**), a soft tissue lesion is present in the anterior epitympanic recess, separated from the middle ear cavity by a thin bony septum, the cog. The diffusion-weighted MR image confirms this to be cholesteatoma

8.3.3 Inner Ear Anomalies

Patients with congenital sensorineural hearing loss (SNHL) often demonstrate no imaging abnormalities. MRI is probably the better modality to image congenital SNHL. A volumetric heavily T2-weighted sequence enables excellent depiction of

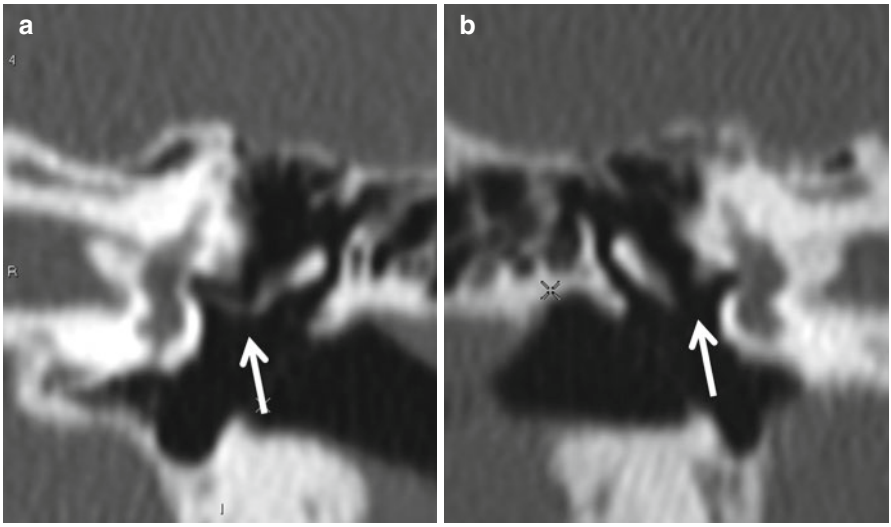

Fig. 8.13 Congenital absence of the long process of the incus. In (**a**), the appearance of the normal incus long process and the incudostapedial articulation (*arrow*) is seen. In (**b**), the long process and stapes are absent

inner ear anatomy. On both CT and MRI, it is useful to have a checklist of what normal inner ear should look like (Box 8.2). The normal cochlea should contain three turns (apical, mid, basal), a central bony modiolus, a spiral interscalar septum and a cochlear aperture. The vestibule and the three semicircular canals must always be accounted for as one or more semicircular canals may be absent. The normal vestibular aqueduct does not exceed the width of the adjacent posterior semicircular canal in caliber.

Box 8.2. Checklist of Inner Ear Anatomy

Presence of three (2 ¾) distinct cochlear turns
Presence of a modiolus
Presence of an interscalar septum
Patent cochlear aperture
Size of the internal auditory canal
Presence of all three semicircular canals
Size of the vestibule
Caliber of the vestibular aqueduct – the diameter should not exceed that of the adjacent posterior semicircular canal

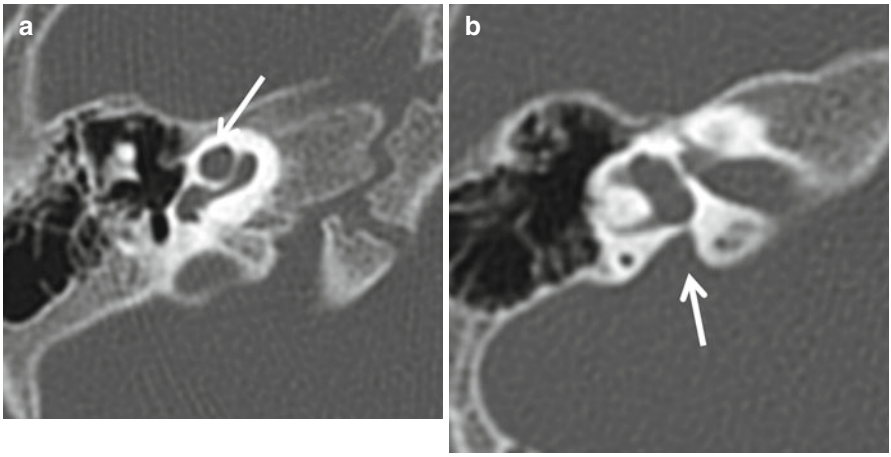

Fig. 8.14 Incomplete partition 2 (Mondini) anomaly. Note the lack of separation between the apical and mid-cochlear turns (*arrow*, **a**). In (**b**), enlargement of the vestibular aqueduct, a finding that frequently coexists with cochlear dysplasia, is seen (*arrow*)

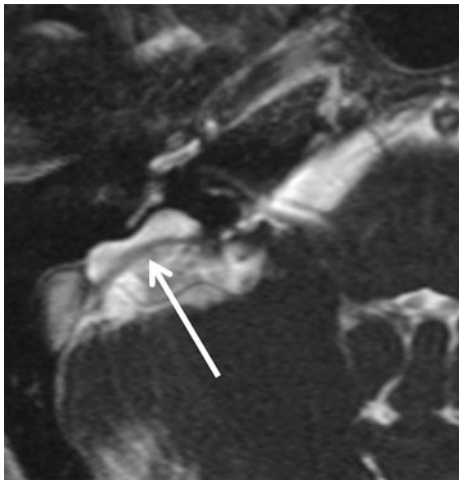

Fig. 8.15 Large endolymphatic sac anomaly. On this axial T2-weighted high-resolution MR image, the vestibular aqueduct and endolymphatic sac are dilated. The dilated (*arrow*) vestibular aqueduct is seen on both CT and MR, whereas the enlarged endolymphatic sac is typically seen only on MRI. This is the most common imaging finding encountered in a patient with congenital sensorineural hearing loss and is frequently associated with dysplasia of the cochlea

The cochlea may be completely absent, sometimes as a part of complete labyrinthine aplasia (Michel anomaly). It may be fused with the vestibule to form a common cavity. When the apical and mid-cochlear turns are fused, the term incomplete partition type II is used. The less common incomplete partition type I anomaly is characterized by a cystic appearance of the cochlea and vestibule and a normal sized vestibular aqueduct. The incomplete partition type III anomaly is the same as the X-linked stapes gusher (see below). Incomplete partition type II is always associated with an enlarged vestibular aqueduct. This may be associated with a large vestibular aqueduct and/or large vestibule (Mondini anomaly) (Fig. 8.14).

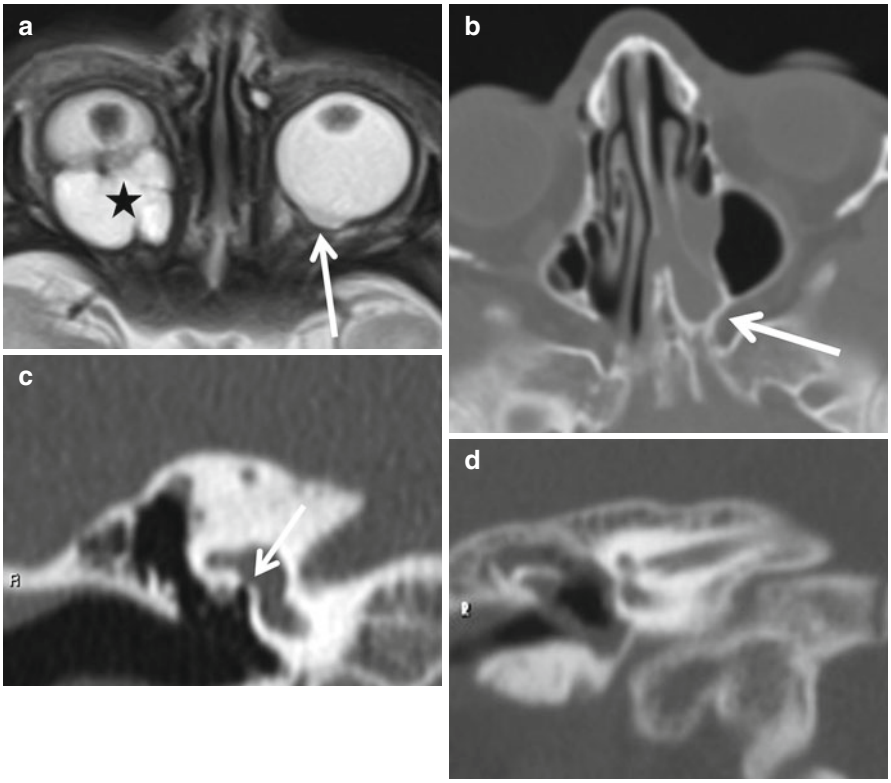

Fig 8.16 The CHARGE association. In (**a**), a colobomatous cyst (*asterisk*) and microphthalmia are seen on the right, while on the left, a small optic nerve head coloboma is seen. Bony atresia of the left nasal choana is seen in (**b**). In (**c**), the oval window is severely stenotic (*arrow*). Note the facial nerve lying directly in front of the oval window. Note the complete absence of the semicircular canals in (**d**)

The *large vestibular aqueduct anomaly* is the most common imaging finding in patients with congenital sensorineural hearing loss. CT demonstrates the enlarged vestibular aqueduct, and MR, the associated enlarged endolymphatic sac (Fig. 8.15). The onset of sensorineural hearing loss in patients with this anomaly may occur in adulthood, sometimes precipitated by trauma. The normal aqueduct is less than 2.5 mm in diameter in its midportion and does not exceed the width of the adjacent posterior semicircular canal. When an enlarged vestibular aqueduct is found, attention must be turned to the cochlea as the incomplete partition anomaly frequently coexists with his entity. The large vestibular aqueduct is a frequent finding with Pendred syndrome (congenital hypothyroidism with deafness).

Absence of one or more semicircular canals may occur as an isolated anomaly. The lateral SCC is most often affected. The CHARGE association is frequently associated with semicircular canal absence (Fig. 8.16). The key head and neck imaging findings of this syndrome are summarized in Box 8.3.

Box 8.3. CHARGE Association: Head and Neck Findings

Temporal bone
Inner ear
Absence of one or more semicircular canals
Dysplastic vestibule
Dysplasia/absence of one or more cochlear turns
Small/absent cochlear aperture
Enlarged vestibular aqueduct
Middle ear
Underpneumatized middle ear cleft
Dysplastic ossicles
Oval window atresia
Round window atresia
Variable course of facial nerve – can lie directly over atretic oval window
Nasal cavity
Choanal atresia
Orbit
Coloboma with/without microphthalmia
Skull base
Basiocciput hypoplasia and basilar invagination
Jugular bulb diverticula
Petrosquamosal sinus
When large, the jugular bulb is hypoplastic
May be injured if unrecognized at cochlear implantation

When the fundus of the internal auditory canal appears bulbous, the diagnosis of X-linked stapes gusher must be considered (Fig. 8.17). This entity, which is bilateral, is associated with congenital mixed hearing loss. The conductive component arises from the associated fixation of the stapes footplate. The base of the cochlea is not separable from the fundus of the IAC. The labyrinthine segment of the facial canal is also widened. If the stapes is manipulated surgically, the increased pressure in the inner ear results in gushing of perilymph at the oval window. Patients with this entity and predominantly conductive hearing loss are therefore best treated with an external hearing aid.

Absence or hypoplasia of the facial or vestibulocochlear nerves is best diagnosed with high-resolution T2-weighted MRI. On a sagittal reconstruction, the facial nerve occupies the anterosuperior quadrant of the IAC, the cochlear nerve, the anteroinferior, the superior and inferior vestibular nerves, and the posterosuperior and posteroinferior quadrants, respectively (Fig. 8.18). Absence or hypoplasia may occur as an isolated abnormality or as a part of entities such as the Möbius syndrome, where absence of the sixth nerve coexists. Evaluation for cochlear nerve deficiency (hypoplasia or absence) is important in the work up for cochlear implantation. Cochlear nerve deficiency can be observed both in association with congenital or acquired (sensorineural hearing loss) SNHL. When present, a hypoplastic internal auditory canal is suggestive for congenital cochlear nerve deficiency.

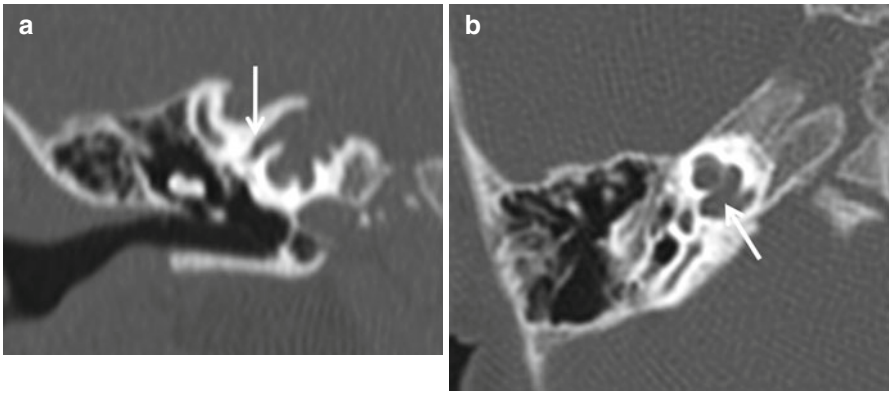

Fig. 8.17 X-linked stapes gusher. In this anomaly, the absence of a bony partition at the fundus of the IAC results in transmission of CSF pressure to the inner ear structures resulting in "gushing" of endolymph at stapedectomy. The increased pressure results in the characteristic widening of the facial nerve canal (*arrow*, **a**) and cochlear aperture (*arrow*, **b**)

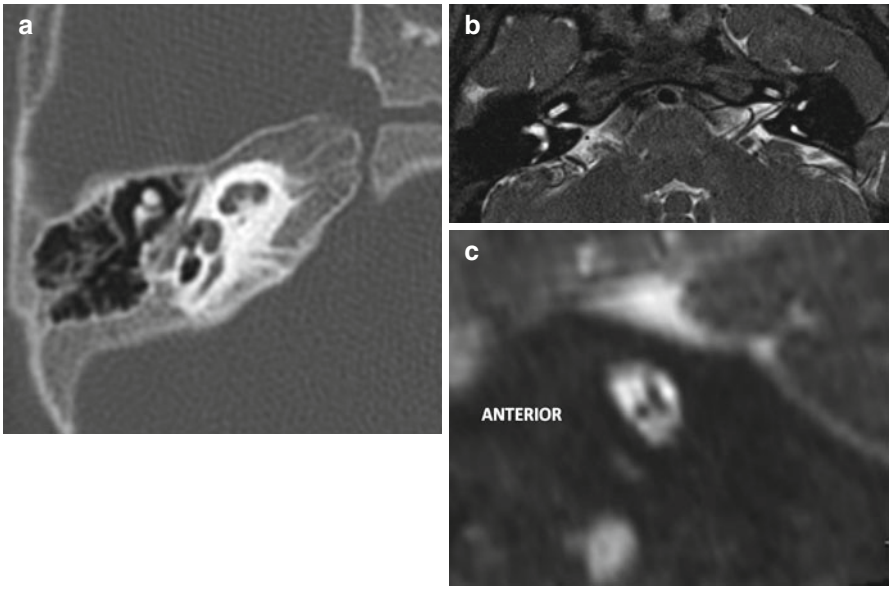

Fig. 8.18 (**a**, **b**) Absence of the cochlear nerve. Note the lack of a cochlear aperture in (a) and the diminutive IAC in (b). The left IAC is normal. (**c**) Absence of the facial nerve. The anterosuperior quadrant of the IAC where the facial nerve would normally be present is empty

8.4 Inflammatory Disorders

8.4.1 External Ear Inflammation

Inflammation of the external ear may manifest as an acute process (acute otitis externa, malignant external otitis) or be chronic in nature (keratosis obturans, cholesteatoma, medial canal fibrosis). Simple acute external otitis is not usually imaged.

Malignant otitis externa (MOE) (Fig. 8.19) is usually caused by Pseudomonas bacteria and is typically encountered in the elderly and diabetic population. It is a type of rapidly spreading skull base osteomyelitis that begins in the EAC. Infection spreads from the floor of the cartilaginous EAC to the skull base through the fissures of Santorini. As the process extends to involve the skull base foramina, cranial neuropathies begin to manifest. Imaging is best achieved with a combination of CT and MRI. Subtle osteolysis at the bony–cartilaginous junction of the EAC may be the only finding on CT. On MRI, the infiltrative nature of the process is revealed by replacement of the fat that is normally encountered in the skull base, such as in the clivus, petrous apex, pterygopalatine fossa, and parapharyngeal spaces. Replacement of fat is best depicted on precontrast T1-weighted images. Postcontrast fat-suppressed T1-weighted images demonstrate abnormal enhancement in the areas involved. Abscesses are revealed as areas of low signal intensity with thick surrounding enhancement. These findings are, however, nonspecific and may be seen with aggressive neoplasms such as invasive nasopharyngeal carcinoma, lymphoma, and metastases. The presence of discrete abscesses, however, points to osteomyelitis.

Cholesteatomas of the external auditory canal manifest clinically as otalgia associated with pearly white soft tissue, usually in the posteroinferior aspect of the EAC, adjacent to the tympanic membrane. Although cholesteatomas usually produce irregular bone destruction, smooth bony remodeling may also be seen (Fig. 8.20). In *keratosis obturans*, a bilateral condition that presents with fairly acute otalgia, the EACs are expanded smoothly by keratin debris.

Medial canal fibrosis is a chronic condition where an indolent tympanic membrane inflammation progressively leads to fibrous obliteration of the medial EAC lumen, resulting in a "false fundus" appearance clinically and on CT (Fig. 8.21).

8.4.2 Middle Ear and Mastoid Inflammation

8.4.2.1 Acute Otitis Media (AOM)

Uncomplicated acute otomastoiditis usually follows a viral upper respiratory tract infection and does not require imaging. On CT, it appears as nonspecific fluid in the middle ear cavity and mastoid air cells. The earliest evidence of inflammation spreading beyond the mucoperiosteum is the loss of the normal mastoid septa, when the entity is referred to as coalescent mastoiditis. Loss of mastoid septa may be

difficult to detect on CT when subtle, and comparison with the unaffected side is helpful (Fig. 8.22). AOM may be complicated by meningitis, intracranial empyema, brain abscess, and cerebral venous thrombosis (Fig. 8.22). These complications

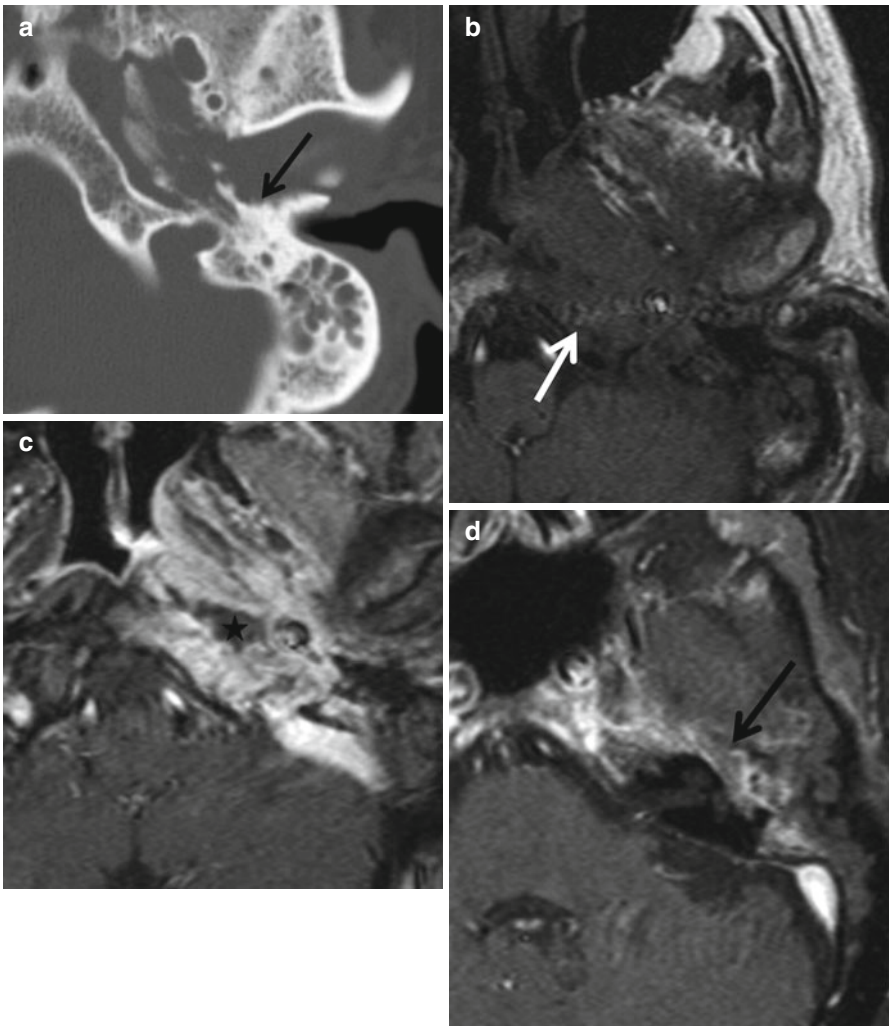

Fig. 8.19 Malignant external otitis. Elderly diabetic patient with otalgia and cranial nerve palsies. (**a**) Destruction of the walls of the bony EAC, glenoid fossa, and petrous ridge (*arrow*). Subtle bone destruction in the anterior wall of the EAC at the bony–cartilaginous junction may be seen in early stages of MOE. This may spread to involve the remainder of the temporal bone and clivus as seen on the unenhanced T1-weighted image (*arrow*, **b**) where replacement of the clival marrow, and an ill-defined inflammatory soft tissue process involving the skull base, extending to the lateral nasopharyngeal wall are evident. On the enhanced fat-suppressed image (**c**), a small abscess deep to the fossa of Rosenmuller (*asterisk*) is noted. In (**d**), extension of inflammation to involve the petrous temporal bone in the region of the geniculate ganglion (*arrow*) is observed. Extension into the jugular foramen is demonstrable in (**e**)

Fig. 8.19 (continued)

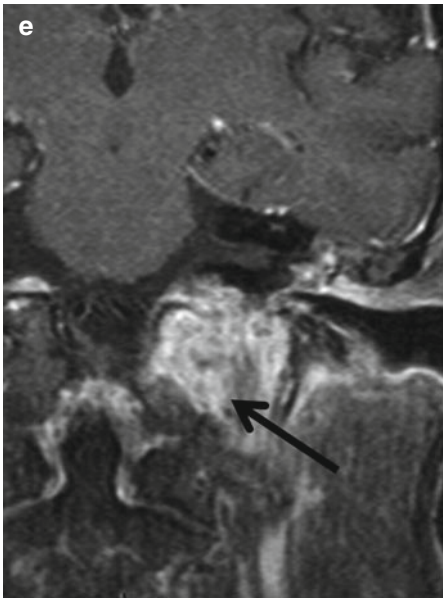

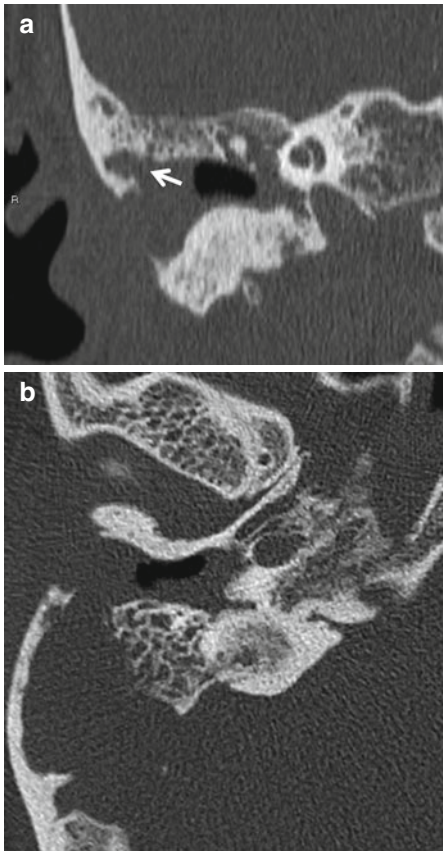

Fig. 8.20 Invasive external canal cholesteatoma in a patient with chronic otalgia. Note destruction of the roof of the EAC by cholesteatoma in (**a**). In (**b**), invasion of the mastoid air cells by cholesteatoma is evident. The diffusion-weighted image (**c**), reveals that almost all of the soft tissue in the EAC and mastoid system is cholesteatoma

Fig. 8.20 (continued)

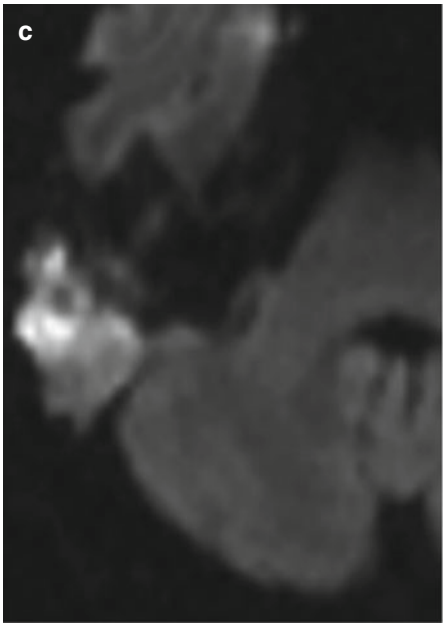

Fig. 8.21 Medial canal fibrosis. Note the "false fundus" appearance of the EAC produced by fibrous tissue

usually follow visible bone destruction in the tegmen tympani, tegmen mastoideum, and the sigmoid sinus plate, structures that must be carefully evaluated on CT. The intracranial complications of AOM are best imaged by contrast-enhanced MRI and MR venography. The detection of venous sinus thrombosis is also possible on contrast-enhanced CT. Occasionally, deep soft tissue abscesses may occur along the sternomastoid sheath (Bezold's abscess), posterior digastric belly, or the zygoma (Fig. 8.22).

8.4.2.2 Chronic Otitis Media (COM)

COM is defined as any ear with a tympanic membrane perforation and may or may not be associated with an acquired cholesteatoma. A cholesteatoma refers to the presence of proliferating epidermis in a place where it is not supposed to

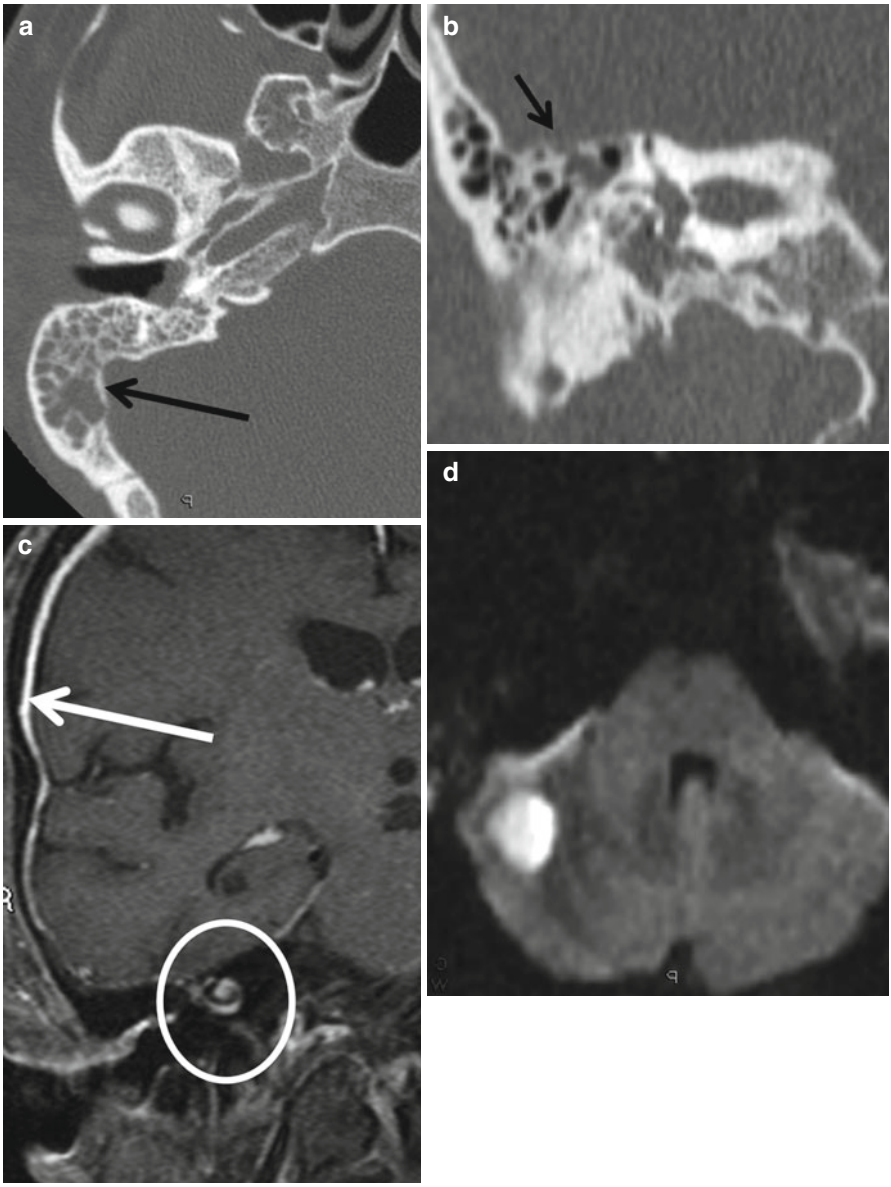

Fig. 8.22 Acute otitis media and its complications. Coalescent mastoiditis is characterized by loss of bony septa (**a**). In (**b**), note the destruction of the tegmen mastoideum. In (**c**), dural and labyrinthine enhancement due to meningitis and labyrinthitis are present. The diffusion-weighted image, (**d**), demonstrates the characteristic bright signal of a pyogenic abscess. The contrast-enhanced image (**e**) shows the peripherally enhancing cerebellar abscess and also a filling defect in the distal transverse sinus, confirmed to be thrombus on the MR venogram

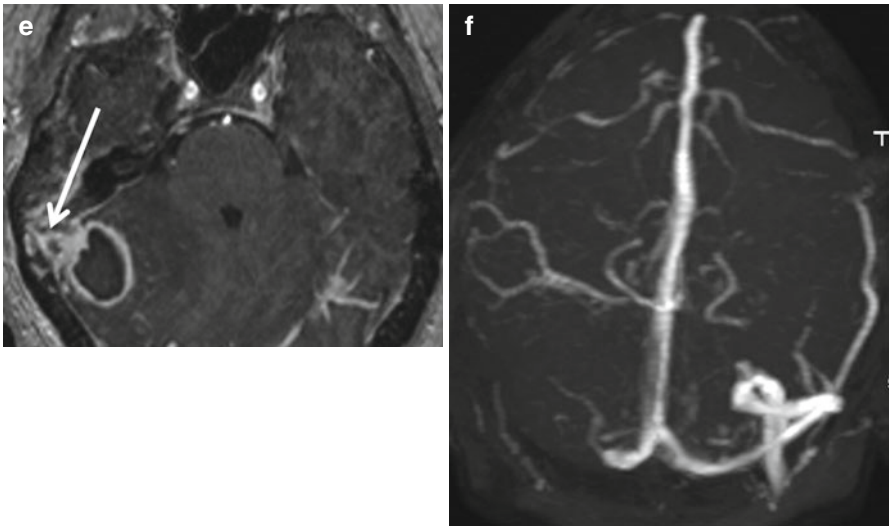

Fig. 8.22 (continued)

exist. Given that COM with acquired cholesteatoma is felt to be a consequence of chronic eustachian tube dysfunction that leads to low intratympanic pressure, the most widely accepted reason for formation of an acquired cholesteatoma is the development of a tympanic membrane retraction pocket containing skin, most often in the pars flaccida. Skin can also grow into the middle ear cavity through a severely retracted pars tensa, usually in the posterior portion of the tympanic membrane, where the eardrum retracts down onto the incudostapedial joint, eventually eroding the joint and causing a conductive hearing loss. Acquired cholesteatoma can also grow through a perforation in the tympanic membrane (usually in the pars tensa). The role of imaging is to identify the presence of cholesteatoma, define its extent, and evaluate the presence of complications. Initial imaging of COM is best accomplished with unenhanced high-resolution CT.

The hallmark of acquired cholesteatoma is bone erosion (Fig. 8.23). Pars flaccida (attic) cholesteatomas are located in Prussak's space and characteristically cause blunting of the scutum, a finding best seen on coronal CT scans. These cholesteatomas displace the ossicular chain medially and extend into the aditus ad antrum. Pars tensa cholesteatomas arise in the mesotympanum and cause early ossicular erosion. The long process of the incus is the structure most likely to be eroded due to its poor vascular supply. Pars tensa cholesteatomas can extend to the medial wall of the middle ear cavity and erode into the lateral semicircular canal creating a horizontal semicircular fistula. Proximity of the cholesteatoma to the facial nerve canal must be evaluated. Erosion of the bony facial nerve canal may be difficult to detect if a

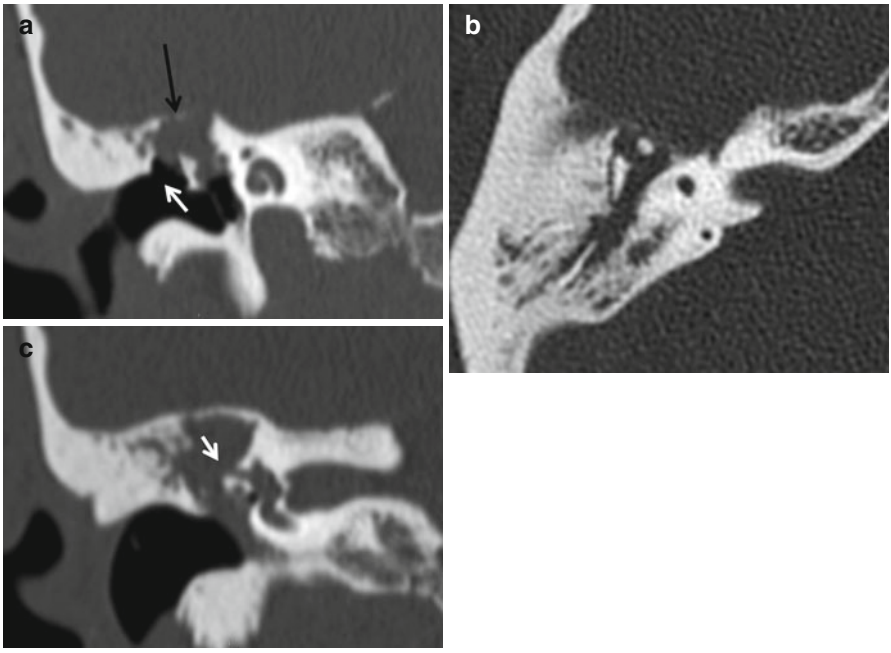

Fig. 8.23 Cholesteatoma and its complications. In (**a**), note the blunting of the scutum produced by this attic cholesteatoma. Erosion of the tegmen tympani (*black arrow*) is also evident. In (**b**), the ossicles are blunted and the malleoincudal joint is disarticulated. Note the erosion of the lateral semicircular canal resulting in a labyrinthine fistula in (**c**)

complete bony canal did not exist in the first place, a not uncommon situation. Therefore, any soft tissue adjacent to the facial nerve canal must be assumed to indicate canal wall erosion. The intracranial complications described with acute otitis media/mastoiditis can also follow COM, and again, the integrity of the tegmen tympani and sigmoid sinus plate must be evaluated.

On CT, an opacified middle ear cavity may contain any combination of fluid, granulation tissue, and cholesteatoma, and distinction between the three is not always possible. The presence of tympanic membrane retraction and bone or ossicular erosion indicates that cholesteatoma is present. MRI may be useful in distinguishing between these three entities, especially if surgery is planned. Granulation tissue enhances with contrast, while fluid and cholesteatoma do not. Cholesteatoma is hyperintense on diffusion-weighted imaging, while granulation tissue and fluid are not (Fig. 8.24).

COM may also result in the development of tympanosclerosis. Tympanosclerosis may be fibrous or osseous in nature and results in a fixed, immobile ossicular chain. Fibrous tympanosclerosis may be difficult to see on CT and appears as delicate bands and strands of soft tissue in the middle ear cavity. In the presence of

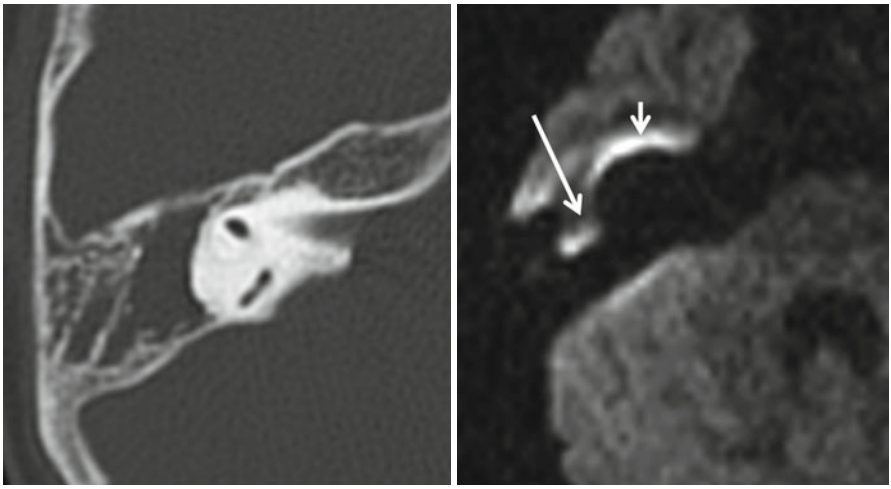

Fig. 8.24 Diffusion MRI in cholesteatoma. On the CT image, the soft tissue in the epitympanum is nonspecific and may represent cholesteatoma, fluid, or granulation tissue. The diffusion image indicates that tissue in the anterior epitympanum is cholesteatoma (*long arrow*). The smaller *arrow* points to artifact that is usually seen in the skull base with diffusion MRI. This must not be misconstrued as abnormality

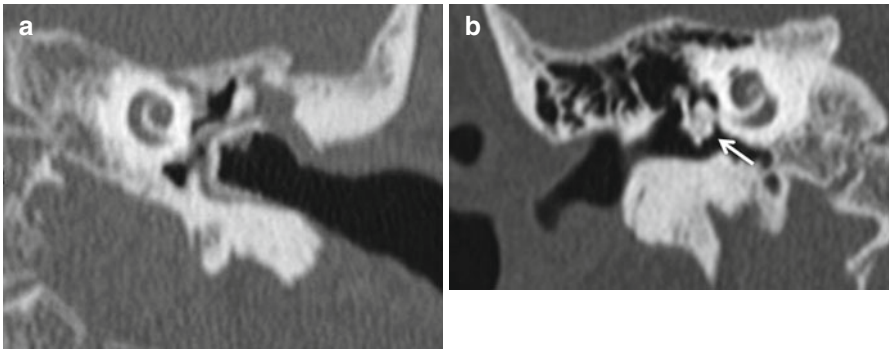

Fig. 8.25 Tympanosclerosis. Florid calcification of the tympanic membrane and EAC walls (**a**) is evident in this patient with long-standing otitis media (note the eroded scutum). Tympanosclerosis may be calcific or fibrous and involve the ligaments and mucosa of the middle ear, ossicles, and tympanic membrane. Early fibrous tympanosclerosis may not be detectable on CT. In (**b**), a densely calcified focus is seen adjacent to the malleus (*arrow*)

conductive hearing loss in a patient with a history of COM, fibrous tympanosclerosis must be suspected in the absence of other more obvious abnormalities. Osseous tympanosclerosis manifests as foci of amorphous calcification in the middle ear cavity and tympanic membrane (Fig. 8.25).

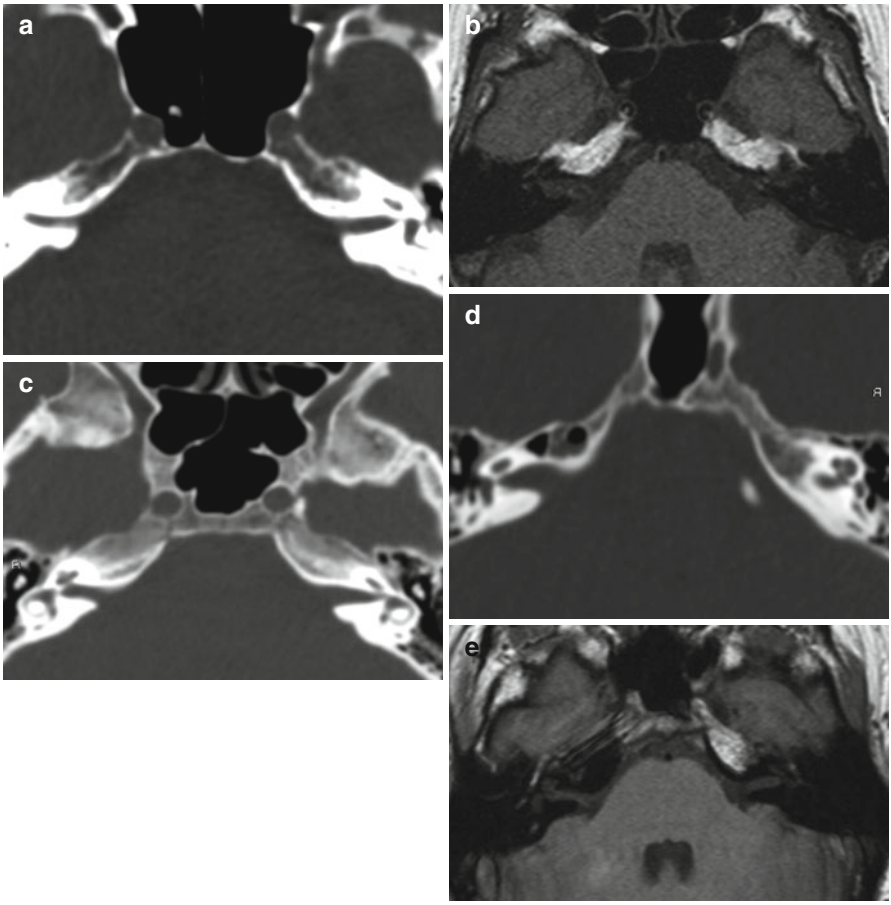

Fig. 8.26 Variations in the appearance of the normal petrous apex. The petrous apex may be pneumatized, sclerotic, or contain fatty marrow. The apices may also be asymmetric from side to side. In (**a**, **b**), the petrous apices are not pneumatized and contain low-density (CT) and high T1 signal intensity fatty marrow. In (**c**), the apices are sclerotic and would be expected to be of low signal on all MR sequences. In (**d**, **e**), the right apex is pneumatized (low signal on the T1W MR image), whereas the left contains fatty marrow (high intensity on T1)

8.4.3 Petrous Apex Inflammation

The imaging appearance of the normal petrous apex is a function of whether it is pneumatized, sclerotic, or contains fatty marrow. The various imaging appearances of the normal petrous apex are important to understand because asymmetry of the normal petrous apex may simulate an abnormality (Fig. 8.26). These are summarized in Box 8.4. Acute petrous apex inflammation usually follows an episode of AOM. Classic petrous apicitis manifests as a deep temporal headache, sixth nerve palsy, and a draining ear (Gradenigo's syndrome). The sixth nerve palsy results from involvement of the nerve where it crosses a fibro-osseous tunnel (Dorello's canal) at the petroclival junction.

Box 8.4. Variations in the Appearance of the Petrous Apex

Content	Density on CT	Signal on T1WI	Signal on T2W
Air (pneumatized)	Very low	Very low	Very low
Bone (nonpneumatized)	Very dense	Very low	Very low
Fatty marrow	Low (negative Hounsfield units)	High, signal disappears on fat-suppressed images	Intermediate to high
Fluid	Intermediate (usually less than 20 HU)	Low, may be slightly high if proteinaceous, signal remains on fat-suppressed images	High

Box 8.5. Differential Diagnosis of Petrous Apex Lesions

Lesion	Key imaging features
Petrous apex effusion	Fluid density on CT; no resorption of osseous septa; signal on T1W images may be variable – higher if proteinaceous; bright on T2W images
Petrous apicitis	Erosion of osseous margins on CT; if the apex was previously pneumatized – septa may be resorbed; enhancement of the petrous apex and overlying dura, best seen on fat-suppressed T1W images
Mucocele	Expansile smoothly marginated lesion, signal intensity of contents dependent on amount of protein
Cholesterol granuloma	Smoothly expansile; characteristically T1 hyperintense
Cephalocele	Mildly expansile; isodense to CSF on CT and isointense to CSF on all sequences on MRI; may be bilateral
Petrous ICA aneurysm	Expansile – complex sometimes laminated signal intensities on MRI due to mural thrombus; pulsation artifact along phase encoding axis may be a telltale sign

On CT, petrous apicitis may, like acute coalescent mastoiditis, be suspected by the loss of bony septa. On MRI, especially on fat-suppressed contrast-enhanced sequences, intense enhancement of the petrous apex, the adjacent meninges, and the fifth and sixth cranial nerves are typical findings. Inflammation may progress to involve the cavernous sinus as well (Fig. 8.27).

Petrous apex inflammation may also be chronic in nature. Chronic effusions of the petrous apex air cells may demonstrate complex signal intensities on MRI due to increasing protein content (Fig. 8.28). Obstruction of a petrous apex air cell may lead to the formation of a mucocele.

A cholesterol granuloma (Fig. 8.29) may also appear following long-standing petrous apex inflammation. These are expansile cystic lesions that are theorized to arise from obstruction of drainage of a petrous apex air cell. The negative pressure in the obstructed cell results in seepage of an exudate and hemorrhagic material. Formation of cholesterol crystals imparts a characteristic T1 hyperintensity. A differential diagnosis of petrous apex lesions is provided in Box 8.5.

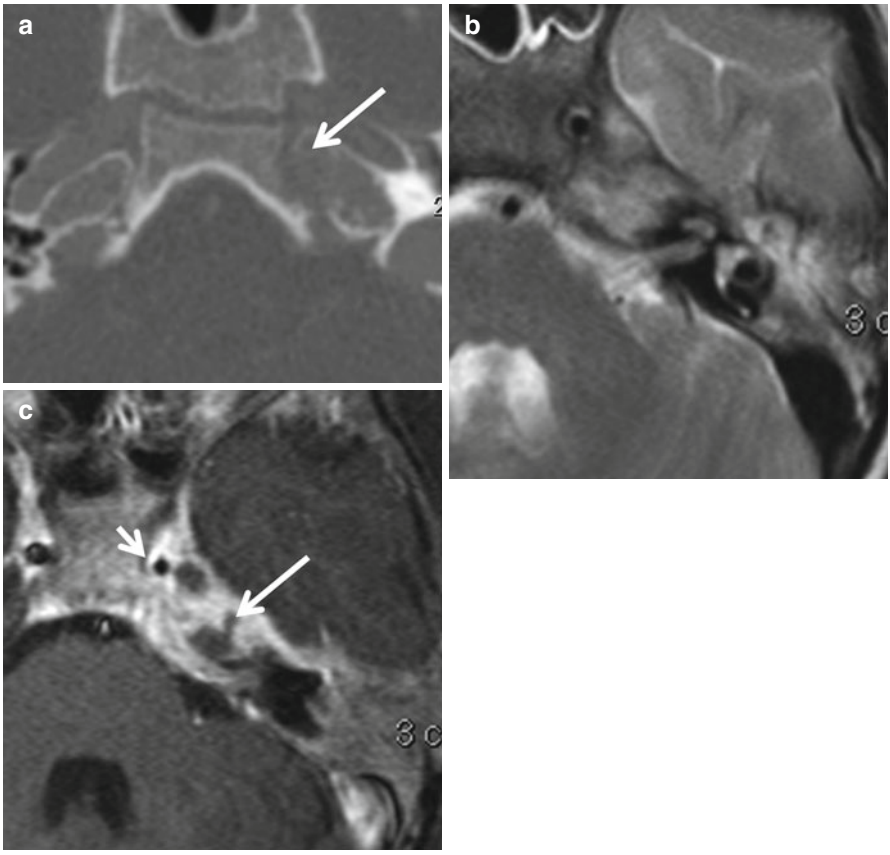

Fig. 8.27 Acute petrous apicitis in a child presenting with fever, headache, and abducens palsy. In (**a**), there is subtle erosion of the petrous apex along the margins of the petroclival fissure (*arrow*). On the T2W MR image, (**b**), fluid is seen in the petrous apex, middle ear cavity, and mastoid air cells. Abnormal enhancement in the apex is seen in (**c**), a fat-suppressed T1-weighted image. The area of nonenhancement (*arrow*) may represent an abscess. Note that the lumen of the cavernous left internal carotid artery is constricted by spread of inflammation to the cavernous sinus (*short arrow*)

8.4.4 Facial Nerve

As discussed earlier, enhancement of the intratemporal course of the facial nerve is a normal finding on MRI. This is due to the presence of a perineural venous plexus. Enhancement of the nerve in the cisternal and canalicular segments is always abnormal. A variety of processes may result in facial nerve enhancement, of which Bell's palsy is overwhelmingly the most common. A list of causes of facial nerve enhancement is indicated in Box 8.6.

Box 8.6. Facial Nerve Enhancement

Bell's palsy
Ramsay Hunt syndrome
Sarcoidosis
Lyme disease
Meningitis
Meningeal carcinomatosis
Lymphoma
Perineural tumor spread

Enhancement of the mastoid and tympanic segments is normal and can be asymmetric from side to side

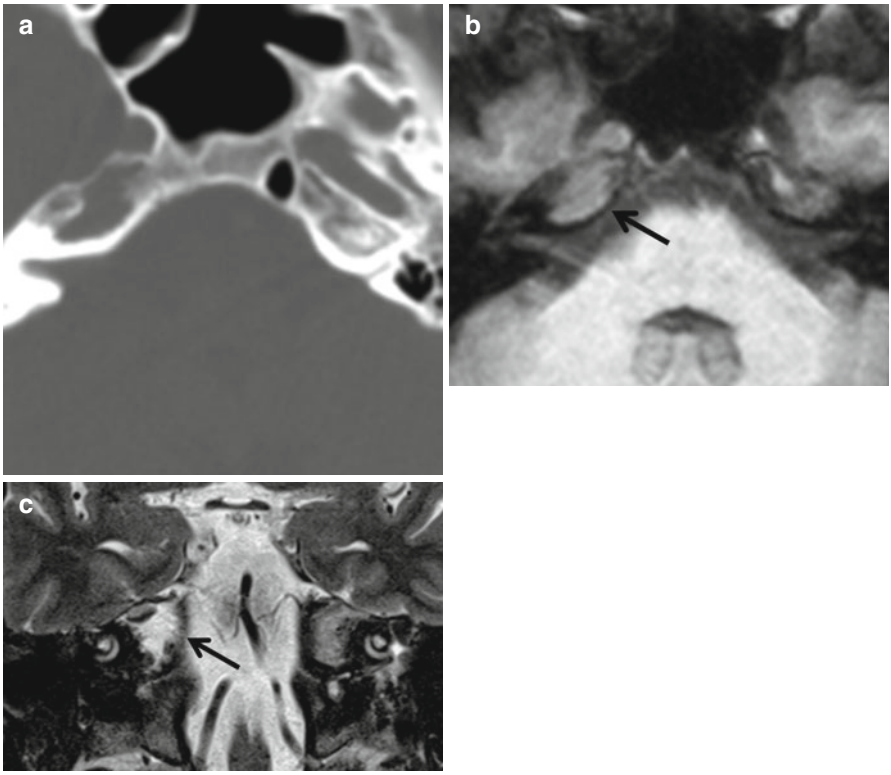

Fig. 8.28 Petrous apex trapped fluid. Incidental finding. The petrous apex is opacified with fluid that is intermediate in signal intensity on the T1WI and of high signal on the T2W image. There is no expansion or erosion of the bony margins

The typical finding of Bell's palsy is ill-defined fuzzy enhancement in the fundus of the IAC (Fig. 8.30). Typical Bell's palsy is of acute onset and self-limited in nature. In herpes zoster oticus (Ramsay Hunt syndrome), enhancement of the seventh and eighth nerves in the IAC may be seen in association with a clinically evident vesicular rash in the external ear. Enhancement of the labyrinth may also occur. This enhancement may persist for several weeks before resolving slowly (Fig. 8.30). The patient with a persistent lower motor neuron facial palsy does not have Bell's

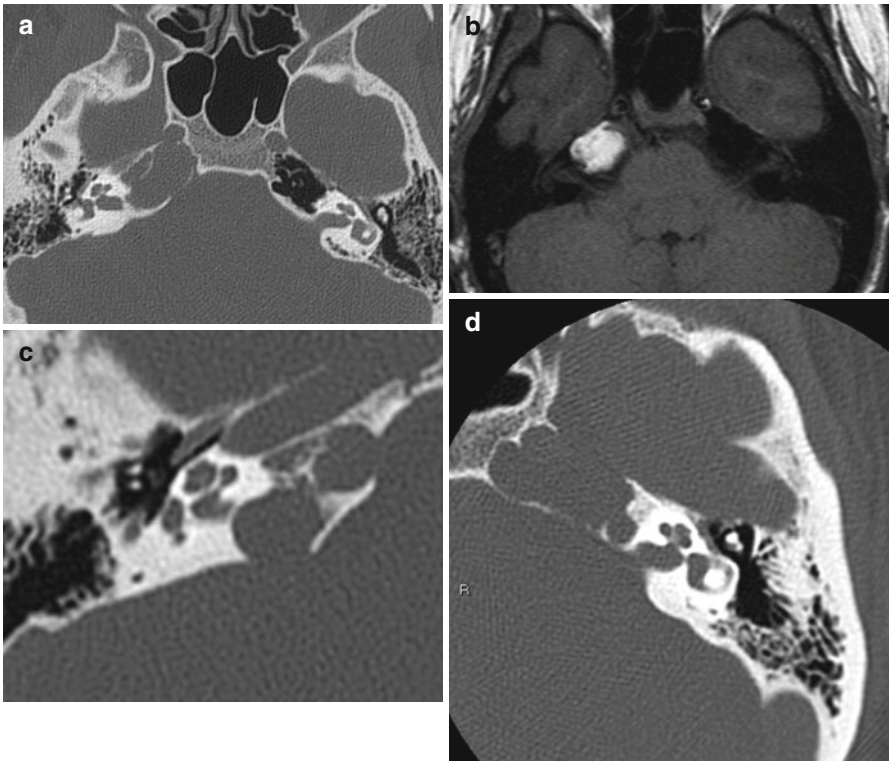

Fig. 8.29 Expansile petrous apex lesions. Cholesterol granuloma (**a**, **b**). The smooth bony expansion and T1 hyperintensity are characteristic of a cholesterol granuloma. (**c**) Petrous apex cholesteatoma. Note that this lesion demonstrates both an expansile and erosive nature. PA cholesteatomas may be congenital or acquired lesions and may erode into the labyrinth or facial nerve canal. They may be distinguished from cholesterol granulomas on MRI by the lack of T1 hyperintensity and presence of high signal on diffusion-weighted imaging. (**d**–**f**) are images of a petrous apex cephalocele. Note the smoothly expansile margins, contiguity with Meckel's cave, and signal intensity that is nearly identical to CSF. These are invariable incidentally detected lesions and not infrequently are bilateral

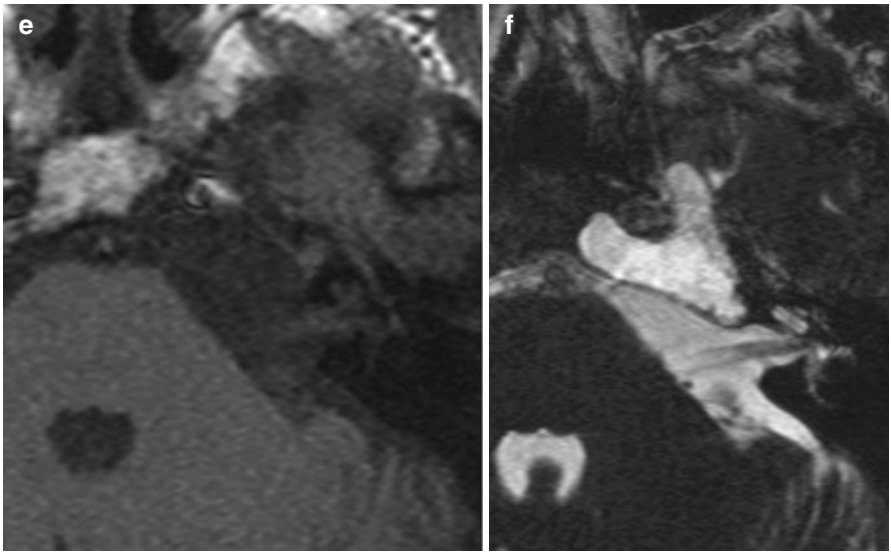

Fig. 8.29 (continued)

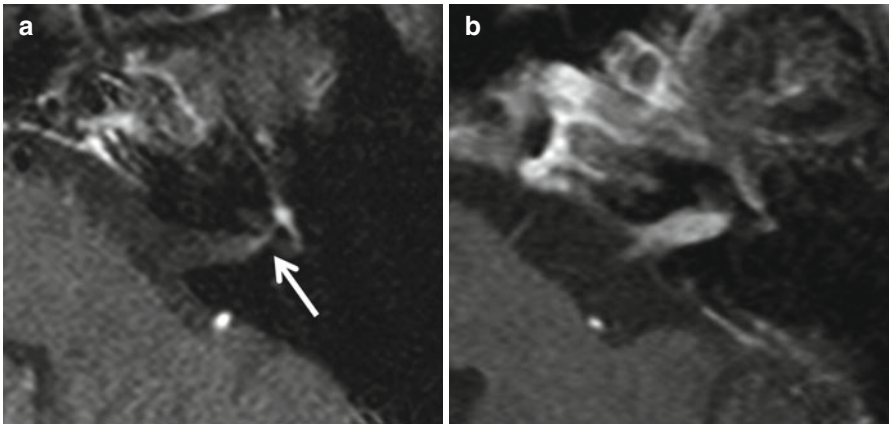

Fig. 8.30 (**a**) Bell's palsy. Ill-defined enhancement is seen in the fundus of the IAC, extending into the labyrinthine facial nerve canal. The enhancement in the geniculate ganglion and tympanic segment may be a normal phenomenon but is perhaps more prominent than one would expect. In band (**c**), a case of Ramsay Hunt syndrome (herpes zoster oticus) where the patient presented with acute facial palsy associated with vertigo and a vesicular facial rash, intense enhancement is present in the IAC and the cisternal segment of the seventh to eigth nerve complex and in the soft tissues of the EAC and periauricular region

Fig. 8.30 (continued)

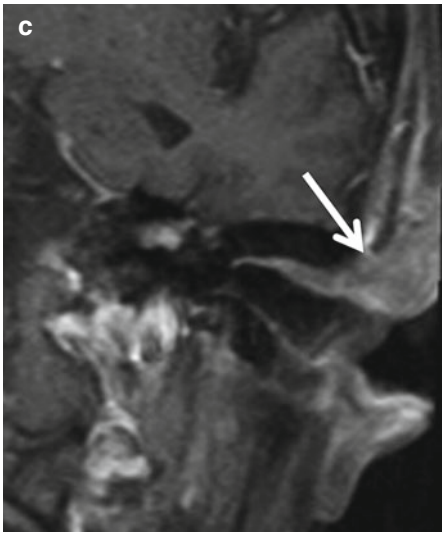

Fig. 8.31 Acute labyrinthitis. Note abnormal enhancement in the cochlea (*long arrow*) and vestibule (*short arrow*). The normal labyrinth does not enhance

palsy, and other inflammatory and neoplastic etiologies must be sought. While evaluating the facial nerve, it is important to study the course of the nerve in its entirety from the brainstem to the parotid gland.

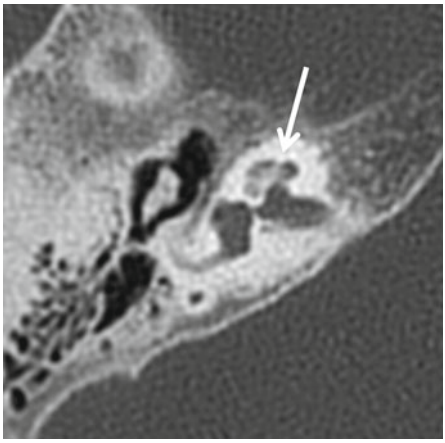

Fig. 8.32 Ossific labyrinthitis. Gradual sensorineural hearing loss in a child after an episode of bacterial meningitis. Note flocculent densities representing dystrophic ossification in the cochlear turns. When severe, ossific labyrinthitis may preclude cochlear implantation

8.4.5 Inner Ear Inflammation

Acute labyrinthitis is a self-limited disease usually viral in etiology. It presents with acute onset of hearing loss or vertigo. Enhancement of the cochlea, vestibule, and the fundus of the internal auditory canal may be seen on MRI (Fig. 8.31). The normal labyrinth does not enhance.

Labyrinthitis may also be bacterial in origin. Bacteria may seed the labyrinth from infection in the meninges or middle ear. This type of pyogenic labyrinthitis may heal with formation of bone, an entity referred to as labyrinthitis ossificans. The disease may be recognized on T2-weighted MR images where there is replacement of the normally hyperintense endolymph with dark bone. It is easier to diagnose this condition on CT where the presence of abnormal bone in the labyrinth can be easily detected. Milder forms of the disease may manifest as subtle thickening of the modiolus. With more florid disease, the entire labyrinth may be replaced by dense bone (Fig. 8.32).

8.5 Trauma

Traditionally, temporal bone fractures are classified as longitudinal or transverse. About three quarters of fractures are longitudinal in orientation. Transverse temporal bone fractures are more likely to be associated with facial nerve injury and labyrinthine involvement. A more practical method classifies temporal bone fractures as those that involve the otic capsule and those that spare it (Fig. 8.33). Clues to the presence of a temporal bone fracture on CT are fluid/blood in the middle ear and mastoids, air in the TM joint, and soft tissues around the external ear, labyrinth, or cranial cavity. Fractures traversing the middle ear may be associated with disruption of the ossicular chain. The weakest link in the chain is the incudostapedial joint. The incus is the most likely ossicle to be dislocated due to its lack of substantial

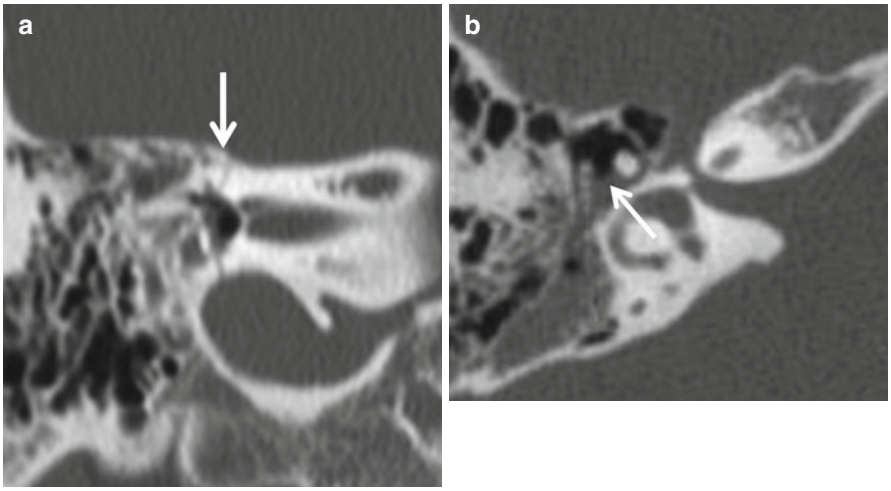

Fig. 8.33 Temporal bone fractures. Note the fracture line traversing the labyrinth in (**a**), resulting in pneumolabyrinth. In (**b**), the malleoincudal joint is dislocated. It is better, in practical terms, to describe temporal bone fractures as those that spare or involve the otic capsule rather than in terms of their orientation

ligamentous support. When fracture lines involve the carotid canal, a CT angiogram is necessary to exclude vascular injury. Long-term sequela of temporal bone fractures includes CSF leaks, perilymph fistulae, sensorineural hearing loss, conductive hearing loss, dizziness, and facial nerve palsy. Temporal bone fractures are discussed in greater detail in the chapter on craniofacial trauma.

8.6 Vascular Abnormalities

8.6.1 Arterial Abnormalities

The aberrant ICA (AbICA) is a rare anomaly, usually incidentally detected. It may produce pulsatile tinnitus and occasionally cause conductive hearing loss. It arises as a consequence of failure of development of the distal cervical internal carotid artery. The AbICA is actually a hypertrophied inferior tympanic artery (a branch of the ascending pharyngeal artery) that has anastomosed with the caroticotympanic artery (a branch of the embryonic hyoid artery) to restore continuity to the ICA. The AbICA enters the tympanic cavity through a dilated inferior tympanic canaliculus, passes across the promontory (where it is visible as a reddish mass behind the eardrum on otoscopy), and enters the horizontal segment of the carotid canal (Fig. 8.34). The anomaly is easily recognized on noncontrast CT scans and does not require a vascular study to confirm the diagnosis. It is obviously important to recognize to prevent injury during myringotomy or an ill-advised biopsy.

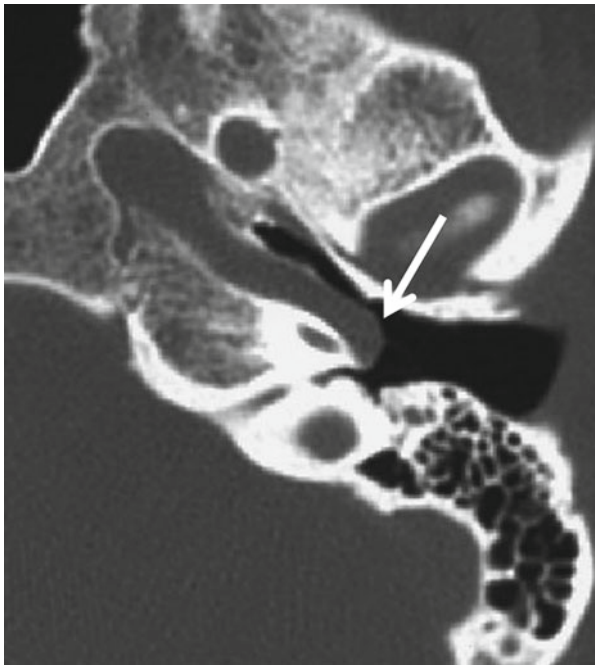

Fig. 8.34 Aberrant internal carotid artery. The anomalous ICA is seen astride the promontory (*arrow*). The jugular bulb on MRI. Side-to-side asymmetry of the bulb is a fairly common finding. Swirling flow in the larger bulb may occasionally be mistaken for a mass

In a third of the cases, the AbICA is associated with a persistent stapedial artery (PSA). The PSA represents persistence of an embryonic branch of the ICA. The PSA enters the tympanic cavity in the anteromedial hypotympanum, passes across the obturator foramen of the stapes to enter the tympanic segment of the facial nerve canal (which is widened on CT), and leaves the canal just posterior to the geniculate ganglion. It then continues as the middle meningeal artery. The foramen spinosum, which otherwise would have transmitted the middle meningeal artery, is absent. The combination of a soft tissue abnormality in the region of the stapes, a widened facial nerve canal, and absent foramen spinosum is diagnostic of a PSA (Fig. 8.35). The PSA may also cause pulsatile tinnitus.

A lateralized internal carotid artery is one in which the bony wall separating the vertical segment of the carotid canal from the tympanic cavity is absent. The ICA continues to remain anterior to the promontory and does not pass across it like the aberrant ICA does. This anomaly is asymptomatic.

8.6.2 Jugular Bulb Anomalies

It is not uncommon for substantial asymmetry in the sizes of the jugular bulb to exist. The right bulb is often larger. The turbulence of blood flow in a large bulb may produce complex signal intensities that simulate the appearance of a mass on MRI.

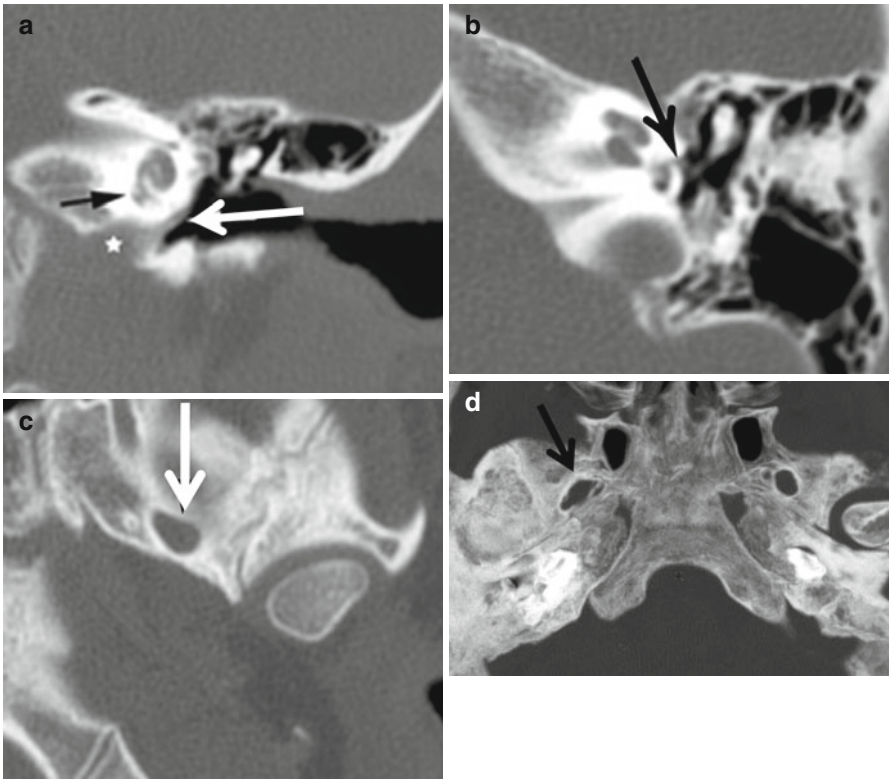

Fig. 8.35 Persistent stapedial artery (black arrows **a**, **b**). The artery arises from the ICA (star, **a**) in the carotid canal (**a**) and passes over the promontory to the oval window niche (**b**) before leaving the middle ear as the middle meningeal artery. Note the absence of the foramen spinosum in (**c**), the *arrow* pointing to foramen ovale. In (**d**), a not uncommon normal variation, the foramen spinosum on the right is incorporated into the foramen ovale and is not truly absent (**a**–**c**, Modified from Jain R, Gandhi D, Gujar S, Mukherji SK (2004) Case 67: persistent stapedial artery1. Radiology 230(2):413–416)

In problematic cases, an MR venogram can help settle the issue. The presence of normal flow-related enhancement helps exclude a mass lesion (Fig. 8.36).

The jugular bulb is said to be dehiscent when the thin bony plate that normally separates it from the hypotympanum is absent. On otoscopy, the dehiscent bulb may be visible as a bluish mass in the posterior hypotympanum that enlarges with compression of the internal jugular vein. The dehiscent bulb may be "high riding," when the dome approximates the level of the promontory (Fig. 8.37).

Focal outpouchings or diverticula may arise from the bulb and project into the tympanic cavity or into the petrous bone adjacent to the semicircular canals or the vestibular aqueduct. It is also possible for diverticula to arise from the distal transverse or sigmoid sinuses and project into the mastoid air cells (Fig. 8.37). These abnormalities can be detected incidentally, and the association between them and tinnitus is controversial.

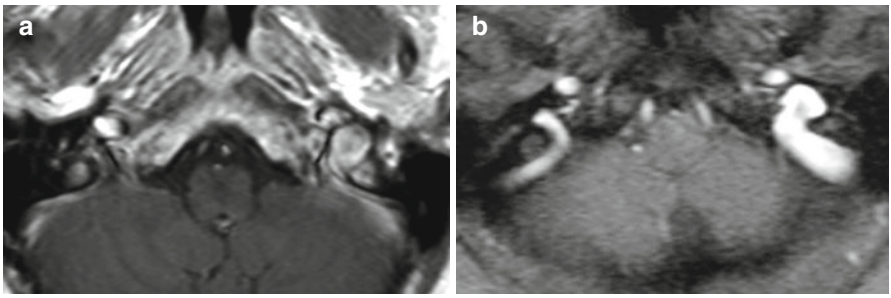

Fig. 8.36 The jugular bulb on MRI. Side-to-side asymmetry of the bulb is a fairly common finding. Swirling flow in the larger bulb may occasionally be mistaken for a mass (**a**). An MR venogram (**b**) is sometimes required to establish that the "lesion" is indeed a normal bulb and not a tumor

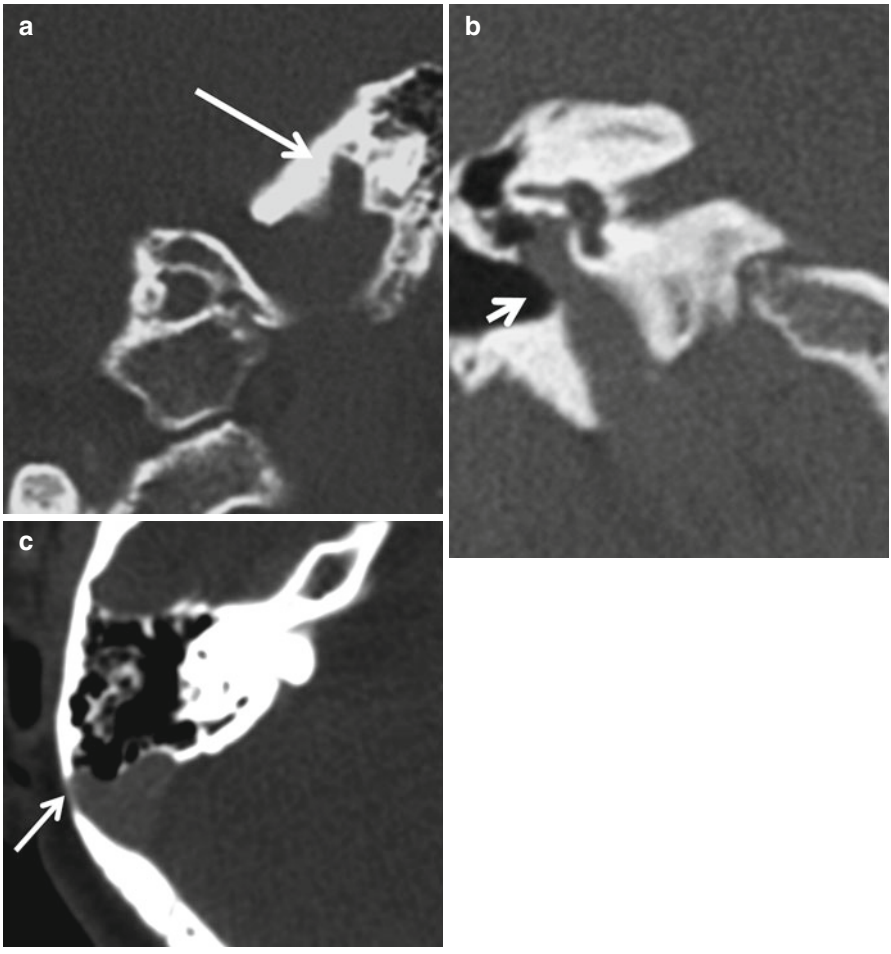

Fig. 8.37 (**a**) Incidental jugular diverticulum. (**b**) Dehiscent jugular bulb astride the promontory in a patient with tinnitus. (**c**) Sigmoid sinus diverticulum in a patient with tinnitus

8.6.3 Radiological Evaluation of Tinnitus

Tinnitus may be pulsatile or nonpulsatile and subjective or objective. The more common causes of tinnitus are discussed in Box 8.7. High-pitched, nonpulsatile binaural tinnitus from presbycusis, noise exposure, or accompanied by a high-frequency sensorineural hearing loss needs no imaging. Other nonpulsatile tinnitus usually arises from pathology in the inner ear or brainstem and is best evaluated with MRI. High-resolution CT with CT angiography is recommended as the study of choice to evaluate the etiology of pulse-synchronous, objective tinnitus, whether it results from dehiscence of the sigmoid sinus plate, an aberrant carotid artery, a high-riding jugular bulb, a jugular/sigmoid diverticulum, or a neoplastic process (e.g., paraganglioma). Dural arteriovenous fistulae are an uncommon but important cause of pulsatile tinnitus (Fig. 8.38). When small, they are difficult to detect on cross-sectional imaging. The presence of unusual vascular structures in the posterior fossa, especially when the sigmoid or transverse sinuses are thrombosed, is highly suggestive of a dural arteriovenous fistula. When the contrast-enhanced CT examination is negative, a time-resolved MR angiogram or a conventional catheter angiogram must be obtained to exclude this entity.

Box 8.7. Causes of Tinnitus

Systemic causes
Hyperdynamic circulatory states (anemia, pregnancy, thyrotoxicosis)
Idiopathic intracranial hypertension and hypotension
Inner ear anomalies
Drug toxicity
Presbycusis
Meniere's disease
Superior semicircular canal dehiscence
Brainstem infarcts
*Arterial causes
Internal carotid artery stenosis
Cervical ICA dissection
Cervical ICA aneurysms
Aberrant ICA
Persistent stapedial artery
Giant cell arteritis
*Venous causes
Jugular bulb dehiscence
Jugular and sigmoid diverticula
*Vascular malformations, especially dural A–V fistulae
Paragangliomas
*These usually cause objective tinnitus. Venous tinnitus can sometimes be suppressed with pressure on the ipsilateral internal jugular vein

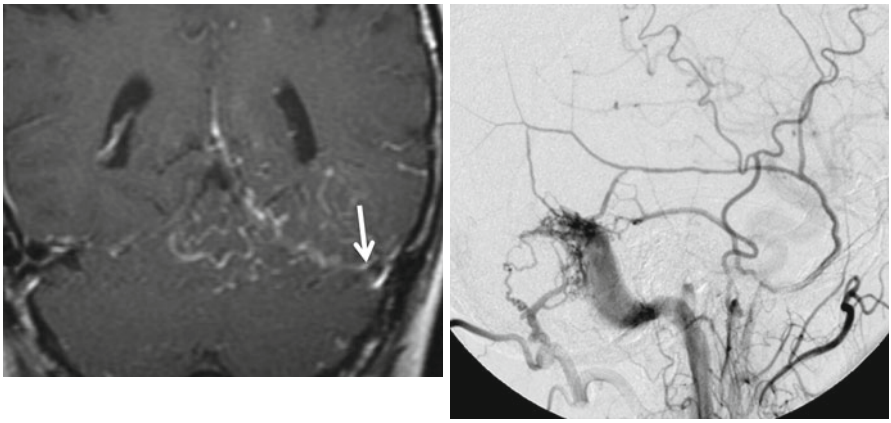

Fig. 8.38 Dural arteriovenous fistula in a patient with pulsatile tinnitus. Numerous abnormal vascular structures are seen on either side of the tentorium. The *arrow* points to a filling defect in the proximal transverse sinus. These findings are compatible with a DAVF, confirmed on angiography which demonstrates feeders arising from the occipital artery, lack of a discrete nidus and shunting into the distal transverse and sigmoid sinuses

8.7 Tumors and Tumorlike Lesions of the Temporal Bone and Skull Base

8.7.1 External Auditory Canal (EAC) Tumors

The most common benign EAC tumors are osteomas, easily identified as bony excrescences on CT scans. Exostoses, which are not actually tumors and occur in response to chronic inflammation, may also be seen in the EAC and appear as sessile bony masses on CT (Fig. 8.39).

The most common malignant neoplasms are squamous cell carcinomas. Squamous cell carcinomas present as infiltrative masses with irregular bone destruction on CT. These tumors carry a poor prognosis, especially when associated with facial palsy or lymphadenopathy. They are treated by a combination of surgery and radiotherapy. Staging is best accomplished by a combination of CT and MR imaging. From a resectability standpoint, involvement of the middle ear cavity, facial nerve canal, temporomandibular joint, and parotid gland are important features that the radiologist must identify (Fig. 8.40).

8.7.2 Middle Ear Tumors

It is often difficult to make a specific pathological diagnosis of a middle ear mass on CT or MR imaging.

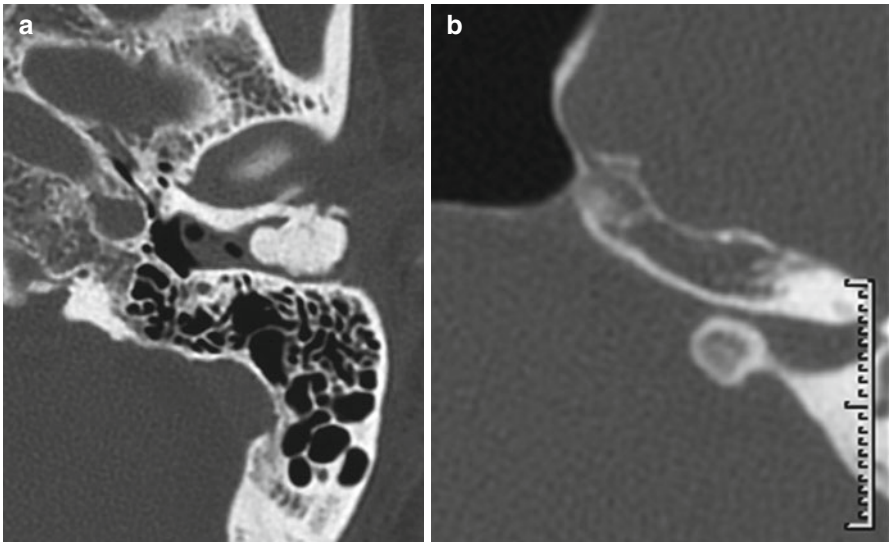

Fig. 8.39 Pedunculated osteomas arising from the EAC (**a**) and IAC (**b**)

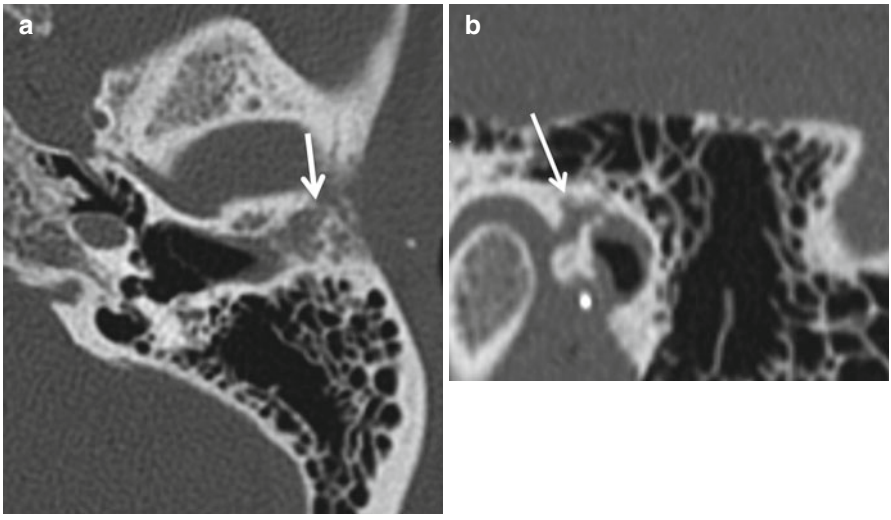

Fig. 8.40 Squamous cell carcinoma of the EAC. Note the permeative bone destruction (*arrow*, **a**) associated with the soft tissue in the EAC. The tumor has extended through the petrotympanic fissure to involve the articular tubercle (*arrow*, **b**). The middle ear cavity is uninvolved. On the coronal and axial enhanced fat-suppressed images (**c**, **d**), abnormal marrow signal in the roof of the EAC and extension into the TM joint space are evident (*arrow*)

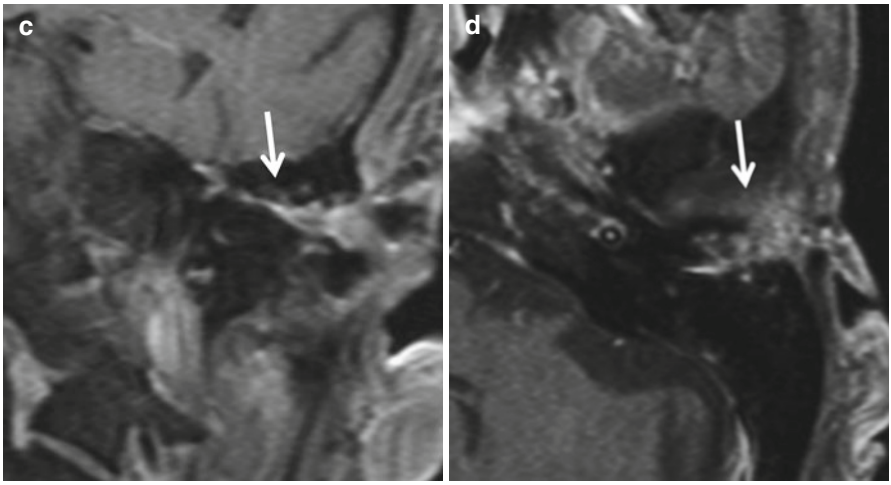

Fig. 8.40 (continued)

Benign processes such as adenomas, glomus tumors (paragangliomas), facial nerve schwannomas, choristomas (ectopic salivary rests), and congenital cholesteatoma may all appear as nonspecific soft tissue masses on CT. The location of these in the middle ear cavity may provide a clue to the diagnosis. A mass situated on the promontory is most likely to be a glomus tumor (Fig. 8.41). A tumor related to the facial nerve canal is likely to be a schwannoma, hemangioma, or choristoma. Facial nerve hemangiomas are often diagnosed by the presence of microcalcifications associated with the neoplasm (see below).

Primary malignant tumors of the middle ear are extremely uncommon. Rhabdomyosarcomas of the embryonal and botryoid types are extremely aggressive tumors that occur in childhood. In the early stages of the disease, both clinically and radiologically, it may mimic a benign middle ear effusion. However, the presence of a bloody ear discharge, facial nerve paralysis, and bone destruction should serve as a clue to the clinician and radiologist that one is dealing with something more than a simple middle ear inflammatory process. A list of middle ear masses is provided in Box 8.8.

Box 8.8. Middle Ear Masses

Adenoma
Paraganglioma
Schwannoma
Cholesteatoma
Choristoma
Meningioma
Rhabdomyosarcoma

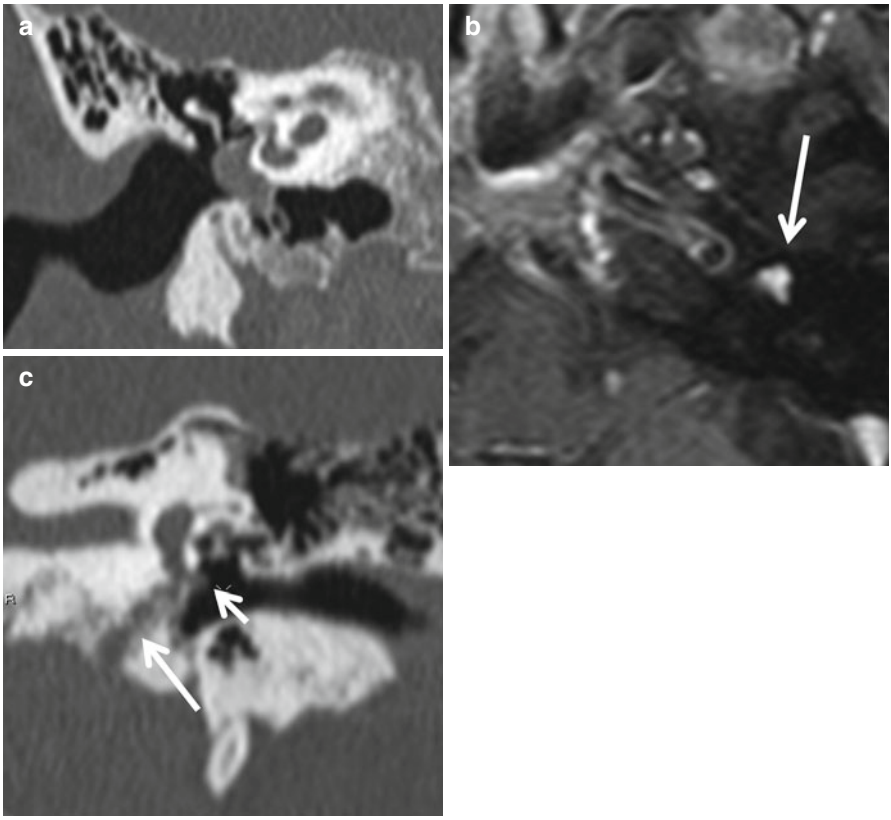

Fig. 8.41 Glomus tympanicum. In (**a**), a sessile mass is seen overlying the promontory. It demonstrates intense enhancement in (**b**). These findings are typical of a glomus tympanicum. In (**c**), note that although the lesion indicated by the *small arrow* resembles a glomus tympanicum, a trail of permeative osteolysis (*long arrow*) extending to the jugular foramen is present. This lesion is actually a small part of a more extensive glomus jugular that has invaded the middle ear

8.7.3 Tumors of the Facial Nerve

Facial nerve schwannomas present as lobulated masses with smooth bony remodeling on CT. On MRI, they tend to enhance homogeneously. The appearance of facial nerve schwannomas may vary depending upon the segment of the nerve they originate from (Fig. 8.42). When they arise in the canalicular segment of the nerve, they are indistinguishable from eigth nerve schwannomas. The short, tight labyrinthine segment of the facial nerve canal does not permit schwannomas in this location to grow to a significant size. However, involvement of the geniculate ganglion can allow a schwannoma to extend considerably into the middle cranial fossa. When one encounters an extra-axial middle fossa mass that rests against the petrous temporal bone, identifying extension into the geniculate ganglion allows distinction from a meningioma. When the tympanic segment is involved, the tumor expands into the

middle ear cavity and is indistinguishable from other middle ear masses described earlier. In the mastoid segment, a schwannoma may have an apparently aggressive appearance as it erodes through the numerous gracile bony septa of the air cells.

Facial nerve hemangiomas or intratemporal benign vascular tumors usually arise in the region of the geniculate ganglion. These present as enhancing masses on MRI and contain characteristic spicules of tumor bone on CT. The larger a hemangioma is, the more likely it is to contain bony spicules (Fig. 8.43). Small lesions are indistinguishable from schwannomas. The important topic of perineural spread of tumor along the facial nerve is discussed in the chapter on salivary gland imaging.

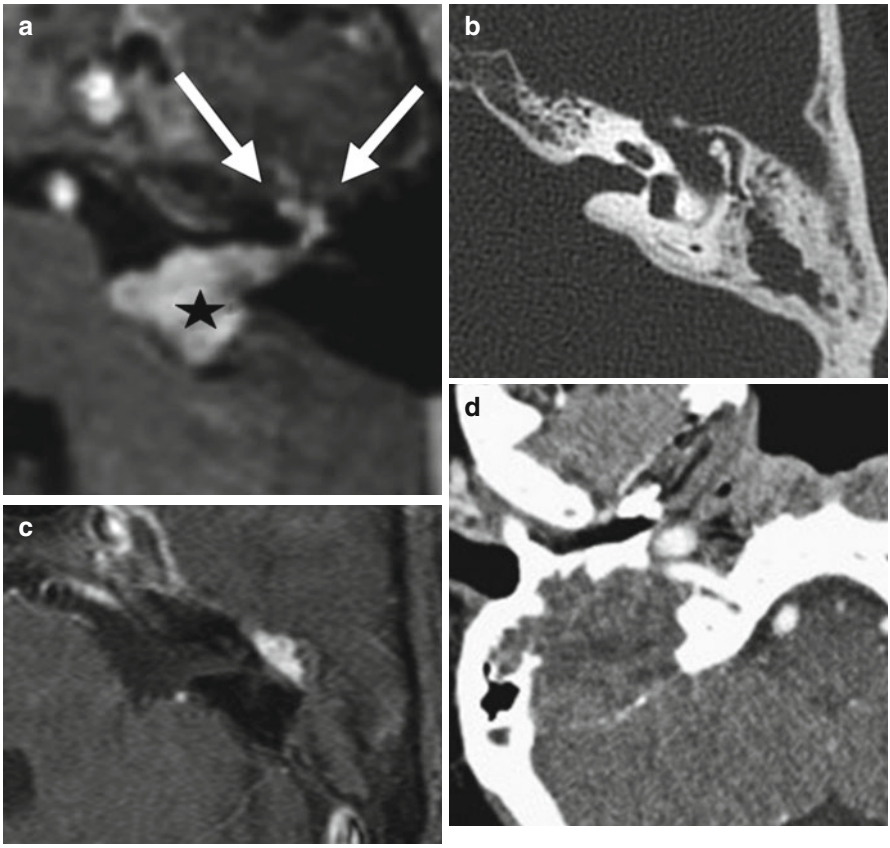

Fig. 8.42 Facial nerve schwannoma. The imaging appearance of FNS depends upon the segment of the nerve it arises from. Schwannomas of the canalicular segment can be indistinguishable from vestibulocochlear schwannomas. Extension into the labyrinthine segment and geniculate ganglion (*arrows*) is a clue to the facial nerve origin of the lesion in (**a**). When they arise from the tympanic segment (**b**, **c**), they present as nonspecific middle ear masses that displace the ossicular chain and enhance on gadolinium MR. Schwannomas arising from the mastoid segment, may demonstrate a pseudo-aggressive appearance as they erode through delicate mastoid septa (**d**, **e**). Occasionally, a schwannoma arising from the geniculate ganglion can project into the middle cranial fossa and present as an extra-axial mass (**f**)

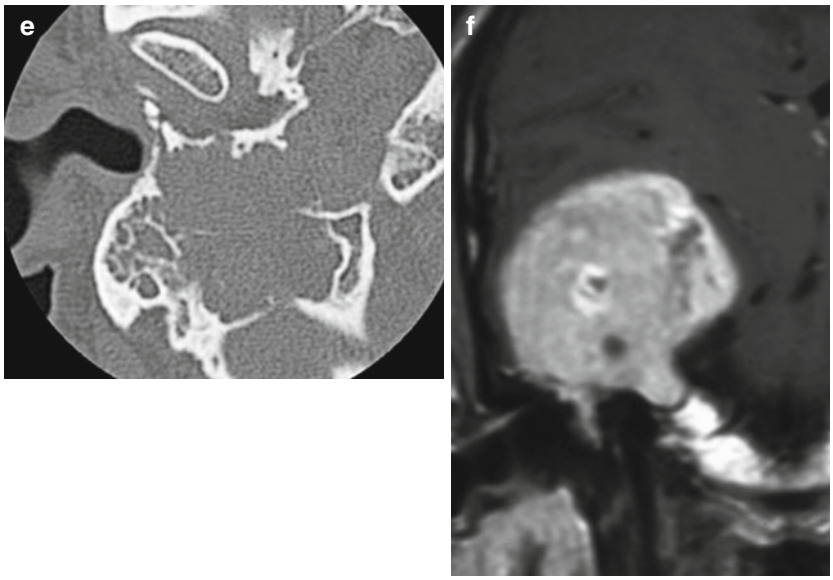

Fig. 8.42 (continued)

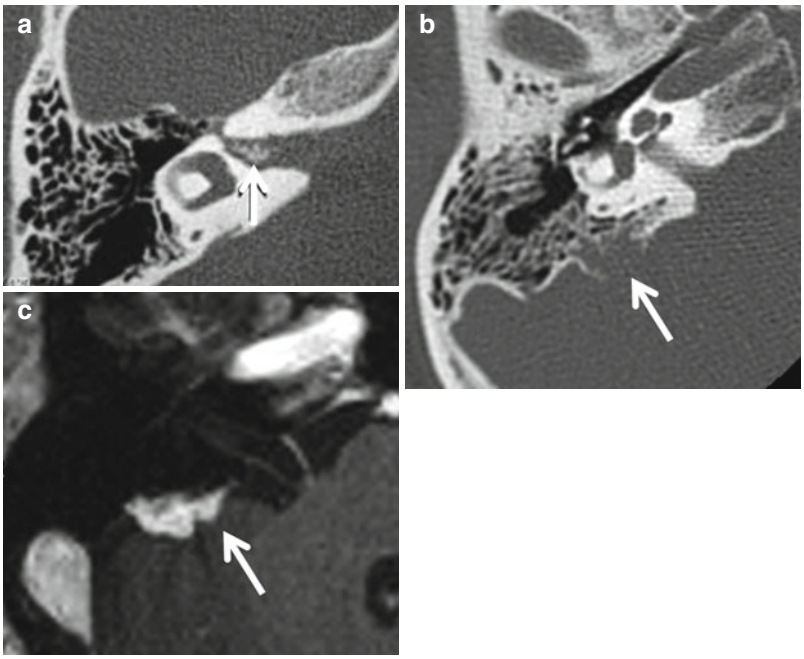

Fig. 8.43 Hemangiomas of the temporal bone. Spicules of bone in an enhancing lesion are typical of ossifying hemangiomas. Although these tumors typically occur along the course of the facial nerve, unusual locations are possible, as shown in images (**b**, **c**) which demonstrate a hemangioma containing spicules of bone that simulated an endolymphatic sac tumor in terms of location and imaging characteristics. The sac was found distinct from tumor at surgery

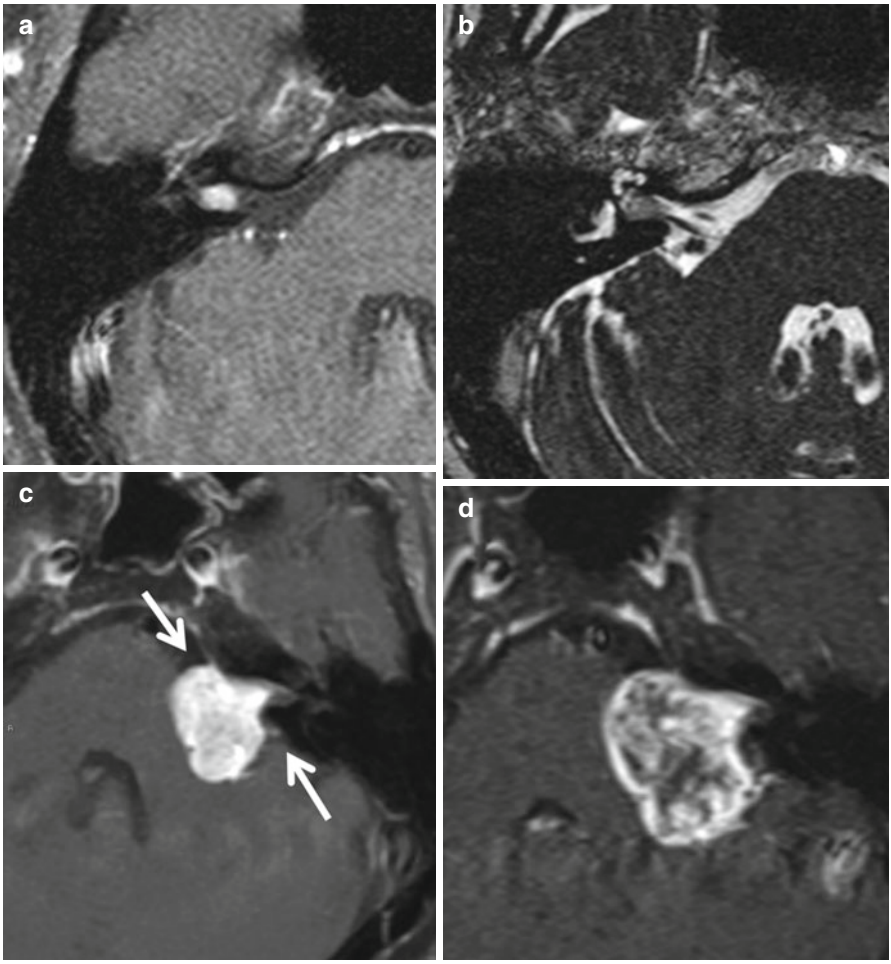

Fig. 8.44 Vestibulocochlear schwannomas. (**a**, **b**) demonstrate typical canalicular schwannomas. (**c**) demonstrates a schwannoma with a typical "ice-cream cone" configuration expanding the IAC and growing into the CP angle cistern. Note the acute angles the tumor makes with the petrous temporal bone (*arrows*). Image (**d**) is of the same tumor 3 months after stereotactic radiosurgery. Mild enlargement and the development of foci of nonenhancement due to liquefaction are expected findings a few weeks after treatment

8.7.4 Tumors of the Cerebellopontine Angle (CPA) Cistern, Internal Auditory Canal (IAC), and Labyrinth

8.7.4.1 Schwannomas

Schwannomas of the CP angle and IAC (Fig. 8.44) arise from the seventh or the eighth nerves. The vestibular nerve is the most likely to be affected, and it is acceptable to refer to all schwannomas limited to the CPA–IAC region as vestibular schwannomas if the nerve of origin cannot be identified on imaging. The typical vestibular

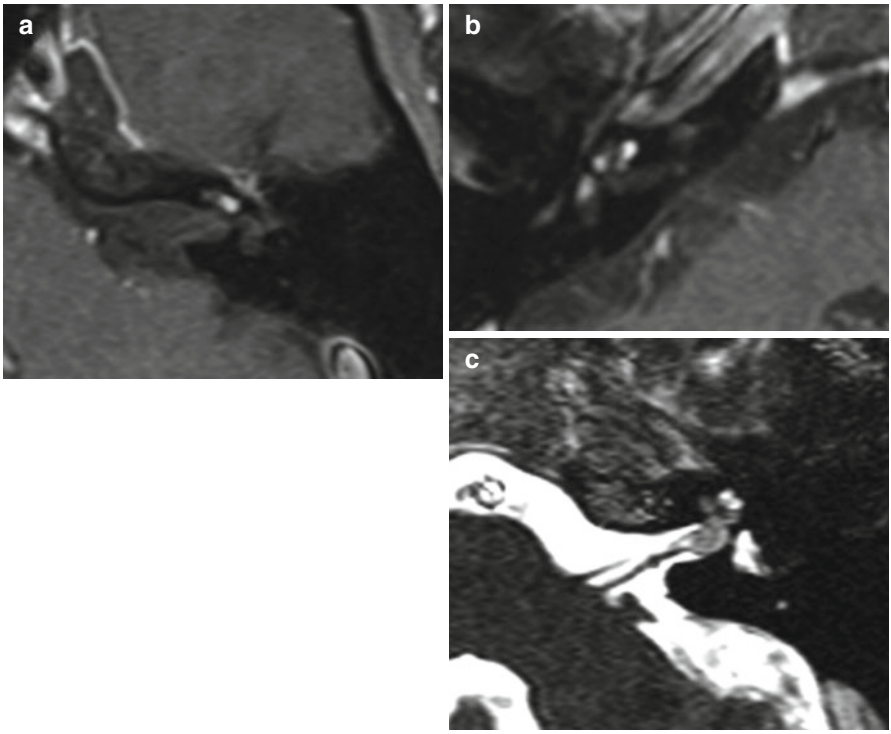

Fig. 8.45 Labyrinthine schwannomas. Cochlear schwannoma (**a**), Trans-otic schwannoma involving the cochlea and vestibule (**b**) and a transmodiolar schwannoma that involves the basal cochlear turn and extends into the fundus of the IAC (**c**)

schwannoma arises at the glial–schwann cell junction which is located at the approximate level of the porous acusticus. These are extremely slow-growing tumors. Bilateral vestibular schwannomas are the hallmark of neurofibromatosis 2. The best way to image schwannomas is to obtain thin section contrast-enhanced MR images. The addition of a volumetric high-resolution heavily T2-weighted sequence enables detection of small tumors against a background of bright CSF or endolymph. Schwannomas can vary greatly in size from punctuate tumors to those that exert considerable mass effect upon the brainstem and cerebellum. Irrespective of size, these tumors always enhance. The smaller tumors enhance homogeneously, while the larger ones may contain foci of liquefaction. Small lesions may assume a cylindrical shape as they fill the internal auditory canal. In larger tumors, the IAC is expanded as the tumor grows into the cerebellopontine angle cistern, assuming the typical "ice-cream cone/mushroom" configuration. The component in the cistern makes acute angles with the petrous temporal bone. Tumors may grow from the IAC into the facial canal, cochlea, or vestibule. Such extension is important to recognize for surgical planning.

Schwannomas may also arise entirely in the labyrinth (Fig. 8.45). Vestibular neuritis and labyrinthitis may give rise to enhancing foci in the IAC or labyrinth and cannot be distinguished from small schwannomas. When such enhancement is noted, it is important to obtain a follow-up MRI study in about 8 weeks. If the enhancement was due to inflammation, it will have likely resolved.

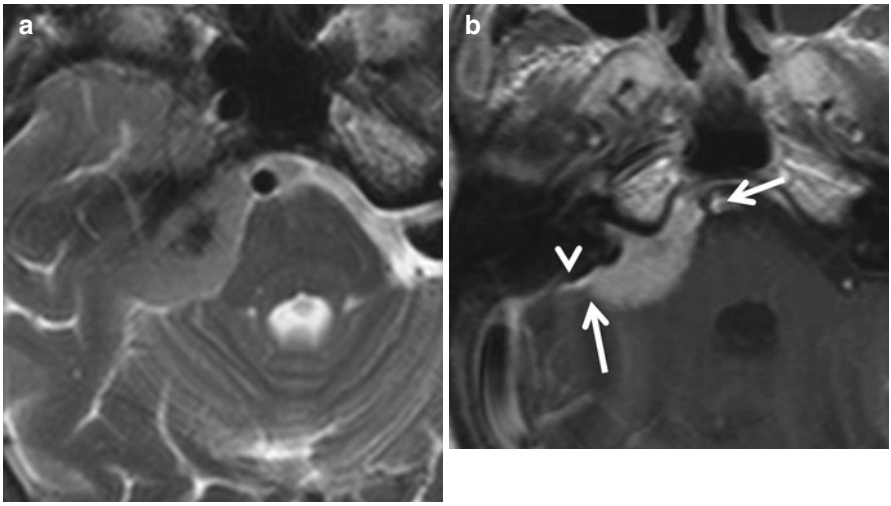

Fig. 8.46 Meningioma of the cerebellopontine angle demonstrating calcification (*arrow*, **a**), lack of IAC expansion, a broad dural base with obtuse angles (*arrows*) to the petrous bone, and a dural tail (*arrowhead*)

Larger schwannomas are treated by open surgery. Medium and small tumors can be treated by surgery or by stereotactic radiosurgery. For small and some medium-sized, asymptomatic lesions, watchful expectancy with repeat MR imaging is a reasonable option. After radiosurgery, it is not uncommon for these lesions to transiently increase in size and for foci of central liquefaction to appear (Fig. 8.44).

8.7.4.2 Meningiomas

Meningiomas of the cerebellopontine angle appear as sessile masses based upon the dura that overly the petrous temporal bone. On CT, they are hyperdense and frequently contain foci of calcification (as opposed to schwannomas that usually do not calcify). On MRI, meningiomas enhance homogeneously and make a characteristic obtuse angle with the dura. An enhancing dural tail may be present. They may extend into the internal artery canal, but do not expand it like schwannomas do (Fig. 8.46). Meningiomas can exert mass effect upon the brainstem and cerebellum and produce considerable vasogenic edema in these structures. Parenchymal edema is something that even large schwannomas are usually not associated with.

8.7.4.3 Epidermoid and Arachnoid Cysts

Congenital epithelial rests in the cerebellopontine angle can give rise to epidermoid tumors. On CT, these tumors can be as hypodense as CSF and resemble the more innocuous arachnoid cysts. On MRI, the signal intensity of arachnoid cysts parallels that of CSF on all sequences, whereas epidermoid cysts are typically hyperintense on FLAIR and diffusion-weighted imaging (Fig. 8.47). The differential diagnosis of the most common cerebellopontine angle cistern lesions is provided in Box 8.9.

Box 8.9. Differential Diagnosis of Cerebellopontine Angle Masses

Lesion	Expansion of IAC	Angle with petrous bone	CT density	Calcification	SI on diffusion-weighted imaging	SI on flair	Enhancement with gadolinium	Dural tail	Adjacent parenchymal edema
Vestibular schwannoma	+	Acute	Intermediate	–	Not bright	Intermediate	+, may be heterogeneous	–	–
Meningioma	–	Obtuse	Hyperdense	+	Variable	Intermediate	+, usually homogeneous	+	May be present
Epidermoid	–	Variable	Low, like CSF	–	Very bright	Very bright	–	–	–
Arachnoid cyst	–	Variable	Low, like CSF	–	Low	Low	–	–	–

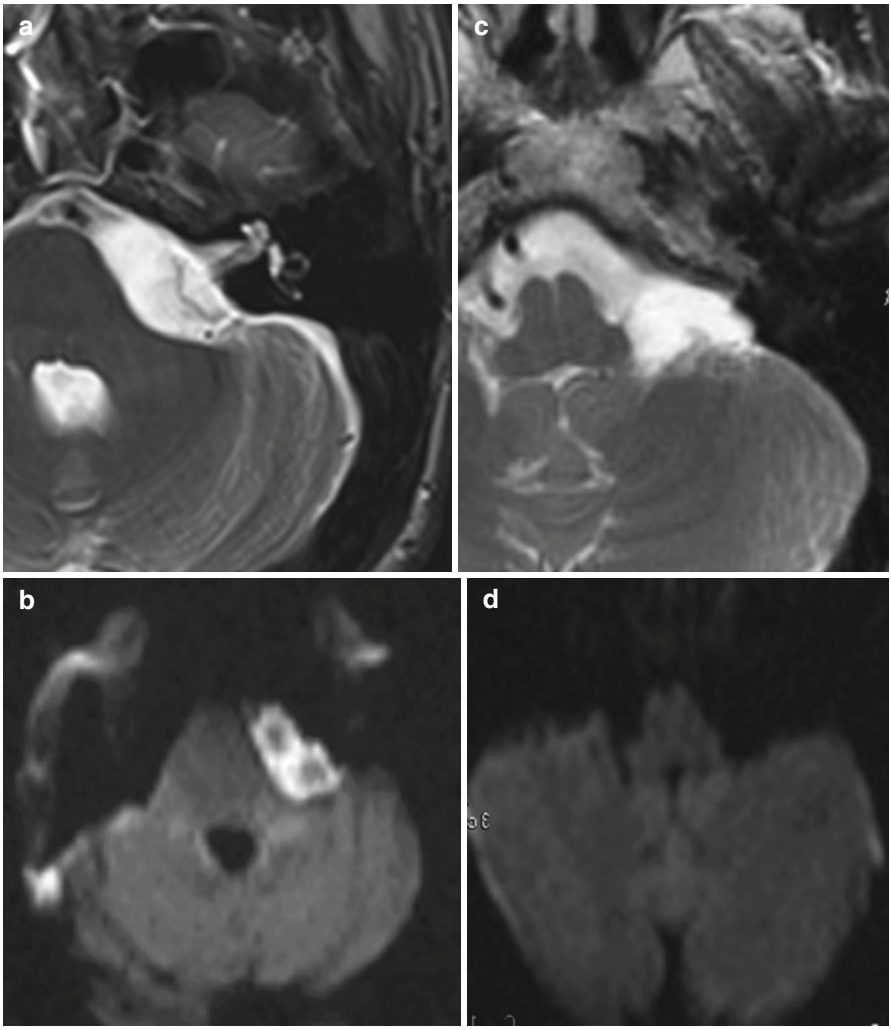

Fig. 8.47 (**a**, **b**) Epidermoid. (**c**, **d**) Arachnoid cyst. Note that both the epidermoid and arachnoid cysts are nearly isointense to CSF on the T2-weighted images. However, the epidermoid is hyperintense on diffusion-weighted imaging, while an arachnoid cyst is not

8.7.4.4 Endolymphatic Sac Tumors (ELST)

These tumors are adenocarcinomas that arise from the lining of the vestibular aqueduct (not the endolymphatic sac itself). An increased incidence of these tumors is found in patients with von Hippel–Lindau syndrome. A heterogeneous, destructive tumor along the posterior aspect of the petrous ridge containing spicules of bone is the typical imaging appearance of this entity (Fig. 8.48). When an ELST is suspected, careful inspection of the brain parenchyma is important to detect small hemangioblastomas, the presence of which indicates von Hippel–Lindau syndrome.

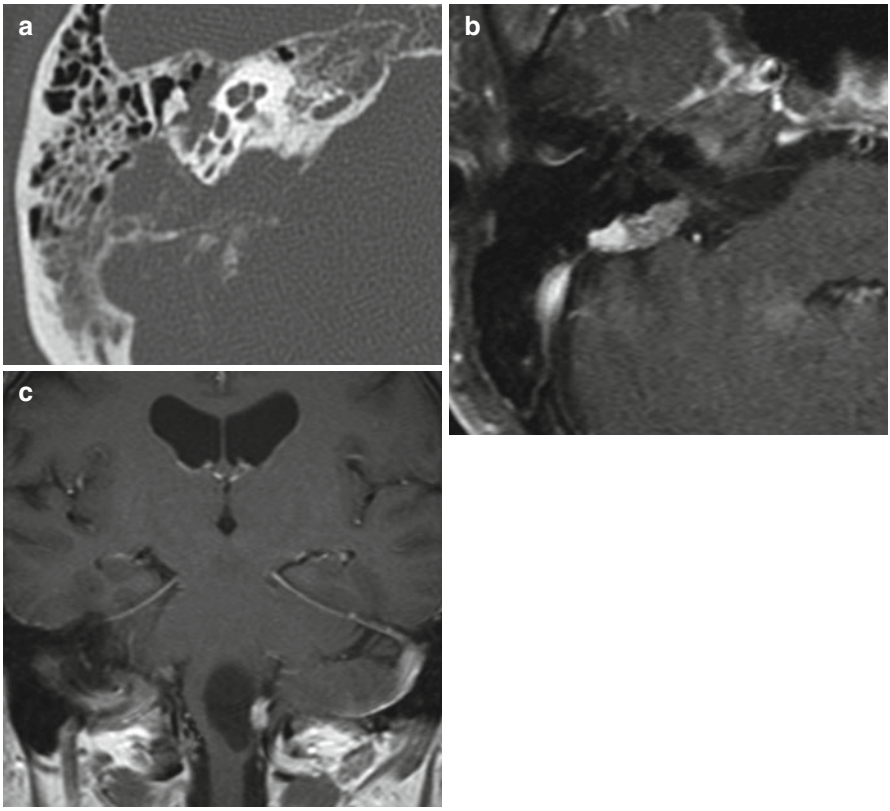

Fig. 8.48 Endolymphatic sac tumor. Note the characteristic spiculated bone destruction along the dorsal aspect of the petrous pyramid in (**a**). On MRI (**b**), these tumors enhance heterogeneously. ELSTs may be sporadic or associated with von Hippel–Lindau syndrome. When an ELST is suspected, the brain must be scrutinized for hemangioblastomas (**c**)

8.7.5 Osseous Tumors of the Temporal Bone and Skull Base

Although a wide variety of benign and malignant tumors and tumorlike lesions may occur in the temporal bone and skull base, they are on the whole very uncommon. The most common benign osseous lesion is fibrous dysplasia (Fig. 8.49). The most common primary osseous malignancy that occurs in the temporal bone is chondrosarcoma (Fig. 8.50). Chondrosarcomas arise from the petroclival and sphenoccipital synchondroses. Chordomas are aggressive tumors that arise from notochordal remnants in the clivus. A destructive midline central skull base containing fragments of bone is invariably a chordoma (Fig. 8.50). The key imaging findings of these lesions are presented in Box 8.10.

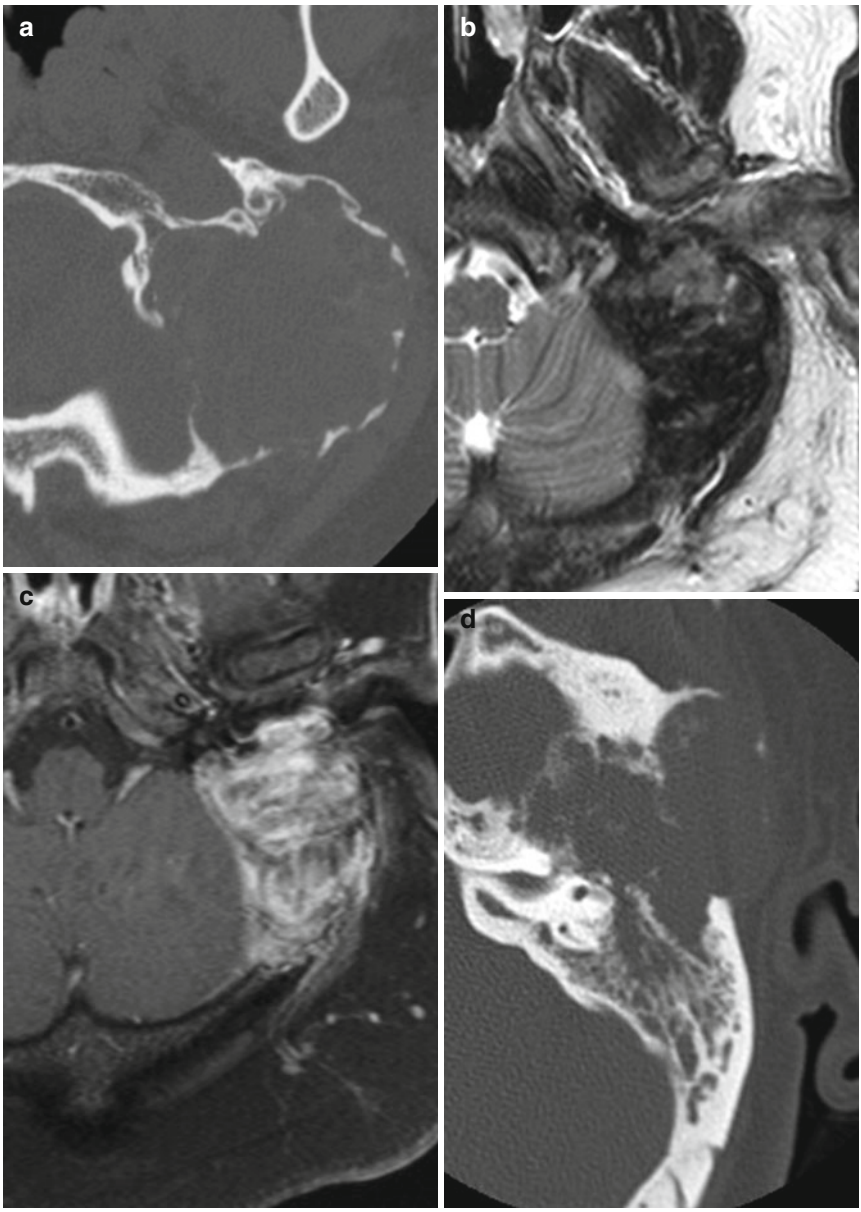

Fig. 8.49 Primary temporal bone tumors. (**a**–**c**) Fibrous dysplasia. (**d**–**f**) Giant cell tumor. Fibrous dysplasia may present as an expansile lesion with a ground glass matrix or as an entirely lytic focus as in this case. The MR signal intensity of FD can be extremely variable and simulate an aggressive process. Giant cell tumors of the temporal bone are fairly uncommon. They tend to present as expansile multiloculated masses with a low T2 signal matrix, as in this case and variable enhancement. The differential diagnosis for an expansile temporal bone lesion would include fibrous dysplasia, giant cell tumor, giant cell reparative granuloma, brown tumor, aneurysmal bone cyst, plasmacytoma, and metastasis

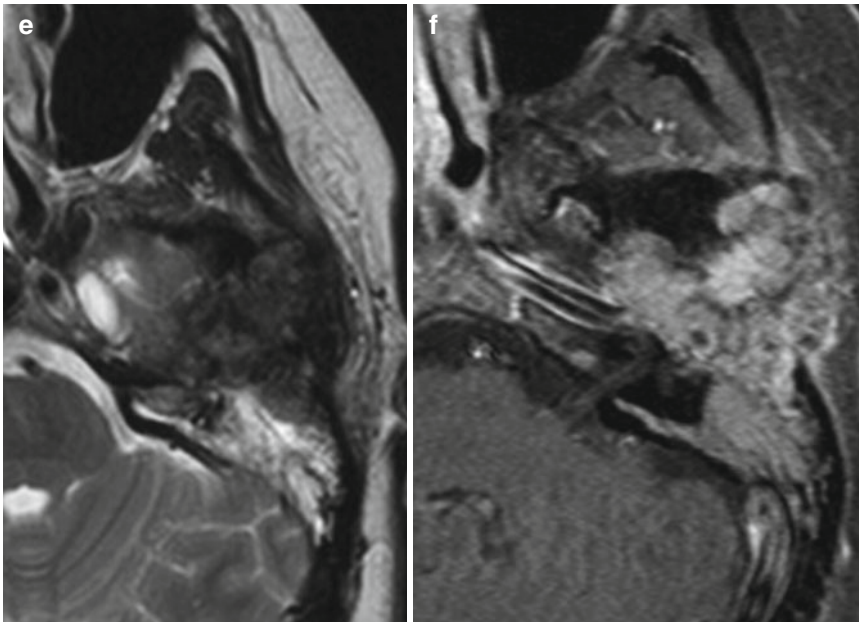

Fig. 8.49 (continued)

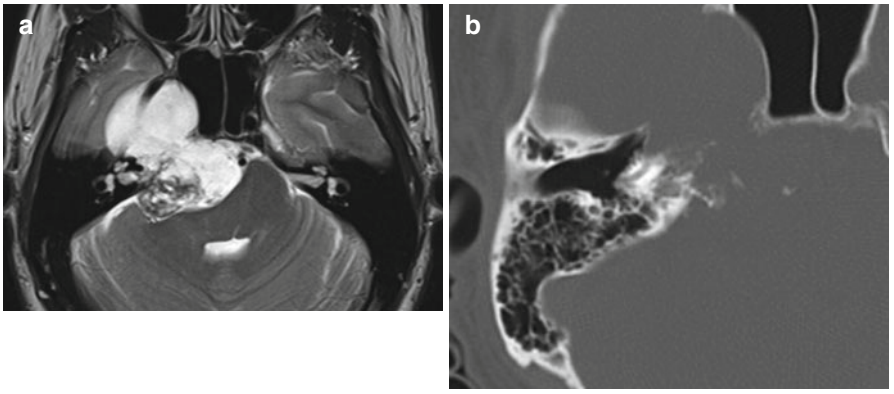

Fig. 8.50 (**a**–**c**) Petrous apex chondrosarcoma. Chondrosarcomas are typically T2 hyperintense lesions that straddle the petrous apex. The presence of the so-called arcs and whorls of calcification, as in this case is a useful but by no means a universal finding. They tend to enhance in a heterogeneous manner. Chordomas (**d**–**g**) are destructive midline central skull base lesions that frequently contain T1 hyperintense hemorrhagic foci (**e**). Shards of destroyed bone can often be seen within them (**d**). They too tend to be fairly hyperintense on T2W imaging and enhance in a heterogeneous fashion. The imaging features of chondrosarcomas and chordomas overlap, and the best way to tell them apart is their location – chondrosarcomas which arise from the petroclival synchondrosis are usually off midline lesions, while chordomas occur in the midline, given their notochordal origin. Very rarely a chondrosarcoma arising from the spheno-occipital synchondrosis may present as a midline lesion indistinguishable from a chordoma

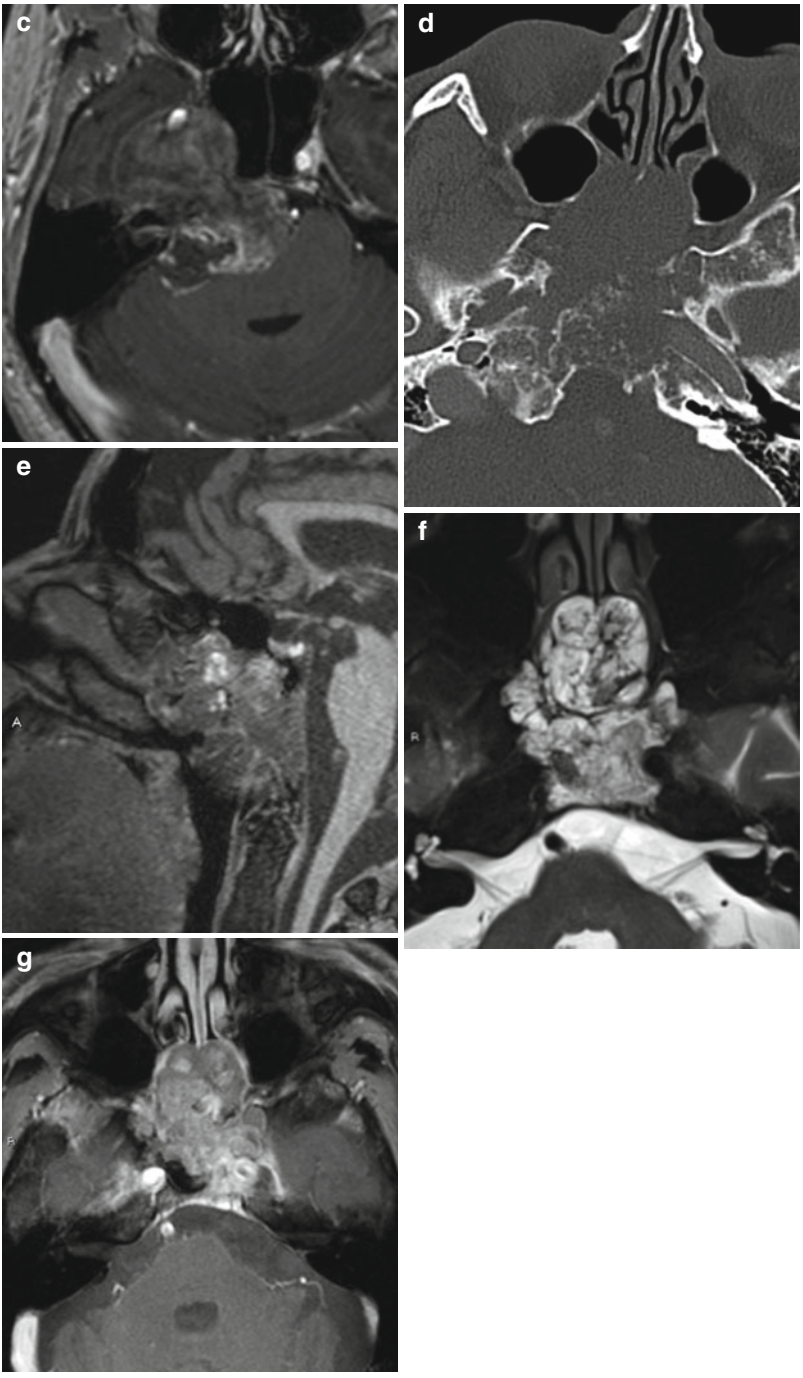

Fig. 8.50 (continued)

Box 8.10. Osseous Skull Base Tumors

Tumor	Key imaging features
Chondrosarcoma	Centered at petroclival fissure, rarely may be midline when origin is from spheno-occipital synchondrosis: curvilinear chondroid calcification typical but not invariable; T2 hyperintense
Chordoma	Destructive almost always midline tumor: contains shards of destroyed bone; T2 hyperintense
Metastasis	Destructive, irregular margins, intense enhancement if primary is hypervascular: may be multiple
Aneurysmal bone cyst	Expansile, multiloculated, blood–fluid levels on MRI
Giant cell tumor	Expansile, multiloculated
Fibrous dysplasia	Expansile, ground glass matrix, may affect multiple bones, heterogeneous enhancement on MR; easier to diagnose on CT

Box 8.11. Jugular Foramen Masses

Tumor	Adjacent bone change	Enhancement	Flow voids	Dural base/tail
Schwannoma	Smooth remodeling	+	None	–
Paraganglioma	Moth-eaten osteolysis	++	+	–
Meningioma	Hyperostosis, sometimes erosion	+	None	+
Metastasis	Irregular destruction	+	Usually none, may be present if from hypervascular primary	_

8.7.6 Jugular Foramen Masses

The most common jugular foramen masses are schwannomas, meningiomas, paragangliomas, and metastases. The two key features that enable differentiation between these lesions are the extent and pattern of enhancement and the changes they produce in the bony walls of the jugular foramen (Box 8.11). Schwannomas enhance homogeneously and produce smooth remodeling of adjacent bone (Fig. 8.51). Meningiomas also enhance homogeneously, may be associated with a broad dural attachment, and induce hyperostosis in the adjacent bone. Hyperostosis is a specific sign for a meningioma (Fig. 8.51). Paragangliomas are hypervascular, enhance intensely and heterogeneously, and are associated with a characteristic pattern of osteolysis (Fig. 8.52). Given the increased vascularity of these tumors, a "salt-and-pepper" appearance – tumor and flow voids of the vascular system – is characteristic on MRI. Metastatic lesions enhance variably and produce aggressive bone destruction (Fig. 8.53).

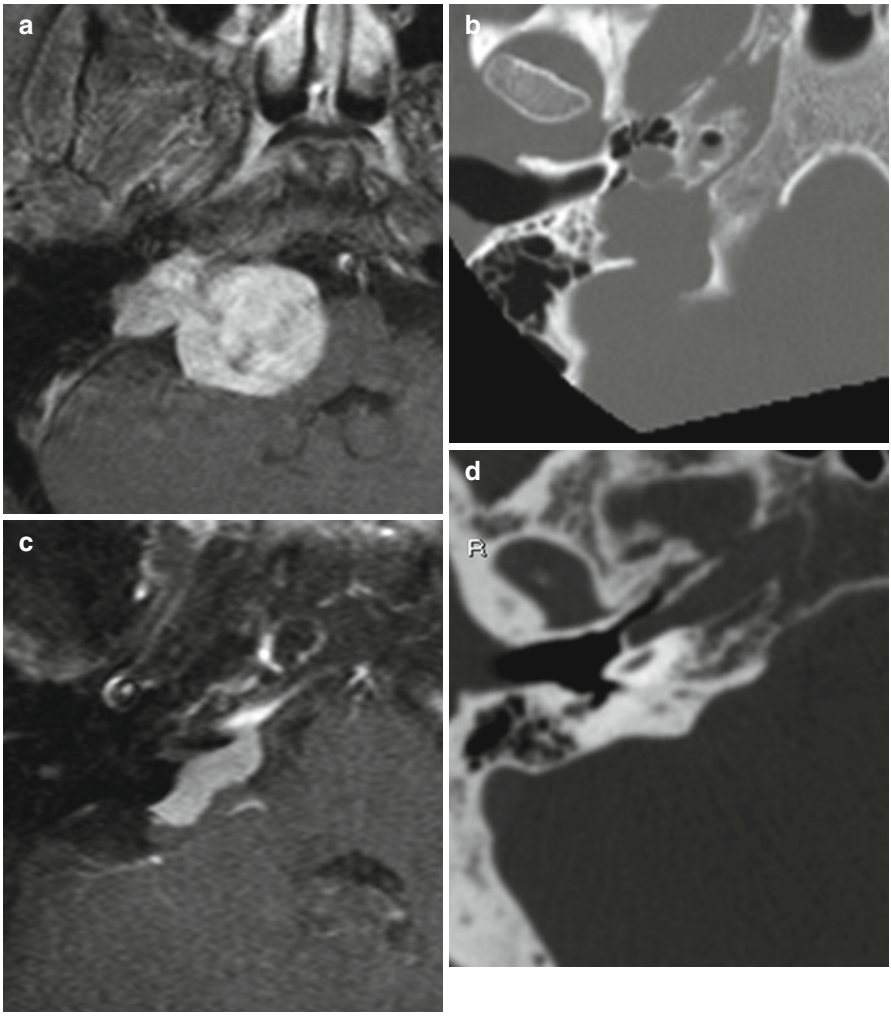

Fig. 8.51 Jugular foramen schwannoma (**a**, **b**) and meningioma (**c**, **d**). Schwannomas of the jugular foramen can arise from cranial nerves 9, 10, or 11. Atypical schwannoma has a lobulated contour, sometimes with a "dumbbell" configuration as it extrudes through the foramen. Note the smooth remodeling of the walls of the foramen in (**b**). Meningiomas demonstrate a broad dural base and may provoke hyperostosis of the underlying bone as shown in image (**d**)

Complete characterization of a jugular foramen mass may require a combination of CT and MR imaging. The contrast-enhanced MR angiogram is often useful in discriminating between paragangliomas and other jugular foramen masses. Due to their hypervascularity, paragangliomas (Fig. 8.52) enhance on dynamic contrast-enhanced MR angiographic images. An enlarged ascending pharyngeal artery supplying these tumors can often be found on cross-sectional imaging. Paragangliomas that arise in the jugular foramen may extend into the middle ear cavity and present

Fig. 8.52 Glomus jugulare. The hallmark of these tumors is the permeative "moth-eaten" pattern of osteolysis that these tumors cause (contrast with schwannomas and meningiomas). These tumors may invade the middle ear by destroying the bone under the hypotympanum, a process sometimes facilitated by the presence of hypotympanic air cells (**b**). The so-called "salt-and-pepper" appearance of these tumors is due to the presence of flow voids, a feature more likely to be seen with larger tumors. Blood supply is derived from the ascending pharyngeal artery, as the external carotid injection from a catheter angiogram shows (**d**)

as a retrotympanic mass. Extension into the middle ear is usually by one of three routes – direct extension, by tracking along the inferior tympanic and mastoid canaliculi and by creeping along hypotympanic air cells. It is important to accurately delineate the extent of these lesions in order to enable optimal surgical planning. Small tumors confined to the jugular foramen, and middle ear may be resected by a

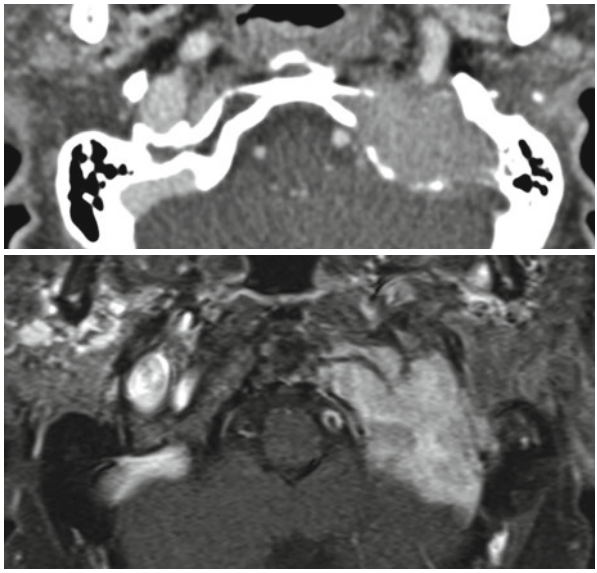

Fig. 8.53 Papillary thyroid carcinoma metastatic to the jugular foramen. The aggressive nature of this lesion is suggested by the extensive bone destruction and infiltration into the adjacent soft tissues

skull base approach. A retrosigmoid approach is required for larger masses which involve the petrous apex or those that extend intracranially. Stereotactic radiosurgery may be employed to treat residual tumors after surgery.

8.8 Miscellaneous Abnormalities

8.8.1 Otosclerosis

Otosclerosis refers to the resorption of the middle endochondral layer of the bone of the otic capsule and its replacement with spongy vascular bone. It is an inherited disorder, common in females, usually encountered in the second and third decades, and characteristically associated with mixed conductive and sensorineural hearing loss. Otosclerosis may be fenestral (confined to the oval window – a process which begins at an embryonic cleft in front of the oval window called the fissula ante fenestram) or retrofenestral (where the bone of the cochlea and vestibule are involved). Retrofenestral otosclerosis is almost always associated with fenestral otosclerosis. The new reactive bone formed at the site of bony resorption impinges upon the stapes and causes fixation of the footplate. This results in conductive hearing loss. The earliest findings of otosclerosis can be extremely subtle and are easily missed (Fig. 8.54). When a history of mixed hearing loss is present, it is important to look for small foci of rarefaction anterior to the oval window. Because the process is frequently bilateral, the contralateral ear must be carefully scrutinized. The bone around the cochlea and vestibule should normally be uniformly hyperdense, and any areas of rarefaction must be viewed with suspicion. The bony demineralization usually begins parallel to the basal turn of the cochlea, resulting in the so-called

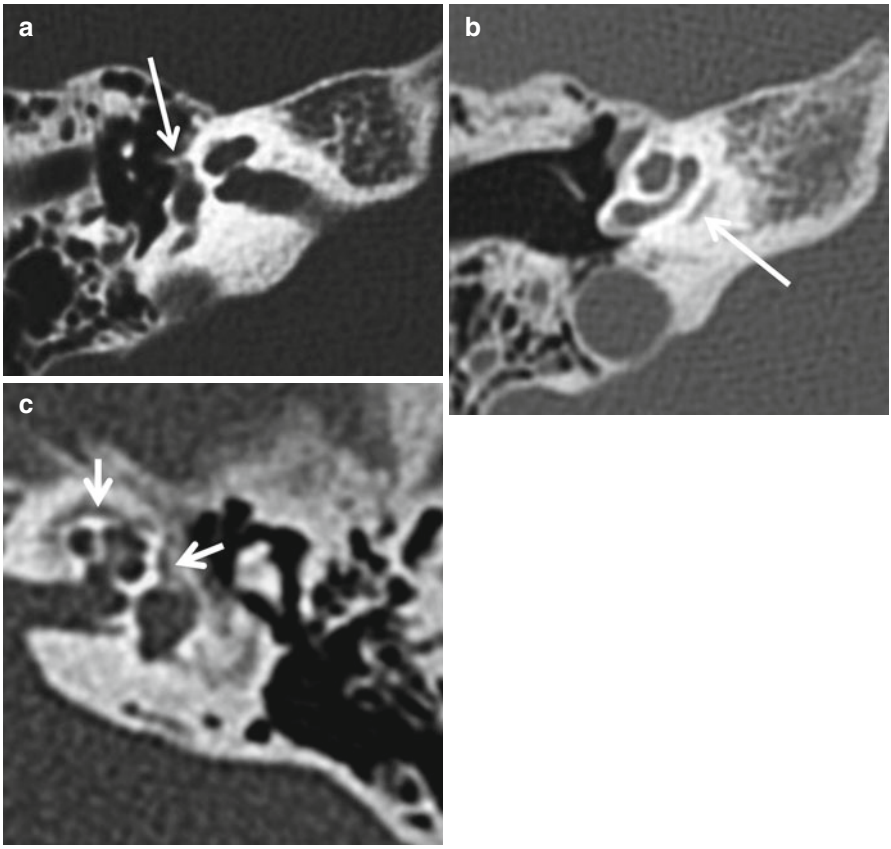

Fig. 8.54 Fenestral (**a**) and retrofenestral otosclerosis (**b**, **c**). In (**a**), note the subtle focus of demineralization anterior to the oval window, the location of the embryonic fissula ante fenestram. In (**b**), a band of demineralization is present parallel to the basal cochlear turn, the "fourth" turn sign. In (**c**), the extensive demineralization around the cochlea produces the "Halo" sign (*arrows*)

"fourth-turn" sign. A complete halo of demineralization may then appear. Otosclerosis can be strikingly symmetric, perhaps accounting for why it is missed fairly often. Otosclerosis may be diffuse, and the extensive demineralization can mimic other entities such as osteogenesis imperfecta, Paget's disease, or syphilis. Fenestral otosclerosis is treated with a stapedotomy with removal of the stapes superstructure and placement of a prosthesis.

8.8.2 Superior Semicircular Canal Dehiscence (SSSD)

Dehiscence of the SCC is a condition that can result in a wide variety of ontological symptoms. Most commonly, patients present with noise-induced vertigo (Tullio's phenomena) and nystagmus (Hennebert's sign). The absence of bone overlying the SCC results in the formation of a third window. The etiology of SSCD is unclear, but a plausible explanation is that long-standing intracranial hypertension causes

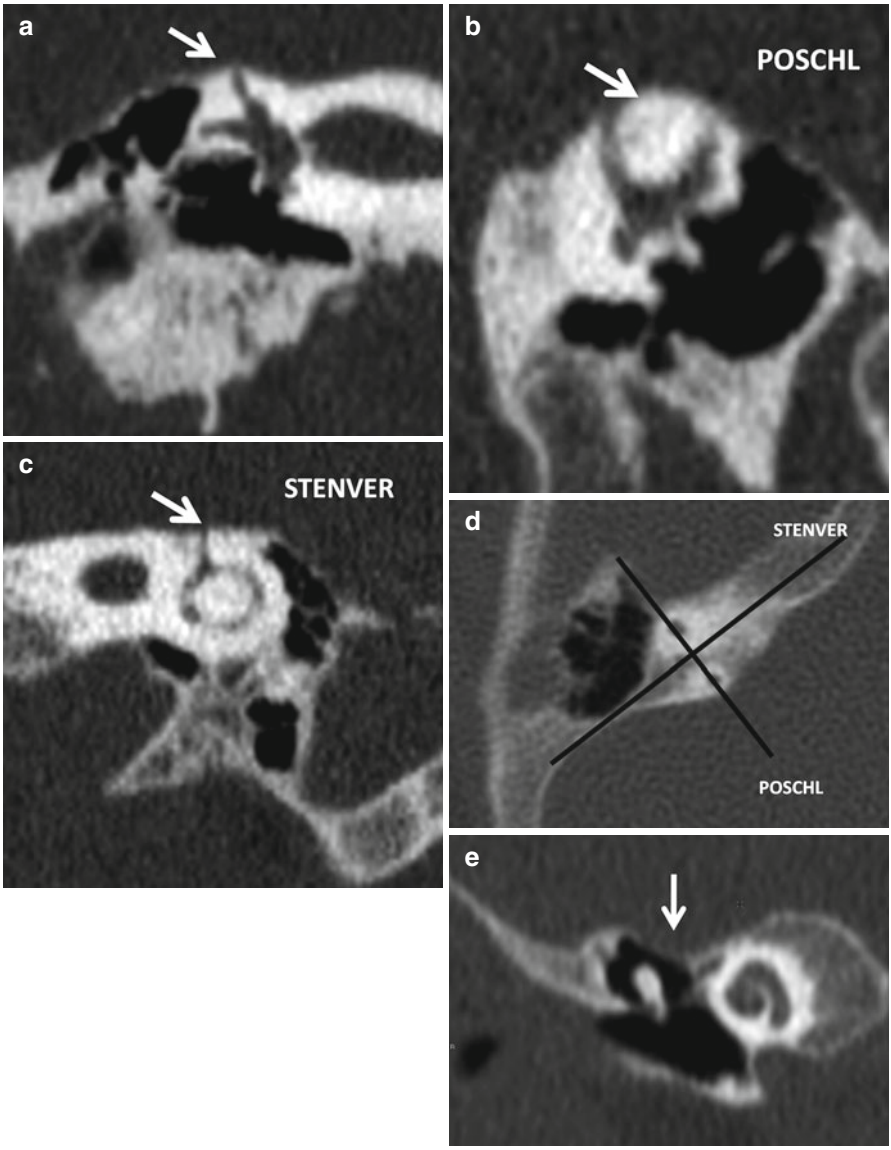

Fig. 8.55 Superior semicircular canal dehiscence. In (**a**), the roof of the SCC appears thin. Dehiscence of the canal roof is confirmed on the transverse and longitudinal oblique reformatted images obtained along the planes of Pöschl and Stenver (**b**–**d**). In (**e**), note the thinning of the tegmen tympani, a finding that frequently accompanies canal dehiscence, leading some to believe that the entity is perhaps caused by chronically elevated intracranial pressure

thinning of the bone exposing the membranous canal. This is supported by the frequent association with a thin tegmen tympani. The best way to confirm bony dehiscence over the SSC is to perhaps obtain oblique reformatted CT images in two orthogonal planes so as not to mistake partial volume averaging defects for small foci of dehiscence (Fig. 8.55).

8.8.3 Cerebrospinal Fluid Leaks

Congenital or acquired defects in the skull base can permit the egress of cerebrospinal fluid into the sinonasal cavities and middle ear, resulting in rhinorrhea and otorrhea. This predisposes patients to recurrent attacks of meningitis. A temporal bone defect can present with rhinorrhea as CSF can leak into the nasopharynx through the eustachian tube. Acquired skull base defects may arise as a consequence of trauma, surgery, invasive tumors, or erosion from cholesteatoma. Examples of congenital skull base defects include those through which meningoencephaloceles protrude and rarely persistent embryonic defects such as the Sternberg's canal (the lateral craniopharyngeal canal that lies medial to the foramen rotundum in the greater sphenoid wing) and Hyrtl's fissure (cleft-like defect between the labyrinth and jugular bulb).

Spontaneous CSF leaks are usually observed in middle-aged overweight women. They are believed to occur as a consequence of "aggressive" arachnoid granulations that burrow into the delicate bone that overlies the sphenoid sinus (especially over pneumatized pterygoid recesses), the middle ear cavity, and mastoid air cells (Fig. 8.56). They may be associated with small meningoencephaloceles.

The first step in the evaluation of suspected CSF leak consists of analyzing the draining fluid for beta-2 transferrin, a protein that is specific for CSF. If the study is positive, the next step is to proceed to a high-resolution CT scan. Important places to look for bone defects are the posterior walls of the frontal sinuses, the cribriform plates and fovea ethmoidales, the greater sphenoid wings, and the tegmen tympani and mastoideum. If the study demonstrates a single skull base defect, no further evaluation is necessary. If the defect associated with soft tissue that is contiguous with the cranial cavity, an MRI needs to be performed to exclude a meningoencephalocele (Fig. 8.56). When multiple defects are encountered, which is not an uncommon scenario, a CT cisternogram is indicated. After obtaining a preprocedure CT of the skull base, about 10–12 mL of a water-soluble nonionic contrast medium is administered intrathecally in the lower lumbar spine and transported to the cranial cavity by placing the patient in a Trendelenburg position. An axial high-resolution CT of the skull base is then acquired from which coronal and sagittal reformations are obtained. Contrast material may be seen traversing the defect (Fig. 8.56). Alternatively, the contents of the sinonasal cavity or middle ear may demonstrate an increase in density indicating that leak has occurred. If no leak is seen, it is worthwhile to have the patient perform a Valsalva maneuver and obtain a direct coronal scan. Rarely, these examinations may fail to reveal a cause of the leak. In such circumstances, there are two options. One is to proceed with intrathecal fluorescein injection followed by endoscopy. The other option is to perform a radionuclide cisternogram with Indium 111 DTPA. Pledgets are placed in the nose and ears before the procedure. Twenty-four hours after the procedure, the pledgets are removed and measured for radioactivity. The presence of a certain level of activity indicates that a leak has occurred. Obviously, this procedure involves substantial patient discomfort and does not provide specific anatomic information.

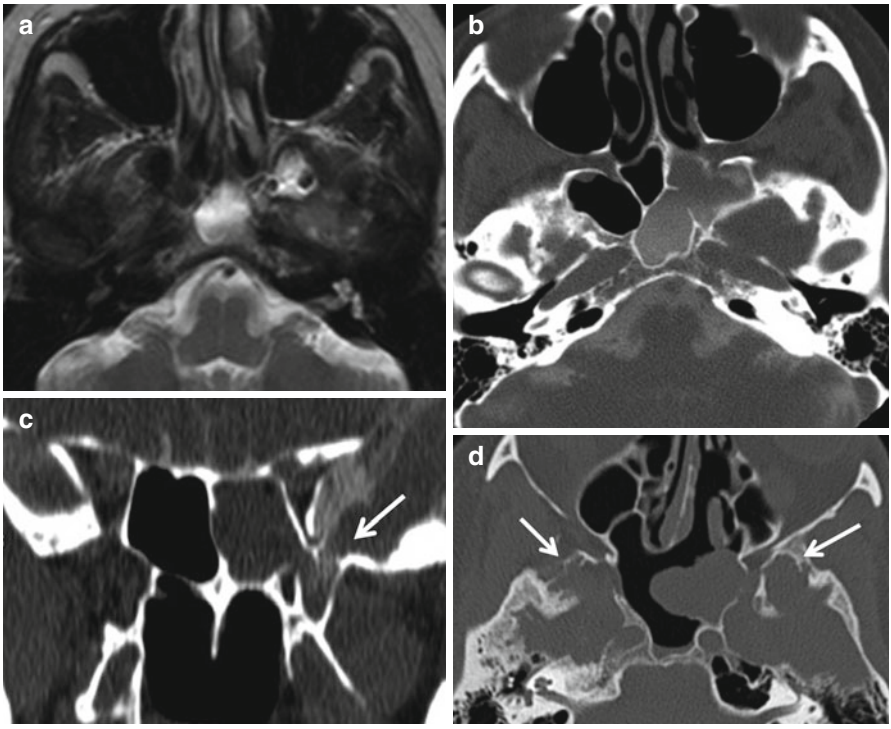

Fig. 8.56 Spontaneous CSF rhinorrhea in a middle-aged female patient. On the T2W MR image (**a**), the sphenoid sinus is filled with CSF intensity fluid. Egress of iodinated contrast into the pterygoid recess sphenoid sinus through a defect in the lateral sinus wall is evident on the CT cisternogram images (**b**, **c**). In (**d**), note erosive changes in the greater sphenoid wings, representing unusually prominent "aggressive" arachnoid granulations (*arrows*)

8.9 The Surgeon's Perspective

The most common otologic complaint among our patients is hearing loss. After taking a careful history, the physical exam is critical in narrowing the differential diagnosis. One of the most important clinical factors is whether the hearing loss is sensorineural (SNHL, problem in the cochlea, cochlear nerve, brainstem, brain) or conductive (CHL, ear canal, eardrum, middle ear, ossicles). The tuning fork exam is indispensible in making this determination, followed by our careful physical exam of the ears under binocular microscopy. Otolaryngologists routinely obtain comprehensive audiometry prior to any imaging studies, and the otolaryngologist should write on the imaging request whether the patient has a conductive or sensorineural hearing loss.

In *very* general terms, a conductive hearing loss may warrant CT imaging because the pathology is most often located in the middle ear or ear canal. It is important to

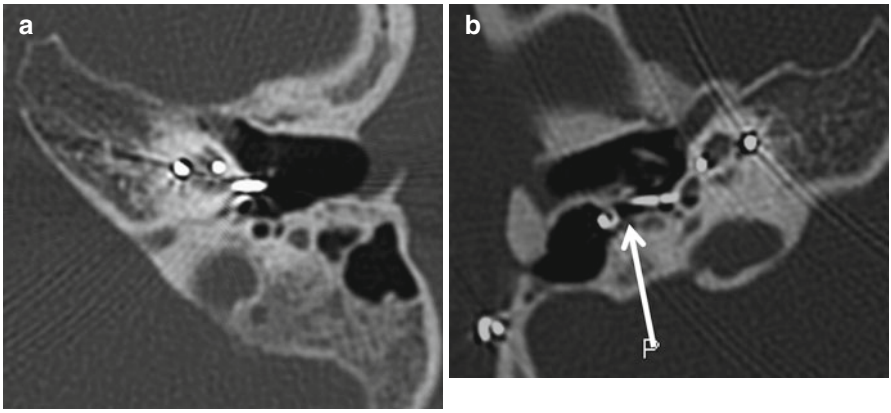

Fig. 8.57 Cochlear implant. The electrode array is introduced into the cochlea through a cochleostomy made anterior to the round window (**a**). Cochlear implants in general present a contraindication to MR imaging. MRI can be performed if the magnet in the implant can be turned off, but the artifact that the implant gives rise to cannot be eliminated. It is best to perform MRI in patients with implants only if indicated and in magnets of field strengths of 1.5 T or lower. In (**b**), note that the electrode wire is fractured (*arrow*)

look beyond the conventional conduction pathway (EAC, tympanic membrane, ossicles, oval window) for dehiscence of the superior semicircular canal, which can present with conductive hearing loss, and is best imaged by CT.

In contrast, sensorineural hearing losses are most commonly imaged by MRI. Indications for MRI in the setting of SNHL include the evaluation of a young child with SNHL, or the evaluation of a patient with an asymmetric SNHL for retrocochlear pathology (e.g., vestibular schwannoma, meningioma, or other CPA neoplasm). When to order an MRI in a patient with asymmetric hearing loss is a matter of clinical judgment based on numerous factors including the history (Does the patient shoot guns – right or left handed? Unilateral tinnitus? Family history of unilateral hearing loss?), physical exam, and audiometric data (degree of asymmetry, speech testing parameters, acoustic reflex testing, presence of speech rollover). There are no clear-cut guidelines mandating imaging for patients with asymmetrical sensorineural hearing loss. The decision to pursue imaging is a purely clinical one, and MRI with and without contrast is the best study.

For patients with severe-profound sensorineural hearing loss not benefited by conventional hearing amplification/hearing aids, a cochlear implant (Fig. 8.57) may greatly improve hearing and quality of life. High-resolution CT scan or MRI preoperatively can investigate the potential etiology of the hearing loss and plan the surgical approach. CT is better to delineate the bony anatomy of the mastoid air cell system, facial recess, round window area, inner ear, and cochlea (e.g., for presence of cochlear hypoplasia, incomplete partition, enlarged vestibular aqueduct, labyrinthine ossification), whereas MRI does not deliver radiation and can still detect cochlear abnormalities and an enlarged vestibular aqueduct. Which study, CT or MRI, in the evaluation of severe-profound SNHL remains a matter of clinician

preference. Findings on imaging that would absolutely contraindicate cochlear implantation would include severe cochlear dysplasia, absence of the cochlear nerve, and severe ossific labyrinthitis.

To evaluate a child with congenital aural atresia for surgery to open the ear canal and restore the natural sound conducting mechanism of the ear canal and middle ear, CT imaging is best to delineate the development of the ossicular chain, the course of the facial nerve, pneumatization of the mastoid and middle ear, and any associated inner ear anomalies. CT imaging is critical in this evaluation, along with a comprehensive audiogram with air and bone conduction testing to determine inner ear function.

Any child with an unexplained conductive hearing loss should undergo CT imaging. An "explained" conductive hearing loss would include fluid in the middle ear (chronic otitis media with effusion) or tympanic membrane perforation, neither of which requires imaging. In the presence of a normal physical exam and CHL, pathologies to investigate radiologically include a congenital cholesteatoma that cannot be seen through the tympanic membrane, congenital stapes gusher, enlarged vestibular aqueduct (which can give a conductive or mixed [conductive and SNHL] hearing loss), congenital middle ear anomaly (e.g., absent oval window, single stapes crus, persistent stapedial artery), or other middle ear mass that cannot be seen on physical examination.

Any retrotympanic mass, adult or child, warrants imaging, and the typical recommendation is to start with noncontrasted CT. MRI may also be necessary for a jugular bulb paraganglioma, facial nerve schwannoma or hemangioma, or other neoplastic process whose extent or properties are not adequately evaluated by CT.

Chronic otitis media with cholesteatoma does not necessarily require imaging, but many practitioners do obtain CT imaging to evaluate the extent of cholesteatoma and its possible complications (e.g., horizontal semicircular fistula). Most practitioners favor CT imaging on any patient undergoing revision chronic ear surgery with residual or recurrent cholesteatoma or if the clinical picture is suspicious for a complication. While MRI is superior to evaluate intracranial extension, this complication is rare, and CT is typically sufficient. CT helps plan surgical approach (transcanal or postauricular) and may inform decisions about staging the operation, taking the canal wall down or leaving it up, and whether to perform ossicular reconstruction and what that reconstruction might entail, depending on the status of the stapes bone and configuration/erosion of the ossicles.

Ossicular prostheses come in many different shapes, sizes, materials, and configurations and may be placed alongside autologous cartilage. Clinical history, if available, is very helpful in the radiologic interpretation and understanding of the reconstructed middle ear.

Evaluation of the ossicular chain is best accomplished by CT. Cholesteatoma or severe eardrum retraction can erode the ossicular chain and cause a conductive hearing loss. Many times in the setting of chronic otitis media, otolaryngologists are able to see in the office under the microscope the etiology for ossicular erosion, but occasionally, patients have had surgery elsewhere and the status of the ossicles is unknown. A CT helps identify the ossicles, any previous attempts at ossicular

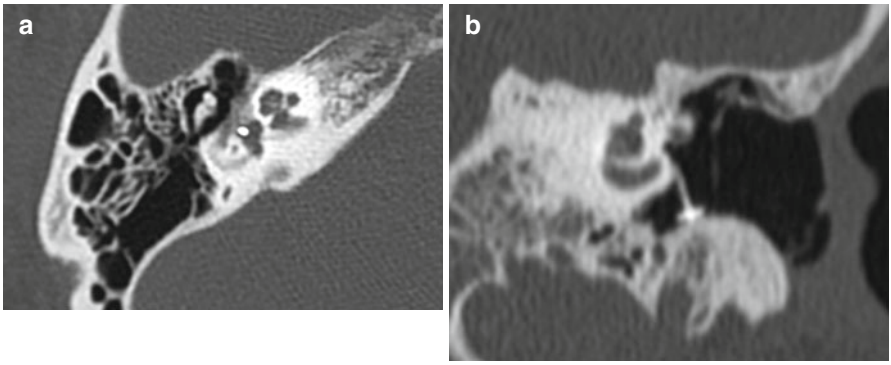

Fig. 8.58 Displaced ossicular prostheses. In (**a**), the stapes prosthesis has penetrated the vestibule, while in (**b**), the TORP lies in the hypotympanum

reconstruction, or any prostheses that have been placed. If the incus is eroded, a PORP (partial ossicular replacement prosthesis) is often used. Made of hydroxyapatite or titanium, PORPs are placed on the capitulum of stapes bone and extend to the tympanic membrane, usually with autologous cartilage placed on the platform of the PORP just under the tympanic membrane (Fig. 8.58).

If the incus and stapes superstructure are eroded, the otolaryngologist will place a TORP (total ossicular replacement prosthesis). Made of hydroxyapatite or titanium, this prosthesis spans the distance between the stapes footplate/oval window and tympanic membrane, also with cartilage on the platform of the prosthesis, just under the eardrum.

If just the incudostapedial joint is eroded, a number of reconstructive options are available, ranging from hydroxyapatite cement to bridge the gap between the incus and stapes, to fluoroplastic, hydroxyapatite, or titanium prostheses of various shapes and sizes.

For patients undergoing stapedectomy for otosclerosis, the prosthesis may be a shepherd's crook cinched around the long process of the incus heading down to the oval window and ending just inside the vestibule or may be a bucket handle prosthesis where the lenticular process of the incus rests in a bucket with the shaft coursing down to the oval window and just peeking into the vestibule.

Otolaryngologists are often faced with the incidentally discovered petrous apex lesion. Evaluation of petrous apex lesions generally benefit from both CT and MR imaging – to evaluate the properties of the lesion (MRI) and its relationship to the surrounding bone and bony structures (CT). Many petrous apex lesions are "leave me alone" lesions – nothing to do but reassure the patient (e.g., asymmetrically pneumatized petrous apex, bone marrow, fluid in a petrous apex air cell). We often follow petrous apex lesions with serial CT scans to document bony expansion, erosion, interval increase in size, and loss of bony septae within the air cells.

An acquired or slowly progressive conductive hearing loss in an adult with a normal physical exam typically does not require imaging. A presumptive diagnosis of fenestral otosclerosis is made, and the patient is offered a middle ear exploration

with possible stapedectomy. If the acoustic reflexes are normal or if, at the time of middle ear exploration, the stapes bone is found to be perfectly mobile, the diagnosis of superior semicircular canal fistula must be entertained; CT is the best imaging modality to investigate.

Evaluating the patient with tinnitus requires taking a careful history and physical examination and includes comprehensive audiometry. Depending on the clinical picture, an imaging study may or may not be indicated. High-pitched, nonpulsatile binaural tinnitus from presbycusis, noise exposure, or accompanied by a high-frequency SNHL needs no imaging. Pulse-synchronous tinnitus often does require an imaging study, and recent investigations have proposed CT/CT angiogram as the study of choice. When patients hear their pulse in their ear, especially if the clinician, too, can hear the pulsing ("objective tinnitus"), the clinician often suspects some organic pathology – dural arteriovenous malformation, high-riding jugular bulb, dehiscence of the sigmoid sinus arterial dissection, carotid–cavernous fistula, or jugular/carotid/sigmoid diverticulum. CT/CTA remains a very good initial study; MRI/MRA may also make the diagnosis (but may not diagnose dehiscence of the sigmoid sinus unless the neuroradiologist is looking for it). Formal four-vessel angiography is the gold standard imaging study.

In summary, the otolaryngologist must give important clinical information to the neuroradiologist with every imaging study ordered. Whether the patient has conductive versus sensorineural hearing loss has implications for the study of choice and for the specific structures on which to focus. Laterality (which ear), clinical symptoms and clinical suspicions should be imparted to the neuroradiologist so that a "shotgun approach" is avoided. Detailed knowledge of the intricate temporal bone anatomy is indispensible when reading CT and MR images of the temporal bone.

Further Reading

Aikele P, Kittner T, Offergeld C, Kaftan H, Hüttenbrink KB, Laniado M (2003) Diffusion-weighted MR imaging of cholesteatoma in pediatric and adult patients who have undergone middle ear surgery. Am J Roentgenol 181(1):261–265

Baráth K, Huber AM, Stämpfli P, Varga Z, Kollias S (2011) Neuroradiology of cholesteatomas. Am J Neuroradiol 32(2):221–229

Caldemeyer KS, Mathews VP, Azzarelli B, Smith RR (1997) The jugular foramen: a review of anatomy, masses, and imaging characteristics. Radiographics 17(5):1123–1139

Kennedy RJ, Shelton C, Salzman KL, Davidson HC, Harnsberger HR (2004) Intralabyrinthine schwannomas: diagnosis, management, and a new classification system. Otol Neurotol 25(2):160–167

Krishnan A, Mattox DE, Fountain AJ, Hudgins PA (2006) CT arteriography and venography in pulsatile tinnitus: preliminary results. Am J Neuroradiol 27(8):1635–1638

Lloyd KM, DelGaudio JM, Hudgins PA (2008) Imaging of skull base cerebrospinal fluid leaks in adults1. Radiology 248(3):725–736

Moore KR, Harnsberger HR, Shelton C, Davidson HC (1998) 'Leave me alone' lesions of the petrous apex. Am J Neuroradiol 19(4):733–738

Morimoto AK, Wiggins RH III, Hudgins PA, Hedlund GL, Hamilton B, Mukherji SK, Harnsberger HR (2006) Absent semicircular canals in CHARGE syndrome: radiologic spectrum of findings. Am J Neuroradiol 27(8):1663–1671

Raghavan P, Mukherjee S, Phillips CD (2009) Imaging of the facial nerve. Neuroimaging Clin N Am 19(3):407

Shonka DC Jr, Livingston WJ III, Kesser BW (2008) The Jahrsdoerfer grading scale in surgery to repair congenital aural atresia. Arch Otolaryngol Head Neck Surg 134(8):873

Stone JA, Mukherji SK, Jewett BS, Carrasco VN, Castillo M (2000) CT evaluation of prosthetic ossicular reconstruction procedures: what the otologist needs to know1. Radiographics 20(3):593–605

Wiggins RH III, Harnsberger HR, Salzman KL, Shelton C, Kertesz TR, Glastonbury CM (2006) The many faces of facial nerve schwannoma. Am J Neuroradiol 27(3):694–699

Witte RJ, Lane JI, Driscoll CL, Lundy LB, Bernstein MA, Kotsenas AL, Kocharian A (2003) Pediatric and adult cochlear implantation1. Radiographics 23(5):1185–1200

Yeakley JW, Jahrsdoerfer RA (1996) CT evaluation of congenital aural atresia: what the radiologist and surgeon need to know. J Comput Assisted Tomogr 20(5):724

Sinonasal Cavities

9

Prashant Raghavan, Mark J. Jameson, Max Wintermark, and Sugoto Mukherjee

9.1 Anatomy and Physiology

9.1.1 Nose and Nasal Cavity

The bony skeleton of the nose is formed by the nasal bones and the nasal processes of the maxillae. The nasal septum is comprised of the septal cartilage anteriorly, the vomer posteroinferiorly and the perpendicular plate of the ethmoid bone superiorly. The Kiesselbach's/Little's area is located in the anterior/inferior septum, and this is where branches of the sphenopalatine, greater palatine, and facial arteries anastomose; it is the most common site of epistaxis.

The piriform aperture is the anterior bony opening of the nasal cavity. The posterior choana is the posterior opening, divided in the midline by the vomer.

The roof of the nasal cavity is formed by the cribriform plate of the ethmoid bone. The floor is formed anteriorly by the palatine processes of the maxilla and posteriorly by the horizontal processes of the palatine bones.

Three meati (spaces) are present along the lateral wall of the nasal cavity lateral to the superior, middle, and inferior turbinates. They contain the sites of drainage of the paranasal sinuses.

9.1.2 Paranasal Sinuses

There are three or four turbinates, designated as supreme (variable), superior, middle, and inferior. The inferior turbinate is a separate bone, while the other three are parts of the ethmoid bone. The middle turbinate is attached to the lateral nasal wall by the basal lamella, which separates the anterior and posterior ethmoid air cells. The space between the basal lamella and the ethmoid bulla is the sinus lateralis or suprabullar recess (Fig. 9.1).

The lateral nasal wall is comprised of two ostiomeatal units. The anterior ostiomeatal unit consists of the frontal sinus ostium, frontal recess, maxillary sinus

P. Raghavan et al., *Manual of Head and Neck Imaging*,
DOI 10.1007/978-3-642-40377-4_9, © Springer-Verlag Berlin Heidelberg 2014

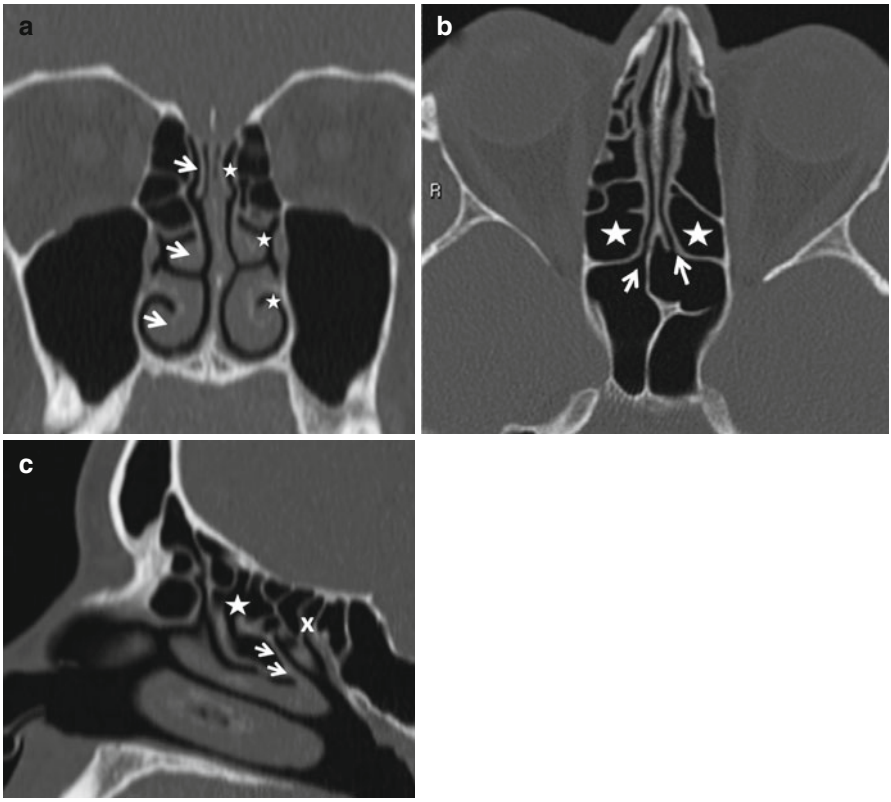

Fig. 9.1 (**a**) The 3 *arrows* point to the superior, middle, and inferior turbinates. The 3 *asterisks* indicate the corresponding meati. (**b**) The *arrows* point to the ostia of the sphenoid sinus, which open into the sphenoethmoidal recesses. The *asterisks* indicate the posterior ethmoid air cells. (**c**) The *arrows* indicate the basal or ground lamella of the middle turbinate, which separates the anterior (*asterisk*) from the posterior ethmoid air cells (*x*)

ostium, infundibulum, and middle meatus. The posterior ostiomeatal unit is comprised of the sphenoid sinus ostium, sphenoethmoidal recess, and the superior meatus (Fig. 9.1).

The uncinate process is a sickle-shaped sheet of bone arising from the lateral nasal wall and directed superiorly. Lateral to the superior free edge is the infundibulum. The ethmoid bulla is the largest anterior ethmoid air cell. Its medial wall forms the lateral wall of the infundibulum. The infundibulum is the air passage bounded medially by the uncinate process and laterally by the ethmoid bulla; it connects the maxillary sinus ostium to the middle meatus. The hiatus semilunaris is the crescentic gap between the free edge of the uncinate process and the ethmoid bulla (Fig. 9.2).

The frontal recess is the funnel-like drainage pathway of the frontal sinus. The term "frontonasal duct" is now avoided as no discrete ductal structure exists. The frontal recess drains into the anterior part of the middle meatus and may be divided into a superior compartment that lies below the frontal sinus ostium in the floor of

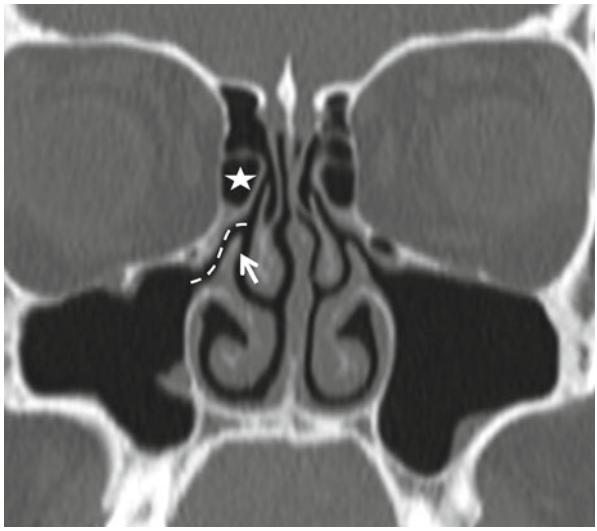

Fig. 9.2 The *curved dashed arrow* represents the infundibulum. Its medial opening is the hiatus semilunaris. It is bounded by the uncinate process (*arrow*) medially and the bulla ethmoidalis (*asterisk*) laterally

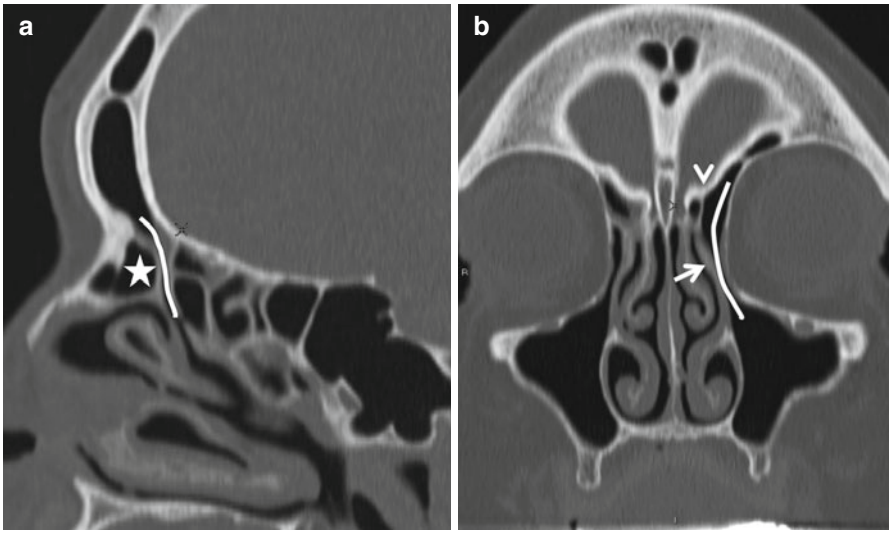

Fig. 9.3 The frontal sinus drainage pathway. The *curved lines* represent the frontal recess. An agger nasi (*asterisk*) cell is seen anterior to the frontal recess in (**a**). In (**b**), note that the uncinate process (*arrow*) is attached superiorly to the fovea ethmoidalis (*arrowhead*). This results in the frontal recess opening into the infundibulum

the sinus and an inferior compartment which either opens into the infundibulum (if the uncinate process is directed towards the skull base) or continues into the middle meatus (if the uncinate process is attached to the lamina papyracea) (Fig. 9.3).

The fovea ethmoidalis is the roof of the ethmoid cavity. The cribriform plates are the portion of the ethmoid bone that forms the roof of the nasal cavity medial to the

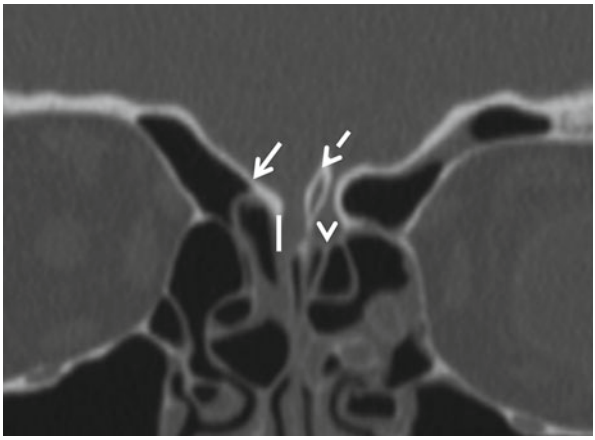

Fig. 9.4 Roof of the nasal cavity. The *arrow* points to the fovea ethmoidalis and the *arrowhead* to the cribriform plate. The *vertical line* represents the depth of the floor of the anterior fossa. The Keros system classifies this as type 1 where the depth is 1–3 mm, type 2 where the depth is 4–7 mm, and type 3 where the depth is between 8 and 11 mm. The greater the depth, the greater the potential for injury during endoscopic surgery. The cribriform plates may be dehiscent, as is the case on the right. The *dashed arrow* indicates the crista galli, to which the falx cerebri is attached. Occasionally the crista may be pneumatized and rarely contain a mucocele

Box 9.1. Paranasal Sinus Drainage

Frontal sinus	Through frontal recess into middle meatus
Anterior ethmoid cells	Middle meatus, mainly into infundibulum
Posterior ethmoid cells	Sphenoethmoidal recess (superior meatus)
Maxillary sinus	Through infundibulum into middle meatus
Sphenoid sinus	Sphenoethmoidal recess (superior meatus)

fovea ethmoidalis. They are perforated by the foramina of the olfactory nerves. The crista galli is a vertically oriented midline ridge of bone arising from the cribriform plates and attaching to the falx cerebri (Fig. 9.4). The anterior and posterior ethmoid air cells are separated by the basal lamella of the middle turbinate. The lamina papyracea is the gracile medial wall of the orbit. The agger nasi designates the most anterior ethmoid cells that form due to pneumatization into the lacrimal bone and the frontal process of the maxillae. They may be anterior, inferior, or posterolateral to the frontal recess and may encroach upon it (Fig. 9.3).

The sphenoethmoidal recess is the site of drainage of the sphenoid and posterior ethmoid air cells (Fig. 9.1).

A summary of sinus drainage is provided in Box 9.1.

Box 9.2. Anatomic Variations

- Nasal septal deviation
- Middle turbinate
  - Paradoxical curvature
  - Concha bullosa
- Uncinate process
  - Pneumatization (uncinate bulla)
  - Variable attachment of free edge to lamina papyracea (atelectatic)/fovea ethmoidalis
- Giant ethmoid bulla
- Lamina papyracea dehiscence
- Variations in ethmoid pneumatization
  - Haller cells
  - Onodi cells
  - Supraorbital cells
  - Frontal cells
  - Agger nasi cells
- Accessory maxillary sinus ostia
- Cribriform plates
  - Variability in depth
  - Dehiscence
- Sphenoid sinus
  - Attachment of septum to lateral wall adjacent to the ICA
  - Lateral wall dehiscence
  - Anterior clinoid process pneumatization

9.1.3 Anatomic Variations of Clinical Importance

The commoner anatomic variations are listed in Box 9.2.

The *nasal septum* is deviated in 25–30 % of the population. Marked deviation, especially with an osteocartilaginous spur, may compromise the middle meatus and predispose to recurrent sinonasal inflammation/infection (Fig. 9.5).

The *middle turbinate* may be completely pneumatized (concha bullosa) or pneumatized only within its vertical portion (lamellar concha or intralamellar air cell). Concha bullosae may become inflamed and rarely transform into a mucocele. In addition to conchae, paradoxically curved middle turbinates may also crowd the middle meatus leading to maxillary sinus obstruction (Fig. 9.6).

The free edge of the *uncinate process* may attach to the lamina papyracea (atelectatic uncinate) resulting in a chronically obstructed maxillary sinus ostium and hypoplasia of the maxillary sinus with associated descent of the orbital floor (silent sinus syndrome) (Fig. 9.7). If not recognized preoperatively, the plunging roof of the maxillary sinus may be inadvertently breached by the surgeon. The uncinate process may attach superiorly to the fovea ethmoidalis, in which case excessive traction during surgery may result in violation of the anterior cranial fossa and a CSF leak. The uncinate

Fig. 9.5 Nasal septal deviation. Septal deviation may predispose one to recurrent sinus inflammatory disease. The sharp leftward deviation in this case has resulted in hypoplasia of the middle turbinate and uncinate process and consequently a narrow infundibulum

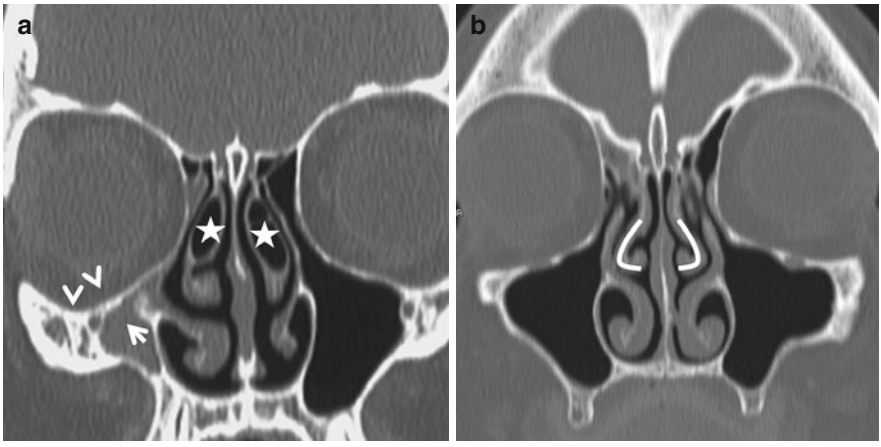

Fig. 9.6 (**a**) Concha bullosa. Pneumatization of the middle turbinates (concha bullosa, *asterisks*) is a fairly common anatomic variation and when substantial, can narrow the middle meatus. In (**a**), note that the right uncinate process (*arrow*) is deviated laterally (atelectatic) closing off the infundibulum, resulting in an obstructed, hypoplastic maxillary antrum. The right orbital floor has descended (*arrowheads*) and is at risk for injury during surgery. When accompanied by enophthalmos, this entity is referred to as the silent sinus syndrome. In (**b**), note that the convexity of the middle turbinates is directed laterally (*curved lines*) rather than towards the midline (paradoxical curvature). This can theoretically compromise the middle meatus

process may also be pneumatized (uncinate bulla), which encroaches upon the infundibulum and impedes frontal and anterior ethmoid sinus drainage (Fig. 9.7).

A *giant ethmoid bulla* is an unusually large ethmoidal bulla that compromises the infundibulum (Fig. 9.7).

Haller cells are infraorbital ethmoidal air cells. They may narrow the infundibulum and predispose patients to recurrent maxillary sinusitis (Fig. 9.8).

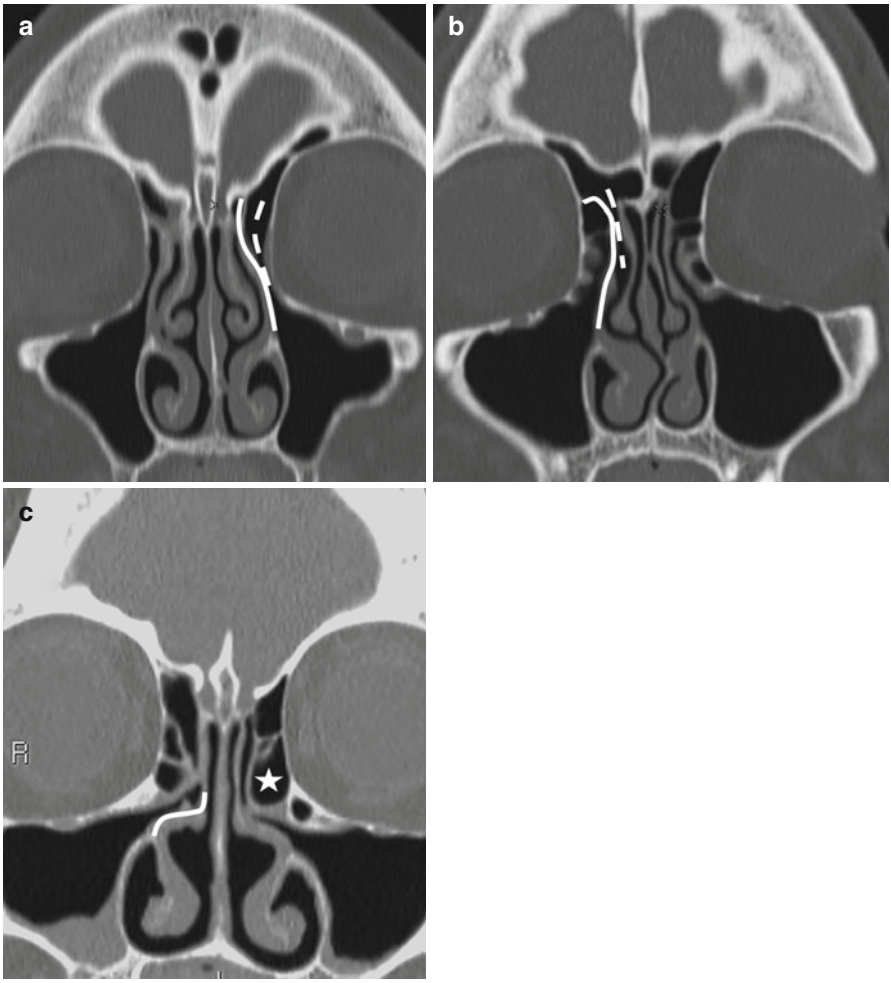

Fig. 9.7 Variations in uncinate process (UP) attachment. In (**a**), the uncinate process is attached superiorly to the fovea ethmoidalis (*continuous line*), resulting in the frontal recess opening into the infundibulum (*dashed line*). This configuration means that infundibular obstruction can result in simultaneous disease in the frontal, maxillary, and anterior ethmoid air cells. In (**b**), the UP is attached to the lamina papyracea (*continuous line*), resulting in the frontal recess (*dashed line*) draining into the middle meatus. This implies that the frontal and anterior ethmoid sinus drainage pathways are separated. Also, traction upon the UP during surgery may result in injury to the delicate lamina. In (**c**), the *continuous line* indicates attachment of the UP to the middle turbinate. The *asterisk* indicates a large ethmoid bulla, likely the cause of the UP being rotated medially

Onodi cells are the most posterior ethmoid air cells and are intimately related to the optic canal; they can completely surround the optic nerve, increasing the risk of optic nerve injury at surgery. Onodi cell mucoceles may compress the optic nerve (Fig. 9.8).

The *sphenoid sinus* is usually divided by a single sagittal septum, but multiple septa may be present. Sphenoid septa that insert laterally adjacent to the cavernous internal carotid artery may be associated with arterial injury at surgery. Pneumatization of the

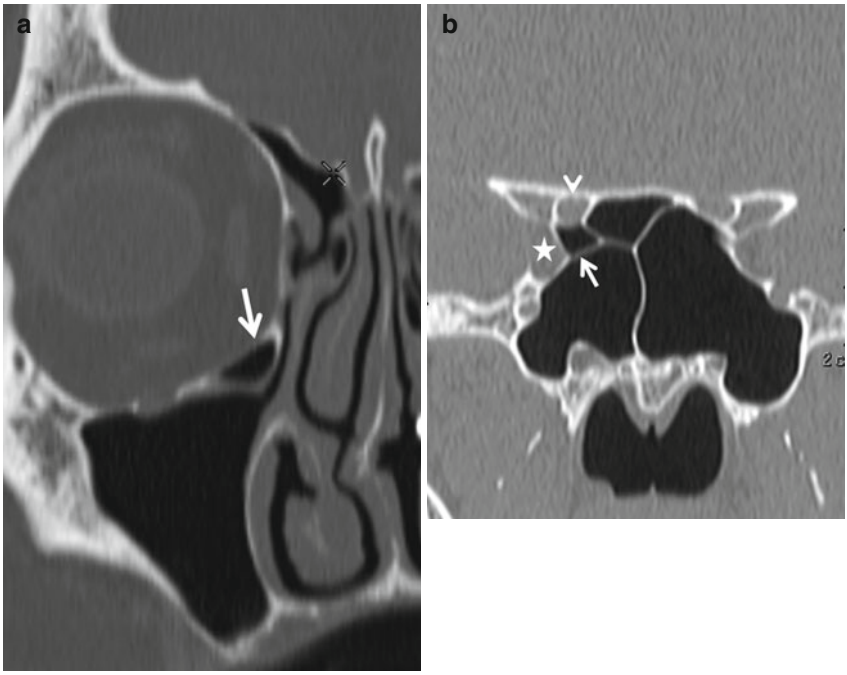

Fig. 9.8 (**a**) A Haller cell (*arrow*) represents an infraorbital ethmoid air cell and can compromise the infundibulum. (**b**) Onodi cells (*arrow*) result from posterior ethmoid pneumatization extending superior and lateral to the sphenoid sinus. These cells lie in close proximity to the optic nerves and occasionally, the internal carotid arteries, structures that may be injured if these cells are violated. Infection in an Onodi cell may also spread to the orbital apex rapidly. The *arrowhead* points to the optic canal and the *asterisk* indicated the superior orbital fissure

sphenoid sinus may extend into the anterior clinoid process and the horizontal carotid canals conferring increased risk of surgical injury to the optic nerves and internal carotid arteries, respectively. The lateral sphenoid sinus walls are occasionally dehiscent allowing the optic nerves and internal carotid arteries to pass through the sinus (Fig. 9.9).

9.1.4 Physiology

The nasal cycle is a normal, cyclical side-to-side alteration in nasal airway resistance. It can be associated with mucosal hypertrophy, which is detectable on CT and MR imaging, especially around the inferior turbinate; this must not be mistaken for pathology (Fig. 9.10).

9.2 Imaging Evaluation

Inflammatory sinonasal disease is evaluated most effectively by CT. Contrast is not usually required, except when spread of infection or inflammation beyond the sinonasal cavities into the orbits or adjacent soft tissues is suspected.

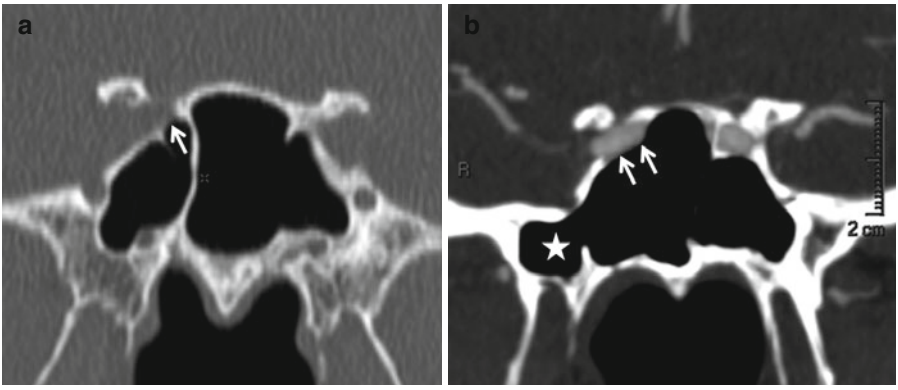

Fig. 9.9 The wall of the sphenoid sinus adjacent to the internal carotid arteries may be variable in thickness. In these images, there is no bony separation between the right ICA and the sinus cavity (*arrows*, **a** and **b**). In (**b**), note that pneumatization of the sphenoid sinus extends to the root of the pterygoid process (*asterisk*, pterygoid recess). A pterygoid recess may be the site of mucocele formation. Also, the greater sphenoid wing overlying, it can be thin enough to permit a CSF leak in some patients

Fig. 9.10 Alternating physiologic congestion and decongestion of the mucosa of the nasal cavity is known as the nasal cycle. Note that the mucosa of the right inferior turbinate is more prominent than on the left on this T2-weighted MR image. This must not be misconstrued as pathology

For effective evaluation using MRI, precontrast T1-weighted images must be obtained without fat suppression. The intrinsic T1 hyperintensity of fat provides a useful contrast against which low T1 signal intensity disease processes are easily seen. Fat suppression is useful on postcontrast T1-weighted sequences and enables the detection of enhancing abnormalities against a background of low fat signal. MRI is best used in mapping the extent of neoplasms and in the evaluation of intracranial spread of infectious diseases.

Plain radiography in the evaluation of sinonasal disease plays a minor role. One may rarely encounter a Waters' view of the paranasal sinuses, obtained to

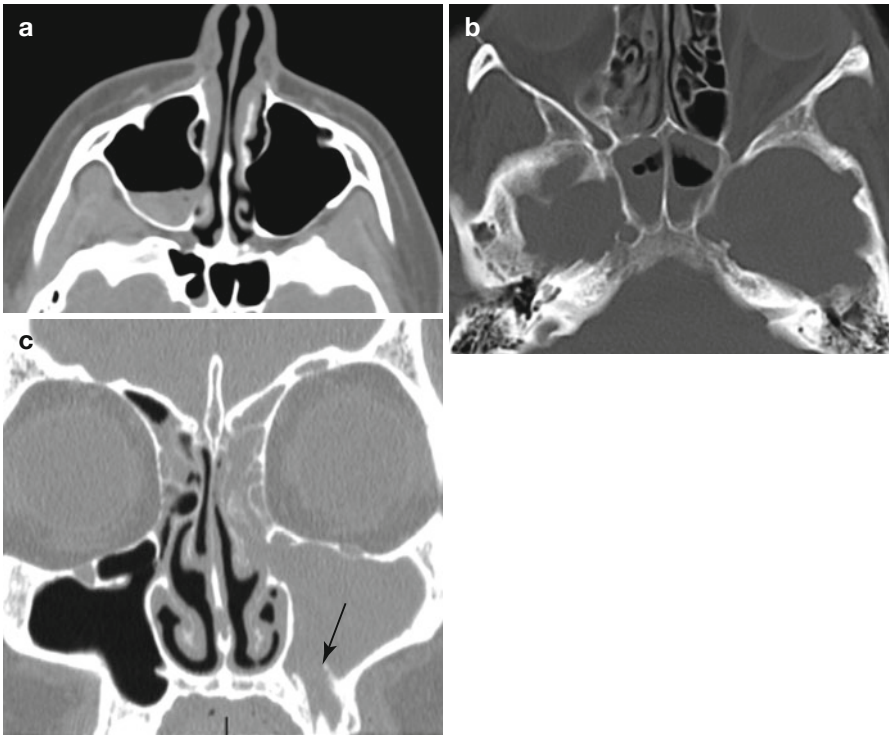

Fig. 9.11 Acute sinusitis. Fluid levels, in the appropriate clinical setting, indicate acute sinusitis (**a**, **b**). In a patient with acute maxillary sinusitis, it is always useful to evaluate the upper teeth. When periodontal disease occurs in a maxillary tooth whose roots project into the antrum, odontogenic sinusitis may occur (**c**, *arrow*)

demonstrate the presence of fluid/fluid levels in the setting of acute sinusitis. Plain films may also be used to evaluate nasal bone fractures, but ideally these are diagnosed clinically. Catheter angiography is best utilized for preoperative embolization of vascular sinonasal lesions such as juvenile nasopharyngeal angiofibromas and in the treatment of epistaxis.

9.3 Inflammatory Sinonasal Disease

9.3.1 Acute Inflammation and Its Complications

Acute inflammation of the sinuses may occur due to viral, bacterial, fungal, or allergic causes. A classic radiographic sign of acute sinusitis is a fluid level, but fluid levels may also be seen in a setting of trauma, prolonged nasogastric intubation, barotrauma, or CSF leak (Fig. 9.11). The presence of frothy secretions in a sinus may also indicate acute inflammation. Given the tendency of acute frontal and

Box 9.3. Complications of Acute Sinusitis

Orbital	
	Preseptal cellulitis
	Postseptal cellulitis
	Subperiosteal abscess
	Intraorbital abscess
	Cavernous sinus thrombophlebitis
Intracranial	
	Meningitis
	Subdural empyema
	Epidural abscess
	Cerebritis
	Brain abscess
	Dural sinus thrombosis
Others	
	Subpericranial abscess (Pott's puffy tumor)
	Calvarial/skull base osteomyelitis

sphenoid sinusitis to progress to life-threatening complications, it is imperative that the clinician be alerted to fluid levels in these areas. Acute sinusitis may also manifest as thickened mucosa on CT. The signs of early acute fungal sinusitis may be subtle and are discussed below.

Complications of acute sinusitis may involve the orbits or cranial cavity (Box 9.3). The orbits are most likely to be affected by ethmoid sinusitis. The lamina papyracea is a poor barrier to the spread of infection. The absence of valves in the anterior and posterior ethmoid veins also permits free spread of infection into the orbits. An extensive intradiploic anastomotic venous network allows spread of infection between the frontal sinuses and the meninges.

Orbital complications follow a loosely defined sequence of events (Fig. 9.12). Preseptal cellulitis (stage I) is manifested on CT by thickening and enhancement of the eyelid soft tissues; this can, however, be the consequence of simple transudative edema from impaired sinus venous outflow. At this stage, inflammation is restricted from posterior spread by the orbital septum. With orbital (postseptal) cellulitis (stage II), the intra- and extraconal fat demonstrates increased attenuation and stranding. The presence of a lentiform peripherally enhancing collection, applied to the lamina papyracea or orbital plate of the frontal bone and confined by the periorbita, indicates a subperiosteal abscess (stage III). A similar collection within the orbit itself indicates an orbital abscess (stage IV). Left untreated, this progresses to thrombophlebitis of the superior and inferior ophthalmic veins and then of the cavernous sinus itself (stage V). Enlargement and lack of enhancement of these venous structures, a convex contour to the cavernous sinus, and extraocular muscle engorgement are signs of cavernous sinus thrombosis. While unenhanced MRI may show T1 hyperintense thrombus in the cavernous sinus, contrast-enhanced CT or MRI is

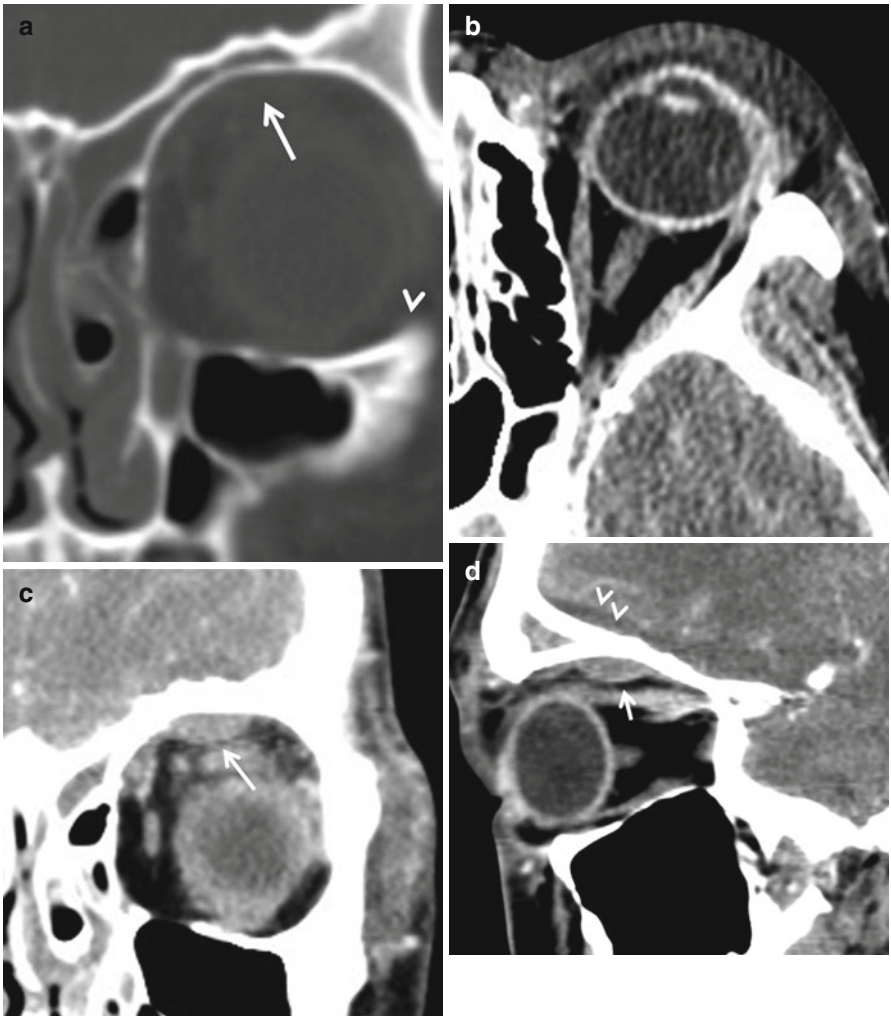

Fig. 9.12 (**a**) Orbital complications of acute frontal and ethmoid sinusitis. Image (**a**) shows fluid in the frontal and ethmoid air cells. In (**b**), edema of the preseptal soft tissues (*arrows*) is evident. The *white lines* roughly indicate the plane of the orbital septum, a fibrous sheet that is an effective but not always reliable barrier to the spread of inflammation. In (**c**, **d**), a lentiform collection (*arrows*) with its base against the orbital roof representing a subperiosteal abscess is present. Also in (d), note a low-density epidural abscess (*arrowheads*) under the right frontal lobe. Inspecting CT images in narrow window settings may help detect subtle findings of intracranial complications. In (**e**), on this contrast-enhanced fat-suppressed MR image, the epidural abscess and the associated meningeal enhancement (*arrowhead*) are obvious. Also, note the stranding and enhancement of the orbital fat (*asterisk*) indicating cellulitis and thickening and enhancement of the superior rectus and oblique muscles representing myositis (*arrows*). Diffusion-weighted images are very useful in demonstrating intracranial purulence (*arrows*, **f**). The graphic, (**g**), illustrates the various complications that may follow acute bacterial sinusitis – preseptal cellulitis (*double arrows*), postseptal cellulitis, subperiosteal abscess (*black asterisk*), meningitis (*arrowheads*), intracranial empyema (*white asterisk*), and cavernous sinus thrombosis (*white arrow*)

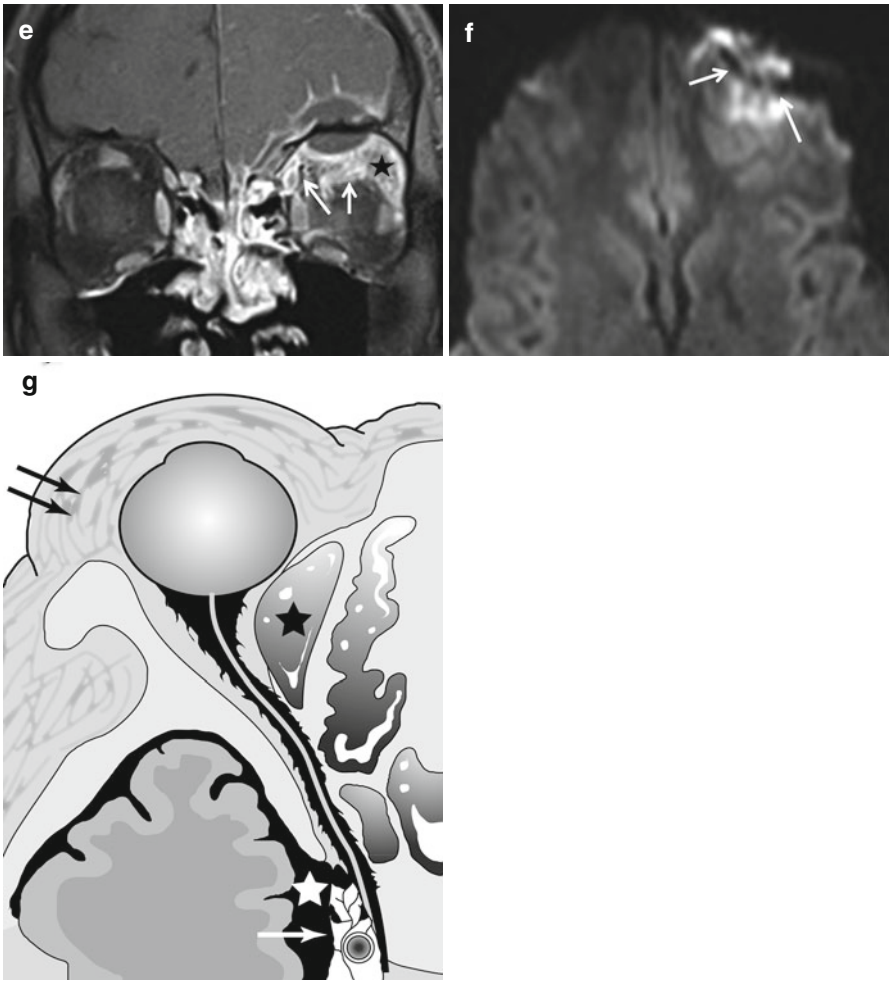

Fig. 9.12 (continued)

the best imaging modality to evaluate this entity. MR venography is usually insensitive to cavernous sinus thrombosis as the normal cavernous sinuses themselves are not well seen.

The intracranial complications of sinusitis are best evaluated by MRI (Fig. 9.13). However, when presented with a CT, it is useful to examine the brain and extra-axial spaces in narrow window settings to detect subtle abnormalities such as small subdural or epidural infectious collections. Meningitis is recognized on MRI by increased signal intensity in the subarachnoid spaces on FLAIR imaging and by leptomeningeal enhancement with administration of contrast. Diffusion-weighted imaging (DWI) is useful in the detection of extra-axial empyemas, which appear

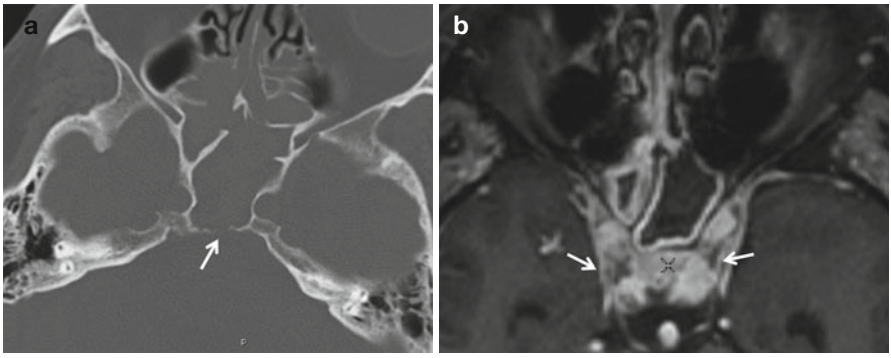

Fig. 9.13 (**a**) Bacterial sphenoid sinusitis with cavernous sinus thrombosis. Note the focus of bone destruction in (a) (*arrows*). This patient presented with fever and headache rapidly followed by chemosis and ophthalmoplegia. In (**b**), the filling defects in the cavernous sinuses bilaterally represent thrombi. Cavernous sinus thrombosis is best depicted on contrast-enhanced MR images (*arrows*). MR venography is not useful because the normal cavernous sinuses are not well depicted on this modality

hyperintense. Sterile effusions are not hyperintense on DWI. Pyogenic brain abscesses are also characteristically hyperintense on DWI. Vascular complications such as dural venous sinus thrombosis and mycotic ICA pseudoaneurysms are best demonstrated by MR venography and angiography, respectively.

9.3.2 Fungal Sinusitis

Fungal sinusitis manifest in four different forms: allergic fungal sinusitis, noninvasive fungal sinus colonization (mycetoma), acute invasive fungal sinusitis, and chronic invasive fungal sinusitis. Of these, allergic fungal sinusitis is the commonest and occurs as a result of an IgE-mediated hypersensitivity response to fungal antigens. It is usually caused by fungi of the *Fusaria*, *Bipolaris*, and *Aspergillus* species, among others. Affected sinuses contain inspissated mucin which gradually accumulates, expands, and thins bony sinus walls. Commonly, all the sinuses and the nasal cavity are simultaneously affected (Fig. 9.14). The mucin contains concentrated protein and fungal elements and heavy metals such as iron and manganese, resulting in hyperdensity on CT and low signal on T1- and T2-weighted MRI, a finding that may simulate a pneumatized sinus. On gadolinium MRI, the mucosa enhances while the sinus contents do not, enabling differentiation from neoplasm. Sinus wall expansion leads to gradual demineralization and erosion, and extension of the disease into the orbits and cranial cavity may follow. A mycetoma results from colonization of a chronically inflamed sinus, usually the maxillary, and appears as a calcified mass on CT. An irregular, calcified mass within a chronically inflamed sinus is almost always a mycetoma (Fig. 9.15).

Acute invasive fungal sinusitis usually occurs in immunocompromised patients. Imaging findings can be exceedingly subtle and must be actively sought in the context of immunosuppression (Fig. 9.16). The culprit fungi are usually *Rhizopus*,

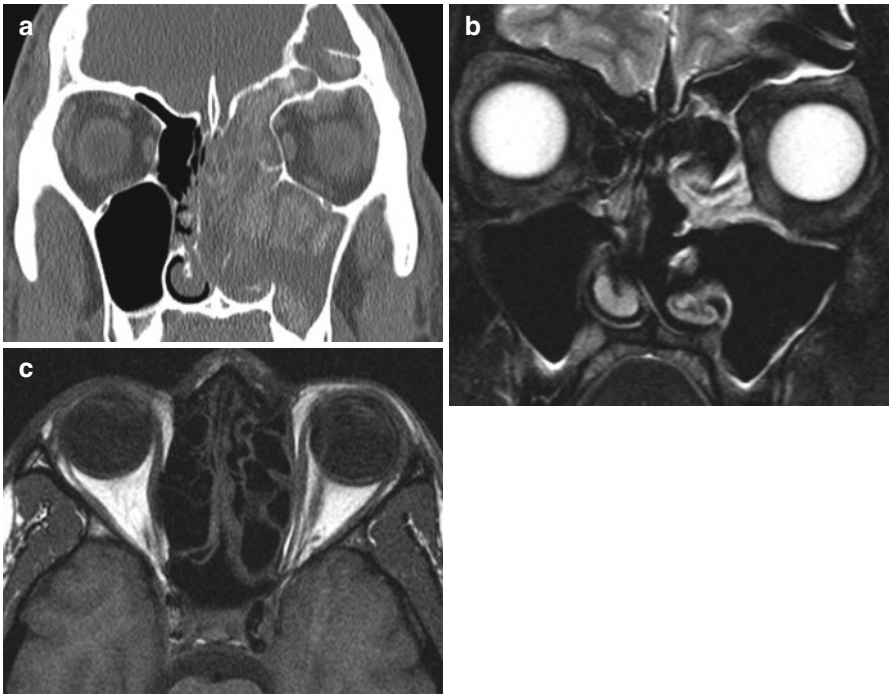

Fig. 9.14 Allergic fungal sinusitis. The hyperdense appearance of the inspissated secretions in the left frontal ethmoid and maxillary sinuses is typical of this entity (**a**). It is not uncommon for the sinuses to be expanded as in this case. It is important to note that in (**b**, **c**), T2- and T1-weighted images, the complete absence of signal in the involved sinuses is not indicative of absence of disease but is a consequence of the extremely high protein and heavy metal concentrations in the secretions

Mucorales, *Absidia*, and *Mucor*. They are angioinvasive and can thus erode the sinus walls and access the orbits and intracranial compartment even in the presence of only minimal sinus imaging findings. The bony changes are best seen on CT while intracranial and orbital spread is best assessed by MRI. Abnormal soft tissue in the retroantral, extraconal, orbital apex, and pterygopalatine fossa (PPF) fat may indicate spread beyond the sinus. The precontrast T1-weighted images are especially useful in evaluating these regions which should show hyperintense fat signal if normal. The flow voids of the cavernous ICA must also be carefully inspected; thrombosis and pseudoaneurysm can occur as a complication of invasive fungal sinusitis. The black turbinate sign, which reflects non-enhancing, ischemic middle turbinate mucosa, may be an early indicator of invasive sinusitis. Fungi may also spread along preexisting canals and foramina, which may simulate perineural tumor spread.

Chronic invasive fungal sinusitis follows a more indolent course and can occur in immunocompetent patients as well. A combination of sinus opacification, bone destruction, and extra-sinus soft tissue is typical. These findings can mimic malignant neoplasms or other entities such as sarcoidosis and Wegener's

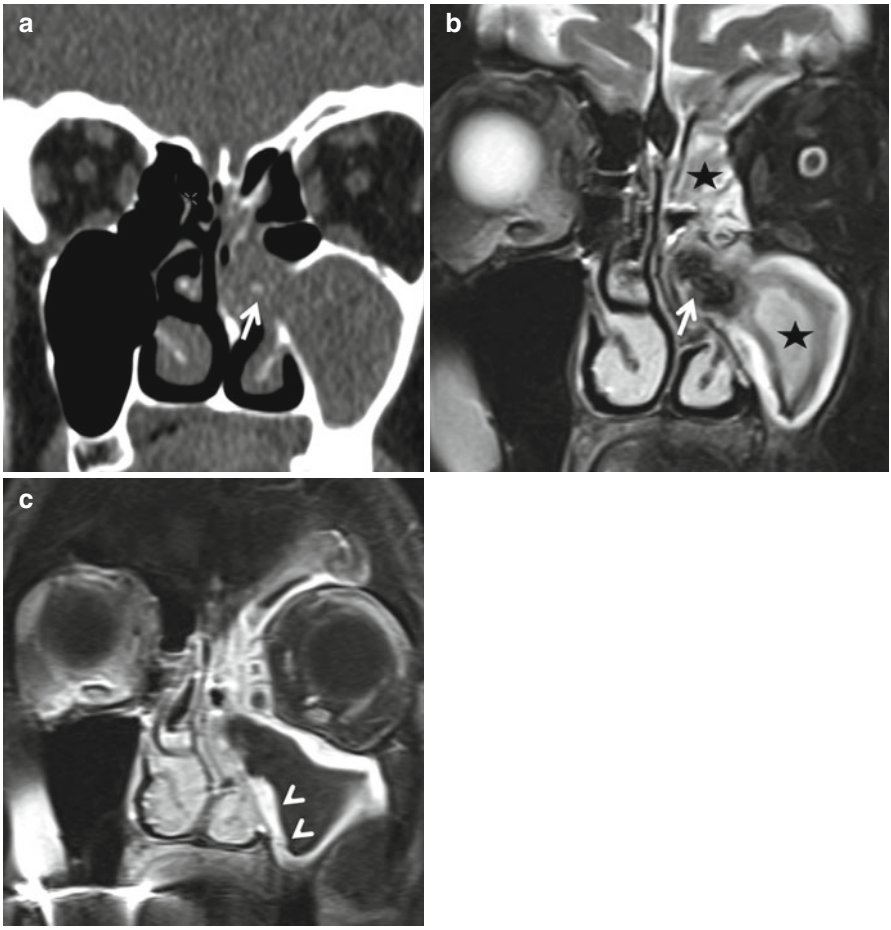

Fig. 9.15 Mycetoma. The CT demonstrates expansion of the left infundibulum by a soft tissue lesion containing foci of calcification (*arrow*, **a**). In (**b**), A T2W image, the infundibular lesion is of low signal intensity. It does not enhance with gadolinium in (**c**). These findings are typical for a mycetoma. The *asterisks* in (b) indicate fluid in the obstructed maxillary and ethmoid air cells. The *arrowheads* in (c) point to enhancement of the edematous sinus mucosa. A pattern of unilateral ostiomeatal unit disease in an adult must always prompt close scrutiny of the middle meatus for an obstructing mass lesion

granulomatosis, and definitive diagnosis may not be possible with imaging alone.

9.3.3 Chronic Rhinosinusitis (CRS)

CRS is manifested by any combination of polyps, retention cysts, sinus wall osteitis, and mucocele formation. The role of anatomic variations such as conchae bullosa, paradoxical turbinates, Haller cells, and pneumatized uncinate processes in

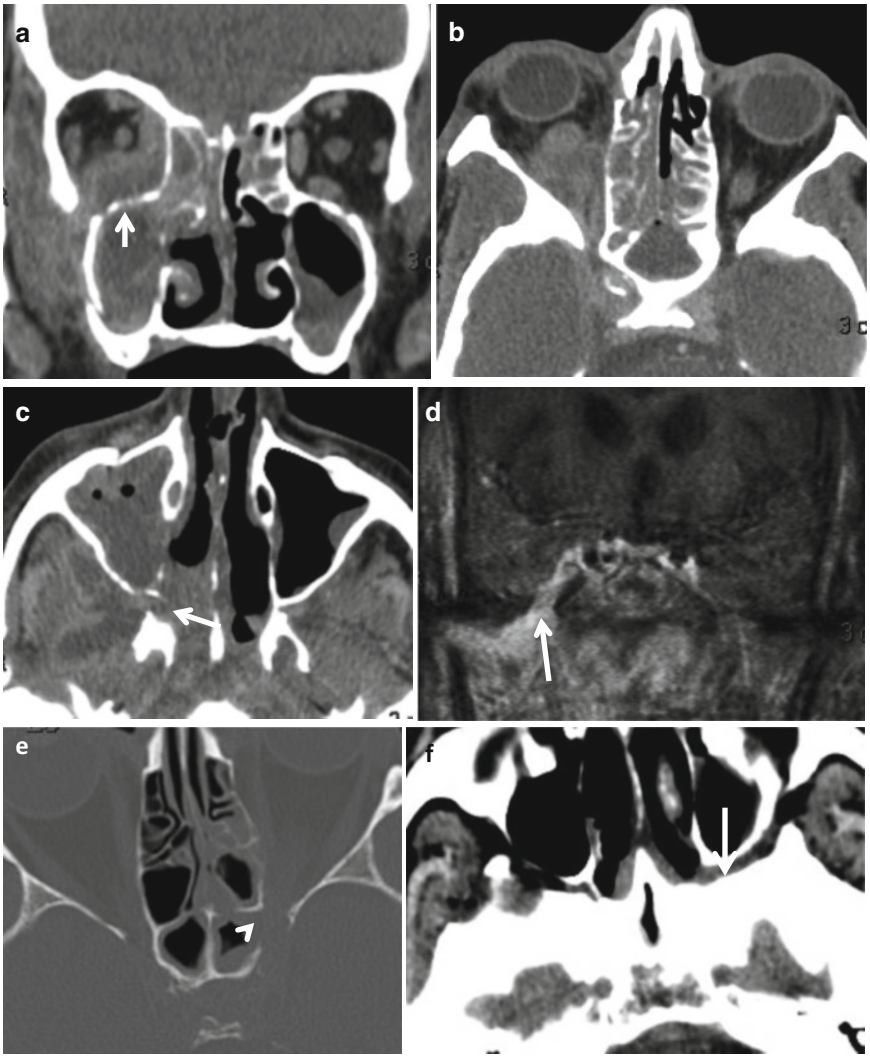

Fig. 9.16 Invasive fungal sinusitis. Images (**a**–**d**) are from a patient with diabetes mellitus and invasive Aspergillus sinusitis. Fungal sinusitis can rapidly spread from the sinonasal cavities to the orbits (**b**) and skull base as in this case. Note the permeative bone destruction of the maxillary sinus wall in (a) (*arrow*), a finding typical of this entity. The inflammatory process can also spread along pathways of least resistance such as the pterygopalatine fossa (*arrow* **c**) and skull base foramina (*arrow*, foramen ovale, **d**) to gain access to the cranial cavity. The sinus inflammation in invasive fungal sinusitis may not be impressive, as in (**e**), where a small amount of ethmoid and sphenoid mucosal thickening is associated with destruction of the wall of the sinus adjacent to the optic canal (*arrowhead*). Spread of infection beyond the sinus and orbits is evident in the left pterygopalatine fossa where the normal fat is replaced by soft tissue (*arrow*, **f**). Images (**g**, **h**) are from a patient with invasive aspergillosis who presented with a sixth nerve palsy. The mucosal inflammation in the sphenoid sinus is not impressive, but the fat-suppressed axial T1-weighted MR image reveals enhancement of the clival and left petrous apex marrow (*arrows*) and of the dura (*arrowheads*) along the posterior aspect of the petrous bone

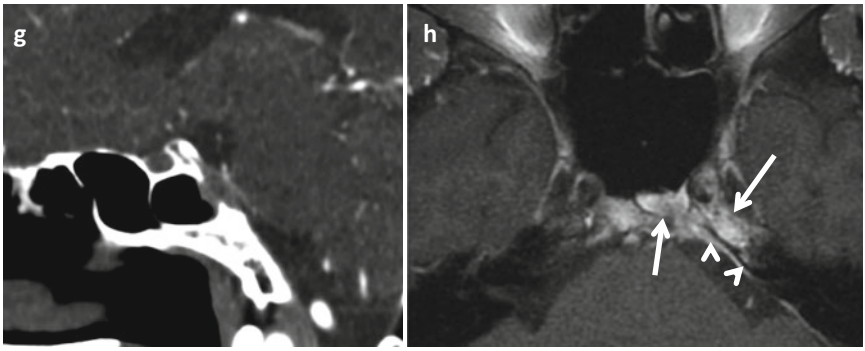

Fig. 9.16 (continued)

predisposing to CRS is debatable. Deviation of the nasal septum and a horizontal orientation of the uncinate process may be more frequent in patients with CRS.

Polyps and mucosal retention cysts are distinct histologically but indistinguishable on noncontrast CT imaging. They are most often seen as incidental findings and are usually of no clinical significance. Polyps may be solitary or numerous and can vary greatly in size. Occasionally a large polyp arising from the maxillary sinus can protrude into the nasal cavity through the maxillary ostium (antrochoanal polyp). Polyps on CT may be indistinguishable from tumors such as inverted papillomas, melanomas, and lymphomas. The presence of smooth remodeling of adjacent bone and internal hyperdensities suggests a benign diagnosis. The hyperdensity is due to the presence of inspissated secretions or fungal colonization. On contrast-enhanced MRI, polyps enhance peripherally while tumors are more likely to enhance in a solid fashion. On MRI, polyps and the fluid collected between them can demonstrate complex signal intensities. Retained sinus secretions demonstrate progressive increase in protein concentration. As protein concentration increases, T1-weighted signal intensity also increases. T1 hyperintensity is usually reassuring for benign disease, with the exception of melanotic melanoma. With very high protein concentrations, T1 signal intensity declines. T2 signal intensity declines with increasing protein concentration and, when protein concentrations exceed 35–40 %, signal may disappear entirely, giving rise to a signal void, which may appear as a falsely aerated sinus (Fig. 9.14).

Chronically inflamed sinuses provoke inflammatory osteitis in the sinus walls that manifests as bone thickening, easily seen on CT (Fig. 9.17). Obstruction of the sinus ostium can result in the formation of a mucocele, which requires expansion of the sinus. Mucoceles (Fig. 9.18) may also arise as a consequence of previous trauma or surgery. The frontal and anterior ethmoid sinuses have relatively small ostia and are more likely to form mucoceles, which can become symptomatic due to extension into the orbits or cranial cavity. Intraorbital extension is more likely to occur with frontal and ethmoid mucoceles. The rare sphenoid mucocele can encroach upon the orbital apex. Mucoceles may also become secondarily infected (mucopyocele) and, in the frontal sinus, give rise to "Pott's puffy tumor," a purulent subpericranial fluid collection (Fig. 9.19).

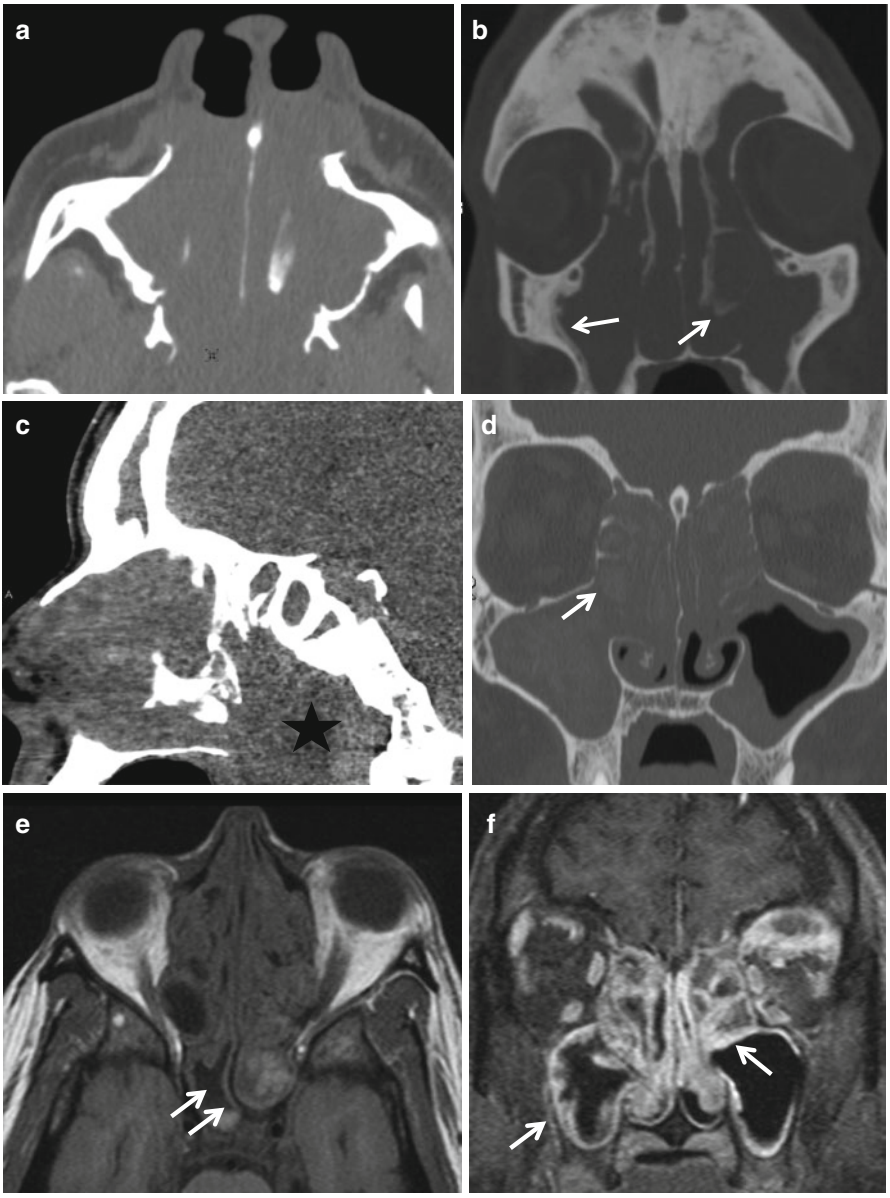

Fig. 9.17 Sinonasal polyposis. Images (**a**–**c**) demonstrate complete opacification of the nasal cavity and paranasal sinuses by diffuse polyposis. Note the extensive demineralization of the ethmoid septa, medial antral walls, and the turbinates in (**a**, **b**). Foci of sclerosis (*arrows*, **b**) are due to chronic osteitis. In (**c**), a large antrochoanal polyp obstructing the posterior choana is noted (*asterisk*). Similar findings are seen in images (**d**) in a patient with long-standing allergic rhinosinusitis. The presence of hyperdense foci and peripheral mucosal enhancement (*arrows* in **d**, **f** respectively) is typical for polyposis. Note trapped secretions of varying signal intensities produced by differing protein concentrations on the unenhanced T1-weighted image (*arrows*, **e**)

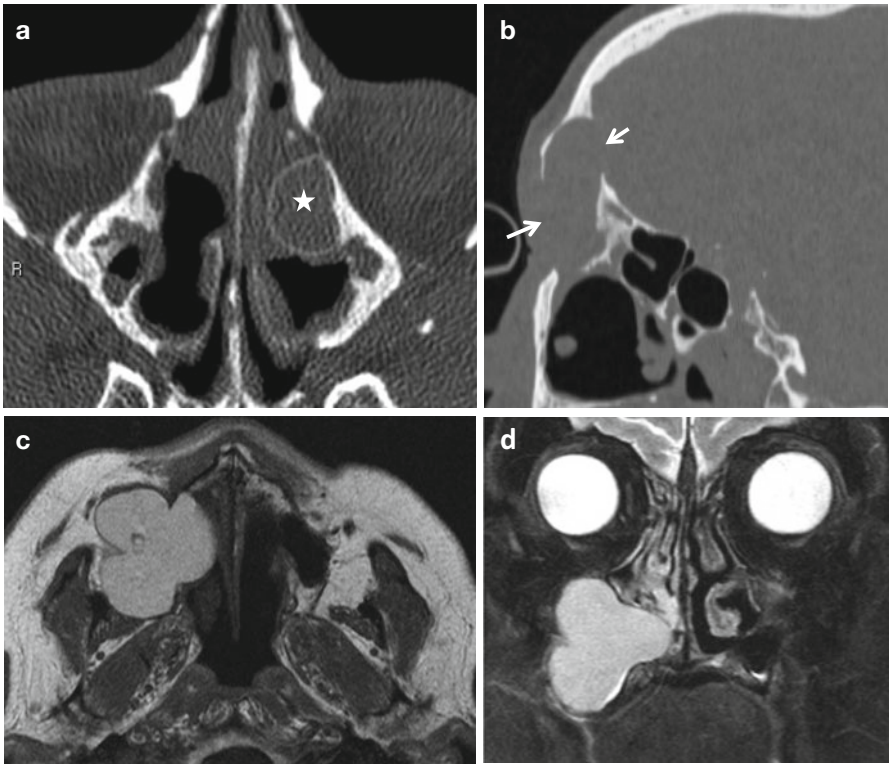

Fig. 9.18 Mucoceles. A mucocele is an obstructed fluid-filled expanded sinus. (**a**) Shows a left anterior ethmoid air cell mucocele (*asterisk*) in a patient with persistent symptoms after sinus surgery. It is not unusual for the wall of large mucoceles to become extremely attenuated as in the case of the frontal mucocele in (**b**) (*arrows*). A maxillary mucocele is shown in (**c**, **d**). The contents of mucoceles on MR are often T1 hyperintense due to their proteinaceous nature

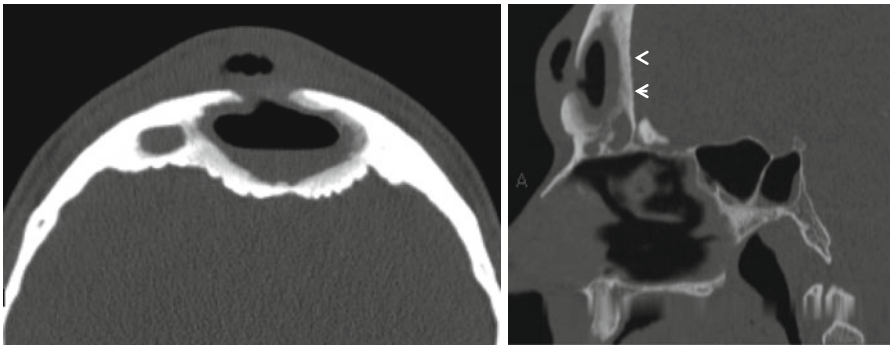

Fig. 9.19 Pott's puffy tumor is the term applied to a collection of pus under the frontal pericranium arising from a frontal sinus mucopyocele. Note the expansion of the frontal sinus, the fluid level, and the chronic osteitis of the frontal sinus walls (*arrowheads*)

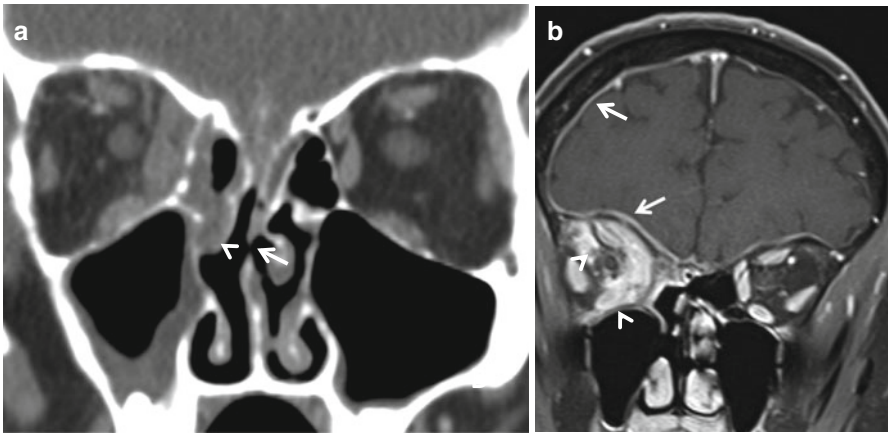

Fig. 9.20 Wegener's granulomatosis. The imaging findings in WG are often indistinguishable from nonspecific chronic rhinosinusitis. However involvement of the nasal septum (*arrow*, **a**) and erosive changes as in the case of the right middle turbinate (*arrowhead* **a**) are highly suggestive of the diagnosis, especially if orbital and meningeal involvements (*arrowheads* and *arrows*, respectively, in **b**) are present

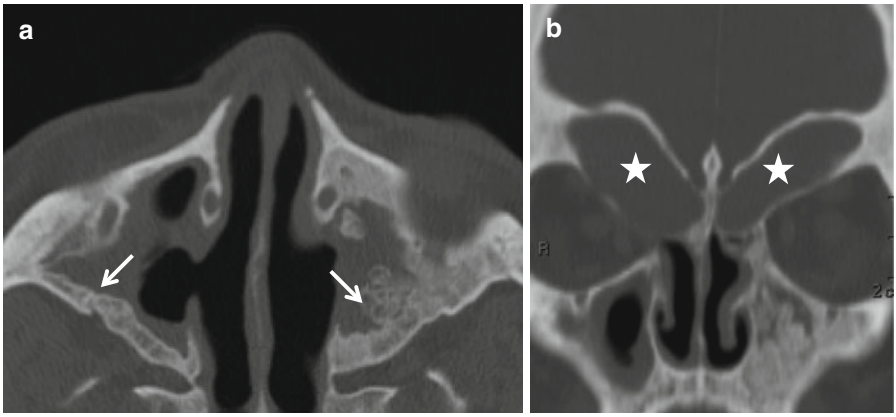

Fig. 9.21 Sarcoidosis. Imaging findings in sinonasal sarcoidosis are nonspecific, reflect long-standing sinus inflammation, and may sometimes resemble those in Wegener's granulomatosis in terms of a tendency to affect the nasal septum and coexistence of orbital and intracranial disease. In this case florid sclerosis of the sinus walls due to chronic osteitis (*arrows*, **a**) and bilateral frontal mucoceles (*asterisks*, **b**) is present

9.3.4 Noninfectious Inflammatory Conditions

The imaging appearance of Wegener's granulomatosis is extremely variable (Fig. 9.20). The diagnosis may be suspected based on involvement of the nasal septum, the presence of soft tissue masses within the sinus cavities, bone sclerosis, and extension into the adjacent soft tissues and the orbits. Sarcoidosis can also affect the sinonasal cavity and presence of any combination of mucosal thickening, bone destruction, soft tissue masses, and extension beyond the sinuses (Fig. 9.21).

A chronic smoldering inflammatory sinonasal process in an African American patient may indicate sarcoidosis. Ultimately, the overall clinical picture and nasal biopsy are crucial in making the final diagnosis. Another more rare diagnostic consideration in the presence of these imaging findings would be inflammatory pseudotumor (IPT), an idiopathic entity of autoimmune/infectious etiology. Perhaps due to the presence of a fibrous component, IPT may appear hypointense on T2-weighted imaging (Fig. 9.22).

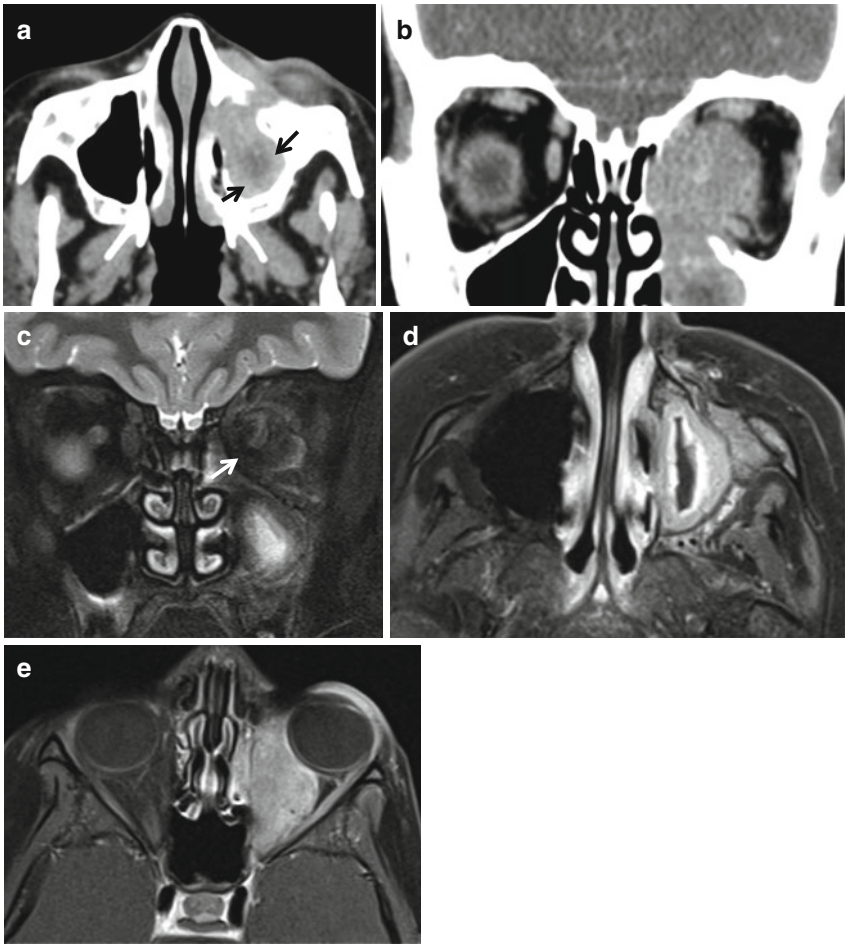

Fig. 9.22 Sino-orbital inflammatory pseudotumor. A thick rind of enhancing soft tissue (*arrows*) is seen in the left maxillary antrum (**a**). It has extended into the left orbit where the medial rectus and superior oblique are engulfed and the intraconal fat invaded (**b**). On the T2-weighted image (**c**), the lesion is profoundly hypointense (*arrow*), a finding that is strongly suggestive of IPT. The contrast-enhanced images (**d**, **e**) reveal fairly intense enhancement. Biopsy revealed IgG4-positive IPT, an entity associated with elevated serum IgG4 which can affect other structures such as the pancreas, salivary glands, thyroid, lungs, pleura, and retroperitoneum among others

9.4 Sinonasal Neoplasms

9.4.1 Malignant Neoplasms

A brief classification of malignant sinonasal tumors is provided in Box 9.4. Although most sinonasal malignant tumors have no characteristic imaging appearance, esthesioneuroblastoma (olfactory neuroblastoma) can occasionally be identified by cysts capping the superior portion of the tumor, and some melanomas are hyperintense on T1-weighted imaging due to a combination of melanin and hemorrhage (Fig. 9.23).

Squamous cell carcinoma is the most common malignant sinonasal tumor; a simplified staging system is provided in Box 9.5. Esthesioneuroblastoma is commonly staged by the Kadish system, with stage A representing tumors confined to the nasal cavity, stage B signifying extension into the paranasal sinuses, and stage C indicating orbital or intracranial extension. A TNM system is also used for esthesioneuroblastoma staging (Box 9.6). The radiologist's primary role is to determine resectability, which requires addressing the following questions:

1. Is there orbital invasion?
2. Is there invasion of the dura or brain parenchyma?
3. Is there perineural tumor spread?
4. Is there skull base invasion?

Box 9.4. Malignant Sinonasal Tumors

- Epithelial origin
  - Squamous cell carcinoma
  - Intestinal type adenocarcinoma
  - Malignant minor salivary gland tumors
    - Adenoid cystic carcinoma
    - Mucoepidermoid carcinoma
- Neuroectodermal origin
  - Esthesioneuroblastoma
  - Sinonasal undifferentiated and neuroendocrine carcinoma
  - Melanoma
- Mesenchymal origin
  - Osteosarcoma
  - Chondrosarcoma
  - Ewing's sarcoma
  - Malignant nerve sheath tumor
  - Rhabdomyosarcoma
  - Fibrosarcoma and malignant fibrous histiocytoma
  - Angiosarcoma
- Lymphoid malignancies
- Metastases

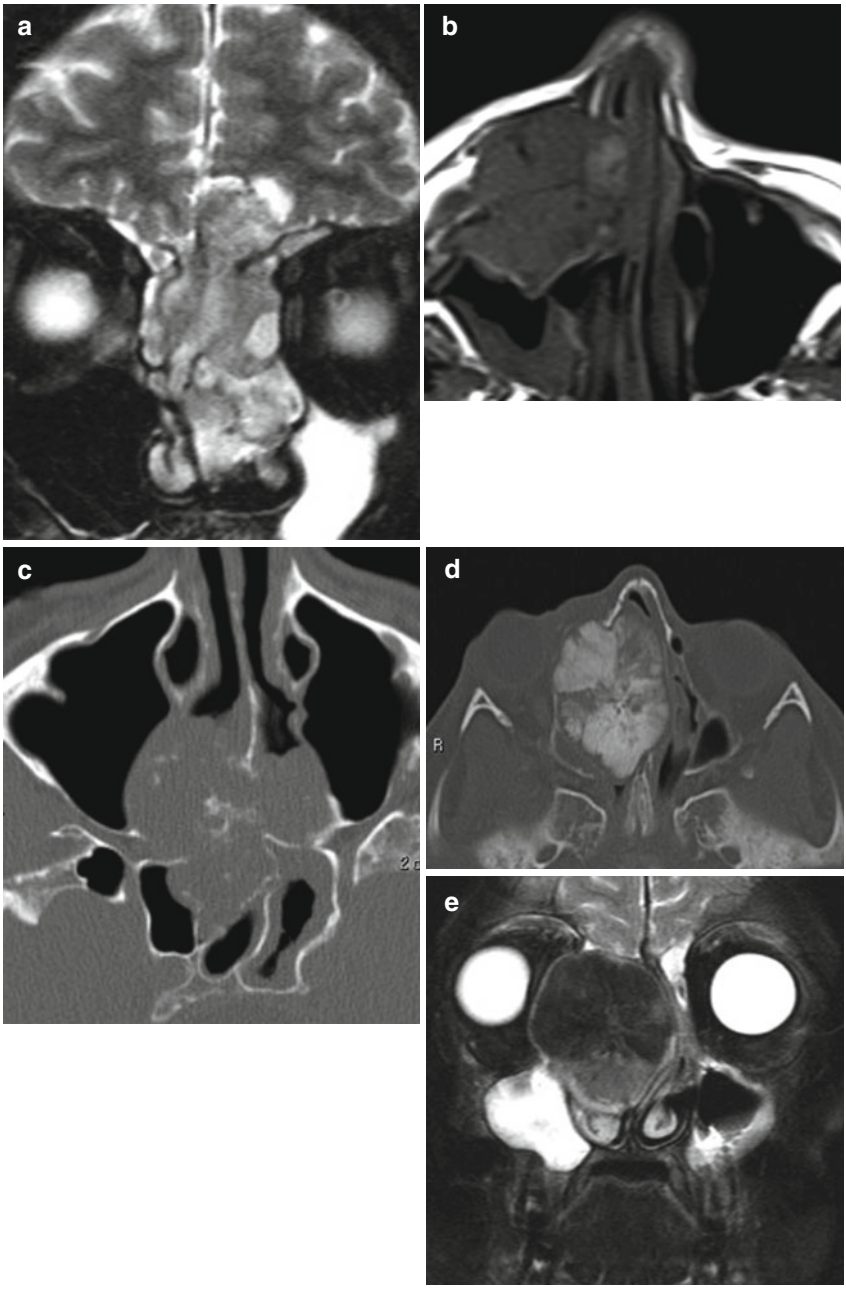

Fig. 9.23 Malignant sinonasal tumors. Sinonasal malignancies rarely demonstrate defining imaging characteristics. However, the presence of cysts capping the intracranial portion of a tumor (**a**) may be a sign of an esthesioneuroblastoma. Areas of T1 hyperintensity due to melanin or hemorrhage (*arrow*, **b**) may be seen with melanomas. Image (**c**) shows arc and whorl-like calcifications, a finding when present is highly suggestive of chondrosarcoma. In (**d**, **e**), a sunburst pattern of tumor bone formation, characteristic of osteosarcoma, is present

Box 9.5. TNM Staging of Nasal Cavity, Maxillary, and Ethmoid Sinus Squamous Cell Carcinoma

TX	Primary tumor cannot be assessed
T0	No evidence of primary tumor
Tis	Carcinoma in situ
Maxillary sinus	
T1	Tumor limited to maxillary sinus mucosa
T2	Tumor causing bone erosion or destruction including extension into the hard palate and/or middle nasal meatus, except extension to posterior wall of maxillary sinus and pterygoid plates
T3	Tumor invading any of the following: posterior wall of maxillary sinus, subcutaneous tissues, floor or medial wall of orbit, pterygoid fossa, or ethmoid sinuses
T4a	Moderately advanced local disease Tumor invades anterior orbital contents, skin of cheek, pterygoid plates, infratemporal fossa, cribriform plate, or sphenoid or frontal sinuses
T4b	Very advanced local disease Tumor invades any of the following: orbital apex, dura, brain, middle cranial fossa, cranial nerves other than maxillary division of trigeminal nerve (V_2), nasopharynx, or clivus
Nasal cavity and ethmoid sinus	
T1	Tumor restricted to any one subsite, with or without bony invasion
T2	Tumor invading two subsites in a single region or extending to involve an adjacent region within the nasoethmoidal complex, with or without bony invasion
T3	Tumor extends to invade the medial wall or floor of the orbit, maxillary sinus, palate, or cribriform plate
T4a	Moderately advanced local disease Tumor invades any of the following: anterior orbital contents, skin of nose or cheek, minimal extension to anterior cranial fossa, pterygoid plates, or sphenoid or frontal sinuses
T4b	Very advanced local disease Tumor invades any of the following: orbital apex, dura, brain, middle cranial fossa, cranial nerves other than (V_2), nasopharynx, or clivus
Regional lymph nodes (*N*)	
NX	Regional lymph nodes cannot be assessed
N0	No regional lymph node metastasis
N1	Metastasis in a single ipsilateral lymph node, ≤3 cm in greatest dimension
N2	Metastasis in a single ipsilateral lymph node, >3 cm but ≤6 cm in greatest dimension, or metastases in multiple ipsilateral lymph nodes, ≤6 cm in greatest dimension, or in bilateral or contralateral lymph nodes, ≤6 cm in greatest dimension
N2a	Metastasis in a single ipsilateral lymph node, >3 cm but ≤6 cm in greatest dimension
N2b	Metastases in multiple ipsilateral lymph nodes, ≤6 cm in greatest dimension
N2c	Metastases in bilateral or contralateral lymph nodes, ≤6 cm in greatest dimension
N3	Metastasis in a lymph node, >6 cm in greatest dimension
Distant metastasis (*M*)	
M0	No distant metastasis
M1	Distant metastasis

Reprinted with permission from AJCC: paranasal sinus and nasal cavity. In: Edge SB, Byrd DR, Compton CC et al (eds) (2010) AJCC cancer staging manual, 7th edn. Springer, New York, p 69–78

These questions are best answered by a combination of CT and MRI. CT is useful to detect destruction of the cribriform plates, fovea ethmoidalis, pterygoid plates, and lamina papyracea. MRI is best used to identify orbital, skull base, and perineural invasion. MRI is also useful in enabling distinction between tumor and obstructed secretions and mucosal inflammation. Given its resistance to tumor spread, the orbit is only considered invaded when the periorbita is breached; when this has occurred, the globe is usually not salvageable. The only reliable sign of orbital invasion is engulfment of one or more extraocular muscles by tumor. While other signs have been described, such as irregular tumor margins, loss of the fat plane between the tumor and the extraocular musculature, and abnormal muscle signal intensity and enhancement, these are unreliable (Fig. 9.24).

Dural invasion may be difficult to determine. Enhancement of the dura can be reactive to tumor; such enhancement is linear and usually less than 5 mm thick. Any nodularity of enhancement or enhancement of the adjacent leptomeninges must be interpreted as meningeal invasion. The presence of parenchymal edema is usually a sign of frank brain invasion (Fig. 9.25).

Perineural tumor spread may occur with any malignancy but is especially common with adenoid cystic carcinoma. The close proximity of the PPF to the sinonasal cavities means that a tumor that invades the PPF has easy access to the skull base. The PPF contains predominantly fat, which is easily seen on CT or on T1-weighted sequences; loss of this fat is always worrisome. Perineural spread may occur in any direction from the PPF and can present as skip lesions. It is therefore important to scrutinize the PPF and all its associated foramina when evaluating a sinonasal malignancy. CT is not very sensitive in the detection of perineural tumor spread, but widening of skull base foramina and loss of the PPF fat can be appreciated. MRI is the best way to evaluate perineural spread using a combination of the precontrast nonfat-suppressed T1-weighted and postcontrast fat-suppressed T1-weighted imaging. Involved nerves are thickened and enhance abnormally (Fig. 9.26).

The skull base is best evaluated with a combination of CT and MRI. The normal skull base marrow is fatty and therefore hyperintense on T1. Replacement of the fatty marrow may indicate tumor invasion, but hematological processes, osteoporosis, chronic smoking, and infection may also produce abnormal marrow signal. A combination of bone erosion on CT and abnormal marrow signal on MRI is the best evidence for skull base invasion.

9.4.2 Benign Neoplasms

The most common benign tumors are osteomas, fibro-osseous lesions, inverted papillomas, and juvenile angiofibromas. Osteomas appear as well-defined radiodense lesions on CT (Fig. 9.27). Multiple osteomas must make one suspect Gardner's syndrome, where there is an increased incidence of sebaceous cysts, extra-abdominal desmoid tumors, and thyroid, breast, and uterine malignancy (Fig. 9.27). Fibrous dysplasia and ossifying fibroma have similar imaging appearances. On plain films and CT, both can demonstrate bone expansion and a ground glass matrix. Ossifying fibromas tend to be less radiodense than fibrosis dysplasia and are usually better

circumscribed. Because they share common imaging features, the term "fibro-osseous lesion" may be used to refer to both. These lesions can demonstrate bizarre signal intensities and enhancement on MRI and can thus appear quite aggressive, which can be erroneously interpreted as malignancy (Fig. 9.28).

Juvenile angiofibromas (Fig. 9.29) are highly vascular tumors and occur exclusively in adolescent males. They originate at the sphenopalatine foramen and have a propensity to infiltrate the PPF, the skull base, and the orbits. Intense enhancement is characteristic on CT and MRI. Flow voids, representing feeding arteries or draining veins, may be seen on MRI. The vascular supply of angiofibromas is from the internal maxillary and ascending pharyngeal arteries, and preoperative embolization is common practice. It is important to note that in older individuals,

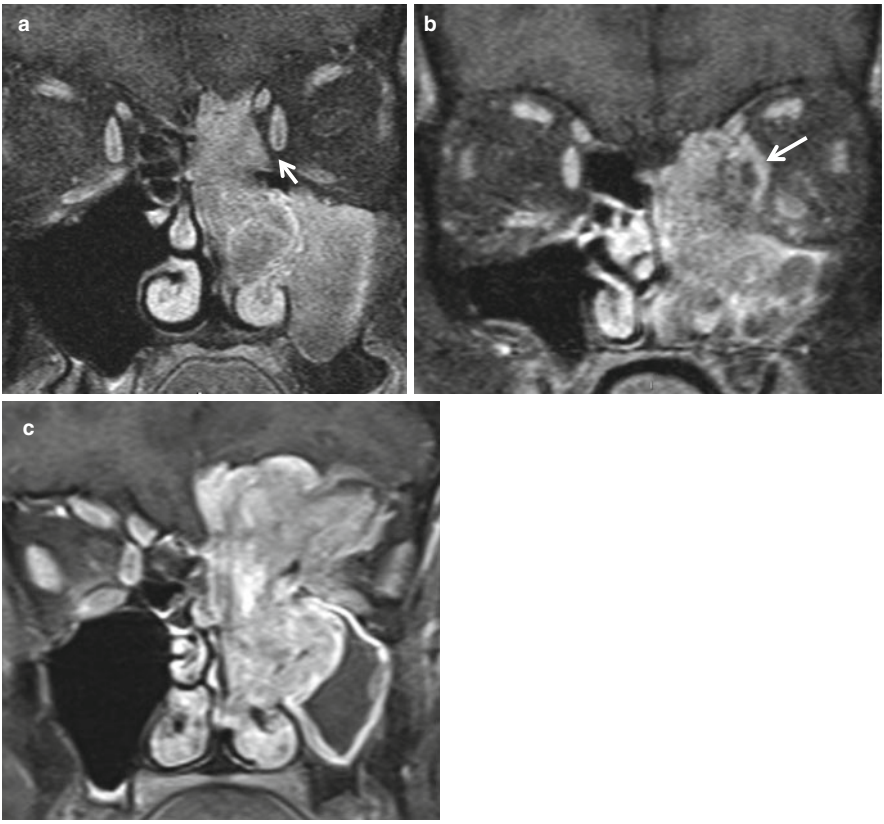

Fig. 9.24 The orbits in sinonasal malignancy. Three different patients with ethmoidal squamous cell carcinoma. In (**a**), a distinct fat plane (*arrow*) is visible between the tumor and the medial rectus indicating that the periorbita is intact and that the orbit is not violated. In (**b**), no fat plane is visible and the tumor displaces the medial rectus (*arrow*). This finding is equivocal for orbital invasion. At surgery, the periorbita was intact. In (**c**), violation of the periorbita is indicated by engulfment of the medial rectus and superior oblique muscles by tumor. It is important to note that destruction of the bony orbital walls does not indicate orbital invasion and that it is violation of the periorbita, a structure not seen on imaging that makes the globe unsalvageable. The graphic, (**d**), illustrates invasion of the periorbita on the right and its displacement on the left

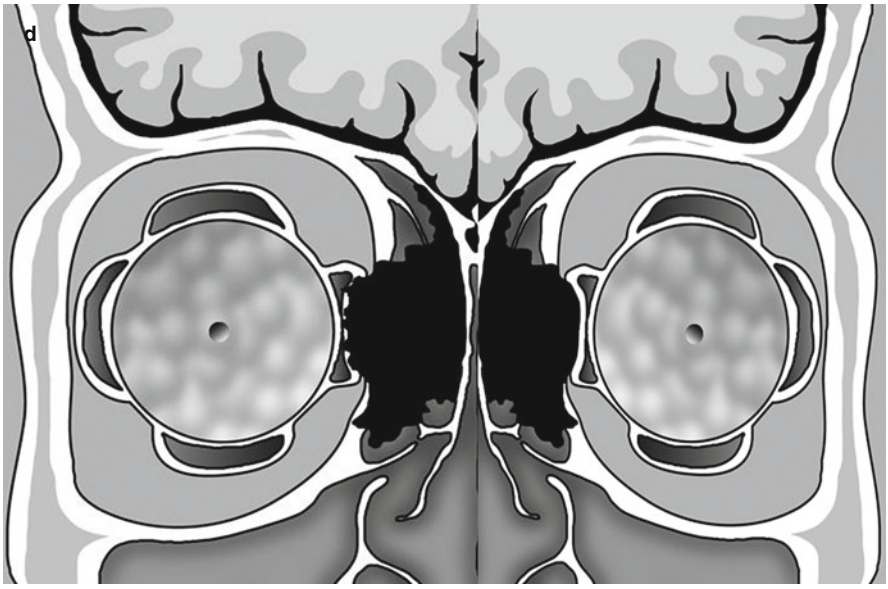

Fig. 9.24 (continued)

angiofibromas may involute spontaneously and, when imaged in the process of doing so, enhancement may not be as intense as expected. The angiomatous polyp is an entity that may appear similar to angiofibromas but does not enhance to the same extent or infiltrate to the same degree as angiofibromas do.

Three types of papillomas arise from the Schneiderian epithelium of the nasal cavity: inverted, fungiform, and cylindrical. Inverted papillomas arise from the lateral nasal walls near the middle turbinate and demonstrate an endophytic pattern of growth into the ethmoid and maxillary sinuses. Due to squamous metaplasia in the adjacent epithelium, inverted papillomas are associated with an increased risk of squamous cell carcinoma and should be removed with clear margins. On CT, inverted papillomas appear as lobulated masses containing fragments of destroyed bone. A focus of sclerosis in the lateral nasal wall may suggest the attachment site. The presence of bone destruction in association with an inverted papilloma is a worrisome sign and may indicate coexisting squamous cell carcinoma. On MRI, an inverted papilloma may demonstrate a convoluted so-called cerebriform appearance on postcontrast images (Fig. 9.30).

9.5 The Surgeon's Perspective

9.5.1 FESS

The mainstay of treatment for both acute and chronic sinusitis is medical. When considering a patient for functional endoscopic sinus surgery (FESS), imaging should be obtained at the point of maximal therapeutic benefit. Functional endoscopic sinus surgery (FESS) relieves obstruction of sinus drainage pathways with

Fig. 9.25 Meningeal invasion. In (**a**), this esthesioneuroblastoma has clearly breached the cribriform plate to enter the anterior cranial fossa. Although the thin dural enhancement (*arrowheads*) may be reactive in nature, the leptomeningeal enhancement (*arrows*) suggests meningeal invasion. In (**b**, **c**), in a patient with an undifferentiated carcinoma, vasogenic edema in the right frontal white matter (*asterisk*) indicates brain parenchymal invasion. (**d**) The graphic illustrates leptomeningeal invasion (*long arrow*), dural invasion (*short arrows*), and vasogenic edema from brain parenchymal invasion (*asterisk*)

reduced inflammation and improved mucociliary clearance (Fig. 9.31). Careful review of anatomic imaging before FESS is crucial to performing a safe and effective operation. Sinus CT clearly delineates the extent and location of disease but also defines the variable anatomy of the paranasal sinuses and key surrounding structures. While performing FESS is not reliant on real-time 3D image guidance, this technology can be assistive in more complex cases and/or when crucial anatomic landmarks are absent.

Preoperatively, the sinus CT should be used to delineate the anatomy of the skull base. As classified by Keros, the vertical height between the cribriform plate and fovea ethmoidalis is variable; as this measurement increases, so does the risk of

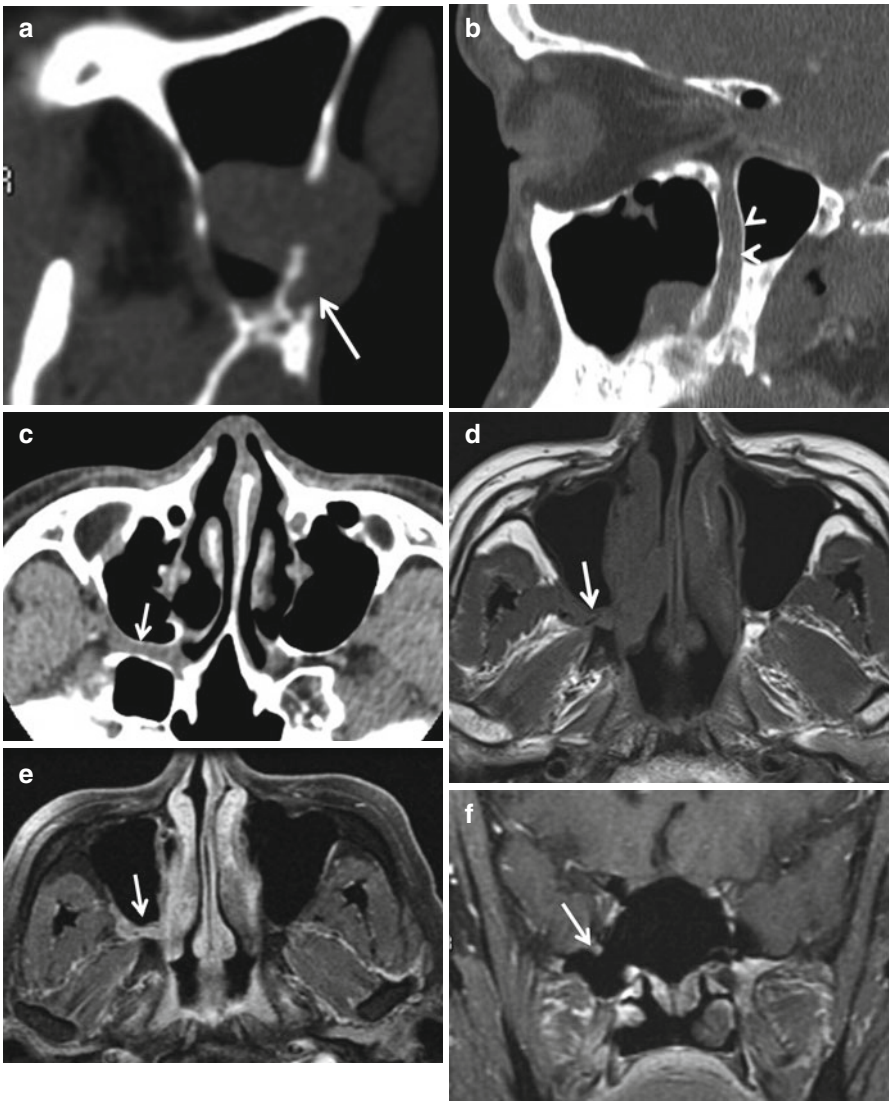

Fig. 9.26 Perineural spread of adenoid cystic carcinoma of the nasal cavity and maxillary sinus. In (**a**), the walls of the greater palatine nerve foramen are destroyed (*arrow*). In (**b**), spread of tumor along the length of the greater palatine nerve into the pterygopalatine fossa (PPF) is evident (*arrowheads*). In (**c**, **d**), note that although the fat density/signal intensity of the PPF is preserved on the left, it has been replaced with soft tissue on the right (*arrows*). Unenhanced T1-weighted images without fat suppression provide excellent depiction of soft tissue intensity tumor against a background of high signal fat. In (**e**), a fat-suppressed contrast-enhanced image, enhancement of tumor in the PPF is evident. In (**f**), note that there is enhancement and expansion of the right foramen rotundum indicating spread along the second division of the trigeminal nerve (*arrow*)

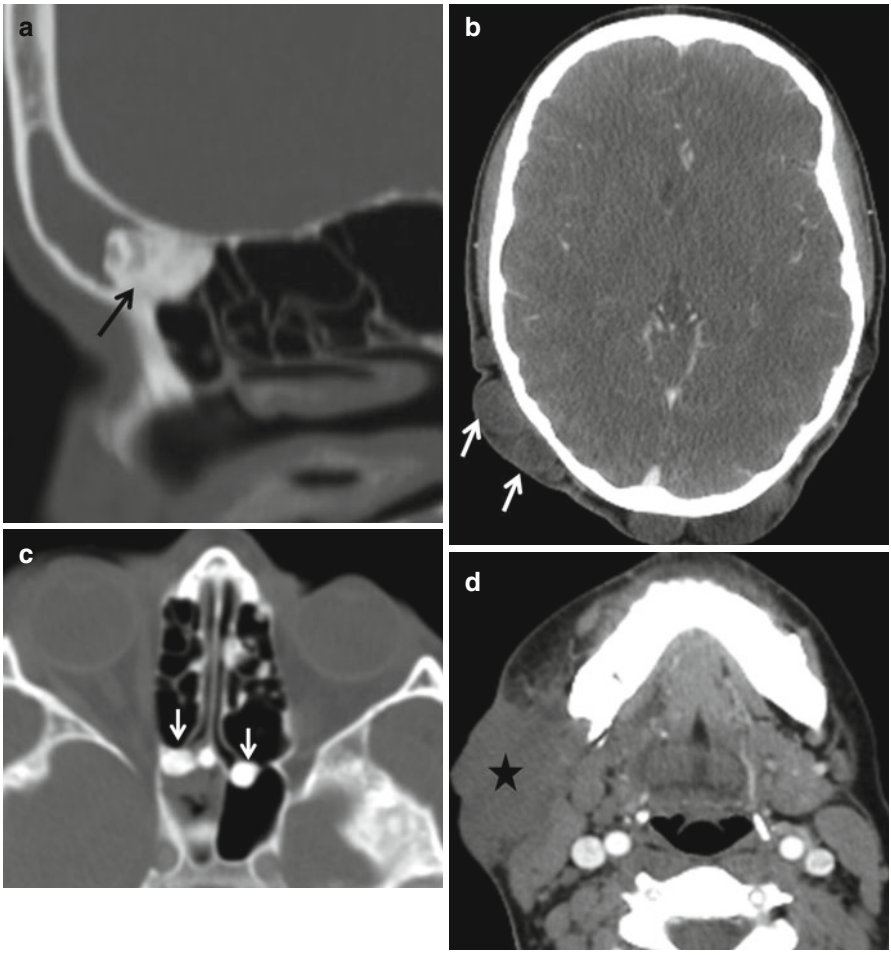

Fig. 9.27 (**a**) Osteoma causing obstruction of the frontal sinus drainage pathway. (**b–d**) Gardner's syndrome with multiple osteomas (*arrows*, **b**), sebaceous cysts (*arrows*, **c**), and a parotid space desmoid tumor (*asterisk*, **d**)

intraoperative skull base injury. Additionally, the superior skull base attachment of the middle turbinate should be noted, and the lamina papyracea should be evaluated for defects. The relationship of the ethmoid bulla to the lamina papyracea and the anterior skull base should be noted, as these landmarks are important for completion of a thorough ethmoidectomy. Identifying dehiscences of the internal carotid artery and optic nerve will help prevent inadvertent injury to these structures during the surgery. Positions of significant vessels that enter the nasal cavity including the anterior and posterior ethmoid arteries and the sphenopalatine artery should be noted.

Unusual air cells may harbor disease or create anatomic confusion when visualized transnasally, and an awareness of these variants is crucial. The CT scan can be used to identify conchae bullosa, Haller cells, agger nasi cells, supraorbital cells,

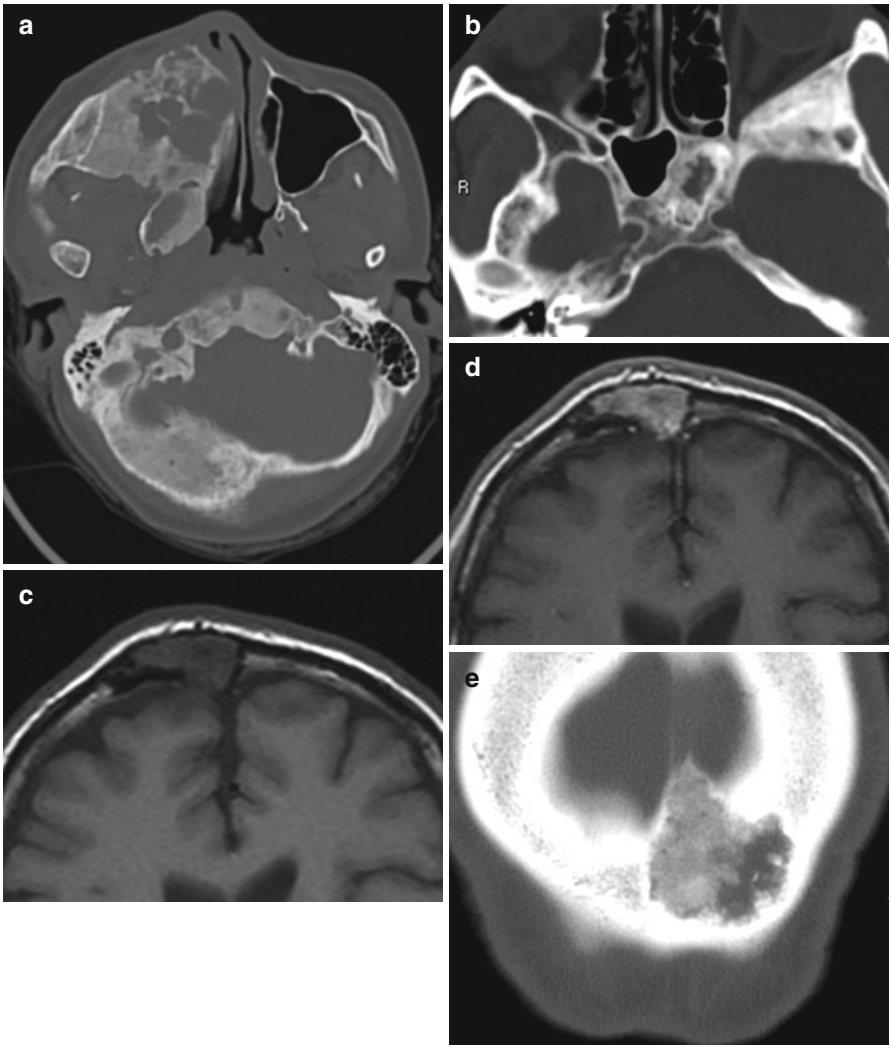

Fig. 9.28 Examples of fibrous dysplasia. In (**a**) the typical features of osseous expansion and involvement of multiple craniofacial bones is evident. In (**b**), the lesion in the left sphenoid sinus demonstrates a sclerotic rind while that in the left pterion is more homogeneously sclerotic. In (**c**, **d**), the lesion on MR simulates an aggressive lesion but the CT (**e**) reveals the ground glass matrix of typical fibrous dysplasia

and Onodi cells. For frontal sinus surgery, the position, orientation, and patency of the frontal outflow tract can be determined. Inter-sinus septa in the sphenoid and frontal sinuses, which are often not midline, should be examined. When correlated with physical exam findings, CT documentation of significant septal deviation and/or inferior turbinate hypertrophy can be useful in planning adjunctive procedures such as septoplasty and inferior turbinate fracture/reduction.

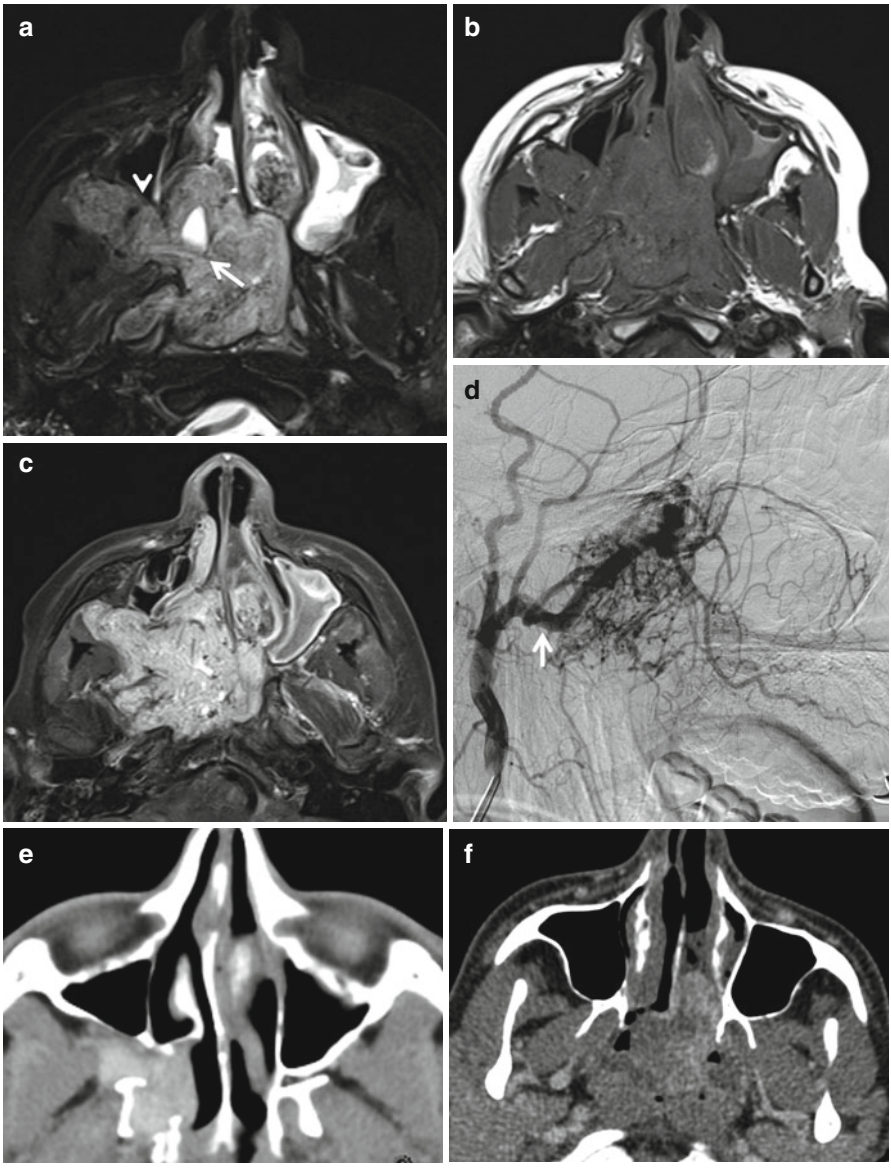

Fig. 9.29 Juvenile nasopharyngeal angiofibroma. Images (**a**–**d**) demonstrate the typical features of a JNA – a lesion centered at the sphenopalatine foramen (*arrow*), extension into the masticator space through the PPF with bowing of the posterior maxillary wall (*arrowhead*), and a large component in the nasal cavity accounting for epistaxis. Note the enlarged maxillary artery in (d) supplying the tumor. (**e**) Demonstrates the typical CT appearance of a JNA, that of an intensely enhancing lesion centered at the sphenopalatine foramen and extending into the PPF. (**f**) Is an atypical JNA in a 28-year-old patient. Note that the lesion lies entirely in the nasal cavity and enhances only moderately

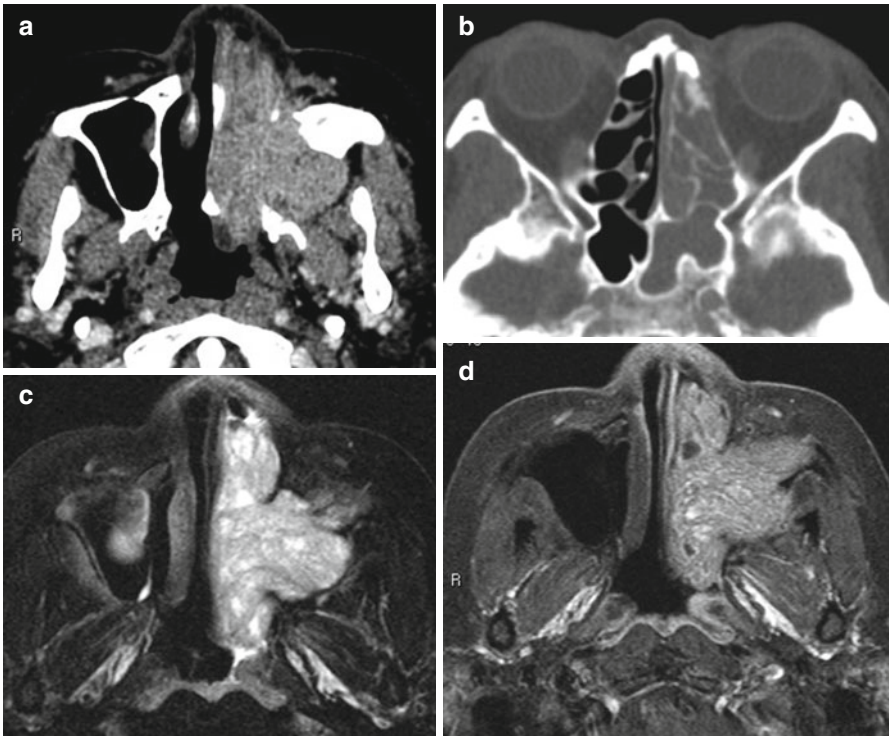

Fig. 9.30 Inverted papilloma in a middle-aged male smoker. An enhancing destructive mass is seen in the left nasal cavity and maxillary sinus. Although the CT appearance of this mass is nonspecific, the "cerebriform" pattern on the T2-weighted (**c**) and contrast-enhanced (**d**) MR image is highly suggestive of the diagnosis. Focal hyperostosis may indicate the site of origin of these tumors as seen in an anterior ethmoid cell in (**b**) (*arrow*)

Failure of FESS to resolve symptoms occurs in up to 20 % of patients (Fig. 9.31); possible causes are listed in Box 9.6. Box 9.7 summarizes the possible complications of FESS. CT is usually sufficient to evaluate these, but the optic nerves and meninges are best evaluated with MRI.

Box 9.6. Causes of Failed Functional Endoscopic Sinus Surgery

Postoperative obstructive synechia
Recurrent polyposis
Inadequate removal of agger nasi or frontal cells
Uncinate remnants
Lateralized middle turbinate
Osteitis of drainage pathway walls
Mucoceles

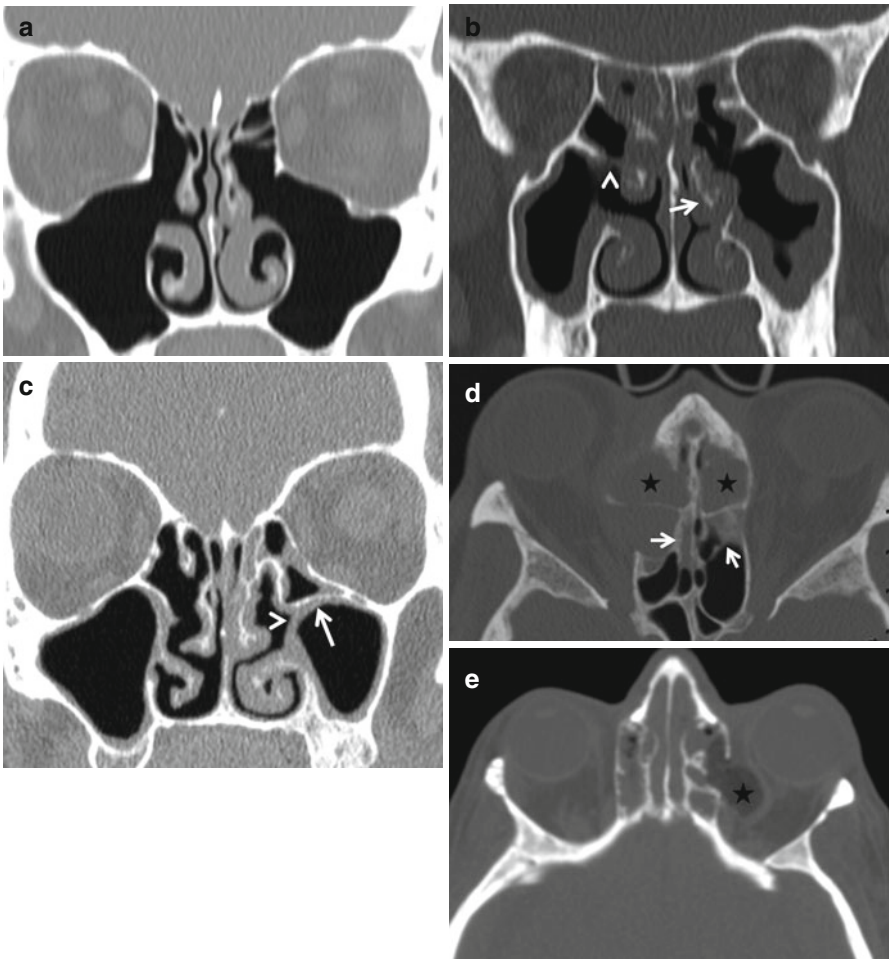

Fig. 9.31 Functional endoscopic sinus surgery. (**a**) Changes after bilateral uncinectomy and anterior ethmoidectomy. (**b**) Recurrent sinonasal polyposis after FESS. Note formation of synechia (*arrowhead*) and lateralization of the left middle turbinate (*arrow*). Persistent symptoms after FESS in (**c**). The left infundibulum is compromised by synechia (*arrowhead*) and an unaddressed Haller cell (*arrow*). The left middle turbinate is also adherent to the septum due to scarring (**d**). Persistent symptoms after FESS due to bilateral anterior ethmoid mucoceles (*asterisks*). Also seen are changes of chronic osteitis in the walls of the ethmoid air cells (*arrows*). In (**e**), inadvertent placement of packing material (*asterisk*) in the left orbit through a preexisting defect in the lamina papyracea is noted

Box 9.7. Complications of Functional Endoscopic Sinus Surgery

- Orbital
  - Intraorbital hematoma – anterior or posterior ethmoid artery injury
  - Extraocular muscle injury
  - Optic nerve injury
    - Direct trauma
    - Nerve compression by hematoma from PE artery injury
  - Nasolacrimal duct trauma
    - Dacryocystitis
    - Epiphora
- Vascular
  - Anterior and posterior ethmoid artery injury
  - Internal carotid artery injury
- Skull base
  - CSF leaks and recurrent meningitis
  - Meningoencephaloceles

9.5.2 Nasal Cavity and Sinus Tumors

While sinusitis is generally a bilateral disease, adults with unilateral nasal obstruction must be evaluated carefully for a tumor. In adults, a unilateral nasal mass that obscures the roof of the nasal vault should be imaged before a biopsy is performed to rule out a meningoencephalocele. This is best done with MRI. When appropriate, biopsy is important to determining treatment approach because imaging characteristics are often inadequate to predict a definitive diagnosis. While benign expansile lesions can be destructive, CT and MRI can generally delineate benign from malignant tumors, and most benign tumors today will be managed using endoscopic surgery. However, management of malignant nasal cavity and sinus tumors is highly variable depending on the location and the histology. In general, management is most impacted by the extent of local disease. Major factors include extension beyond the nasal and sinus cavities, particularly into the cranial vault, orbit, or nasopharynx. Again, it is important to determine invasion into and through these structures versus erosion by a benign expansile mass. Once intracranial, it is important to determine the presence and degree of dural and parenchymal involvement. With more extensive malignant lesions, neck imaging may be appropriate to evaluate for regional metastases.

Resection of malignant tumors involving the superior nasal vault can be performed by open (i.e., craniofacial), endoscopic, or combined approaches. Immediate postoperative CT imaging often shows thick enhancement of the frontal dura, a reactive phenomenon that must not be mistaken for infection or tumor. Pericranial or myofascial flaps are commonly used to fill the skull base defect; these can demonstrate a convex masslike appearance on imaging for an extended

period of time. The presence of a walled-off fluid collection on a postoperative scan is not normal and may indicate infection, hematoma, or a CSF leak (Fig. 9.32). Likewise, postoperative enhancement is usually linear and smooth; any nodularity, especially if it increases in size on serial imaging, must be presumed to represent recurrent tumor.

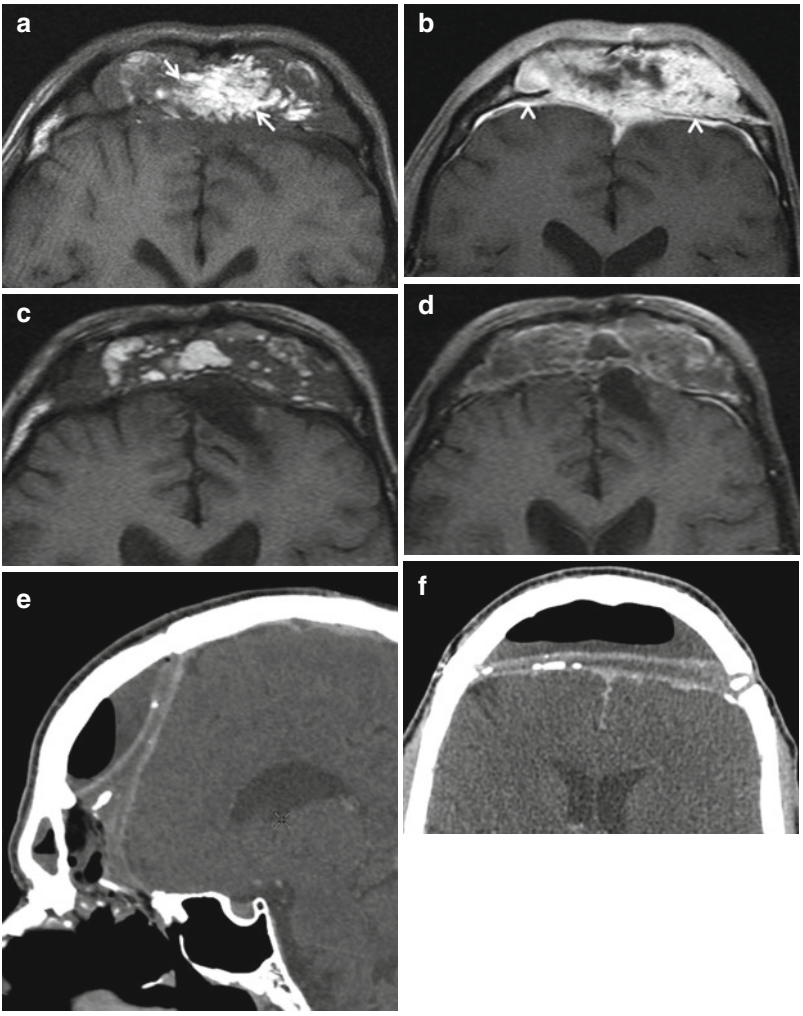

Fig. 9.32 Postoperative findings after craniofacial resection for esthesioneuroblastoma. Images (**a**, **b**) were obtained immediately after surgery, while (**c**, **d**) are from a study 6 months after the procedure. Note the persistent masslike appearance of the myofascial flap. The T1 hyperintense foci (*arrows*), representing fat involute with time. Enhancement of the flap and of the underlying dura (*arrowheads* in **b**) is not unusual and subsides with time. The presence of a fluid collection or of air-fluid levels (**e**, **f**) is not an expected postoperative finding and may indicate infection as in this case

Further Reading

Aribandi M, McCoy VA, Bazan C (2007) Imaging features of invasive and noninvasive fungal sinusitis: a review. Radiographics 27(5):1283–1296

Daniels DL, Mafee MF, Smith MM, Smith TL, Naidich TP, Brown WD, … Strottmann JM (2003) The frontal sinus drainage pathway and related structures. Am J Neuroradiol 24(8): 1618–1627

Eden BV, Debo RF, Larner JM, Kelly MD, Levine PA, Stewart FM, Cantrell RW, Constable WC (2006) Esthesioneuroblastoma. Long term outcome and patterns of failure—the University of Virginia experience. Cancer 73(10):2556–2562

Hoang JK, Eastwood JD, Tebbit CL, Glastonbury CM (2010) Multiplanar sinus CT: a systematic approach to imaging before functional endoscopic sinus surgery. Am J Roentgenol 194(6):W527–W536

Huang BY, Lloyd KM, DelGaudio JM, Jablonowski E, Hudgins PA (2009) Failed endoscopic sinus surgery: spectrum of CT findings in the frontal recess. Radiographics 29(1):177–195

Raghavan P, Phillips CD (2007) Magnetic resonance imaging of sinonasal malignancies. Top Magn Reson Imaging 18(4):259–267

Schuster JJ, Phillips CD, Levine PA (1994) MR of esthesioneuroblastoma (olfactory neuroblastoma) and appearance after craniofacial resection. AJNR Am J Neuroradiol 15(6):1169–1177

Yousem DM, Gad K, Tufano RP (2006) Resectability issues with head and neck cancer. AJNR Am J Neuroradiol 27(10):2024–2036

Head and Neck Trauma

10

David Clopton, Sugoto Mukherjee, J. Jared Christophel, Max Wintermark, and Prashant Raghavan

10.1 Introduction

The overwhelming majority of craniofacial traumatic injuries however are caused by motor vehicle accidents with about 70 % of these including some type of facial injury. The objectives of this chapter are to review the standard imaging techniques used to evaluate craniofacial trauma, discuss the various patterns of facial fractures with emphasis on the pertinent findings and relevant anatomical considerations, and finally present some special considerations pertaining to pediatric patients.

10.2 Imaging Evaluation

Plain films no longer play a significant role in evaluating craniofacial trauma. Facial injuries are best evaluated by CT using 1.25 mm or thinner images through the face. Images should include both soft tissue and bone algorithms, with coronal and sagittal reformatting. While axial, coronal, and sagittal images are sensitive at identifying fractures, 3D reconstructions play a significant role in surgical planning and should be made available.

First, the skin and soft tissues are inspected; traumatic soft tissue findings will direct the radiologist to more closely examine the adjacent deeper structures. The superficial bony structures are evaluated next, followed by the deeper bony structures. Finally, it is useful to consider typical fracture patterns and areas that are easy to miss, including the lamina papyracea, orbital rims and floor, nasolacrimal duct, carotid canal, temporal bones, and orbital apex. The craniocervical junction is often included on these examinations, and it is important to evaluate the occipital condyles and the atlas and axis vertebra and their joints.

P. Raghavan et al., *Manual of Head and Neck Imaging*,
DOI 10.1007/978-3-642-40377-4_10,

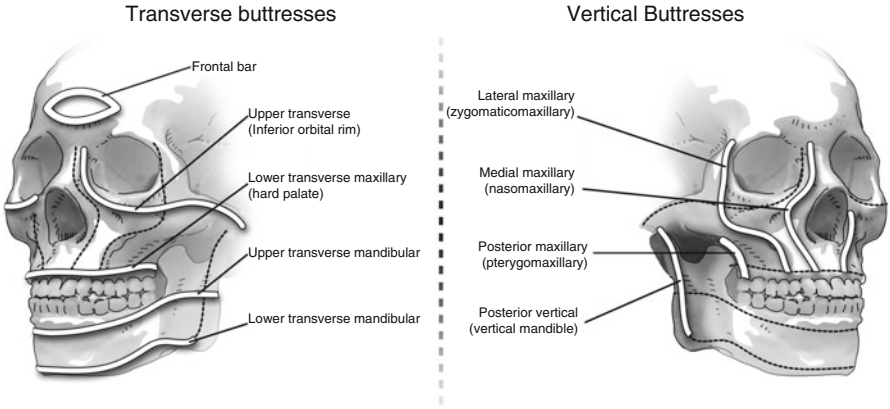

Fig. 10.1 Facial buttress graphic. The facial buttress system is divided into vertical and horizontal buttresses. As shown in the above figure, the vertical buttresses run on the medial and lateral aspects of the maxillary sinus/orbits and mandible, whereas the horizontal buttresses run below the orbits, above and below the teeth, and at the bottom of the mandible

10.3 The Facial Buttress Concept

The facial buttress concept describes the regions of thicker bone that provide structural support to the facial skeleton. The buttresses play key roles in maintaining facial stability (e.g., with mastication) and appropriate midface projection. Accordingly, repair of fractured buttresses is crucial to maintain form and function of the face, orbits, sinuses, nose, and teeth. As they have sufficient bone thickness to accept screws and anchor titanium plates, the buttresses are a focus of surgical planning for fracture repair. The strongest buttresses are vertically oriented: the medial nasomaxillary buttress and the lateral zygomaticomaxillary buttress (Fig. 10.1). The pterygomaxillary buttress has also been described but is less commonly addressed in fracture repair. The horizontal buttresses are weaker and include the superior orbital rims and frontal bones superiorly, the inferior orbital rims and nasal bones across the midface, and the maxillary alveolus and hard palate inferiorly (Fig. 10.1).

10.4 Fracture Patterns

10.4.1 Nasal Fractures

The nasal bones are the most commonly fractured bones of the face. The nasal bone is thicker cephalically and becomes progressively thinner inferiorly. Eighty percent of nasal fractures occur within the thinner portion below the

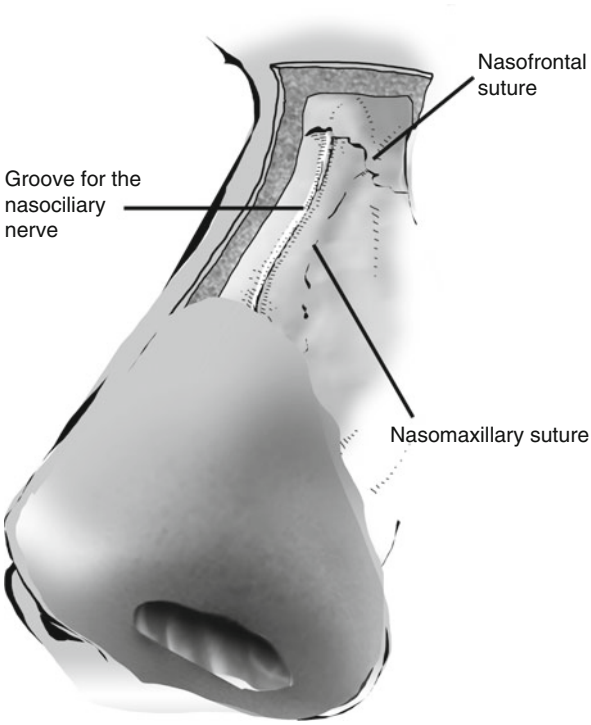

Fig. 10.2 Nasal bone anatomy. The nasofrontal and nasomaxillary sutures and the groove for the nasociliary nerve are common mimics of nasal fractures. A lucency inferior to the nasofrontal suture should not cross the midline

intercanthal line (axial line connecting the orbital rims at the level of the lateral canthi). The most common pitfall is confusing a suture line for a nasal fracture (and vice versa). Confusion is most frequently centered around the so-called high defect (thinning of the nasal wall) and low defect (nasomaxillary suture). Most nasal fractures occur in the transverse plane, while normal sutures and nasociliary grooves are longitudinally oriented and do not cross the midline; lucencies that cross the midline are fractures. Additionally, short lucent lines that reach the anterior cortex of the nasal bone, regardless of displacement, should be considered nasal fractures (Fig. 10.2).

The nasal bones comprise only one third of the structural support of the nose; the majority of the nasal structure is cartilage which can also be injured. Cartilaginous fractures can result in perichondrial separation resulting in hematoma formation. Cartilage hematomas interfere with native blood supply to the cartilage and can result in necrosis, infection, and long-term saddling of the nose. The radiologist should always evaluate the nasal septum for localized septal swelling or traumatic deviation. A septal hematoma can result in sclerotic septal distortion and disordered or obstructed airflow, or it can become a nidus for infection (Fig. 10.3). To avoid these complications, septal hematomas require prompt evacuation (Box 10.1).

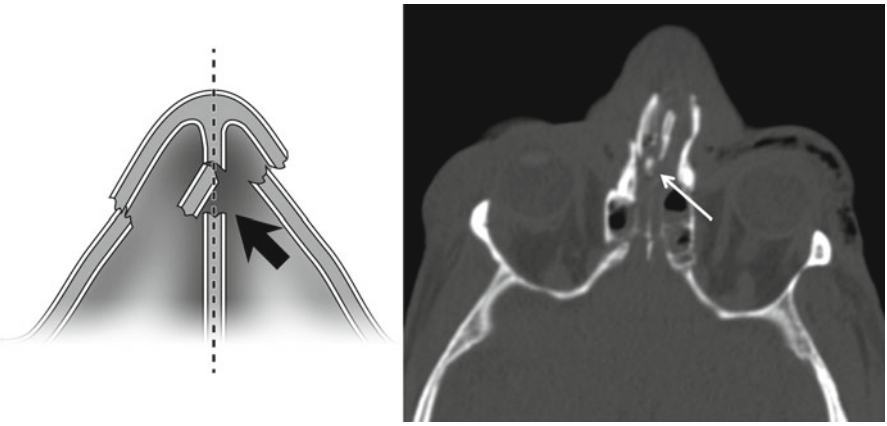

Fig. 10.3 Nasal septum fracture. In the setting of nasal trauma, it is important to identify traumatic deviation of the nasal septum (*white arrow*), and any associated soft tissue hematoma.

Box 10.1. Nasal Bone Fractures: Pearls and Pitfalls

Don't confuse the high and low defects for fractures

Old or new? Remote fractures may mimic a recent fracture; look for soft tissue swelling

Most nasal bone fractures occur in the transverse plane

The nasociliary groove does not cross the plane of the nasal bone; but a fracture can

Look at the nasal septum to identify signs of septal hematoma (localized septal swelling or traumatic deviation)

10.4.2 Naso-Orbital-Ethmoid (NOE) Fractures

Naso-orbital-ethmoid (NOE) fractures involve the nasal bones, the ethmoid sinuses, and the medial orbital rims. This type of fracture tends to disrupt the confluence of the medial maxillary buttress with the upper transverse maxillary buttress (Fig. 10.4). Classically, the anterior nasal structures are displaced posteriorly into the lacrimal bones and ethmoid sinuses.

A key finding in NOE fractures is an increased distance between the medial orbital walls and the attachments of the medial canthal tendons (MCTs, which arise from the anterior and posterior lacrimal crests) (Fig. 10.5). Splaying of the medial orbital walls will result in telecanthus and malposition of the globes. Grading of NOE fractures depends on the status of the MCT: grade I involves MCT attachment to a large bone fragment of the lacrimal fossa; grade II demonstrates multiple smaller comminuted fragments; and grade III indicates avulsion of the MCT. Often accurate grading requires physical exam and/or intraoperative assessment (Fig. 10.6).

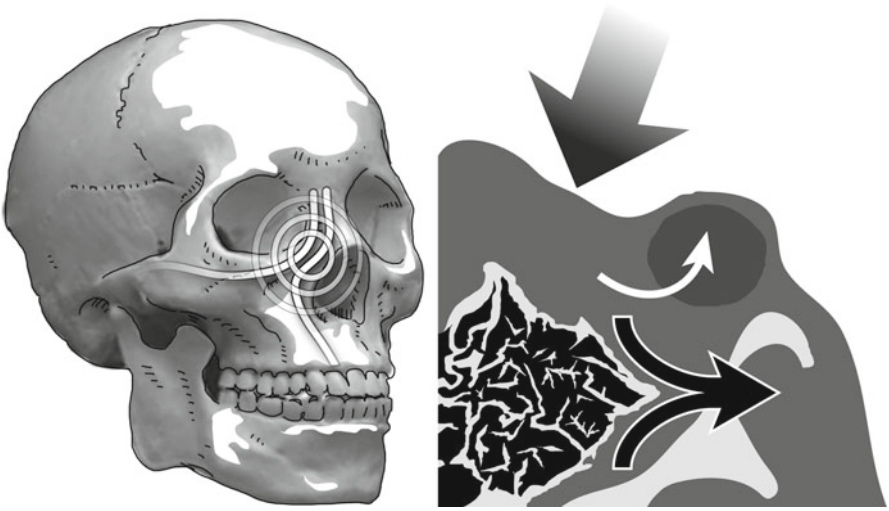

Fig. 10.4 NOE fracture. Posterior displacement of the anterior nasal bony structures can result in lateral displacement of the medial orbital walls causing proptosis

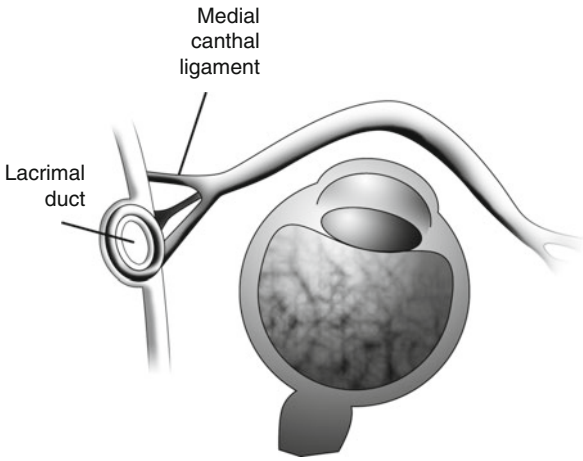

Fig. 10.5 Medial canthal ligament anatomy. The medial canthal ligaments are not visible on CT. However, their bony attachments anterior and posterior to the lacrimal crest can be identified

NOE fractures are commonly associated with frontal sinus fractures. Injury to the frontal sinus outflow tract (FSOT) may lead to formation of adhesions, obstruction, and subsequent frontal mucocele (Fig. 10.7). If the FSOT is involved, a frontal sinus obliteration procedure may be required (Box 10.2).

10.4.3 Frontal Sinus Fractures

In general, fractures through sinus walls tear mucosa and produce hemorrhage; thus, in the acute phase, the absence of free fluid in a sinus cavity excludes a fracture. When the frontal sinus is fractured, only the anterior table is disrupted in

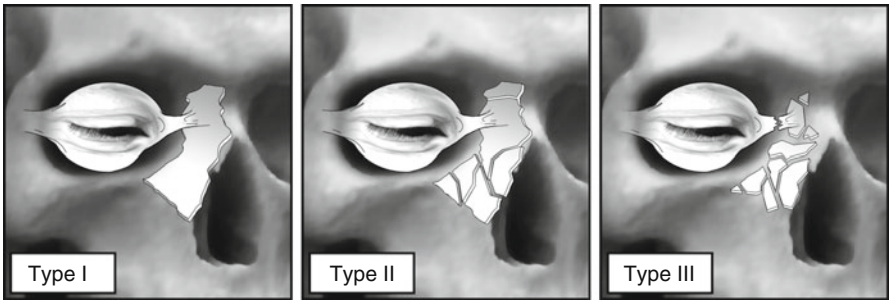

Fig. 10.6 Manson classification. The Manson system classifies NOE fractures based on the medial canthus. In type 1, the fractured piece is large and the insertion of the medial canthal ligament around the lacrimal fossa is intact. In type II, there is a comminuted fracture of the buttress and the canthus is attached to a small bone fragment. In type III, there has been avulsion of the ligament from its osseous insertion. The distinction between type II and type III cannot be done with imaging and requires physical exam

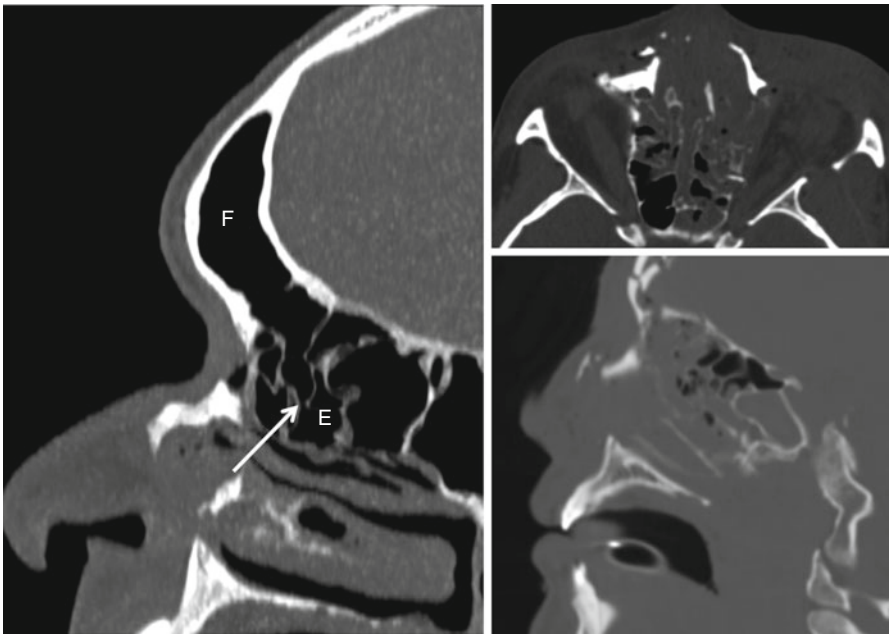

Fig. 10.7 Frontal ethmoid sinus drainage. The above image demonstrates the drainage pathway (*arrow*) between the frontal sinus *F* and the ethmoid sinuses *E*. A fracture that disrupts this drainage can predispose the patient for frontal sinus mucocele formation

approximately two thirds of cases. Repair for these is considered in the setting of cosmetic deformity. The implications are much more significant when the posterior table is involved; in this case, the degree of posterior table displacement and amount of pneumocephalus must be reported, as these are the indications for surgical repair.

Box 10.2. Naso-Orbital-Ethmoid (NOE) Fractures: Checklist

Evaluate for a fracture of the medial orbital wall in the region of the nasal lacrimal duct If present, is the fracture fragment large or comminuted?

Assess the distance between the two lacrimal fossae in the coronal plane, to identify a potential deformity that requires repair

Evaluate for disruption of the nasofrontal drainage pathways

Posterior table fractures are associated with CSF leaks, meningitis, and traumatic brain injury. As discussed above, the status of the FSOT should be reviewed.

10.4.4 Orbital Fractures

10.4.4.1 Inferior Blowout Fracture

"Blowout" fractures occur as the result of a direct blow to the orbit by an object that is too large to enter the orbit. The force of the blow is absorbed by the thick orbital rim and is transmitted to the thin orbital floor. Alternative theories describe force transmitted through the globe to the orbital floor which is the path of least resistance in the orbit. The typical result is a fracture of the middle third of the orbital floor near the infraorbital canal; the orbital rim remains intact. (By strict definition, if the orbital rim is fractured, the floor fracture cannot be referred to as a "blowout.") An important complication of orbital floor disruption is orbital entrapment. While the diagnosis of entrapment can only be made on physical exam, noting herniation of orbital fat, the inferior rectus muscle, or the inferior oblique muscle through the orbital floor is strongly suggestive. An abrupt kink in the herniated muscle as opposed to a smooth prolapse through the site of fracture is convincing evidence of entrapment. If the inferior rectus muscle remains flattened in cross section and in the correct position, the fascial sling is likely intact. Alternatively, if the muscle is round in cross section and inferiorly displaced, the fascial sling is likely disrupted increasing the likelihood of entrapment. Rounding of the inferior rectus is associated with development of enophthalmos with nonoperative treatment, and reporting of height-to-width ratio of this muscle can be useful in treatment planning. Regardless of imaging findings, an ophthalmologic exam is recommended for all orbital injuries and is critical to evaluate for entrapment; this is particularly true in the pediatric setting (Fig. 10.8).

10.4.4.2 Medial Blowout Fracture

Fractures of the lamina papyracea can be very subtle. Orbital emphysema in the absence of an obvious fracture of the orbital roof or floor suggests a medial wall fracture. Herniation of orbital fat and entrapment of the medial rectus muscle may occur through the fracture defect. If the fracture results in loss of the posterior medial orbital bulge (Fig. 10.9), the normal bony orbital volume will be increased and enophthalmos can result; this is actually the most common cause of enophthalmos.

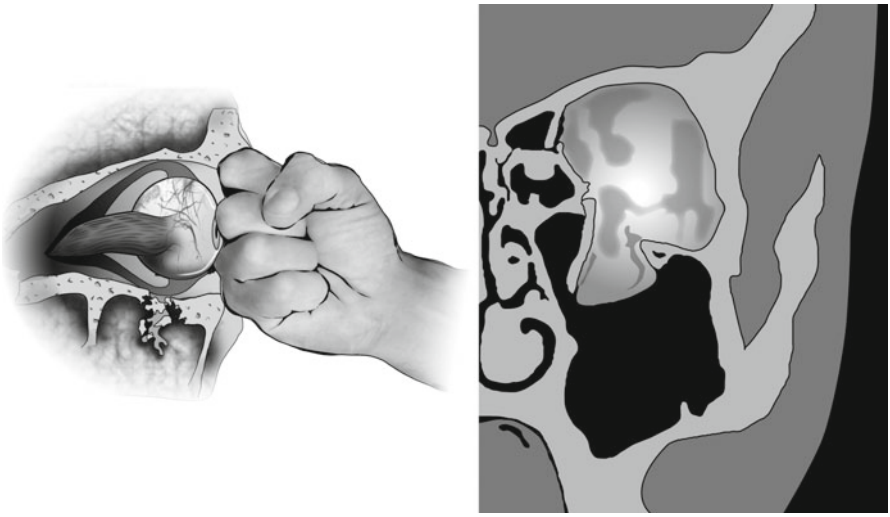

Fig. 10.8 Blowout facture. The above diaphragm demonstrates inferior displacement of the inferior orbital floor with some herniation of intraorbital fat. The inferior rectus muscle normally has a flat appearance. A more rounded appearance can be seen with a contused muscle and can raise suspicion for entrapment

Fig. 10.9 Medial orbital bulge. The above diaphragm demonstrates loss of the normal orbital bulge, compared to the normal contralateral contour. This expands the orbital volume and can cause enophthalmos

10.4.4.3 Orbital Roof and Blow-In Fractures

Fracture of the orbital roof is more common in the pediatric population (see below). However, this fracture still occurs in the adult population and is frequently associated with frontal sinus and skull base fractures, dural tears, intracranial hemorrhage, and meningoencephaloceles. When orbital roof fractures demonstrate inferior displacement of fracture fragments into the soft tissues of the orbit, they are called

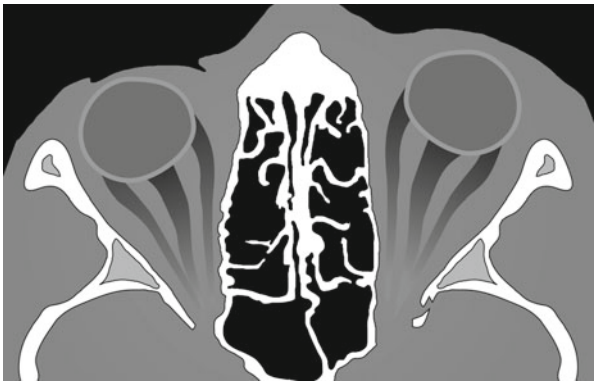

Fig. 10.10 Orbital apex fracture. The above diaphragm demonstrates how subtle a fracture involving the orbital apex can be. In the setting of trauma, careful scrutiny of this area is important because of the potentially devastating complication to the optic nerve and vessels

Box 10.3. Globe Trauma: Checklist

Evaluate the anterior chamber. Increased attenuation = hyphema. Decreased depth = corneal laceration or anterior subluxation. Increased depth is associated with open globe injury

Evaluate the lens. Remember it is usually dislocated posteriorly (but can be anteriorly)

Evaluate the posterior globe. Look specifically for blood or evidence for retinal or choroidal detachment

Evaluate the ophthalmic veins. Dilatation may indicate a carotid-cavernous fistula

Evaluate for the presence of retinal hemorrhage. In a child this is concerning for possible non-accidental trauma

"blow-in" fractures. While ocular injury is uncommon with "blowout" fracture, it has been reported in 14–29 % of patients with blow-in fractures.

10.4.4.4 Orbital Apex Fractures

Fracture of the orbital apex is rare and can be associated with optic nerve impingement. When this fracture is identified, it is important to evaluate for a retrobulbar hematoma and for a bone fragment impinging on the optic nerve. It is critical to realize that even a small fracture can cause nerve injury (Fig. 10.10) (Box 10.3).

10.4.4.5 Traumatic Globe Injury

Evaluation of the globes should begin with the anterior chambers to ensure they are symmetric. If the volume of the anterior chamber appears decreased, it may indicate a corneal laceration or anterior displacement of the lens. Increase in anterior chamber size is associated with globe rupture (less posterior chamber volume allows the anterior chamber to expand). The position of the lens must be evaluated as trauma is the

Fig. 10.11 Vitreous hemorrhage. Disruption of the left globe with vitreous hemorrhage (*asterisk*) and posterior lens dislocation (*white arrow*). There is a small amount of right retinal hemorrhage (*white arrowhead*)

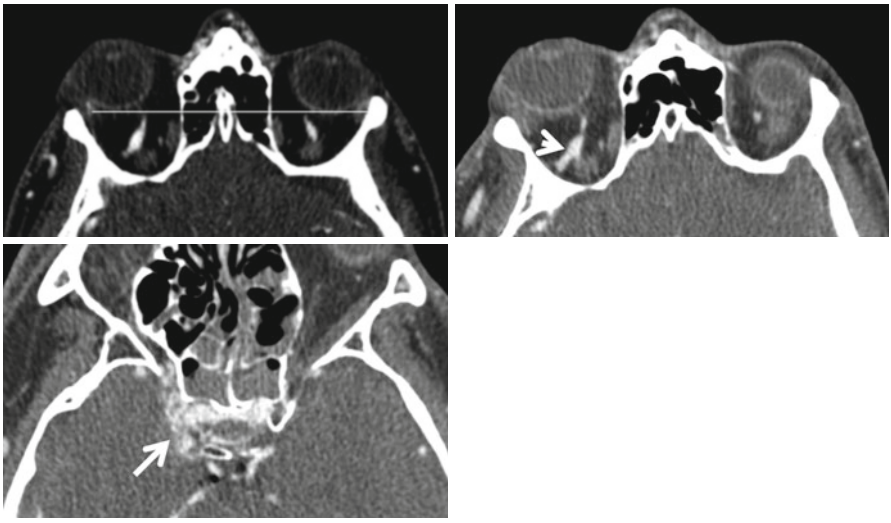

Fig. 10.12 Carotid-cavernous fistula. The right cavernous sinus is relatively enlarged (*arrow*) and shows more contrast opacification compared to the left side. This is associated with a prominent right superior ophthalmic vein (*arrow head*) and right proptosis. This combination of findings is concerning for a carotid-cavernous sinus fistula

most common cause of lens dislocation, usually into the posterior chamber. However, it must be remembered that the lens may dislocate for nontraumatic reasons (Marfan and Ehlers-Danlos syndromes, homocystinuria), particularly if the dislocation is bilateral. The posterior chamber must be assessed for hemorrhage (Fig. 10.11). Retinal detachment may occur, especially in the setting of a globe rupture; collections of subretinal fluid may assume a characteristic V-shaped configuration on cross-sectional imaging. In children, retinal hemorrhage should raise concern for non-accidental trauma. The orbit should also be evaluated for foreign bodies, remembering that wood can mimic air on CT, and for dilation of the ophthalmic veins, which may be a sign of a carotid-cavernous fistula (Fig. 10.12) (Box 10.4).

Box 10.4. Orbital Fracture: Checklist

Evaluate the integrity of the lamina papyracea
Evaluate for involvement of the infraorbital canal
Evaluate for herniation of orbital fat. Is there clear evidence for ocular muscle entrapment?
Evaluate for ocular muscle contusion. Do the ocular muscles appear contused (swollen/round), compared with the contralateral side?
In the pediatric setting look for a "trapdoor" fracture
Evaluate for a large volume of intraorbital fat herniation. This can lead to chronic enophthalmos
Evaluate for fracture of the orbital apex
Evaluate the globe. Confirm the lens is intact and in the correct position

10.4.5 Zygomaticomaxillary Complex (ZMC) Fractures

The zygoma is a paired facial bone that has sites of articulation with the maxilla, the temporal bone, the sphenoid bone, and the frontal bone. The zygoma forms portions of the orbital floor and lateral wall and is responsible for establishing appropriate orbital volume. ZMC fractures are typically the result of a blow to the malar eminence. They have classically been known as "tripod fractures" but actually involve four fractures ("quadripod"): (1) zygomatic arch fracture, (2) inferior orbital rim and orbital floor fracture, (3) anterior and posterior maxillary sinus wall fractures, and (4) lateral orbital rim and wall fracture. The classic term "tripod fracture" fails to recognize the posterior relationship of the zygoma with the sphenoid bone, and the current preferred terminology is "ZMC fracture."

This complex fracture pattern occurs across the two major buttresses of the ZMC – the vertical zygomaticomaxillary (lateral) buttress and the horizontal inferior orbital rim buttress. Specifically, the fracture line involves the zygomaticomaxillary, zygomaticotemporal, frontozygomatic, and zygomaticosphenoid sutures. Because of the 3-dimensional complexity of this fracture, it is possible to reduce the two buttresses and still have rotational misalignment about the zygomaticosphenoid suture. If this angulation is not reduced prior to addressing the remaining fractures, the facial width will be increased and the cheek will be underprojected. Of note, the component of ZMC fractures involving the zygomaticomaxillary suture line often traverses the infraorbital nerve foramen. Clinically, V2 function should be carefully documented prior to surgical repair (Figs. 10.13 and 10.14).

10.4.6 Zygomatic Arch Fracture

Fractures of the zygomatic arch frequently occur in isolation. It is worth knowing that fractures of the zygomatic arch usually show two distinct fracture fragments that are displaced medially and inferiorly. The fracture is not without consequence

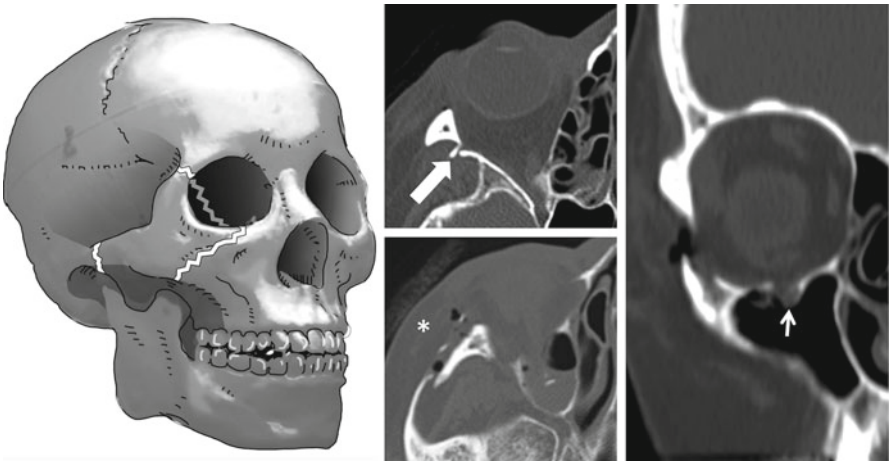

Fig. 10.13 ZMC fracture. The above image series demonstrates substantial rotation deformity at the zygomaticosphenoid suture (*white arrow*), fracture line through the infraorbital nerve foramen (*arrowhead*), and fracture involving the zygomaticotemporal suture (*asterisk*)

Fig. 10.14 The above image demonstrates a fracture of the zygomatic arch, with the classic two distinct fracture fragments (*arrows*)

Fig. 10.15 Le Fort fracture patterns

as fragments may impinge on the temporalis muscle or the coronoid process of the mandible and in some cases alter dental occlusion.

10.4.7 Midface Fractures (Le Fort Classification)

René Le Fort described his classic fracture patterns based on dropping cadaver skulls from several stories or striking them with a wooden club. The results of the experiments demonstrated three distinct fracture patterns: (I) palatofacial disjunction (palate separated from the maxilla), (II) midfacial separation (maxilla separated from the face), and (III) craniofacial disjunction (face separated from the cranium). The forces Le Fort used are similar to low-velocity impacts similar to those seen in fist fights and sporting events. Given the current predominance of high-speed injuries such as vehicular accidents, a combination of Le Fort fractures is more frequently encountered, and it may provide more clarity to describe the fractures rather than trying to identify a pre-classified pattern. Additionally, most midface fractures have some degree of comminution and are complicated by fractures and displacement not addressed by the Le Fort system. Regardless of its shortcomings, the Le Fort system is still the most commonly accepted method for classifying fractures (Fig. 10.15).

10.4.7.1 Le Fort I: Palatofacial Disjunction ("The Palate Separated from the Maxilla")

Fractures of the pterygoid processes are a necessary component of all 3 Le Fort subtypes. Fracture of the anterolateral margin of the pyriform aperture immediately superior to the maxillary alveolar process (best seen on coronal imaging) is unique to the Le Fort I fracture. This pattern is classically seen with a direct blow to the upper jaw and results in a clinically mobile palate. The fracture lines extend through the inferior aspect of the maxillary sinuses and the pterygoid plates. This approach is sometimes used surgically for access to the deep midface.

10.4.7.2 Le Fort II: Midfacial Separation ("The Maxilla Separated from the Face")

Fracture of the inferior orbital rim and orbital floor is unique to the Le Fort II fracture (best seen on coronal imaging). This pattern is classically seen from a direct blow to the central face, resulting in posterior displacement of the central midface. The fracture line will extend through the nasion (separating the nose from the cranium), through the lacrimal bone, medial orbital wall, orbital rim, orbital floor, anterolateral maxillary wall, and pterygoid plates. The midface complex (palate, maxilla, and nose) is mobile on clinical exam.

10.4.7.3 Le Fort III: Craniofacial Disjunction ("The Face Separated from the Cranium")

Fractures of the lateral orbital rim and wall and zygomatic arch are unique to the Le Fort III fracture. The fracture line passes through the nasoethmoid complex, extends horizontally through the medial and lateral orbital walls, transverses the pterygoid plates, and involves the zygomatic arch. This results in complete mobility of the face relative to the cranial vault, including the palate, maxilla, nose, and eyes.

10.4.7.4 Combinations

The search for facial fractures should not end with recognition of a Le Fort pattern, and combinations and unexpected elements are possible. For example, it is possible for Le Fort II and III fractures to exist together on the same side, as it is possible to encounter different subtypes on opposite sides. Most commonly, one or more Le Fort patterns can be recognized with imperfect characteristics; thus, it should always be the rule to describe in careful detail the fractures observed rather than simply remarking on a pattern (Figs. 10.16 and 10.17) (Box 10.5).

10.4.8 Mandibular Fractures

The mandible is the second most commonly fractured facial bone; it is frequently fractured in association with severe midface injures, particularly Le Fort fractures. Because the mandible and the temporomandibular joints (TMJs) form a ring, mandibular fractures are often accompanied by a second fracture or a TMJ dislocation.

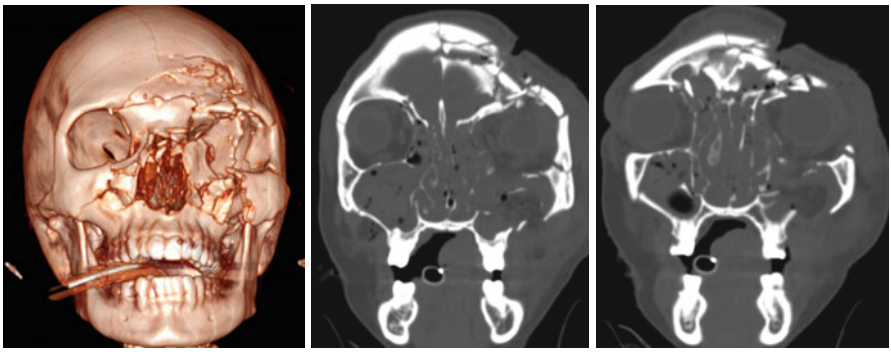

Fig. 10.16 Modern high-velocity fracture patterns often result in complex mixed fracture patterns, with fractures and displacement not covered by the Le Fort system

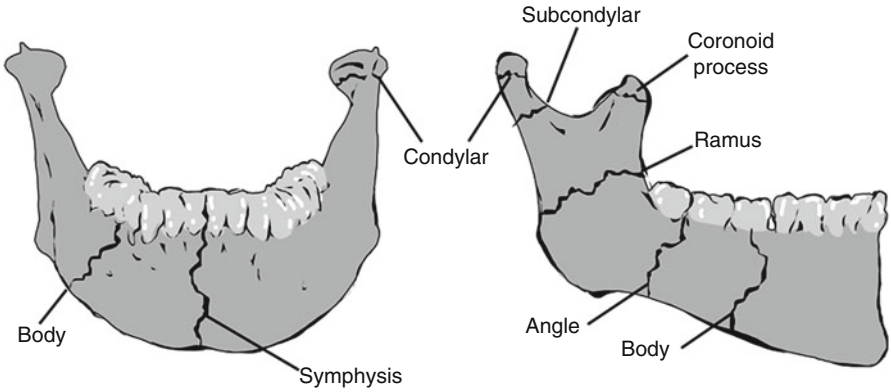

Fig. 10.17 Common mandibular fracture sites

Box 10.5. Le Fort Fracture Key Components

	Common component	Unique component
Type I	Pterygoid processes	Lateral nasal aperture
Type II	Pterygoid processes	Inferior orbital rim Orbital floor
Type III	Pterygoid processes	Zygomatic arch Lateral orbital rim/wall

Mandibular fracture lines tend to follow the long axis of the teeth; all fractures that involve dentoalveolar structures are considered open fractures. When fractures are multiple, one fracture usually approximates the site of impact (e.g., symphysis) and the site of force distribution (e.g., condylar neck) suggests the site of the other.

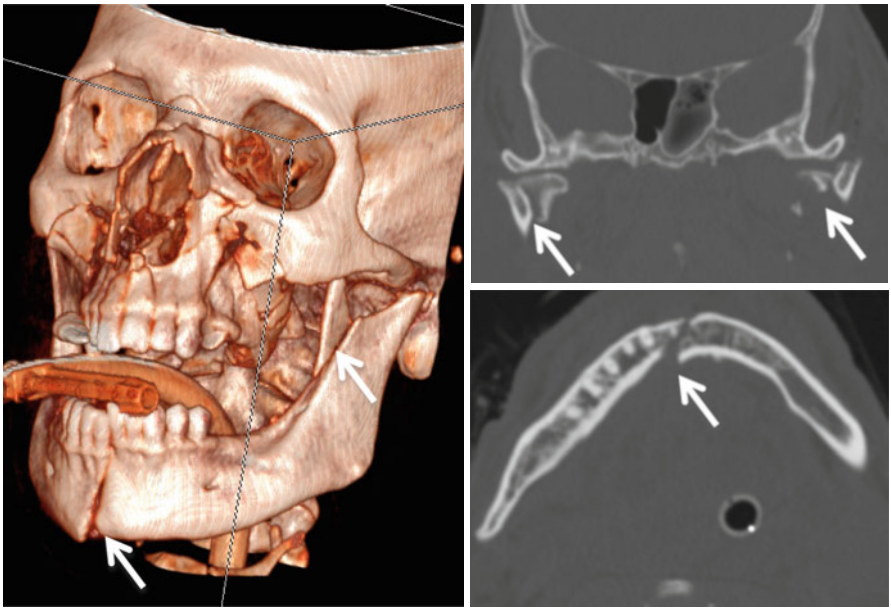

Fig. 10.18 An example of a complex mandible fracture, with fracture sites at the symphysis (*arrow* on axial image) and the bilateral condyles (*arrows* on coronal image)

When a condylar fracture occurs, the force of traction applied by the lateral pterygoid muscle displaces the condylar fragments medially and anteriorly resulting in an "empty glenoid fossa." A fracture through the mandibular canal may cause injury to the inferior alveolar nerve and associate hypesthesia or anesthesia in the V3 distribution. Although uncommon, bilateral temporomandibular joint dislocations can occur without a fracture in the trauma setting (Fig. 10.18).

10.4.9 Temporal Bone Fractures

Temporal bone fractures are classically divided into longitudinal and transverse fractures. However, most temporal bone fractures represent a mixture of these orientations. For the purpose of understanding and predicting the complications associated with temporal bones, it is still useful to discuss the two classic subtypes as isolated entities. However, a more modern classification system based on violation of the otic capsule has recently been shown to be superior to the classic system at predicting outcomes.

10.4.9.1 Longitudinal Fractures

The longitudinal fracture is more common, representing about 80 % of temporal bone fractures. The fracture line traverses the long axis of the petrous ridge. This fracture type more commonly involves the internal auditory canal, but cochlear and/

Box 10.6. Longitudinal Versus Temporal Bone Fractures

Longitudinal	Transverse
Along the long axis of the petrous bone	Right angles to the longitudinal axis
More common	Less common
Ossicular dislocation	Injury to the carotid and/or jugular
Facial paralysis (20 %)	Facial paralysis (>30 %)
Conductive hearing loss	Sensorineural hearing loss

or vestibular damage is uncommon. Conductive hearing loss is frequent, resulting from tympanic membrane and/or ossicular injury (~50 % of cases). The most commonly dislocated ossicle is the incus, resulting from the disruption of the incudostapedial joint. Dislocations of the stapes and the malleus occur but are less common. Facial nerve injury occurs in a much lower percentage of longitudinal fractures (~20 %) compared to transverse fractures and is usually delayed and incomplete when it does occur.

10.4.9.2 Transverse Fractures

The remaining 20 % of temporal bone fractures are transverse fractures, with the fracture line running at right angle to the longitudinal axis of the petrous ridge. Transverse fractures commonly result in sensorineural hearing loss, either due to a transection of the cochlear nerve or to a cochlear injury. Additionally, vertigo, dizziness, and tinnitus may result from injury to vestibular nerves, the vestibule, the semicircular canals, and/or the vestibular aqueduct. Injury to the facial nerve occurs in a greater percentage of cases (~50 %), and paralysis is typically immediate from nerve transection or severe compression by fracture fragments. Delayed onset of facial nerve paralysis may be secondary to edema or intraneural hematoma. A facial nerve hematoma can be recognized as T1 high signal along the damaged nerve segment with strong enhancement on gadolinium-enhanced T1-weighted images. It is important to note that because they are much less common, transverse fractures account for fewer cases of facial nerve paralysis overall, despite the incidence of facial nerve injury being much higher with this fracture type (Box 10.6).

10.4.9.3 Significance of Pneumolabyrinth

Persistent vertigo after a temporal bone fracture may indicate a perilymph fistula. This can develop secondary to a tear either in the round window membrane or in the ligamentous attachment of the stapedial footplate. Neither of these findings can easily be seen on CT. In the absence of a definite fracture, the presence of pneumolabyrinth is strongly suggestive of a perilymph fistula (Fig. 10.19).

10.4.9.4 Classification Based on Otic Capsule Involvement

The majority of modern temporal bone fractures occur secondary to high-velocity impacts that result in more complex fracture orientations not accounted for in the classic

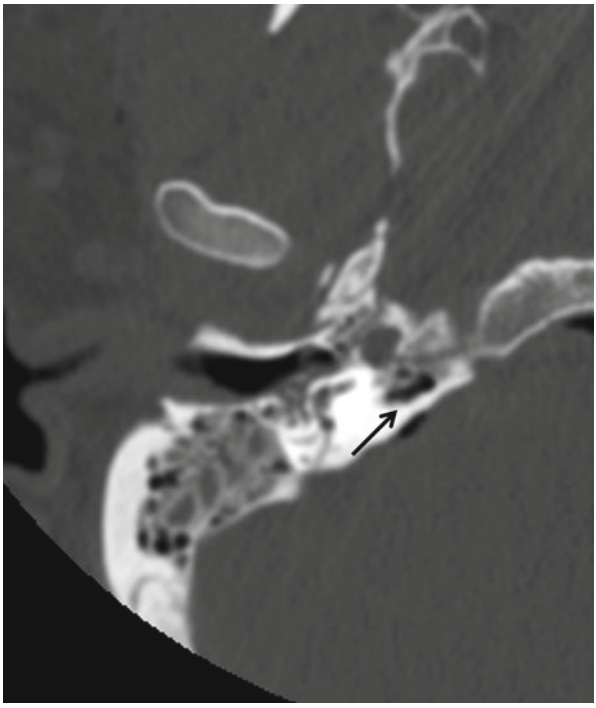

Fig. 10.19 Pneumolabyrinth (*black arrow*). Noted after violation of the otic capsule by a temporal bone fracture

system. An updated classification system, originally proposed by Dahiya et al., has two categories: fractures that violate the otic capsule and fractures that do not. This system has been shown to be a superior predictor of clinical outcome, with fractures violating the otic capsule showing statistically significant increases in facial nerve injury, sensorineural hearing loss, and CSF otorrhea. The effectiveness of the new system is intuitive, as the vital structures housed in and around the otic capsule are protected by the densest bone in the body. Therefore, the force needed to fracture this bone is more likely to lead to injury of the vestibular system, cochlea, facial nerve, and dura (Fig. 10.20) (Box 10.7).

10.5 Vascular Injuries of the Neck

CTA and MRA are the two primary imaging modalities used for evaluation of vascular injuries to the neck. In general, the two techniques have different strengths and weaknesses. MRA can detect intramural hematoma within the false lumen of a dissection. This T1 bright signal is sometimes called the "crescent sign." Additionally, MRI can add increased sensitivity by demonstrating acute stroke with diffusion-weighted sequences and therefore increase scrutiny to the upstream arterial tree. CTA tends to be more widely available, has fewer contraindications, and provides greater spatial resolution than MR imaging/MRA. Acquisition of CTA is also faster, which is an advantage especially in a trauma setting with an unstable patient.

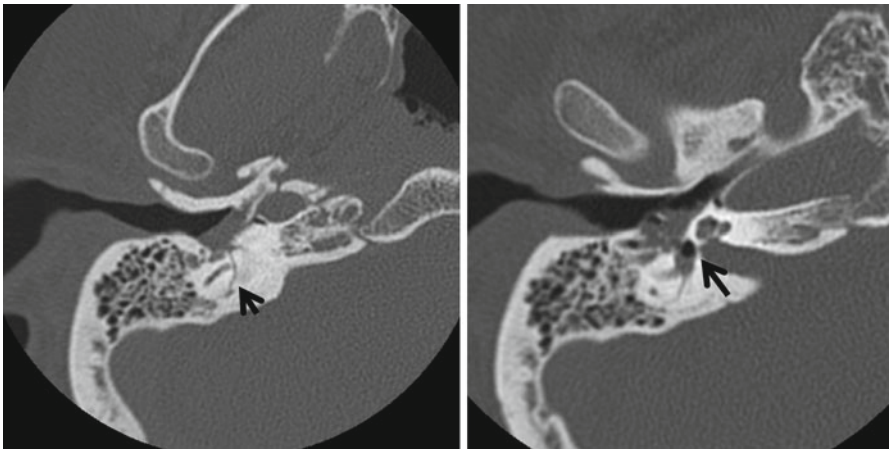

Fig. 10.20 Transverse fracture through the temporal bone that violates the otic capsule (*arrowhead*). Air is noted in the inner ear cavities (*arrow*). This fracture pattern is more predictive of facial nerve injury, sensorineural hearing loss, and CSF otorrhea when compared to otic capsule-sparing fractures

Box 10.7. Temporal Bone Fracture: Checklist
Violation of the otic capsule. Is there pneumolabyrinth?
Ossicular chain involvement
Integrity of the tegmen tympani
Involvement of the facial nerve canal
Involvement of the carotid canal
Evaluate for jugular vein/sigmoid sinus thrombosis

The mechanisms of vascular trauma to the neck can be grouped in blunt trauma or penetrating trauma, both of which have the potential for significant morbidity and mortality. Blunt trauma tends to affect the vertebral arteries more than the carotids, with the most common arterial injury being arterial dissection. Direct signs of dissection include vessel wall irregularity, pseudoaneurysms, thrombi, and arterial occlusions. Penetrating trauma more commonly affects the carotid arteries more than the vertebral arties and has a higher rate of occlusion and transection. In the setting of penetrating trauma, it is especially important to look for nearby associated vascular injuries with the external jugular vein and external carotid artery being the most frequently affected. Traditionally, penetrating trauma has been classified into three zones, based on the need for surgical exploration (Fig. 10.21).

Regardless of the mechanism, the vessel injury is going to result in either partial wall damage or total wall disruption. Specific signs of arterial injury include occlusion, free extravasation, contained extravasation (pseudoaneurysm), intimal flap, dissection, and arteriovenous fistula (Fig. 10.22).

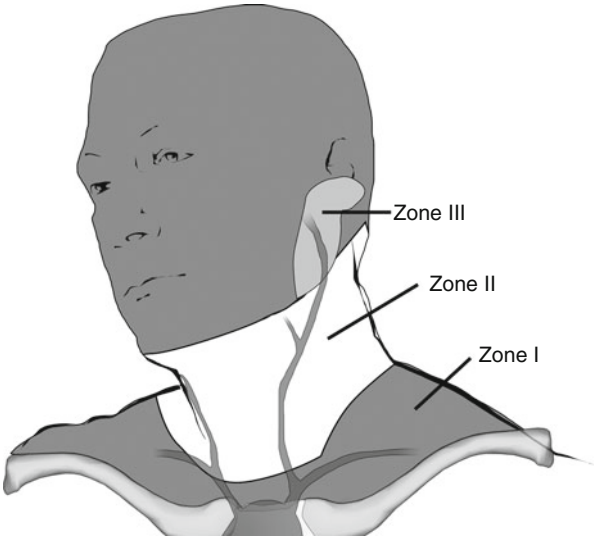

Fig. 10.21 *Zone I* extends from the thoracic inlet to the cricoid cartilage. *Zone II* is located between the cricoid cartilage and the mandible. *Zone III* extends from the mandible to the skull base. Injuries involving zones I and III are prone to major intrathoracic injuries. Zone III is at risk of concomitant major intracranial injuries

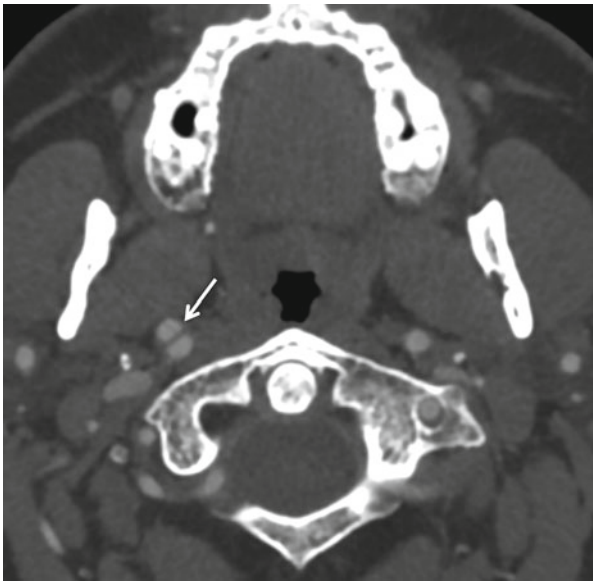

Fig. 10.22 There is an intimal flap (*arrow*) within the right internal carotid artery consistent with a dissection

10.6 Pediatric Considerations

Special considerations must be made when dealing with craniofacial injury in children, as the patterns of injury are frequently different that those in adults. This difference is a result of both anatomic and physiologic characteristics (such as the extent of paranasal sinus pneumatization and phases of dentition) seen at different

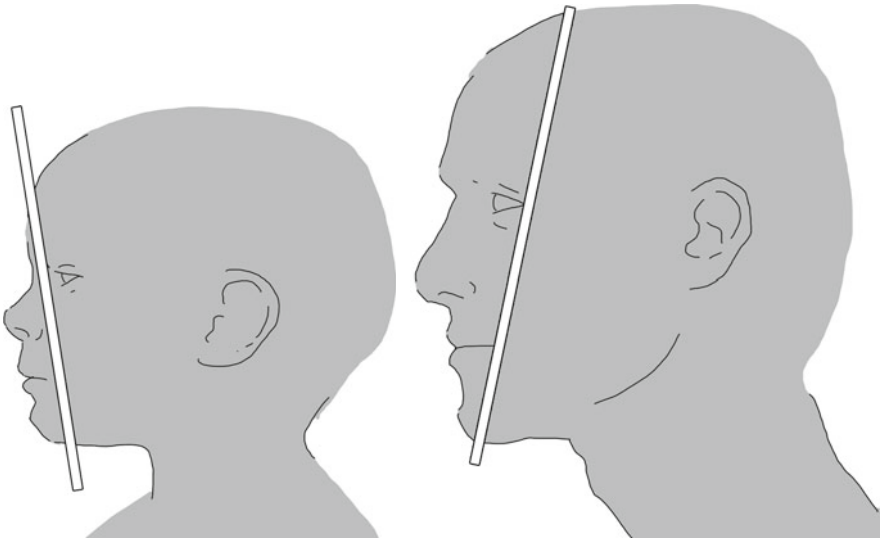

Fig. 10.23 Change in head-to-face ratio with age

stages of craniofacial development. With half of all injuries in battered children (especially in infants and children younger than 5 years) including injuries to the head and neck, it is always important to consider the possibility of child abuse when dealing with pediatric trauma.

10.6.1 Age and Development

In very young children, the relative risk for skull fracture is greater than facial fracture secondary to the frontal protrusion of the cranium and the relative retrusion of the face. Normal development favors the face over the cranium, with the cranium quadrupling in size from birth to adulthood, while the face undergoes a 12-fold increase in size. With age, facial projection increases with the midface and mandible becoming dramatically more prominent. The frequency of pediatric facial fractures thus increases with age (Fig. 10.23).

Pneumatization of the paranasal sinuses progresses in the following order: ethmoid, maxillary, sphenoid, and frontal. The sinuses reach their full size only after puberty and the complete emergence of all the teeth. The maxillary and frontal sinuses play an important role in pediatric facial fracture patterns, with an incidence of midfacial fractures increasing along with the stage of development and pneumatization.

Dental development also plays a role in fracture susceptibility. The presence of tooth buds within the jaw increases the stability and elasticity of the bone. As a result, incomplete dentition provides additional strength to the maxilla and mandible.

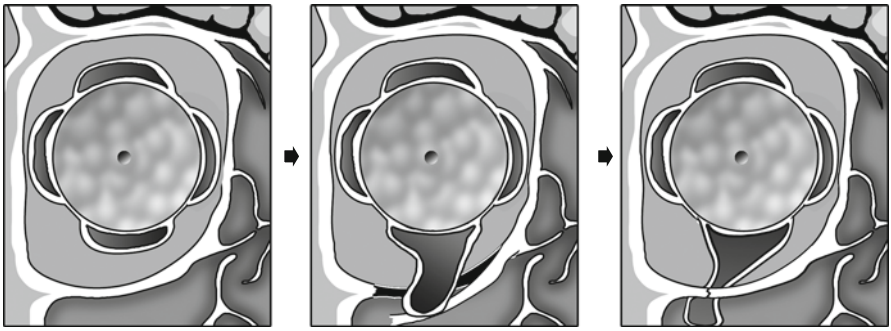

Fig. 10.24 Trapdoor fracture of the orbital floor, causing impingement of the inferior rectus muscle

10.6.2 Fractures

10.6.2.1 Nasal Bone

As in adults, nasal bone fractures are the most common facial fracture in pediatric children. Septal fractures are common and septal hematoma is a concern.

10.6.2.2 Mandibular Fractures

The mandible is the most commonly fractured facial bone in the hospitalized pediatric trauma patient. Fracture of the mandible is more common in the pediatric setting when compared to adults. The "ring" rule for the mandible tends to hold up less well in children, with a solitary mandibular fracture being the most common pattern. The most common fracture locations are the condylar and subcondylar areas.

10.6.2.3 Frontal Bone/Orbital Roof

Fractures of the frontal bone are common in the pediatric setting, due to the prominence of the forehead. Prior to age 7 (before the frontal sinus begins to pneumatize), frontal bone fractures tend to affect the orbital roof in almost every case. With fractures of the orbital roof, it is important to evaluate for signs of muscle entrapment (specifically along the superior oblique and superior rectus muscles).

10.6.2.4 Orbital Rim/Floor Fractures

Fractures of the orbital floor are rare in young children; frequency increases with age due to pneumatization of the maxillary sinuses. After age 7, orbital fractures tend to affect the medial and lateral walls. Although uncommon, the most characteristic blowout fracture in children is the "trapdoor fracture." In this fracture pattern, the orbital floor fracture is a "greenstick" fracture that allows the bony fragment to stay attached at a hinge (usually on the medial side). If the displaced fragment pops back into place, the prolapsed orbital tissues may be entrapped. Such fractures are easy to miss, with the only imaging findings being periorbital fat or rectus muscle entrapped beneath the floor of the orbit (Fig. 10.24).

Box 10.8. Pediatric Facial Fractures with Age

Younger than 3	Usually isolated, nondisplaced, and caused by low-energy forces
Younger than 5	Cranial, frontal, and orbital fractures >>> midfacial and mandibular fractures
Older than 10	Mandibular and midfacial fractures

10.6.2.5 Maxillary Fractures

These are rare in children and basically do not occur under the age of two. They tend to increase in prevalence as the maxillary sinus develops and the permanent teeth erupt (Box 10.8).

10.7 The Surgeon's Perspective

The face is a "high rent" district of the body, with injuries in this area causing relatively higher distress and quality of life impacts than similar injuries elsewhere. Similar to other intricate areas of the body like the hand, trauma to the face is treated by specialists familiar with the complex anatomy and function of the craniofacial skeleton.

The craniofacial skeleton is a unique area of the bony skeleton with regard to function and composition of the bones. Whereas most bones exist primarily to facilitate movement by providing levers for muscles, those in the face serve more of a structural and protective role. The majority of the bones of the craniofacial skeleton are flat (vs. tubular) and do not contain diaphyses, metaphyses, or epiphyses. Flat bones are composed predominantly of cancellous bone with thin cortical shells. The blood supply to the facial bones is predominantly via the overlying periosteum, with some areas receiving dual supply from nutrient arteries (e.g., inferior alveolar artery to mandible). These differences in purpose and physiology affect the techniques used to treat craniofacial fractures.

Compression techniques used on the axial skeleton to achieve primary bone healing have not been shown as effective in the craniofacial skeleton, save the lag screw technique for mandible fractures. Instead, the majority of open reduction and internal fixation of the craniofacial skeleton utilizes semirigid, load-sharing techniques that are best suited for secondary bone healing (endochondral bone formation via an intermediary cartilaginous callous). Secondary bone healing occurs best when there is initial stability followed by a small amount of micromotion across the fracture site. Hence, load-sharing techniques use smaller plates and screws placed across lines of ideal osteosynthesis. These ideal lines of osteosynthesis generally correlate with the facial buttresses described above.

Imaging plays a key role in the care of facial trauma patients. First, it is important to identify and characterize almost all fractures. Second, the majority of patients with fractures of the facial skeleton will require some sort of operative

intervention, and treatment is almost always guided by imaging. Fine-cut CT is the referent standard for imaging the craniofacial skeleton. While many emergency rooms will screen for suspected mandible fractures with an orthopantomogram (dental panoramic radiograph or Panorex), the cost of a CT is nominally higher, and the CT imaging is much more sensitive, especially in the areas of the ascending ramus and condyle. Even if a fracture is identified on an orthopantomogram, a CT is usually ordered to better characterize the fracture. An important exception to obtaining CT imaging for facial fractures is the isolated nasal bone fracture; while CT will image these effectively, treatment decisions are usually based on physical exam. Nasal bone fractures warrant clinical treatment when there is a significant change in cosmesis or nasal air flow. Thus, unless there is a suspicion of other facial fractures, nasal bone injuries should not undergo imaging.

Axial, coronal, and sagittal images are important for identifying all fractures of the craniofacial skeleton and useful in guiding management of fractures deeper in the skeleton. The orbital floors, orbital walls, frontal sinuses, frontal sinus outflow tract, and pterygoids are best seen in these 2D cuts. The more superficial fractures of the midface and mandible are still easily identified by 2D cuts, but the advent of 3D reconstructions has been a significant help to the facial traumatologist in these areas. Viewing the skeleton in 3D improves visualization of relative displacement of the midface buttresses, as well as comminuted fractures that may require grafting. In the mandible, 3D reconstructions help with surgical approach planning. In panfacial fractures, 3D imaging is key as it gives the surgeon a more global view instead of focusing on individual parts and helps identify areas of stability where plating can begin.

Facial traumatologists vary in their use of post-reduction imaging. In some centers, it is standard to obtain a post-reduction orthopantomogram after reduction and fixation of a mandible fracture. Proponents note that it establishes a baseline for hardware positioning and fracture reduction for future comparison. However, as most are well visualized during surgery, studies have shown that post-reduction imaging of mandible fractures does not affect return to the operating room (OR) or clinical outcomes. As most of the fractures treated by facial traumatologist are well visualized during surgery, post-reduction imaging does not add clinical significance. When treating panfacial fractures or "deeper" fractures such as the orbital floor, a post-reduction CT is often obtained to assure proper reduction. In these complex cases, intraoperative imaging with CT is increasingly being used.

10.8 Summary and Conclusions

Facial trauma can be complex, but knowledge of common fracture patterns aids in imaging interpretation. It is important to have a systematic approach to interpretation and to communicate all findings clearly to support therapeutic decision-making.

Further Reading

Alcalá-Galiano A et al (2008) Pediatric facial fractures: children are not just small adults1. Radiographics 28(2):441–461

Dahiya R et al (1999) Temporal bone fractures: otic capsule sparing versus otic capsule violating clinical and radiographic considerations. J Trauma Acute Care Surg 47(6):1079

Hopper RA, Salemy S, Sze RW (2006) Diagnosis of midface fractures with CT: what the surgeon needs to know1. Radiographics 26(3):783–793

Kubal WS (2008) Imaging of orbital trauma. Radiographics 28(6):1729–1739

Little SC, Kesser BW (2006) Radiographic classification of temporal bone fractures: clinical predictability using a new system. Arch Otolaryngol Head Neck Surg 132(12):1300

Parbhu KC et al (2008) Underestimation of soft tissue entrapment by computed tomography in orbital floor fractures in the pediatric population. Ophthalmology 115(9):1620–1625

Rhea JT, Novelline RA (2005) How to simplify the CT diagnosis of Le Fort fractures. Am J Roentgenol 184(5):1700–1705

Schuknecht B, Graetz K (2005) Radiologic assessment of maxillofacial, mandibular, and skull base trauma. Eur Radiol 15(3):560–568

Maxilla and Mandible

11

Prashant Raghavan, Mark J. Jameson, Matthew A. Hubbard, Max Wintermark, and Sugoto Mukherjee

11.1 Introduction

A bewildering variety of lesions occurs in the maxilla and the mandible. Although a specific diagnosis of these can be difficult on imaging, it is important to be familiar with the key imaging characteristics of a few common entities and to be facile at detecting imaging signs of aggressive neoplastic, inflammatory, and infectious processes. This chapter describes a fundamental approach to commonly encountered jaw lesions; it does not address dental or temporomandibular joint pathology in detail.

11.2 Anatomy

The term "jaws" refers to the teeth-bearing bones including both the mandible and the maxilla. Because of their arched contour, the anatomic positions anterior and posterior are somewhat inexact, and the terms mesial (toward the midline) and distal (toward the molars) are favored.

The mandible is comprised of a body and paired rami, coronoid processes, and condylar processes. The ramus meets the body at the angle. The midline of the body is the mandibular symphysis (Fig. 11.1). The buccal surface of the mandible attaches multiple muscles: the lateral pterygoid at the condylar process, the medial pterygoid at the posterior-inferior ramus near the angle, the temporalis at the coronoid process, and the masseter at the ramus. The temporalis, medial pterygoid, and masseter close the jaw. The lateral pterygoid opens the jaw and moves it from side to side (Fig. 11.2).

The lingual surface of the ramus contains the inferior alveolar foramen through which pass the inferior alveolar nerve and artery into the canal of the same name. The inferior alveolar nerve, a branch of the mandibular (third) division of the trigeminal nerve (V3), exits the mandible through the mental foramen on the buccal aspect of the body. The mental foramen is generally in line with the longitudinal axis of the second premolar.

P. Raghavan et al., *Manual of Head and Neck Imaging*,
DOI 10.1007/978-3-642-40377-4_11, © Springer-Verlag Berlin Heidelberg 2014

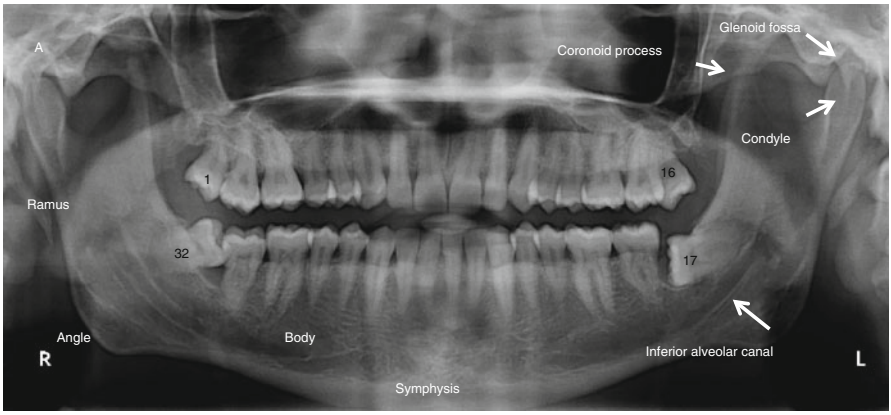

Fig. 11.1 Orthopantomogram depicting mandibular anatomy and teeth numbering

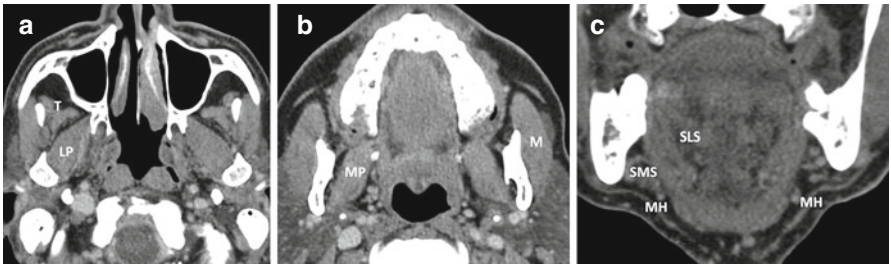

Fig. 11.2 Muscles attached to the mandible. *LP* lateral pterygoid, *MP* medial pterygoid, *M* masseter, *T* temporalis, *MH* mylohyoid, *SMS* submandibular space, *SLS* sublingual space

The lingual surface of the body attaches to the mylohyoid muscle at the mylohyoid line. The left and right mylohyoid muscles combine to form a sling that separates the submandibular and sublingual spaces (Fig. 11.2). Posteriorly, the mylohyoid sling has a free margin where the two spaces are contiguous. In the midline, the lingual surface contains the genial tubercle that attaches to the genioglossus superiorly and the geniohyoid inferiorly. Below the genial tubercle on each side is a shallow groove for the attachment of the anterior belly of the digastric.

The alveolar process of both the mandible and maxilla supports the teeth. The mandibular alveolar process tapers distally to a triangular plateau called the retromolar trigone (Fig. 11.1). Lateral to this is a depression, the retromolar fossa, limited externally by a ridge contiguous with the coronoid process called the temporal crest. Squamous cell carcinomas arising from the mucosa in this region can present with early osseous and deep space invasion.

The temporomandibular joint (TMJ) is formed by the articulation of the mandibular condyle with the concave glenoid fossa in the temporal bone which is positioned just posterior to a convex articular eminence. The TMJ space is divided by a biconcave fibrocartilaginous disc that moves in conjunction with the mandibular condyle.

The 32 adult teeth are bound to dental sockets in the alveolar processes by the periodontal ligaments that form the lucencies around the tooth roots seen on radiographs. The teeth may be named by descriptors including the side, the jaw (mandibular or maxillary), the position (lateral/medial, first/second/third), and the tooth type (incisor, canine, premolar, molar) or by a single number from 1 to 32, starting at the right upper jaw and ending in the right lower. Children have 20 deciduous teeth which are numbered from the right upper jaw to the right lower. The teeth have occlusal, buccal, lingual, mesial, and distal surfaces.

11.3 Imaging Evaluation

Plain radiographs and pantomograms are extremely useful in the initial evaluation of the jaws. It is possible to characterize some small jaw lesions definitively using plain films alone. Lesions greater than 2 cm are better evaluated with CT or MRI. In a setting of suspected odontogenic infection, osteomyelitis, or osteonecrosis, CT is the modality of choice. CT is also useful in the detection of osseous invasion by malignancy. The role of MRI is limited to those cases where CT or plain radiography is equivocal.

11.4 Benign Lesions

11.4.1 Cystic Lesions

It is important to note that the term "cystic" as used here refers to the imaging appearance (bone lysis with resulting cystic appearance) and does not necessarily indicate a pathological characteristic. Radiographically, these lesions present as discrete, well-marginated, sometimes expansile osteolytic lesions.

The vast majority of small discrete lytic jaw lesions are *periapical cysts*. These are associated with chronic infection that progresses from the pulp of a tooth through its root into the alveolar bone. Initially, a periapical granuloma is formed, which transforms with time into a sterile cavity (Fig. 11.3).

Dentigerous cysts arise from odontogenic epithelium around the crown of an unerupted tooth, usually a molar. They typically appear as a well-defined expansile lytic lesion which contains an unerupted tooth. Very rarely, an ameloblastoma may arise from the lining of a dentigerous cyst (Fig. 11.4).

Odontogenic keratocysts are lined by stratified squamous epithelium and contain keratin. They tend to grow along the long axis of the mandible, insinuating themselves between the dental roots and thus do not contain a tooth. When multiple odontogenic keratocysts are seen, a diagnosis of basal cell nevus (Gorlin's) syndrome must be entertained. This syndrome is characterized by the appearance of nevoid basal cell carcinomas at a young age (Fig. 11.5).

Unicameral bone cysts, similar to those seen in the long bones, may also be encountered in the maxilla and mandible of young people. They are well-defined

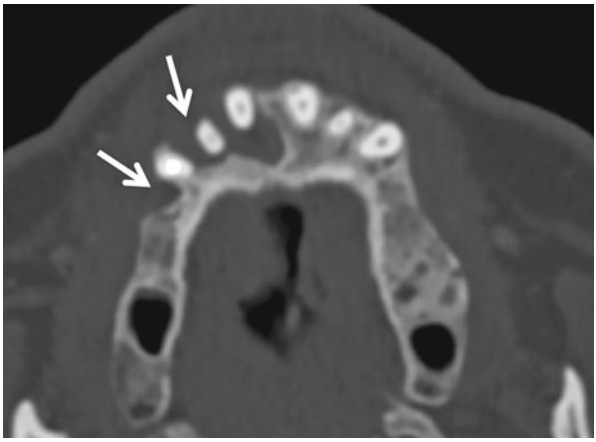

Fig. 11.3 Typical periapical granulomas on CT

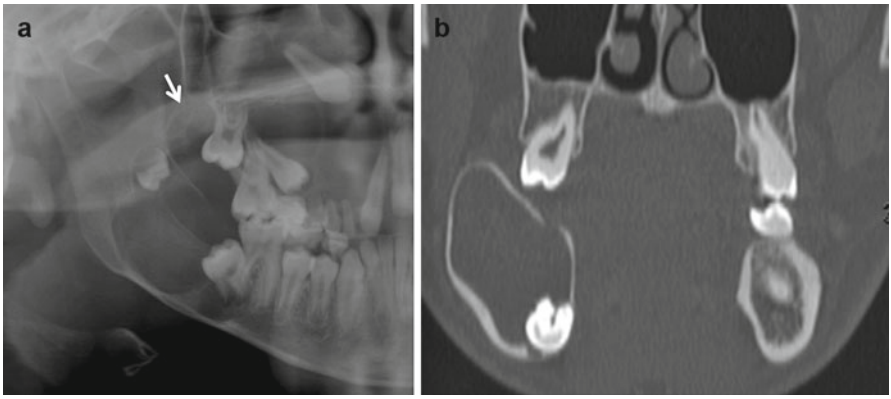

Fig. 11.4 Dentigerous cyst. Radiograph (**a**) and CT (**b**) images of dentigerous cysts. A typical dentigerous cyst is an expansile unilocular lesion containing an unerupted tooth. Occasionally more than one cyst may be present (*arrow*, **a**)

expansile lesions with no other distinguishing characteristics. They are postulated to arise as a consequence of liquefaction of an intraosseous hematoma.

A *Stafne cyst* or cavity is a developmental variation found at the angle of the mandible. They may be bilateral and contain a rest of salivary glandular tissue.

Fissural cysts occur along mandibular and maxillary embryonic fusion lines. The most common fissural cyst is the nasopalatine duct (incisive canal) cyst seen between the premaxilla and the hard palate in the midline. These are usually incidentally detected but occasionally erode into the oral cavity forming a submucosal mass on the anterior hard palate (Fig. 11.6).

Ameloblastomas (Fig. 11.7) are benign tumors arising from odontogenic epithelium that appear as unilocular or multilocular expansile lytic masses. When septations are present, they can produce a characteristic "soap bubble" appearance. Although ameloblastomas tend to breach the cortex and extend into adjacent soft tissues, only a tiny fraction is malignant. Ameloblastomas can exhibit

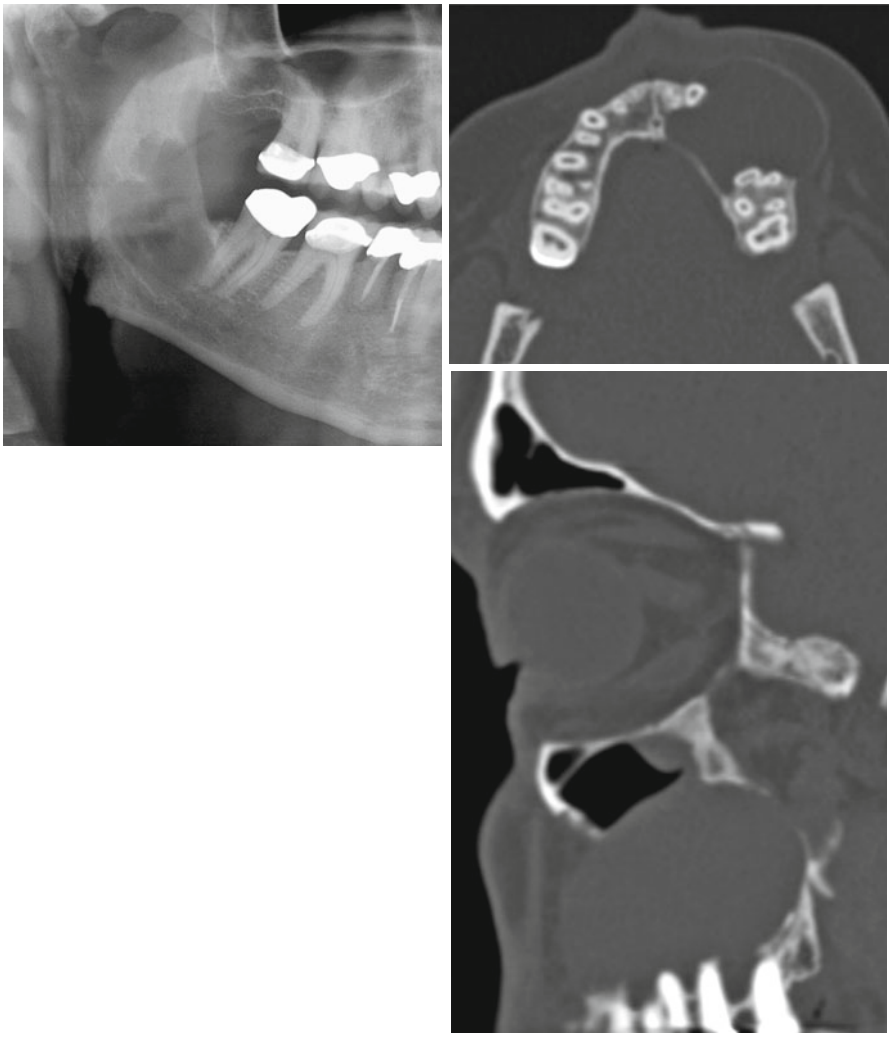

Fig. 11.5 Odontogenic keratocyst. A typical OKC is expansile, is unilocular, and does not contain an unerupted tooth. Multiple odontogenic keratocysts suggest Gorlin's syndrome, a condition characterized by multiple nevoid basal cell carcinomas in childhood, cardiac and ovarian fibromas, and macrocephaly along with higher incidence of medulloblastomas

enhancing papillary projections that distinguish them from other radiographic cysts (lytic lesions) that are not tumors; these projections can sometimes be seen on contrast-enhanced CT but are more reliably detected with MRI.

When one encounters a lytic expansile jaw lesion in a middle-aged or older patient that does not conform to the appearance of one of the more typical benign cysts discussed above, a contrast-enhanced CT or MRI must be recommended to characterize it further. These can demonstrate the enhancing papillary projections that, when present, are highly suggestive of ameloblastoma. Ameloblastomas are treated with wide excision as they have a tendency to recur.

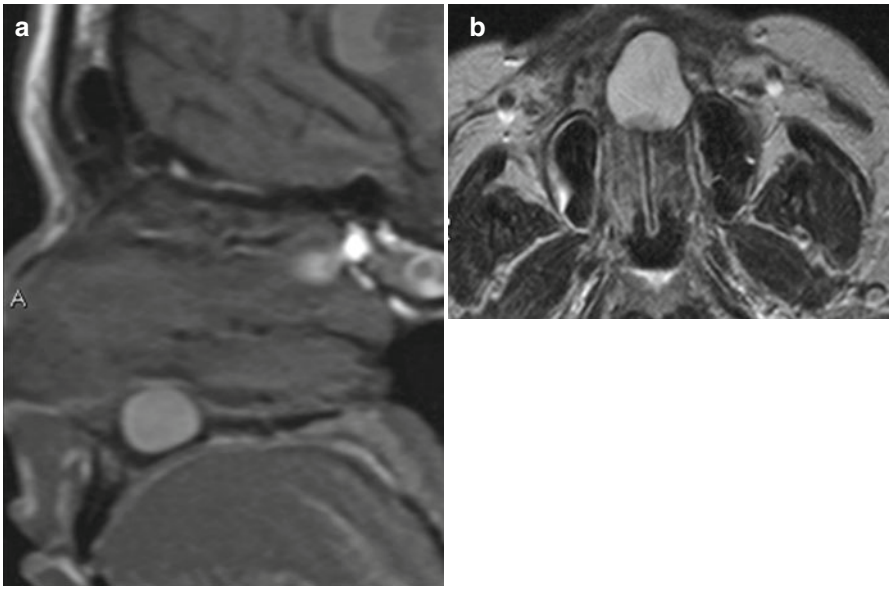

Fig. 11.6 Incisive canal or nasopalatine duct cysts. (**a**, **b**) Are examples of incisive canal cysts. They occur in the midline at the junction of the hard palate and premaxilla and are usually found incidentally. Occasionally they may be large enough to cause cosmetic deformity. Rarely secondary infection may occur. The high T1 signal of the cyst contents in these images reflects elevated protein concentration

Odontogenic myxomas are benign but locally aggressive expansile tumors seen in young adults; they may be indistinguishable from ameloblastomas (Fig. 11.8).

Aneurysmal bone cysts of the jaws present as expansile multilocular masses containing characteristic blood-fluid levels on MRI. They resemble giant cell lesions, a category that includes brown tumors of hyperparathyroidism, giant cell reparative granulomas, and true giant cell tumors. Brown tumors are unilocular lesions that may be associated with loss of the lamina dura, a finding typical of the bone resorption of hyperparathyroidism. Giant cell reparative granulomas and giant cell tumors are multilocular expansile lesions that may be indistinguishable from ameloblastomas and aneurysmal bone cysts (Fig. 11.9).

When one encounters a lytic jaw lesion in an older patient, especially one with irregular margins, the possibility of metastasis and myeloma should be considered. Likewise, the possibility of eosinophilic granuloma must be entertained in a child with a discrete punched-out lytic focus, especially if associated with fever and systemic signs of inflammation (Fig. 11.10).

11.4.1.1 Sclerotic Lesions

These lesions demonstrate a predominant pattern of increased bone density on radiographs and CT scans. The increased density may be due to the presence of osseous or odontogenic elements.

Fig. 11.7 Ameloblastoma. The radiograph (**a**) demonstrates a lytic multiloculated lesion. The contrast-enhanced CT (**b**) depicts the solid papillary projections (*arrow*) that characterize this tumor. Ameloblastomas can sometimes be unilocular. When a benign lesion cannot be definitively excluded on radiography, it is prudent to obtain a cross-sectional study to characterize the internal architecture of these lesions and establish the diagnosis as in the fat-suppressed contrast-enhanced image, (**c**) (Courtesy of Dr William P. Dillon, University of California, San Francisco), where *solid areas* of enhancement are evident

Odontomas are benign tumors comprised of normal dental elements (enamel, cementum, dentine, and/or pulp). When well differentiated, they tend to occur in the anterior mandible and are called compound odontomas. These are well defined on radiographs and contain numerous dense toothlike elements. When less well differentiated, they tend to occur in the posterior mandible and are called complex odontomas. They are similar to compound odontomas radiographically, but the internal densities are more amorphous and less toothlike. Rarely, an odontoma may be associated with an undifferentiated component that histologically resembles an ameloblastoma (ameloblastic odontoma). The lesions contain a lytic component in addition to the typical radiodensities of odontomas (Fig. 11.11).

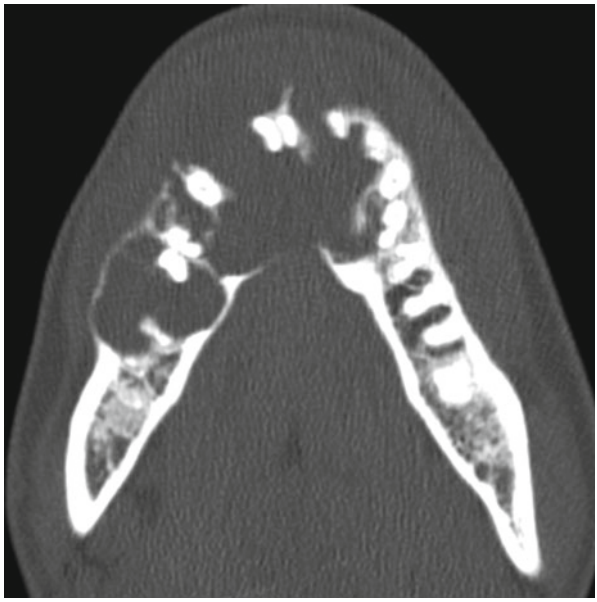

Fig. 11.8 Odontogenic myxoma. These tumors resemble ameloblastomas on imaging and must be suspected when an expansile multiloculated lesion is encountered in a young patient

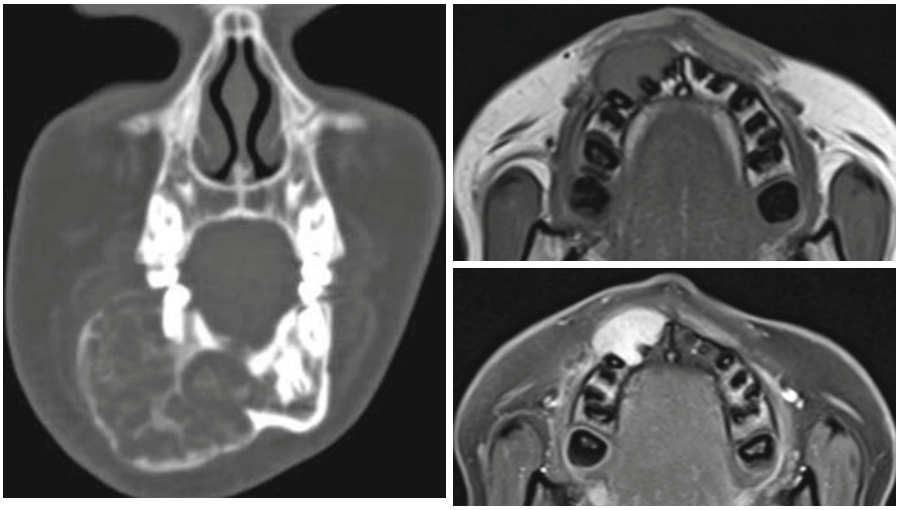

Fig. 11.9 Giant cell reparative granuloma. GCRGs are poorly understood nonneoplastic lesions that may represent a reparative response to intraosseous hemorrhage from prior trauma. They can occur on the jaw bones as well as in the overlying gingiva (epulis). They resemble brown tumors of hyperparathyroidism histologically. There is nothing specific about the radiological appearance of GCRGs, and they can be indistinguishable from aneurysmal bone cysts, giant cell tumors, ameloblastomas, and myxomas. The most common finding is that of an expansile multiloculated mass with variable degrees of cortical thickening, usually affecting the mandibular body. However, as seen in the pre- and postcontrast T1-weighted image from a 12-year-old with tooth pain, they may be unilocular as well

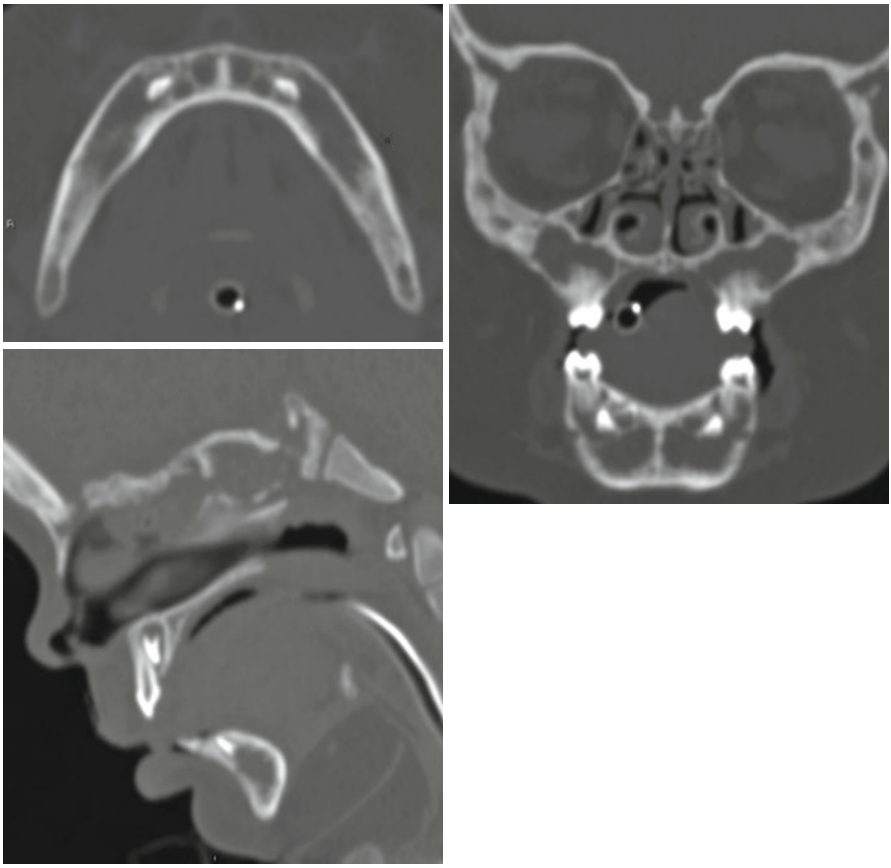

Fig. 11.10 Disseminated Langerhans cell histiocytosis. When a lytic jaw lesion is encountered in a child, histiocytosis must always be suspected. It may be a unifocal process or, as in this case, present with widespread lytic foci and systemic manifestations

Cemento-osseous dysplasia of the mandible occurs in two forms. The more common periapical type can be painful, is common in black females, and presents as a discrete radiodensity with a lucent periphery adjacent to a tooth root. The less common florid type involves several teeth and is usually asymptomatic.

*Tori a*re benign, usually asymptomatic osseous excrescences that arise from characteristic locations in the mandible (torus mandibularis), hard palate (torus palatinus), and maxilla (torus maxillaris) in response to chronic irritative stress. Clinically, these can be misidentified as tumors by unfamiliar practitioners (Fig. 11.12).

Fibrous dysplasia (Fig. 11.13) of the jawbones has two distinct appearances depending on the degree of mineralization: (1) a well-defined lucent expansile lesion containing foci of mineralization and confined by a sclerotic rind or (2) a more homogeneous sclerotic lesion with a ground-glass matrix. Ossifying fibromas are benign fibrous neoplasms containing bony trabeculae. These are slow-growing tumors that begin as lucent lesions that gradually mineralize. Often they are

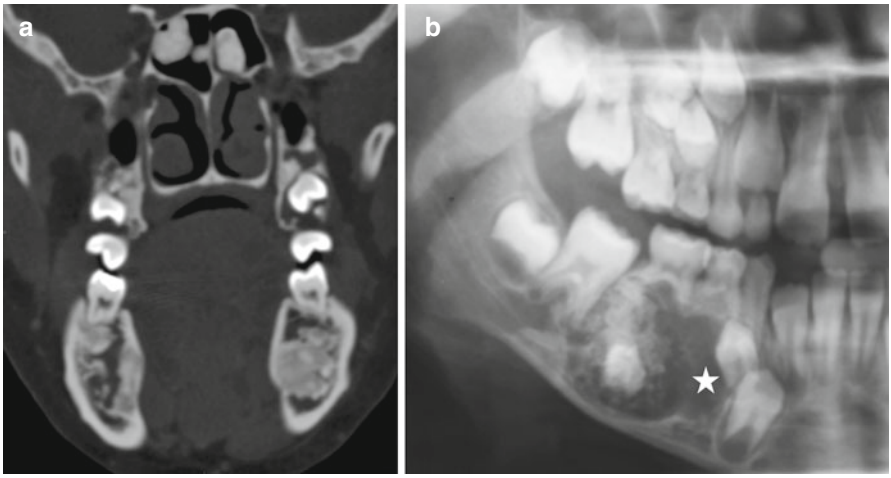

Fig. 11.11 Odontomas are usually incidentally detected lesions and are comprised of numerous dense toothlike elements. They can sometimes be associated with pain. Multiple odontomas can be seen in Gardner's syndrome (**a**). Rarely an ameloblastoma (*asterisk*, **b**) may be associated with an odontoma (ameloblastic odontoma)

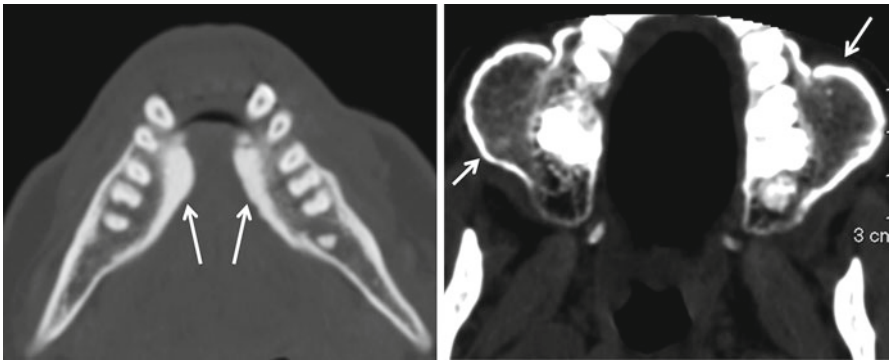

Fig. 11.12 Mandibular and maxillary tori. Tori are reactive osseous excrescences that arise as a consequence of repetitive trauma. Maxillary tori are also called buccal alveolar exostoses

indistinguishable from fibrous dysplasia. It is important to remember that fibro-osseous lesions may demonstrate bizarre signal intensities and enhancement patterns on MRI that can lead to a misinterpretation of malignancy; their true nature is easier to recognize on plain radiographs or CT. Cherubism, an extremely rare autosomal dominant condition that may be considered a variant of fibrous dysplasia, is characterized by symmetric overgrowth of the maxillae and mandible due to the formation of multiple cystic fibro-osseous lesions.

Osteochondromas tend to arise from the coronoid or condylar processes. Like long bone osteochondromas, these osseous excrescences have a medullary cavity that is contiguous with the mandibular medullary cavity, a characteristic radiographic appearance. They can cause cosmetic deformity and TMJ malalignment (Fig. 11.14).

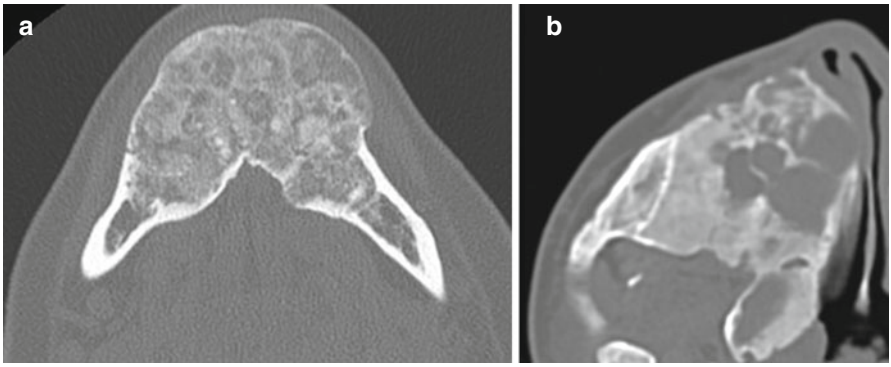

Fig. 11.13 Fibrous dysplasia of the mandible (**a**, Courtesy of Dr William P. Dillon, University of California, San Francisco) and maxilla (**b**). Note the "ground-glass" appearance of the expanded bone

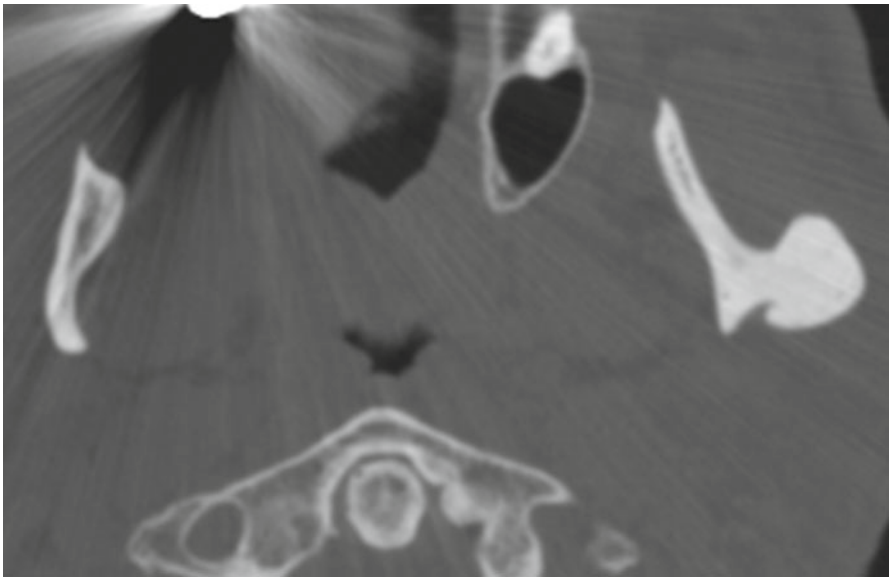

Fig. 11.14 Osteochondromas present as pedunculated mushroom-shaped excrescences usually from the mandibular ramus. They may cause cosmetic deformity or, if located in proximity to the condyle, result in TM joint malalignment

11.5 Malignant Lesions

11.5.1 Osteosarcoma

The diagnosis of osteosarcoma must always be considered in the setting of a destructive jaw lesion. Gnathic osteosarcomas occur across a wide age range and have a better prognosis than long bone osteosarcomas. The imaging appearance is

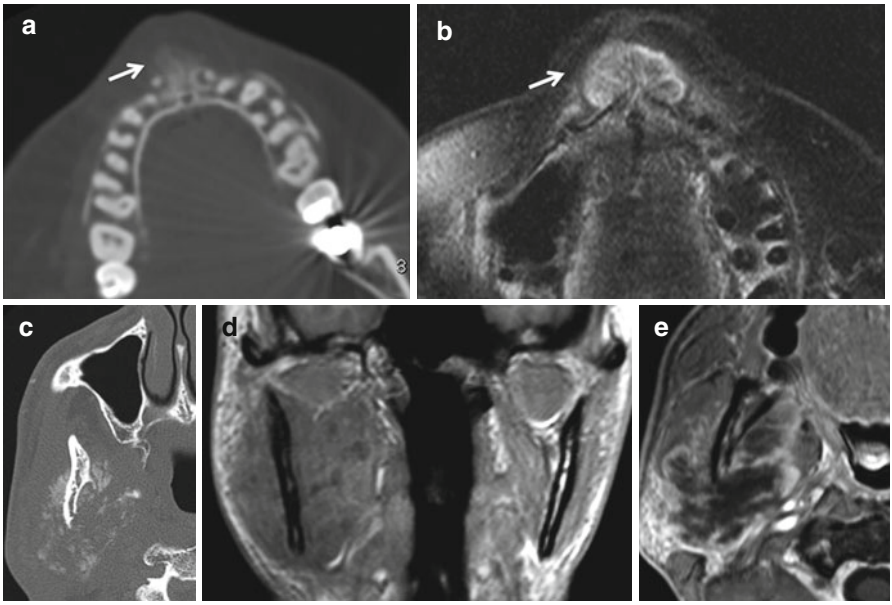

Fig. 11.15 Osteosarcoma. (**a**, **b**) Are from a patient with a premaxillary osteosarcoma. The presence of ill-defined tumor bone (*arrows* **a** and **b**) is a clue to the diagnosis. (**c**–**e**) Are from a patient with a radiation-induced mandibular osteosarcoma. Tumor bone is evident in CT, while the soft tissue component and extent of mandibular medullary involvement are better demonstrated on the MR images. Tumor bone, however, by no means is a universal radiological feature of osteosarcoma

extremely variable; the classic "sunburst" pattern of periosteal tumor bone formation seen in the long bones is infrequently seen in the jaws. More commonly, there is a nonspecific expansile, destructive mass associated with a soft tissue component. Tumor bone, when visible, may be amorphous and irregular. MRI is necessary to clearly define tumor extent, but there are no MR characteristics that are specific of this tumor (Fig. 11.15).

11.5.2 Osseous Involvement by Squamous Cell Carcinoma

Penetration of the cortical bone of the maxilla or mandible by upper aerodigestive squamous cell carcinoma (SCCA) upstages the primary tumor to T4. On CT, cortical involvement typically appears as a saucer-shaped bone defect adjacent to the tumor (Fig. 11.16). Subtle cortical invasion can also be detected on CT by using dedicated processing software (DentaScan, GE, Milwaukee) but is not routinely required. Loss of medullary trabeculae and replacement of fatty marrow by soft tissue imply deep bony invasion. MRI can also be used to evaluate the extent of mandible invasion but is best reserved for equivocal cases. On MRI, the tumor is of low to intermediate signal intensity on T1-weighted images, is intermediate to high signal intensity on T2-weighted images, and enhances with gadolinium. However,

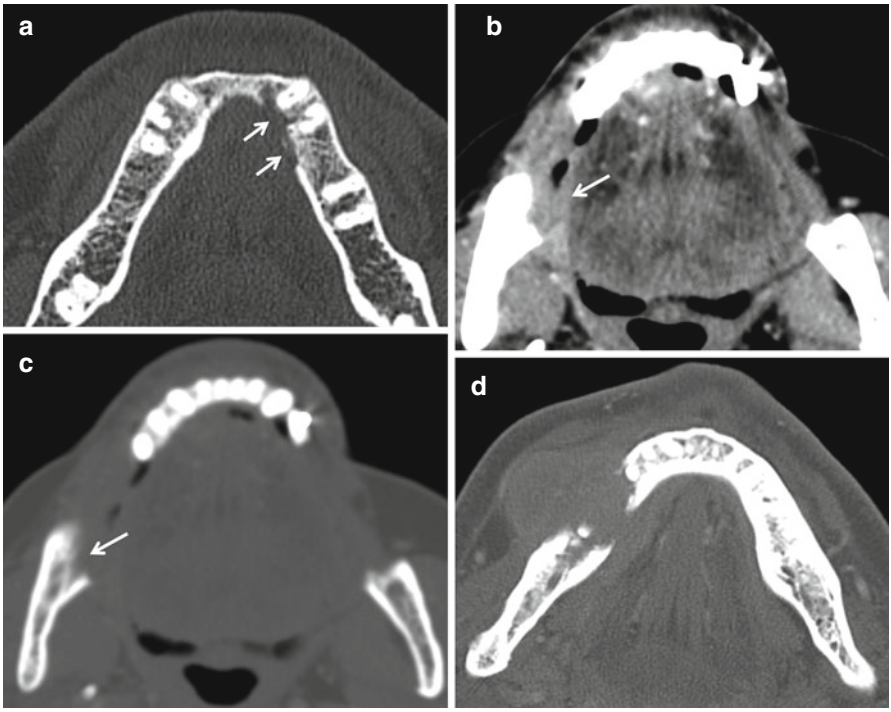

Fig. 11.16 Mandibular invasion (*arrows*) in squamous cell carcinoma. In (**a**), the lingual mandibular cortex is invaded by tumor. (**b**, **c**) Show a retromolar trigone squamous cell cancer invading the adjacent mandibular cortex. RMT cancers are notorious for early bone involvement. In (**d**), full-thickness mandibular invasion by a gingival mucosal squamous cell cancer is evident

edema and granulation tissue can also demonstrate similar characteristics, which may lead to overestimation of bone involvement by MRI (Fig. 11.17).

11.6 Osteomyelitis

The simplest classification of osteomyelitis defines two broad varieties – acute and chronic. Chronic osteomyelitis (COM) is either primary, when there is no antecedent episode of acute osteomyelitis (AOM), or secondary, when AOM persists beyond 4 weeks.

AOM (Fig. 11.18) is usually a pyogenic infection that follows periodontal disease. Infection spreads from the root of the affected tooth to the alveolar bone. Suppuration in the affected bone leads to increased intraosseous pressure, necrosis, cortical destruction, and formation of soft tissue abscesses in the adjacent spaces. Bone destruction, periostitis, and abscesses are best demonstrated on contrast-enhanced CT. Abscesses in this setting are often small and may be obscured by dental artifact; to detect these, it is important to examine CT images in narrow

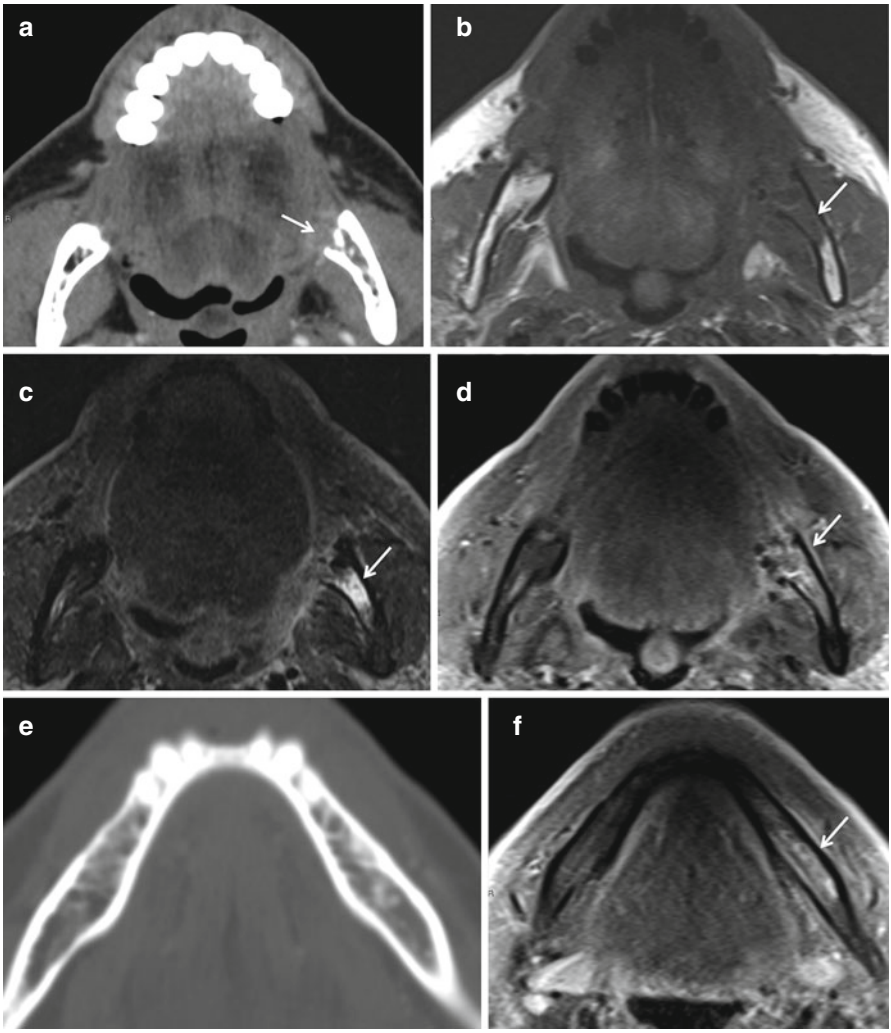

Fig. 11.17 Role of MRI in osseous invasion by squamous cell carcinoma. In (**a**), erosion of the cortex by a retromolar trigone cancer is noted. On the T1 (**b**) and fat-suppressed T2 (**c**) MR images, abnormal marrow signal is present in the medullary cavity (*arrows*). This is observed to enhance on the contrast-enhanced T1W fat-suppressed image (*arrow*, **d**). Abnormal marrow signal is non-specific and may indicate edema or tumor infiltration. In (**e**), an image through the mandibular body in the same patient, no osseous abnormality is apparent. However, the enhanced MR image (**f**) indicates that the marrow cavity is infiltrated with tumor. MR can aid in assessing tumor involvement in bone in equivocal cases, but the presence of masticator space abscess enveloping the mandibular ramus is noted

window. Secondary COM may follow untreated or inadequately treated AOM. Permeative bone destructions, periosteal thickening, fragmented bone representing sequestra, soft tissue inflammatory changes, and sinus tracts may be seen on CT.

Primary COM is a complex disorder. It may be caused by an identifiable infectious organism (*Actinomyces*, *Mycobacteria*, or fungi) or may occur as an idiopathic

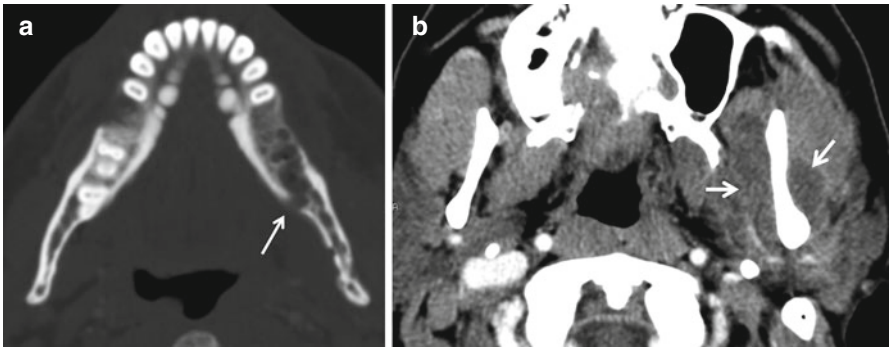

Fig. 11.18 Acute osteomyelitis arising from odontogenic infection. Mottled bone destruction is present in the left hemimandibular body and angle. A focal breach of the lingual cortex adjacent to the root of the third molar is present (*arrow*). In (**b**), a large masticator space abscess enveloping the mandibular ramus is noted

disorder (Fig. 11.19). A subset of patients with idiopathic COM fall under the spectrum of chronic recurrent multifocal osteomyelitis (CRMO), also known as the SAPHO (synovitis, acne, palmoplantar pustulosis, hyperostosis, and osteitis) syndrome characterized by recurrent episodes of osteomyelitis of the long bones and thoracic spine, sternoclavicular hyperostosis, and polyarthritis. Dense sclerosis and periostitis on CT and plain radiographs are characteristic of this entity. The mandible is involved in about 10 % of cases (Fig. 11.19).

11.7 Osteonecrosis

Osteonecrosis of the mandible is seen either as a consequence of radiotherapy or due to bisphosphonate treatment. Radiation-induced osteonecrosis (osteoradionecrosis, ORN) can be seen in patients with upper aerodigestive tract cancers who receive radiation to the jaw in excess of 60 Gy. The disease may be precipitated by a seemingly innocuous event that results in bony exposure, e.g., progressive dental decay, dental extraction, or minor trauma. ORN is a consequence of failure of the radiated bone to mount adequate immunologic and reparative responses. Grade 1 ORN is limited to the alveolar process and characterized clinically by exposure of devitalized bone. In grade 2 ORN, the necrosis extends to involve the body to a greater depth, down to the inferior alveolar canal. Grade 3 ORN involves the mandible below the level of the inferior alveolar canal and may be associated with pathological fractures. On CT, a combination of permeative bone loss and sclerosis in the absence of a significant soft tissue abnormality is typical. Foci of gas may be evident in necrosed bone (Fig. 11.20). ORN can sometimes be difficult to distinguish from tumor recurrence. Absence of a soft tissue mass adjacent to destroyed bone favors ORN over tumor.

Bisphosphonate-associated osteonecrosis (sometimes referred to as osteochemonecrosis) (Fig. 11.20) is seen in patients who receive one of these drugs for management of osteoporosis, osseous metastatic disease, or Paget's disease. Bisphosphonate

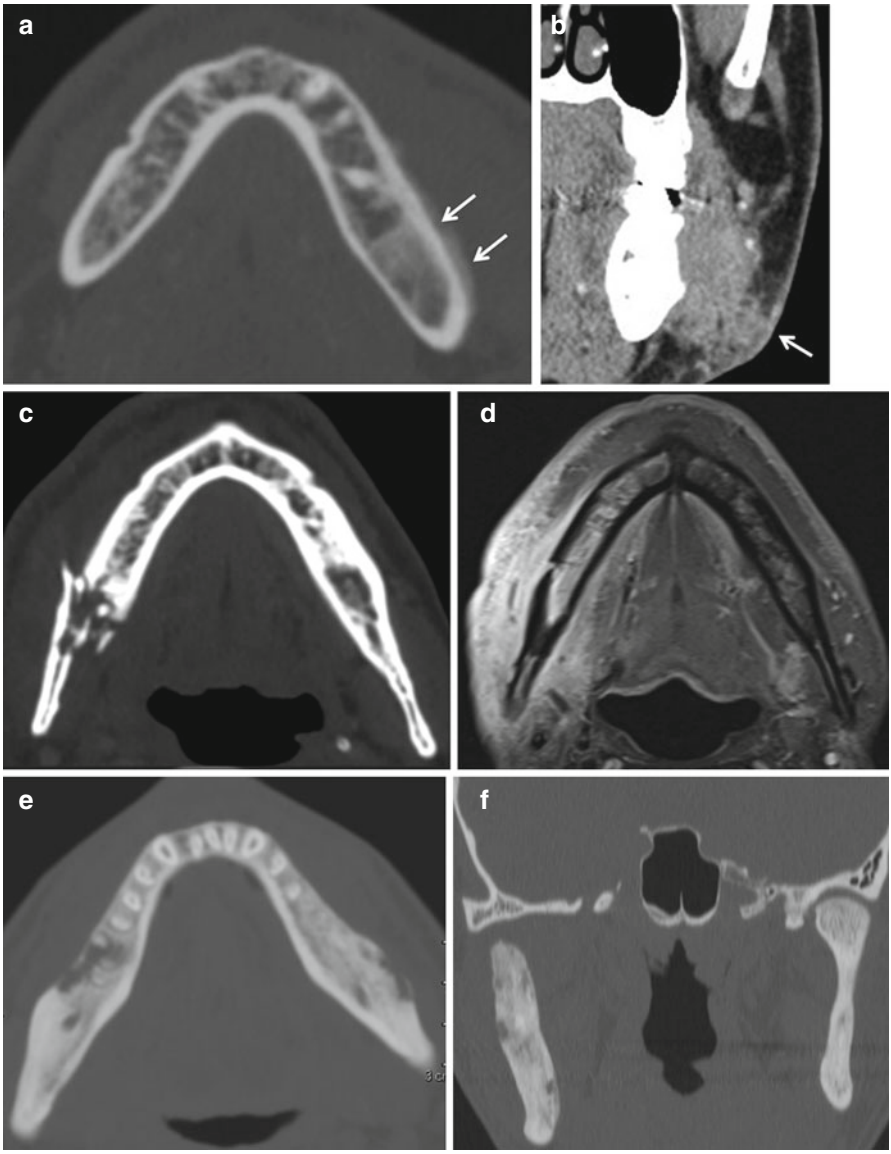

Fig. 11.19 (**a**, **b**) Chronic actinomycotic infection of the mandible. Sclerosis, a periosteal reaction (*arrow*), and an adjacent soft tissue abnormality (*arrow*) that extends to the skin surface, where draining sinuses were present, are evident. (**c**–**e**) Chronic candida osteomyelitis. The CT image shows a pathological fracture and small sequestra. On the enhanced MR image, extensive marrow inflammation/edema and loss of adjacent tissue planes are observed. (**e**, **f**) Chronic osteomyelitis in a patient with the SAPHO syndrome. Note the dense sclerosis and periosteal thickening cloaking the entirety of the mandible

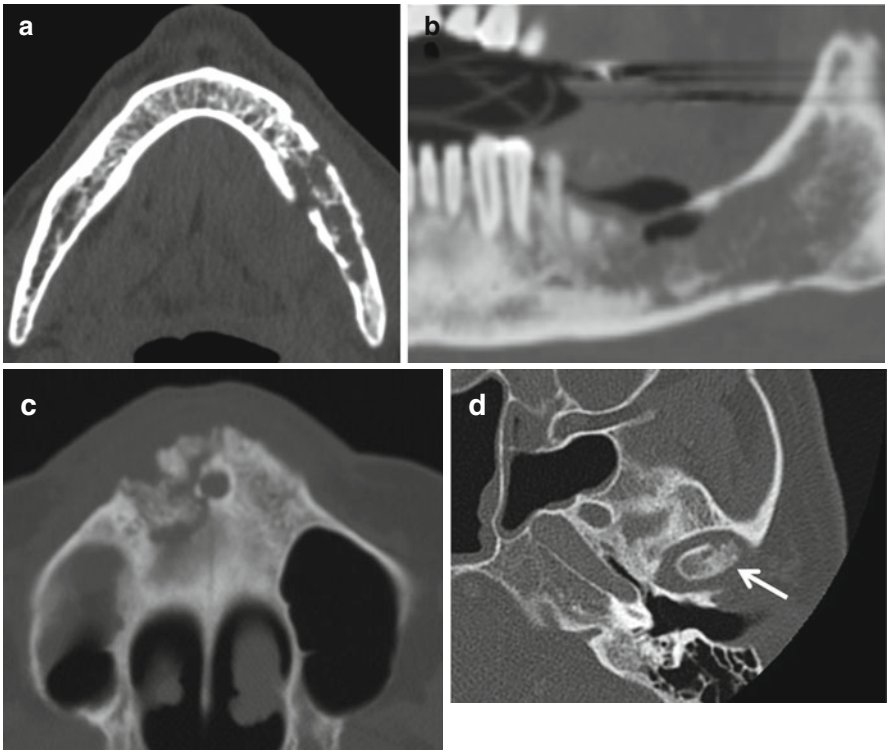

Fig. 11.20 (**a**, **b**) Osteonecrosis in a patient who received radiotherapy for a tonsillar malignancy. Note the osseous fragmentation and pathological fracture in (a) and the focus of gas in the medullary cavity in (b). The typical picture of a patient with ORN is that of bone exposure, pain, and the absence of an adjacent soft tissue mass. (**c**, **d**) depict mottled osteolysis from maxillary alveolus and mandibular condyle osteonecrosis respectively in patients receiving bisphosphonate (Image **d**, Courtesy of Dr William P. Dillon, University of California, San Francisco)

inhibits bone turnover and therefore prevents the mandible from mounting a reparative response to insults such as dental extraction. The risk of developing osteonecrosis increases with the dose of bisphosphonate and with IV administration. Early bisphosphonate-induced osteonecrosis is seen on CT as subtle foci of sclerosis adjacent to a dental socket or wound. With time, increased fragmentation, sclerosis, and formation of sequestra can be seen. MRI can demonstrate marrow edema, sclerosis, and enhancement but does not offer any significant advantage over CT.

11.8 The Surgeon's Perspective

As a general rule, definitive treatment of jaw lesions requires surgical resection and appropriate reconstruction. Rather than the exact histologic diagnosis, the most fundamental question to be answered by imaging is whether the process is benign, malignant, or infectious/necrotic.

Benign lesions tend to grow slowly but persistently and are detected when they cause dental symptoms (dental pain, loose teeth, etc.), masses, or functional deficits (masticatory pain, dental malalignment, etc.). While many of the benign cystic lesions can be successfully treated with curettage or even marsupialization (e.g., maxillary cysts opened into the maxillary sinus endoscopically), they have a high recurrence rate after these approaches. Thus, consideration must be given to the specific patient context when the treatment approach is determined. Unless resection is contraindicated, conservative treatment should not be repeated multiple times as this can lead to much more extensive anatomic deficits when compared to early definitive treatment. Odontogenic keratocysts and ameloblastomas, in particular, have a high recurrence rate after conservative approaches.

Malignant tumors require aggressive resection, and defining the extent of tumor radiographically is crucial. When tumor is in contact with the periosteum on imaging but mobile on examination, tumor excision with removal of the adjacent periosteum is adequate. When tumor is immobile on exam, periosteal invasion is likely. In this case, if imaging does not show frank cortical invasion, an alveolectomy/rim mandibulectomy is appropriate. This approach is generally adequate even when there is subtle cortical erosion, but penetration of the cortex (i.e., T4 tumor) requires segmental mandibulectomy. In this situation, the degree of progression through the medullary cavity is important in determining the extent of mandibular resection. If the extent is unclear on CT, MRI is often helpful. The head and neck surgeon will often encounter tumors in the context of a recently extracted tooth (at which time the dentist or oral surgeon performed a biopsy and documented cancer), and this can complicate the interpretation of bony erosion somewhat since the dental socket sometimes mimics cortical erosion on CT. Such sockets have smooth margins as opposed to invaded bone which is invariably irregular. It should be noted that alveolar carcinomas often cause significant erosion of the alveolar ridge without progression to medullary invasion, and these are often treated with alveolectomy only despite somewhat more extensive apparent cortical destruction on CT. Again, MRI can be helpful to clearly define the status of the medullary bone.

In the maxilla, in addition to jaw lesions, bony destruction can occur from maxillary sinus tumors which require partial or total maxillectomy and appropriate reconstruction.

Osteonecrosis of the jaws is becoming more common with the increasing use of radiation for head and neck cancer therapy and the increasing use of bisphosphonates. Careful imaging evaluation is important because biopsies can actually worsen osteonecrosis and should be avoided if possible. In addition to review of the imaging for evidence of recurrent tumor, careful and thorough clinical exam is crucial. Osteonecrosis should always be managed as conservatively as possible, remembering that clinical findings and symptoms are more important that the apparent degree and extent of abnormal bone on imaging. When aggressive treatment is appropriate, CT is the modality of choice to determine the extent of bone necrosis and plan reconstruction.

When planning advanced jaw reconstruction, it is common to use high-resolution CT to produce medical models and/or perform software-based planning of plate and flap size, position, and contour.

Conclusion

Jaw lesions on imaging may be broadly classified as those that are lytic, those that are sclerotic, and those that demonstrate both features (Box 11.1). They may also be divided into those with well-defined margins and those that produce more diffuse permeative bone loss. Well-defined lytic lesions may be unilocular or multilocular. The commonly encountered unilocular lesions are periapical cysts, dentigerous cysts, odontogenic keratocysts, unicameral bone cysts, and, sometimes, ameloblastomas. Multilocular lesions include ameloblastomas, aneurysmal bone cysts, and giant cell lesions. Predominantly sclerotic lesions include odontomas, cemento-osseous dysplasia, tori, and fibro-osseous lesions. Diffuse aggressive destructive processes include osteomyelitis, osteonecrosis, and malignancies such as osteosarcoma and invasive squamous cell carcinoma. The key imaging characteristics of these lesions are presented in Box 11.2. Jaw imaging is almost always most effectively performed with CT, but MRI and plain films have a place depending on the clinical situation. Figure 11.21 illustrates the key imaging appearances of the more commonly encountered jaw lesions.

Box 11.1. Differential Diagnosis of Jaw Lesions

- Cystic lesions
  - Unilocular
    - Periapical cyst
    - Dentigerous cyst
    - Odontogenic keratocyst
    - Unicameral bone cyst
    - Stafne bone cavity
    - Ameloblastoma
    - Brown tumor
    - Eosinophilic granuloma
  - Multilocular
    - Ameloblastoma
    - Odontogenic myxoma
    - Aneurysmal bone cyst
    - Giant cell lesions
- Sclerotic lesions
  - Odontoma
  - Cemento-osseous dysplasia
  - Fibro-osseous lesions
  - Tori
  - Osteoma
- Diffuse destructive processes
  - Osteomyelitis
  - Osteonecrosis
  - Invasion by squamous cell carcinoma
  - Metastatic disease
  - Sarcoma – osteosarcoma, Ewing's sarcoma

Box 11.2. Key Imaging Characteristics of the More Common Discrete Jaw Lesions

Lesion	Key imaging feature(s)
Periapical cyst	Well defined, related to root of tooth
Dentigerous cyst	Unerupted tooth at base of cyst
	Multiple, consider Gorlin's (basal cell nevus) syndrome
Unicameral bone cyst	Smoothly marginated unilocular lesion, no distinguishing characteristics
Stafne bone cavity	Well-defined lucent focus at angle of mandible, contains rest of submandibular salivary tissue
Incisive canal cyst	Midline cyst at junction of hard palate and premaxilla
Ameloblastoma	Uni- or multilocular expansile lytic lesion, papillary projections on enhanced CT or MR
Odontogenic myxoma	Resembles ameloblastoma, seen in younger patients
Aneurysmal bone cyst	Multilocular expansile cyst with blood-fluid levels on MRI
Giant Cell Lesions	Multilocular expansile lesions indistinguishable from aneurysmal bone cysts
Odontoma – complex	Posterior mandible, contains amorphous densities
Odontoma – compound	Anterior mandible, contains well-defined small toothlike densities
Cemento-osseous dysplasia	Periapical circumscribed density with lucent periphery adjacent to tooth root; florid type – widespread lesions
Fibro-osseous lesions	Lytic focus with sclerotic rim, ground-glass mineralized matrix, may involve other craniofacial bones
Tori	Well-defined osseous excrescences arising from the inner surface of the mandibular body, from the undersurface of the hard palate in the midline, or from the outer aspect of the maxillary alveolus
Osteochondroma	Pedunculated osseous excrescence arising most commonly from the mandibular ramus with a cartilage cap
Osteosarcoma	Variable appearance, destructive lesion with a soft tissue mass sometimes containing tumor bone, sunburst periosteal reaction if present is highly suggestive

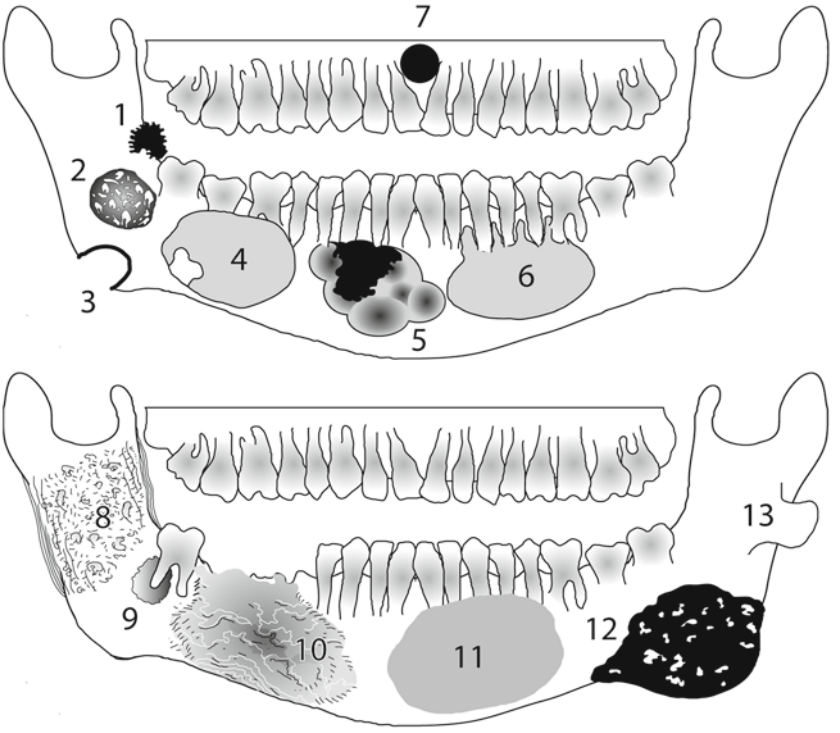

Fig. 11.21 Graphic demonstrating the basic imaging appearances of the more common jaw lesions. (*1*) Invasion by a retromolar trigone squamous cell cancer, (*2*) odontoma, (*3*) Stafne bone cavity, (*4*) dentigerous cyst, (*5*) ameloblastoma, (*6*) odontogenic keratocyst, (*7*) incisive canal cyst, (*8*) osteomyelitis, (*9*) periapical abscess, (*10*) osteoradionecrosis, (*11*) fibrous dysplasia, (*12*) osteosarcoma, (*13*) osteochondroma

Further Reading

Curé JK, Vattoth S, Shah R (2012) Radiopaque jaw lesions: an approach to the differential diagnosis. Radiographics 32(7):1909–1925

Morag Y, Morag-Hezroni M, Jamadar DA, Ward BB, Jacobson JA, Zwetchkenbaum SR, Helman J (2009) Bisphosphonate-related osteonecrosis of the jaw: a pictorial review1. Radiographics 29(7):1971–1984

Scholl RJ, Kellett HM, Neumann DP, Lurie AG (1999) Cysts and cystic lesions of the mandible: clinical and radiologic-histopathologic review1. Radiographics 19(5):1107–1124

Suei Y, Taguchi A, Tanimoto K (2005) Diagnosis and classification of mandibular osteomyelitis. Oral Surg Oral Med Oral Pathol Oral Radiol Endod 100(2):207–214

Thyroid and Parathyroids

12

Rachita Khot, David C. Shonka Jr., Prashant Raghavan, Max Wintermark, and Sugoto Mukherjee

12.1 Introduction

The thyroid gland is an essential component of our endocrine system and regulates a wide range of critical metabolic functions. Both focal and diffuse thyroid disorders can impact function. The parathyroid glands regulate serum calcium levels. Parathyroid evaluation is almost always done in the setting of hyperparathyroidism and hypercalcemia. A combination of imaging techniques are used to evaluate thyroid and parathyroid pathology and function, including ultrasound, CT, MRI, and radionuclide imaging.

12.2 Anatomy

The thyroid gland consists of two lobes connected by midline isthmus. It lies in the visceral space, anteromedial to the carotid space, between the prevertebral muscles posteriorly and the infrahyoid strap muscles anteriorly (Fig. 12.1). An accessory pyramidal lobe can extend superiorly from the isthmus toward the hyoid bone. The tubercle of Zuckerkandl can often be reliably identified on CT and is located on the posterior aspect of each lobe; it serves as a surgical landmark for the recurrent laryngeal nerve, which passes posterior to it (Fig. 12.2).

The thyroid gland develops from the third and fourth pharyngeal pouches and descends during fetal development from the foramen cecum at the midline base of the tongue to the thyroid bed along the course of the thyroglossal duct (Fig. 12.3).

The thyroid gland is supplied by paired superior and inferior thyroid arteries, which arise from the external carotid and thyrocervical trunk, respectively. The thyroidea ima artery is present in 4–10 % of the population and can have a variable origin from the arch of the aorta or the innominate artery. The venous drainage is via the superior and middle thyroid veins into the internal jugular veins and the inferior thyroid veins into the brachiocephalic veins. The lymphatic drainage is to adjacent pretracheal, paratracheal, and prelaryngeal nodes in the visceral space (level VI). Regional drainage can occur to levels II–V in the lateral neck. The gland is closely associated with the superior and recurrent laryngeal nerves.

P. Raghavan et al., *Manual of Head and Neck Imaging*,
DOI 10.1007/978-3-642-40377-4_12, © Springer-Verlag Berlin Heidelberg 2014

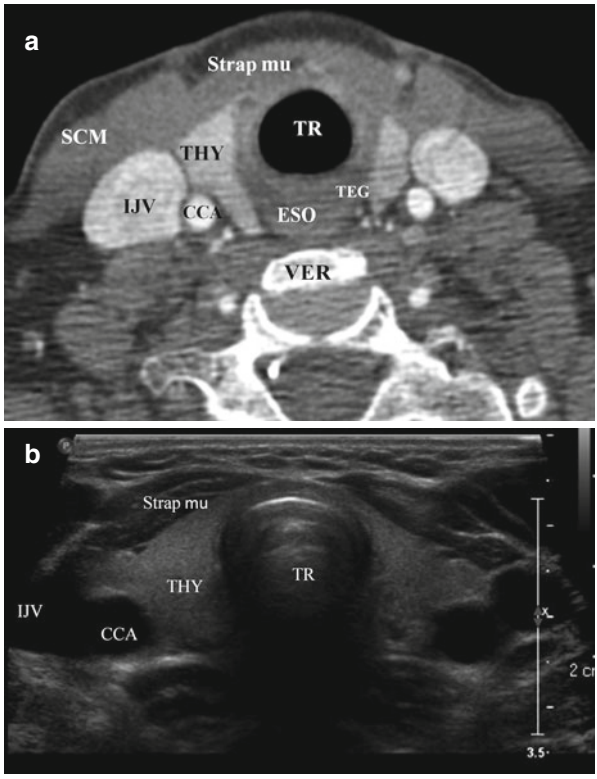

Fig. 12.1 Normal CT and US images of the thyroid gland. Contrast-enhanced axial CT (**a**) and axial grayscale US images (**b**) of the thyroid gland in the infrahyoid neck show the normal anatomical relationships of the relevant structures. These include the following: *Strap mu* strap muscles, *SCM* sternocleidomastoid muscle, *IJV* internal jugular vein, *VER* cervical vertebra, *CCA* common carotid artery, *TEG* tracheoesophageal groove, *TR* trachea, *ESO* esophagus, *THY* thyroid

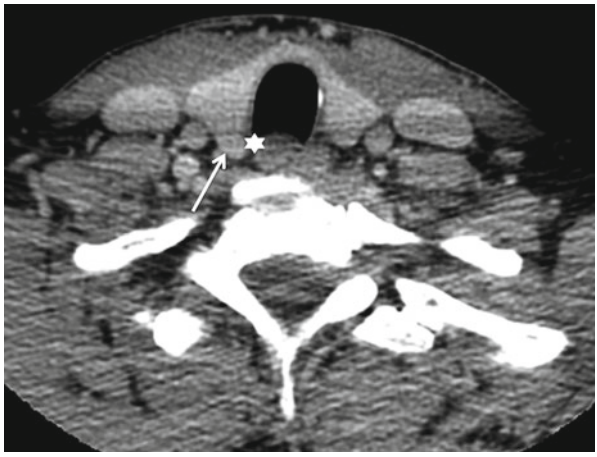

Fig. 12.2 Zuckerkandl tubercle. The Zuckerkandl tubercle (also referred to as the posterior thyroid tubercle) is usually identified as a nodular posterior extension (*arrow*) of thyroid tissue beyond the tracheoesophageal groove (*star*). It serves as an important surgical landmark for the recurrent laryngeal nerve, which courses medial to it

The thyroid gland uses iodine to produce thyroxine (T4) and triiodothyronine (T3); production is regulated by the hypothalamic-pituitary axis via secretion of thyroid-stimulating hormone (TSH). Circulating thyroid hormone is predominantly bound to thyroglobulin, also produced by the thyroid. Calcitonin is produced and

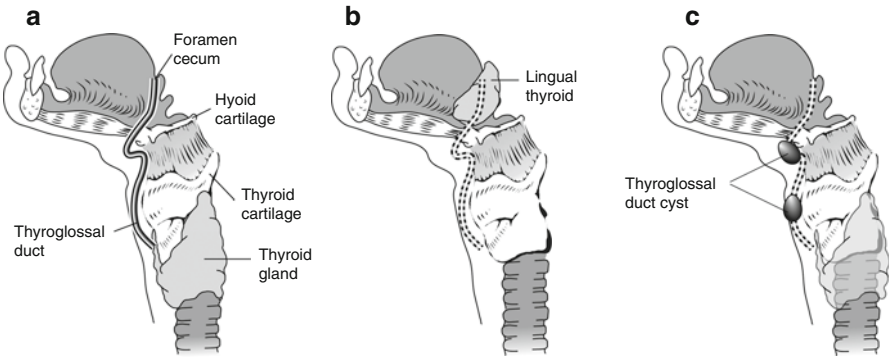

Fig. 12.3 Graphic showing the course of the thyroglossal duct cyst from the foramen cecum in the base of the tongue, passing anterior to the hyoid bone and laryngeal cartilages to its final destination in a pretracheal location (**a**). Abnormal descent of the thyroid gland or failure of obliteration of the thyroglossal duct can lead to ectopic thyroid tissue (**b**) and thyroglossal cysts (**c**) along the course of the thyroglossal duct

secreted by parafollicular C cells, which are derived from the ultimobranchial bodies.

12.3 Imaging Evaluation

12.3.1 Ultrasound

The initial imaging modality for the thyroid gland is ultrasound (US), performed using a high-resolution linear probe (7–13 MHz). US is useful for evaluating thyroid nodules and cervical nodes, guiding fine-needle aspirate (FNA) biopsies, and performing surveillance for disease progression or recurrence. US can also be used to assess for fetal goiters and to screen for the presence of thyroid nodules in high-risk groups (e.g., history of childhood radiation exposure).

On US, the thyroid parenchyma appears homogeneous with echogenicity greater than the adjacent muscles. The longus colli muscle and trachea can be seen posteriorly to the thyroid gland on sagittal views. On axial views, the common carotid artery and internal jugular vein are present laterally; sternohyoid, sternothyroid, and sternocleidomastoid muscles are present anteriorly (Fig. 12.4).

Ultrasonography findings suspicious for thyroid cancer include a taller-than-wide shape, spiculated or microlobulated margins, marked hypoechogenicity, and micro- and macrocalcifications. A combination of size and suspicious US features is more predictive of malignancy than size alone. When FNA biopsy of a nodule is clinically appropriate, US guidance is recommended for nodules that are nonpalpable, predominantly solid, and/or located posteriorly in the thyroid lobe. US-guided FNA is done using narrow-gauge needles (22G or 25G), with or without local anesthesia, and adequate samples can be obtained in 90–97 % of solid nodules (Fig. 12.5). The American Thyroid Association and Society of Radiologists in Ultrasound recommendations are summarized in Box 12.1.

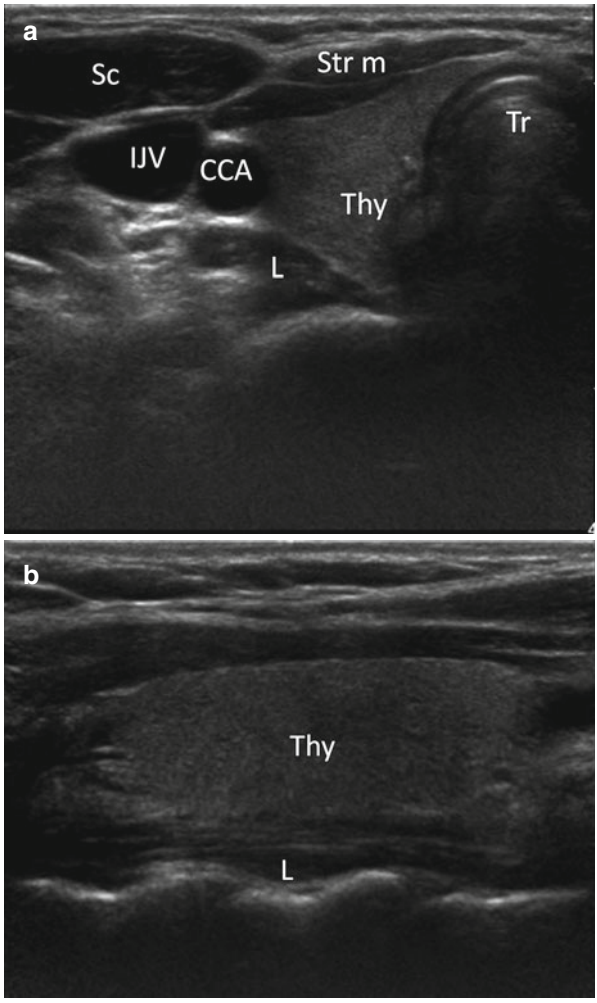

Fig. 12.4 Axial (**a**) and sagittal (**b**) grayscale ultrasound images of the right thyroid lobe with adjacent structures. *Thy* right thyroid lobe, *Tr* trachea, *CCA* common carotid artery, *IJV* internal jugular vein, *L* longus coli muscle, *Sc* sternocleidomastoid muscle, *Str m* strap muscle

12.3.2 Radionuclide Scintigraphy and PET

In the past, radionuclide imaging was used to assess the functionality of all thyroid nodules as a predictor of malignancy (hot nodules are rarely malignant). Given the effectiveness of thyroid US and FNA to clearly delineate malignant nodules, nuclear thyroid scans are currently used to distinguish between various causes of hyperfunctioning thyroid (Graves' disease, toxic multinodular goiter, autonomous adenoma) and in the workup of ectopic thyroid tissue. Whole body imaging using iodine-123 (^{123}I) or iodine-131 (^{131}I) is used to monitor post-thyroidectomy patients for recurrence or metastasis and to assess the response to therapy. ^{123}I is the imaging agent of choice for benign thyroid processes due to its short half-life (13 h) and lower energy (159 keV). Because of its longer half-life (8 days) and higher energy (364 keV), ^{131}I is the radionuclide of choice for treatment of Graves' disease, toxic multinodular goiter, and well differentiated thyroid cancers

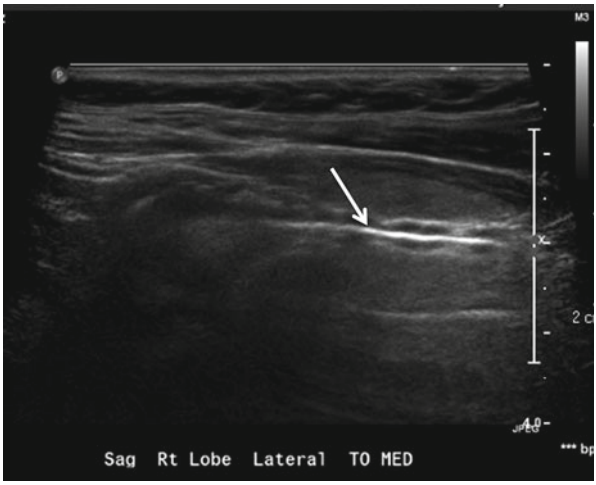

Fig. 12.5 Fine-needle aspiration of thyroid lesion. Sagittal ultrasound image showing the entire needle (*arrow*) as a hyperechoic structure. This appearance is seen using the parallel needle technique, with both the needle and ultrasound transducer in a plane parallel to each other

Box 12.1. Summary of FNA Recommendations for Thyroid Nodules Based on Clinical and Sonographic Criteria

Sonographic and clinical features	American Thyroid Association	Society of Radiologists in Ultrasound (≥1 cm)
High-risk history[a] and suspicious sonographic features[b]	Strongly recommend FNA if >5 mm	None
Substantial growth	None	Consider FNA
Cystic nodule	FNA not indicated	FNA not indicated
Solid composition	Recommend FNA if >1 cm and hypoechoic	Strongly recommend FNA if ≥1.5 cm
Solid and cystic	Recommend FNA if >2 cm	Consider FNA if ≥2 cm
Coarse calcification	None	Strongly recommend FNA if ≥1.5 cm
Microcalcifications	Recommend FNA if >1 cm	Strongly recommend FNA if ≥1 cm

MEN multiple endocrine neoplasia, *FMTC* familial medullary thyroid cancer
[a]High-risk history: history of thyroid cancer in one or more first-degree relatives, history of external bean radiation as a child, exposure to ionizing radiation in childhood or adolescence, prior hemithyroidectomy with discovery of thyroid cancer, FDG avidity on PET scanning, MEN II-/FMTC-associated RET proto-oncogene mutation, and calcitonin >100 pg/mL
[b]Suspicious features: microcalcifications, hypoechoic, increased nodular vascularity, infiltrative margins, taller than wide on transverse view

(papillary and follicular thyroid cancers). ^{131}I is also used for posttreatment surveillance of well-differentiated thyroid cancer. Medullary and anaplastic thyroid carcinomas do not take up radioiodine, but can be evaluated by either technetium-99 m (^{99m}Tc) sestamibi imaging or fluorine-18 deoxyglucose (FDG) PET-CT, which are discussed below. ^{99m}Tc pertechnetate is the preferred thyroid imaging agent in children due to its low radiation dose, short half-life (6 h), and high count rate.

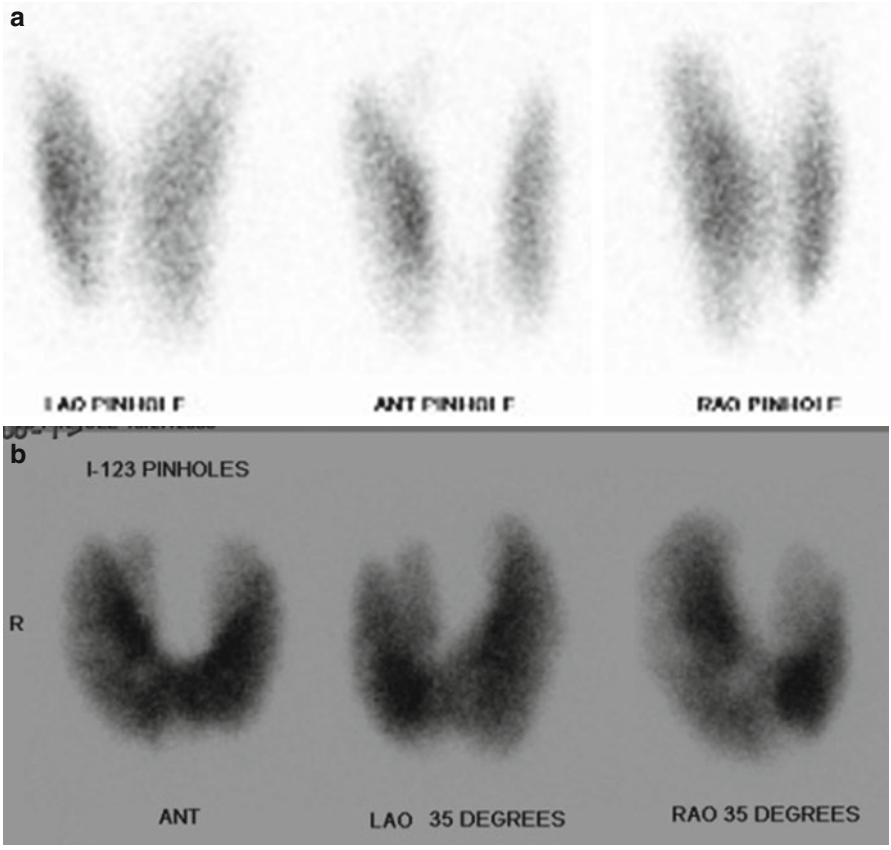

Fig. 12.6 Normal I-123 thyroid scan (**a**) with uniform uptake of radiotracer by the thyroid gland. Iodine uptake equals 10.3 % at 4 h and 21.2 % at 24 h. Values less than 18 % at 4 h and less than 35 % at 24 h are normal. Abnormal I-123 scan (**b**) in a hyperthyroid patient shows a diffusely enlarged gland with an identifiable pyramidal lobe. This patient had an iodine uptake of 85.7 % at 3 h

A normal thyroid gland shows homogeneous radiotracer uptake with areas of increased uptake in the region of greater gland thickness. The pyramidal lobe can be seen as linear uptake extending superiorly from the isthmus in cases of hyperthyroidism (Fig. 12.6). Most cold nodules represent benign lesions such as cyst, adenomas, or colloid nodules; the incidence of cancer in a cold nodule is 15–20 %; thus, they warrant further assessment with US. If a cold nodule is solid on US, biopsy is recommended. Almost all hot nodules represent benign hyperfunctioning adenomas. Given the limited diagnostic information and the frequent need for follow-up US, iodine uptake imaging is no longer considered the preferred initial evaluation for a thyroid nodule.

PET-CT is performed using ^{18}F-FDG and is useful in detecting recurrent thyroid cancers in the setting of negative radioiodine scans. The sensitivity of PET-CT is

more than 90 % in the setting of elevated thyroglobulin and negative ^{131}I scan after thyroidectomy. Due to their low ^{18}F-FDG uptake, PET-CT is limited in its ability to evaluate poorly differentiated and aggressive thyroid tumors, except to identify distant metastasis.

12.3.3 CT and MRI

The primary role of cross-sectional imaging (CT or MRI) is for presurgical evaluation for extra thyroidal extension and regional metastasis of thyroid cancers. This includes evaluation for invasion of the trachea, esophagus, larynx, recurrent laryngeal nerve, infrahyoid strap muscles, subcutaneous soft tissue, mediastinal and great vessels, and prevertebral fascia. While US can evaluate for cervical lymphadenopathy, retropharyngeal and mediastinal nodes are difficult to access with US and are better evaluated by CT or MRI. Contrast-enhanced CT is discouraged prior to surgery as it can impact the uptake of ^{131}I used for postoperative thyroid ablation. When iodinated contrast agents have been used, ^{131}I treatment is typically withheld for 6 weeks and urine iodine measurements may be necessary to ensure uptake. Thus, non-contrast CT or contrast-enhanced MRI is preferred preoperatively; of the two, MR provides better soft tissue resolution.

12.3.4 Imaging Incidentalomas

Thyroid incidentalomas are nonpalpable thyroid nodules that are detected during imaging procedures ordered for other reasons. Nonpalpable nodules have approximately the same risk of malignancy as palpable nodules. However, ^{18}F-FDG-avid nodules discovered on PET scans have a higher risk of malignancy relative to those discovered on CT or MRI. The American Thyroid Association (ATA) and Society of Radiologists in Ultrasound (SRUS) guidelines, summarized in Box 12.1, are based on clinical risk factors and ultrasound evaluation. Although there are no uniform guidelines for non-US (CT, MRI, or PET)-detected incidentalomas, a practical approach includes further work based on imaging findings and clinical history. This has been summarized in Box 12.2.

12.4 Pathology

From an imaging perspective, the diseases of the thyroid gland can be divided into congenital/developmental, diffuse, and focal diseases. The congenital diseases include thyroglossal duct cysts (TGDCs) and ectopic thyroid. The diffuse disease includes goiter, Graves' disease, and multinodular goiter, along with various forms of thyroiditis. The focal diseases consist of thyroid nodules, which are broadly divided into colloid nodules, adenomatous nodules, adenoma, and tumors.

Box 12.2. Practical Approach for Incidental CT-, MRI-, or PET-Detected Thyroid Nodules

Malignancy risk category	Imaging characteristics	Workup recommendations
Low risk	<1 cm sized nodule with absence of risk factors	Description in body and/or impression of radiology report
High risk	>1 cm size nodule High-risk[a] clinical history, younger patients <20 years, or males <35 years or females 20–35 years Concerning imaging features (associated lymphadenopathy, extrathyroid spread of lesion, vocal cord palsy, distant metastasis, PET avid lesion, etc.)	Ultrasound for further characterization and possibly FNA (dependent on the additional workup)

Modified from Hoang JK, Raduazo P, Yousem DM, Eastwood JD. What to do with incidental thyroid nodules on imaging? An approach for the radiologist. Semin Ultrasound CT MR 2012;33:150–157

MEN multiple endocrine neoplasia, *FMTC* familial medullary thyroid cancer

[a]High-risk history: history of thyroid cancer in one or more first-degree relatives, history of external beam radiation as a child, exposure to ionizing radiation in childhood or adolescence, prior hemithyroidectomy with discovery of thyroid cancer, MEN II-/FMTC-associated RET proto-oncogene mutation, calcitonin >100 pg/mL

12.4.1 Congenital/Developmental Diseases

12.4.1.1 Thyroglossal Duct Cyst

TGDCs represent thyroglossal duct remnants anywhere between the foramen cecum (tongue base) and the thyroid gland (Fig. 12.3); they are among the most common congenital anomalies in the head and neck. TGDCs are usually midline at or above the hyoid and paramidline below. On CT, these are thin-walled, uni- or multilocular cystic masses and may enhance if infected (Fig. 12.7). Approximately 50 % occur at the level of the hyoid, either anterior to hyoid or extending into the preepiglottic space. About 25 % are suprahyoid, within the tongue base or floor of mouth, and about 25 % are infrahyoid, embedded within the strap muscles. TGDCs are most effectively treated with the Sistrunk procedure, which, in addition to the cyst, resects the entire tract and central hyoid bone to reduce recurrence. Rarely, these can have associated papillary thyroid cancers, noted as an enhancing solid nodule within the cyst (Fig. 12.8).

12.4.1.2 Ectopic and Lingual Thyroid

Ectopic thyroid tissue may be found anywhere (Fig. 12.9) within the central neck along the course of the thyroglossal duct (Fig. 12.3). While lingual thyroid represents the most common location (90 %), ectopic thyroid tissue has been identified as far inferiorly as the mediastinum. Lingual thyroid tissue is usually asymptomatic but may present with irritative or obstructive symptoms. Due to its iodine content, it appears as a hyperdense midline mass within the tongue on non-contrast CT (Fig. 12.10). The presence of thyroid in the normal location should be verified as the

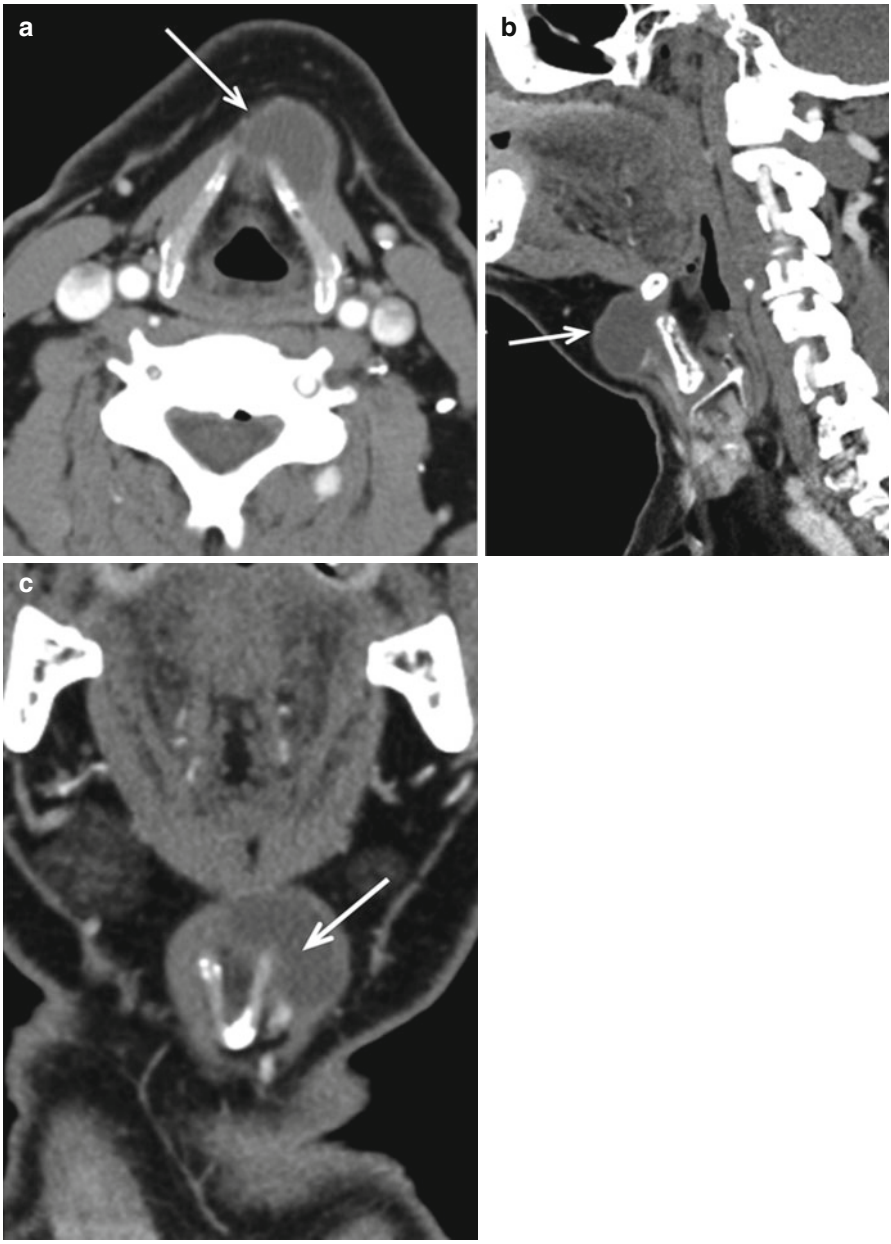

Fig. 12.7 Infrahyoid thyroglossal duct cyst. Rim-enhancing cystic lesion (*white arrow* in **a**, **b** and **c**), in the left paramedian location, wrapping around the left thyroid lamina and embedded within the strap muscles on axial (**a**), sagittal (**b**) and coronal (**c**) scans. Unlike suprahyoid thyroglossal duct cysts which are usually midline, infrahyoid cysts are paramedian in location. Enhancing solid nodules or thick calcifications within the cyst suggest an associated thyroid carcinoma

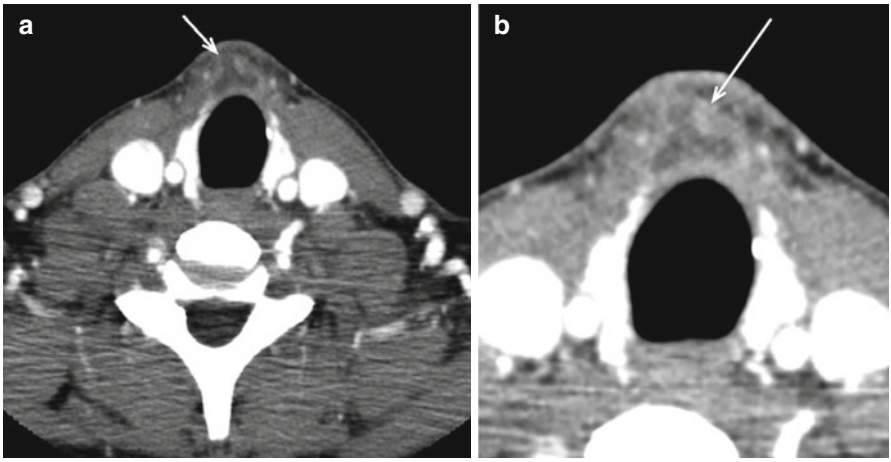

Fig. 12.8 Papillary carcinoma in thyroglossal duct cyst. Heterogeneously enhancing lesion in the pretracheal location (*arrow* in **a**) with a more nodular focus within it (*arrow* in **b**). FNA of the lesion came back as a papillary carcinoma arising within a thyroglossal duct cyst

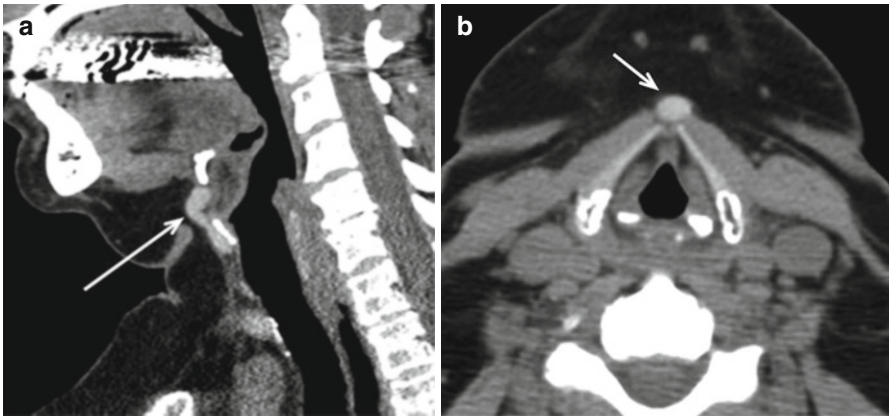

Fig. 12.9 Ectopic thyroid. Sagittal (**a**) and axial (**b**) non-enhanced CT images demonstrate a well-defined hyperdense (*arrows*) lesion just below the hyoid, representing an ectopic thyroid tissue. The presence of iodine in thyroid tissue makes them hyperdense on non-contrast CT scans, making it an easy diagnosis

ectopic thyroid tissue may represent the only functioning thyroid tissue (75 %). Rarely, these may undergo goitrous or malignant transformation (3 %). Rarely, two separate ectopic thyroid tissues can be identified (Fig. 12.11).

12.4.2 Diffuse Thyroid Diseases

Despite the overlapping imaging features of diffuse thyroid disease, the clinical presentation is different, aiding in diagnosis. These conditions can present with both morphological and functional changes of the thyroid gland.

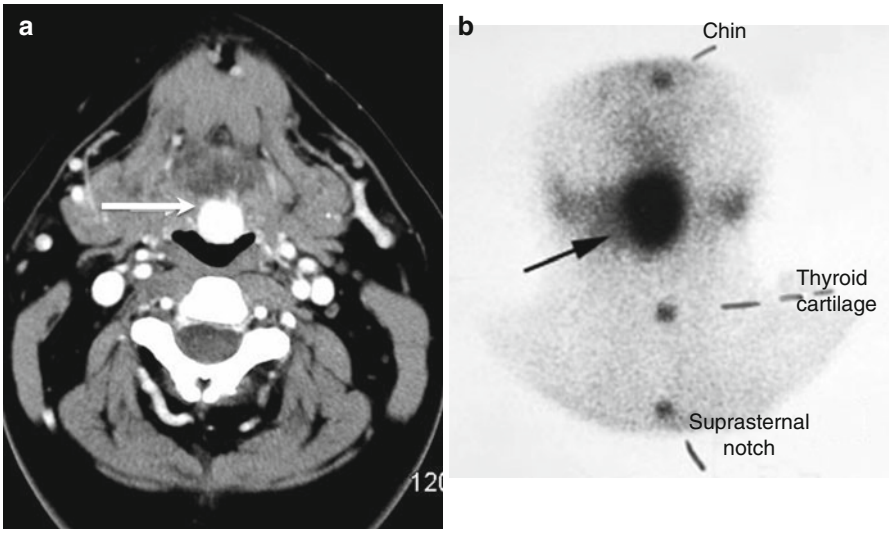

Fig. 12.10 Lingual thyroid. Enhancing mass (*arrow*) in the characteristic midline location at the tongue base on axial CT (**a**), along with the technetium-99 pertechnetate scan (**b**), confirming the focal increased activity at the tongue base and absence of any uptake in the thyroid bed inferiorly

12.4.2.1 Goiter

Goiter refers to abnormal thyroid growth with enlargement of the gland and can be associated with normal, decreased, or increased thyroid hormone production; both size and function impact clinical management. In North America, multinodular goiter, chronic autoimmune (Hashimoto's) thyroiditis, and Graves' disease are common causes of goiter. However, worldwide iodine deficiency is the most common cause of goiter. Compressive symptoms (dyspnea, dysphagia) can occur due to massive or asymmetric enlargement or retrosternal extension. As the growth is slow, patients with symptoms are often well compensated. Radionuclide studies and thyroid function tests are used to categorize these lesions, based on the change in normal uptake and the focality. Nodules should be considered for FNA biopsy based on clinical and imaging features.

On US, the nodules in multinodular goiter can have varied echogenicity representing mixed solid and cystic components along with occasional hemorrhage or calcification. US characteristics of the nodules should be carefully reported, as suspicious nodules must be addressed. On radionuclide scan, these nodules are generally cold, and the gland appears irregular and heterogeneous. On CT, the gland is nodular with areas of low density corresponding to nodules, hemorrhage, or necrosis. Coarse calcification is commonly seen (Fig. 12.12). On MRI, varying signal intensities are noted on T1-weighted images depending on presence of colloid or hemorrhage, which has high signal intensity. On T2-weighted images, heterogeneous signal intensity is noted. On both T1- and T2-weighted images, calcifications appear as signal voids and fibrosis appears as low signal foci. The entire gland demonstrates heterogeneous enhancement. CT and MRI are very helpful to evaluate for retrosternal extension and for compression of adjacent structures (Fig. 12.12).

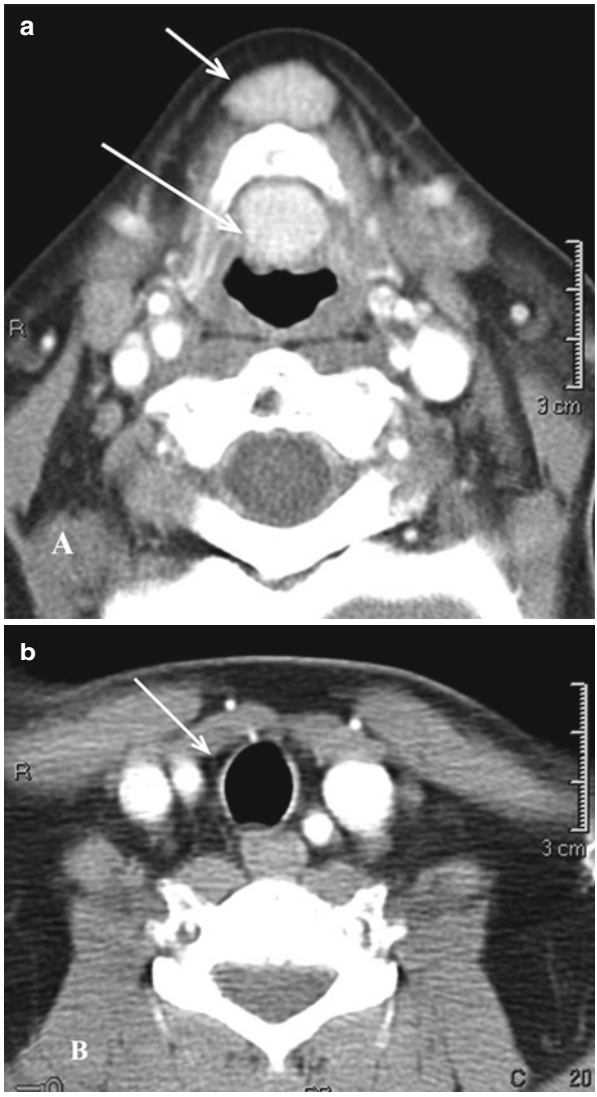

Fig. 12.11 Double ectopic thyroid. Two hyperenhancing masses are seen in the midline, anterior and posterior to the hyoid bone in this patient with midline neck swelling (*arrows* in **a**). Axial scan through the thyroid bed demonstrates an absent thyroid gland (*arrow* in **b**). This represents a rare double ectopic thyroid tissue. It is extremely important to check the thyroid bed for thyroid remnant. Resection of ectopic thyroids without reimplantation in a patient with absent normal thyroid tissues ends up leaving the patient hypothyroid and on lifelong thyroid hormone replacement therapy

12.4.2.2 Graves' Disease

Graves' disease is a hyperthyroid autoimmune disease caused by anti-TSH receptor autoantibodies. It is more common in females with peak incidence in the third to fourth decades. On US, the thyroid gland appears enlarged with heterogeneous parenchyma. A condition called "thyroid inferno" can be seen on color Doppler in untreated cases that have significantly increased vascularity; this resolves with treatment (Fig. 12.13). On CT and MRI, the gland appears heterogeneous with diffuse

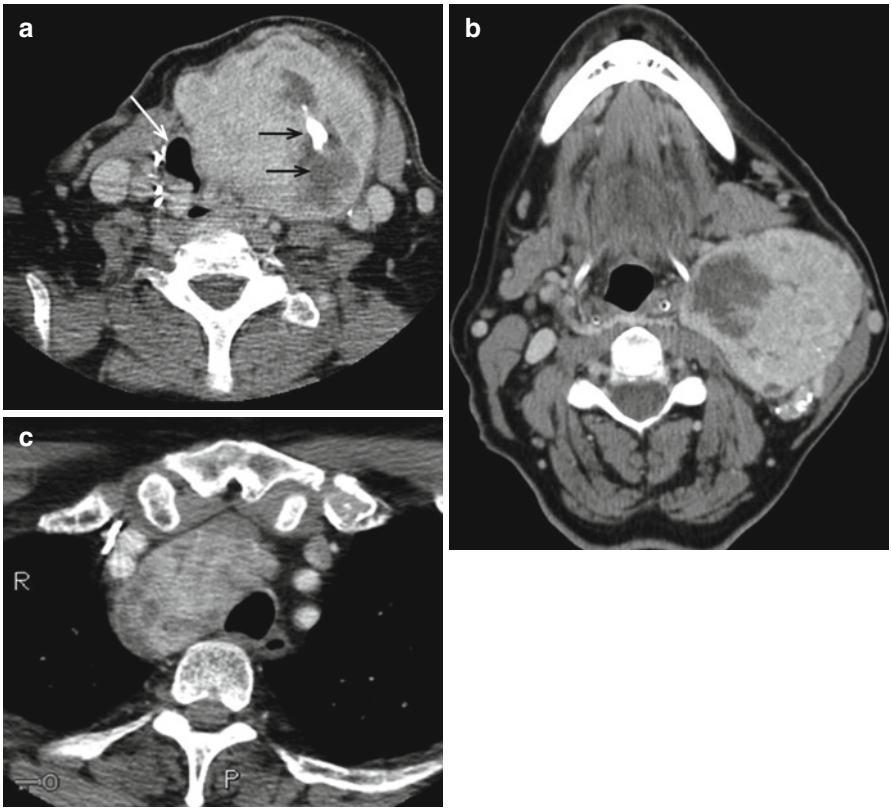

Fig. 12.12 Multinodular goiter. Large multinodular goiter, displacing the trachea to the right (*white arrow* in **a**), with superior extension on the left (**b**) and substernal extension (**c**). Note the multiple areas of hypodensity as well as thick calcifications (*black arrows* in **a**)

irregular enlargement. Graves' disease-related hyperthyroidism can be associated with thyroid orbitopathy involving the extraocular muscles with increased orbital fat volume (Fig. 12.14).

12.4.2.3 Hashimoto's Thyroiditis

Hashimoto's thyroiditis is an autoimmune disease characterized by diffuse lymphocytic infiltration and an increased risk of lymphoma. It is associated with autoantibodies to thyroid peroxidase and thyroglobulin, is more common in females, and is the most common cause of goitrous hypothyroidism in the United States. In the early hyperthyroid stage, the gland appears normal in size or enlarged on US. Due to fibrous septae, the parenchyma is heterogeneous with a multinodular pattern; most of the nodules are less than 5 mm and hypoechoic. Color Doppler demonstrates increased vascularity (Fig. 12.15). In the later hypothyroid stage, the gland

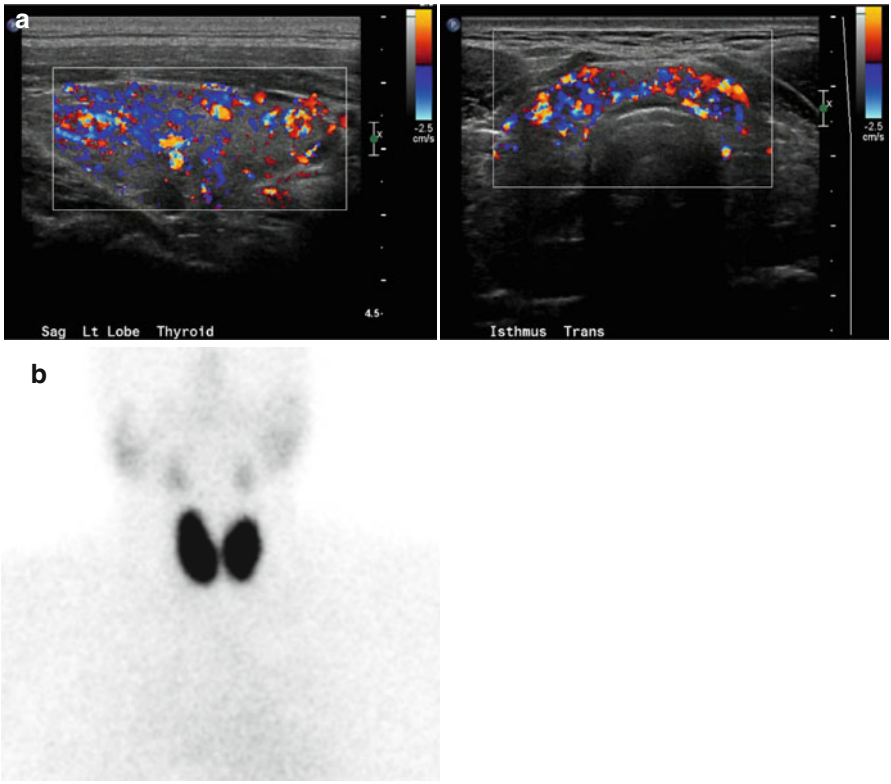

Fig. 12.13 (**a**) Graves' disease. Color Doppler images of the left thyroid lobe and isthmus shows increased vascularity ("thyroid inferno") in a patient with hyperthyroidism secondary to Graves' diseases. (**b**) Graves's disease. Technetium-99m pertechnetate scan in this patient with Graves' disease shows diffusely increased uptake with enlarged thyroid gland. The 24-h iodine uptake in this patient was 65 %

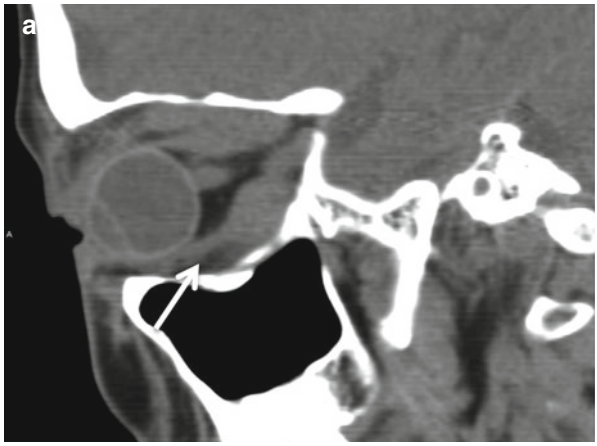

Fig. 12.14 Thyroid orbitopathy. Sagittal (**a**) and coronal CT (**b**) images demonstrate the characteristic findings of thyroid orbitopathy with enlarged extraocular muscles in this patient with hyperthyroidism due to Graves' disease. Note the sparing of the tendinous insertions (*arrow* in **a**)

Fig. 12.14 (continued)

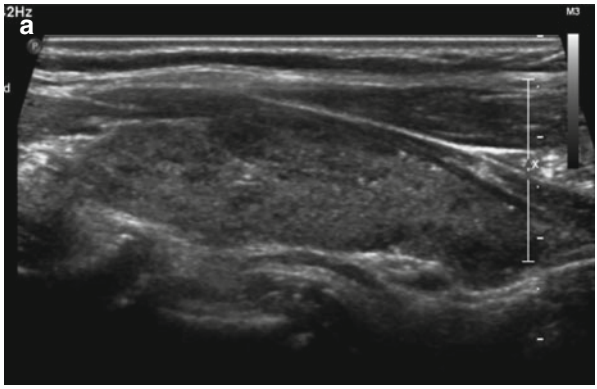

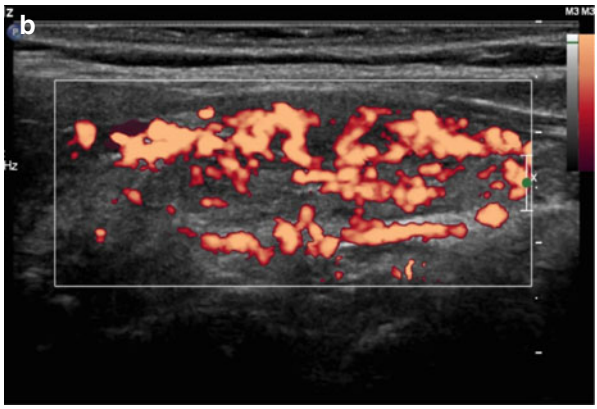

Fig. 12.15 Hashimoto's thyroiditis. Grayscale US image shows enlarged, heterogeneous thyroid, with small hypoechoic nodules with thin echogenic septa (**a**), and color Doppler shows increased vascularity (**b**) in a case of early Hashimoto's thyroiditis with positive thyroid peroxidase antibodies. Late cases of Hashimoto's demonstrate decreased vascularity

may be small and fibrotic with heterogeneous echotexture. On radionuclide scan, radiotracer uptake is increased and irregular (Fig. 12.16). On CT, the gland shows heterogeneous enhancement, usually without necrosis and calcification. On MRI, the gland demonstrates diffusely increased T2 signal intensity, with numerous lower-signal fibrotic bands.

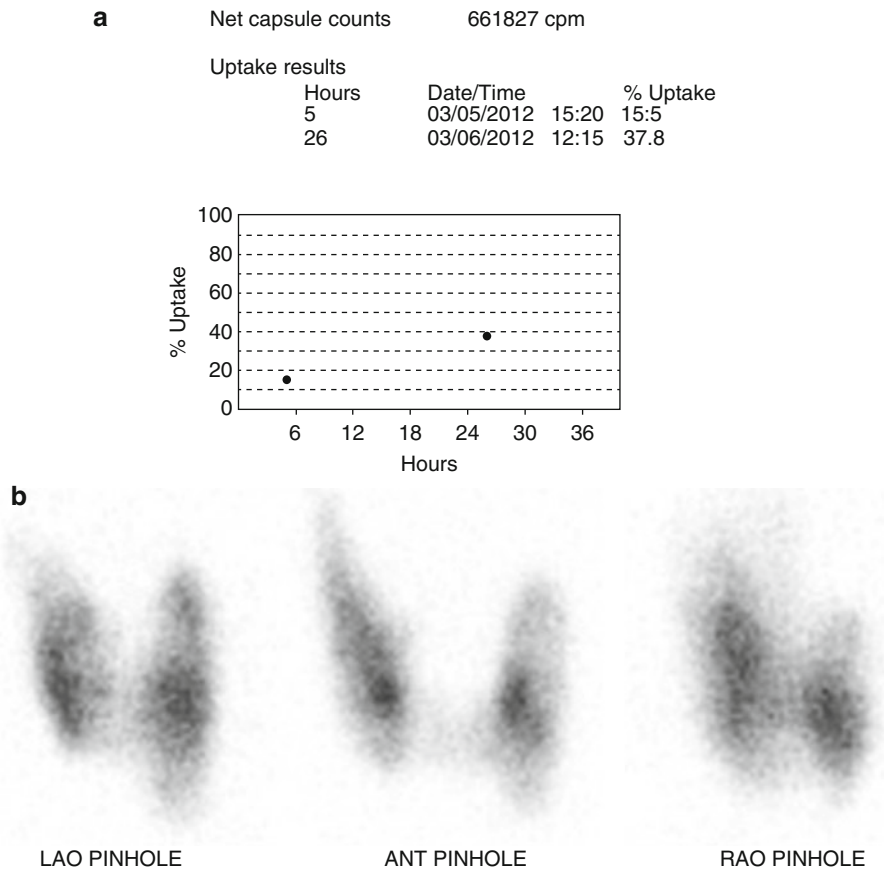

Fig. 12.16 Hashimoto's thyroiditis. I-123 thyroid scan shows patchy and heterogeneous mildly elevated thyroid uptake. Findings compatible with Hashimoto's thyroiditis in active phase, given pattern and elevated serum thyroid peroxidase antibodies

12.4.2.4 Subacute Thyroiditis

Subacute thyroiditis also commonly referred to as de Quervain's Thyroiditis, is a self-limiting viral disease that is more common in females. Clinical symptoms include a painful, tender gland after an upper respiratory infection. There is granulomatous inflammation of the thyroid gland and initial hyperthyroidism followed by hypothyroidism. After recovery from the respiratory infection, the gland returns to its normal function. A painless variant occurs in postpartum patients. On US, the gland is enlarged with hypoechoic parenchyma and increased vascularity on color Doppler. On radionuclide scan, there is decreased radiotracer uptake during acute phase with return to normal uptake following resolution of the infection (Fig. 12.17).

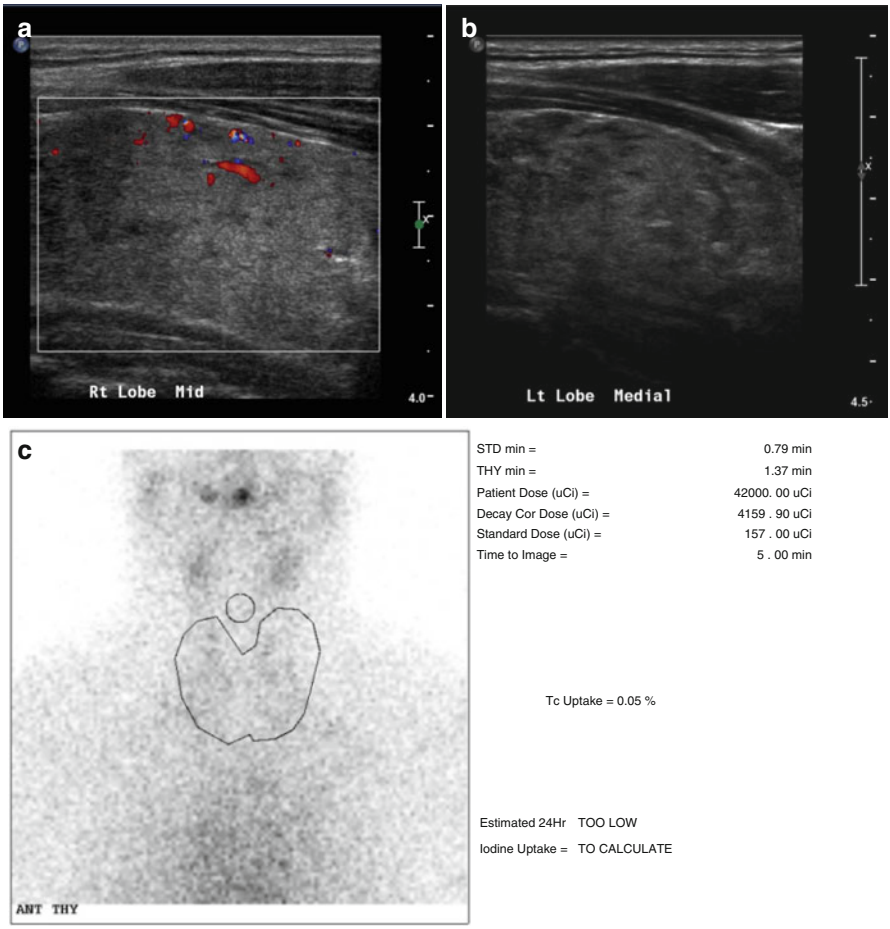

Fig. 12.17 Subacute thyroiditis. Mildly enlarged and heterogeneous thyroid gland is evident on the US images with diffusely decreased iodine uptake on Tc-99 pertechnetate scan. This patient presented with atrial fibrillation and low TSH with raised T3 and T4 values. The combination of findings is most compatible with subacute thyroiditis

12.4.2.5 Riedel's Thyroiditis (Struma)

Riedel's thyroiditis (struma) is a rare form of chronic thyroiditis that tends to occur in females in the fourth through seventh decades. The gland is diffusely enlarged and replaced by fibrous tissue, and patients present with dysphagia, stridor, and even vocal cord palsy, which raise concern for malignancy. The gland is quite firm on palpation. US demonstrates decreased echogenicity and vascularity with decreased or no uptake in the areas of fibrosis on radionuclide scans. On CT, the thyroid is hypodense, and it appears hypointense on all MR sequences due to fibrosis. Riedel's thyroiditis is sometimes associated with orbital pseudotumor, retroperitoneal or mediastinal fibrosis, or sclerosing cholangitis.

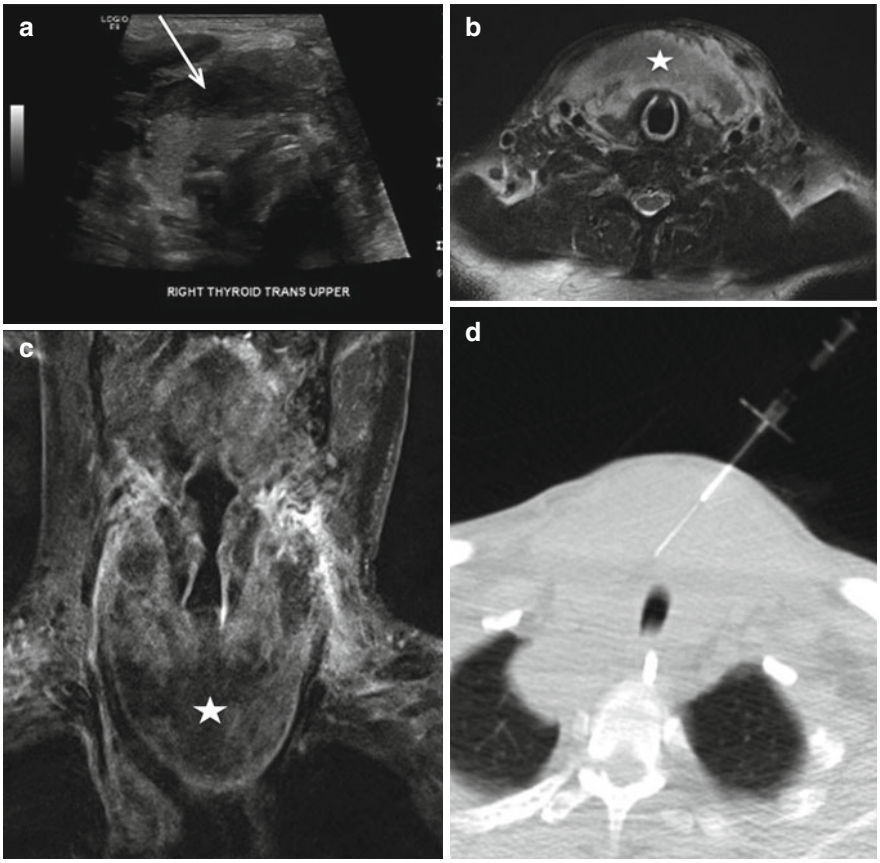

Fig. 12.18 Suppurative thyroiditis. Acute suppurative thyroiditis complicated by intrathyroidal abscess. US (**a**) shows a heterogeneous mixed echogenic collection anterior to the thyroid with abnormal glandular echogenicity. T2 and post contrast MR (*star* in **b** and **c**) shows the inflammatory changes and the abscess, mimicking a necrotic thyroid mass. The clinical history (rapid onset after an episode of flu and acute symptoms) along with needle aspiration (frank pus) (**d**) helped in making the correct diagnosis

12.4.2.6 Acute Suppurative Thyroiditis

Acute suppurative thyroiditis is usually secondary to bacterial infection by *Streptococcus, Staphylococcus,* and *Pneumococcus* species. A US is performed to evaluate for an abscess. The gland is enlarged and diffusely hypoechoic. An abscess appears as a well-defined collection of varying echogenicity due to presence of complex fluid and air. On CT and MR, the gland is enlarged with heterogeneous parenchyma (Fig. 12.18). Complications such as abscesses are better evaluated with CT or MRI, which can also demonstrate the inflammatory changes in the adjacent soft tissue planes. Particularly in children, the infection can originate from a pyriform fistula representing a fourth branchial cleft anomaly, which is more common on the left.

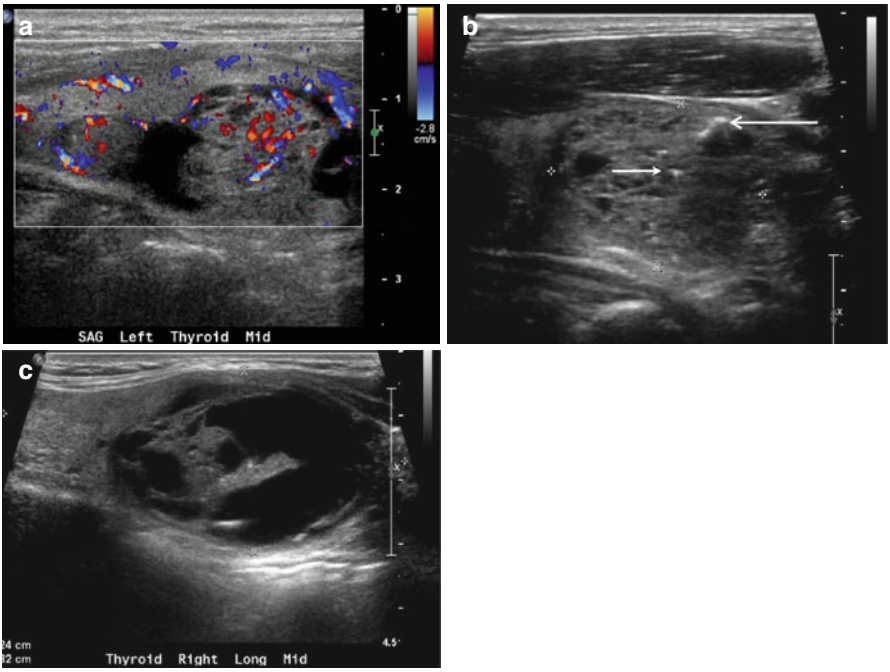

Fig. 12.19 Colloid nodule. Grayscale US images demonstrating mixed solid-cystic lesion (**a**) with dystrophic calcification (*long arrow*) causing posterior acoustic shadowing, colloid crystal (*short arrow*) with ring-down artifact, and small cystic changes giving the honeycombing appearance (**b**). All the features favor a colloid nodule. A predominantly cystic colloid thyroid nodule is seen on the third image (**c**)

12.4.3 Focal Thyroid Diseases

12.4.3.1 Colloid Nodules

Colloid nodules are the most common cystic lesions within the thyroid gland. These develop as a result of cystic degeneration of the hyperplastic nodule or adenoma. They can be multiple and vary in appearance from predominantly solid, solid-cystic, to purely cystic. On US, these usually appear anechoic with posterior acoustic enhancement. There may be associated calcification along the margins of the lesion (Fig. 12.19). Both colloid material (thyroglobulin) and hemorrhage can appear T1 bright on MR. These colloid nodules/cysts usually appear as "cold" spots with decreased or absent uptake on nuclear medicine studies.

12.4.3.2 Thyroid Adenomas

Adenomas are similar in appearance to the solid colloid nodules. Some of the adenomas are hyperfunctioning and cause compression of the normal thyroid parenchyma. Identification of such nodules is easy with radionuclide scan in which the nodule appears as a hot lesion (Fig. 12.20). Sometimes the adenomas are autonomous in which the activity in the normal thyroid parenchyma is suppressed. These

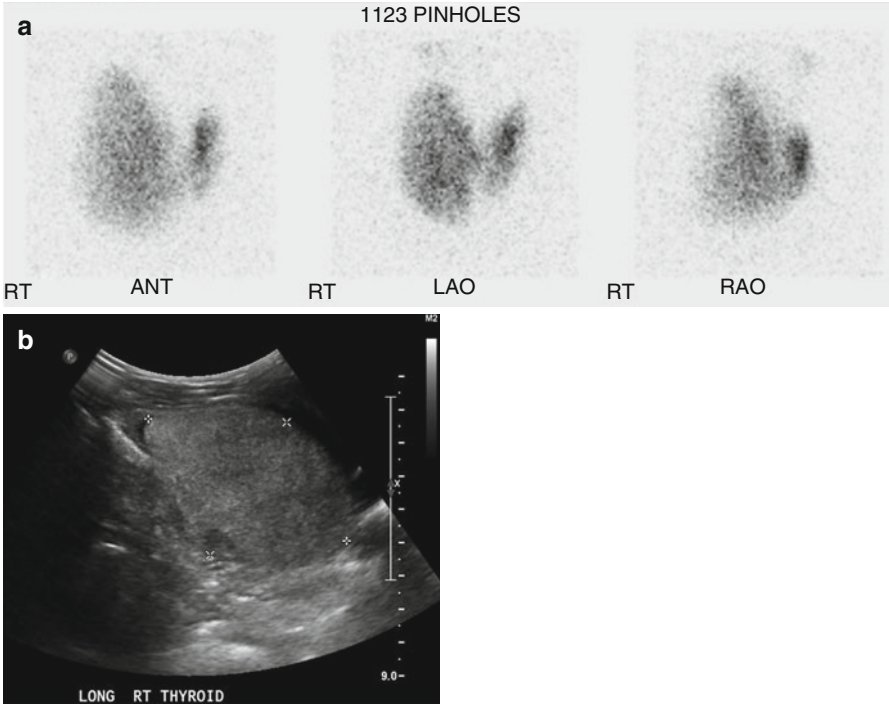

Fig. 12.20 I-123 thyroid scan (**a**) shows enlarged right thyroid lobe secondary to a large functioning nodule, adenoma. The corresponding grayscale ultrasound image (**b**) shows a solid nodule

nodules cause hyperthyroidism and show good response to radioiodine therapy treatment (Fig. 12.21).

12.4.3.3 Thyroid Carcinomas

Well-differentiated thyroid cancers (WDTCs), including papillary and follicular thyroid carcinomas, make up the vast majority of thyroid malignancies. Other rarer types include medullary and anaplastic carcinomas. The thyroid gland can be involved in lymphoma, sarcoma, and metastatic lesions, all of which are quite rare. The thyroid gland can be secondarily invaded by malignant tumors arising from adjacent organs. Box 12.3 summarizes the TNM classification for thyroid cancers.

Papillary thyroid carcinoma (PTC) is the most common thyroid cancer (70–80 %). On US, PTC usually presents as solitary solid hypoechoic nodule with microcalcifications (Fig. 12.22), which represent psammoma bodies on microscopy. At times multifocal nodules or invasion of adjacent larynx, trachea, or esophagus is seen. Metastases occur via lymphatics to the pre- and paratracheal lymph nodes and the deep cervical nodes. Involved nodes are usually hyperechoic compared to adjacent muscles and can also demonstrate microcalcifications. On CT, the nodes appear cystic and can be hyperenhancing with calcifications. They are T1 bright on MRI (Fig. 12.23). Larger papillary carcinomas may demonstrate irregular

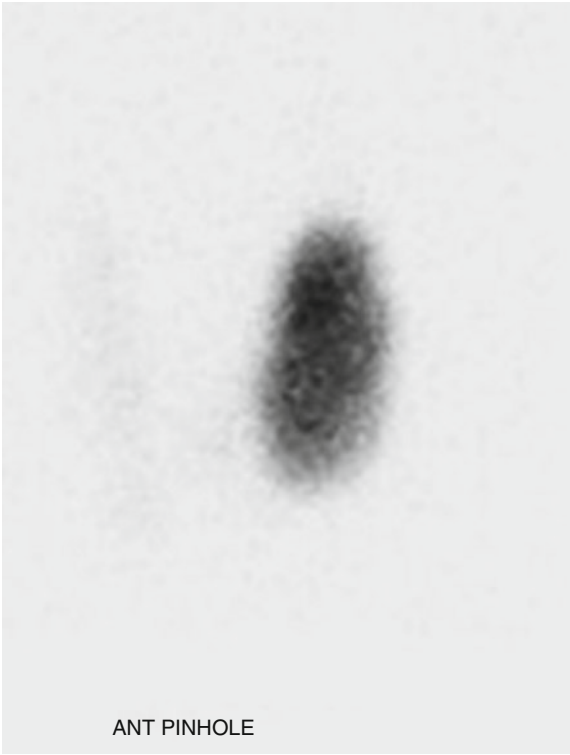

Fig. 12.21 Anterior pinhole view of 4-h delayed I-123 thyroid scan shows focal increased uptake in the left thyroid lobe with suppressed activity in the remaining thyroid gland due to autonomous hyperfunctioning thyroid nodule

Box 12.3. AJCC/UICC Staging of Thyroid Cancer

Primary tumor (T)	
TX	Primary tumor cannot be assessed
TO	No evidence of primary tumor
T1	Tumor ≤2 cm in greatest dimension limited to the thyroid
T1a	Tumor ≤1 cm, limited to the thyroid
T1b	Tumor >1 cm but ≤2 cm in greatest dimension, limited to the thyroid
T2	Tumor 2 to 4 cm in greatest dimension, limited to the thyroid
T3	Tumor >4 cm in greatest dimension limited to the thyroid or any tumor with minimal extrathyroid extension (e.g., extension to sternothyroid muscle or perithyroid soft tissues)
T4	All anaplastic carcinomas are considered T4 tumors
T4a	Moderately advanced. Intrathyroidal anaplastic carcinoma. Tumor of any size extending beyond the thyroid capsule to invade subcutaneous soft tissues, larynx, trachea, esophagus, or recurrent laryngeal nerve
T4b	Very advanced. Anaplastic carcinoma with gross extrathyroid extension. Tumor invades prevertebral fascia or encases carotid artery or mediastinal vessels
Note: All categories may be subdivided: (s) solitary tumor, (m) multifocal tumor (the largest determines the classification)	

(continued)

Box 12.3 (continued)

Regional lymph nodes (N)						
NX	Regional lymph nodes cannot be assessed					
NO	No regional lymph node metastasis					
N1	Regional lymph node metastasis					
N1a	Metastasis to level VI (pretracheal, paratracheal, and prelaryngeal/Delphian lymph nodes)					
N1b	Metastasis to unilateral, bilateral, or contralateral cervical (level I, II, III, IV, or V) or retropharyngeal or superior mediastinal lymph nodes (level VII)					
Distant metastasis (M)						
MX	Distant metastasis cannot be assessed					
MO	No distant metastasis					
M1	Distant metastasis					
Stage grouping						
	Papillary or follicular <45 years old			**Papillary or follicular (≥45 years old) or medullary (any age patient)**		
Stage I	Any T	Any N	MO	Stage I	T1	NO	MO
Stage II	Any T	Any N	M1	Stage II	T2	NO	MO
Stage III				Stage III	T3	NO	MO
					T1	N1a	MO
					T2	N1a	MO
					T3	N1a	MO
Stage IVA				Stage IVA	T4a	NO	MO
					T4a	N1a	MO
					T1	N1b	MO
					T2	N1b	MO
					T3	N1b	MO
					T4a	N1b	MO
					T4a	Any N	MO
Stage IVB				Stage IVB	T4b	Any N	MO
Stage IVC				Stage IVC	Any T	Any N	M1
Stage grouping Undifferentiated (anaplastic)[a]							
Stage IV	Any T	Any N	Any M				

Modified from Edge SB, Byrd DR, Compton CC et al (eds) (2010) AJCC cancer staging manual, 7th edn. Springer, New York

AJCC American Joint Committee on Cancer, *UICC* International Union Against Cancer

[a]For undifferentiated cancers, all cases are classified as stage IV

ill-defined margins, extraglandular spread with invasion of trachea, and regional nodal metastases on CT or MRI, which are used to differentiate between T3 (minimal extension beyond thyroid), T4a (invasion into trachea, esophagus, larynx, or recurrent laryngeal nerve), and T4b (invasion into prevertebral fascia or great

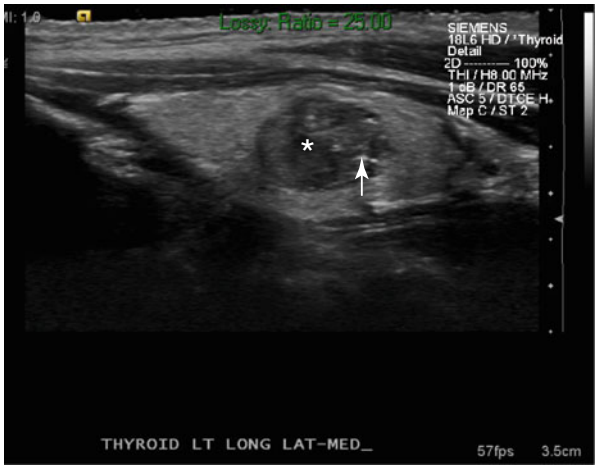

Fig. 12.22 Papillary cancer. A well-defined hypoechoic (*star*) lesion in the left thyroid lobe with small echogenic foci representing microcalcification (*arrow*) in papillary thyroid cancer

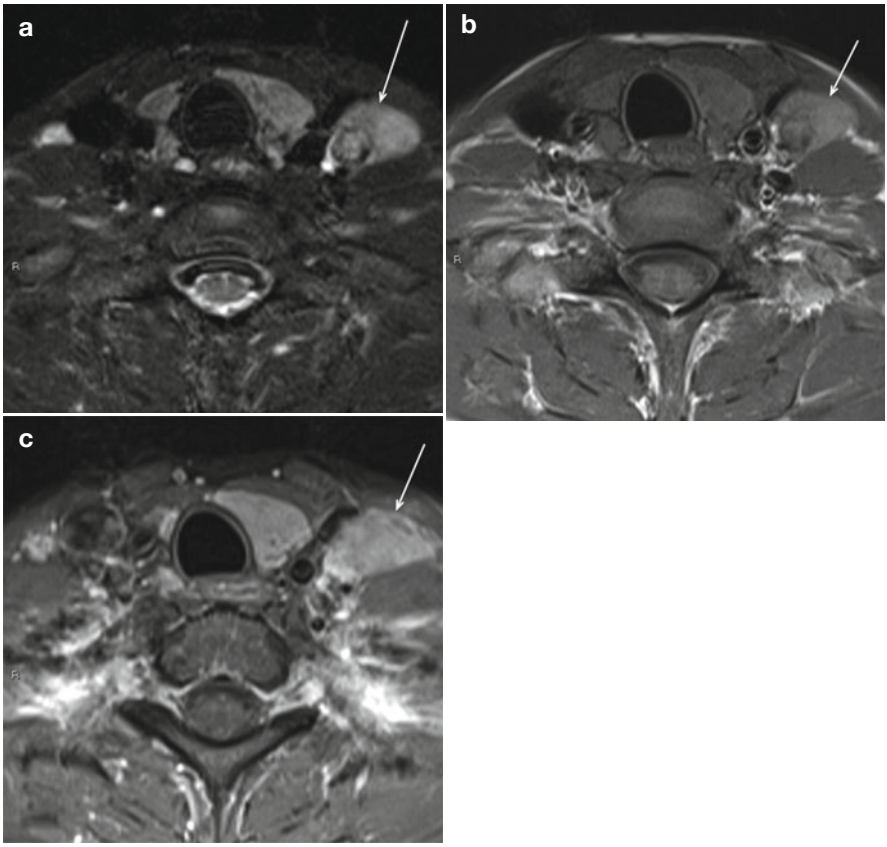

Fig. 12.23 Pathological left level IV nodes (*arrow*) in this patient with papillary cancer demonstrate both T1 (**b**) and T2 (**a**) hyperintensity, with intense enhancement (**c**). The increased signal on T1-weighted sequences is believed to be due to thyroglobulin in these metastatic nodes

vessels) lesions (Figs. 12.24 and 12.25). Tracheal invasion is predicted by increased signal on T2-weighted MR, intratracheal mass, and/or circumferential encasement by more than 180–270°. Similarly, esophageal invasion is predicted by abnormal MR signal in the esophageal wall, intraluminal tumor, abnormal wall enhancement, and/or more than 270° of encasement. Initial treatment of PTC is surgical, and it is usually responsive to radioactive iodine (RAI) therapy. Overall, it has an excellent prognosis with survival of 90–95 % at 30 years.

Follicular thyroid carcinoma is the second most common thyroid cancer (10–20 %). It metastasizes hematogenously to bones, lungs, liver, brain, and lymph nodes. Imaging appearance is very similar to PTC. Differentiation from follicular adenoma is difficult on both imaging and FNA biopsy, and surgical removal is often necessary to make the definitive diagnosis. Overall 10-year survival is 70–95 %. Initial treatment is surgical and adjunctive RAI is usually effective.

Medullary thyroid carcinoma is an uncommon form of thyroid cancer (5–10 %) that arises from calcitonin-secreting parafollicular cells (C cells) and is more aggressive than the WDTCs. Calcitonin is a specific marker for the tumor, and 10–20 %

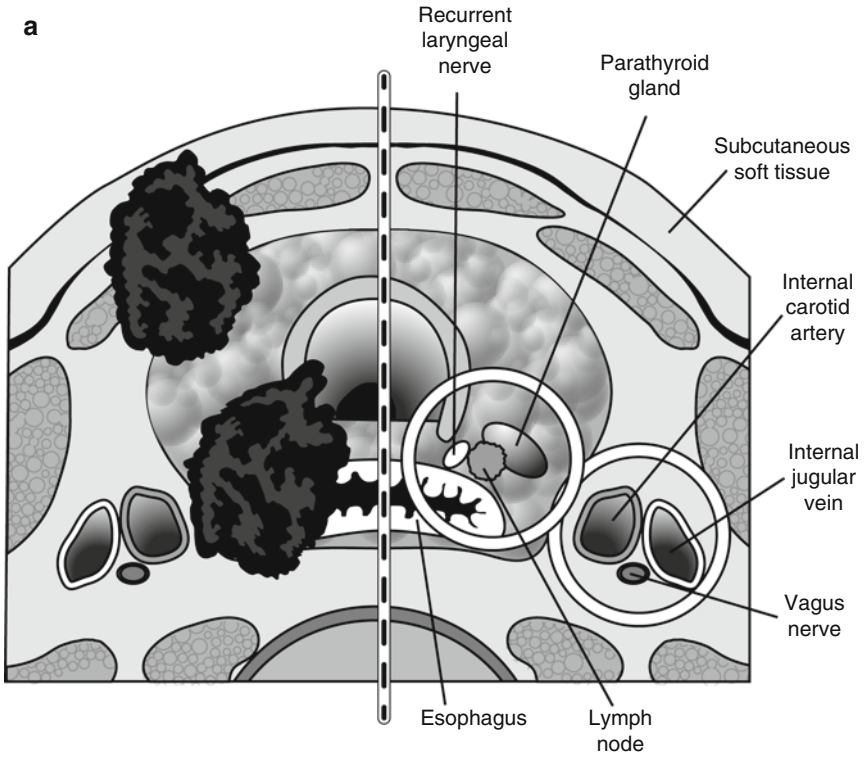

Fig. 12.24 (**a**) T4a thyroid lesions are tumors of any size, which extend beyond the thyroid capsule to invade subcutaneous soft tissues, larynx, trachea, esophagus, or recurrent laryngeal nerve. (**b**) T4b tumors invade prevertebral fascia or encase carotid artery or mediastinal vessels

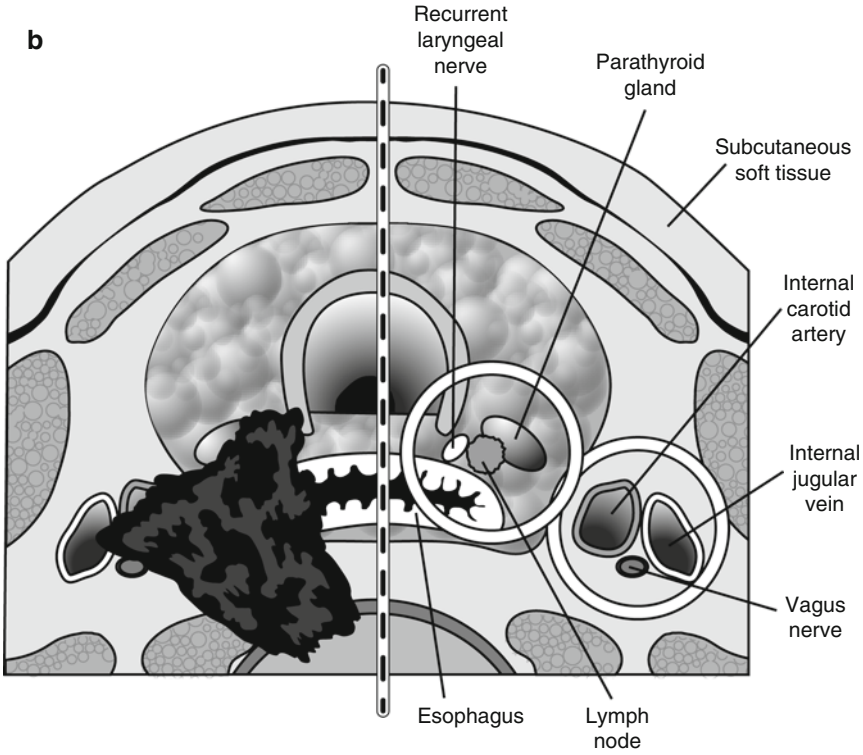

Fig. 12.24 (continued)

are associated with multiple endocrine neoplasia (MEN) type II. Except for stippled calcification, the imaging appearance is nonspecific and similar to papillary and follicular carcinomas (Fig. 12.26). Medullary carcinoma has a tendency for local invasion, cervical lymph node metastasis, and distant metastasis via hematogenous route to lungs, bones, and liver. It does not respond to RAI.

Anaplastic thyroid carcinomas are highly aggressive cancers (all classified as T4) that account for less than 5 % of thyroid malignancies. They are more common in elderly patients, and their incidence increases following radiation therapy to the neck. The tumors are usually large at the time of diagnosis with extrathyroidal extension, cervical lymphadenopathy, and distant metastases. The cancer shows rapid growth and invasion of the adjacent structures (Fig. 12.27). Lymphatic metastasis is the primary mode of spread. RAI is not effective.

Rarely, the thyroid gland is involved by lymphoma or metastasis. Breast, renal, skin (melanoma), and lung cancers can metastasize to the thyroid. The sonographic appearance is very similar to primary thyroid cancer. On ultrasound, lymphomas are usually large, hypoechoic, solid masses replacing the thyroid parenchyma. The differentiation from primary thyroid cancer can be difficult (especially anaplastic), but thyroid lymphoma often shows a more homogeneous appearance with lack of calcification. Lymphomas demonstrate mild enhancement following contrast

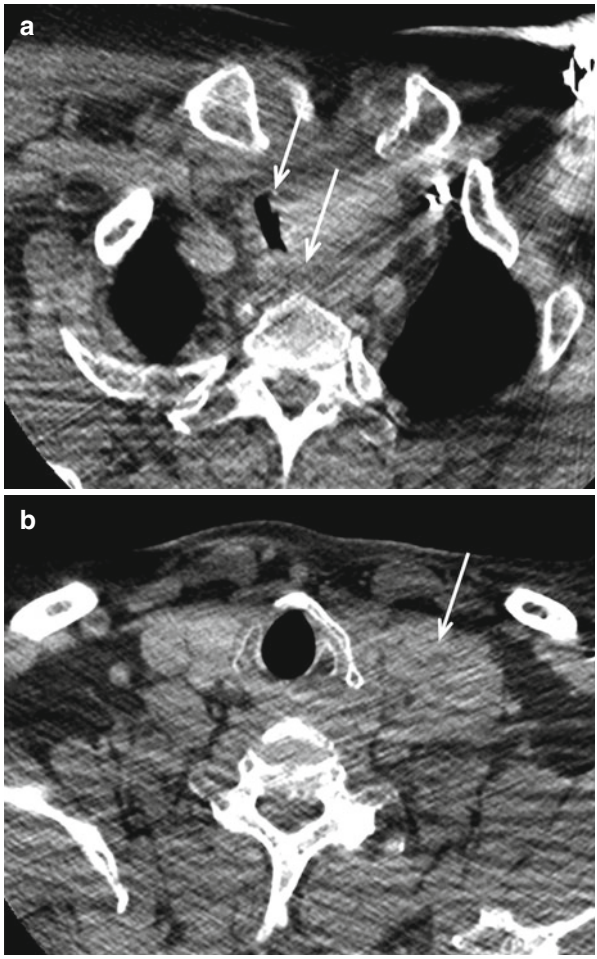

Fig. 12.25 Biopsy-proven papillary cancer with tracheal and esophageal invasion (*arrows* in **a**) (confirmed on endoscopy) with conglomerate pathological left level IV/VI adenopathy (*arrow* in **b**)

administration on CT. On MRI, they are iso intense on T1 and mildly T2 hyperintense compared to the adjacent thyroid parenchyma.

12.5 Parathyroid Glands

12.5.1 Anatomy

The parathyroid glands are located in the posterior visceral space, posterior to the thyroid gland. Normal parathyroid glands measure approximately 5 × 3 × 2 mm and weigh 30–40 mg. There are four parathyroid glands, but 5–10 % of individuals have more or fewer. The superior parathyroid glands are derived from the fourth

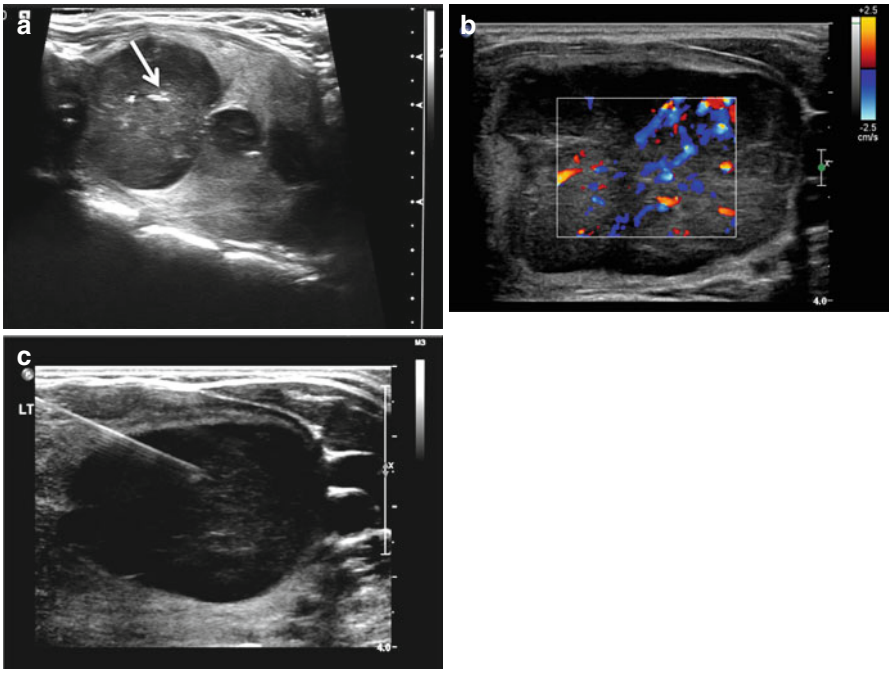

Fig. 12.26 Well-defined hypoechoic lobulated left thyroid mass (**a**), with internal punctate hyperechoic foci, suggestive for microcalcifications (*arrow*) and increased vascularity on color Doppler (**b**). US-guided FNA was performed (**c**) using a 22 gauge 2.5 cm needle, which demonstrated medullary carcinoma on cytopathology

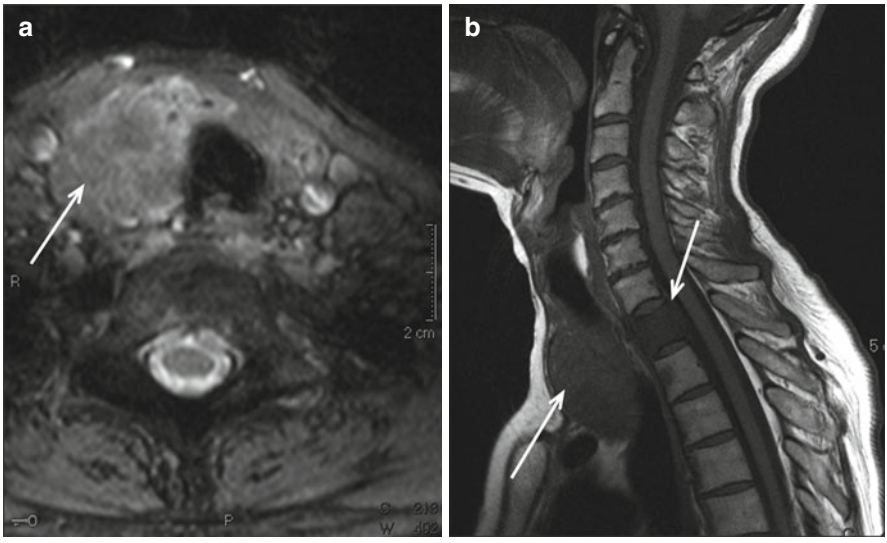

Fig. 12.27 Anaplastic carcinoma. Right thyroid lobe anaplastic carcinoma (*arrow* in **a**) with T1 vertebral body metastasis (*arrow* in **b**)

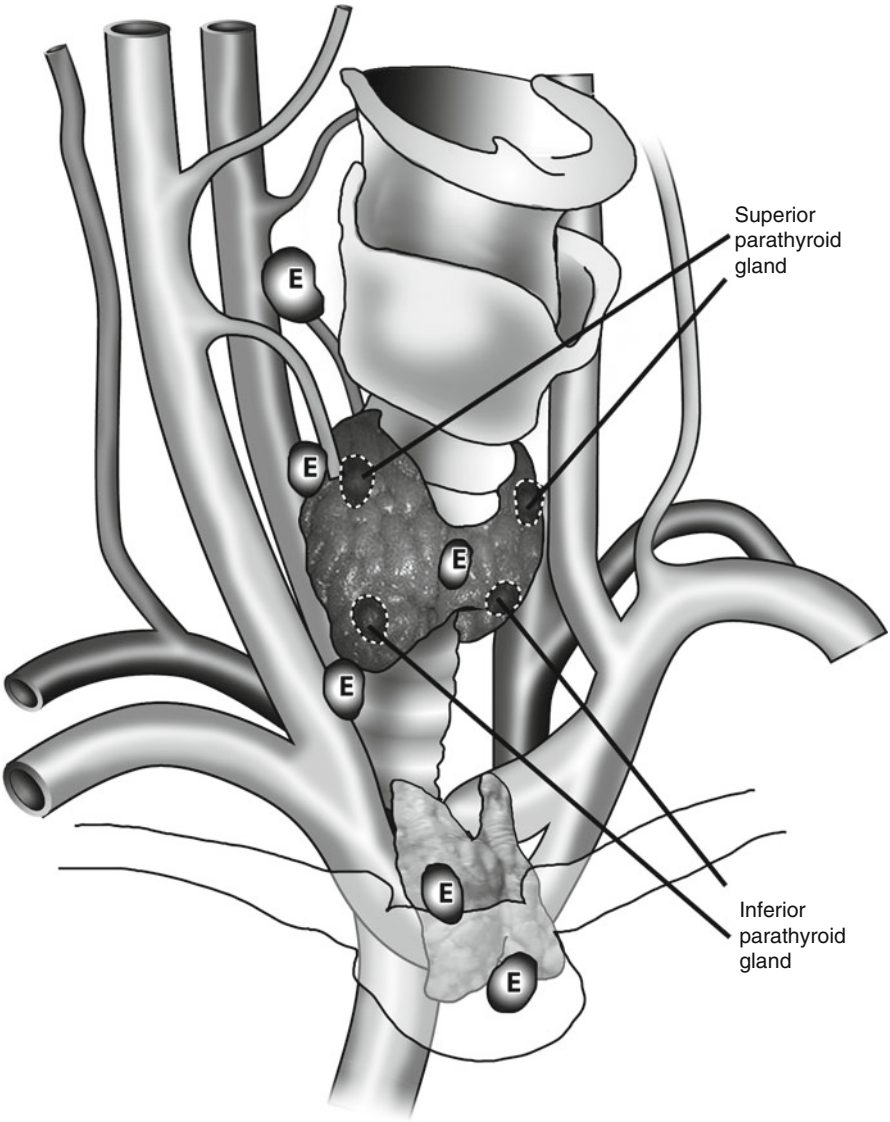

Fig. 12.28 Graphic shows the variable sites for ectopic location of parathyroid adenomas, from the upper neck to the thoracic inlet. It is important to cover this entire area on imaging

branchial pouch and are usually located at the level of the cricoid cartilage posterolateral to the upper pole of the thyroid. The inferior parathyroid glands are derived from the third branchial pouch and are more variable in location. Parathyroid glands can be found anywhere from the angle of the mandible to the superior mediastinum including para- and retroesophageal regions, carotid sheath, thymus, and within the thyroid (Figs. 12.28 and 12.29). The superior and inferior parathyroid glands are

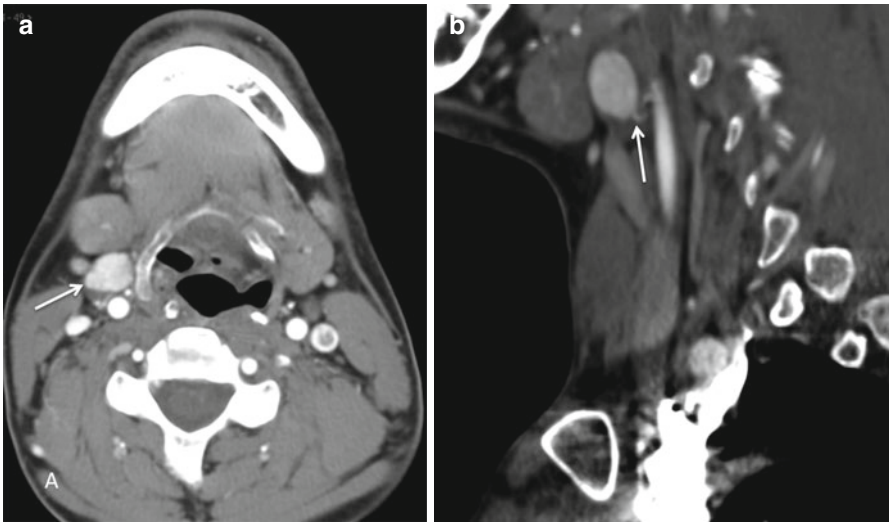

Fig. 12.29 Parathyroid adenoma. Contrast-enhanced axial CT scan (**a**) in a 40-year-old male with recurrent hyperparathyroidism postsurgery demonstrates an avidly enhancing ectopic right superior parathyroid adenoma anterior to the carotid space (*arrow*). Sagittal image (**b**) demonstrates a prominent vessel coursing into the lesion (*arrow*), which is frequently seen in larger adenomas

usually supplied by branches of the inferior thyroid artery and are drained by the thyroid veins. The parathyroid glands contain a mix of chief, intermediate, and oxyphil cells; the chief cells secrete PTH.

12.5.2 Imaging Evaluation

The parathyroid glands are usually imaged for preoperative localization for parathyroid adenomas. Ultrasonography performed using a high-resolution linear array transducer (7–13 MHz) can identify enlarged parathyroid glands in approximately 70–90 % of cases. Nuclear scintigraphy with ^{99m}Tc sestamibi can localize adenomas as it tends to concentrate in parathyroid tissue. Finally, high-resolution multiphase CT and thin-section MR are also used for anatomic localization of ectopic parathyroid adenomas.

12.5.3 Pathology

12.5.3.1 Parathyroid Cysts

These are developmental or represent colloid retention cysts. Alternatively, they might represent cystic degeneration of parathyroid adenomas. These can sometimes lead to hypercalcemia, secondary to increased levels of parathyroid hormone within the cyst (Fig. 12.30).

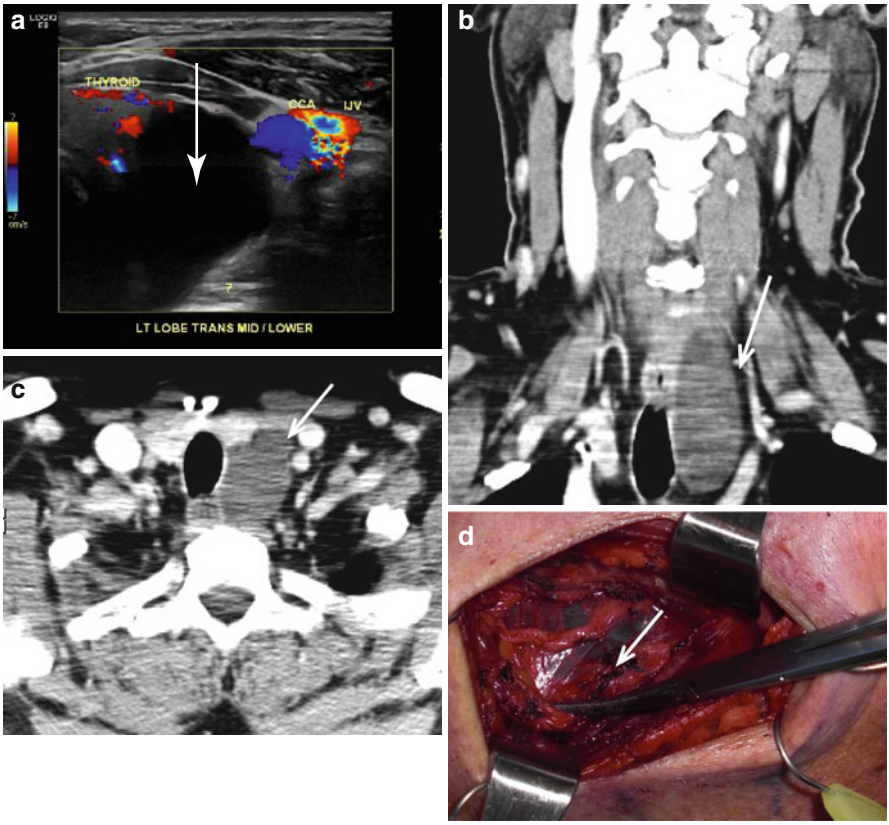

Fig. 12.30 Parathyroid cyst. US demonstrates a cystic (anechoic lesion with posterior acoustic enhancement) lesion (*arrow* in **a**), adjacent to the left thyroid lobe. Note the absence of vascularity within the lesion. CT images demonstrate the well-defined hypodense lesion in between the left thyroid lobe and left carotid sheath (*arrow* in **b** and **c**). Intraoperative images show the glistening surface of the cyst after retraction of adjacent soft tissues (*arrow* in **d**)

12.5.3.2 Multiple Endocrine Neoplasias (MEN)

MEN I and IIa syndromes are associated with hyperparathyroidism due to parathyroid adenoma or hyperplasia. MEN I is characterized by primary hyperparathyroidism, pancreatic endocrine tumors, and anterior pituitary neoplasms, while MEN IIa is characterized by pheochromocytomas, medullary thyroid carcinomas, and hyperparathyroidism (Fig. 12.31). Patients with MEN I typically present with hyperparathyroidism.

12.5.3.3 Parathyroid Adenomas

The most common indication for parathyroid imaging is to localize the hyperfunctioning gland either in the thyroid bed or in an ectopic location (usually lower neck or mediastinum). Parathyroid adenomas represent the most common cause (~90 %) for primary hyperparathyroidism; the remaining patients have

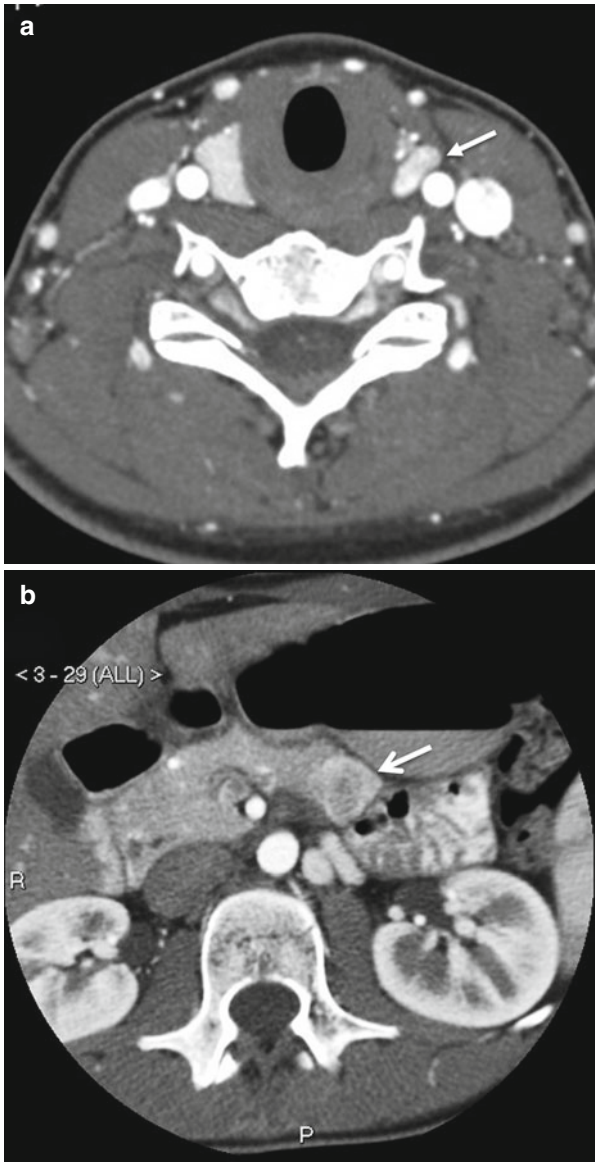

Fig. 12.31 MEN I with parathyroid adenoma. 18-year-old with MEN I syndrome with enhancing left superior parathyroid adenoma (*arrow* in **a**) and a hyperenhancing insulinoma on the arterial phase in abdominal CT (*arrow* in **b**)

multiglandular parathyroid hyperplasia or carcinoma; often this distinction cannot be made without parathyroidectomy. Parathyroid imaging is performed either to localize an adenoma preoperatively or in the setting of persistent postoperative hypercalcemia.

^{99m}Tc sestamibi is the best initial imaging choice with approximately 90 % sensitivity and high specificity. It is performed using 20 mCi of ^{99m}Tc sestamibi with sequential imaging. Normal thyroid tissue and thyroid adenomas usually

fade over 2 h, whereas parathyroid adenomas demonstrate emission in that time frame. This technique is less sensitive for parathyroid hyperplasias (~50–60 %) and for multiglandular disease. ^{99m}Tc sestamibi scanning exhibits reduced sensitivity in the setting of thyroid lesions (adenoma, goiter, etc.), mediastinal parathyroid adenomas, and postsurgical evaluation. Use of additional single-photon emission computed tomography (SPECT) can increase the sensitivity and also helps in better localization of the adenoma. In patients with a known thyroid lesion, using subtraction techniques (Iodine -123/^{99m}Tc sestamibi) can more vividly display the abnormal parathyroid uptake after removal of the thyroid component (Fig. 12.32).

On ultrasound using high-frequency linear probes (7–13 MHz), the parathyroid adenoma is seen as a well-defined, bean-shaped, hypoechoic, homogenous structure posterior to the thyroid gland. On color Doppler, they appear hypervascular, with a characteristic feeding artery extending into one of the poles (Fig. 12.32). False-positive results may be seen on US due thyroid nodules or reactive lymph nodes. Also, the scanning field must include the entire central neck, including the bilateral carotid sheath from the level of the mandibular angle to the suprasternal notch to avoid false negatives. US is limited in the evaluation for retrosternal or mediastinal parathyroids. Heterogeneity and cystic degeneration suggest malignancy, but parathyroid carcinomas are generally larger than adenomas.

CT and MRI are usually reserved for patients with equivocal sestamibi or US findings and for a postsurgical setting. On CT, parathyroid adenomas are variably enhancing, soft tissue masses adjacent to the thyroid gland. Sometimes, a vessel can be seen entering the lesion. More recently, CT techniques such as 4D-CT have developed; this approach uses time-delayed sequential CT acquisitions to demonstrate contrast wash-in and washout to better identify adenomas (Fig. 12.33). The downside of 4D-CT is increased radiation exposure compared to conventional contrast-enhanced CT scans. On MRI, parathyroid adenomas usually appear T1 iso- to hypointense and T2 iso- to hyperintense relative to the thyroid gland; they avidly enhance. Although they are slightly less sensitive than sestamibi scans, CT and MRI offer better spatial localization and are often preferred by surgeons. CT and MR imaging are more effective than nuclear medicine and ultrasound scans in evaluation of aberrant adenomas within the mediastinum or tracheoesophageal groove (Fig. 12.34).

Persistent hyperparathyroidism after surgery is an imaging challenge that usually requires a combined multimodality approach for identifying ectopic adenomas or identifying small adenomas within the scarred surgical bed. A combination of CT and MRI along with ^{99m}Tc sestamibi scanning is frequently performed. US has an adjunctive role in this setting.

12.5.3.4 Parathyroid Carcinomas

Parathyroid carcinoma is quite rare and occurs in less than 1 % of patients with primary hyperparathyroidism. On imaging, these are usually indistinguishable from benign adenomas, but the diagnosis may be suspected based on cervical lymphadenopathy or invasion of adjacent neck structures.

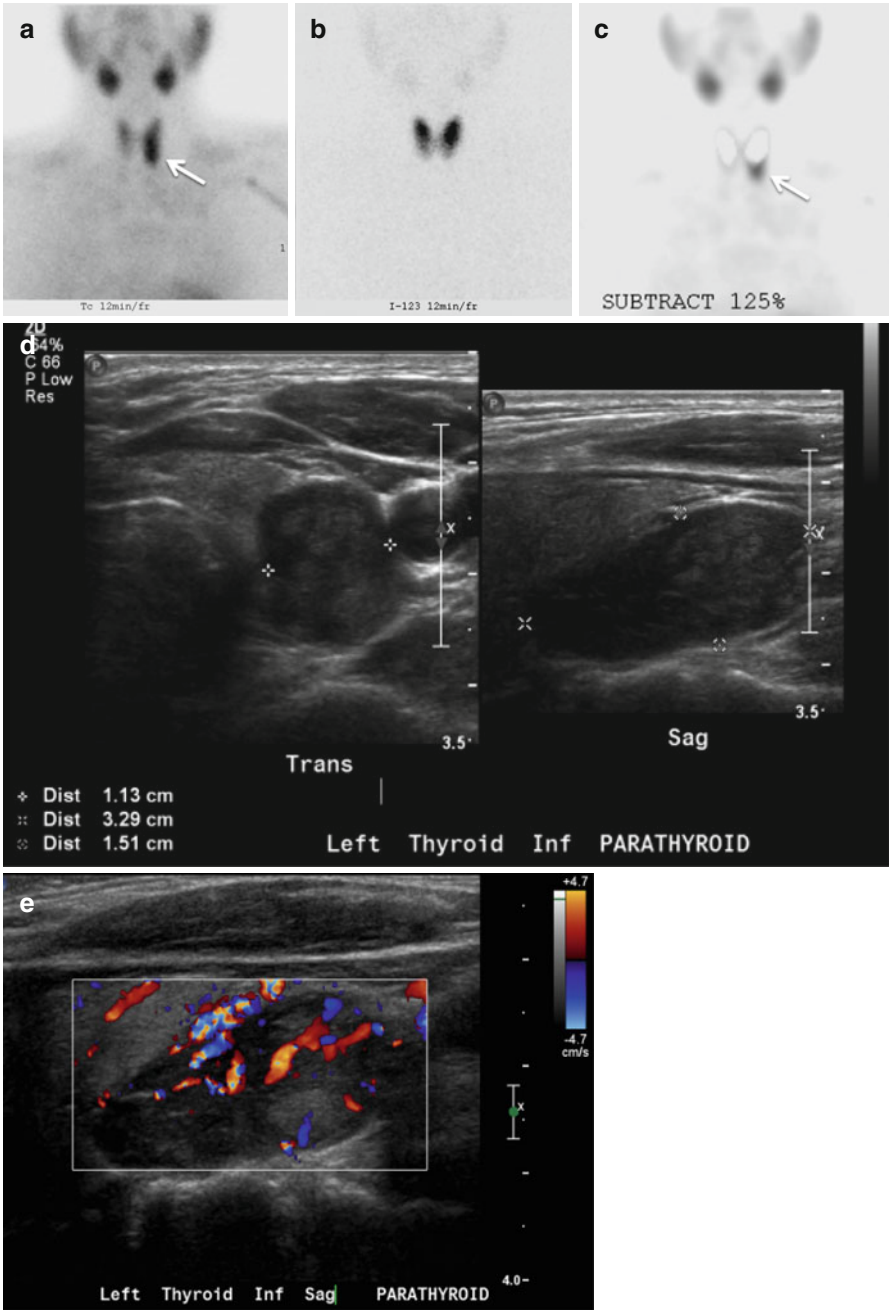

Fig. 12.32 Parathyroid subtraction scan consisting of Tc-99m sestamibi (**a**), I-123 scan (**b**), and subtracted images (**c**) demonstrate left inferior parathyroid adenoma (*arrow*). The abnormal increased uptake on the sestamibi images (*arrow*) is more obvious on the subtracted scan. Grayscale (**d**) and color Doppler (**e**) USG images show the same left inferior paratracheal parathyroid adenoma with intense vascularity on color Doppler

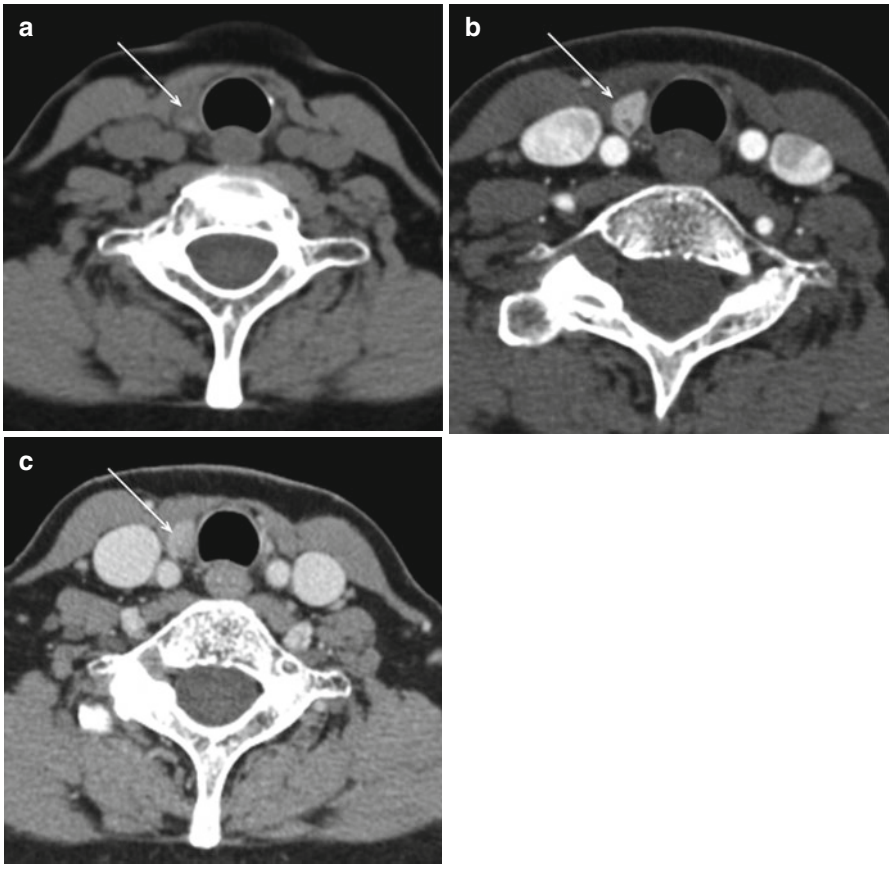

Fig. 12.33 Three axial CT images, unenhanced (**a**), early post contrast (**b**), and delayed post contrast (**c**) images, show an intensely enhancing right paratracheal parathyroid adenoma with washout. A lymph node does not demonstrate this early enhancement and washout characteristic

12.6 The Surgeon's Perspective

Thyroid and parathyroid disorders commonly managed surgically include hyperthyroidism, thyroid nodules (benign and malignant), goiter, and hyperparathyroidism. Thyroid nodules are occasionally noted on palpation by the patient or a perceptive primary care provider but are often imaging incidentalomas. Because a substantial percentage of the population has thyroid nodules, the ATA has recommended a standard algorithm for evaluation of a patient with a thyroid nodule detected by palpation or imaging, which begins with a thorough history and physical exam. Patients may report a history of hyperthyroid symptoms such as flushing, palpitations, tachycardia, heat intolerance, weight loss, anxiety/nervousness, diarrhea, or sweating. Patients should have a TSH checked. If this is low, indicating hyperthyroidism, a nuclear scan is recommended which may demonstrate a hyperfunctioning nodule.

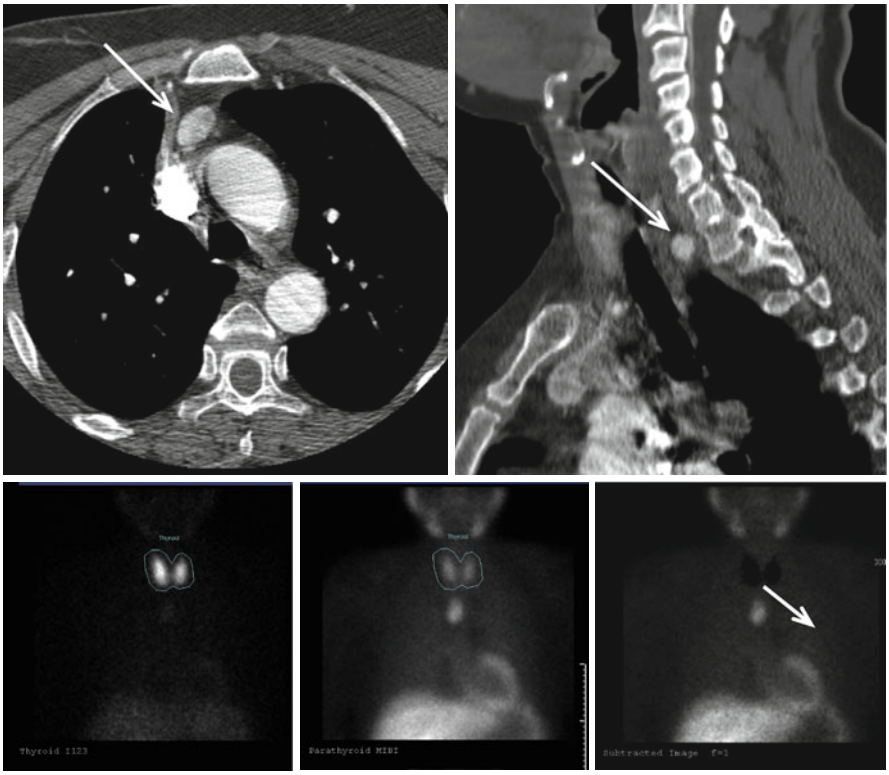

Fig. 12.34 Axial and sagittal enhanced CT scans, in this patient with primary hyperparathyroidism, show an enhancing lesion (*arrow*) in the prevascular compartment of the superior mediastinum. An ectopic parathyroid adenoma was confirmed on surgical excision. Sequential Tc-99m sestamibi images show persistent increased activity within the mediastinum corresponding to the ectopic parathyroid adenoma

A normal or elevated TSH should prompt further evaluation of the nodule with US. As discussed above, certain US features correspond with an increased risk of malignancy and should be considered when deciding on FNA biopsy. If FNA biopsy confirms the diagnosis of malignancy, US or MRI is used to evaluate for cervical nodal metastasis as CT with contrast may delay treatment with RAI. In cases where there is concern for substernal extension, invasion of local structures, or unusual locations for metastasis (e.g., retropharyngeal or mediastinal), MRI or CT is preferred over ultrasound to help determine the necessary extent of surgery.

Goiter is often diagnosed as an enlarging neck mass or occasionally due to compressive symptoms such as dysphagia, neck fullness/pressure, or shortness of breath, particularly when recumbent. Because malignancy is rare and substernal extension is common, CT with contrast is often used to evaluate thyroid goiters and helps to demonstrate the extent of tracheal deviation or compression. One or both thyroid lobes may be involved, and imaging helps to determine if a unilateral lobectomy will be sufficient to manage the goiter.

Patients with primary hyperparathyroidism present with signs and symptoms of hypercalcemia including nephrolithiasis, depression, constipation, bone pain, fragile fractures, and even memory loss. Often patients are asymptomatic and elevated calcium is noted on routine lab testing or evaluation for osteoporosis. DEXA bone density scans are useful to evaluate the degree of bone loss, and osteoporosis on a DEXA scan is an indication for parathyroidectomy. Primary hyperparathyroidism is a laboratory diagnosis, and other than the results of the DEXA scan, all of the indications for parathyroidectomy are related to clinical or lab findings. Parathyroid imaging studies are performed only after it has been determined that a patient has an indication for parathyroidectomy. US, 99mTc sestamibi scan with SPECT, and contrasted neck CT are often useful for preoperative localization of parathyroid adenomas as described above. Coupled with intraoperative rapid PTH testing, preoperative localization of an adenoma permits a directed approach to parathyroidectomy instead of four-gland exploration. A US is useful because parathyroid adenomas have characteristics that distinguish them from lymph nodes and ectopic thyroid tissue, and synchronous thyroid pathology can be evaluated. Sestamibi-SPECT provides functional information in a format that most surgeons are comfortable reading and can identify adenomas in locations where ultrasound is limited such as the superior mediastinum and retroesophageal neck. Fine-cut CT or 4D-CT has also been described for localization of parathyroid adenomas, but all of these studies are limited in their ability to detect four-gland hyperplasia. False positives occur when ectopic thyroid tissue or central compartment lymph nodes occasionally masquerade as a potential adenoma. In these cases where preoperative localization studies are non-diagnostic or misleading, four-gland exploration may be necessary.

Further Reading

Cooper DS, Doherty GM, Haugen BR, Kloos RT, Lee SL, Mandel SJ, Mazzaferri EL, McIver B, Pacini F, Schlumberger M, Sherman SI, Steward DL, Tuttle RM (2009) Revised American Thyroid Association management guidelines for patients with thyroid nodules and differentiated thyroid cancer. American Thyroid Association (ATA) Guidelines Taskforce on Thyroid Nodules and Differentiated Thyroid Cancer. Thyroid 19(11):1167–1214, Erratum in: Thyroid. 2010 Aug;20(8):942

Frates MC, Benson CB, Charboneau JW, Cibas ES, Clark OH, Coleman BG, Cronan JJ, Doubilet PM, Evans DB, Goellner JR, Hay ID, Hertzberg BS, Intenzo CM, Jeffrey RB, Langer JE, Larsen PR, Mandel SJ, Middleton WD, Reading CC, Sherman SI, Tessler FN (2005) Management of thyroid nodules detected at US: society of radiologists in ultrasound consensus conference statement. Radiology 237:794–800

Greenspan, B. S., et al. (2012) SNM practice guideline for parathyroid scintigraphy 4.0. Journal of Nuclear Medicine Technology 111:40.2

Hoang JK, Lee WK, Lee M, Johnson D, Farrell S (2007) US features of thyroid malignancy: pearls and pitfalls. Radiographics 27:847–860

Rodgers SE, Hunter GJ, Hamberg LM, et al. (2006) Improved preoperative planning for directed parathyroidectomy with 4-dimensional computed tomography. Surgery. 140(6):932–40

Pediatric Head and Neck Lesions

13

Prashant Raghavan, Mark J. Jameson, David C. Shonka Jr., Max Wintermark, and Sugoto Mukherjee

13.1 Embryology: Key Concepts

The structures of the face are formed from five mesodermal processes: the midline frontonasal process and the paired maxillary and mandibular processes (Figs. 13.1 and 13.2).

The nose is formed by the union of two nasal placodes, each comprised of a nasal pit surrounded by a medial and lateral nasal eminence. The medial nasal eminences unite to form the septum, primary palate, and philtrum. The lateral nasal eminences form the lateral nasal walls and nasal ala. These are separated from the maxillary processes by the nasolacrimal groove, within which the nasolacrimal duct develops as a solid cord of cells that later canalizes.

The nasal cavity is separated from the oral cavity by the oronasal membrane.

The maxillary processes give rise to the zygoma, maxilla, and hard palate.

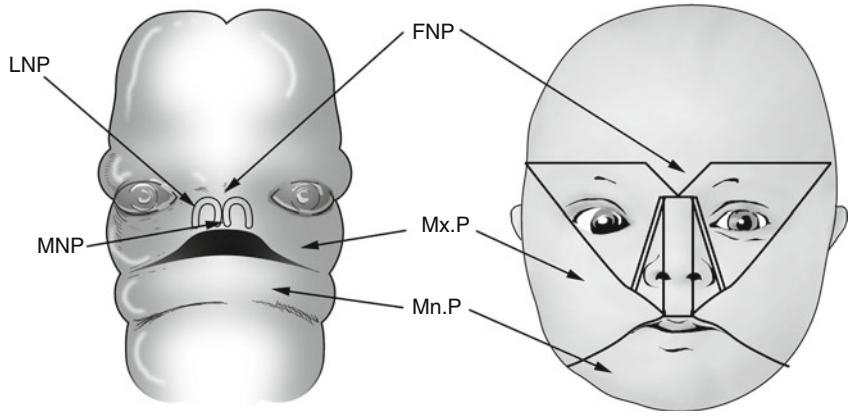

Fig. 13.1 Development of the face. *FNP* frontonasal process, *Mx.P* maxillary process, *Mn.P* mandibular process, *LNP* lateral nasal process, *MNP* medial nasal process

P. Raghavan et al., *Manual of Head and Neck Imaging*,
DOI 10.1007/978-3-642-40377-4_13, © Springer-Verlag Berlin Heidelberg 2014

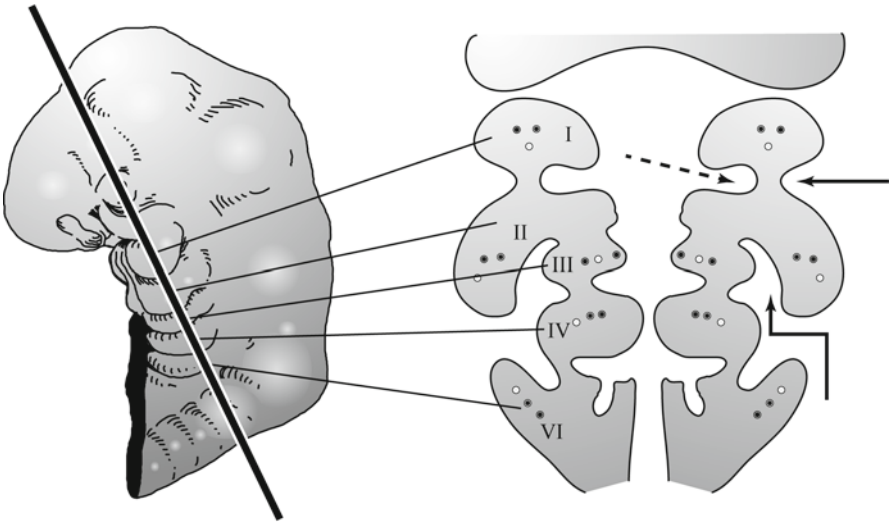

Fig. 13.2 Coronal section through the branchial arches. The branchial arches are paired mesodermal structures in the fetal neck, each with its own artery, vein, and nerve. The *straight arrow* points to a branchial cleft and the *dashed arrow* to a branchial pouch. The clefts are lined by ectoderm and the pouches by endoderm. The *bent arrow* points to the sinus of His, a cleft between the overgrown second arch and the external surface of the branchial apparatus. Second branchial anomalies are believed by some to arise from persistence of remnants of the sinus of His

The developing nasal bones are separated from the frontal bone by a transient fontanelle – the frontonasal fonticulus. The nasal bones are separated from the underlying cartilaginous nasal capsule by the prenasal space, which transmits a dural diverticulum. This diverticulum exits the cranial cavity through the foramen cecum in the midline anterior skull base and extends to the tip of the nose. Both the fontanelle and the diverticulum are obliterated by growth of the frontal and nasal bones.

The branchial arches are five bars of mesenchyme (numbered 1 to 4 and 6) in the developing neck. Each arch contains a nerve, artery, and vein. The arches are separated on their external aspect by ectoderm-lined clefts and on their internal (luminal) aspect by endoderm-lined pouches. The derivatives of the branchial arches are indicated in Box 13.1.

Box 13.1. Derivatives of the Branchial Arches

Branchial arch	Nerve	Muscles	Ligaments	Bones	Pouch derivative	Cleft derivative
I	Trigeminal	Muscles of mastication, tensor palati, anterior belly of digastric, mylohyoid	Lateral ligament of the malleus	Malleus, incus	Eustachian tube, middle ear cavity	External auditory canal

Branchial arch	Nerve	Muscles	Ligaments	Bones	Pouch derivative	Cleft derivative
II	Facial	Muscles of facial expression, stylohyoid, posterior belly of digastric, stapedius	Stylohyoid ligament	Stapes, lesser horn of the hyoid, styloid process		Faucial tonsillar crypts
III	Glossopharyngeal	Stylopharyngeus		Greater horn of the hyoid	Inferior parathyroid gland, thymus	
IV	Vagus	Laryngeal and pharyngeal musculature, except the stylopharyngeus and tensor palati			Superior parathyroid gland, C cells of the thyroid	
V	Spinal accessory	Trapezius, sternomastoid				

13.2 Congenital Anomalies of the Nose and Nasal Cavity

The three most important developmental nasal abnormalities that result in respiratory distress at birth are choanal atresia, congenital piriform aperture stenosis, and congenital nasolacrimal duct mucoceles. These all cause nasal obstruction and are symptomatic because infants are obligate nasal breathers at rest. Midline nasal anomalies include nasal dermal sinuses, dermoid and epidermoid cysts, nasal gliomas, and encephaloceles.

13.2.1 Choanal Atresia

Choanal atresia (Fig. 13.3) results from persistence of the primitive oronasal membrane that separates the nasal cavity from the oral cavity, either unilaterally or bilaterally. When choanal atresia is bilateral, it is symptomatic at birth. In the absence of symptoms, choanal atresia is suspected when the pediatrician is unable to pass a nasogastric tube. The atresia may be osseous, membranous, or osteomembranous and is best evaluated by CT. The most common finding on imaging is thickening of the vomer. It is important to obtain axial images of the nasal cavity in a plane parallel to the hard palate; if this is not done, the posterior choanae may appear artifactually narrowed. It is also important to suction secretions from the nasal cavity prior to imaging in order to be able to assess the cause of atresia

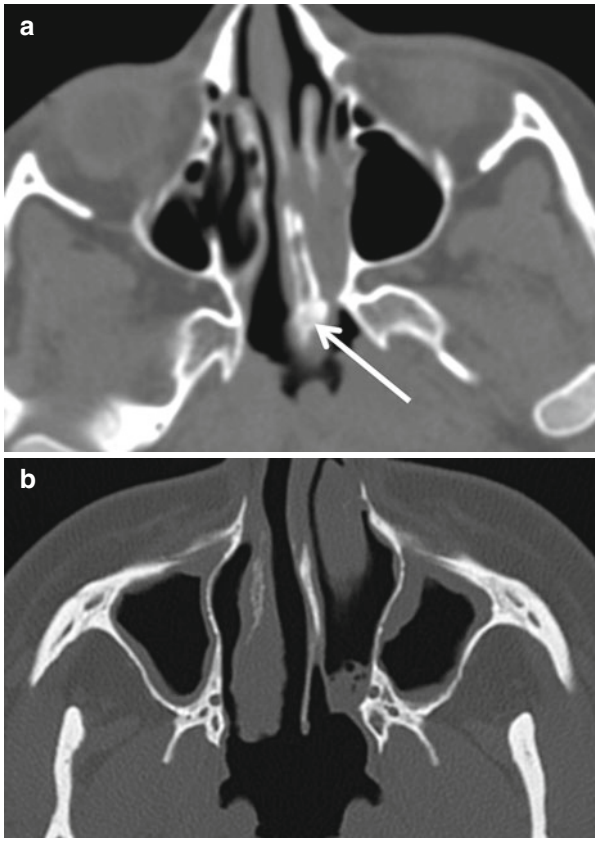

Fig. 13.3 Choanal atresia. (**a**) Osteomembranous atresia. Note the thickened vomer (*arrow*). (**b**) Membranous atresia

accurately. The orbits and temporal bones should be evaluated for coexisting anomalies that may indicate the CHARGE association (coloboma of the eye, heart defects, atresia of the choanae, retardation of growth and/or development, genital and/or urinary abnormalities, and ear abnormalities/deafness). Imaging features of the CHARGE association are discussed in the chapter on the temporal bone and skull base.

13.2.2 Congenital Piriform Aperture Stenosis

Piriform aperture stenosis (Fig. 13.4) arises from abnormal development of the medial nasal eminences which results in failure of formation of the primary palate. The piriform aperture of the nasal cavity is therefore stenotic and the palate is

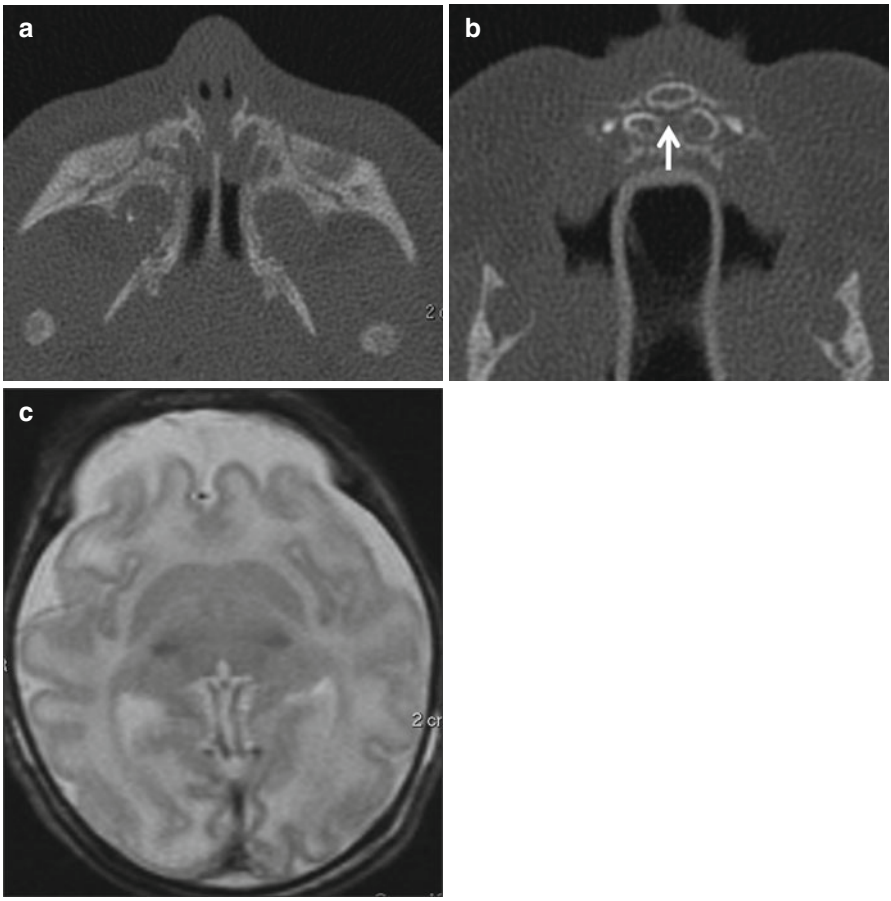

Fig. 13.4 Congenital piriform aperture stenosis. (**a**) The nasal processes of the maxillae approximate each other closely to narrow the piriform aperture. CPAS is considered to be present if the width of each PA is less than 3 mm or if the total width is less than 8 mm. The presence of a single unerupted maxillary megaincisor (**b**) should prompt evaluation for intracranial anomalies (holoprosencephaly – note the forebrain fusion in (**c**) (Images courtesy of C. Douglas Phillips, MD)

narrow. It may be recognized clinically by a complete inability to pass a nasal catheter. This abnormality may be associated with fusion of the central maxillary incisors, forming a single central or mega incisor. Midline abnormalities of the brain including corpus callosal agenesis and holoprosencephaly may coexist. The stenotic piriform aperture is best evaluated with CT; it is useful to obtain an MRI to evaluate for coexisting brain abnormalities.

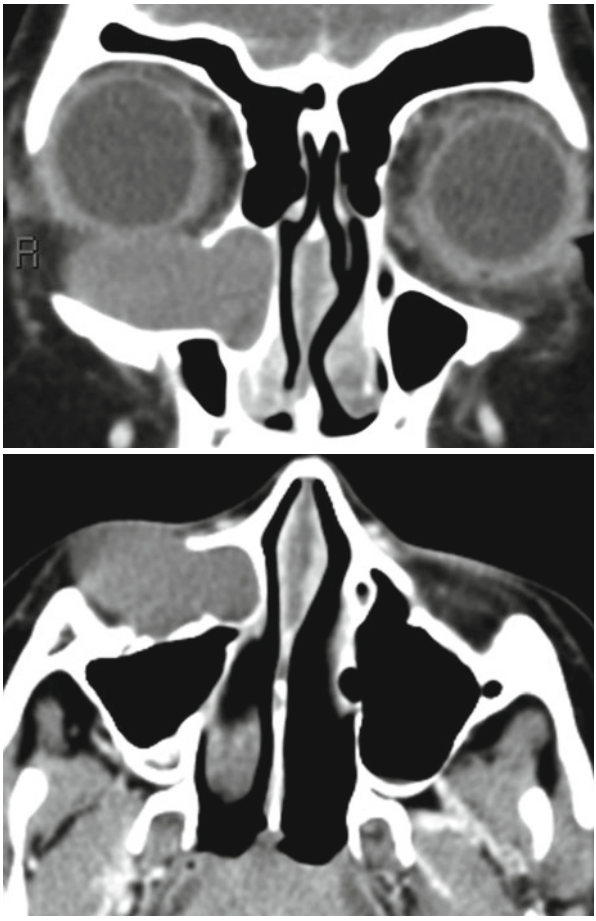

Fig. 13.5 Dacryocystocele. Dacryocystoceles may be unilateral or bilateral, with the latter tending to present at birth with respiratory distress. Unilateral lesions may go undetected until later in childhood. A smoothly expansile lesion, conforming to the course of the nasolacrimal duct is the typical appearance of a dacryocystocele (Images courtesy of C. Douglas Phillips, MD)

13.2.3 Nasolacrimal Duct Mucoceles

These mucoceles (Fig. 13.5) result from obstruction of the nasolacrimal duct by an imperforate valve of Hasner, a membrane that guards the inferior opening of the nasolacrimal duct. Normally, perforation of the valve of Hasner occurs immediately after birth due to increase in pressure within the lacrimal system when the infant cries. If perforation does not occur, a mucocele results. The process may be bilateral, and when the mucoceles are large enough, they may encroach upon the nasal cavity to produce respiratory distress. The lacrimal sac may also be dilated, especially if the valve of Rosenmuller, a membrane that is normally present at the junction of the common lacrimal canaliculus and the sac, is also imperforate. These are best evaluated by unenhanced CT. The most important differential diagnoses for an

intranasal mass in a neonate are encephaloceles, dermoids, teratomas, and hemangiomas. The characteristic low density of the mucocele and its location along the course of the nasolacrimal duct are usually diagnostic.

13.2.4 Midline Nasal Anomalies

Box 13.2 summarizes the embryological mechanisms that underlie the four types of midline nasal anomalies (Figs. 13.6, 13.7, and 13.8) and their typical imaging features. Each of these may present as a sinus or as a midline mass. An encephalocele is likely when the mass increases in size with crying. A firm mass may be a nasal heterotopia or a dermoid. Nasal glial heterotopias (also called nasal gliomas) are nonneoplastic disorganized rests of brain tissue that present as firm midline nasal masses and are best investigated with a combination of CT and MRI. The most important determination is if there is communication with the cranial cavity. With larger encephaloceles, this is usually not problematic and the herniation of meninges, CSF, and brain tissue through the midline frontonasal defect is usually obvious on MRI. Intracranial extension may not be as obvious in the case of dermal sinuses, nasal gliomas, and dermoid/epidermoid cysts. The presence of a widened foramen cecum or of a bifid crista galli is indicative of intracranial extension.

Box 13.2. Midline Nasal Anomalies

Anomaly	Embryological defect	Key imaging findings
Nasal dermal sinus	Patent dural diverticulum, failure of closure of frontonasal fonticulus	Evaluate for intracranial extension which is best indicated by widened foramen cecum or bifid crista galli
Dermoid/epidermoid	Incorporation of ectodermal elements into the diverticulum as it retracts	Well-defined mass with low density on CT and high T1 signal on MRI due to fat; epidermoid cysts are hyperintense on diffusion-weighted imaging
Nasal glial heterotopia	Sequestration of neural elements within the dural diverticulum	Well-defined mass, extranasal or intranasal, usually without direct intracranial extension; variable intensity on T1, hyperintense on T2
Encephalocele	Herniation of intracranial contents through patent dural diverticulum	May contain any combination of CSF, meninges, and brain tissue; contiguity with intracranial subarachnoid space usually apparent

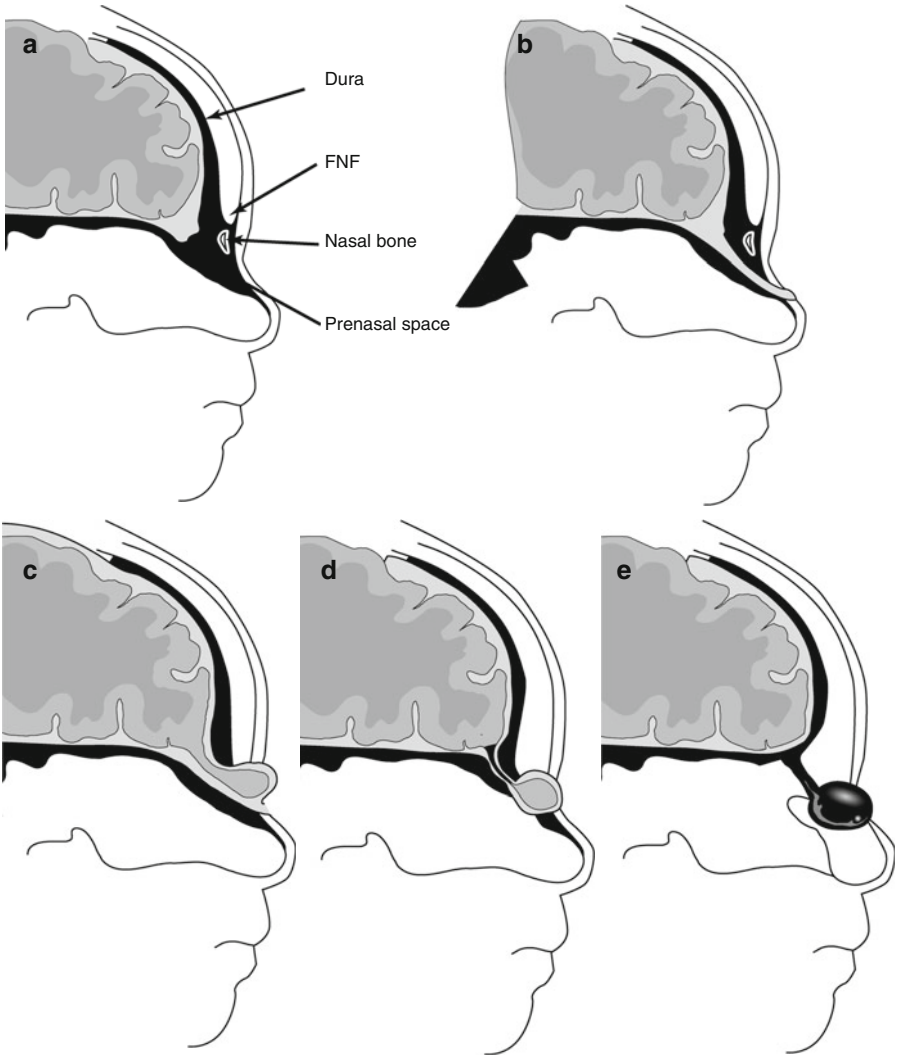

Fig. 13.6 Midline nasal anomalies. (**a**) Normal development. *FNF* fonticulus nasofrontalis – a transient opening that closes during normal development. *FC* foramen cecum. (**b**) Nasal dermal sinus. (**c**) Encephalocele. (**d**) Nasal cerebral heterotopia (nasal glioma). (**e**) Dermoid cyst. Modified from Lowe et al. (2000)

13.3 Branchial Cleft Cysts, Sinuses, and Fistulae

A branchial cleft anomaly may present as a draining sinus or fistula or as a cystic neck mass. First branchial sinuses and cysts (Fig. 13.9) are located adjacent to the angle of the mandible. Second, third, and fourth branchial sinuses and cysts are usually encountered along the anterior margin of the sternocleidomastoid (SCM) muscle in the middle third of the neck.

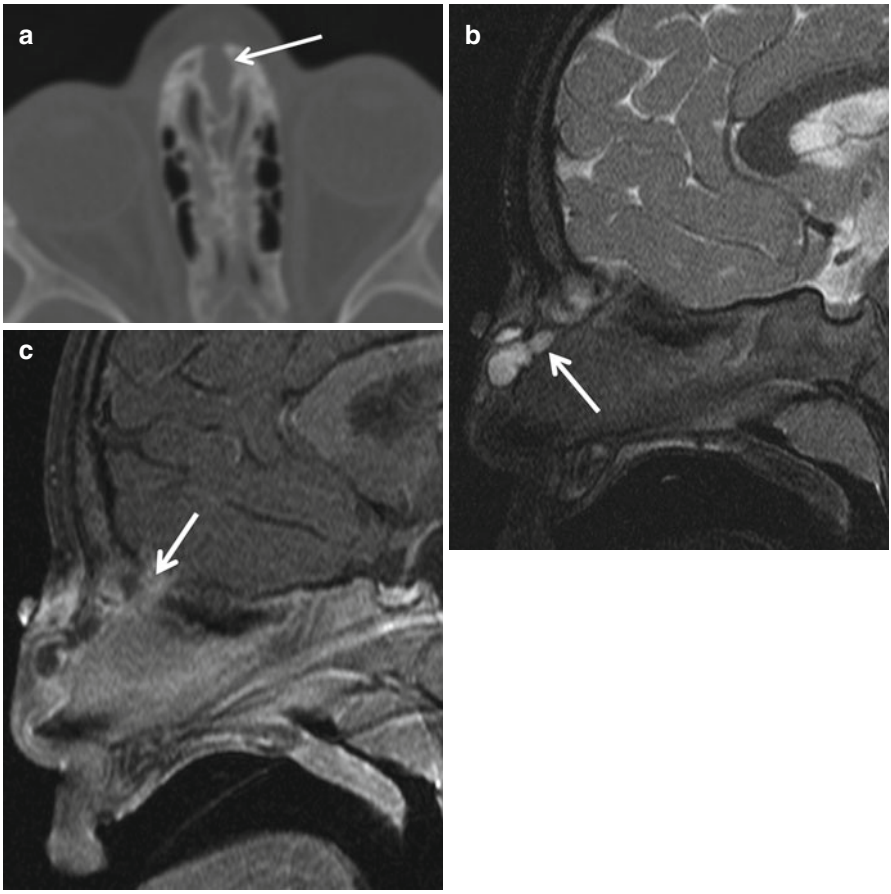

Fig. 13.7 Infected nasal dermal sinus with dermoid. The sinus tract (*arrow*) at surgery was found to extend between the nasal bones and split the crista galli (**a**). Also, a lobulated dermoid cyst, as demonstrated on the sagittal T2 (**b**) and contrast-enhanced T1 (**c**), was found. In (**c**), the intracranial extent of the sinus tract is evident. The enhancement along the sinus tract was due to infection. Dermoid and epidermoid cysts can coexist with dermal sinuses (Images courtesy of C. Douglas Phillips, MD)

The external opening of the first branchial cleft sinus/fistula is usually adjacent to the angle of the mandible although it may occur anywhere from the angle to the external auditory canal (EAC). The internal opening is typically encountered in the floor of the EAC. The sinus tract can be intimately related to the facial nerve within the parotid gland. The relationship with the facial nerve is variable. The tract may lie superficial or deep to it or be entwined with the smaller branches of the nerve. First branchial cysts may be also found in close proximity to the EAC or within the parotid gland.

A type 1 first branchial cyst/sinus lies in proximity to the pinna and may be considered to embryologically represent a duplication of the membranous EAC. Type 1 anomalies lie lateral to the facial nerve. A type 2 first branchial sinus/cyst

Fig. 13.8 Nasal cerebral heterotopia (nasal glioma). These are heterotopic disorganized dysplastic rests of brain tissue that may be extranasal, intranasal, or both. They present as firm sessile masses that do not change in size when the infant cries. They are isointense to gray matter on T1WI (**a**, **c**), are hyperintense on T2WI (**b**), and may sometimes enhance (**d**), as in this case (Images courtesy of C. Douglas Phillips, MD)

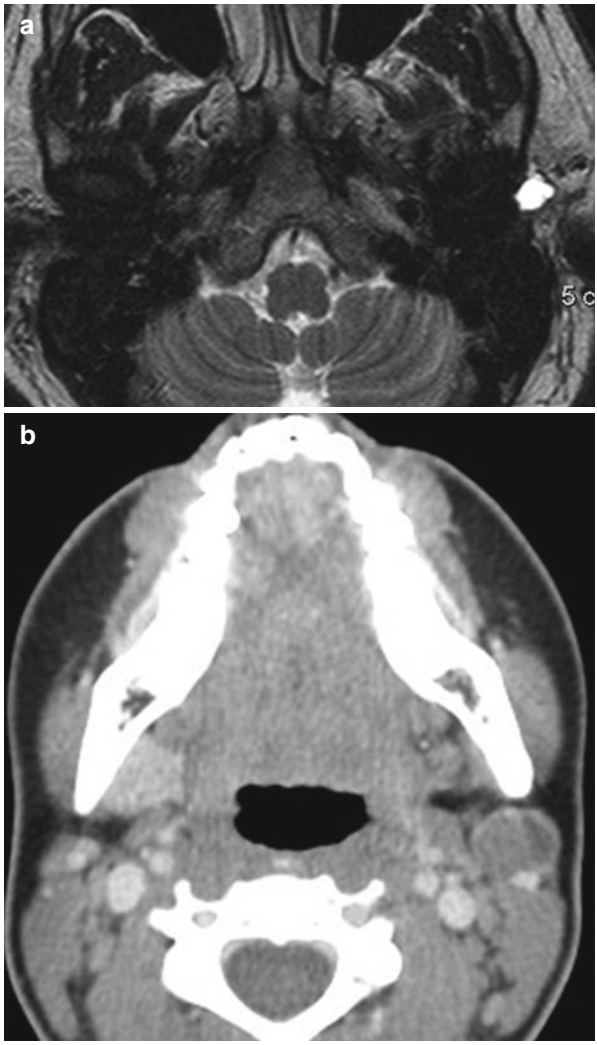

Fig. 13.9 First branchial cleft cyst. (**a**) A Work type 1 cyst in the parotid gland, (**b**) a Work type 2 cyst adjacent to the angle of the mandible

lies adjacent to the angle of the mandible and may lie external or internal to the facial nerve.

The fistulous tract of a second branchial anomaly (Fig. 13.10) passes from the external opening at the anterior margin of the SCM, between the internal and external carotid arteries, and terminates in the tonsillar fossa. Second branchial cleft cysts are usually located between the SCM and the carotid sheath, deep to the submandibular gland.

Third and fourth branchial cysts (Fig. 13.11) are also found along the anterior margin of the SCM in the middle third of the neck. Both fistulae terminate in the

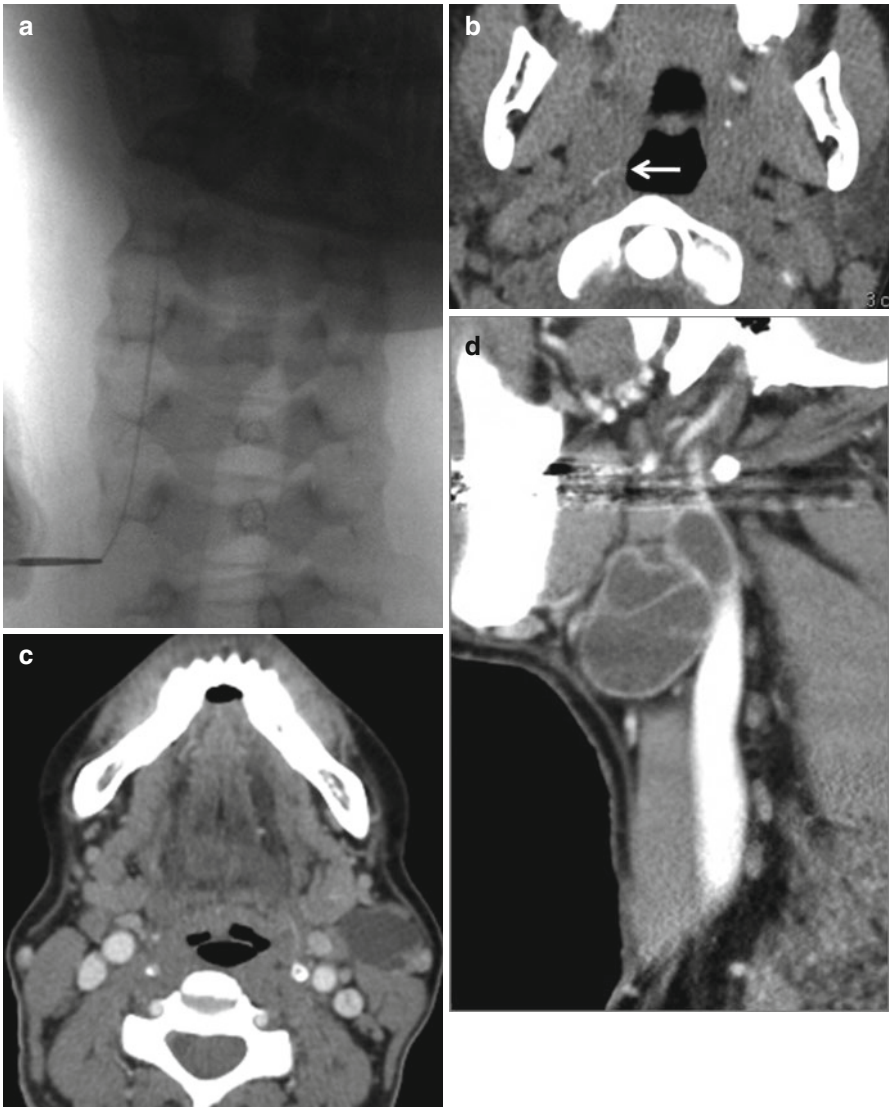

Fig. 13.10 Second branchial anomalies. The fistulogram (**a**, **b**), obtained by injecting dilute contrast medium into the external neck opening through a Rabinov catheter, shows the fistulous tact terminating in the tonsillar fossa (*arrow*, **b**). (**c**) Typical second branchial cyst located anteromedial to the sternomastoid and external to the submandibular gland. (**d**) Shows a multilocular cystic lesion adjacent to the mandibular angle. This lesion in this middle-aged patient was a metastatic lymph node and not a branchial cyst

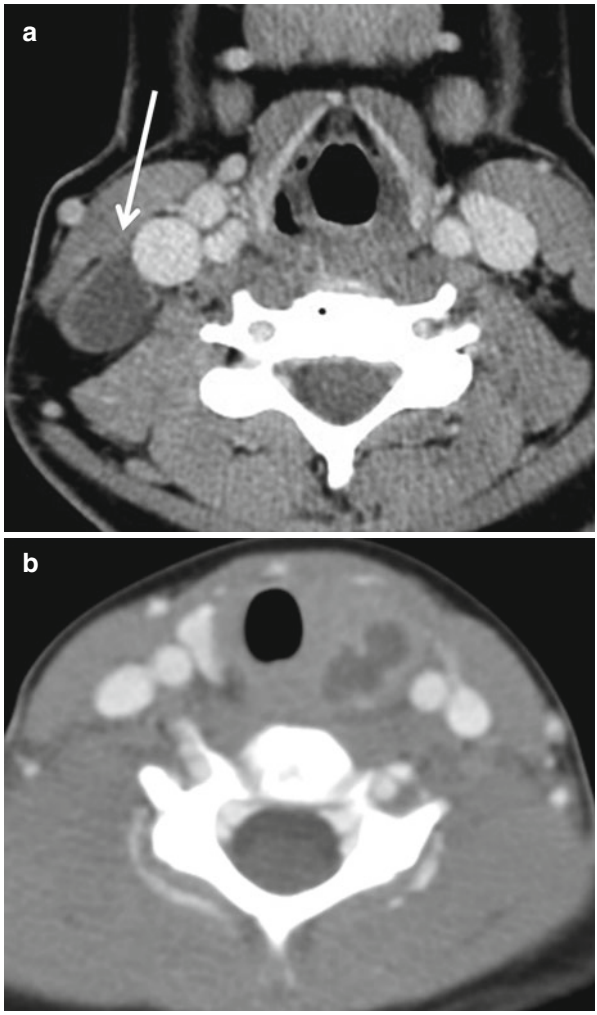

Fig. 13.11 Third (**a**) and fourth (**b**) branchial anomalies. Third branchial cysts are indistinguishable from second branchial cysts but tend to occur lower in the neck (*arrow*). In (**b**), infection along a fourth branchial sinus tract has resulted in a thyroid abscess. Sometimes edema in the ipsilateral (usually left) piriform sinus may be present and is a clue to the presence of the underlying sinus tract

piriform sinus: the third at the base and the fourth at the apex. The proximity of third and fourth branchial cleft abnormalities to the thyroid gland may result in thyroiditis when these are infected. Recurrent thyroiditis in a child must always raise suspicion for a third or fourth branchial anomaly.

The course of the four types of branchial cleft sinuses/fistulae is summarized in Box 13.3.

Box 13.3. Courses of Branchial Sinuses/Fistulae

Branchial anomaly	External opening	Sinus tract course	Internal opening
I	Angle of mandible or preauricular region	May be superficial or deep to facial nerve	Floor of the EAC
II	Anterior border of SCM	Tract passes between the carotids	Tonsillar fossa
III	Anterior border of SCM	Tract passes posterior to the carotid sheath, pierces the thyrohyoid membrane	Base of the piriform sinus
IV	Anterior border of SCM	Tract follows course of the recurrent laryngeal nerve – on the right side, it loops under the right subclavian artery; on the left, it passes under the arch of the aorta before ascending into the tracheoesophageal groove	Apex of the piriform sinus

Branchial sinuses and fistulae are best evaluated with a CT fistulogram (Fig. 13.10).

This procedure involves injection of small amount of dilute water-soluble contrast medium into the sinus orifice under fluoroscopic guidance. It is best not to perform this procedure when active infection is present. After a sufficient amount contrast is injected (usually about 1 cc), CT images are obtained. MR fistulography, performed with fat-suppressed heavily T2-weighted sequences, is an alternative. While no injection of contrast is necessary, the spatial resolution may not be sufficient to map the entirety of the tract adequately.

Branchial cysts are best evaluated with contrast-enhanced CT. Uninfected cysts are unilocular and demonstrate no mural enhancement, nodularity, or septations. When any of these features are present, especially in an adult patient, the diagnosis of branchial cyst must be seriously reconsidered. Metastatic cervical lymphadenopathy from HPV-associated oropharyngeal squamous cell carcinoma can closely mimic branchial cysts, and initial presentation of a branchial cyst in adulthood is rare. It is not infrequent for metastatic lymph nodes to be misdiagnosed as branchial cysts and for appropriate treatment to be delayed. Therefore, a cystic neck lesion with septations, nodularity, and enhancement in an adult must be assumed to represent a metastatic necrotic lymph node until proven otherwise (Fig. 13.11).

A thymic cyst is a closely related abnormality thought to arise from incomplete regression of the thymopharyngeal duct, which is a third branchial pouch derivative. The typical thymic cyst is an elongated, unilocular, low-density structure that straddles the thoracic inlet (Fig. 13.12).

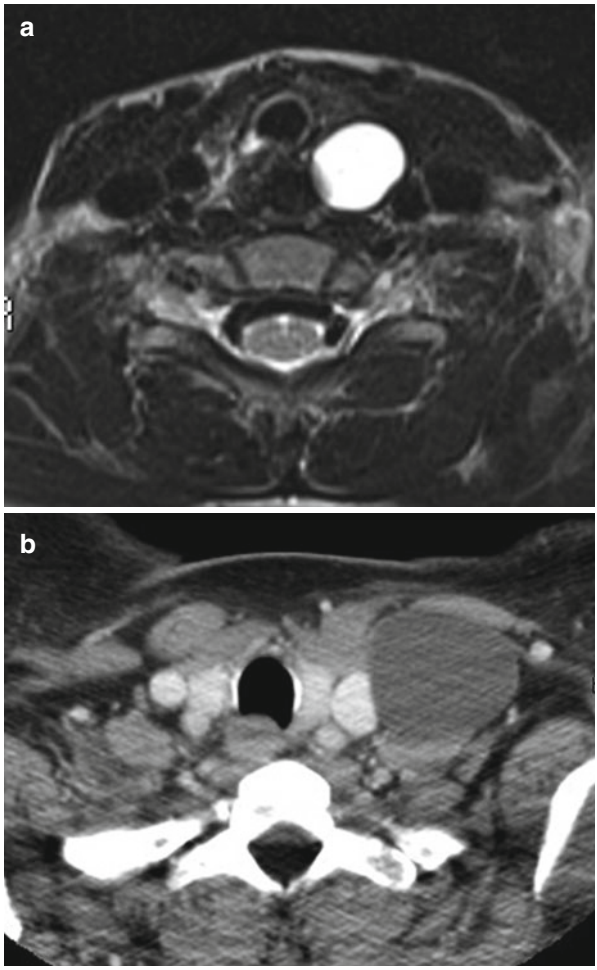

Fig. 13.12 Typical thymic cysts. Thymic cysts are usually left-sided unilocular lesions that straddle the thoracic inlet

13.4 Congenital Skull Base Anomalies

13.4.1 Arrested Pneumatization

This is an asymptomatic variant of the sphenoid sinus, occasionally mistaken for pathology. The sphenoid sinus normally undergoes fatty marrow replacement prior to pneumatization. Incomplete pneumatization results in residual foci of fatty marrow that are easily recognized by their low density on CT and high signal intensity on T1-weighted MRI (Fig. 13.13).

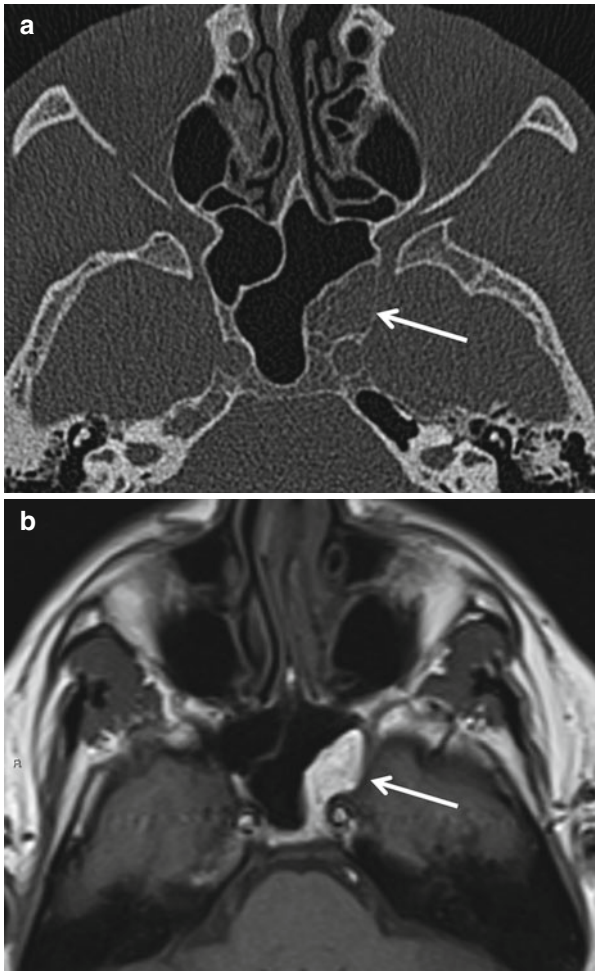

Fig. 13.13 Arrested pneumatization. This is a developmental variation usually encountered in the central skull base, often misdiagnosed as pathology. The fat contained within it (easily identified on T1W MRI) is characteristic of this process. The fat is also detectable on CT with narrow window settings

13.4.2 Encephalocele

Skull base encephaloceles are broadly classified into two types: median (transsphenoidal, sphenoethmoidal, and transethmoidal) and lateral (transalar, sphenoorbital, and sphenomaxillary). These may present with nasal obstruction, CSF rhinorrhea, or recurrent meningitis. There are two theories regarding the origin of these encephaloceles. One holds that they occur due to persistence of embryonic canals such as the pharyngohypophyseal and lateral craniopharyngeal (Sternberg) canals. Another theory, perhaps more plausible, holds that they occur due to herniation of intracranial contents between embryonic ossification centers. Acquired transalar encephaloceles may also arise from gradual rarefaction of bone by arachnoid granulations, possibly due to chronically raised intracranial pressure. Encephaloceles

are best evaluated with a combination of CT and MRI (Fig. 13.14). CT is useful in the demonstration of the osseous defect, while MRI enables evaluation of their contents. Any combination of CSF and brain tissue may be present within them. Although herniated brain tissue is usually isointense to brain parenchyma, it may also appear heterogeneous due to gliosis and encephalomalacia. Rarely, the contents of an encephalocele may enhance.

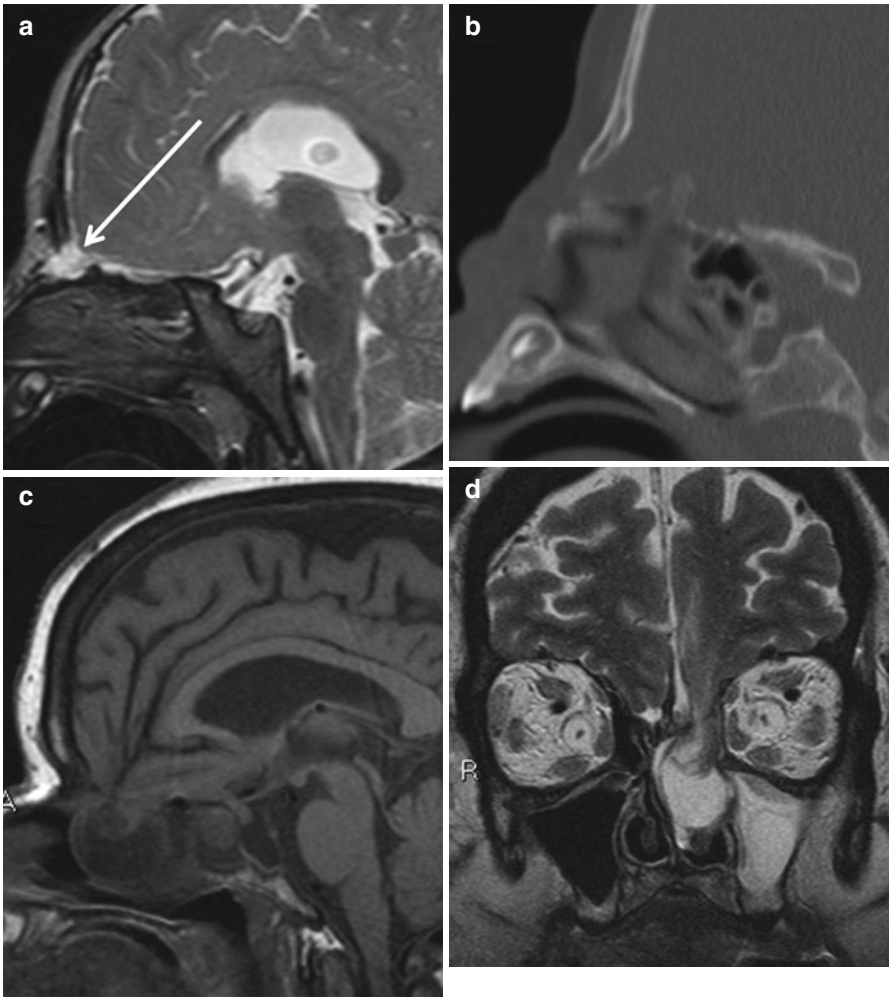

Fig. 13.14 Encephaloceles. (**a**, **b**) Small frontonasal meningocele (*arrow*) in a child presenting with a nasal root mass that increased in size with crying. (**c**, **d**) Sphenoethmoidal encephalocele containing CSF and gliotic brain tissue in an adult. (**e**, **f**) Massive sincipital encephalocele containing hemorrhagic brain tissue (dark areas on the susceptibility-weighted image, **f**). The contents of encephaloceles can be very variable and so therefore can their signal intensities on MRI. It is important to remember that they can present later in life. Indeed, the first question that comes to the surgeon's mind when determining if a nasal mass needs a biopsy is "Am I dealing with an encephalocele?"

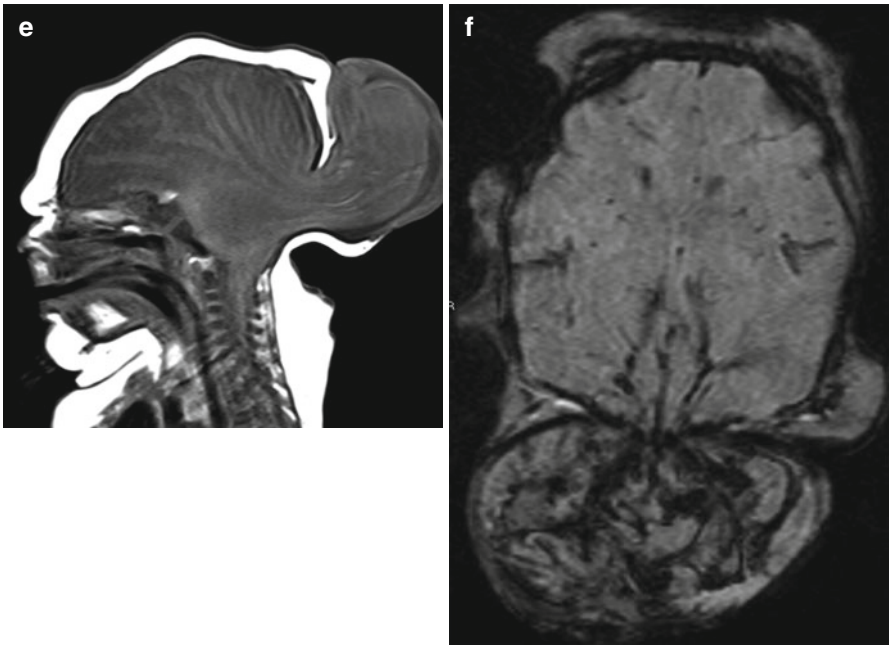

Fig. 13.14 (continued)

13.5 Hemangiomas and Vascular Malformations

The terminology used to describe pediatric head and neck vascular lesions can be confusing. It is important to realize that hemangiomas are true neoplasms, whereas vascular malformations (VMs) are hamartomas. Hemangiomas are present at birth, grow rapidly in the first few months of life, and then tend to involute spontaneously. VMs, on the other hand, grow proportionately with the patient and do not involute. VMs are subclassified into venous, lymphatic, capillary, arteriovenous, and mixed malformations.

13.5.1 Hemangiomas

Hemangiomas (Fig. 13.15) can be broadly divided into two types: infantile and congenital. Infantile hemangiomas are the most common head and neck tumor of childhood, can occur anywhere in the head and neck, and can involve both superficial and deep soft tissues. They can be solitary or multiple. Most hemangiomas of infancy are not obviously visible at birth, but present within the first several weeks of life. These often demonstrate a period of rapid growth followed by quiescence and involution.

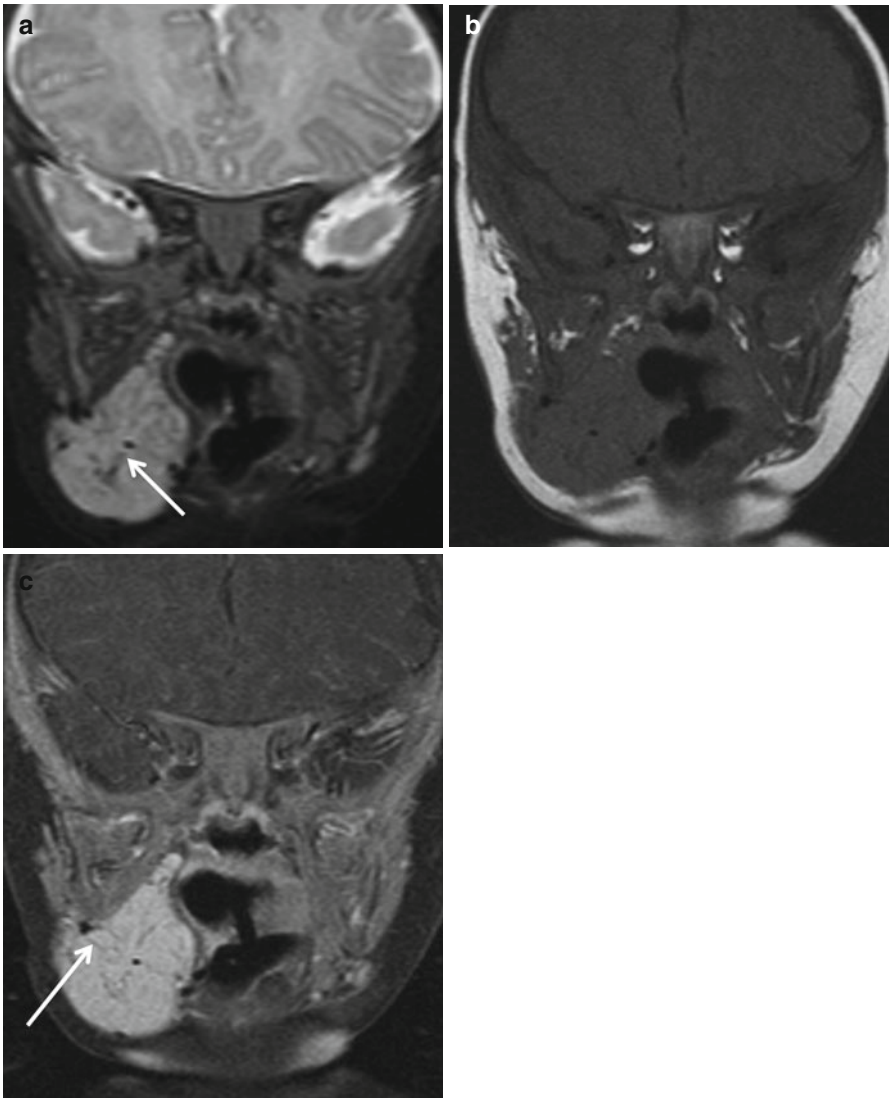

Fig. 13.15 Well defined mass centered in the right parapharyngeal space. The high T2 signal (**a**), flow voids (*arrows*), and intense enhancement (**c**) are typical of a hemangioma

Unlike infantile hemangiomas, congenital hemangiomas complete their proliferative phase before birth. Two distinct forms have been described with the acronyms, the rapidly involuting congenital hemangioma (RICH) and the noninvoluting congenital hemangioma (NICH), based on their clinical behavior.

A combination of ultrasound and MRI is typically used to confirm the clinical diagnosis and assess tumor extent. Ultrasound alone may suffice in cases where the lesion is superficial. MRI is frequently performed to assess the extent of deeper

lesions. On MRI, hemangiomas appear as discrete, lobulated, T2-hyperintense lesions with intense enhancement. On ultrasound, they demonstrate a well-marginated, mixed echogenic appearance, with low-velocity flow on color Doppler.

13.5.2 Vascular Malformations

It is also useful from a therapeutic point of view, to classify vascular malformations based on the presence of arteriovenous shunting; they are thus classified as high flow (arteriovenous malformations) or low flow (venous, lymphatic, and capillary malformations). Treatment of high-flow lesions may require catheter angiography and embolization of arterial feeders, whereas low-flow lesions may be addressed with direct puncture embolization and sclerotherapy or surgical resection.

13.5.3 Venous Vascular Malformations

Venous vascular malformations (VVMs), also referred to as cavernous hemangiomas (Fig. 13.16), are the most common vascular malformation in the head and neck. Although they can be well defined, most are infiltrative in nature and cross fascial and spatial boundaries.

On ultrasound they appear as infiltrative, poorly defined, compressible hypoechoic lesions, with low-velocity flow on Doppler. On CT, VVMs appear as

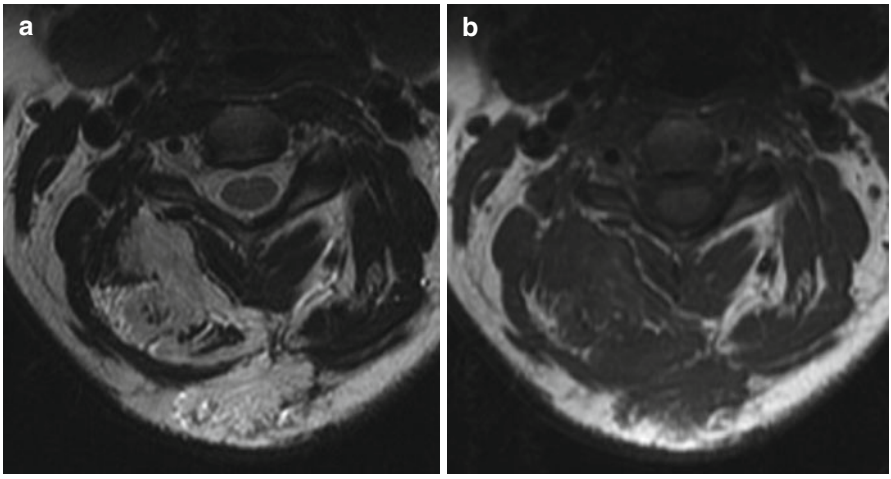

Fig. 13.16 Venous vascular malformation. These are poorly defined trans-spatial lesions (**a**, **b**) that enhance variably with contrast. The presence of phleboliths (**d**) is a typical finding. (**e, f**) are fluoroscopic images obtained during and after percutaneous injection of the sclerosant 3 % sodium tetradecyl sulfate. Note that the lesion has been nearly obliterated in (**f**)

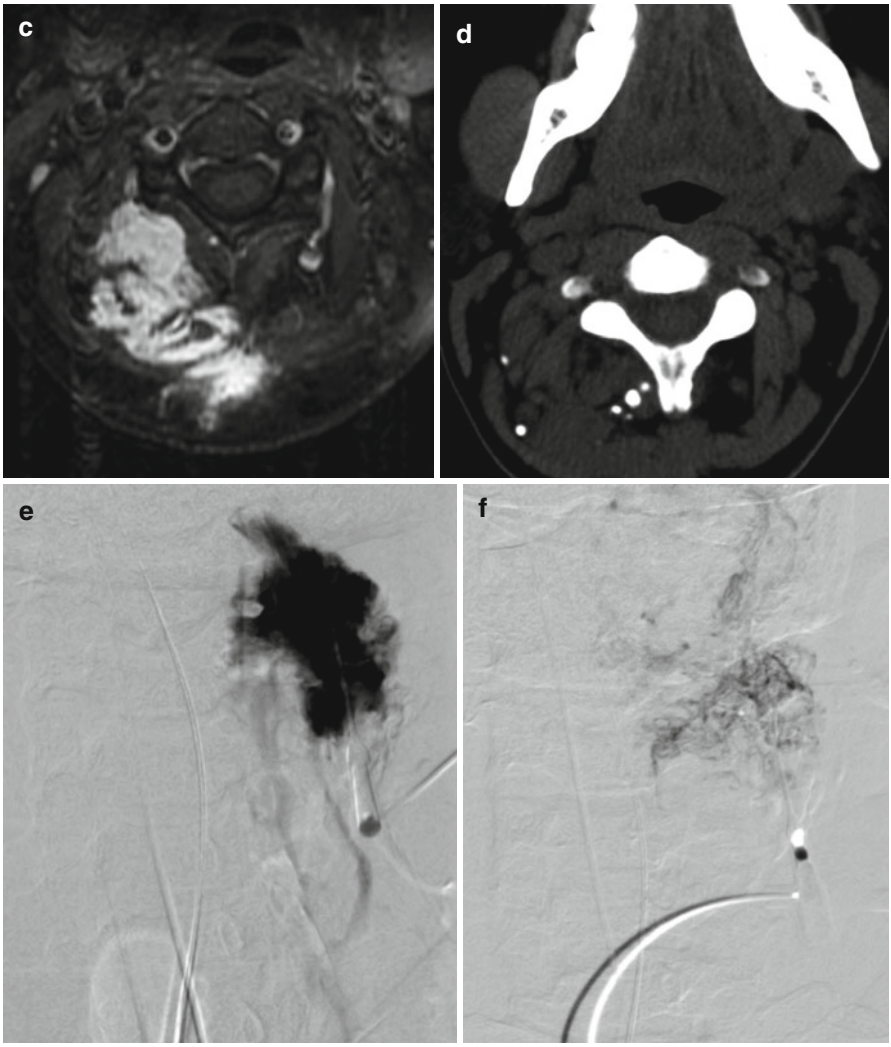

Fig. 13.16 (continued)

lobulated enhancing lesions containing phleboliths that may remodel adjacent bone. Prominent arterial feeders and draining veins are not present. On MRI, an infiltrative contour, transgression of spatial boundaries, and variable heterogeneous enhancement are typical features. When a significant lymphatic component is present, T2-hyperintense cystic foci may be evident, sometimes containing fluid levels from past hemorrhage. Flow voids are typically absent. Phleboliths, which may be evident as discrete areas of signal void, should not be confused for true flow voids.

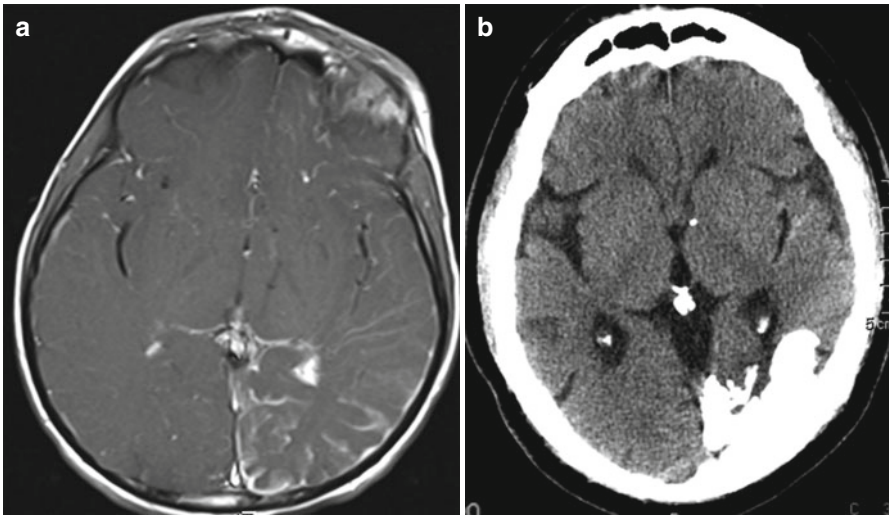

Fig. 13.17 Sturge-Weber syndrome. Capillary hemangiomas manifest as areas of skin discoloration and are usually not imaged. However, when they occur in the distribution of the trigeminal nerve, they may be associated with epilepsy caused by an intracranial pial venous angioma (**a**) and focal parenchymal atrophy and calcification (**b**)

13.5.4 Capillary Malformations

Capillary malformations (nevus flammeus, port-wine stains) are superficial lesions that do not require imaging. However, a patient with such a lesion in the distribution of the trigeminal nerve must be evaluated with MRI for Sturge-Weber syndrome, characterized by epilepsy, ipsilateral cerebral leptomeningeal angiomatosis, "tram track" gyral calcifications on CT, and cerebral hemiatrophy (Fig. 13.17).

13.5.5 Arterial Malformations

These high-flow lesions include arteriovenous malformations (AVMs) (Fig. 13.18) and arteriovenous fistulae (AVF). Histologically, there is a direct connection between feeding arteries and draining veins without a normal intervening capillary network. In fistulae, no nidus of abnormal vasculature is present and the arterial feeders communicate directly with the venous circulation. On ultrasound and Doppler imaging, they present as a loosely defined tangle of blood vessels with rapid flow. MR and CT may be used to assess extent. These malformations often require evaluation with catheter angiography.

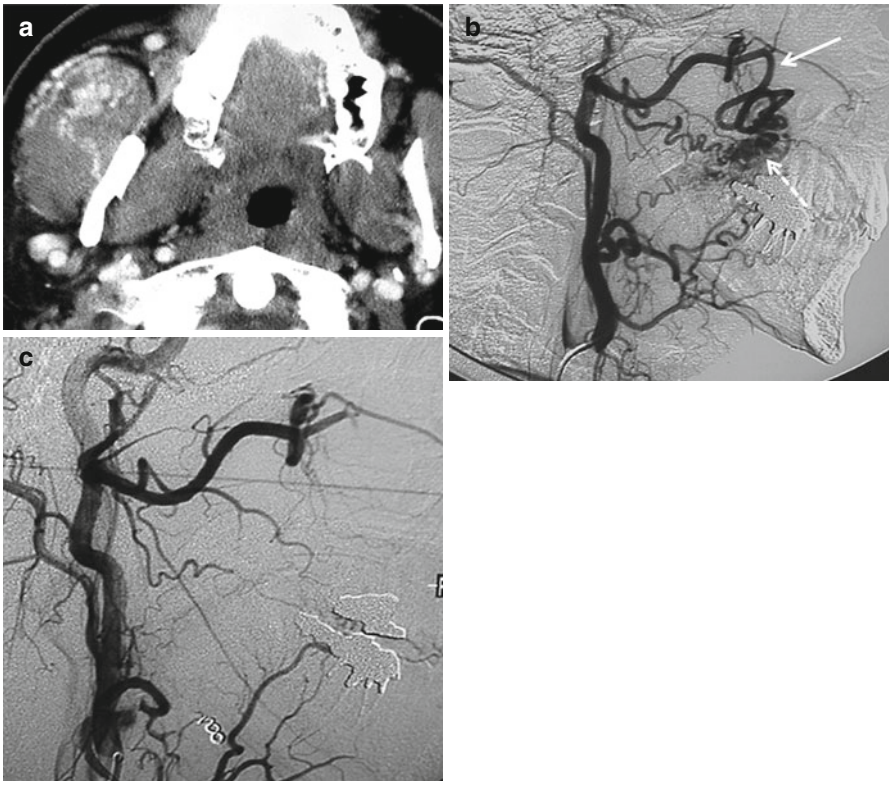

Fig. 13.18 Arteriovenous malformation of the masticator space. (**a**) Depicts tortuous vascular structures in the enlarged right masseter. This is a high-flow lesion as evidenced by the presence of arteriovenous shunting (note the enlarged internal maxillary artery (*arrow*) and the early draining veins (*dashed arrow* in **b**). The post embolization angiogram (**c**) shows that the lesion has effectively been obliterated

13.5.6 Lymphatic Malformations

Lymphatic malformations (LMs) (Fig. 13.19), also referred to as cystic hygromas or lymphangiomas, are most commonly seen in the posterior cervical triangle. Their appearance on imaging depends upon whether they are microcystic or macrocystic in nature and also upon the proportion of a coexisting venous component. On ultrasound, macrocystic lesions are comprised of one or more discrete hypoechoic foci, whereas the microcystic lymphangiomas appear hyperechoic because of the close apposition of small cysts. Uncomplicated LMs demonstrate low density on CT and high T2 signal on MRI and do not enhance significantly. Fluid levels due

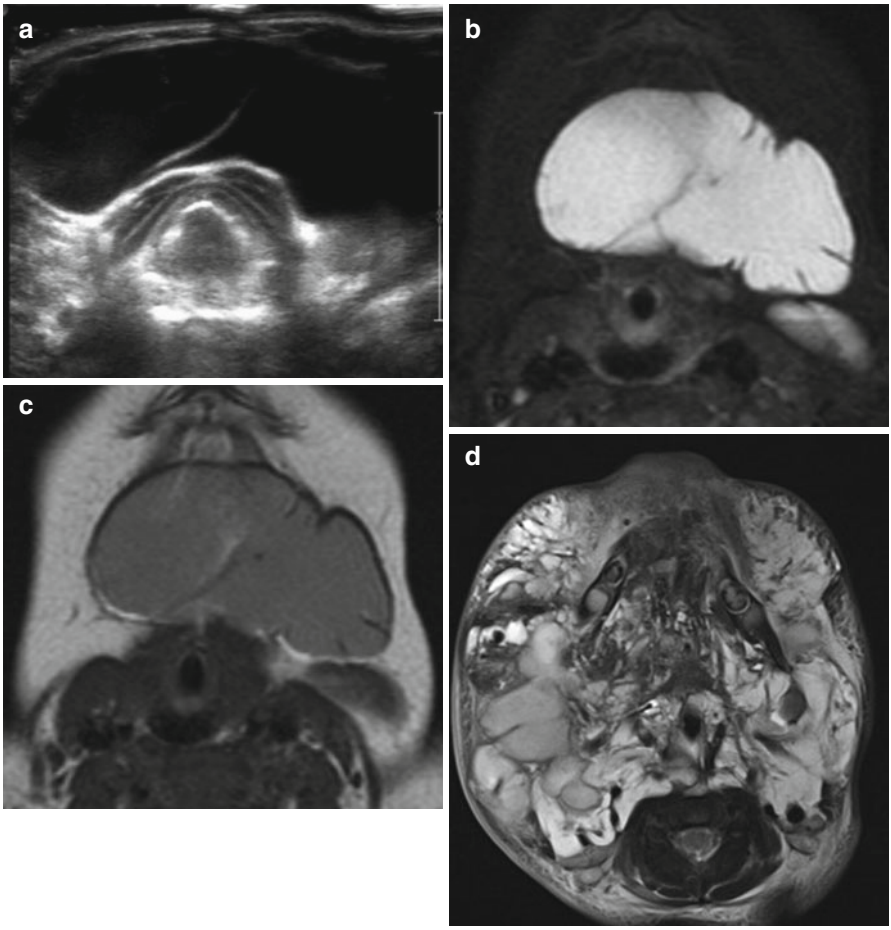

Fig. 13.19 Lymphatic malformations. (**a**–**c**) Depict a large macrocystic submandibular space lymphatic malformation. The large cystic spaces are evident on the ultrasound image (**a**). In (**b**), a T2W MR image, a fluid level, indicated past hemorrhage is present. In (**c**), a T1W image, note that the cyst fluid is of high signal intensity, also likely due to past hemorrhage. The cyst in lymphatic malformations can vary greatly in size. These lesions can also be very infiltrative and transgress spatial boundaries to the extent that complete surgical extirpation can be impossible, as in the example in (**d**)

to hemorrhage and areas of solid enhancement may indicate an associated venous component. Enhancement of the walls and septa may be seen when they are infected. Like VVMs, LMs can be extremely infiltrative in nature. Unilocular lymphangiomas can be mistaken for branchial cysts, thymic cysts, and ranulas.

The imaging features and treatment options for hemangiomas and vascular malformations are summarized in Box 13.4.

Box 13.4. Vascular Anomalies: Imaging Findings and Treatment

Vascular anomaly	Imaging findings	Management
Hemangioma	MR/CT: lobulated, well demarcated, T2 hyperintense, intense enhancement US: mixed echogenicity with low flow on Doppler DSA: intense, persistent stain, enlarged feeding vessels. A-V shunting may be present	Systemic ± intralesional steroids, particle embolization alone or embolization with surgery
Venous malformation	MR/CT: multiloculated, infiltrative, phleboliths (pathognomic), T2 hyperintense with delayed enhancement, no flow voids US: ill-defined variably echogenic lesions with phleboliths; low-flow monophasic pattern on Doppler without an arterial waveform DSA: no A-V shunting or stain; multiloculated pouches that fill with contrast in direct puncture	Percutaneous sclerotherapy with sodium tetradecyl sulfate, ethanol, with surgical excision in selected cases
Lymphatic malformation	CT/MR: uni- or multilocular cystic lesions, may be well defined or very infiltrative; enhancement and hemorrhage with fluid levels may indicate associated venous component; enhancement and thickening of septa when infected US: multiple hypoechoic cysts; may be echogenic when predominantly microcystic; insignificant flow on color Doppler DSA: avascular on angiography. Cysts fill with contrast on direct puncture	Usually surgical excision or direct puncture sclerotherapy
Arteriovenous malformations and fistulae	MR/CT: enhancing lesion with flow voids. (MR) Prominent feeding arteries and draining veins US: biphasic Doppler waveforms suggestive of shunting DSA: high-flow lesions with rapid A-V shunting; AVF shows no nidus, while AVMs have a nidus of multiple small fistulae	Fistulae: embolization at point of fistulization with balloons and coils for larger lesions and liquid adhesive (n-butyl cyanoacrylate) for smaller lesions AVM: rarely cured by embolization alone. Role of endovascular treatment usually to aid surgery

13.6 The Surgeon's Perspective

13.6.1 Choanal Atresia

Because newborns are obligate nasal breathers, bilateral choanal atresia often presents with respiratory distress or cyanosis during feeding. Unilateral choanal atresia may be asymptomatic and only identified with inability to pass a suction catheter to the nasopharynx. For newborns with choanal atresia, CT is the imaging modality of choice. In order to confirm the extent of the atresia (unilateral vs. bilateral) and to determine the type and thickness of obstructive tissue (membrane vs. soft tissue vs. bone), the CT should be performed after careful suctioning of the nasal cavity to clear secretions. Some protocols use a decongestant to further improve the CT evaluation. Choanal atresia is usually repaired via an endoscopic transnasal approach, which results in low recurrence rate and few complications.

13.6.2 Congenital Nasal Malformations

Congenital nasal malformations are best evaluated by a combination of CT and MRI. Biopsy of a congenital nasal mass should be avoided until imaging has been obtained. Often the diagnosis can be made with imaging alone. The treatment of nasal dermoids and gliomas involves surgery to completely remove the tumor and any associated sinus tract. If these extend intracranially, a more extensive craniofacial approach may be required in conjunction with a neurosurgical specialist. For encephaloceles, repair of the bony defect is usually required, which may necessitate a craniotomy.

13.6.3 Branchial Cleft Anomalies

Branchial cleft anomalies are an important diagnostic consideration in the pediatric and young adult population. Branchial cleft cysts are much more common than fistulae or sinuses. Specialized imaging modalities such as fistulograms are useful for defining the tract in fistulae and sinuses to assist with complete surgical extirpation, but are of no utility for the branchial cleft cyst. Branchial cleft cysts can be diagnosed for the first time in an adult without a prior history of a neck mass. However, this is uncommon. Thus, a mass in an adult that appears consistent with a branchial cleft cyst on imaging must be carefully evaluated for malignancy. Cystic metastatic nodes are common with HPV-related oropharyngeal squamous cell carcinoma, which often presents with a subtle primary lesion in young nonsmokers. In an adult with a newly diagnosed cystic neck mass, a thorough head and neck exam including endoscopy should be performed. If no primary lesion is noted, a careful ultrasound-guided fine-needle aspirate biopsy of the rim or any solid component of the cyst should be performed. Even when a diagnosis of cancer is absent and a decision is

made to proceed with surgical removal of the cyst, adult patients should be consented for a completion neck dissection and appropriate staging exam under anesthesia if intraoperative evaluation of the cyst by frozen section demonstrates squamous cell cancer.

13.6.4 Vascular Malformations

It is extremely important to differentiate hemangiomas from other congenital vascular malformations. Hemangiomas can be treated with observation, steroids, or beta-blockers, and parents can be assured that, while these lesions may initially grow, the expectation is complete involution over time. Other congenital vascular malformations are not expected to spontaneously resolve. Management of these lesions is by observation, embolization/sclerosis, or surgical removal. These tumors are often infiltrative and difficult to completely extirpate. Thus, they frequently recur, and careful consideration should be given to nonsurgical therapy when possible. However, when expansion is destructive (e.g., erosion of the mandible), more aggressive surgical intervention may be warranted.

Further Reading

Hudgins PA, Gillison M (2009) Second branchial cleft cyst: NOT!! Am J Neuroradiol 30(9):1628–1629

Johnson JM, Moonis G, Green GE, Carmody R, Burbank HN (2011) Syndromes of the first and second branchial arches, part 1: embryology and characteristic defects. Am J Neuroradiol 32(1):14–19

Johnson JM, Moonis G, Green GE, Carmody R, Burbank HN (2011) Syndromes of the first and second branchial arches, part 2: syndromes. Am J Neuroradiol 32(2):230–237

Lowe LH, Booth TN, Joglar JM, Rollins NK (2000) Midface anomalies in children1. Radiographics 20(4):907–922

Morón FE, Morriss MC, Jones JJ, Hunter JV (2004) Lumps and bumps on the head in children: use of CT and MR imaging in solving the clinical diagnostic Dilemma1. Radiographics 24(6):1655–1674

Index

P. Raghavan et al., *Manual of Head and Neck Imaging*,
DOI 10.1007/978-3-642-40377-4, © Springer-Verlag Berlin Heidelberg 2014